The Design of a Fast Neutron Radiography System for Non-Destructive Analysis of Thick, Dense Objects

A Dissertation Presented for the

Doctor of Philosophy

Degree

The University of Tennessee, Knoxville

Alicia Lauren Swift

May 2016

© by Alicia Lauren Swift, 2016
All Rights Reserved.

This dissertation is dedicated to the numerous people who supported me through graduate school, in particular my family and friends, as well as to all the teachers I had along the way who challenged me and taught me that, if you try hard enough, you can always find an answer to "Why?".

Acknowledgements

The author would like to thank Thomas Zocco of Los Alamos National Laboratory (LANL) and the National Nuclear Security Administration for funding this work. Many scientists at LANL have been integral in completing this work by providing advice and guidance, including Avneet Sood, Brian Temple, Douglas Mayo, and Edward McKigney of XCP-3; Richard Schirato of ISR-1; James Hunter of AET-6; Bill Myers of NEN-2; and many others. Thanks are also due for the experimental support at the Los Alamos Neutron Science Center that was provided by Ron Nelson and Nikolaos Fotiadis of P-27. Finally, I would like to thank my committee members for their invaluable input and support during my studies: Jason Hayward, Howard Hall, Lawrence Heilbronn, and Mariya Zhuravleva.

I was born not knowing and have had only a little time to change that here and there.

-Richard Feynman

All truths are easy to understand once they are discovered; the point is to discover them.

-Galileo Galilei

Abstract

This dissertation describes the development of a novel time-of-flight (TOF) fast neutron radiography system, TiGReSSE ("Time Gating to Reject Scatter and Select Energy"), for non-destructive analysis of thick, dense objects, such as a spent nuclear fuel cask. Such objects create large scatter fields that mask interior flaws in an image, and are impenetrable with traditional x-ray or low-energy neutron radiography. By using a fast pulsed, high-energy monoenergetic neutron source with TiGReSSE, TOF methods may be employed to completely reject this problematic scatter. If using TOF methods with a fast pulsed, high-energy polyenergetic neutron source instead, partial scatter rejection is possible, as is the variation of image contrast by selecting the neutron interrogation energy(ies). To accomplish scatter rejection and energy selection, the system uses a fast plastic scintillator to convert neutrons to visible light, which then enter an intensified charge coupled device camera to form a radiograph. The camera shutter is opened and closed at specific times to apply TOF methods. Experiments were conducted using a deuterium-tritium generator, as well as with polyenergetic spallation neutrons in two Los Alamos Neutron Science Center accelerator flight paths. These experiments were carried out to improve system design and determine system characteristics, while demonstrating that TiGReSSE could partially reject scatter and select energy in novel neutron energy ranges up to 600 MeV (i.e., 80% of the speed of light). It was also shown that optimal neutron radiography energies vary between objects. Simulations were also conducted using Los Alamos National Laboratory's radiation transport code, MCNP6, to further support

system design and characterization, modeling properties including detector efficiency, dose to radiography objects during imaging, and direct-to-scatter ratios. MCNP6 was also used to design an optimal shielding configuration for the camera. Based on all work conducted, it is recommended that a pulsed monoenergetic neutron source with energy from 10 to 14 MeV be used for scatter rejection, and that a spallation target be used to create a polyenergetic pulsed source to also enable energy selection, while being mindful that other objects may exist that require higher energy neutrons.

Table of Contents

1 Introduction **1**

1.1 An Overview of Radiography . . . 3

1.1.1 Photon Radiography . . . 3

1.1.2 Neutron Radiography . . . 4

1.2 Detectors for Radiography Applications . . . 7

1.2.1 Film Systems . . . 7

1.2.2 Digital Systems . . . 8

1.3 Optical Considerations for a Radiography System . . . 12

1.3.1 Spatial Resolution . . . 14

1.3.2 Time and Energy Resolution . . . 29

1.3.3 Contrast Resolution . . . 30

1.3.4 Magnification and Field of View . . . 30

1.3.5 Depth of Field and Lens Aperture Size . . . 31

1.3.6 Tomographic Reconstruction . . . 32

1.3.7 Source Intensity and Exposure Time . . . 33

1.3.8 Time-of-Flight Concepts . . . 33

1.3.9 Noise . . . 38

2 Gaps in Technology **40**

2.1 Current Work in Neutron Imaging . . . 40

2.1.1 Continuous Neutron Radiography . . . 40

2.1.2 Pulsed Neutron Radiography 41
2.2 Gaps in Technology 44

3 Novel Contributions **46**

4 Initial System Design **49**
4.1 Neutron Time-of-Flight Estimations 49
4.1.1 Overview of Neutron Time-of-Flight Analysis 49
4.1.2 MCNP6 FMESH Tally Simulations 50
4.1.3 Analytic Calculations 53
4.1.4 MCNP6 F4 Tally Simulations 56
4.1.5 Results 56
4.1.6 Discussion of MCNP6 Error 64
4.1.7 Conclusions 64
4.2 System Design 65
4.2.1 Fast Plastic Scintillator 66
4.2.2 ICCD Camera 68
4.2.3 ICCD Camera Lenses 70
4.2.4 Front Surface Mirror 70
4.2.5 Pulsed Light Source for Testing 73
4.2.6 Delay Generator for Time Gating 73
4.2.7 Other Equipment 75
4.2.8 Typical Experimental Set-up 77
4.3 First Light Measurement 77
4.4 Conclusions 80

5 Initial Neutron Radiography Testing **83**
5.1 D-T Radiography 83
5.1.1 Experimental Overview and Results 84
5.1.2 Total System Efficiency Calculations 84

5.1.3 Lessons Learned . . . 90
5.2 LANSCE Radiography . . . 90
5.2.1 Overview . . . 90
5.2.2 Experimental Set-up . . . 94
5.2.3 Radiography Objects . . . 108
5.2.4 Scatter Evaluation . . . 108
5.2.5 Time-of-Flight Scan . . . 111
5.2.6 Radiography Data . . . 115
5.2.7 Evaluation of Radiography Data . . . 132
5.2.8 Discussion of System Performance . . . 171
5.3 Conclusions . . . 180

6 System Properties **181**
6.1 Scintillator Properties . . . 181
6.1.1 Theory: Fast Neutrons and Plastic Converters . . . 181
6.1.2 MCNP6 Simulations of Detector Efficiency . . . 186
6.1.3 Simulation Results . . . 189
6.2 Limiting Contrast Resolution . . . 199
6.2.1 Overview . . . 199
6.2.2 Experimental Set-up . . . 204
6.2.3 Experimental Procedure . . . 206
6.2.4 Data Processing and Results . . . 210
6.2.5 Conclusions . . . 218

7 Shielding Studies **220**
7.1 Theory . . . 220
7.2 Simulated Case Studies . . . 222
7.2.1 Overview of Simulations . . . 222
7.2.2 Simulated Geometry . . . 223
7.2.3 Shielding Configurations . . . 227

7.2.4 Results . . . 229
7.2.5 Source of Scatter and Secondary Particles . . . 299
7.3 Conclusions . . . 308

8 System Design Considerations 310
8.1 Direct-to-Scatter Ratio . . . 310
8.1.1 Overview . . . 310
8.1.2 MCNP6 Simulations . . . 311
8.1.3 Simulated Radiograph Observations . . . 313
8.1.4 Simulated Direct-to-Scatter Ratio Results . . . 315
8.2 Dose Delivered to the Radiography Object . . . 333
8.2.1 Overview . . . 333
8.2.2 Simulation Description . . . 338
8.2.3 Results and Conclusions . . . 340

9 Additional Neutron Radiography Testing 350
9.1 Overview . . . 352
9.1.1 FP60R Beam Description . . . 352
9.1.2 Flight Path Geometry . . . 353
9.1.3 Experimental Set-up . . . 353
9.2 System Performance Evaluations . . . 373
9.3 Time-of-Flight Scan . . . 382
9.3.1 Error in TOF Calculation . . . 389
9.4 Description of Experiments . . . 393
9.4.1 Optimal Source Energy . . . 393
9.4.2 Optimal Location for Radiography Object . . . 397
9.4.3 Comparison between FP60R and FP15R . . . 399
9.4.4 Long Exposure Radiographs . . . 403
9.4.5 Depleted Uranium Radiographs . . . 403
9.5 Results and Conclusions . . . 406

9.5.1 Optimal Source Energy 411
9.5.2 Optimal Location for Radiography Object 423
9.5.3 Comparison between FP60R and FP15R 429
9.5.4 Long Exposure Radiographs 441
9.5.5 Depleted Uranium Radiographs 453
9.5.6 Material Transmission Properties 465
9.5.7 Challenge Object 473
9.5.8 Comments on Line-out Noise 485
9.5.9 Flatfield Images 487
9.6 Summary 489

10 Conclusions and Future Work **493**

Bibliography **498**

Vita **508**

List of Tables

4.1 Comparison of simulated TOF data for F4 and FMESH tallies. 60

4.2 Comparison of the TOF for analytic elastic single neutron scatter to simulated FMESH tally TOF data for Ring 1. 61

4.3 Comparison of the TOF for analytic elastic single neutron scatter to simulated FMESH tally TOF data for Ring 2. 62

4.4 Comparison of the TOF for analytic elastic single neutron scatter to simulated FMESH tally TOF data for Ring 3. 63

5.1 Variable values used in Equation 5.2 for 14 MeV neutrons incident on EJ-212 scintillator of 5 mm thickness [53, 54, 63, 64]. 87

5.2 Properties of the four Object 1 radiographs, including the particle type, particle energy, added signal delay, camera gate width, and the number of integrated pulses per frame. 118

5.3 Properties of the six Object 2 radiographs, including the particle type, particle energy, added signal delay, camera gate width, and the number of integrated pulses per frame. 125

5.4 Properties of the three Object 3 radiographs, including the particle type, particle energy, added signal delay, camera gate width, and the number of integrated pulses per frame. 133

5.5 Experimental and calculated transmission data for three of the neutron energy bins used to radiograph Object 1, composed of borated polyethylene ("b-poly"), graphite, and lead. I/I_0 values larger than 1.0 indicate net particle birth, whereas values less than 1.0 indicate net particle attenuation. 155

5.6 Experimental and simulated transmission data for three of the neutron energy bins used to radiograph Object 1, composed of borated polyethylene ("b-poly"), graphite, and lead. I/I_0 values larger than 1.0 indicate net particle birth, whereas values less than 1.0 indicate net particle attenuation. 165

5.7 Calculated and simulated direct transmission data three of the neutron energy bins used to radiograph Object 1, composed of borated polyethylene ("b-poly"), graphite, and lead. Note that I/I_0 values larger than 1.0 indicate net particle birth, whereas values less than 1.0 indicate net particle attenuation. 170

6.1 Values used with MCNP6 F6 tally to convert from deposited proton energy (MeV) to generated photon energy ($MeVee$) and thus simulate EJ-212 efficiency. 188

6.2 Upper detectable neutron energy for 2 mm and 5 mm EJ-212 screens and for Generation I and II system designs. 197

6.3 Upper detectable neutron energy for 2 mm and 5 mm EJ-212 screens and for Generation I and II system designs, if the source strength is reduced to 10^6 neutrons per second. 198

6.4 Normalized MTF values for apertures of $f/2$ and $f/4$. 217

7.1 The three volumes with the largest "LANSCE" flux values for neutrons, photons, protons, and alphas. Here, NPS is the number of particles simulated, and flux values shown are normalized to this value. 300

7.2 The three volumes with the largest "Configuration 15" flux values for neutrons, photons, protons, and alphas. Here, NPS is the number of particles simulated, and flux values shown are normalized to this value. 302
7.3 The three largest sources of particle births and deaths for the "LANSCE" configuration. Here, NPS is the number of particles simulated, and values shown are normalized to this value but not to cell volume. MCNP6 does not generate error for these values. Note that for alpha particles, there are no net births, only net deaths. . . . 306
7.4 The three largest sources of particle births and deaths for "Configuration 15". Here, NPS is the number of particles simulated, and values shown are normalized to this value. MCNP6 does not generate error for these values. Note that for alpha particles, there are no net births, only net deaths. 307

9.1 FP60R TOF time gates for particles and energy ranges of interest. . . 388
9.2 Corrected FP60R time-of-flight time gates for neutron time gates of interest, showing what time gates were thought to have been used ("imagined energy") and those that were actually used ("actual energy") during experiments. 391
9.3 Equipment settings for the five Object 2 neutron radiographs conducted to determine optimal source energy, including the neutron energy, added signal delay, camera gate width, and the number of integrated pulses per frame. 396
9.4 Equipment settings for the four Object 2 radiographs taken to compare FP60R image quality to that of FP15R, including the particle type, particle energy, added signal delay, camera gate width, and the number of integrated pulses per frame. 402

9.5 Equipment settings for the three radiographs of the crack test object, taken through 3 *in* of DU, including the particle type, particle energy, added signal delay, camera gate width, and the number of integrated pulses per frame. 409
9.6 The number of frames, rounded up to the nearest whole number, used to generate the radiography and flatfield images for the optimal energy study. A varying number of frames was used in order to normalize the images to the average flatfield intensity. 413
9.7 Experimental and calculated transmission data for two thicknesses of DU: 1 *in* and 3 *in*. 468
9.8 Experimental and simulated total transmission data for two thicknesses of DU: 1 *in* and 3 *in*. 472
9.9 Theoretical results and simulated direct transmission data for two thicknesses of DU: 1 *in* and 3 *in*. 475
9.10 Materials and their thicknesses as used in FP15R and FP60R experiments. The thickness of tungsten is listed for the thickest part of the cylinder internal to Object 2. Isotopes used for ENDF/B-VII.1 total cross-sections are also listed [52]. 477
9.11 Transmission through five materials radiographed in FP15R or FP60R: borated polyethylene ("b-poly."), graphite (^{12}C), lead (^{207}Pb), depleted uranium (^{238}U), and tungsten (^{184}W). Energies shown cover most of the LANSCE spectrum, and materials are listed in order of their increasing density. Transmission was calculated for experimental thicknesses of materials using ENDF/B-VII.1 total cross-section data (note: ^{238}U data only listed for energies up to 30 MeV.) [52]. 478

List of Figures

1.1 Left: Three knife-edge images, each generated by a different scintillator (top: granular; middle: glass; bottom: foil). Resolution of the edge visibly increases from top to bottom. Right: Graph of "line-outs", corresponding to the three images at left, that plot the change in grayscale value across the edge and thus quantify the resolution [10]. . 9

1.2 Diagram of a typical CCD radiography system. Radiation, after interacting in the radiography object, strikes a screen and is converted into visible light. A mirror angled at 45° then reflects this light into the lens of the CCD camera, so as to form an image on a digital array. 11

1.3 Neutron radiograph of a rose inside a lead cylinder. This example illustrates the ability of a neutron source to penetrate high-Z material, such as lead, and differentiate between densities [2]. 13

1.4 Feature blur, a result of source spot size, is reduced by maximizing the L/D ratio. 16

1.5 Illustration of period, T, and amplitude, A, on the plot of $y = \sin x$ [19]. 18

1.6 Illustration of the modulation depth of a system, with A_{max} and A_{min} equal to the maximum and minimum signal amplitude, respectively [16]. 20

1.7 Top: The input frequency increases as position in the object changes. Middle: The brightness of a real-world image, after blurring terms have been applied, decreases in amplitude as the input frequency increases. Bottom: The MTF of the system, $H(\xi, \eta)$, also decreases with increase in frequency. The system user would need to decide, based on their needs, what the minimum acceptable resolution limit would be [16]. . 21

1.8 An illustration of the MTF for two systems, A and B. Although A and B have the same resolution limit, A is a better system because it has higher modulation [16]. 22

1.9 The 1951 Air Force test pattern used to determine the modulation transfer function of an imaging system [18]. 25

1.10 An illustration of a perfectly resolved ideal image of a sequence of bars with increasing frequency (A). The corresponding ideal MTF can be seen in (C). A real-world system, however, adds blur to the sequence of bars (B) and its associated MTF (D) [22]. 26

1.11 An illustration of ringing, where the central peak interferes with another signal and forms lesser peaks at regular intervals on either side [18]. 27

1.12 Example of the Siemens star pattern used to find the system CTF and the optimized system focus. This pattern was used for lens focusing in the experiments that will be outlined later in this paper [25]. 28

1.13 Illustration of a two-dimensional projection (white) of a radiography object (gray) used to form a three-dimensional tomograph, where ρ and θ describe the projection view, s, and $P(\rho, \theta)$ describes the resultant two-dimensional projection. The incident particle fluence, I_0, is affected by interactions within the object to become the transmitted signal, I [17]. 34

4.1 Illustration of the MCNP6 geometry used to simulate neutron time-of-flight. A 10 MeV pencil beam neutron source was incident on the radiography object (a graphite slab), with a distance of 100 cm between the center of the graphite slab and the front face of an ideal detector [51]. 51

4.2 Diagram of the pulsed high-energy neutron source proposed by LLNL. According to Reference [50], A is a 7 MeV deuteron linear accelerator, B is the beam transport, C is the deuterium gas target, D is the imaging object, and E is the imaging system. This system is a boosted D-D source with endpoint energy of 10.2 MeV. 52

4.3 Illustration of the three locations selected on the detector face for neutron time-of-flight analysis. Case I is located in the detector center, Case II is located in the center of the top edge of the detector, and Case III is located in the upper left corner of the detector. Blue arrows indicate neutron travel from the graphite slab to these three locations [51]. 54

4.4 Illustration of the three F4 tally volumes located at Case I, Case II, and Case III. The FMESH tally border on the detector surface is shown for reference [51]. 57

4.5 MCNP6 FMESH simulated radiographs of neutrons that underwent a single elastic scatter in the graphite target prior to reaching the detector plane. TOF from the source origin to the detection location is shown above each image. Top: Elastically-scattered neutrons arrive at Case I first because it is the shortest distance between the interaction site and the detector. Middle: The elastic scatter, emitted isotropically, forms a cone as the deflection angle increases, causing the TOF to also increase. Neutrons are detected between Case I and II locations. Bottom: Elastic scatter reaches Case II, with an additional increase in deflection angle and thus TOF [51]. 59

4.6 Eljen EJ-212 scintillator emission spectrum with a peak wavelength of 423 *nm* [53]. 67
4.7 Photograph of the PI-Max4 emICCD camera and power supply [56]. . 69
4.8 Diagram of the PI-Max4 intensifier that is fiberoptically coupled to the CCD array. The PI-Max4 is unique because it has gain applied to the microchannel plate, as well as to the CCD chip [56]. 71
4.9 Illustration of the difference between a front surface mirror (top; also called "first surface mirror") and a standard surface mirror (bottom) [57]. 72
4.10 Photograph of the DeltaDiode control unit (white) with a laser head (black) resting on top [60]. 74
4.11 Photograph of the front display of the Stanford Research Systems DG645 digital delay generator [61]. 76
4.12 Block diagram of the typical TiGReSSE experimental system set-up. For cases with an external neutron source, the waveform generator and LED laser are not used. Instead, the accelerator provides the trigger signal. 78
4.13 Photograph of the interior of the light-tight box showing the ICCD camera and lens (bottom left), the mirror and its mount (bottom right), and the laser head with an attached diffuser (center). The scintillator is behind the paper with the smiley face used to mimic an imaging object (top center). An optical breadboard can be seen on the bottom of the box and is used for attaching and aligning TiGReSSE components. An 18 *in* ruler is shown for scale (center). 79
4.14 A computer screen shot of LightField software showing a focused image of a smiley face drawing. Tape used to affix the drawing to the light-tight box can be seen in the corners of the image. The orange and purple plots above and to the left of the image are horizontal and vertical line-outs of the image, respectively, and show how pixel values vary with location in the image. 81

5.1 D-T generator and control equipment that were used for initial system testing [62]. 85
5.2 Diagram of LANSCE beam lines, with the red arrow pointing to Target 4 and the blue arrow pointing to FP15R [67]. 92
5.3 Neutron flux profile of four of the six Target 4 flight paths: FP15R at an angle of 15° from the tungsten spallation target, FP30R (angle of 30°), FP60R (angle of 60°), and FP90R (angle of 90°). Note that, as the flight path angle from the target increases, the neutron flux shifts to lower energies. The source of this graphic unfortunately did not include a y-axis label on the plot [67]. 93
5.4 Photograph of various LANSCE beam collimators, with the 2 *in* beam collimators used in this experiment. 95
5.5 Photograph of the beam port where the beam exits the wall. The attached fission chamber was used to measure beam flux. 96
5.6 Illustration of the time-of-flight (black) of the FP15R beam as a function of energy (red) for a flight path distance of 23.7 m. Diagram is to scale, with each block equal to ∼24 ns. Note that $t = 0$ ns indicates the time of arrival of the spallation photons (γ), and that $t = 1784$ ns is the end of the micropulse. 98
5.7 Camera shielding composed of polyethylene (white), borated polyethylene (green), and concrete blocks (gray). Yellow tape was used to hold the shielding in place. Top left: Front view of the shielding around the camera, with lens cap on the camera lens. Top right: Top view of the shielding around the camera, with the lens pointed to the right (not shown). Bottom left: Back view of the shielding around the camera, with coolant tubes visible. Bottom right: Shielding underneath the camera and external to the light-tight box to shield scatter from the floor. 99

5.8 External shielding for camera (rusty steel blocks and green-colored borated polyethylene). The gray light-tight box can be seen behind the shielding, with the scintillator exposed. Note that the light-tight box was placed on top of stacked steel blocks to lift the box to the height of the beam. 100
5.9 Diagram of FP15R and the equipment set-up. 101
5.10 Photographs of the equipment set-up in the beam line. Left: Photograph of the light-tight box, wooden sample stand, and shielding blocks with the beam to the photographer's back. Center: Photograph of the light-tight box looking toward the beam. The liquid chiller and camera power supply, also shielded, are visible below the light-tight box. Note the other equipment in the beam line that increases scatter. Right: Equipment used to control the camera, which was located behind the shielding wall for personnel safety. 102
5.11 Diagrams of the external shielding placement (top) and the placement of equipment within the light-tight box (bottom). Units are in *cm*, and dimensions are not to scale. 103
5.12 Diagram of the components within the light-tight box to illustrate their distance above the bottom of the box. The mirror and its stand are on the left, and the camera and its stand are on the right. The two stands are highly simplistic in this diagram. Units are in *cm*, and dimensions are not to scale. 104
5.13 Diagram of the light-tight box within the flight path. The beam port is behind the viewer. Thicknesses of the floors and walls are not indicated because those dimensions are unknown. Units are in *cm*, and dimensions are not to scale. 105
5.14 Block diagram of the equipment set-up in FP15R. 106
5.15 Photographs of the trigger signal equipment provided by LANSCE (top) and a view of the trigger signal on an oscilloscope (bottom). . . 107

5.16 Photographs of Object 1, Object 2, and Object 3, the radiography objects that were imaged during the FP15R experiment, as placed in front of the scintillator. 109
5.17 Diagram of Object 2, shown here in the orientation used for radiography. A valve is fitted to the object (not shown) and is located at the top of the object. The diagonal lines indicate stainless steel. 110
5.18 Initial time-of-flight scan results taken with 50 ns gate widths. The peak in average intensity, and thus arrival of photons at the scintillator, occurs between 600 to 750 ns. 113
5.19 Initial time-of-flight scan with a gate width of 50 ns shown for reference, as well as increasingly narrow time-of-flight scans of gate widths of 25 ns and 10 ns around the previous peak in intensity. It was found that the peak in intensity, attributable to photons, occurs between 715 and 725 ns. 114
5.20 Radiographs taken with added time delays of 0 ns (left) and 1784 ns (right) are shown to have approximately equal intensities, which signifies the LANSCE beam is relatively stable from pulse to pulse. . 116
5.21 Time gating shown on the time-of-flight scan for the four radiographs taken of Object 1: 10 to ∼600 MeV neutrons (top left), ∼0.1 to 10 MeV neutrons (bottom left), 2.5 to 10 MeV neutrons (bottom right), and photons (top right). 119
5.22 Spallation photon radiograph of Object 1. Note that the beam forms a circle on the scintillator around Object 1. 121
5.23 High-energy neutron radiograph of Object 1 taken with 10 to 600 MeV neutrons. Note that the beam forms a circle on the scintillator around Object 1. 122
5.24 Mid-energy neutron radiograph of Object 1 taken with 2.5 to 10 MeV neutrons. Note that the beam forms a circle on the scintillator around Object 1. 123

5.25 Low- and mid-energy neutron radiograph of Object 1 taken with ∼0.1 to 10 MeV neutrons. Note that the beam forms a circle on the scintillator around Object 1. 124
5.26 Spallation photon radiograph of Object 2. Note that the beam forms a circle on the scintillator around Object 2. 126
5.27 High-energy neutron radiograph of Object 2 with 10 to 600 MeV neutrons. Note that the beam forms a circle on the scintillator around Object 2. 127
5.28 Mid-energy neutron radiograph of Object 2 taken with 2.5 to 10 MeV neutrons. Note that the beam forms a circle on the scintillator around Object 2. 128
5.29 Low- and mid-energy neutron radiograph of Object 2 taken with ∼0.1 to 10 MeV neutrons. Note that the beam forms a circle on the scintillator around Object 2. 129
5.30 Low-energy neutron radiograph of Object 2 taken with ∼0.1 to 2.5 MeV neutrons. Note that the beam forms a circle on the scintillator around Object 2. 130
5.31 Radiograph of Object 2 using the total LANSCE spectrum (photons and neutrons). This radiograph approximates a traditional neutron radiograph that does not use time gating to reject signal. Note that the beam forms a circle on the scintillator around Object 2. 131
5.32 Radiographs of Object 3 without collimation (left) and with 2 in collimation (right), showing that collimation reduces scatter and improves feature visibility. Radiographs were generated with 10 to 600 MeV neutrons. Note that the beam forms a circle on the scintillator around Object 3, and that this circle shrinks with the 2 in collimation. 134
5.33 Spallation photon radiograph of Object 3. Note that the beam forms a circle on the scintillator around Object 3. 135

5.34 High-energy neutron radiograph of Object 3 taken with 10 to 600 MeV neutrons. Note that the beam forms a circle on the scintillator around Object 3. 136
5.35 Mid-energy neutron radiograph of Object 3 taken with 2.5 to 10 MeV neutrons. Note that the beam forms a circle on the scintillator around Object 3. 137
5.36 The 10 to 600 MeV neutron radiograph of Object 1 after it has been rotated 0.9° clockwise. The region of interest that was used to determine the averaged vertical line-out is shown in yellow. 141
5.37 Averaged vertical line-out across the high-energy (i.e., 10 to 600 MeV) neutron radiograph of Object 1. The dip at Pixel 210 indicates the sheet of paper is visible. 142
5.38 Averaged vertical line-out across the mid-energy (i.e., 2.5 to 10 MeV) neutron radiograph of Object 1. Note there is no dip at Pixel 210 and thus the sheet of paper is not visible at this energy range. 143
5.39 An averaged vertical line-out was generated for each of the three regions shown on Object 2 (white) to illustrate that features can be seen only with the 2.5 to 10 MeV time gate. The radiograph shown here was taken with 2.5 to 10 MeV neutrons and has been rotated 0.9° counter-clockwise. 145
5.40 Averaged vertical line-out for the top feature in radiographs of Object 2 taken with 2.5 to 10 MeV and ∼0.1 to 10 MeV neutrons. The peak of interest is indicated by an arrow and is only visible with 2.5 to 10 MeV neutrons. 146
5.41 Averaged vertical line-out for the middle feature in radiographs of Object 2 taken with 2.5 to 10 MeV and ∼0.1 to 10 MeV neutrons. The peaks of interest are indicated by an arrow and are only visible with 2.5 to 10 MeV neutrons. 147

5.42 Averaged vertical line-out for the bottom feature in radiographs of Object 2 taken with 2.5 to 10 MeV and ∼0.1 to 10 MeV neutrons. The peak of interest is indicated by an arrow and is only visible with 2.5 to 10 MeV neutrons. 148
5.43 An averaged horizontal line-out was generated for a region spanning the three holes in Object 3 (yellow). The radiograph of Object 3 shown here was taken with 10 to 600 MeV neutrons and has been rotated 1.5° clockwise. 149
5.44 Averaged horizontal line-out for radiographs of Object 3 taken with 10 to 600 MeV, 2.5 to 10 MeV, and the photon time gate. The peaks of interest are indicated by an arrow. 150
5.45 Transmission images (I/I_0) of Object 1 in FP15R generated with ∼0.1 to 10 MeV (top), 2.5 to 10 MeV (middle), and 10 to 600 MeV (bottom) neutrons. 152
5.46 ROIs (red) used to find average I/I_0 values in lead (top), borated polyethylene (middle), and graphite (bottom). The ROIs are shown on the 2.5 to 10 MeV radiograph of Object 1. 153
5.47 The inelastic ("inel."), total ("tot."), and $(n, 2n)$ ENDF/B-VII.1 microscopic cross-sections for ^{207}Pb [52]. 158
5.48 The inelastic ("inel.") and total ("tot.") ENDF/B-VII.1 microscopic cross-sections for graphite (natural carbon, or "nat. C") [52]. 159
5.49 The inelastic ("inel.") and total ("tot.") ENDF/B-VII.1 microscopic cross-sections for ^{10}B ("B-10"), which is used as a dopant in polyethylene to better absorb thermal neutrons [52]. 160

5.50 Simulated total (i.e., direct plus scatter) neutron radiographs of Object 1 in FP15R using MCNP6 FMESH tallies. These three radiographs are set to the same contrast levels. Top: Simulated ∼0.1 to 10 MeV total neutron radiograph. Middle: Simulated 2.5 to 10 MeV total neutron radiograph. Bottom: Simulated 10 to 600 MeV total neutron radiograph. 163
5.51 ROIs (red) used to find average simulated I/I_0 values in lead (top), borated polyethylene (middle), and graphite (bottom). The ROIs are shown on the 10 to 600 MeV simulated neutron radiograph of Object 1. 164
5.52 Simulations of FP15R total radiographs of Object 1, as well as simulations of corresponding flatfield images, allowed for determination of the number of secondary particles generated in each image type. The difference in secondary particles between the image types indicates the number of secondary particles born in the radiography object. Top: The number of secondary neutrons generated via the (n, xn) reaction. Bottom: The number of secondary photons generated via (n, γ), x-ray fluorescence, and photon annihilation reactions. 167
5.53 Simulated direct radiographs of Object 1 in FP15R using MCNP6 FMESH tallies. These three radiographs, set to different contrast levels, do not include secondary particles or scatter. Top: Simulated ∼0.1 to 10 MeV direct neutron radiograph. Middle: Simulated 2.5 to 10 MeV direct neutron radiograph. Bottom: Simulated 10 to 600 MeV direct neutron radiograph. 168
5.54 Photograph of the controlled access door to FP15R. The position of the shutter here is closed, as indicated by the glowing lights above the door. 172

5.55 Two radiographs of the Siemens star pattern, one taken at a temperature of -10 °C (left) and one taken at a temperature of -20 °C (right). Both radiographs are set to the same contrast range to compare the effect of temperature on noise. 174
5.56 Line-outs of the Siemens star pattern as a function of camera operating temperature. Top: Line-out location indicated by the yellow line and demonstrated on the -20 °C image. Bottom: Line-out values plotted for both the -10 °C and -20 °C images. 175
5.57 Example of stars and tracks in one of the frames taken of Object 1 with 2.5 to 10 MeV neutrons. 176
5.58 Top: Example of the line-out used to quantify FP15R beam non-uniformity. The line is shown on the full spectrum flatfield. Bottom: Line-outs for the six flatfield images taken in FP15R. Pixel grayscale values were normalized to the number of total pulse accumulations in each energy bin. 179

6.1 Semi-*log* plot of the proton CSDA range for a neutron of 800 MeV incident on various materials, taken from the NIST PSTAR database [71]. 184
6.2 Semi-*log* plot of the alpha CSDA range for a neutron of 800 MeV incident on various materials, taken from the NIST ASTAR database [72]. 185
6.3 Simulated pulse height distributions for monoenergetic neutrons incident on EJ-212, ranging in energy from 500 keV to 20 MeV. The scintillator thickness was either 2 mm (top) or 5 mm (bottom), and had a face 20.32 $\times$ 20.32 cm^2 in area. MCNP6 relative error is indicated. 191

6.4 Power trendlines fit to the average light output data for monoenergetic neutrons incident on a 2 mm or 5 mm EJ-212 scintillator with face 20.32 $\times$ 20.32 cm^2 in area. Neutron energies range from 500 keV to 20 MeV. Trendline equations and corresponding R^2 values are indicated on the plot. MCNP6 relative error is so small that is does not appear on the plot. 193
6.5 *Log* plot of the average light output for neutrons incident on EJ-212 of 2 mm or 5 mm thickness. 194
6.6 *Log* plot of the average number of photons per pixel reaching the CCD chip as a function of incident neutron energy and EJ-212 thickness. The detection limit of 3.0×10^2 photons per pixel per second is shown in red, with values below this red line not detected by TiGReSSE. The top plot is for the Generation I design used in FP15R, whereas the bottom plot is for the Generation II design used in FP60R. 196
6.7 Illustration of the test pattern used in the MTF experiment [76]. . . . 200
6.8 Photograph of the light source used in the MTF experiment [77]. . . . 201
6.9 Bottom: An input stimulus of three line pairs, such as those in a line pair test pattern, is used to find the MTF of a system. Middle: A perfect system images the line pairs as a square wave. Top: A real-world system adds blur that rounds edges and reduces amplitude. The MTF represents such blur and determines the limiting contrast resolution of an optical system. 202
6.10 Photograph of the experimental set-up to determine the contrast resolution of the system. The light source and test pattern were placed where the scintillator is typically located, while the camera and mirror remained in the same position as that in FP15R. Blue tape was used to affix the test pattern to the light source. 205
6.11 Photograph of the test pattern used in the MTF experiment, along with the blue tape used to affix the test pattern to the light source. . 207

6.12 Averaged image taken of the test pattern prior to adjusting the lens focus. 208
6.13 Averaged image taken of the test pattern after adjusting the lens focus. 209
6.14 Post-processed cropped image of the test pattern at $f/2$. 211
6.15 Post-processed cropped image of the test pattern at $f/4$. 212
6.16 Vertical line-out (top) and horizontal line-out (bottom) for a frequency of 1.0 lp/mm and aperture of $f/2$. 214
6.17 Vertical line-out for a frequency of 2.2 lp/mm and aperture of $f/2$. Note that the peaks and valleys are virtually indistinguishable. 215
6.18 Plot of the normalized MTF at the imaging plane for apertures of $f/2$ and $f/4$. 216

7.1 Diagram of the beam pipe and scintillator, designed in MCNP6 simulations to approximate experimental conditions. The source was angled to provide an 8 in spot size on the front face of the scintillator. Dimensions are in cm and are not to scale. 225
7.2 Baseline energy distribution (top) and surface current (bottom) for neutrons entering the camera body and for "No object, no shield", "No shield", and "LANSCE". 231
7.3 Baseline energy distribution (top) and surface current (bottom) for photons entering the camera body and for "No object, no shield", "No shield", and "LANSCE". 232
7.4 Baseline energy distribution (top) and surface current (bottom) for protons entering the camera body and for "No object, no shield", "No shield", and "LANSCE". 233
7.5 Baseline energy distribution (top) and surface current (bottom) for alphas entering the camera body and for "No object, no shield", "No shield", and "LANSCE". 234

7.6 Energy distribution (top) and surface current (bottom) for neutrons entering the camera body and for Configurations 00 and 000. 235
7.7 Energy distribution (top) and surface current (bottom) for photons entering the camera body and for Configurations 00 and 000. 236
7.8 Energy distribution (top) and surface current (bottom) for protons entering the camera body and for Configurations 00 and 000. 237
7.9 Energy distribution (top) and surface current (bottom) for alphas entering the camera body and for Configurations 00 and 000. 238
7.10 Energy distribution (top) and surface current (bottom) for neutrons entering the camera body and for Configurations 1 and 3. 240
7.11 Energy distribution (top) and surface current (bottom) for photons entering the camera body and for Configurations 1 and 3. 241
7.12 Energy distribution (top) and surface current (bottom) for protons entering the camera body and for Configurations 1 and 3. 242
7.13 Energy distribution (top) and surface current (bottom) for alphas entering the camera body and for Configurations 1 and 3. 243
7.14 Energy distribution (top) and surface current (bottom) for neutrons entering the camera body and for Configurations 1 and 2. 245
7.15 Energy distribution (top) and surface current (bottom) for photons entering the camera body and for Configurations 1 and 2. 246
7.16 Energy distribution (top) and surface current (bottom) for protons entering the camera body and for Configurations 1 and 2. 247
7.17 Energy distribution (top) and surface current (bottom) for alphas entering the camera body and for Configurations 1 and 2. 248
7.18 Energy distribution (top) and surface current (bottom) for neutrons entering the camera body and for Configurations 1, 10, 11, and 12 as compared to the LANSCE set-up. 250

7.19 Energy distribution (top) and surface current (bottom) for photons entering the camera body and for Configurations 1, 10, 11, and 12 as compared to the LANSCE set-up. 251
7.20 Energy distribution (top) and surface current (bottom) for protons entering the camera body and for Configurations 1, 10, 11, and 12 as compared to the LANSCE set-up. 252
7.21 Energy distribution (top) and surface current (bottom) for alphas entering the camera body and for Configurations 1, 10, 11, and 12 as compared to the LANSCE set-up. 253
7.22 Energy distribution (top) and surface current (bottom) for neutrons entering the camera body and for Configuration 13 as compared to the LANSCE set-up. 254
7.23 Energy distribution (top) and surface current (bottom) for photons entering the camera body and for Configuration 13 as compared to the LANSCE set-up. 255
7.24 Energy distribution (top) and surface current (bottom) for protons entering the camera body and for Configuration 13 as compared to the LANSCE set-up. 256
7.25 Energy distribution (top) and surface current (bottom) for alphas entering the camera body and for Configuration 13 as compared to the LANSCE set-up. 257
7.26 Energy distribution (top) and surface current (bottom) for neutrons entering the camera body and for Configuration 0 as compared to the LANSCE set-up. 259
7.27 Energy distribution (top) and surface current (bottom) for photons entering the camera body and for Configuration 0 as compared to the LANSCE set-up. 260

7.28 Energy distribution (top) and surface current (bottom) for protons entering the camera body and for Configuration 0 as compared to the LANSCE set-up. 261
7.29 Energy distribution (top) and surface current (bottom) for alphas entering the camera body and for Configuration 0 as compared to the LANSCE set-up. 262
7.30 Energy distribution (top) and surface current (bottom) for neutrons entering the camera body and for Configurations 4 and 7 as compared to the LANSCE set-up. 264
7.31 Energy distribution (top) and surface current (bottom) for photons entering the camera body and for Configurations 4 and 7 as compared to the LANSCE set-up. 265
7.32 Energy distribution (top) and surface current (bottom) for protons entering the camera body and for Configurations 4 and 7 as compared to the LANSCE set-up. 266
7.33 Energy distribution (top) and surface current (bottom) for alphas entering the camera body and for Configurations 4 and 7 as compared to the LANSCE set-up. 267
7.34 Energy distribution (top) and surface current (bottom) for neutrons entering the camera body and for Configurations 4, 7, and 8. 269
7.35 Energy distribution (top) and surface current (bottom) for photons entering the camera body and for Configurations 4, 7, and 8. 270
7.36 Energy distribution (top) and surface current (bottom) for protons entering the camera body and for Configurations 4, 7, and 8. 271
7.37 Energy distribution (top) and surface current (bottom) for alphas entering the camera body and for Configurations 4, 7, and 8. 272
7.38 Energy distribution (top) and surface current (bottom) for neutrons entering the camera body and for Configurations 00, 5, and 9 as compared to the LANSCE set-up. 273

7.39 Energy distribution (top) and surface current (bottom) for photons entering the camera body and for Configurations 00, 5, and 9 as compared to the LANSCE set-up. 274
7.40 Energy distribution (top) and surface current (bottom) for protons entering the camera body and for Configurations 00, 5, and 9 as compared to the LANSCE set-up. 275
7.41 Energy distribution (top) and surface current (bottom) for alphas entering the camera body and for Configurations 00, 5, and 9 as compared to the LANSCE set-up. 276
7.42 Energy distribution (top) and surface current (bottom) for neutrons entering the camera body and for Configurations 4, 5, and 6. 278
7.43 Energy distribution (top) and surface current (bottom) for photons entering the camera body and for Configurations 4, 5, and 6. 279
7.44 Energy distribution (top) and surface current (bottom) for protons entering the camera body and for Configurations 4, 5, and 6. 280
7.45 Energy distribution (top) and surface current (bottom) for alphas entering the camera body and for Configurations 4, 5, and 6. 281
7.46 Energy distribution (top) and surface current (bottom) for neutrons entering the camera body and for Configurations 14 and 15. 282
7.47 Energy distribution (top) and surface current (bottom) for photons entering the camera body and for Configurations 14 and 15. 283
7.48 Energy distribution (top) and surface current (bottom) for protons entering the camera body and for Configurations 14 and 15. 284
7.49 Energy distribution (top) and surface current (bottom) for alphas entering the camera body and for Configurations 14 and 15. 285
7.50 Energy distribution (top) and surface current (bottom) for neutrons entering the camera body and for Configurations 15 and 16. 287
7.51 Energy distribution (top) and surface current (bottom) for photons entering the camera body and for Configurations 15 and 16. 288

7.52 Energy distribution (top) and surface current (bottom) for protons entering the camera body and for Configurations 15 and 16. 289
7.53 Energy distribution (top) and surface current (bottom) for alphas entering the camera body and for Configurations 15 and 16. 290
7.54 Energy distribution (top) and surface current (bottom) for neutrons entering the camera body and for all configurations simulated. 291
7.55 Energy distribution (top) and surface current (bottom) for photons entering the camera body and for all configurations simulated. 292
7.56 Energy distribution (top) and surface current (bottom) for protons entering the camera body and for all configurations simulated. 293
7.57 Energy distribution (top) and surface current (bottom) for alphas entering the camera body and for all configurations simulated. 294
7.58 Energy distribution (top) and surface current (bottom) for neutrons entering the camera body and for Configuration 15 as compared to the LANSCE set-up. 295
7.59 Energy distribution (top) and surface current (bottom) for photons entering the camera body and for Configuration 15 as compared to the LANSCE set-up. 296
7.60 Energy distribution (top) and surface current (bottom) for protons entering the camera body and for Configuration 15 as compared to the LANSCE set-up. 297
7.61 Energy distribution (top) and surface current (bottom) for alphas entering the camera body and for Configuration 15 as compared to the LANSCE set-up. 298
7.62 Histogram of the (n, γ) reaction for "Configuration 15" and "LANSCE" shielding designs. The number of secondary gammas is not normalized to the number of particles simulated. 304

7.63 Semi-*log* histogram of the (n, γ) reaction for "Configuration 15" and "LANSCE" shielding designs. The number of secondary gammas is not normalized to the number of particles simulated. 305

8.1 Diagram of the cylindrically symmetric NAC-I28 spent nuclear fuel cask, with dimensions in *cm* (not to scale). 312

8.2 Simulated direct 14 MeV neutron radiographs of the NAC-I28 SNF cask, with one image cropped (left) and the other image the full size of the detector (right). Note that cropping the image to remove the beam area outside the edges of the cask increases the range of contrast within the cask (notice that the center of the cask now appears darker as a result of cropping). 314

8.3 Simulated direct 10 MeV neutron radiographs of the NAC-I28 SNF cask, arranged according to the procedure to convert pixel grayscale values to areal density, σt. The direct data (left) is divided by the value of the beam incident on the detector (middle left), a natural *log* filter is applied (middle right), and the data is multiplied by -1 before image contrast is adjusted for optimal feature visibility (right). 316

8.4 Comparison of a 10 MeV direct-to-scatter (D/S) neutron radiograph (left) to a 10 MeV direct (D) neutron radiograph (right). Note that the grayscale values are inverted because the D radiograph is multiplied by -1, and that the grayscale values differ slightly between the two radiographs because they represent different quantities. 317

8.5 Simulated 10 MeV neutron radiographs of the NAC-I28 SNF cask, with the total (direct plus scatter; left) image compared to the direct (right) image. 318

8.6 Simulated direct (D) radiographs of the NAC-I28 SNF cask, with the 10 MeV neutron radiograph (left) compared to the 15 MeV x-ray radiograph (right). The x-ray image appears to show a void (circled in red) that does not exist because x-rays, unlike fast neutrons, are unable to penetrate the thickest part of the lead. 320
8.7 Simulated 15 MeV total (T) x-ray radiograph of the NAC-I28 SNF cask. 321
8.8 Simulated D/S neutron radiographs for 10 MeV (left), 14 MeV (center), and 20 MeV (right) monoenergetic neutrons. The three radiographs are set to the same logarithmic contrast range, [-70,6]. . . 322
8.9 Simulated D/S x-ray radiographs for 6 MeV (left) and 15 MeV (right) bremsstrahlung x-rays. The two radiographs are set to the same contrast range, [-70,6]. 324
8.10 Plot of the horizontal line-out data for the simulated neutron (10, 14 and 20 MeV) and x-ray (6 and 15 MeV) D/S radiographs. 325
8.11 Plot of the vertical line-out data for the simulated neutron (10, 14 and 20 MeV) and x-ray (6 and 15 MeV) D/S radiographs, where Pixel 0 is the bottom of the radiograph. 326
8.12 Plot of the horizontal line-out data for the simulated 10 MeV neutron radiograph, with all material boundaries visible. 328
8.13 Plot of the horizontal line-out data for the simulated 14 MeV neutron radiograph, with all material boundaries visible. 329
8.14 Plot of the horizontal line-out data for the simulated 6 MeV x-ray radiograph, with all material boundaries visible. 330
8.15 Plot of the horizontal line-out data for the simulated 15 MeV x-ray radiograph, with all material boundaries visible. 331
8.16 Plot of the horizontal line-out data for the simulated 20 MeV neutron radiograph, with only some material boundaries visible. 332

8.17 Horizontal line-outs were taken in two locations within the 10 MeV neutron radiograph of the SNF cask ($y = 68$ and $y = 239$) in order to determine the impact of the line-out location on the ability to find material boundaries. 334
8.18 Vertical line-outs were taken in two locations within the 10 MeV neutron radiograph of the SNF cask ($x = 68$ and $x = 119$) in order to determine the impact of the line-out location on the ability to find material boundaries. Pixel 0 indicates the bottom of the cask. 335
8.19 Simulated D neutron radiographs for 10 MeV (left), 14 MeV (center), and 20 MeV (right) neutrons. The three radiographs are set to different contrast ranges, which are determined to be optimal by an ImageJ "Auto" algorithm. 336
8.20 Two views of the 20 MeV simulated D neutron radiograph, one with a custom contrast setting (left) and one with the "Auto" contrast setting in ImageJ (right). Note that, while the "Auto" setting provides the most useful overall image, changing the contrast to a custom setting allows for features to be preferentially viewed while ignoring others and thus reveals features that may otherwise be hidden. 337
8.21 Not-to-scale diagram of the tungsten (blue) and polyethylene (beige) radiography object simulated in MCNP6 to estimate dose-to-object values. Cracks (red) are shown in their locations. Top left: External view of the object. Top right: Internal view of the center of the object, with full-length and half-length cracks shown. Bottom: View of the object from the top, with the crack coordinates listed. 339

8.22 Dose per source particle that is delivered to the polyethylene region as a function of source type and energy, particle type delivering dose (neutron or photon), and crack size (1 cm, 5 mm, or 1 mm). Neutrons deliver neutron dose and, via the (n, γ) reaction, photon dose. X-rays deliver photon dose, with neutron dose via the (γ, n) reaction equal to zero for this radiography object. The polyenergetic sources (LANSCE, 6 MeV, and 15 MeV) are indicated by their endpoint energy. Error bars are indicated. 342

8.23 Dose per source particle that is delivered to the tungsten region as a function of source type and energy, particle type delivering dose (neutron or photon), and crack size (1 cm, 5 mm, or 1 mm). Neutrons deliver neutron dose and, via the (n, γ) reaction, photon dose. X-rays deliver photon dose, with neutron dose via the (γ, n) reaction equal to zero for this radiography object. The polyenergetic sources (LANSCE, 6 MeV, and 15 MeV) are indicated by their endpoint energy. Error bars are indicated. 343

8.24 Simulated direct radiographs of the cylindrical object, generated by an MCNP6 FMESH tally. Source and geometry specifications remained the same as the MCNP6 F6 dose tally outlined in this section. The cylindrical object, composed of tungsten and polyethylene, has three 1 cm cracks. Top: Radiography source is 14 MeV neutrons. Note that the tungsten-polyethylene border and two of the three cracks are visible (indicated by arrows), with the third most likely in a contrast-stretched region. Bottom: Bremsstrahlung x-ray radiography source with a 15 MeV endpoint energy. Note that hardly any x-rays are penetrating the center, which is the thinnest (and therefore easiest) part of the object for x-rays to image, and that no cracks are visible. 344

8.25 Dose per source particle that is delivered to the entire radiography object (tungsten plus polyethylene) as a function of source type and energy, particle type delivering dose (neutron or photon), and crack size (1 cm, 5 mm, or 1 mm). Neutrons deliver neutron dose and, via the (n, γ) reaction, photon dose. X-rays deliver photon dose, with neutron dose via the (γ, n) reaction equal to zero for this radiography object. The polyenergetic sources (LANSCE, 6 MeV, and 15 MeV) are indicated by their endpoint energy. Error bars are indicated. . . . 346

8.26 Total dose (neutron plus photon) per source particle that is delivered to each material region as a function of source type and energy, particle type delivering dose (neutron or photon), and crack size (1 cm, 5 mm, or 1 mm). Neutrons deliver neutron dose and, via the (n, γ) reaction, photon dose. X-rays deliver photon dose, with neutron dose via the (γ, n) reaction equal to zero for this radiography object. The polyenergetic sources (LANSCE, 6 MeV, and 15 MeV) are indicated by their endpoint energy. Error bars are indicated. 347

8.27 Total dose (neutron plus photon) per source particle that is delivered to the entire radiography object as a function of source energy and crack size (1 cm, 5 mm, or 1 mm). The polyenergetic sources (LANSCE, 6 MeV, and 15 MeV) are indicated by their endpoint energy. Error bars are indicated. 348

9.1 Diagram of LANSCE beam lines, with the red arrow pointing to Target 4 and the blue arrow pointing to FP15R. The new flight path, FP60R, is indicated by an orange oval [67]. 351

9.2 A photograph of the beam pipe, the fission chamber, and the concrete shielding blocks placed around it to reduce scatter and dose to personnel. 354

9.3 A photograph of front of the fission chamber, with its instrumentation and the beam pipe visible behind it. Note how the fission chamber has three large holes, one in each corner of its support, and that the beam pipe also has smaller holes along its edge. 355
9.4 A not-to-scale diagram of FP60R. The FP60R building is shown in light blue, hand stack shielding (mostly concrete) is shown in yellow, and magnetite concrete is shown in red. The cave, beam pipe, beam dump (used to stop particles that would exit the flight path in order to protect workers), a neighboring building, and experimental operation area are indicated. This diagram was provided by R. Nelson of LANSCE. 356
9.5 A not-to-scale diagram of the front view of the cave used to shield staff from scatter off of the radiography object. The beam pipe is shown in gray, and the fission chamber used to monitor beam flux is shown in blue. Concrete magnetite blocks (white) are of identical dimensions. . 357
9.6 A not-to-scale diagram of the side view of the concrete cave used to shield staff from scatter off of the radiography object. The beam pipe is shown in gray, and the fission chamber used to monitor beam flux is shown in blue. Concrete magnetite blocks (white) are of the same dimensions. 358
9.7 A not-to-scale diagram of the sliding concrete block that is used to protect staff walking outside of FP60R. The block is placed on rails (gray) so its position can be changed as needed. Note that there is no gap between the sliding block and the concrete cave behind it. 359
9.8 A photograph of the magnetite cave during set-up of the experiment. Note that a table is inside the cave for the purpose of supporting external shielding, and a second table to support the light-tight box is seen outside the cave but not yet in position. 360

9.9 TiGReSSE was reconfigured for the experiments in FP60R. The light-tight box remained the same size, with overall dimensions of 76.2 cm × 91.4 cm × 32.8 cm. 361
9.10 A photograph of one of the team members, A. Madden, with the light-tight box for a sense of scale. 363
9.11 A photograph of the products used to clean the scintillator (right) and the mirrors (left) within the light-tight box. 364
9.12 A not-to-scale diagram of the translation stage used to rotate and translate the radiography object. Top: Top view of the translation stage. The object is placed on the 8 in^2 plate, shown as dark gray. Bottom: Side view of the translation stage. 365
9.13 A photograph of the translation stage within the concrete cave. . . . 366
9.14 A not-to-scale diagram of the two tables used in the beam line, one for the light-tight box (left table) and one for the external shielding and translation stage (right table). The beam pipe is shown for reference. The right table was placed within the concrete cave (not shown), and both tables sat flush with the edge of the concrete cave. The shielding is shown as a red dashed line. The lower shelves on the left table were used to store the chiller and the camera power supply, which were shielded with borated polyethylene and concrete (not shown). 367
9.15 A not-to-scale diagram of the external shielding used to protect the camera from the direct beam. Steel plates (blue) were stacked on top of concrete blocks (beige) in order to get the steel shielding to the correct height while saving weight. Left: The shielding as viewed looking from the light-tight box toward the beam pipe. Right: Side view of the shielding. 369
9.16 A photograph of the external shielding composed of steel plates and concrete blocks. The translation stage can be seen in the foreground, with the light-tight box in the background. 370

9.17 A not-to-scale diagram of the shielding placed within the light-tight box to protect the camera from the direct beam. Top: Shielding inside the light-tight box as viewed from above. Lithiated polyethylene is indicated by solid purple, and an assortment of polyethylene, borated polyethylene, and lithiated polyethylene blocks is indicated by vertical purple stripes. The camera, mirrors, and scintillator are shown for reference. Bottom left: Front view of the shielding within the light-tight box. Here, diagonal purple stripes indicate polyethylene. The camera and its stand are shown for reference. The lead shield, bent to wrap around the camera while leaving a gap between it and the camera, is shown as gray. Not shown is 1 *in* thick lithiated polyethylene placed between the wall of the light-tight box and the right side of the camera. Bottom right: Detailed diagram of the lead shield, which is also seen in the bottom left diagram. The lead shield is 1 *in* thick. 371

9.18 A photograph of the shielding within the light-tight box. The mirrors, light source (used for testing lens focus), and the scintillator (located where the light source reflection can be seen) are also visible. The camera lens and lens cap are visible beneath the bent lead shielding (which was covered in yellow tape to allow safe handling). On top of the lead, borated polyethylene blocks are held together with black tape, and an assortment of lithiated polyethylene, borated polyethylene, and polyethylene is seen to its left. 372

9.19 A diagram of the polyethylene penetrameter used to test system resolution at the object plane. Both the object and this diagram were provided by J. Hall of Lawrence Livermore National Laboratory. . . . 374

9.20 A diagram of the polyethylene (yellow) and steel (gray) crack test object used to determine system resolution at the object plane. Both the object and this diagram were provided by J. Hall of Lawrence Livermore National Laboratory. 375

9.21 A photograph of the disassembled crack test object. A tape measure is shown for reference. Left: The interior of the crack test object showing the four cracks in the polyethylene and the holes of various depths and diameters in the steel. The various pieces are held together by an aluminum frame that can be tightened via the screw at the top of the frame in order to vary the crack spacing. Right: The front cover of the crack test object, made of aluminum, would be rotated 90° clockwise and attached via four screws. 376
9.22 A diagram of the DU plates imaged in FP60R. Each plate has an identical hole of unknown diameter. Top: Two plates are shaped like the semi-circle depicted here. Bottom: One plate is shaped like the rectangle shown here. 377
9.23 A photograph of the interior of the light-tight box, with the Siemens star pattern placed at the center of the scintillator plane. The light source used to illuminate the test pattern is also visible. 379
9.24 Image of the Siemens star pattern, located at the center of the scintillator plane, at the system's best focus. 380
9.25 Scatter as seen by the camera with the FP15R configuration. 381
9.26 Scatter as seen by the camera with the FP60R configuration. 383
9.27 Histogram of the scatter seen in FP60R and FP15R, with the number and intensity of large pixel grayscale values (caused by stars) decreased in FP60R. 384
9.28 A photograph of the flat panel detector used to determine the true beam shape and location. This allowed for the light-tight box's position to be adjusted so that the scintillator was centered in the beam. The detector and its stand are visible behind the light-tight box. 385

9.29 Top: Graph of the FP60R results for the time-of-flight scan, which plots average scintillator intensity as a function of time. Gate widths of 10 (purple), 25 (green), 50 (red), and 200 ns (blue) are shown. Bottom: A close-up view of the top plot so that the peaks for both photons and neutrons can be seen in the 50, 25, and 10 ns time gates (the 200 ns time gate was too broad in time to capture this behavior). The photons arrive between 990 and 1000 ns. 387
9.30 Semi-*log* plot of the difference, in MeV, between the imagined energy and the actual energy measured in FP60R. 392
9.31 Semi-*log* plot of the percent difference between the imagined energy and the energy actually measured in FP60R. 394
9.32 These two plots show the balance that must be struck between spatial and contrast resolution, with the best location for the object shown in yellow on both plots. Top: Plot of the magnification in FP60R as a function of object-to-detector distance. Bottom: Plot of the scintillator's field of view of the scatter off the radiography object. . . 398
9.33 Photograph of Object 2 at a distance of 78.7 cm from the scintillator. 400
9.34 Photograph of Object 2 at a distance of 5.5 cm from the scintillator. . 401
9.35 Not-to-scale diagram of the set-up for the long exposures of Object 2 (dark blue), the crack test object (dark green), and the penetrameter (green). The optical table (blue), aluminum plates (white with gray border), and the foam (beige) used to raise the height of the objects are also shown. The steel shielding, shielding support table, and concrete cave wall are shown for reference, and the point-of-view is from the beam looking toward the scintillator. 404
9.36 Photograph of the set-up for the long exposure radiographs. Object 2 is on the left, and the two LLNL objects are stacked on the right, with the penetrameter above and the crack test object below. 405

9.37 Photograph of the experimental set-up to radiograph the crack test object behind three DU plates. 407
9.38 Photograph of the top of the crack test object. 408
9.39 Averaged vertical line-outs for the normalized 10 to 600 MeV radiograph (27 frames) and the unnormalized 10 to 600 MeV radiograph (all 100 frames were used), both taken of Object 2 in FP60R. Note that while smoothness is affected by normalization, contrast is not. . 412
9.40 FP60R radiograph of Object 2 using 2 to 3 MeV neutrons and 84 frames. The image was rotated 1.5° counter-clockwise to straighten the object in the field of view. 414
9.41 FP60R radiograph of Object 2 using 8 to 12 MeV neutrons and 64 frames. The image was rotated 1.5° counter-clockwise to straighten the object in the field of view. 415
9.42 FP60R radiograph of Object 2 using 9 to 11 MeV neutrons and 100 frames. The image was rotated 1.5° counter-clockwise to straighten the object in the field of view. 416
9.43 FP60R radiograph of Object 2 using 12 to 16 MeV neutrons and 92 frames. The image was rotated 1.5° counter-clockwise to straighten the object in the field of view. 417
9.44 FP60R radiograph of Object 2 using 50 to 70 MeV neutrons and 79 frames. The image was rotated 1.5° counter-clockwise to straighten the object in the field of view. 418
9.45 Features of interest indicated on the FP60R radiograph of Object 2 that was generated with 8 to 12 MeV neutrons. 419
9.46 Two ROIs were selected on the radiographs of Object 2 to generate averaged line-outs and thus gauge the impact of neutron source energy on the ability to image internal features. ROIs are shown in red. . . . 420

9.47 The line-outs associated with the optimal source energy study, which took radiographs of Object 2 with five different energy ranges. Regions and features are labelled, with "GCS" representing gold-coated steel. Only major materials were listed on the line-outs; for a full list, refer to the diagram of Object 2. Top: The averaged vertical line-out associated with the middle ROI. Bottom: The averaged vertical line-out associated with the top ROI. 422
9.48 Close radiograph generated of Object 2 with neutrons of energy 2.5 MeV and below. The centerline of Object 2 is located 5.5 cm from the scintillator. The radiograph was rotated 1.9° counter-clockwise to straighten the object. 425
9.49 Far radiograph generated of Object 2 with neutrons of energy 2.5 MeV and below. The centerline of Object 2 is located 78.7 cm from the scintillator. The radiograph was rotated 2.3° counter-clockwise to straighten the object. 426
9.50 Regions of interest (red) on the close radiograph taken with 2.5 MeV and below neutrons in FP60R. These same ROIs were used on the far radiograph. 427
9.51 Averaged vertical line-outs taken to determine the impact of object location on image quality. Regions and features are labelled, with "GCS" representing gold-coated steel. Only major materials were listed on the line-outs; for a full list, refer to the diagram of Object 2. Top: Top ROI with the close radiograph shown in blue and the far radiograph shown in red. Bottom: Middle ROI with the close radiograph shown in blue and the far radiograph shown in red. 428

9.52 Radiographs from FP15R and FP60R, taken with 2.5 MeV neutrons and below. Top row: Radiographs from FP15R of Object 2, with the left radiograph at an optimal contrast range and the right radiograph at a contrast range matching that of the FP60R radiograph. Both radiographs were cropped. Note that the edge of the scintillator is visible because the mirror was misaligned. Bottom: Radiograph from FP60R of Object 2, set to an optimal contrast range, rotated, and cropped to the same size as the radiographs in the top row. 430

9.53 Radiographs from FP15R and FP60R, taken with 10 to 600 MeV neutrons and below. Top row: Radiographs from FP15R of Object 2, with the left radiograph at an optimal contrast range and the right radiograph at a contrast range matching that of the FP60R radiograph. Both radiographs were cropped. Note that the edge of the scintillator is visible because the mirror was misaligned. Bottom: Radiograph from FP60R of Object 2, set to an optimal contrast range, rotated, and cropped to the same size as the radiographs in the top row. . . . 431

9.54 Radiographs from FP15R and FP60R, taken with spallation photons. Top row: Radiographs from FP15R of Object 2, with the left radiograph at an optimal contrast range and the right radiograph at a contrast range matching that of the FP60R radiograph. Both radiographs were cropped. Note that the edge of the scintillator is visible because the mirror was misaligned. Bottom: Radiograph from FP60R of Object 2, set to an optimal contrast range, rotated, and cropped to the same size as the radiographs in the top row. 432

9.55 Radiographs from FP15R and FP60R, taken with the full LANSCE spectrum. Top row: Radiographs from FP15R of Object 2, with the left radiograph at an optimal contrast range and the right radiograph at a contrast range matching that of the FP60R radiograph. Both radiographs were cropped. Note that the edge of the scintillator is visible because the mirror was misaligned. Bottom: Radiograph from FP60R of Object 2, set to an optimal contrast range, rotated, and cropped to the same size as the radiographs in the top row. 433
9.56 Regions of interest shown in red on 2.5 MeV and below neutron radiographs for FP15R (left) and FP60R (right). 436
9.57 Averaged vertical line-outs taken for Object 2's top ROI in FP60R (top) and FP15R (bottom). Results plotted here have not been normalized to the average flatfield intensity. Regions and features are labelled. Only major materials were listed on the line-outs; for a full list, refer to the diagram of Object 2. 437
9.58 Averaged vertical line-outs taken for Object 2's middle ROI in FP60R (top) and FP15R (bottom). Results plotted here have not been normalized to the average flatfield intensity. Note that the FP15R data has been shifted to the right so features line up vertically. Regions and features are labelled, with "GCS" representing gold-coated steel. Only major materials were listed on the line-outs; for a full list, refer to the diagram of Object 2. 438
9.59 Averaged vertical line-outs taken for Object 2's top and middle ROIs for unnormalized radiographs generated in FP60R and FP15R. For FP60R, the top ROI is shown in blue and the middle ROI is shown in red. For FP15R, the top ROI is shown in green and the middle ROI is shown in purple. Top: Radiography data taken with neutrons of energy 2.5 MeV and below. Bottom: Radiography data taken with the full LANSCE spectrum. 439

9.60 Averaged vertical line-outs taken for Object 2's top and middle ROIs for unnormalized radiographs generated in FP60R and FP15R. For FP60R, the top ROI is shown in blue and the middle ROI is shown in red. For FP15R, the top ROI is shown in green and the middle ROI is shown in purple. Top: Radiography data taken with neutrons of energy 10 to 600 MeV. Bottom: Radiography data taken with spallation photons. 440
9.61 Long exposure radiograph of Object 2 (right), the penetrameter object (top left), and the crack test object (bottom left). This FP60R radiograph was generated with 8 to 12 MeV neutrons and with 1268 frames. 442
9.62 Long exposure radiograph of Object 2 (right), the penetrameter object (top left), and the crack test object (bottom left). This FP60R radiograph was generated with 12 to 16 MeV neutrons and with 1800 frames. 443
9.63 The five ROIs used to generate averaged line-outs of the 8 to 12 MeV and 12 to 16 MeV long exposure neutron radiographs of Object 2 (right), the penetrameter object (top left), and the crack test object (bottom left). 444
9.64 The features of interest in the long exposure radiographs, which are contained within the five selected ROIs, depicted on the 8 to 12 MeV normalized neutron radiograph. 445
9.65 Averaged line-outs for the long exposure radiographs of the penetrameter object, with features of interest labelled with the hole depth indicated. Top: Averaged vertical line-out of the ROI in the penetrameter object for radiographs generated with 8 to 12 MeV and 12 to 16 MeV. Bottom: Averaged horizontal line-out of the ROI in the penetrameter object for radiographs generated with 8 to 12 MeV and 12 to 16 MeV. 446

9.66 Averaged line-outs of the crack test object for the long exposure radiographs. No features of interest are seen in these line-outs. Top: Averaged vertical line-out of the ROI in the polyethylene region of the crack test object for radiographs generated with 8 to 12 MeV and 12 to 16 MeV neutrons. Bottom: Averaged horizontal line-out of the ROI in the steel region of the crack test object for radiographs generated with 8 to 12 MeV and 12 to 16 MeV neutrons. 448
9.67 Long exposure (1268 frames) radiograph of Object 2 (left) compared to the short exposure (70 frames) radiograph (right). Both radiographs were taken in FP60R and used 8 to 12 MeV neutrons. 450
9.68 Long exposure (1800 frames) radiograph of Object 2 (left) compared to the short exposure (100 frames) radiograph (right). Both radiographs were taken in FP60R and used 12 to 16 MeV neutrons. 451
9.69 Averaged line-outs for the long exposure ("long exp.") and short exposure ("short exp.") radiographs of Object 2. Regions and features are labelled, with "GCS" representing gold-coated steel. Only major materials were listed on the line-outs; for a full list, refer to the diagram of Object 2. Top: Averaged vertical line-out of the ROI in the top of Object 2 for radiographs generated with 8 to 12 MeV and 12 to 16 MeV neutrons. Bottom: Averaged vertical line-out of the ROI in the middle of Object 2 for radiographs generated with 8 to 12 MeV and 12 to 16 MeV neutrons. 452
9.70 Radiographs of the crack test object through 3 in of DU and using the 8 to 12 MeV time gate. Top: Long-exposure flatfield used for normalization. Bottom: Short-exposure flatfield used for normalization. Note that the image quality is worse than the top radiograph. 455

9.71 Radiographs of the crack test object through 3 *in* of DU and using the 12 to 16 MeV time gate. Top: Long-exposure flatfield used for normalization. Bottom: Short-exposure flatfield used for normalization. Note that the image quality is worse than the top radiograph. 456

9.72 Features of interest in the 8 to 12 MeV radiograph processed with the long exposure flatfield. The fission chamber attached to the beam pipe can be seen as a circular object with three holes in it. The crack test object appears as three objects in this radiograph, and the boundaries of the DU plates are also visible. 457

9.73 The ROI selected on the DU radiographs, after rotating the images 1.5° counter-clockwise, to generate averaged vertical and horizontal line-outs. 458

9.74 Unnormalized averaged vertical line-outs for the neutron radiographs of the DU plates and crack test object (labelled as "frame", "poly." (polyethylene), and "steel"). Features of interest in the radiograph are labelled on the plots. Top: Generated with the 600 frame ("fr.") flatfield image and 600 frame radiograph. Bottom: Generated with the 1800 frame flatfield and 600 frame radiograph. 459

9.75 Unnormalized averaged horizontal line-outs for the neutron radiographs of the DU plates and crack test object (labelled as "frame", "poly." (polyethylene), and "steel"). Features of interest in the radiograph are labelled on the plots. Top: Generated with the 600 frame ("fr.") flatfield image and 600 frame radiograph. Bottom: Generated with the 1800 frame flatfield and 600 frame radiograph. . . 460

9.76 Radiographs of the crack test object through 3 *in* of DU at its thickest location. The average intensity of the short-exposure flatfield was used for normalization. The radiographs were formed with neutrons of 8 to 12 MeV (top left), 12 to 16 MeV (top right), and 50 to 70 MeV (bottom) in energy. 462

9.77 Normalized averaged line-outs for the neutron radiographs of the DU plates and crack test object (labelled as "frame", "poly." (polyethylene), and "steel"). Features of interest in the radiograph are labelled on the plots. Top: Averaged vertical line-out. Bottom: Averaged horizontal line-out. 464
9.78 DU radiographs post-processed to represent I/I_0 values. Top: Radiograph generated with 8 to 12 MeV neutrons. Bottom: Radiograph generated with 12 to 16 MeV neutrons. 466
9.79 Two ROIs used to find the average I/I_0 value for 1 in and 3 in thicknesses of DU. The ROIs are shown in red on the 8 to 12 MeV neutron radiograph. 467
9.80 Simulated total (direct and scatter) neutron radiographs (including effects from secondary photons) for an 8 to 12 MeV neutron source (top) or a 12 to 16 MeV neutron source (bottom). 470
9.81 ROIs (red) used to find the average I/I_0 values for simulated radiographs of DU plates. 471
9.82 Simulated direct neutron radiographs generated with an 8 to 12 MeV neutron source (top) or a 12 to 16 MeV neutron source (bottom). . . 474
9.83 *Log* plot of transmission as a function of incident neutron energy for five materials radiographed in FP15R or FP60R: borated polyethylene ("b-poly."), graphite (^{12}C), lead (^{207}Pb), depleted uranium (^{238}U), and tungsten (^{184}W). Materials are listed in the legend according to increasing density, and calculations are based on ENDF/B-VII.1 total cross-section data (note: ^{238}U data only listed for energies up to 30 MeV) [52]. 479

9.84 *Log* plot of mean free path as a function of incident neutron energy for five materials radiographed in FP15R or FP60R: borated polyethylene ("b-poly."), graphite (^{12}C), lead (^{207}Pb), depleted uranium (^{238}U), and tungsten (^{184}W). Materials are listed in the legend according to increasing density, and calculations are based on ENDF/B-VII.1 total cross-section data (note: ^{238}U data only listed for energies up to 30 MeV) [52]. 481

9.85 Semi-*log* plot of the number of mean free paths in each of the five materials radiographed in FP15R or FP60R: borated polyethylene ("b-poly."), graphite (^{12}C), lead (^{207}Pb), depleted uranium (^{238}U), and tungsten (^{184}W). Materials are listed in the legend according to increasing density, and calculations are based on ENDF/B-VII.1 total cross-section data (note: ^{238}U data only listed for energies up to 30 MeV) [52]. 482

9.86 *Log* plot of the material thickness necessary, as a function of incident neutron energy, to reduce the incident neutron flux to 1% (top) or 0.1% (bottom) of its initial value. Materials are listed in the legend according to increasing density, and calculations are based on ENDF/B-VII.1 total cross-section data (note: ^{238}U data only listed for energies up to 30 MeV) [52]. 483

9.87 Semi-*log* plot of the fraction of the 1% (top) and 0.1% (bottom) thickness that was radiographed at LANSCE. Materials are listed in the legend according to increasing density, and calculations are based on ENDF/B-VII.1 total cross-section data (note: ^{238}U data only listed for energies up to 30 MeV) [52]. 484

9.88 Semi-*log* plot of transmission through the experimental thicknesses of the graphite cylinder (^{12}C) and tungsten sphere (^{184}W) that were radiographed in FP15R. Monoenergetic neutrons of 2.5 and 10 MeV were compared to monoenergetic x-rays of the same energies. Neutron total microscopic cross-section data were taken from the ENDF/B-VII.1 library, while x-ray total attenuation coefficients were taken from the NIST XCOM database [52, 81]. 486

9.89 Top: Example of the line-out used to quantify FP60R beam non-uniformity. The line is demonstrated on the 2 to 3 MeV neutron flatfield. Bottom: Line-outs for the four flatfield images taken in FP60R that match some of the energy bins used in FP15R. Pixel grayscale values were normalized to the number of total pulse accumulations in each energy bin. 488

9.90 Line-outs for the five flatfield images taken in FP60R for several studies. Pixel grayscale values were normalized to the number of total pulse accumulations in each energy bin. 490

Nomenclature

σ	Cross-section
ALARA	As low as reasonably achievable
B-poly	Borated polyethylene
CCD	Charge-coupled device
Crack test object	Polyethylene and steel blocks, with cracks in the polyethylene and holes in the steel; radiographed in FP60R
CSDA	Continuous slowing-down approximation
CTF	Contrast transfer function
D-D	Deuterium-deuterium neutron source
D-T	Deuterium-tritium neutron source
DU	Depleted uranium; three 1 *in* plates were radiographed in FP60R
EJ-212	Fast plastic scintillator manufactured by Eljen
$f/\#$	Aperture size
*F*4	Volumetric flux tally

FIR	Voxellated radiography tally
$FMESH$	Voxellated volumetric flux tally
FOV	Field of view
$FP15R$	Flight Path 15 Right
$FP60R$	Flight Path 60 Right
$ICCD$	Intensified charge-coupled device
$ImageJ$	Freeware used for image editing
keV	Kilo-electron volt
$LANL$	Los Alamos National Laboratory
$LANSCE$	Los Alamos Neutron Science Center
LED	Light-emitting diode
Li-poly	Lithiated polyethylene
$LLNL$	Lawrence Livermore National Laboratory
LSF	Line spread function
$MCNP6$	Monte Carlo N-Particle code, Release 6
MeV	Mega-electron volt
Mod	System modulation
MTF	Modulation transfer function
NDA	Non-destructive analysis
Object 1	Configuration of graphite cylinder, lead block, sheet of paper, and borated polyethylene block; radiographed in FP15R

Object 2	Cylindrical object composed of polypropylene, tungsten, nylon, stainless steel, and gold-coated stainless steel; radiographed in FP15R and FP60R
Object 3	Tungsten sphere; radiographed in FP15R
ORNL	Oak Ridge National Laboratory
Penetrameter	Block with holes of various diameter and depth to determine spatial and contrast resolution; a polyethylene version was radiographed in FP60R
Q	Threshold energy for an inelastic scattering reaction
ROI	Region of interest
SNF	Spent nuclear fuel
TiGReSSE	Time Gating to Reject Scatter and Select Energy
TOF	Time-of-flight
Z	Atomic number

Chapter 1

Introduction

For many reasons in the field of engineering, it is desirable to assess the physical characteristics of a system, such as structure, composition, strength, and other similar properties. Such system characteristics often affect the safety, integrity, longevity, and operation of the system in question, making it very important to ascertain system properties in a timely and effective manner. As a result, a wide range of measurement techniques have been developed over the years to meet this need. Such investigative methods are often divided into two categories: destructive and non-destructive analysis.

Destructive analysis is defined as an assay method that alters the object being measured in some irreversible way, such as a stress test to determine when a material will deform or break. Non-destructive analysis (NDA), on the other hand, preserves the integrity of the object by not significantly changing its properties. NDA is therefore useful for analyzing systems that must remain operational after testing (e.g., an airplane wing) or when population sample sizes are too small to warrant destructive testing (e.g., a nuclear reactor containment vessel). Examples of NDA techniques include weighing an object to determine mass, performing ultrasonic inspection, injecting dyes to track liquid flow, using a microscope to examine object surfaces, and generating images of an object's interior via radiography [1].

This latter method, radiography, is especially useful because it allows an inspector to find internal flaws that may otherwise go unnoticed until system failure. Radiography is similar to photography in that a radiation source is allowed to interact with an object and an image is formed by measuring these interactions via a sensor, such as film or a digital array. In photography, the source is visible light and the interaction is light reflection from the object surface onto the sensor. Radiography, on the other hand, passes radiation through the object so it may interact in the object via a reaction of interest (e.g., scatter or fission) before being measured by a sensor.

Often in radiography, the radiation, after interacting in the object, is converted into light in order for the signal to be measured by a sensor. For such visible light radiography systems, optical considerations are important for two stages of the imaging process: pre-converter (i.e., the radiation passing through the object and falling upon the converter), and post-converter (i.e., the visible light leaving the converter and reaching the sensor) [2]. The quality of the radiography images is thus a direct result of the successful application of optical principles during system design and use. For this reason, a radiography system (i.e., the interrogation source, the imaging sensor(s), and the method of imaging) must be tailored to the particular object being studied and the type and location of flaws that are of interest to NDA [2].

One particularly challenging area in NDA is the radiography of large, dense objects. Objects such as these can be difficult to penetrate with radiation, and thus require the use of high-energy radiation sources. These sources can increase dose to employees and the object being evaluated, and tend to activate their housing. Additionally, large, dense objects create large scatter fields that reduce image quality and in general make imaging very difficult. For these reasons, a radiography system for large, dense objects requires special engineering considerations that have prevented the design of such a system to date.

This introductory chapter will begin by providing background on general radiography principles as they apply to NDA, focusing in particular on the imaging sensors and radiography source that comprise the system. An explanation of the general

optics principles that must be employed in the design of a visible light radiography system will follow. Subsequent chapters will discuss current gaps in radiography technology, the novel contributions of this project to the field of radiography, and completed and future work toward the development of this system.

1.1 An Overview of Radiography

This section will provide an overview of radiography systems by discussing common radiation sources used for radiography. The category of imaging system is typically defined by the type of interrogation source, so it is logical to begin this chapter with the source. Starting the discussion with the source also allows the reader to move through the imaging process in a step-by-step manner and follow the radiation, so to speak, from the source to the detector.

Radiation sources for imaging vary widely according to the application. Charged particles, such as protons and electrons, are used for radiography but only are capable of imaging shallow depths. This is because charged particles interact with the electrons of the material, resulting in a much shorter average travel distance than uncharged particles, such as neutrons. While charged particles are useful for imaging object surfaces, such as with an electron microscope, they cannot be used to image an object interior. Uncharged particles, commonly x-rays but also neutrons, are therefore preferable for NDA imaging because they penetrate farther into the object being imaged and can radiograph more attenuating objects. Since the imaging system that is currently being designed will image dense, large objects, only uncharged particle sources are considered in this paper.

1.1.1 Photon Radiography

Almost everyone in their lives has had a medical x-ray image taken for reasons like a broken bone. This ubiquitous technology is very useful for imaging objects that

have a clear distinction between high density and low density regions (e.g., bone and skin). This is because photons are attenuated by high-Z materials but pass through low-Z materials relatively unattenuated. As a result, thick, high-Z material regions are not imaged well with x-rays, due to reduced image statistics and image resolution. Thus, to radiograph large, dense objects, another form of neutral radiation must be employed, even if employing higher energy photon sources (such as 9 or 15 MeV bremsstrahlung sources) [2–4].

1.1.2 Neutron Radiography

Unlike x-rays, which interact with the orbital electrons of the materials in the object being imaged, neutrons interact with the nucleus. This results in image properties that are dependent on the object's elemental (i.e., nuclear) composition instead of the object's density (which is directly related to the number of electrons and thus the property seen in x-ray radiographs) [2]. This fact is useful because neutrons (and in particular, high-energy neutrons) can penetrate much deeper into a thick, dense object than x-rays. It is for this reason that high-energy neutrons were selected as the radiation source, and for the remainder of this document, the source will be assumed to be neutrons unless otherwise stated.

As stated earlier, neutrons interact with the nucleus. For this reason, neutron radiography provides material-dependent information as a function of material location in the object being imaged. More specifically, neutron imaging generates a map of the attenuation coefficients of the material, where each pixel value is the sum of the attenuation of the materials that the pixel "sees". Mathematically, this concept is described by the flux attenuation relationship for uncharged particles,

$$I(x) = I_0 \; exp\left(-\sum_n \sigma_n t_n\right), \tag{1.1}$$

where I_0 is the initial flux incident on the object ($particles/\left(cm^2 s\right)$), t_n is the chordal length of region n (cm), σ_n is the macroscopic cross-section of region n (cm^{-1}), and $I(x)$ is the transmitted flux through the object ($particles/\left(cm^2 s\right)$). Here, I_0 is the source strength and $I(x)$ is the pixel signal. Thus, image contrast varies with attenuation according to σ_n, where the contrast is the pixel grayscale value that can range from white to black [2, 3, 5].

Many types of neutron sources exist, including isotopic sources, nuclear reactor beam ports, and particle accelerators. Some sources contain neutrons with many energies ("polyenergetic"), whereas other sources are of a single energy ("monoenergetic"). Polyenergetic neutron sources are often formed using a conversion target with a charged particle beam or a photon source [2]. Target 4 at the Los Alamos Neutron Science Center (LANSCE), for example, uses a pulsed 800 MeV proton beam incident on a tungsten target to generate spallation neutrons and, as a by-product, photons. The neutron spectrum varies according to angle and distance from the tungsten target and intermediate shielding of the beam itself, but at unmoderated Flight Path 15R (FP15R), neutrons range in energy from hundreds of keV to approximately 600 MeV [6, 7]. Another example of a polyenergetic neutron source is Lawrence Livermore National Laboratory's (LLNL's) proposed boosted deuterium-deuterium (D-D) source that generates neutrons ranging in energy from 1.7 MeV to 10.2 MeV as a function of angle [8].

As for monoenergetic sources (noting that they still have small ranges in energy as a function of angle), the deuterium-tritium (D-T) reaction generates monoenergetic fast neutrons ($E_n = 14\ MeV$). Another common monoenergetic neutron source is the unboosted D-D reaction which yields moderately fast neutrons of $E_n = 2.5\ MeV$ [9].

When choosing the source, it is important to consider whether a monoenergetic or polyenergetic source is desired for the NDA problem at hand. As stated earlier, large, dense objects contribute a large amount of scatter to the image which reduces contrast and degrades image quality. According to time-of-flight principles, scattered neutrons arrive much later in time than the direct, unscattered signal because they

have suffered energy losses and/or directional changes. A fast-pulsed monoenergetic source and a fast detector system, in theory, allows for a clean rejection of scatter if time binning of the detector(s) is properly applied. Thus, for the types of objects being considered in this document, a monoenergetic source is much preferred so as to improve image quality through the rejection of scatter.

Conversely, a pulsed polyenergetic source is not ideal for time-of-flight scatter rejection. Downscatter from upper energy bins can arrive at the same time as direct signal from a lower energy bin. This causes scatter to contaminate direct signal, preventing the two from being completely separated by time-of-flight methods. While it is true that partial scatter rejection is better than no scatter rejection, images do not benefit nearly as much as they would with a monoenergetic source [2].

A pulsed polyenergetic source is, however, useful for material identification. As defined in Equation 1.1, neutron transmission properties are dependent on the neutron macroscopic cross-section, which, in turn, is dependent on the incident neutron energy. By varying the incident neutron energy, material attenuation in a transmission image is also varied, and thus contrast may provide material-dependent information. Gating the detector(s) in time can thus be used to image with specific portions of the polyenergetic neutron spectrum and allow for comparison of contrast changes as a function of energy. A monoenergetic source could be employed for this application if a spallation target is added to the system design; the spallation target would allow for the generation of a polyenergetic spectrum and allow for dual-use of the monoenergetic source.

It should be noted that some neutron energies may be more desirable than others for imaging certain materials or features. This is because material cross-section values may drive energy selection, and features in one material region may require a different incident neutron energy than another region. Therefore, source energy can and should be tailored to the object undergoing NDA to maximize the visibility of features of interest [2].

1.2 Detectors for Radiography Applications

Now that the types and uses of uncharged radiation sources for radiography applications have been discussed, detector systems mentioned briefly in Section 1.1 will be more completely addressed. The imaging sensors are particularly important because they form the image after the radiation interacts in the object of interest. In this section, imaging detectors are divided into two categories: film and digital.

1.2.1 Film Systems

The original form of imaging sensor, film systems come in a variety of forms that have been expanded over many decades of use. The benefits of using film include its simple and cost-effective implementation; the generation of a permanent, physical image; excellent spatial resolution; and the ability to take long exposures without the in-growth of electronic noise. When imaging with visible light, such as with photography, the light induces a physical change in the film that can then be treated with chemicals to produce a photograph. However, when using a radiation source that does not directly expose film (e.g., neutrons), a converter screen must be used to convert the incident radiation into photoeffective radiation such as charged particles or photons [10].

For fast neutrons, the conversion process is dependent upon the (n, p) scatter reaction. Once scattered, the kinetic energy of the recoiling proton is absorbed by the scintillator and released in the form of heat and visible light. A good scintillator is thus transparent to allow light emission, and should yield more light than heat (which is wasted energy since it is not used for radiography). Once emitted, this light is then used to expose the film. Typically, organic scintillators are used as converters for fast neutron radiography due to large hydrogen (and thus large proton) content. While carbon recoil is possible in a plastic scintillator, a neutron can only transfer up to 28% of its energy to a carbon nucleus, as compared to 100% of its energy in a head-on collision with a proton [2, 11, 12]. Thermal neutrons, on the other hand,

require a scintillator converter that emits charged particles, either from capture or from internal conversion electrons, such as lithium-doped glass [2].

Another method of using film to image high-energy neutrons is to use a plastic detector, such as a cellulose nitrate plastic produced by Kodak. The high-energy neutrons etch tracks in the plastic, with track density directly correlated to neutron flux through an object. Reference [13] describes a neutron radiography system in which helium gas was used to convert the neutrons into alpha particles, a photoeffective radiation, thereby increasing the detection efficiency of the plastic detectors.

Other types of converter materials for use with film include granular composites, doped glass, and metal foils. Converter materials are chosen according to the incident radiation energy and their particular properties (e.g., inherent spatial resolution and stopping power). Referring to Figure 1.1, it can be seen in a typical knife-edge measurement (described in detail later in this chapter) that three screens of different materials have a varying ability to image an object edge due to their differing material properties. As will be explained later, the sharper that this edge appears in the image, the better the imaging performance [10].

1.2.2 Digital Systems

Digital systems, such as CCD cameras, use methods similar to film, but instead of exposing film with visible light, a digital array of pixels is exposed inside a camera-lens system. The image is then formed when the pixel values are read out of the camera and transferred to a storage system such as a computer or a storage card internal to the camera [2]. Intensifiers can be used to multiply the signal levels detected by the camera, thereby increasing light sensitivity and improving the signal-to-noise ratio of the device [14]. Similar to film methods, digital systems must use converters to obtain an optical light signal that can be detected to form images. The two methods differ,

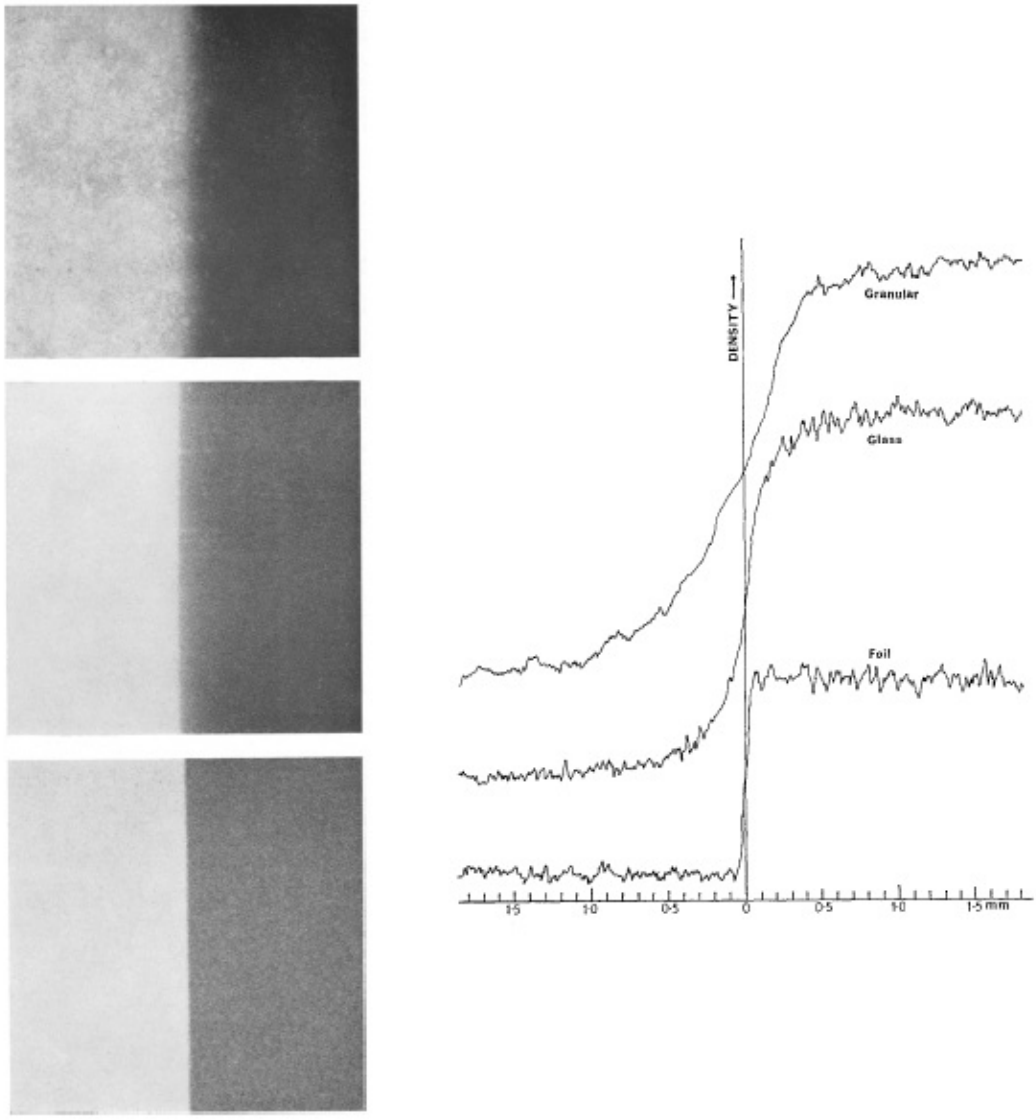


Figure 1.1: Left: Three knife-edge images, each generated by a different scintillator (top: granular; middle: glass; bottom: foil). Resolution of the edge visibly increases from top to bottom. Right: Graph of "line-outs", corresponding to the three images at left, that plot the change in grayscale value across the edge and thus quantify the resolution [10].

however, in that film systems can use charged particles or visible light for imaging, whereas digital systems (e.g., CCD camera) must solely use visible light [11].

For imaging large, dense objects, a gated CCD camera is particularly of interest because it may be used with time-of-flight methods to reject the scatter that is problematic for radiographing these types of objects. A gated detector can be turned on and off at appropriate times, as determined by time-of-flight calculations, to accept direct neutrons and reject scatter. In contrast, time-insensitive detectors, such as storage phosphors, cannot differentiate between direct signal and scatter and are therefore ill-suited for this application [2].

Often, a mirror is used to reflect light from the converter onto the digital sensor so that the electronics can be kept out of the direct path of the radiation source, reducing the likelihood of activation of and damage to the sensor (Figure 1.2). This also reduces radiation interference on the pixellated sensor that can lead to bright spots in the image, commonly called "stars". These stars make image post-processing difficult, particularly by distorting the contrast range of the image. If used, mirrors must be treated with an anti-reflective front surface coating so that optical scatter within the mirror is not reflected toward the camera, but is stopped at the front of the mirror [11].

Reference [14] outlines some of the desirable features of digital imaging systems, including high sensitivity and efficiency; fast readout/high frame rate; good linearity and spatial resolution; a post-processing ability; and the ability to employ tomographic methods. Another positive feature of a digital radiography system is real-time imaging that allows for immediate image viewing and manipulation, whereas film which must undergo a comparatively lengthy development process [10].

As a final note on converter screens, several factors in their design must be taken into account. First, as stated earlier, a high-energy neutron source typically uses plastic screens due to the high density of hydrogen in the material. However, the probability of the (n, p) reaction decreases as the neutron energy increases because of

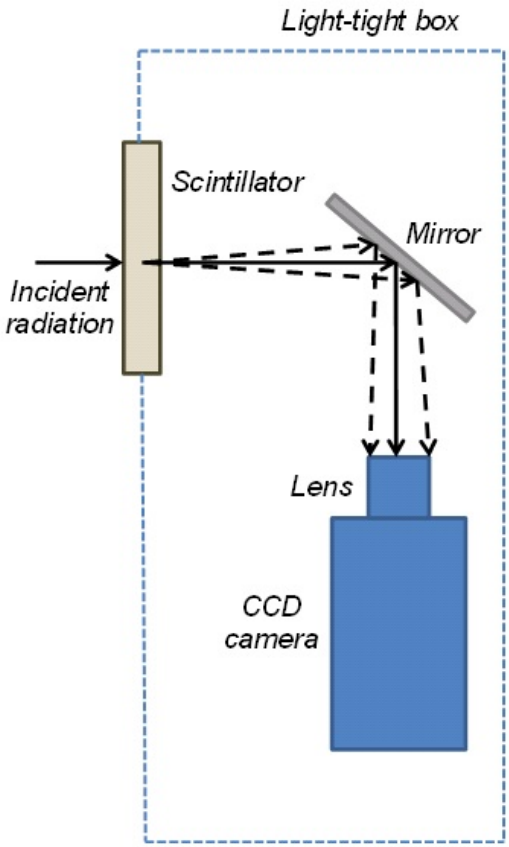


Figure 1.2: Diagram of a typical CCD radiography system. Radiation, after interacting in the radiography object, strikes a screen and is converted into visible light. A mirror angled at 45° then reflects this light into the lens of the CCD camera, so as to form an image on a digital array.

the decreasing interaction cross-section. Rough calculations have shown an interaction probability of approximately 2% for 14 MeV neutrons incident on a Eljen $EJ-212$ 5 mm thick plastic scintillator. Logically, this would suggest a converter screen should be thick to increase the probability of neutron interactions in the screen. However, a thicker screen reduces spatial resolution by increasing image blur, and so a balance must be struck between detector efficiency and resolution [15].

The second design consideration is that the scintillator converter must have a short decay time for use with high-energy time-of-flight neutron radiography; slow decay times lead to blurring and uncertainty in the time resolution of the system. This is undesirable for employing scatter rejection principles, which require very precise timing. Additionally, for conducting neutron radiography with a mixed source (such as an isotope that emits both gammas and neutrons or the LANSCE source described earlier in this chapter), a neutron converter with a low photon cross-section is desirable to reject photons that would pollute the image and could contribute to scatter [2].

1.3 Optical Considerations for a Radiography System

For radiography to be useful for NDA, the principles of optics must be properly applied during the design and operation of the imaging system. For example, the system must have the correct focus and magnification of features for easy and accurate NDA. Figure 1.3 is an example of a radiography image taken by a carefully-designed neutron radiography system. Neutrons are able to penetrate the high-Z container to image the rose located inside of it, which would most likely not be possible with an x-ray source [2]. This section outlines optical properties that directly affect image quality and provide quality images such as that in Figure 1.3.

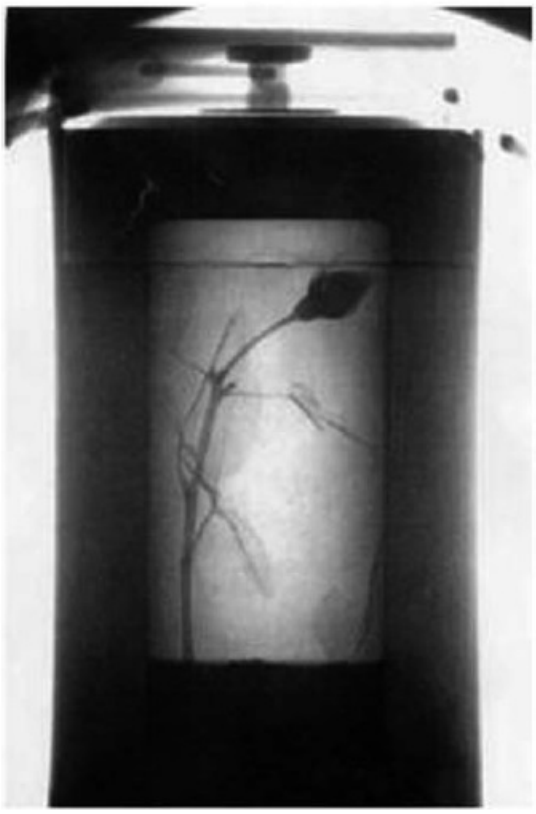


Figure 1.3: Neutron radiograph of a rose inside a lead cylinder. This example illustrates the ability of a neutron source to penetrate high-Z material, such as lead, and differentiate between densities [2].

1.3.1 Spatial Resolution

One very important parameter to consider when designing a useful radiography system is the spatial resolution of the system. The concept of spatial resolution, as defined in optics, describes the ability to distinguish two separate, parallel lines (referred to as line pairs) in an image. To determine the system's spatial resolution limit, the space between the lines is reduced until the two lines appear as a single line and they are no longer resolvable [16]. This implies that a system with a higher spatial resolution can discern smaller object features, such as a crack or material boundary, in the image. Thus, the smaller the feature that can be seen in the image, the better the spatial resolution.

Spatial resolution can be degraded by many system characteristics, such as the type of radiation source, the thickness of the scintillator screen, and the resolution of the detector [2]. If a radiation source results in increased scatter, this can hinder the ability to resolve features by increasing noise. This is because scattered radiation loses its directional and energy information and is rendered useless for image generation while still contributing to the detected signal. Similarly, a thick scintillator screen can lead to blurring, or "unsharpness", due to increased scatter within the screen [17]. Background noise, such as electronic noise in a digital system, also reduces spatial resolution [2].

Thus, the spatial resolution is a function of the imaging system and is comprised of a geometry component and a detector component [10]. Empirically, the total system unsharpness, U_{tot}, is the convolution of the geometric unsharpness and the inherent unsharpness, U_i, present in the detector. One such empirical relationship for U_{tot} is found by

$$U_{tot} = \left(U_g^3 + U_i^3\right)^{\frac{1}{3}}, \tag{1.2}$$

although other equations exist in the literature [10].

The geometry component is affected primarily by the distances between the source and object, and between the object and detector. This effect can be reduced by careful

collimation of the source. Often this is done by maximizing the "L/D ratio", which is a ratio of the source-to-object distance (L) to the beam aperture diameter (D) such that

$$Collimation \propto L/D. \tag{1.3}$$

The greater this ratio (i.e., the farther the source is from the object), the more parallel the beam becomes at the object and the smaller the geometric blurring becomes in the image. However, this improved resolution must be balanced with a reduction in the source flux reaching the detector, since flux decreases in space according to $1/\left(L+S\right)^2$ if S is the distance from the object to the detector. This trade-off is logically determined by the system's parameter space [17]. Additionally, if the object is close to the detector, geometric blur is further minimized. This concept is shown in Figure 1.4.

Once the L/D ratio is maximized, some geometric unsharpness, U_g, will inevitably remain. The geometrical component of the total blur can thus be calculated by

$$Blur = S\left(\frac{D}{L}\right), \tag{1.4}$$

using previously-defined variables [17].

The blur resulting from the detector, or the inherent resolution of a system, U_i, should also be characterized. The standard practice for determining the system resolution is to find the modulation transfer function (MTF) of the system [18]. As defined, a transfer function is the Fourier transform of an equation, converting it from the spatial domain to the frequency domain. This is useful because in the spatial domain, convolutions are often necessary to determine the response of a system (e.g., a detector) to a stimulus (e.g., incident radiation). However, in the frequency domain, these components can simply be multiplied, making the mathematics much easier.

It should be noted that, because of how it is defined, the MTF only applies to sinusoidal stimuli. Common properties of sinusoids include the frequency (f; units of

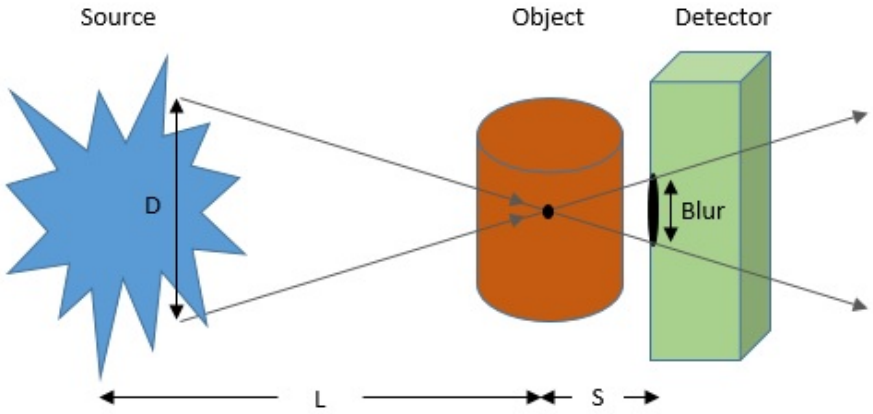


Figure 1.4: Feature blur, a result of source spot size, is reduced by maximizing the L/D ratio.

Hz or $cycles/s$), period (T; units of s), and wavelength (λ; units of nm, typically), where T describes the length of the wave for exactly one cycle, f describes the number of cycles in one second, and A describes the amplitude, or height, of the wave (Figure 1.5) [16, 19]. These three quantities are related by

$$f = \frac{1}{T} = \frac{v_{wave}}{\lambda}, \tag{1.5}$$

where v_{wave} is the wave velocity and is equal to the speed of light for a light wave [20].

With transfer functions thus defined, their application to imaging systems can be explained. In an ideal imaging system, a point source would appear as a point in the image. However, real-world systems are imperfect and have some amount of distortion and blurring. In the frequency space, this addition of blur is described by

$$F(\xi, \eta) \times H(\xi, \eta) = G(\xi, \eta), \tag{1.6}$$

where ξ is the spatial frequency in the x-direction, η is the spatial frequency in the y-direction, $F(\xi, \eta)$ is Fourier transform of the ideal image, $H(\xi, \eta)$ is the system response to stimulus (i.e., a blurring term), and $G(\xi, \eta)$ is the resultant Fourier transform of the real-world image that has some degradation in resolution [16].

Equation 1.6 can be applied to each component of the system to generate i individual transfer functions, $H_i(\xi, \eta)$ (e.g., in a CCD imaging system, one for the camera lens, one for the mirror, and one for the converter screen). These transfer functions are then multiplied together to form a total transfer function for the entire system, which is then applied to the stimulus $F(\xi, \eta)$ [16]. If the system is linear, $H(\xi, \eta)$ will remain the same, regardless of the stimulus. While real-world systems are not truly linear, this approximation is typically valid.

As ξ and η of the sinusoidal input increase, the sinusoidal output amplitude, A, decreases due to blurring and optical interference. This variation in amplitude as a function of input frequency is called the system modulation, Mod, that has values

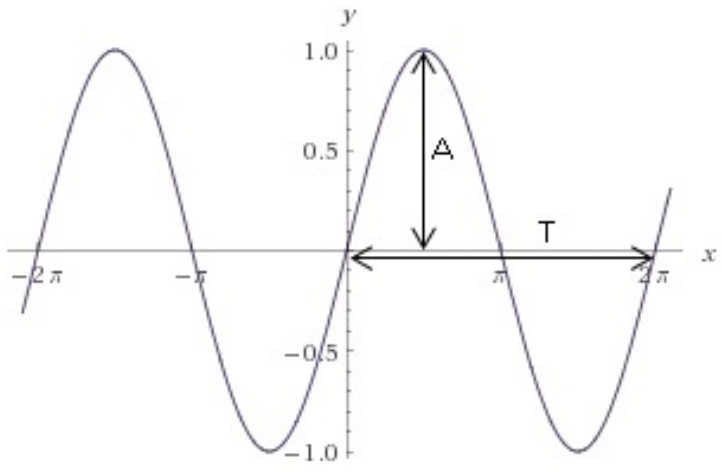


Figure 1.5: Illustration of period, T, and amplitude, A, on the plot of $y = \sin x$ [19].

between 0 and 1 such that

$$Mod = \frac{A_{max} - A_{min}}{A_{max} + A_{min}}, \tag{1.7}$$

where A_{max} is the maximum amplitude value and A_{min} is the minimum amplitude value. Eventually, ξ and η reach values where the resultant modulation is very small and the blurring term is very large, so that features in the image are no longer resolvable. This corresponding modulation value is known as the modulation limit of the system and is illustrated in Figure 1.6 [16].

Consider the modulation of a grayscale image, where A_{min} corresponds to black (i.e., total absorption) and A_{max} corresponds to white (i.e., pure reflection). Mid-scale values that lie somewhere in the middle are gray. Based on this definition, a perfectly-resolved image would range between pure black and white because it would span the entire modulation scale [21]. In a real-world system with decreased resolution, the image would have a reduced modulation scale that does not extend all the way up to white or down to black, resulting in an image purely in shades of gray. Eventually, as input frequency increased, the gray shades would become so close together in contrast that they would no longer be distinguishable. This is defined as the modulation limit (and thus the contrast resolution limit) of the system [22]. By then converting from the frequency domain back to the spatial domain, the corresponding spatial resolution can be found. Sinusoids with full and reduced modulation are illustrated in Figure 1.7 [16].

It is not enough, when comparing systems, to simply state the modulation limit of the system. Two systems could have the same modulation limit, but have vastly different MTF curves. In Figure 1.8, curves A and B have the same limiting resolution. However, A has a much higher, and therefore better, modulation than B, making it a better system. Thus, it is important not to oversimplify the ability of a system by citing a single number [16].

Now that the theory of the MTF has been introduced, methods for measurement of the MTF in the laboratory will be discussed. First, to determine the blurring

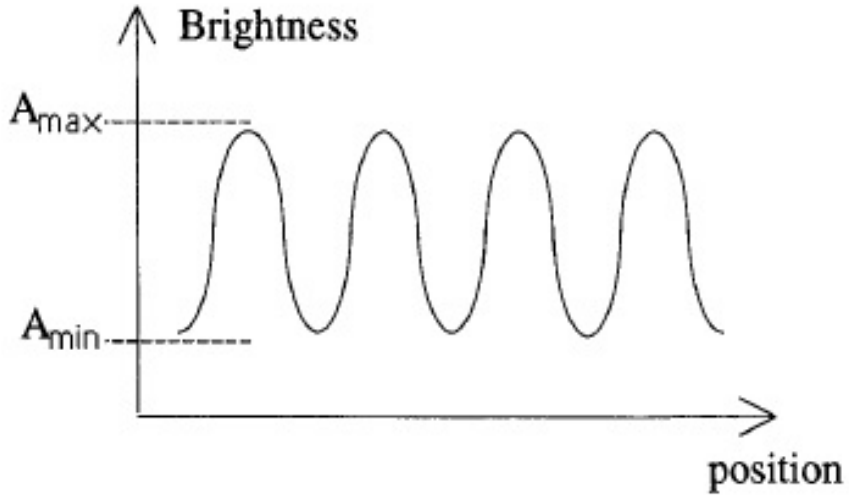


Figure 1.6: Illustration of the modulation depth of a system, with A_{max} and A_{min} equal to the maximum and minimum signal amplitude, respectively [16].

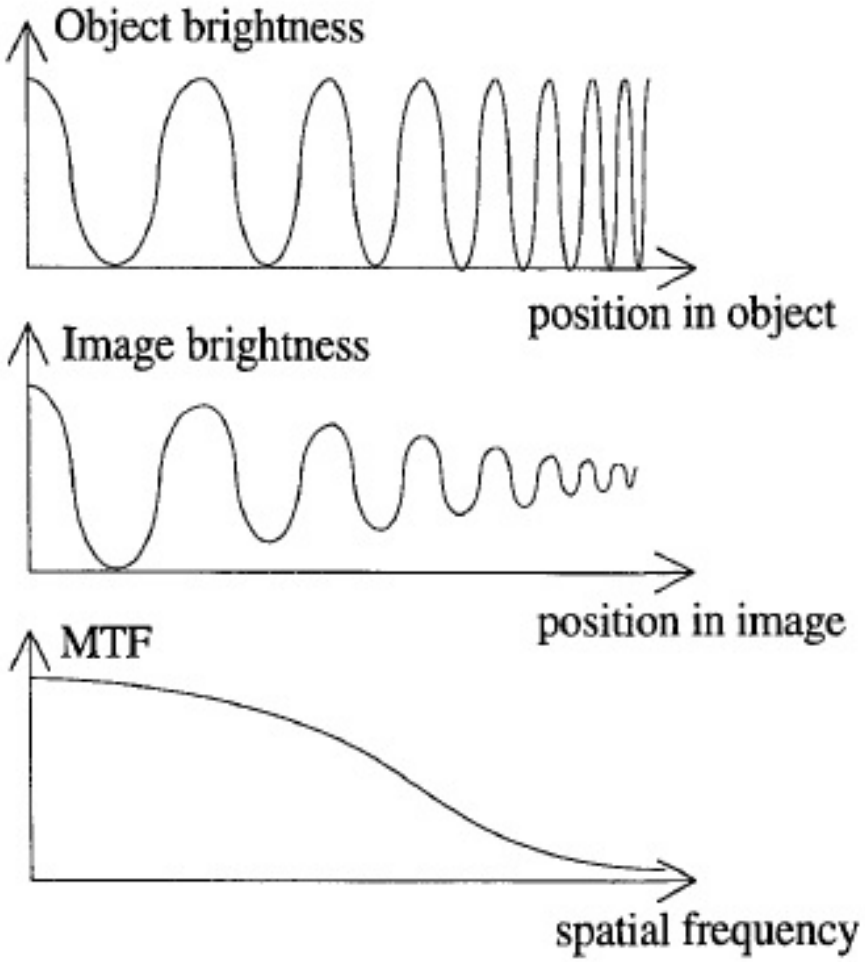


Figure 1.7: Top: The input frequency increases as position in the object changes. Middle: The brightness of a real-world image, after blurring terms have been applied, decreases in amplitude as the input frequency increases. Bottom: The MTF of the system, $H(\xi, \eta)$, also decreases with increase in frequency. The system user would need to decide, based on their needs, what the minimum acceptable resolution limit would be [16].

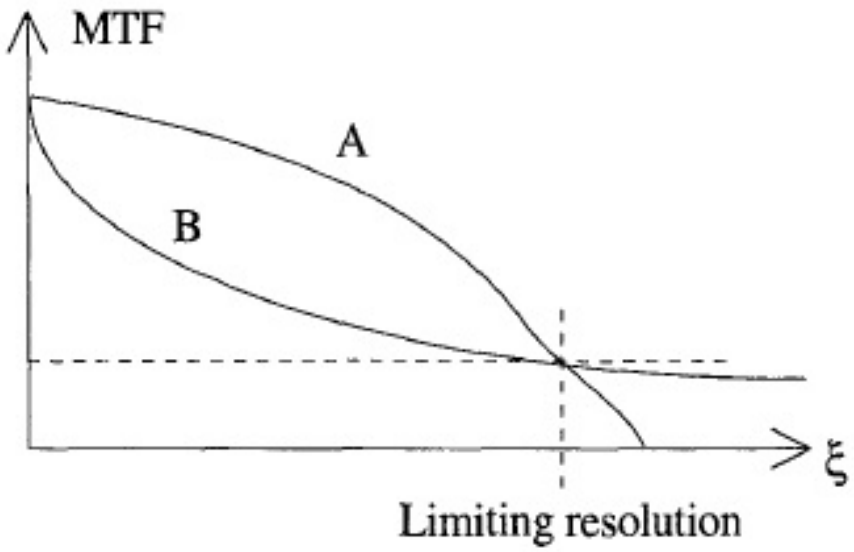


Figure 1.8: An illustration of the MTF for two systems, A and B. Although A and B have the same resolution limit, A is a better system because it has higher modulation [16].

term of the detector, $H(\xi, \eta)$, flatfield (i.e., shutter is open to detect the beam, but no object is present) and background (i.e., shutter is closed, but beam is on) images must be taken. The background image is subtracted from the experimental image to remove noise, and this result is then divided by the flatfield image for normalization to variations in source intensity across the field of view [2].

Next, to determine the MTF of the entire system, a "knife-edge" experimental image of an object edge is generated. A vertical edge, such as the edge of a block of tungsten, is placed in front of the lens system and the lens is focused until the edge comes into the best focus possible for the system. An experimental image is taken, the background image is subtracted, and the result is divided by the flatfield image. To determine system blur, a horizontal "line-out" across the vertical edge is obtained for a row of pixels to determine the change in intensity as one moves across the edge. In a perfect system, a jump discontinuity is formed in the line-out because the edge is perfectly defined. However, in a real-world system, there is a slope across the edge as a result of blurring. An example of knife-edge images and corresponding line-out plots can be seen in Figure 1.1, with decreased image blur having a sharper slope across the edge [2, 10]. This line-out is called the edge spread function (ESF). To obtain the MTF of the imaging system, the ESF is converted to a line spread function (LSF) by taking the derivative. A Fourier transform of the LSF thus generates the MTF [5, 23].

To directly solve for the MTF, another method generates experimental images of sinusoid patterns with varying frequency. Images are taken at increasingly higher frequencies so that the corresponding decrease in amplitude can be studied. The MTF is then generated by plotting f against Mod. However, since this method requires many sinusoidal targets and is only applicable to light sources, a different approach is needed for a source such as a neutron generator. Thus, many people use the contrast transfer function (CTF) instead to approximate the MTF, and often the CTF is referred to as the MTF in the literature.

The CTF is similar to the MTF, but instead of a sinusoidal pattern, a bar target is used that represents a square wave. A CTF target test pattern is typically referred to as a three-bar or four-bar target based on the number of blocks at each spatial frequency [24]. One example is the 1951 Air Force three-bar test pattern, shown in Figure 1.9 [18]. Figure 1.10 is an example of the modulation limit as it would appear for a different bar target [22].

The CTF measurement is only an approximation of the MTF and it is important to address its limitations. Due to the small area of each bar pattern, the system is not adequately stressed to get a true degradation in modulation from optical interference. For example, "ringing", a result of optical interference that decreases image resolution, will not necessarily be seen (Figure 1.11). Additionally, the bar target is either white or black; there is no intermediate value in the test pattern such as that seen in a sinusoidal pattern, so the CTF can only approximate a sinusoidal input [18].

However, for non-light systems, measuring the CTF is the first step in obtaining the MTF and thus serves as a useful approximation of the MTF. By using a series expansion as outlined in Reference [24], one can convert the CTF into an approximate MTF, with the approximation improving as the number of bars increases for the reasons stated in the previous paragraph [24].

Another related test pattern is the "Siemens star" pattern (Figure 1.12). Frequency increases as one moves toward the center of the pattern, and so the resolution limit is somewhere in the inner region of the circle. This makes the Siemens star especially useful for lens focusing.

Another cause of resolution degradation in an image can be the imaging object itself. Images can be degraded by scatter from the object that increases background noise and causes a loss of position-sensitive information. Additionally, because the formation of an image is the projection of a three-dimensional object onto a two-dimensional image plane, there can be overlap of features of interest. This, in turn, degrades the resolution of the image. One way to address this problem is through the application of tomography, which forms a three-dimensional reconstructed image

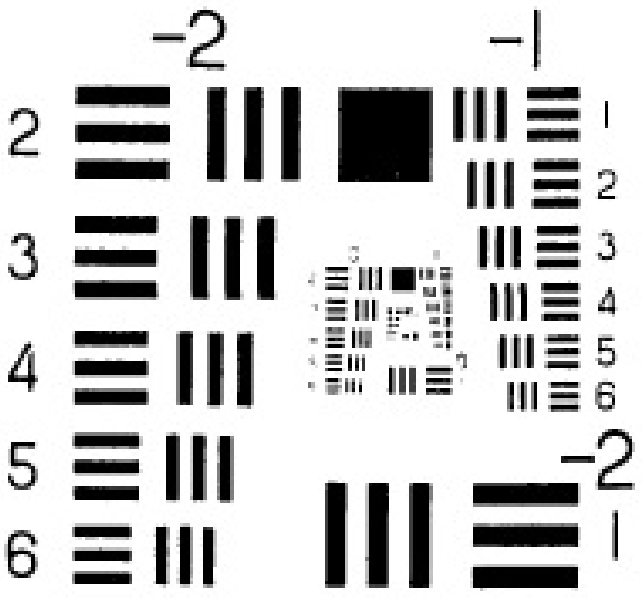


Figure 1.9: The 1951 Air Force test pattern used to determine the modulation transfer function of an imaging system [18].

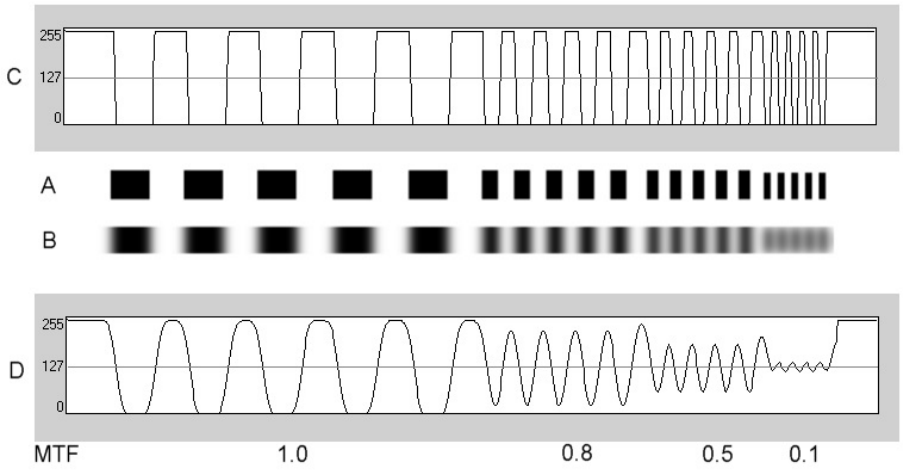


Figure 1.10: An illustration of a perfectly resolved ideal image of a sequence of bars with increasing frequency (A). The corresponding ideal MTF can be seen in (C). A real-world system, however, adds blur to the sequence of bars (B) and its associated MTF (D) [22].

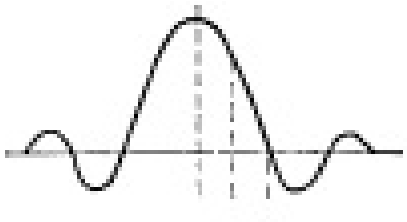


Figure 1.11: An illustration of ringing, where the central peak interferes with another signal and forms lesser peaks at regular intervals on either side [18].

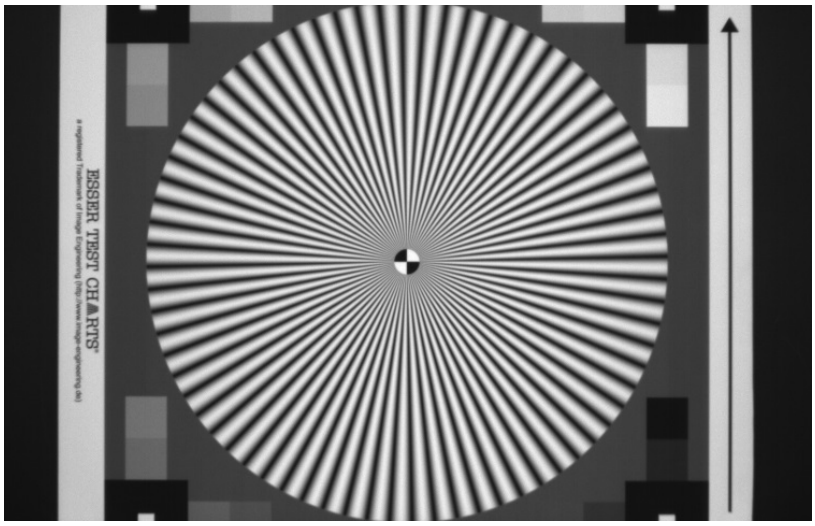


Figure 1.12: Example of the Siemens star pattern used to find the system CTF and the optimized system focus. This pattern was used for lens focusing in the experiments that will be outlined later in this paper [25].

of the object from two-dimensional images of the object taken at regular rotational intervals [3]. The concept of tomography will be elaborated later in this chapter [15].

1.3.2 Time and Energy Resolution

Similar to spatial resolution, time resolution refers to the inherent uncertainty in the time of arrival of the incident radiation at the detector. The better the time resolution, the more this uncertainty is reduced [2]. Related to time resolution is the concept of energy resolution because of the relationship between energy and velocity in particle time-of-flight (TOF) systems (see Section 1.3.8). Thus, energy resolution is found by

$$\Delta E_n = \frac{(2E_n)^{\frac{3}{2}}}{(L+S)\sqrt{m_n}}\Delta t, \tag{1.8}$$

where Δt is the uncertainty in particle time-of-flight from the source to the detector (s), ΔE_n is the resulting uncertainty in the particle energy (MeV), and m_n is the neutron mass (MeV/c^2) with c equal to the speed of light [15]. Therefore, by increasing the distance from the source to the scintillator screen $(L+S)$, one reduces the uncertainty in the energy resolution.

Good time resolution is needed for dynamic measurements where the object is changing in time (e.g., a running engine) or for TOF methods where particles incident on the detector are discriminated by their time of arrival (and, correspondingly, their energy and velocity) in order to form time-binned images [2]. Time resolution is very important if images of events at particular times are desired, or if only a certain signal is of interest, and thus uncertainty in the time bin boundaries must be minimized. This is true of scatter rejection and energy selection, both of which need precise time and energy resolution, respectively.

1.3.3 Contrast Resolution

Contrast resolution in an image is defined by how well a given radiography system can distinguish between grayscale values, and thus how well a system can distinguish between low- and high-density regions in the radiography object. A crack, for example, will have a lower density than the surrounding material, and a good imaging system will allow for these differences in density to be visible in the image as differences in contrast. This is because, ideally, contrast is directly determined by source energy, material cross-sections, and material thicknesses [2, 5].

However, in a real-world system, source particles that are scattered within the radiography object can enter void regions (such as the crack) and re-scatter into the detector, reducing contrast by brightening darker areas of the image. Scatter within the detector itself also reduces image contrast. These scatter effects can thus mask the presence of the crack by reducing contrast resolution, and careful system design must be employed to mitigate these detrimental scatter effects [15].

The contrast resolution is measured directly by the CTF and is obtained using the methods previously discussed in Section 1.3.1. The limiting contrast resolution of the system is the spatial frequency of line pairs where the black and white bars appear as the same color gray, and peaks and valleys such as those in Figure 1.10 are no longer resolved.

1.3.4 Magnification and Field of View

Magnification, M, is an optics term that refers to the size of the object in an image relative to itself. Using the notation from Equation 1.4, this is mathematically described by

$$M = \frac{L + S}{L - S}, \tag{1.9}$$

where L and S were defined previously in Equation 1.4 as the source-to-object distance and the object-to-detector distance, respectively. As magnification is increased,

feature size in the image is increased, and the percent of the object projected onto the screen is decreased. This mimics the "zoom" feature in photography and microscopy [15].

A related concept is the field of view (FOV), which is defined as the solid angle that can be seen by the detector; this is therefore determined by the image magnification. The FOV is also dependent on the detector. If using a CCD camera with a digital array, the FOV is limited by the number of pixels in the array and the lens properties. As a result, magnification and FOV must be determined for each system so that images of the regions of interest are taken [16].

1.3.5 Depth of Field and Lens Aperture Size

Imagine there are three objects on a table, each at a different distance from the camera lens. If the photographer wanted all three objects to be in focus in their image, they would need a large depth of field to do so, where the depth of field describes the range of focusing distances where image quality is not impacted. A short depth of field might result in an image where only the closest object is in focus and the remaining two objects are blurry because the range of acceptable focusing distances is reduced.

A related concept is the lens focal length, which is the distance from the lens center to the focal point for an object at infinity. The focal point is where the rays converge to a single point, and this is the location of minimum blurring. Objects not at the focal point will therefore appear blurry. With an increased depth of field, the size of the focus range increases, and multiple objects can be in focus at once. This is relevant to a CCD camera set-up because the lens needs to be focused at the center of the scintillator. If it is not focused to the proper depth, images will be blurry [16].

Depth of field is determined by the lens aperture size, with smaller aperture diameters causing a larger depth of field. This is because less light divergence occurs with a smaller aperture [26]. However, with a smaller aperture, there is less light

entering the lens and a longer exposure time is needed, so an optical imaging system must balance light quantity with depth of field.

A typical indicator of the lens aperture size is the quantity $f/\#$, pronounced "f-number". The $f/\#$ describes the relationship between aperture size and lens focal length, F (mm), such that

$$f/\# = \frac{F}{2R}, \tag{1.10}$$

where R is the radius of the lens aperture (mm). For example, using Equation 1.10, a 50 mm lens set to $f/2$ (just "2" in the equation) has an aperture radius of 12.5 mm. If the same lens is increased to a setting of $f/8$, the aperture radius is decreased to 3.1 mm. Therefore, by increasing the $f/\#$ by a factor of 4, the aperture radius is similarly decreased by a factor of 4, but the area available to incident photons is decreased by a factor of 16 (due to its dependence on R^2) [16]. Similarly, by increasing the lens setting from $f/2$ to $f/1$, the amount of available light increases by a factor of 4. As a result, a system using a large $f/\#$ (and therefore small aperture) is called a "slow" system because it takes longer to form an image than a "fast" system with a small $f/\#$ and a large aperture that allows more light to enter the lens and yields faster exposure times [16].

The $f/\#$ is traditionally printed on camera lenses to enable the user to more accurately select the lens focal length and aperture size. The maximum aperture size is limited to values between approximately $f/0.8$ and $f/1.0$, even for highly optimized lenses, due to physical limits that place an upper limit on exposure times [5, 16].

1.3.6 Tomographic Reconstruction

Although not currently being considered, tomographic methods will still be mentioned as they may be included in future versions of the proposed imaging system. As stated earlier, tomography uses post-processing to combine two-dimensional radiographs (called "views") into a three-dimensional representation of the object. To achieve good resolution, tomographic reconstruction requires many views, and, as a result,

tomographic imaging can be a lengthy process. However, tomography is useful for visualizing the interior of an object, which is, after all, three-dimensional [2]. An example of a two-dimensional projection, which is later combined with other projections to form a three-dimensional tomograph, can be seen in Figure 1.13 [17]. There are numerous mathematical methods that can be used to complete this reconstruction, but since tomography is not part of this project, they are not discussed here.

1.3.7 Source Intensity and Exposure Time

The length of time that the shutter is open and the film (or CCD array) is exposed to incident radiation is known as the exposure time. One must open the shutter long enough to allow features to be resolved; if the exposure time is too long or too short, the image will be too bright or too dark, respectively, to distinguish object features. As a result, the exposure time is directly related to the amount of radiation transmitted through the object. Referring to Equation 1.1, where $I(x)$ is the transmitted source intensity, the exposure time decreases as $I(x)$ increases. It should be noted that secondary effects on the exposure time are the imaging system geometry (e.g., distances between the source, object, and detector), camera-lens configuration, and the scintillation efficiency of the screen [2].

1.3.8 Time-of-Flight Concepts

The idea of using particle time-of-flight for imaging applications has been around for decades, with many diverse applications taking advantage of differences in arrival time between particles of varying energy. Photons, traveling at the speed of light, are detected earlier than particles with mass, such as neutrons. As an illustration, 14 MeV neutrons travel at a relativistic velocity of 5.12 cm/ns; this is about six times slower than photons, which have a velocity of 30 cm/ns [15, 27]. By extension, high-energy neutrons arrive prior to thermal or epithermal neutrons. For example,

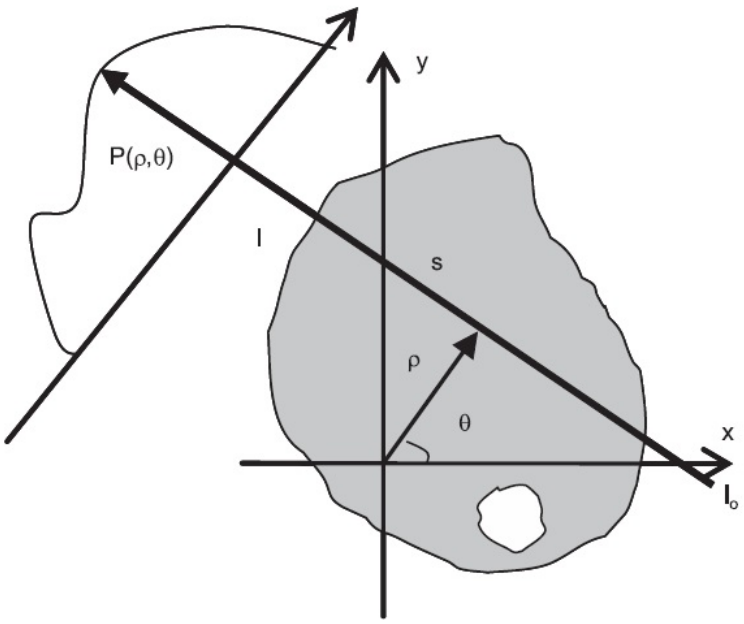


Figure 1.13: Illustration of a two-dimensional projection (white) of a radiography object (gray) used to form a three-dimensional tomograph, where ρ and θ describe the projection view, s, and $P(\rho, \theta)$ describes the resultant two-dimensional projection. The incident particle fluence, I_0, is affected by interactions within the object to become the transmitted signal, I [17].

8 MeV neutrons have a relativistic velocity of 3.9 cm/ns, which is slower than the aforementioned value for 14 MeV neutrons [27].

The TOF of a neutron, in this example, is approximated non-relativistically by

$$v_n = \sqrt{\frac{2E_n}{m_n}}, \tag{1.11}$$

where v_n is the neutron velocity (m/s) and E_n is the neutron energy (MeV) [15]. Equation 1.11 can then be used to solve for the TOF, t_{TOF} (s), of the neutron using simple kinematics. This equation, taken from Reference [15], is

$$t_{TOF} = \frac{L+S}{v_n}, \tag{1.12}$$

where $L+S$ is the distance from the source to the detector. In the case of a CCD camera-lens system, the lens location is used to calculate $L+S$, not the converter screen.

As a rule of thumb, Equation 1.12 can be used for neutrons below 10 MeV in energy because relativistic effects are minimal in this energy range. However, for neutrons above 10 MeV, relativistic equations must be used to calculate the TOF. The distinction between relativistic and non-relativistic particles is especially important for experiments at large, high-energy particle accelerators. The relativistic neutron kinetic energy, T, is described in Reference [28] by

$$T = (\gamma - 1)\, m_0 c^2, \tag{1.13}$$

where m_0 is the rest mass of the neutron (MeV/c^2), c is the speed of light, and γ is defined as

$$\gamma = \frac{1}{\sqrt{1 - v_n^2/c^2}}. \tag{1.14}$$

Solving Equation 1.13 for v_n yields

$$v_n = c\left(\sqrt{1-\left(\frac{1}{1+T/(m_0c^2)}\right)^2}\right). \tag{1.15}$$

By setting m_0 equal to the neutron rest mass of 939.565 MeV/c^2, v_n as a function of T can be found and then used with Equation 1.12 to calculate the relativistic time-of-flight.

With proper time gating and careful implementation of kinematics, one can generate a radiograph with neutron energies of interest and reject the remainder of the source [15]. For example, if using a polyenergetic neutron source ranging from 1 to 15 MeV, a time gate width could be set to detect neutrons from 5 to 10 MeV. This time gate would thus reject faster neutrons from 10 to 15 MeV, slower neutrons from 1 to 5 MeV, slower scatter from all energies, and background. In this way, scatter is reduced and signal-to-noise is improved, resulting in higher resolution images [29]. An additional benefit is that images also have higher dynamic ranges because the scatter is not "filling in" voids in the image, allowing smaller features to be seen with greater contrast [30].

TOF gating techniques can be used to form images from both neutrons and neutron-induced photons in a single measurement. This is especially useful because only one source is needed to measure two signals. Moreover, the differences in attenuation between the two radiation types allow for the formation of complementary images [29].

Another common use of time-of-flight principles is imaging crystal structure using neutron scattering from the crystal's Bragg edges [31]. This type of imaging is sensitive to the shift in wavelength resulting from neutron scatter off of the crystal lattice. Mathematically, this is described by

$$\lambda = \frac{h}{m_n v_n}, \tag{1.16}$$

where h is Planck's constant ($h = 6.6261 \times 10^{-34}\ Js$). Such small shifts in wavelength and short penetration depths require cold neutrons (on the order of meV) [2]. Cold neutrons also allow for larger variations in material contrast (since there is more variation in cross sections at low energies), as well as increased detection efficiency (since they are more easily stopped by a detector) [14]. Sources are often pulsed to allow particles to be detected with minimum background [32]. These cold neutrons, however, are not useful for imaging thick, dense objects because they are easily attenuated.

Time-of-flight techniques can also be used to take images of dynamic systems, such as two-phase liquid flow. TOF methods are necessary to reduce blur from movement in the object because blur decreases as the gate width decreases. Such a technique requires a camera with a very fast shutter speed, usually a high frame rate CCD camera [15].

In fact, all time-of-flight methods require fast systems in order to properly employ the technique and maximize time resolution. Fast cameras must be used in conjunction with scintillator screens with fast decay times since this is also a limiting factor in high frame rate imaging. Often, a faster decay time means less light output, but in fast timing applications, this is a necessary trade-off [11]. Monoenergetic sources are also preferable in TOF measurements, since it is much easier to separate direct signal from scatter. Pulsed sources are also typically used for TOF studies for this same reason [33]. In pulsed systems, there is a maximum pulse frequency that can be allowed before particles from the previous pulse begin to overlap with the subsequent pulse. This maximum frequency, f_{max} (s^{-1}), for a non-relativistic neutron source is described by

$$f_{max} = \frac{1}{L+S}\sqrt{\frac{2E_{n,min}}{m_n}}, \tag{1.17}$$

where $E_{n,min}$ (MeV) is the minimum neutron energy in the pulse [15]. Equation 1.17 thus addresses downscatter that can interfere with time discrimination efforts.

A high readout rate is also necessary for time-of-flight measurements with digital CCD systems because, once the pixel has been exposed, the data must be transferred very quickly out of the pixel and into the data processor before the arrival of the next pulse. As a result, the true frame rate, FR (s^{-1}), of the camera is defined by

$$FR = \frac{1}{t_{exposure} + t_{readout}} \tag{1.18}$$

and is dependent on the exposure time, $t_{exposure}$, and readout time, $t_{readout}$ [14].

1.3.9 Noise

Briefly mentioned earlier in this chapter, noise is a very important contributor to image degradation because it decreases the signal-to-noise ratio. Noise has three contributions, which differ in weight depending on the system characteristics. The total noise, N_{total}, is proportional to the square root of the quadrature sum of the noise inherent in the detection process ("shot noise"), N_{shot}, the noise resulting from data readout, $N_{readout}$, and the noise from dark current (electronic noise resulting from circuitry) and other background effects, N_{dark}. N_{total} is thus described by

$$N_{total} = \sqrt{{N_{shot}}^2 + {N_{readout}}^2 + {N_{dark}}^2}. \tag{1.19}$$

It should be noted that noise tends to increase as exposure time and readout rate increase, so these should be limited if possible [14].

Noise also increases as the photodetector temperature, T, rises. Thermal energy excites electrons present in the sensor, which then deposit their energy in the sensor as dark current. Dark current is problematic because this signal is indistinguishable from that of the incident radiation and therefore reduces the signal-to-noise ratio of the image. This dark current can be a significant contributor to background noise [16].

The dark current can be modeled as leakage current in the semiconductor chip in the CCD camera. The probability per unit time and as a function of temperature,

$P(T)$, that an electron-hole pair is thermally generated in the silicon chip (an approximation of dark current) is found by

$$P(T) = CT^{3/2}\left(exp\left(-\frac{E_g}{2kT}\right)\right), \tag{1.20}$$

where T (K) is the temperature of the chip, E_g (eV) is the bandgap energy for the semiconductor, k $(= 8.617 \times 10^{-5}\ eV/K)$ is the Boltzmann constant, and C is a material-dependent proportionality constant. By cooling the CCD chip and reducing T, the probability of dark current exponentially decreases and image quality improves [34].

Chapter 2

Gaps in Technology

With the principles of optics and imaging explained in the previous chapter, Chapter 2 will explain current gaps in neutron radiography. This chapter will first explore existing work in neutron radiography to provide background for the reader, and conclude by describing areas of improvement in the field that will be addressed by this project.

2.1 Current Work in Neutron Imaging

While some current work in neutron imaging was discussed in Chapter 1, this section will go into deeper detail on neutron radiography to allow for differentiation of this project from others previously conducted. Tomographic methods will not be included here, as they will not be used in this project.

2.1.1 Continuous Neutron Radiography

The traditional form of neutron radiography uses a continuous source that is off before and after an imaging measurement and is on continuously during the measurement. A continuous source may be an isotopic source that is removed from shielding during the course of the measurement and then turned "off" by placing it back in its shielding.

Other examples include a reactor beam port or a continuous wave accelerator beam [2]. These sources have many applications depending on the required flux and neutron energy, but all may be used to form an image.

The continuous method requires opening a shutter on the film or digital array for part or all of the time the beam is on to allow the light from the converter to expose the image medium [13, 35]. While this shutter is open, the imaging medium is exposed to all other background sources that cause light in the scintillator, such as heavy charged particles, photons, electrons, and light itself. For these reasons, continuous imaging is not ideal for high background or low flux situations because there is no good way to reject the extraneous signal that reduces image quality and contaminates the signal of interest. It is for these situations that pulsed neutron imaging was developed, and why this project will design a neutron radiography system for use with a pulsed neutron source.

2.1.2 Pulsed Neutron Radiography

Pulsed neutron radiography, by design, requires a source that can be turned on and off during the measurement, sometimes quite rapidly. This is done mechanically with a shutter or shielding, or electronically by turning the power on and off. Sometimes, such as with large accelerator facilities, the beam is pulsed electronically but the beam structure is determined by mechanical beam choppers or other means [6]. For both low and high-energy particles, a pulsed source can be used to reduce scatter through time gating, improve signal-to-noise, and allow the use time-of-flight methods when the beam is off to differentiate features of interest.

Pulsed low-energy neutrons are useful for imaging shallow depths (e.g., a surface) or small features (e.g., microscopic material structure). One example is Bragg edge imaging, which images the microscopic structure of materials by allowing cold neutrons to scatter and diffract from the crystal structure. These material-dependent changes in neutron energy and scattering angle can then be reconstructed to form

an image. In addition to time-of-flight scatter rejection, detectors may be placed at certain angles so that scatter is also rejected geometrically. Research has been conducted on Bragg edge imaging with linear accelerators, including LANSCE in the United States, J-PARC in Japan, and SINQ in Switzerland, to name a few [6, 14, 31–33, 36–38].

High-energy neutrons, on the other hand, are useful for imaging deep inside an object or imaging large objects or features. It is this property of high-energy neutrons that make them of interest to this project. Original technology used film for fast neutron radiography [13, 35]. However, film has mostly been replaced by digital methods that provide on-line imaging, with some of the most relevant digital systems described below.

One research group is developing high-energy neutron imaging with a CCD camera to scan luggage at the airport. They propose time gating for energy selection to manipulate image contrast and identify materials, but not for scatter rejection. They have developed two detector designs for this application: a fiber-optic, pixellated plastic scintillator, and a gas-filled detector. In Reference [39], they conducted simulations of the detector response to incident neutrons up to 14 MeV in energy. In a subsequent paper, the characteristics of the optical system were determined, and experimental radiographs were generated with various monoenergetic neutron sources ranging from 3.1 MeV to 10.5 MeV, as well as photons resulting from the $^{9}Be(d,n)$ reaction. Radiography objects were optically thin and/or small, including wire, batteries, a small toy gun made of plastic, and a small vial filled with several grams of uranium [11].

Other research has been conducted to develop a system to scan large cargo containers that is capable of both x-ray and neutron radiography. A pulsed neutron source of 8.5 MeV is proposed so that it is of high enough energy to stimulate secondary photons within the cargo. An array of 128 plastic detectors is then proposed to generate radiographs from the primary neutrons and secondary photons. These signals are then later reconstructed into images. A boosted D-D reaction is used

to generate the source neutrons, and has a pulse width of 1 ns and frequency of 5 MHz. The source is moved vertically along the container in sync with the detectors, addressing scatter by the typically hydrogenous cargo via geometric methods. Called "slot-scanning," this particular geometric method images only part of the radiography object at a time; by moving the source and detector, scatter in other parts of the object can be ignored. The image resolution is not great, with the purpose of the system to roughly locate contraband within the shipping container, and ranges from $20 \times 20 \times 10$ cm^3 to $45 \times 45 \times 20$ cm^3 [27, 29, 30].

Another example of a pulsed, high-energy neutron radiography system employs a 2.5 MeV D-D source of flux of 10^{10} neutrons per second. A CCD camera and plastic scintillator converter are proposed as a detection system to generate radiographs with fast and, if using a moderator with the D-D source, thermal neutrons. Simulations were completed to develop a beam collimator for the purpose of reducing both imaging time and gamma background. This project found that the best shielding configuration for fast neutrons was composed of borated polyethylene, iron, and lead [40].

Along with a D-D source, radiography with a 14 MeV D-T source is also fairly common. The Nuclear Materials Identification System (NMIS) at Oak Ridge National Laboratory (ORNL) uses an associated particle D-T generator to provide time-of-flight information and reject scatter. A single row of detectors is used to geometrically reject scatter via the slot scanning method. NMIS is different from other scatter rejection methods that will be employed with the proposed imaging system (i.e., gating a CCD camera in time to reject scatter instead of correlating in time the D-T reaction with detector events) [41]. Another fast neutron imaging system at ORNL is the Associated Particle Neutron Imaging System (APNIS). APNIS uses a pixellated plastic scintillator in the form of a block detector to provide timing and spatial information that can be used to form images using gammas, transmission neutrons, and fission neutrons [42]. Thus, APNIS uses the scintillator to gate in time.

Another D-T imaging system is the Neutron Imaging System (NIS) designed for the National Ignition Facility (NIF). NIF is currently conducting experiments to evaluate the possibility of fusion of D-T plasma. Plastic capsules containing D-T ice and gas are imploded, emitting 10^{14} 14 MeV neutrons. The source is pulsed once in a single shot, with neutrons generated during the short time that the capsule is imploding, but not after the implosion process is complete. NIS was designed to image the implosion and provide an experimental diagnostic. Using pinhole and coded aperture imaging, NIS uses two gated CCD cameras to generate two images of the imploding capsule: one with 14 MeV neutrons, and one with 6 to 13 MeV neutrons. System tests have been conducted at LANSCE [43–45].

2.2 Gaps in Technology

While Bragg edge imaging and other low-energy neutron imaging techniques employ time-of-flight to reject scatter, TOF scatter rejection has not been accomplished at high neutron energies. This is mostly due to the small differences in time-of-flight for neutrons above 1 MeV, which requires very fast and precise timing that makes scatter rejection very difficult. Only recently has technology (i.e., CCD cameras) evolved to allow imaging with very fast (on the order of MHz) pulsed neutron sources. This work will thus apply methods currently used for low-energy neutron imaging to high-energy situations, which will expand the arsenal of techniques currently available to neutron radiography for NDA.

Additionally, radiography systems are not yet developed to image the interior of large, dense objects that tend to scatter neutrons back into the field of view. As stated in Chapter 1, such objects cause images to have low spatial and contrast resolution. A literature search has shown that existing neutron radiography systems are either developed for and/or are tested with small objects of higher density (e.g., vial of powdered uranium) or large objects with low density (e.g., cargo container), which allows such systems to avoid the negative effects of scatter. Additionally, such

objects can be imaged with x-rays because they do not cause a large attenuation in the transmitted signal. The neutron radiography system being designed in this project, however, will be capable of radiographing large, dense objects that cannot be radiographed with x-rays. Thus, this project will fill an existing gap in current radiography research.

Chapter 3

Novel Contributions

The neutron radiography system, Time Gating to Reject Scatter and Select Energy (TiGReSSE), under development in this project will make several novel contributions to the existing body of work on pulsed high energy neutron imaging. First, the principle of time gating to reject scatter will be applied to high energy neutron sources that can penetrate large, dense objects (i.e., greater than several MeV). As stated in Chapter 2, this is rather easily conducted at low energies due to large differences in time-of-flight for neutrons in this energy range. For example, non-relativistically, a 1 MeV neutron travels 10 m in 722 ns. A 2 MeV neutron travels the same distance in 511 ns, which is an easily gated difference of 211 ns between the two energies. However, this is much more difficult at high energies, with a non-relativistic difference of 6 ns between 14 MeV and 15 MeV neutrons traveling 10 m. As a result, this project will be the first to apply this method of scatter rejection to neutrons of energy greater than 10 MeV (up to ~600 MeV at LANSCE) [27, 29, 30].

A second novel contribution of this project is that TiGReSSE is being designed to radiograph objects that cannot be clearly imaged at their center due to their geometry (which scatters neutrons back into the field of view) and their density (which attenuates other interrogation sources, such as x-rays). Large, dense objects have a large range in image contrast values, with high-density regions appearing much

darker than low-density regions because fewer source particles are able to penetrate the former. Scatter from low-density regions into high-density regions, either within the object itself or within the converter screen, causes dark regions to appear much brighter. The artificially-brightened region is thus portrayed as less dense than it actually is, and also has reduced contrast resolution that can hide object features. For these reasons, large, dense objects are a challenge to radiograph. By reducing or eliminating scatter via TOF or geometric means (and also by increasing the flux of the neutron source to improve signal-to-noise), image quality can be improved and contrast for a given material becomes more uniform. Scatter rejection has been demonstrated with cold and thermal neutrons, but not for thick, dense objects or for fast neutrons [46]. Work referenced in Chapter 2 simply does not address this type of object composition and geometry, nor high-energy neutron sources.

Third, this project will conduct proof-of-principle imaging experiments at the LANSCE linear accelerator. With LANSCE neutrons ranging in energy from several hundred keV to upwards of 600 MeV, time-of-flight principles will be applied to allow for energy selection of certain neutrons. By imaging with neutrons of different energies, specific interaction cross-sections can intentionally be selected to vary image contrast and provide material information. Additionally, and possibly more importantly, gating in time to radiograph with varying neutron energy provides the ability to see features at certain energies that are not visible at other energies as a direct result of resonances and other effects [10]. Energy selection such as this has not been conducted above energies of 14 MeV, so this experiment will expand our understanding of imaging at higher energies and determine whether it is worthwhile [41, 43–45].

Finally, component designs and studies that are specific to this system are considered novel. Many novel design features will need to be implemented to allow for radiography to be conducted at LANSCE with neutrons up to $\sim$600 MeV in energy; such design features are unnecessary at lower neutron energies. For example, shielding

to protect the camera against high-energy spallation particles will be designed and tailored to the radiography system.

Chapter 4

Initial System Design

This chapter details work completed in support of initial TiGReSSE design, and includes theoretical and simulated results that guided the purchase of system equipment. Experimental results from initial testing of the system are also included in this chapter.

4.1 Neutron Time-of-Flight Estimations

4.1.1 Overview of Neutron Time-of-Flight Analysis

The first step taken in TiGReSSE design was to simulate and calculate typical experimental conditions that would be experienced during radiography. Since the main feature of TiGReSSE is rejecting scatter, it was necessary to estimate the difference in TOF between unscatttered ("direct") and scatter neutrons. Such results would then guide system design and equipment selection.

The simulation code selected for this purpose was Los Alamos National Laboratory's Monte Carlo radiation transport code, MCNP6. MCNP6 has many capabilities, such as criticality calculations, flux-to-dose conversions, and radiography [47]. For the latter application, MCNP6 can simulate radiographs using an FMESH tally. This tally places a voxellated mesh over a detector volume, which represents the image

plane. The tally simulates the amount of particle fluence in each pixel by dividing the voxel volume by the total particle track length in that voxel. Plotting the results thus allows for a two-dimensional visualization of a simulated radiograph [48]. The simulated fluence is measured in units of $1/n/cm^2$, where n is the total number of simulated source particles; in other words, MCNP6 normalizes the fluence values to n [49]. The FMESH tally can be further specified by tallying in time, by source energy, and by source particle type, which makes the FMESH tally particularly appropriate for time-of-flight radiography simulations.

4.1.2 MCNP6 FMESH Tally Simulations

A simple geometry was intentionally simulated so that FMESH results could easily be compared to analytic calculations and the results of another MCNP6 tally, the F4 tally, which calculates fluence the same way but for un-voxellated volumes (Figure 4.1). The F4 tally thus provides additional verification of the FMESH results.

The simulated geometry is as follows. A monoenergetic ($E = 10.2\ MeV$) neutron pencil beam was incident on a graphite slab ($5 \times 50 \times 50\ cm^3$), which was selected to represent an object being radiographed. The neutron source was located 0.25 cm from the front of the graphite target. A neutron energy of 10.2 MeV was selected to approximate the boosted D-D source proposed by Dietrich et al. at LLNL for neutron radiography and first mentioned in Section 1.1.2 (Figure 4.2) [8, 50]. This proposed source generates a spectrum of neutrons with an upper energy of 10.2 MeV, but for ease of comparison to analytic calculations, the source was modeled as monoenergetic.

An ideal detector with 100% efficiency and size of $5 \times 100 \times 100\ cm^3$ was simulated so as to represent an ideal CCD camera. The front detector face was located at a distance of 100 cm from the graphite slab centerline. A voxellated mesh was placed over the front of the detector face, with voxels $7 \times 2 \times 2\ cm^3$ in size. The source was simulated as 100×10^9 neutrons. For ease of verification with theoretical calculations,

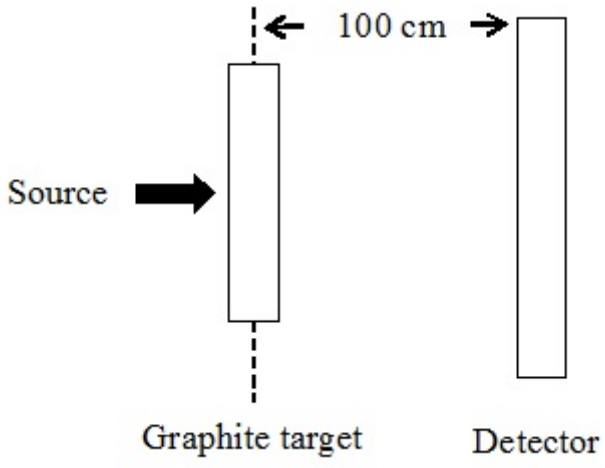


Figure 4.1: Illustration of the MCNP6 geometry used to simulate neutron time-of-flight. A 10 MeV pencil beam neutron source was incident on the radiography object (a graphite slab), with a distance of 100 cm between the center of the graphite slab and the front face of an ideal detector [51].

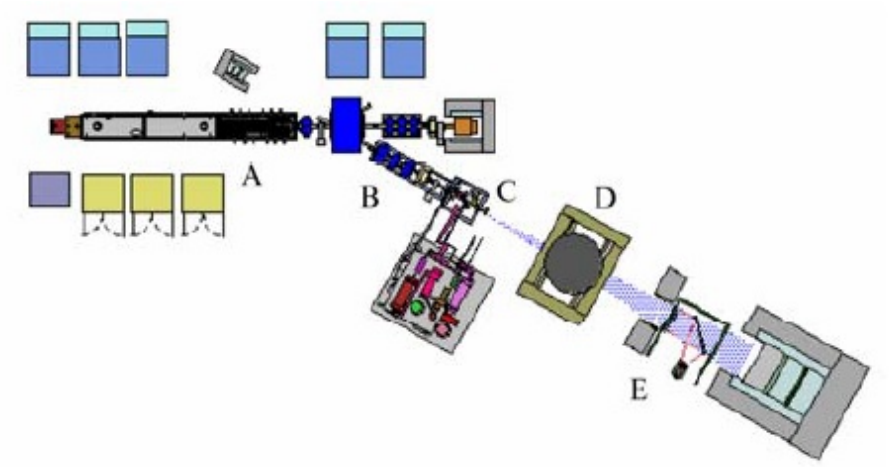


Figure 4.2: Diagram of the pulsed high-energy neutron source proposed by LLNL. According to Reference [50], A is a 7 MeV deuteron linear accelerator, B is the beam transport, C is the deuterium gas target, D is the imaging object, and E is the imaging system. This system is a boosted D-D source with endpoint energy of 10.2 MeV.

the FMESH tally only counted neutrons undergoing a single scatter in the graphite target, and the geometry was simulated in a vacuum.

FMESH results were separated into time bins to determine the time-of-flight from the source to the detector plane for particles suffering a given reaction. The FMESH time bins were 1.0 ns wide and covered an interval of 50 μs. To bound the problem and determine when direct and scattered neutrons were arriving at the detector plane, voxels were selected in three locations on the detector face: the center ("Case I"), the center of the top edge ("Case II"), and the upper left corner ("Case III") (Figure 4.3). Case I is the shortest object-detector distance, and so neutrons would arrive at the detector center first, followed by Case II. Case III, with the largest object-to-detector distance, would see neutrons arrive last. Choosing these three locations also allowed for easy comparison of FMESH results to F4 tally results and analytic calculations.

4.1.3 Analytic Calculations

As additional confirmation of MCNP6 results, elastic and inelastic non-relativistic time-of-flight calculations were completed. For both simplicity and to bound the problem, scatter locations were assumed to occur either at the front or back of the graphite target and then travel to Case I, II, or III locations after a single scatter. Simple trigonometry was used to determine the scattering angle and distance, d (cm), traveled by the particle from its scattering location to the detector so that the time-of-flight could be calculated according to the principles in Equation 1.11 and Equation 1.12 in Chapter 1. The scattering velocity, v' (cm/s), was calculated using non-relativistic kinematics of a neutron scattering from carbon. The elastic scatter (or "billiard ball" reaction) from the front of the graphite target is described by

$$TOF_{front,el} = \frac{L}{v} + \frac{d}{v'}, \tag{4.1}$$

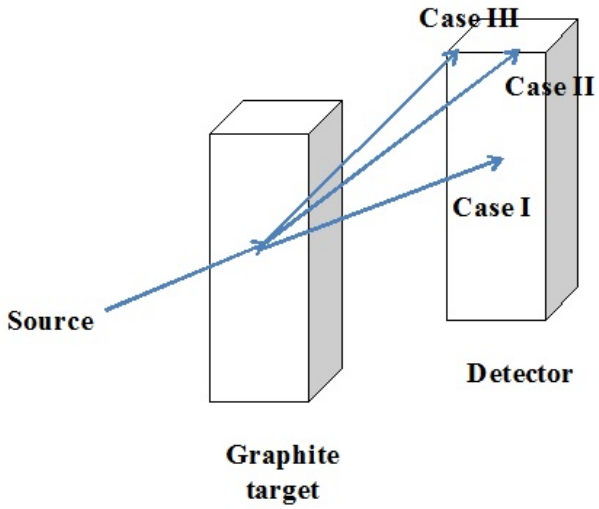


Figure 4.3: Illustration of the three locations selected on the detector face for neutron time-of-flight analysis. Case I is located in the detector center, Case II is located in the center of the top edge of the detector, and Case III is located in the upper left corner of the detector. Blue arrows indicate neutron travel from the graphite slab to these three locations [51].

and from the back of the graphite target by

$$TOF_{back,el} = \frac{L+h}{v} + \frac{d}{v'}, \tag{4.2}$$

where L (equal to 0.25 cm) is the distance from the source to the front of the graphite target and h (cm) is the thickness of the graphite slab that is traveled at the initial velocity, v (cm/s), before scattering. For a scatter at the front of the graphite slab, $h = 0$ cm; for a scatter from the back of the slab, $h = 5$ cm. The initial velocity is determined by the neutron source energy, or 10.2 MeV in this case. Note that an elastic scatter from the graphite slab to Case I involves no angular deflection of the neutron and thus no energy loss; therefore, Case I elastic scatter is equivalent to the direct signal. All other signal (elastic scatter to Case II and III, as well as inelastic scatter to Case I, II, and III) would be rejected by TiGReSSE to improve image quality.

Inelastic scattering from the graphite slab is a more complicated reaction to calculate than elastic scattering because, for inelastic scattering to occur, the incident neutron energy must be greater than the reaction threshold energy, Q. This is because inelastic scattering typically causes the incident neutron to be absorbed by the nucleus, which (in most cases) excites it and forms a compound nucleus. This excited state then decays and yields reaction-dependent ejectiles, which in this case are neutrons. As a result, the inelastic scatter reaction results in greater energy loss and, consequently, slower neutrons than the elastic scatter reaction [12].

The value of Q depends on the nuclear structure of the target atom and the inelastic scattering level. As atomic structures become more complex, more inelastic scattering reactions are possible and levels become more narrowly spaced in energy. According to tabulated MCNP6 ENDF/B-VII.0 neutron cross-section data, graphite has thirteen possible inelastic scattering reactions with neutrons. However, given the problem geometry and the neutron source constraints (i.e., the incident neutron energy of 10.2 MeV and the solid angle that the detector plane intersects outgoing

scatter), only two of these reactions are feasible: Level 1 ($Q = 4.44\ MeV$) and Level 2 ($Q = 7.65\ MeV$) inelastic scatter. Inelastic TOF calculations were performed similarly to elastic scatter (Equations 4.1 and 4.2), while taking into account the reduced incident neutron energy that results from overcoming the reaction threshold energy.

4.1.4 MCNP6 F4 Tally Simulations

In addition to the analytic calculations, MCNP6 FMESH results were also compared to those from an F4 tally. As stated earlier, the F4 tally was selected because it averages neutron track length over volume to yield fluence in the same way that the FMESH tally does. However, instead of finding the fluence in voxels like the FMESH tally, the F4 tally does so for the entire tally volume. This difference allows the F4 tally to use more rigorous statistical checks, making it particularly useful for verification of FMESH results.

The geometry of the F4 tally was designed to mimic the FMESH study. Three F4 volumes of the same size as the FMESH voxels ($7 \times 2 \times 2\ cm^3$) were placed at Case I, Case II, and Case III locations (Figure 4.4). To remain consistent with the FMESH tally, the F4 tally immediately killed neutrons entering the cells, thereby simulating an ideal detector. The F4 tally also only tallied neutrons that had suffered a single scatter and similarly simulated a source strength of 100×10^9 neutrons. Time bins for the F4 tally were the same as those used in the FMESH tally, with 1.0 ns width. To conduct verification, the F4 time bins when counts first appeared in the three cells were noted and compared to first counts in the FMESH time bins at Case I, II, and III locations.

4.1.5 Results

Time-binned FMESH results were plotted to form simulated images, which were then visually examined to determine the neutron arrival time at Case I, II, and III locations.

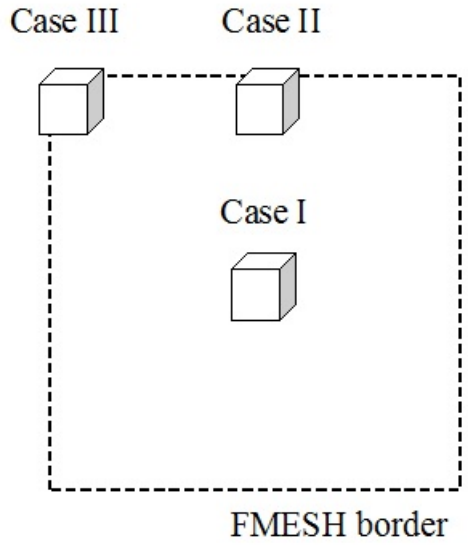


Figure 4.4: Illustration of the three F4 tally volumes located at Case I, Case II, and Case III. The FMESH tally border on the detector surface is shown for reference [51].

An example of FMESH simulated results, plotted to represent a radiograph, can be seen in Figure 4.5. A ring structure was seen to start at the detector center and grow with time, and was determined to result from intersection of the detector plane with the cone of scattered neutrons leaving the graphite slab. The cone increases radially in size because of increased deflection angles, with larger deflection angles resulting in greater energy loss and thus larger TOF.

FMESH results showed that elastic scatter composed the first ring, Ring 1, because it does not lose energy in the center-of-mass during the scatter reaction. Two other subsequent series of rings followed this pattern of radial growth, with the second (Ring 2) and third (Ring 3) series of rings corresponding to the two possible inelastic scatter reactions for this geometry ($Q = 4.44\ MeV$ for Level 1 (L1) or $Q = 7.65\ MeV$ for Level 2 (L2) inelastic scattering, respectively).

F4 time-of-flight results were similarly determined for Case I, II, and II, but in this case by examining the MCNP6 output data files instead of plotting data to form a simulated radiograph. FMESH and F4 tally time-of-flight results were seen to match with 0% error, with results shown in Table 4.1. This indicates that FMESH results agree with other tallies that have more rigorous statistical checks (in this case, the F4 tally).

FMESH and analytic results were also compared, matching within 3.8% or better (with differences most likely resulting from using non-relativistic equations, and the method of visually determining from FMESH data when neutrons reach Case I, II, and III locations). Thus, FMESH results are further verified by the analytic calculations described earlier in this chapter. Percent error was calculated if the analytic results fell outside of the FMESH time bin, and was calculated for the nearest time bin endpoint. The sign of the error indicates whether it is above (+) or below (−) the FMESH time bin. It was seen that, if the FMESH and analytic data did not agree, the FMESH tally results consistently fall below the analytic results. Results for Rings 1, 2, and 3 can be seen in Tables 4.2 through 4.4, respectively.

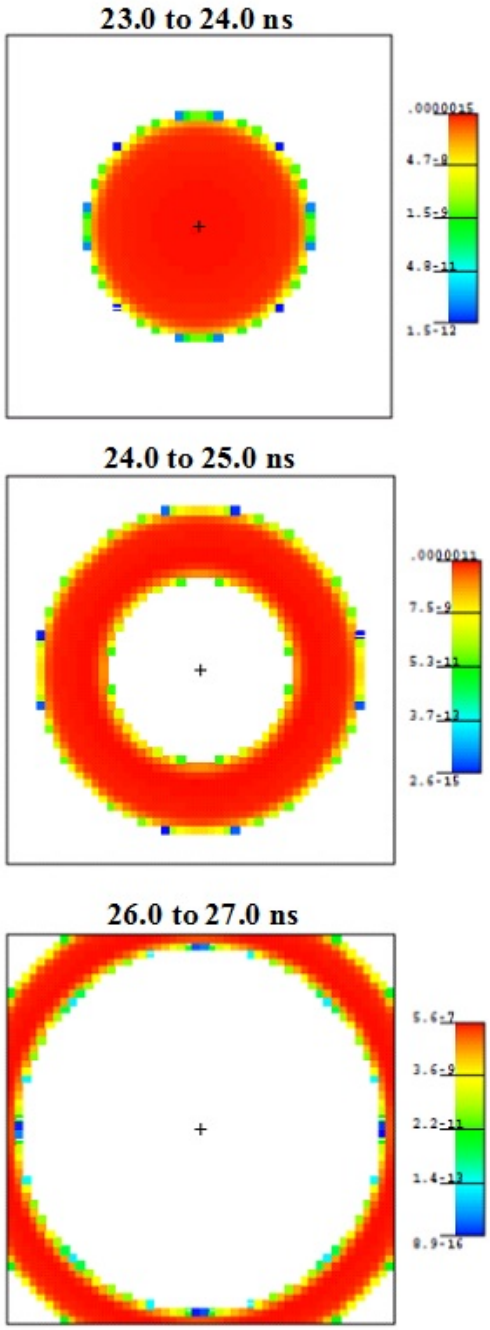


Figure 4.5: MCNP6 FMESH simulated radiographs of neutrons that underwent a single elastic scatter in the graphite target prior to reaching the detector plane. TOF from the source origin to the detection location is shown above each image. Top: Elastically-scattered neutrons arrive at Case I first because it is the shortest distance between the interaction site and the detector. Middle: The elastic scatter, emitted isotropically, forms a cone as the deflection angle increases, causing the TOF to also increase. Neutrons are detected between Case I and II locations. Bottom: Elastic scatter reaches Case II, with an additional increase in deflection angle and thus TOF [51].

Table 4.1: Comparison of simulated TOF data for F4 and FMESH tallies.

Ring Number	Location	FMESH TOF (ns)	F4 TOF (ns)	Percent Difference (%)
Ring 1	Case I	23.0 to 24.0	23.0 to 24.0	—
	Case II	24.0 to 25.0	24.0 to 25.0	—
	Case III	28.0 to 29.0	28.0 to 29.0	—
Ring 2	Case I	30.0 to 31.0	30.0 to 31.0	—
	Case II	34.0 to 35.0	34.0 to 35.0	—
	Case III	37.0 to 38.0	37.0 to 38.0	—
Ring 3	Case I	47.0 to 48.0	47.0 to 48.0	—
	Case II	53.0 to 54.0	53.0 to 54.0	—
	Case III	58.0 to 59.0	58.0 to 59.0	—

Table 4.2: Comparison of the TOF for analytic elastic single neutron scatter to simulated FMESH tally TOF data for Ring 1.

Scatter Location	Detection Location	Analytic TOF (ns)	FMESH TOF (ns)	Percent Difference (%)
Front of graphite slab	Case I	23.0	23.0 to 24.0	—
	Case II	25.9	24.0 to 25.0	—
	Case III	28.5	28.0 to 29.0	—
Back of graphite slab	Case I	23.0	23.0 to 24.0	—
	Case II	25.9	24.0 to 25.0	—
	Case III	28.6	28.0 to 29.0	—

Table 4.3: Comparison of the TOF for analytic elastic single neutron scatter to simulated FMESH tally TOF data for Ring 2.

Scatter Location	Detection Location	Analytic TOF (ns)	FMESH TOF (ns)	Percent Difference (%)
Front of graphite slab	Case I	30.8	30.0 to 31.0	—
	Case II	34.7	34.0 to 35.0	—
	Case III	38.3	37.0 to 38.0	−0.8
Back of graphite slab	Case I	30.6	30.0 to 31.0	—
	Case II	34.6	34.0 to 35.0	—
	Case III	38.3	37.0 to 38.0	−0.8

Table 4.4: Comparison of the TOF for analytic elastic single neutron scatter to simulated FMESH tally TOF data for Ring 3.

Scatter Location	Detection Location	Analytic TOF (ns)	FMESH TOF (ns)	Percent Difference (%)
Front of graphite slab	Case I	48.6	47.0 to 48.0	-1.2
	Case II	55.3	53.0 to 54.0	-2.4
	Case III	61.3	58.0 to 59.0	-3.8
Back of graphite slab	Case I	47.8	47.0 to 48.0	—
	Case II	54.7	53.0 to 54.0	-1.3
	Case III	60.9	58.0 to 59.0	-3.1

4.1.6 Discussion of MCNP6 Error

FMESH and F4 relative error, while generally low, increased in two instances. First, the fluence reaching a given location on the detector face decreased as the neutron path length increased, which caused statistical relative error to increase. For example, Case III had the lowest fluence, the longest path length, and the highest relative error when compared to Case I or Case II. For example, the average FMESH voxel counts per simulated source particle and per unit volume were approximately 10^{-7} for Case I and II, compared to approximately 10^{-12} for Ring 3. This led to a respective average relative error of 0.08%, 0.17%, and 24.5% for the three locations.

A second factor driving MCNP6 error is that the fluence for a particular scattering reaction decreased directly with the reaction cross-section, where $\sigma_{inelastic,\ L2} < \sigma_{inelastic,\ L1} < \sigma_{elastic}$, with error again increasing when fluence decreased [52]. Thus, Ring 1 data has a smaller relative error than Ring 2, which has a smaller relative error than Ring 3.

For these two reasons, the highest MCNP6 error was seen for Ring 3 at the Case III location, with the F4 data having a 49.2% relative error and the FMESH data having a 57.4% relative error. This also corresponds to the largest percent difference between the analytic and FMESH TOF results (3.8%). In the future, the relative error can be decreased by simulating more neutrons and employing variance reduction techniques.

4.1.7 Conclusions

In conclusion, the simulated FMESH results showed that elastic scatter arrives between 23.0 and 29.0 ns, with direct (no deflection) signal arriving between 23.0 and 24.0 ns and the first elastic scatter arriving at Case II between 24.0 and 25.0 ns. Inelastic scatter arrives between 30.0 and 59.0 ns. Since direct signal arrives very close in time to elastic scatter (a difference of $\sim$3 ns if using the analytic data, but only a $\sim$1 ns difference if using the FMESH data!), a CCD camera with ns time gating capabilities is necessary for the system to operate. This is especially true if

a neutron source with energy greater than 10 MeV is used (e.g., a 14 MeV D-T generator), since faster neutrons travel at higher speeds and become more difficult to discriminate. Thus, to reject scatter, a very fast camera is necessary.

Results also show that inelastic scatter is much easier to discriminate from the direct signal than elastic scatter, since inelastic scatter arrives $\sim$6 ns after the direct signal. Inelastic scatter, however, arrives only 1 ns after the elastic scatter and is not that much slower than elastic scatter. This geometry would require a source to be pulsed once every 37 ns. Such a pulse structure would allow the next wave of direct neutrons to arrive 1 ns after the arrival time of the last inelastic scatter at Case III. Thus, the frequency of the pulse must be optimized for the radiography object and geometry being imaged to maximize the amount of scatter rejected by the system. For this geometry, inelastic scatter has a TOF $\sim$2.5 times larger than that of the direct signal, and the effect of inelastic scatter should not be ignored in the development of TiGReSSE.

4.2 System Design

Based on the simulations and calculations outlined above, which suggest a necessary time resolution on the order of 1 ns to successfully reject scatter, equipment that could operate within these time constraints was purchased to build TiGReSSE. Purchases were made by R. Schirato of Los Alamos National Laboratory. This section outlines the equipment properties and the general experimental set-up of TiGReSSE.

Based on the principles covered in Chapter 1, TiGReSSE uses a scintillator to convert neutrons transmitted through the radiography object into visible light. This light is then reflected by a mirror into a gated intensified CCD (ICCD) camera. The camera, opening and closing its shutter electronically by turning the intensifier (i.e., gain) on and off, then integrates this light signal to form a radiograph of the object being imaged. Multiple pulses are integrated into one image to increase the amount

of neutrons, and thus light, used for radiography in order to improve the signal-to-noise ratio. Multiple, identical images (called "frames") are combined into one image during post-processing to further improve signal-to-noise. The system is enclosed in a light-tight box so that only visible light from neutrons hitting the scintillator is integrated on the camera.

4.2.1 Fast Plastic Scintillator

Because of the fast timing required for scatter rejection and energy selection, Eljen EJ-212 was chosen as the neutron converter screen. A fast plastic scintillator, EJ-212 emits light with a peak wavelength of 423 nm, which is easily visible with a blue-sensitive camera (Figure 4.6). EJ-212 was desirable because of its fast rise (0.9 ns) and decay (2.4 ns) times, which are necessary for fast neutron radiography. The fast decay time is especially important because it limits scintillator afterglow that would otherwise negatively impact TOF methods. With a full-width, half-maximum pulse width of 2.7 ns, imaging gate widths must be at least this wide to prevent loss of signal [53]. EJ-212 has a polyvinyltoluene (PVT) base (where PVT has the molecular formula of $C_{27}H_{30}$) and a density of 1.023 g/cc [53, 54]. The scintillation efficiency for this material is 10,000 $photons/(1\ MeVee)$, which is 65% that of anthracene, but the sacrifice in scintillation efficiency is necessary in this case because fast timing is a more important design consideration than scintillator brightness.

Scintillator screens with thicknesses of 2 mm, 3 mm, and 5 mm were purchased so that a trade-off study could be conducted between resolution (which decreases as screen thickness increases) and efficiency (which increases as screen thickness increases). Additionally, the two thinnest screens sum to the thickness of the 5 mm screen, which would allow focusing studies for the 5 mm scintillator to be performed by sandwiching a resolution test pattern between the 2 mm and 3 mm screens. This is necessary because, for the best focus, the CCD lens should be focused at the center of the screen.

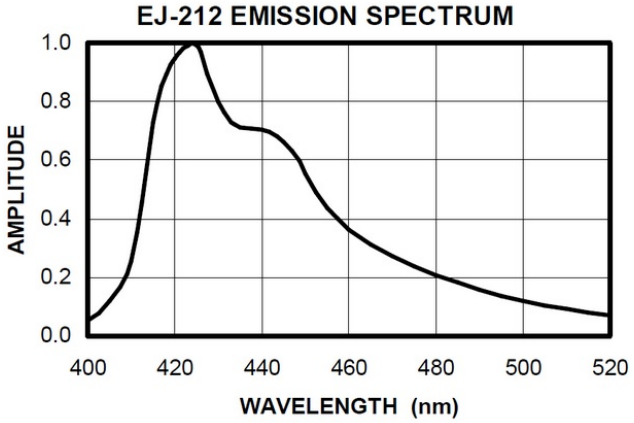


Figure 4.6: Eljen EJ-212 scintillator emission spectrum with a peak wavelength of 423 nm [53].

Screen edges were either rough-cut or diamond-milled. Diamond-milled edges are better for imaging because there is less scatter from the edges of the scintillator, but they are more costly and time-intensive to produce. The scintillator was placed in an aluminum frame that attached to the outside of a light-tight box. The frame surrounded the outside of the scintillator to block external light from entering the scintillator and contaminating the neutron signal. The back of the screens were painted black with a plastic-compatible paint to prevent photon scatter into the scintillator from the aluminum scintillator holder.

4.2.2 ICCD Camera

Since the scintillator emits light with a peak wavelength of 423 nm (see Figure 4.6), a blue-sensitive intensified CCD camera was necessary. The ICCD also needed to have the capability of narrow time gating in order to reject scatter and select energy (which arrives $\sim$1 ns after the direct signal according to work in Section 4.1), as well as operate at the high repetition rates seen with pulsed accelerator sources ($f\sim$1 MHz). The Princeton Instruments PI-Max4 emICCD camera met these requirements, with possible gate widths as narrow as 500 ps and repetition rates of up to 1 MHz. The camera can gate in time by turning the camera intensifier on and off, with light from the converter screen integrated only when the intensifier is gated on. In this way, by opening the camera "shutter" at a specified time and for a given duration, only signal of interest will be integrated while other signal is simply rejected.

The PI-Max4 camera intensifier is coupled with fiber-optics to the CCD chip [53]. The CCD chip has 1024 x 1024 pixels (13×13 μm^2 in size) and a vertical shift rate of 3.4 μs per row of pixels. The camera is run by Princeton Instrument's LightField software, which controls camera settings such as gain, triggering, time gating, and the like. A photograph of the PI-Max4 camera can be seen in Figure 4.7 [55].

This camera is unique in that it has the ability to have two sources of gain applied to it, making it sensitive to single photons. Gain is applied to the CCD chip, which is



Figure 4.7: Photograph of the PI-Max4 emICCD camera and power supply [56].

typical of CCD cameras. The additional gain is applied to the microchannel plate so as to allow for high sensitivity in low-light situations (Figure 4.8) [56]. Each source of gain, however, contributes to noise within the image; studies to determine their individual contribution to noise will be discussed in Chapter 5.

To reduce electronic noise in the camera that degrades image quality, the PI-Max4 camera has the ability to be cooled with an external liquid chiller. The chiller allows the camera to maintain the recommended operating temperature of -20 °C, which is difficult to maintain inside the light-tight box in the absence of a coolant [55].

4.2.3 ICCD Camera Lenses

Two Edmund Optics C-mount lenses were used with the initial system design. The first lens had a 75 mm focal length and $f/4$ maximum aperture, and the second lens had a 50 mm focal length and $f/2$ maximum aperture. For almost all of the measurements, the latter lens was used because of the relatively short distance between the mirror and the camera, which required a shorter lens focal length and wider field of view. The 50 mm lens also has the benefit of letting in more light due to its larger maximum aperture, a useful characteristic in low-light situations (such as a high-energy neutron source incident on a plastic scintillator).

4.2.4 Front Surface Mirror

An optical-grade (1 μm resolution) front surface mirror made of float glass was purchased to reflect light from the scintillator into the camera lens (Figure 4.9). A front surface mirror (also called a first surface mirror) is a particular type of mirror often used in optical applications because it it designed to prevent "ghosting", or internal reflections that degrade image quality, by placing an aluminum coating on the front of the mirror [57]. The coating is stable at the temperature range used for this system. The mirror has dimensions of 15.1 cm × 21.5 cm × 0.25 in. Interpolating between the values listed in Reference [58], light of 425 nm (nearly the

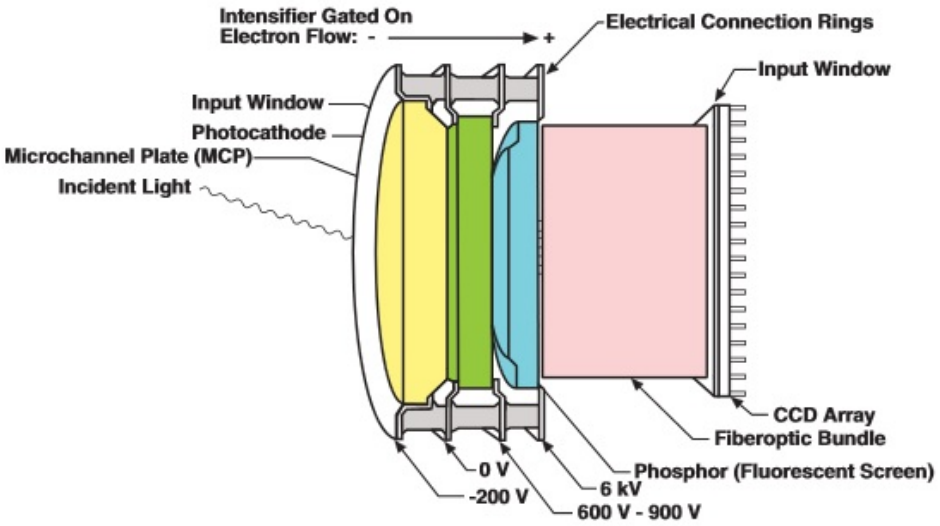


Figure 4.8: Diagram of the PI-Max4 intensifier that is fiberoptically coupled to the CCD array. The PI-Max4 is unique because it has gain applied to the microchannel plate, as well as to the CCD chip [56].

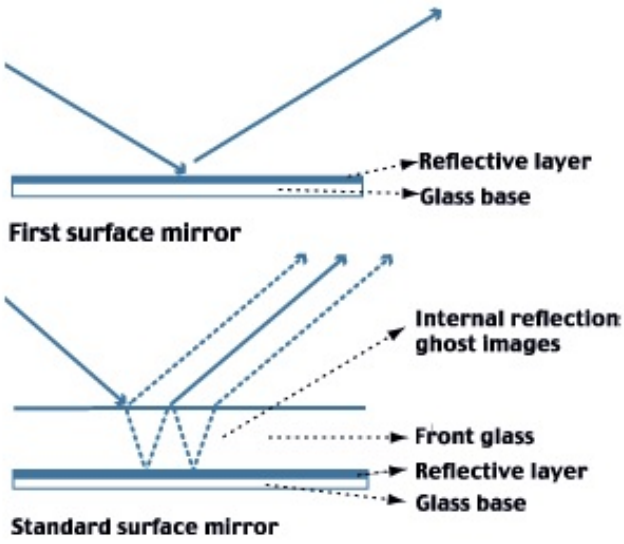


Figure 4.9: Illustration of the difference between a front surface mirror (top; also called "first surface mirror") and a standard surface mirror (bottom) [57].

peak wavelength of light emitted by EJ-212) has a reflectivity of 92.5% for 6° and 45° angles of incidence on the mirror [58].

The mirror was mounted in an aluminum mirror mount and placed in the light-tight box at a 45° angle to both the scintillator and the camera. Light emitted from the scintillator is thus reflected 90° into the camera lens. The mount was adjusted so the mirror was vertical. Both of these adjustments were important to prevent distortion of the object being imaged.

4.2.5 Pulsed Light Source for Testing

A pulsed light-emitting diode (LED) laser, the Horiba DeltaDiode, was purchased to test the timing and gating of the camera in the absence of a pulsed neutron source (Figure 4.10) [59, 60]. The LED wavelength is controlled by the attachment of a laser head to the laser system. For this project, the Horiba 425L laser head was used, which emits light at a wavelength of 425 nm (nearly the peak wavelength of EJ-212) and has a peak power of 230 mW. Laser pulses are 70 ps wide at a frequency of up to 100 MHz [59]. A diffuser with a shutter was attached to the front of the laser head; with the shutter closed, the diffuser increased safety and converted the collimated laser beam into a diffuse source of light.

The LED laser served as a visible light source to focus the lens in lieu of neutrons incident on the scintillator. The laser head was placed inside the light-tight box and aimed at a printed resolution pattern (i.e., the Siemens test pattern shown in Figure 1.12) that had been placed over the scintillator. Thus, instead of using neutron-generated light from the scintillator to focus the camera, the ICCD camera detected LED light reflected off the printed resolution pattern.

4.2.6 Delay Generator for Time Gating

The ICCD camera opens its shutter based on when it receives an input signal, typically referred to as a "trigger signal". The trigger signal is generated by a waveform



Figure 4.10: Photograph of the DeltaDiode control unit (white) with a laser head (black) resting on top [60].

generator in pulser mode if imaging with the LED laser, or by a pulsed neutron source if imaging with neutrons. A delay generator was purchased to add delay to the trigger signal, and thus control the opening and closing of the camera shutter so that time bins could be moved to select neutrons of interest (e.g., neutrons that were unscattered and/or of a particular energy).

The Stanford Research Systems DG645, shown in Figure 4.11, was purchased to delay the trigger signal for several reasons. First, the DG645 has 4 independent trigger outputs, as well as many combinatorial trigger outputs [61]. Multiple outputs are necessary to allow for separate delays to be applied to distinct pieces of equipment. This was found to be necessary when using the LED laser for system testing; the camera and the laser had different internal delays, so the laser needed a delay independent from the camera so that laser pulses aligned with the opening of the camera shutter. The smallest internal delay for the CCD camera is 36 ns, but that of the LED laser was seen experimentally to be 15 ns, and therefore needed a longer delay than the camera.

The DG645 was also selected due to a very small internal delay (85 ns) and very short output pulse rise time (100 ps), both which are necessary for fast timing applications. In addition, the DG645 has time resolution of 5 ps and jitter of 12 ps, due to the use of a rubidium timebase that allows for extremely stable timing [61].

4.2.7 Other Equipment

An oscilloscope (Tektronix TDS 3032B) and waveform generator (Agilent 33522A; run in pulser mode) were used for system development and testing. The oscilloscope was used to view waveforms and confirm correct delays were added by the delay generator. The waveform generator was used during system testing to generate input pulses for the delay generator, and was used in lieu of the external accelerator trigger signal from a pulsed neutron source. These two pieces of equipment were already owned by the group and did not need to be purchased.



Figure 4.11: Photograph of the front display of the Stanford Research Systems DG645 digital delay generator [61].

4.2.8 Typical Experimental Set-up

A block diagram of the laboratory experimental set-up in absence of a pulsed neutron source can be seen in Figure 4.12. For experiments with a pulsed neutron source, the waveform generator is disconnected and the laser head is removed from the interior of the box. A photograph of the interior of the light-tight box can be seen in Figure 4.13. An optical breadboard was placed in the bottom of the light-tight box so that equipment could be bolted in place and easily lined up. Areas of potential light leaks were covered with black electrical tape, and the interior of the light-tight box was covered with a black velvet-like material to prevent scatter within the box. The lid, not shown in Figure 4.13, is simply closed and locked shut when an experiment is in progress.

4.3 First Light Measurement

The first time that an ICCD camera generates an image is dubbed by the imaging community as the camera's "first light". The purpose of such a measurement is to ensure components are working properly and to learn how to use the equipment and software. A photograph of the set-up for the first light can be seen in Figure 4.13. A "smiley face" was drawn on a sheet of paper, placed over the scintillator, and illuminated by the laser in order to ensure that the camera could "see" the drawing. Once it was confirmed that the camera could take images, the smiley face was replaced by a Siemens star pattern in order to focus the lens.

The 50 mm lens was set to an aperture of $f/2$. The lens was then adjusted to bring the smiley face into focus, which is a rather slow process. First, a reference image was taken to judge the camera focus. If out of focus, the laser was turned off and the light-tight box was opened so that the lens' focusing ring could be slightly moved. The box was then closed and the laser again turned on in order to take a subsequent photo. The images were compared and the process repeated until the

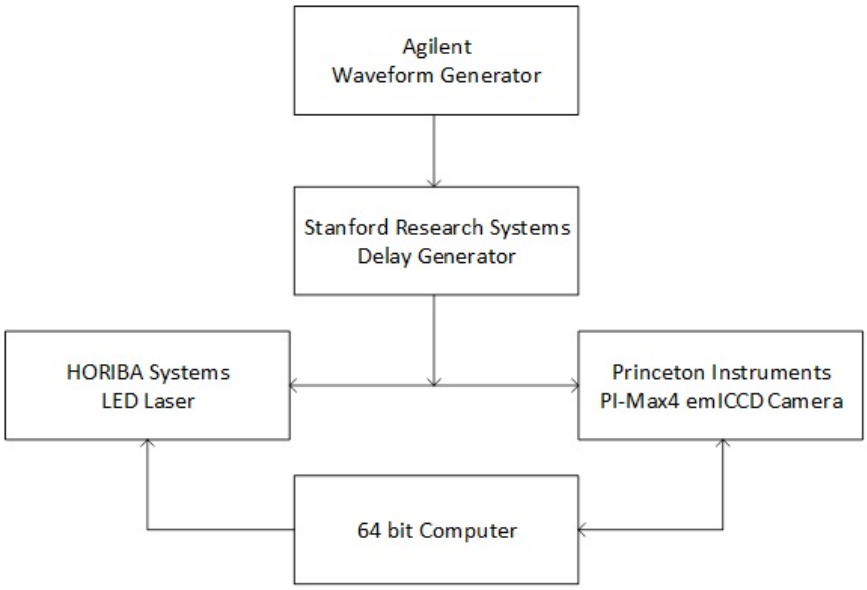


Figure 4.12: Block diagram of the typical TiGReSSE experimental system set-up. For cases with an external neutron source, the waveform generator and LED laser are not used. Instead, the accelerator provides the trigger signal.

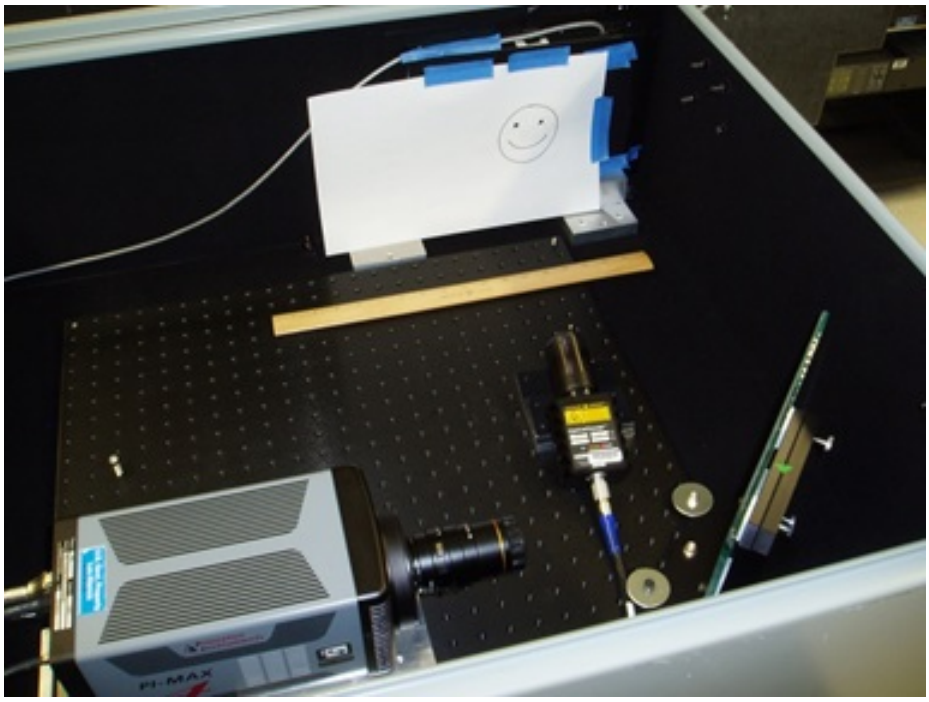


Figure 4.13: Photograph of the interior of the light-tight box showing the ICCD camera and lens (bottom left), the mirror and its mount (bottom right), and the laser head with an attached diffuser (center). The scintillator is behind the paper with the smiley face used to mimic an imaging object (top center). An optical breadboard can be seen on the bottom of the box and is used for attaching and aligning TiGReSSE components. An 18 *in* ruler is shown for scale (center).

smiley face appeared to the viewer to be at the best focus. The lens was then locked in place so that this process would not need to be repeated. The resultant image can be seen in Figure 4.14.

Figure 4.14 was generated with the following settings and system geometry. The diffused laser was placed approximately 6 in from the smiley face drawing to further diffuse the LED light and keep the laser head out of the camera's field of view. The CCD camera was set to integrate 10,000 laser pulses per frame (i.e., the shutter was opened and closed 10,000 times). Only 10 ns of each laser pulse was integrated. To form a sharp image, 15 frames were taken and then averaged together using LightField software. The camera's intensifier gain was set to 10 and the EM gain on the microchannel plate was set to 50 in the LightField camera software. Also in the software, the camera temperature was set to 0 °C. The waveform generator, used to trigger the delay generator, formed pulses with width of 200 ns and frequency of 10 kHz. The delay generator independently delayed the camera 5 ns and the laser 20 ns.

Once a focused smiley face image was formed, the lens was further focused with a Siemens star pattern. To provide more uniform light, the laser head was moved to a location 12 in from the pattern. Forty frames, each generated with 100,000 pulse accumulations, were averaged together in post-processing to generate a clean image. The lens was then locked in place so the focus could not be accidentally changed by bumping or moving the camera. At this point, TiGReSSE was ready for initial experimental testing with a pulsed neutron source.

4.4 Conclusions

This section outlined the initial design of TiGReSSE. MCNP6 simulations, as well as analytic calculations, were conducted to determine the approximate difference in TOF between direct neutrons, elastic scatter, and inelastic scatter. It was seen that the direct signal arrives $\sim$1 to 3 ns before the elastic scatter, and thus an ICCD



Figure 4.14: A computer screen shot of LightField software showing a focused image of a smiley face drawing. Tape used to affix the drawing to the light-tight box can be seen in the corners of the image. The orange and purple plots above and to the left of the image are horizontal and vertical line-outs of the image, respectively, and show how pixel values vary with location in the image.

camera with narrow time gating capabilities was necessary. Inelastic scatter was also seen to arrive much later in time than the direct signal, and care must be taken so that direct signal from a subsequent pulse does not overlap with the inelastic scatter from a previous pulse. The camera also needed to operate at high repetition rates to match the frequency of pulsed sources such as LANSCE.

Equipment was purchased that met the requirements of a fast neutron radiography system employing TOF scatter rejection and energy selection. Equipment was tested using a waveform generator in pulser mode to mimic the neutron accelerator trigger signal. The generator's signal was then used to trigger the LED laser and the camera, with independent delays added by the delay generator. The camera had a successful first light measurement, and the lens was properly focused at the scintillator plane. With initial testing completed, the LED laser could be replaced with a neutron source for additional system testing and development.

Chapter 5

Initial Neutron Radiography Testing

This chapter outlines the initial experimental testing of TiGReSSE with a pulsed, high-energy neutron source, replacing the laser light source used for system development in Chapter 4. Experiments described in this chapter used a pulsed D-T generator as a source of 14.1 MeV neutrons, as well as the LANSCE pulsed spallation source that generates neutrons ranging in energy from ∼0.1 to 600 MeV. Goals of these tests were to determine whether the camera could survive in a high flux, high-energy environment; find the approximate length of time required to form radiographs; define general system behavior; and identify the system design elements that needed improvement.

5.1 D-T Radiography

Initial tests of the radiography system were conducted with a D-T generator. Unfortunately, the D-T signal was too weak to be detected by the camera, in part because the camera overheated in the light-tight box with prolonged use and caused an increase in electronic noise that masked the neutron signal. Mostly, however, the

source could not be detected because of geometric losses resulting from the system design. Thus, while images could not be generated, it was learned that a liquid chiller was necessary to keep the camera cool during subsequent experiments at LANSCE.

5.1.1 Experimental Overview and Results

For initial TiGReSSE testing with a neutron source, B. Myers of Los Alamos National Laboratory offered the use of his D-T generator (Figure 5.1). The Thermo Scientific D-T generator (Model P 211) provides a monoenergetic source (which, as stated earlier, is preferable for scatter rejection). The generator operates at a frequency of up to 100 Hz and emitted, on average, 1.5×10^6 neutrons per pulse with a 10 μs pulse width [62]. This yields an average flux of 1.5×10^8 $neutrons/s$.

However, as stated in this chapter's introduction, it was discovered via experimentation that the D-T flux was too low to be used for imaging with TiGReSSE. In principle, a low-intensity source could be integrated for many hours so that enough signal could be accumulated to form an image. However, the camera warmed up very quickly in the light-tight box (most likely because of the light-absorbing black velvet-like material lining the box), which forced the operators to run the camera in the range of 0 °C to 10 °C, far above the recommended operating temperature of -20 °C. As a result, the electronic noise at the warmer camera temperatures competed with the neutron signal, overwhelming the neutron signal and preventing the formation of a radiograph. Nonetheless, the experiment was useful because it showed that the purchase and installation of a liquid chiller was necessary to keep the camera at the recommended -20 °C.

5.1.2 Total System Efficiency Calculations

To lend credence to the idea that the camera was too warm and the source was too weak to generate radiographs, rough calculations were conducted to determine the number of photons received in the lens per D-T neutron pulse. This value could then

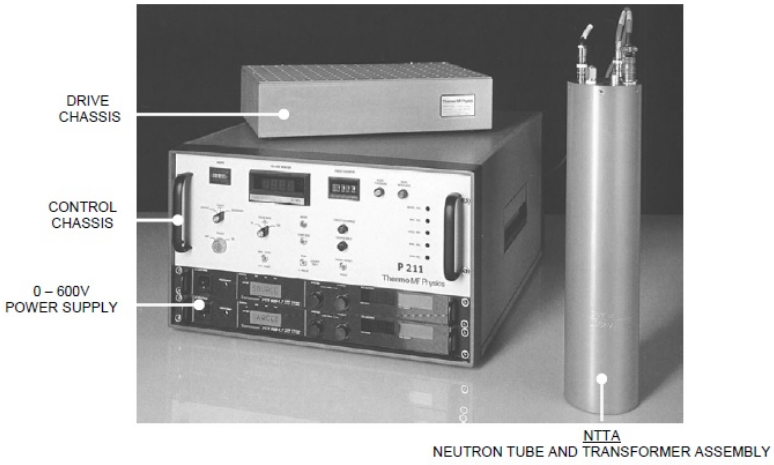


Figure 5.1: D-T generator and control equipment that were used for initial system testing [62].

be compared to documented electronic noise levels to show that the D-T signal could not compete with the electronic noise within the camera.

During the experiments, the D-T generator was placed 0.5 m from the 5 mm thick scintillator screen and emitted, on average, 1.5×10^6 neutrons per pulse into 4π with energy of 14 MeV. The source is designed to emit neutrons isotropically, so only a fraction of the pulse's flux reaches the scintillator. Assuming the neutrons are emitted into a sphere with radius r and surface area SA (where $SA = 4\pi r^2$), the TiGReSSE scintillator with surface area of 64.0 in^2 (or 412.9 cm^2) receives only 1.3% of the emitted neutron pulse, or 2.01×10^4 neutrons per pulse.

A small fraction of these neutrons then react in the plastic scintillator by elastically scattering from the hydrogen in a "proton knock-on" reaction; the majority of the neutrons, however, simply pass through the screen without interacting. According to Reference [63], the small fraction, F, of neutrons that undergo an elastic scatter collision in the screen can be described by

$$F = 1 - e^{-\sigma d}, \tag{5.1}$$

where d (cm) is the thickness of the scintillator screen. The variable σ (cm^{-1}) is the linear attenuation coefficient that is described by

$$\sigma = \frac{\rho N_A H \sigma_s}{W}, \tag{5.2}$$

where ρ is the density of the plastic scintillator, N_A is Avogadro's number, H is the number of hydrogen atoms per polymer unit, σ_s is the neutron elastic scattering cross section, and W is the molecular weight of the plastic polymer [53, 54, 63, 64]. Using the values listed in Table 5.1, Equations 5.1 and 5.2 yield $\sigma = 3.587 \times 10^{-2}$ cm^{-1} and $F = 1.78 \times 10^{-2}$.

Thus, only 1.78% of the 2.01×10^4 neutrons per pulse that reach the screen actually interact with the screen, which is equal to $F = 358$ scattered neutrons

Table 5.1: Variable values used in Equation 5.2 for 14 MeV neutrons incident on EJ-212 scintillator of 5 mm thickness [53, 54, 63, 64].

Variable	Value	Units
ρ	1.023	g/cm^3
N_A	6.022×10^{23}	mol^{-1}
H	30	$atoms/polymer$
σ_s	6.87115×10^{-25}	cm^2
W	354	g/mol

perD-T pulse. Ignoring neutron scatter from carbon atoms in the plastic scintillator, the number of scattered protons equals the number of scattered neutrons, such that there are also 358 scattered protons per D-T pulse.

The average amount of energy transferred from a neutron to a proton, ΔE, is found by

$$\Delta E = \left(\frac{1-\alpha}{2}\right) E_i, \tag{5.3}$$

where E_i (MeV) is the incident neutron energy (here, $E_i = 14\ MeV$). The term α in Equation 5.3 is described by

$$\alpha = \left(\frac{A-1}{A+1}\right)^2, \tag{5.4}$$

with A equal to the charge of the target atom [63]. For hydrogen (which is essentially a proton), $A = 1$ and $\alpha = 0.5$, so $\Delta E = 0.5E_i$. Thus, the neutron loses, and the proton gains, an average of 7 MeV during an elastic scatter in the scintillator.

Once the proton is scattered, some fraction of its kinetic energy, δE, is deposited in the scintillator screen, which is then converted to light via scintillation mechanisms. Assuming all proton energy is deposited in the screen (i.e., ignoring leakage out of the surfaces so that $\delta E = 7\ MeV$), the scintillator efficiency, ε, can be defined as

$$\varepsilon = (\delta E)\, R\epsilon, \tag{5.5}$$

where R is the ratio between the efficiency of a photon at creating light to that of a proton (thus converting units from MeV to $MeVee$) and ϵ is the number of photons created per $MeVee$ deposited in the screen. As a rough estimate for this application, Reference [65] states that a 1 MeV photon produces 6 times as much light as a 1 MeV proton; thus, $R = \frac{1}{6}$. As stated on the Eljen website, $\epsilon = 1 \times 10^4$ photons are generated per deposited $MeVee$ [53]. Solving Equation 5.5, $\varepsilon = 1.17 \times 10^4$ photons are generated per scattered proton (or $\varepsilon = 4.19 \times 10^6$ photons per D-T pulse).

Only a fraction of these photons, however, reach the lens and pass through the lens aperture due to geometry losses in the TiGReSSE design. Combining terms, the number of photons entering the lens, N_γ, is found by

$$N_\gamma = \varepsilon F \left(\frac{Area_{lens\ aperture}}{SA_{emitted\ light}} \right), \tag{5.6}$$

where $Area_{lens\ aperture}$ is the area of the lens aperture and $SA_{emitted\ light}$ is the surface area of the sphere into which photons are isotropically emitted from the scintillator. The aperture area available to detect photons for a 50 mm lens set to $f/2$ is found with Equation 1.10 to be $4.91 \times 10^{-4}\ m^2$. The distance between the scintillator and the camera equals 0.8 m, a value which is used to find $SA_{emitted\ light}$.

Substituting values, Equation 5.6 therefore becomes

$$N_\gamma = \left(1.17 \times 10^4\ \frac{gammas}{proton} \right) \times \left(358\ \frac{protons}{pulse} \right) \times \left(\frac{4.91 \times 10^{-4}\ m^2}{4\pi\ (0.8)^2\ m^2} \right), \tag{5.7}$$

which yields a value of $N_\gamma = 256$ gammas entering the lens per pulse. This is equivalent to $1.7 \times 10^{-4}\ \frac{\gamma}{neutron}$, or, with $(1024)^2$ pixels on the CCD chip, $2.4 \times 10^{-4}\ \frac{\gamma}{pixel/pulse}$. This means that, at the D-T generator's operating frequency of 100 Hz, there are 100 pulses per second and thus only $2.4 \times 10^{-2}\ \frac{\gamma}{pixel/s}$.

Documentation on the PI-Max4 states that the dark current noise is approximately 2.5 electrons per pixel per second [55]. The dark current is thus nearly 100 times greater than the signal entering the camera from the neutron source. This is especially true when one considers that these calculations overestimate N_γ. It was assumed that all protons were stopped in the scintillator, ignoring leakage effects that result in partial energy deposition and a smaller number of photons generated by the scintillator than was calculated. Additional light loss that occurs in the mirror and lens due to attenuation and reflection was also ignored for this rough calculation. Attenuation of the D-T pulse in the radiography object, which would result in fewer neutrons incident on the scintillator, was also ignored, as were efficiency losses in the

CCD chip and photon multiplication effects within the camera resulting from added gain.

Additionally, the value for R from Reference [65] was for 1 MeV protons, much lower than the average proton energy of 7 MeV. Reference [65] also cited this value for a different plastic scintillator. For these two reasons, R is probably much less than the value used here, since increasing the proton energy (here, from 1 to 7 MeV) decreases proton stopping power and increases leakage. Thus, fewer photons would be generated because less energy is deposited in the scintillator.

5.1.3 Lessons Learned

While the D-T generator signal was too weak to form neutron radiographs, this experiment led to the purchase of a chiller to keep the camera at its recommended -20 °C. The chiller pumps an antifreeze-deionized water mixture through the camera so it may operate in a safe environment that leads to reductions in electronic noise. This experiment and the subsequent calculations also underscored the importance of the neutron source characteristics, including source strength. The source flux at the scintillator plane will need to be ∼100 times greater than that of the D-T generator to approximately equal the camera's electronic noise, and ∼1000 times greater for the radiography signal to be greater than the camera noise.

5.2 LANSCE Radiography

5.2.1 Overview

The next set of neutron radiography experiments were conducted at LANSCE in January, 2015. The scientists on this project were given the opportunity to share one week of beam time at LANSCE with another scientist at LANL, J. Hunter. While the LANSCE accelerator is polyenergetic, which makes only partial scatter rejection possible, the LANSCE beam does have the high flux, high-energy, and fast timing

source characteristics that make it a desirable pulsed source for proof-of-principle testing of TiGReSSE.

The experiment was conducted in LANSCE's Flight Path 15 Right (FP15R), where "15" signifies the beam line's angle from the spallation target's centerline, and "R" signifies that the flight path is to the right of the spallation target from the target's point-of-view [66]. The target, a tungsten cylinder, is referred to as Target 4 and has six flight paths radiating off of it. A diagram of the beam lines can be seen in Figure 5.2, with Target 4 indicated by a red arrow and FP15R indicated by a blue arrow [67].

The spallation photons and neutrons are generated via a proton reaction in the tungsten target. LANSCE accelerates protons to 800 MeV and bunches them into micropulses, some of which then collide with Target 4 (other micropulses are sent to additional LANSCE spallation targets or are directly used for proton radiography). Spallation neutrons are created in the target via the (p, n) reaction in the tungsten cylinder. FP15R is at a very small angle from the target and thus receives mostly forward-peaked spallation particles. As a result, FP15R receives neutrons ranging in energy from several hundred keV to ~600 MeV, or up to ~80% of the speed of light [66]. As the angle of the flight path from the target's centerline increases, the neutron flux is seen to shift to lower energies (Figure 5.3) [67]. In addition to neutrons, Target 4 also generates spallation photons. The photons are arrive at the detector immediately before the neutron pulse since photons travel at the speed of light and are by definition much faster than neutrons.

The timing of the Target 4 pulses is affected by two factors. First, the macropulse is defined by the time that the radiofrequency (RF) drive is on and accelerating protons toward the target, which typically yields 50 or 100 macropulses per second with a period of 625 μs. Second, the micropulse timing is driven by the frequency of the RF driver, which is what bunches protons into groups before striking the spallation target [68]. The micropulse period was seen to be 1.784 μs (i.e., a pulse of spallation neutrons and photons from the target occurs every 1.784 μs). With a

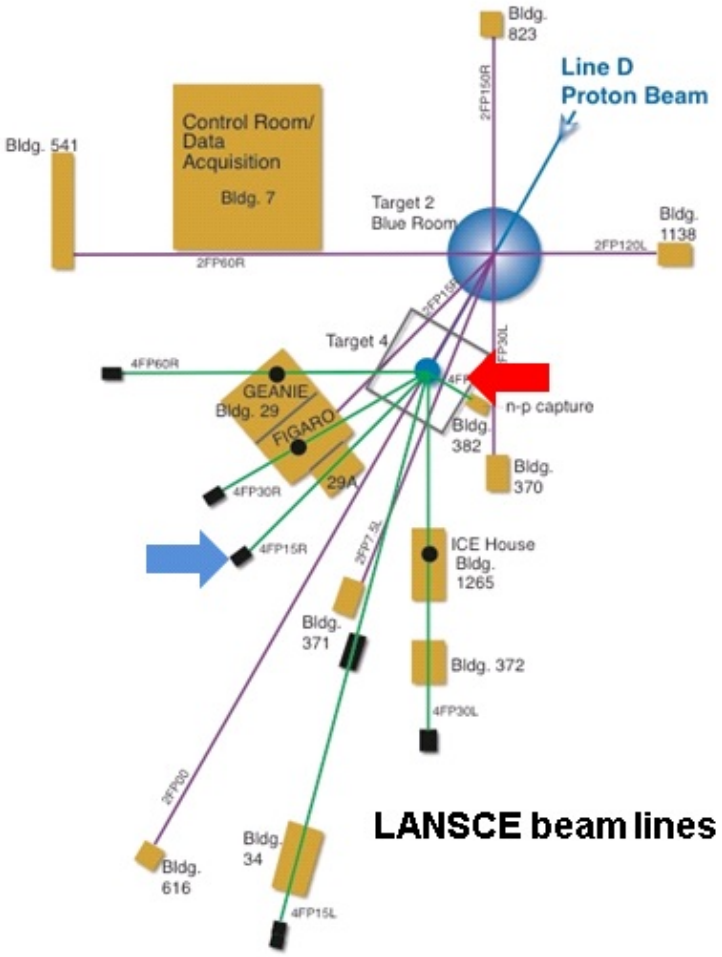


Figure 5.2: Diagram of LANSCE beam lines, with the red arrow pointing to Target 4 and the blue arrow pointing to FP15R [67].

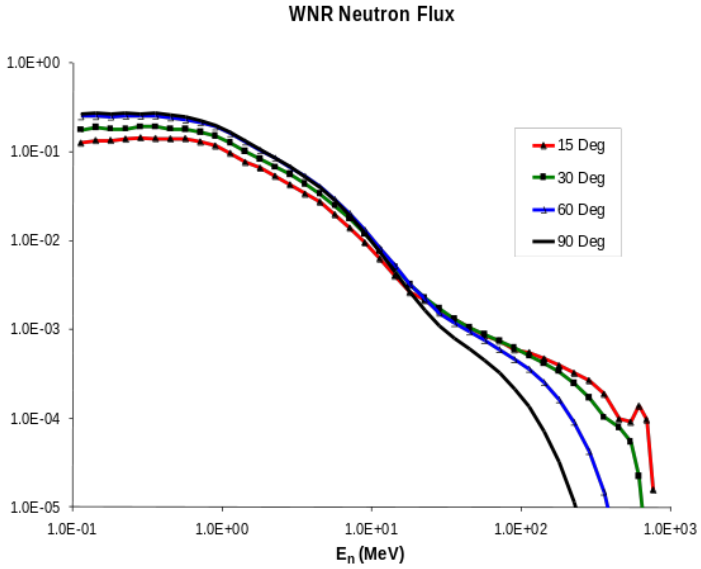


Figure 5.3: Neutron flux profile of four of the six Target 4 flight paths: FP15R at an angle of 15° from the tungsten spallation target, FP30R (angle of 30°), FP60R (angle of 60°), and FP90R (angle of 90°). Note that, as the flight path angle from the target increases, the neutron flux shifts to lower energies. The source of this graphic unfortunately did not include a y-axis label on the plot [67].

macropulse width of 625 μs, there are approximately 347 micropulses per macropulse. To provide an idea of the number of pulses the ICCD camera integrates, a macropulse frequency of 100 Hz yields 3.48×10^4 micropulses per second.

The beam port where the beam enters FP15R consists of a thick steel tube with a 4 in internal diameter. The beam port could be run "full open" with no collimation, or thick, steel cylindrical collimators with bore holes could be slid inside the tube to narrow the beam port diameter. The imaging experiments conducted at LANSCE were mostly run with no collimation in order to get an approximate beam spot of 8 in at the scintillator location (a result of beam divergence), but for some instances, a 2 in collimation was used that provided an approximate beam spot of 4 in at the scintillator. Photographs of the beam port collimators and of the beam port (with an attached fission chamber to measure beam flux) can be seen in Figures 5.4 and 5.5, respectively.

5.2.2 Experimental Set-up

The light-tight box, the camera power supply, and the liquid chiller were placed in the FP15R beam line. The light-tight box was placed on blocks on top of a rolling cart to allow for proper positioning of the box in the beam, with the bottom of the light-tight box at a height of 92.75 cm above the floor. The camera power supply and liquid chiller placed on a lower shelf on the cart. The camera control equipment (i.e., computer with LightField software, delay generator, waveform generator, and oscilloscope) was placed on the other side of the shielding wall to allow for safe operation of the system while generating neutron radiographs.

Time-of-flight for the FP15R beam was next calculated from measured distances between the detector and various components of FP15R. The scintillator, attached to the outside of the light-tight box, was located 10.3 m from the front edge of the beam pipe, which was 13.4 m below the tungsten target. Thus, the spallation particles travel 23.7 m from the tungsten target to the scintillator, which takes



Figure 5.4: Photograph of various LANSCE beam collimators, with the 2 *in* beam collimators used in this experiment.



Figure 5.5: Photograph of the beam port where the beam exits the wall. The attached fission chamber was used to measure beam flux.

600 MeV neutrons approximately 21 ns longer than photons. The time-of-flight for other neutron energies can be seen in Figure 5.6. Incident photons and neutrons are converted by the scintillator into optical photons that then travel an additional distance of 1 m to the ICCD camera; this process adds 3 ns to the time-of-flight calculations.

To protect sensitive camera electronics, shielding materials, such as polyethylene and borated polyethylene, were next placed in and around the light-tight box. Borated polyethylene and polyethylene blocks were placed around the camera inside the light-tight box, with similar blocks placed around the camera power supply and other electronics on the cart's lower shelf (Figure 5.7). A second cart, rolled partially in front of the light-tight box, was used to support steel and borated polyethylene shielding blocks. The cart was placed so that the scintillator was exposed to the neutron beam, but the remainder of the light-tight box was shielded (Figure 5.8).

Figure 5.9 shows a not-to-scale diagram of the experimental set-up in FP15R, which shares a building with neighboring Flight Path 15 Left (FP15L). Photographs of the TiGReSSE set-up can be seen in Figure 5.10. Diagrams of the light-tight box dimensions, shielding placement, and TiGReSSE placement within the flight path can be seen in Figures 5.11 through 5.13.

Final set-up consisted of connecting equipment and obtaining the appropriate timing signals from the accelerator to accurately employ TOF methods according to the block diagram shown in Figure 5.14. The accelerator trigger signal originated from a beam pick-off located approximately 30 to 40 m upstream of Target 4 and was provided by LANSCE. This signal had many unknown inherent delays due to an inexact beam pick-off location, unknown length of signal cable, and unknown signal generation equipment. It was therefore necessary to do additional experiments to determine the relationship between the trigger signal and the arrival of photons at the scintillator, which is the true start of the pulse. These experiments will be detailed in Section 5.2.5 later in this chapter. The accelerator trigger signal was provided by LANSCE and had negative polarity and a pulse width of 20 ns (Figure 5.15).

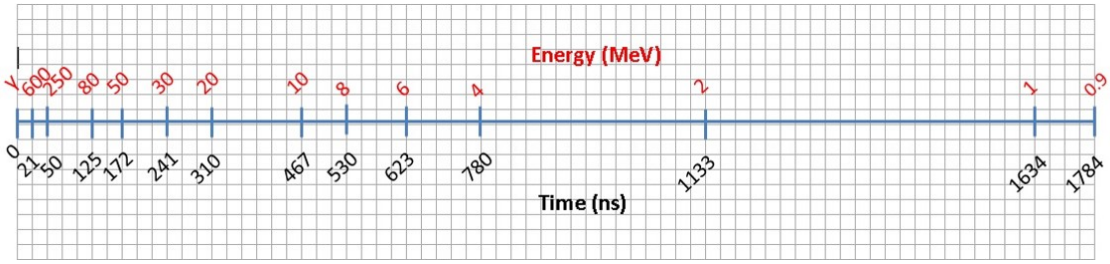


Figure 5.6: Illustration of the time-of-flight (black) of the FP15R beam as a function of energy (red) for a flight path distance of 23.7 m. Diagram is to scale, with each block equal to $\sim$24 ns. Note that $t = 0$ ns indicates the time of arrival of the spallation photons (γ), and that $t = 1784$ ns is the end of the micropulse.

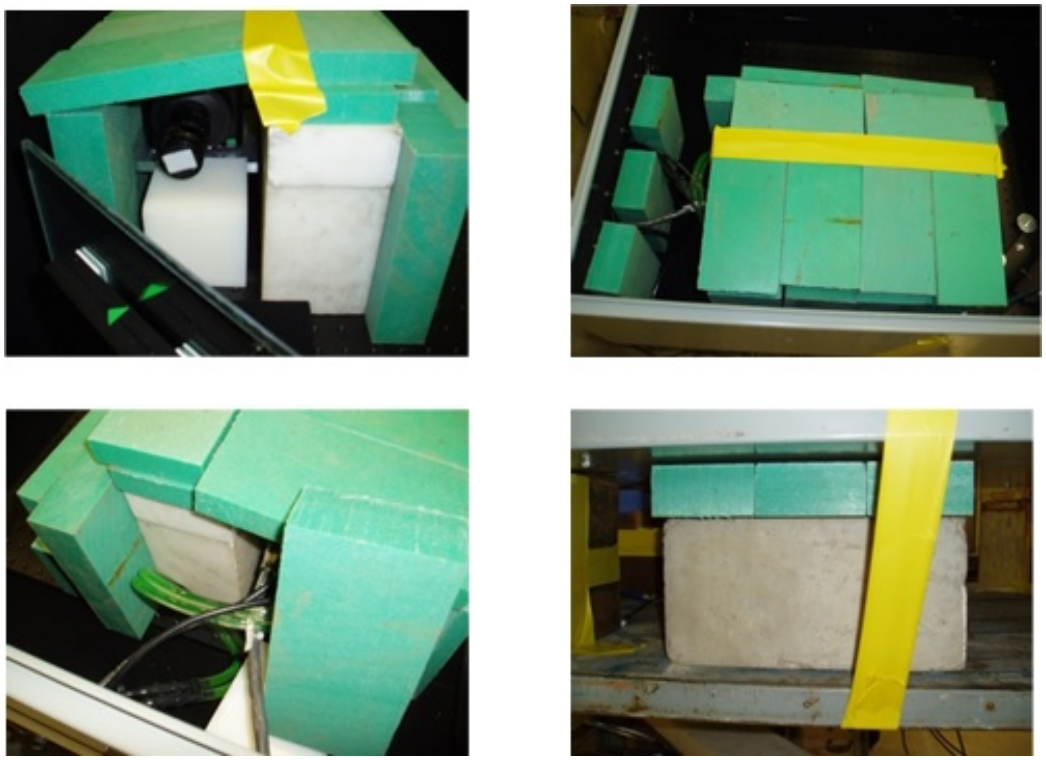


Figure 5.7: Camera shielding composed of polyethylene (white), borated polyethylene (green), and concrete blocks (gray). Yellow tape was used to hold the shielding in place. Top left: Front view of the shielding around the camera, with lens cap on the camera lens. Top right: Top view of the shielding around the camera, with the lens pointed to the right (not shown). Bottom left: Back view of the shielding around the camera, with coolant tubes visible. Bottom right: Shielding underneath the camera and external to the light-tight box to shield scatter from the floor.



Figure 5.8: External shielding for camera (rusty steel blocks and green-colored borated polyethylene). The gray light-tight box can be seen behind the shielding, with the scintillator exposed. Note that the light-tight box was placed on top of stacked steel blocks to lift the box to the height of the beam.

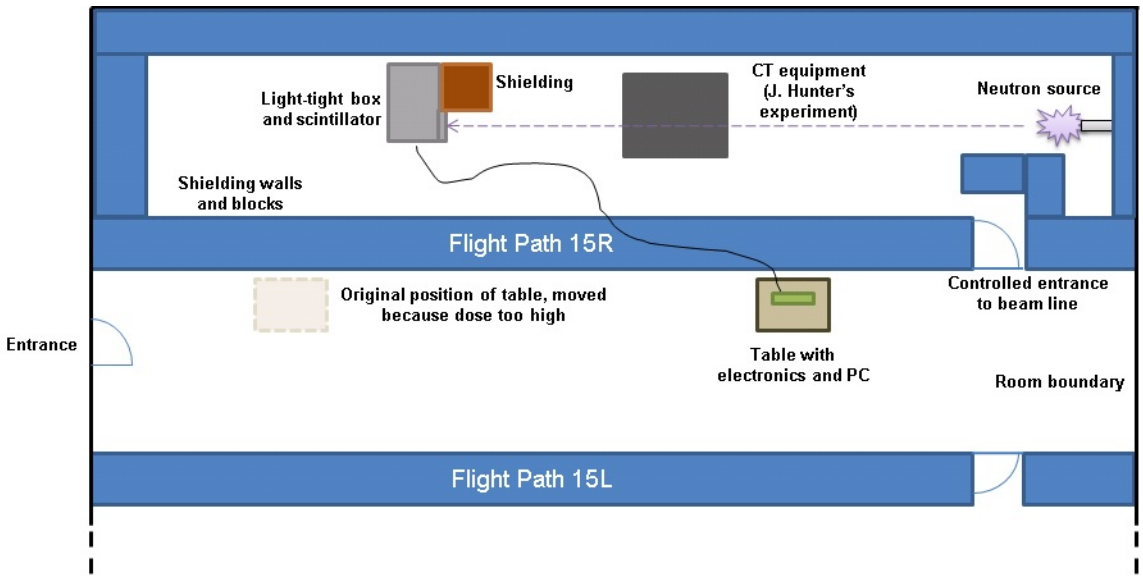


Figure 5.9: Diagram of FP15R and the equipment set-up.

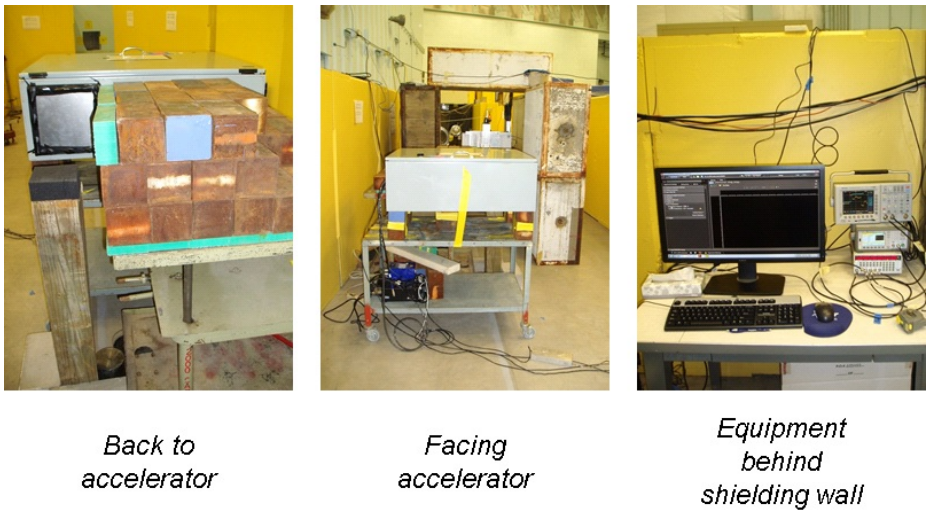


Figure 5.10: Photographs of the equipment set-up in the beam line. Left: Photograph of the light-tight box, wooden sample stand, and shielding blocks with the beam to the photographer's back. Center: Photograph of the light-tight box looking toward the beam. The liquid chiller and camera power supply, also shielded, are visible below the light-tight box. Note the other equipment in the beam line that increases scatter. Right: Equipment used to control the camera, which was located behind the shielding wall for personnel safety.

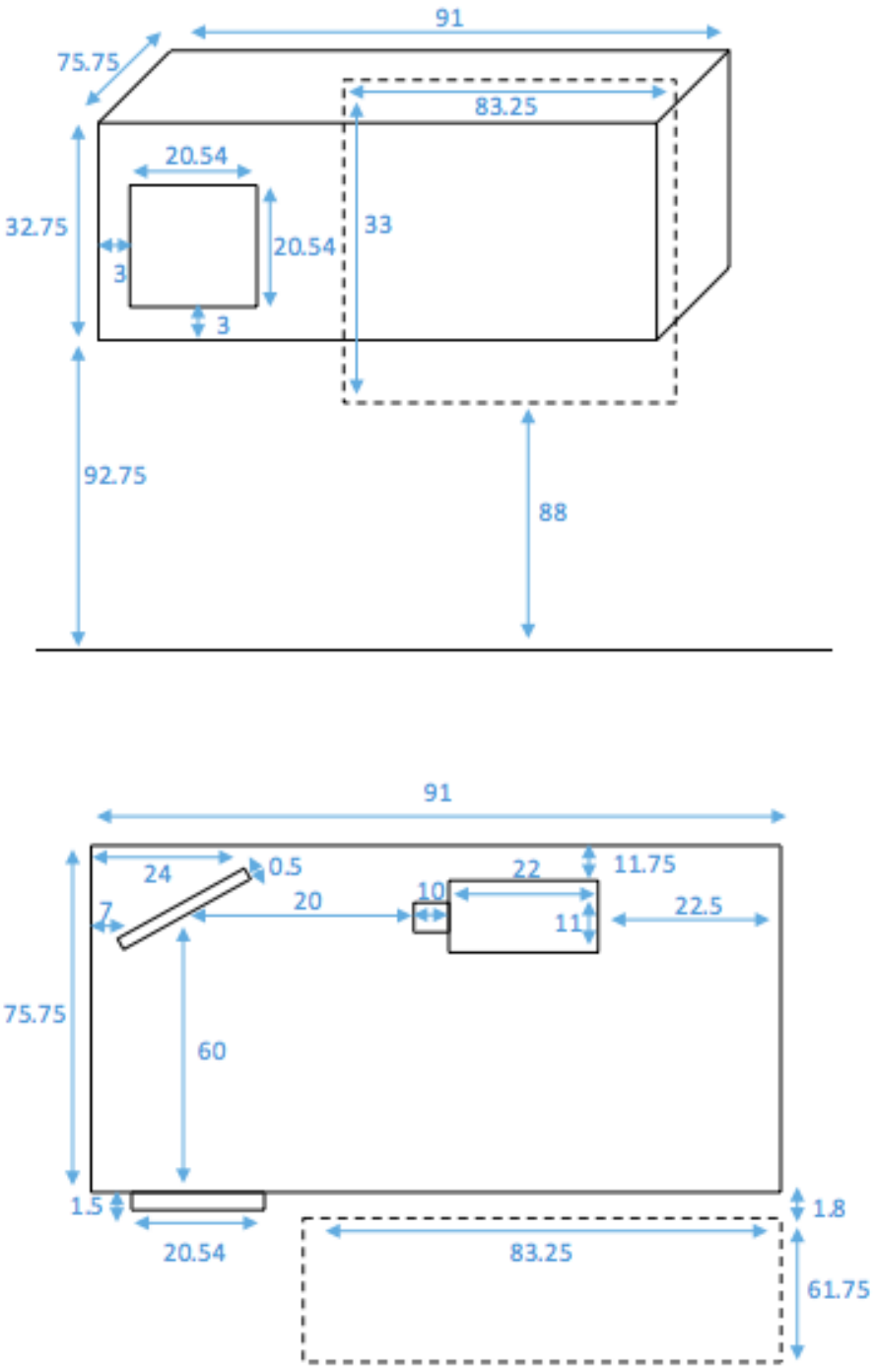


Figure 5.11: Diagrams of the external shielding placement (top) and the placement of equipment within the light-tight box (bottom). Units are in *cm*, and dimensions are not to scale.

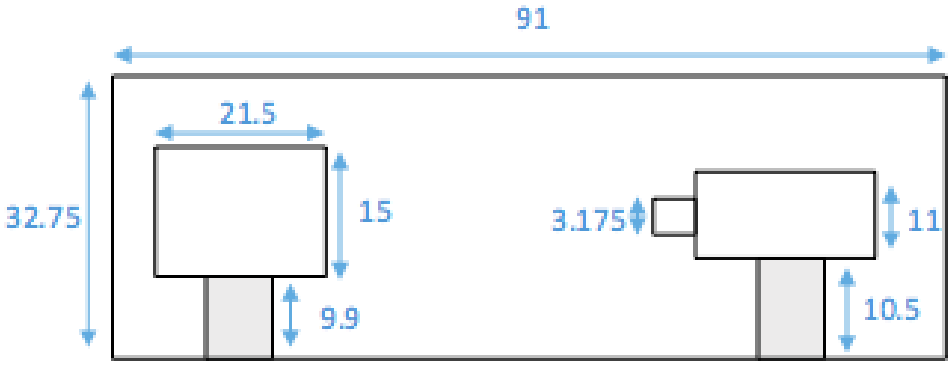


Figure 5.12: Diagram of the components within the light-tight box to illustrate their distance above the bottom of the box. The mirror and its stand are on the left, and the camera and its stand are on the right. The two stands are highly simplistic in this diagram. Units are in *cm*, and dimensions are not to scale.

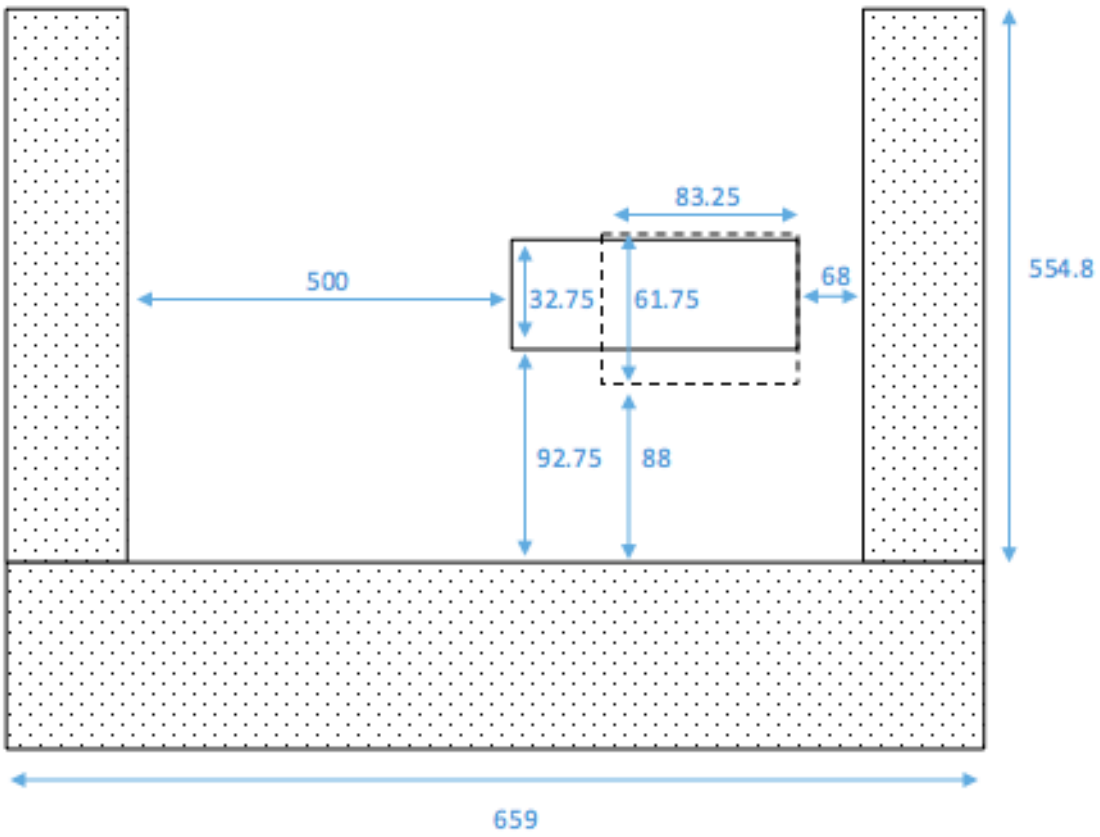


Figure 5.13: Diagram of the light-tight box within the flight path. The beam port is behind the viewer. Thicknesses of the floors and walls are not indicated because those dimensions are unknown. Units are in *cm*, and dimensions are not to scale.

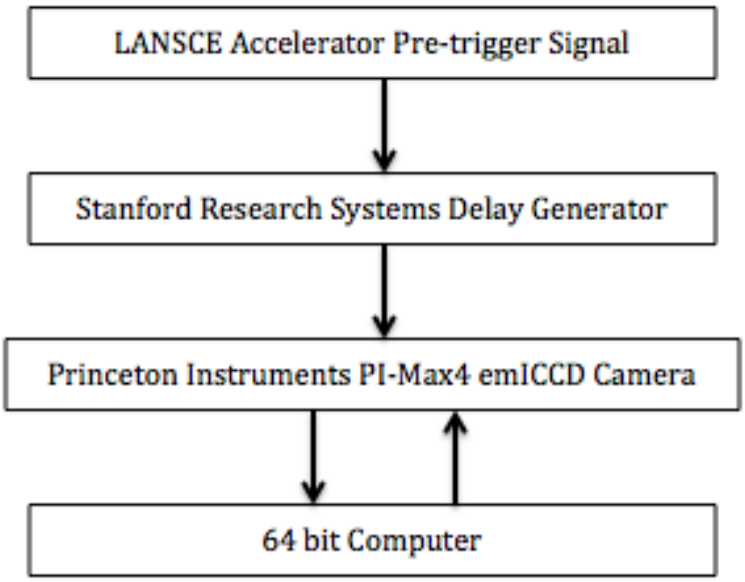


Figure 5.14: Block diagram of the equipment set-up in FP15R.

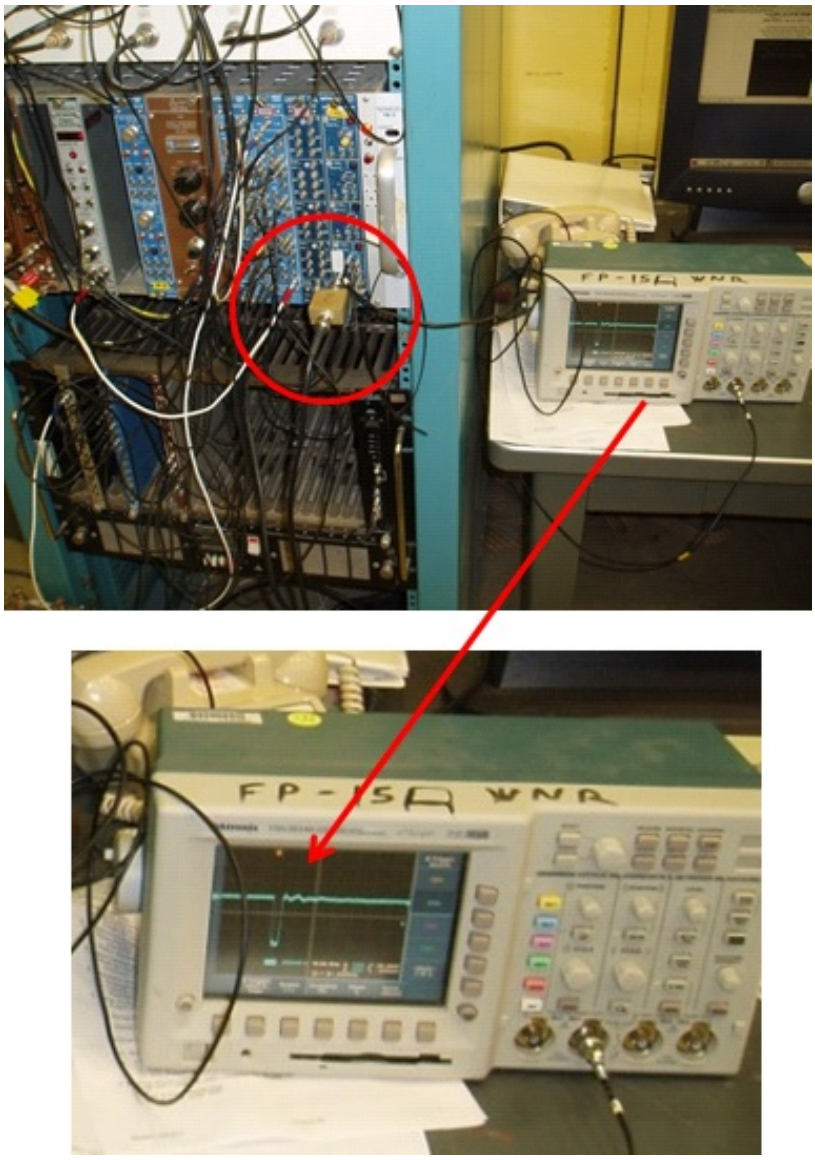


Figure 5.15: Photographs of the trigger signal equipment provided by LANSCE (top) and a view of the trigger signal on an oscilloscope (bottom).

5.2.3 Radiography Objects

Three radiography objects were selected for FP15R system testing and placed in front of the scintillator on a wooden stand 91.5 cm in height (Figure 5.16). The first object, "Object 1", consisted of a lead block measuring $5.7 \times 10.2 \times 20.5$ cm^3, a borated polyethylene block measuring $5.0 \times 9.75 \times 20.0$ cm^3, and a graphite cylinder measuring 4 in in both diameter and height. The three components were stacked such that the lead block was on top of the borated polyethylene block, which was on top of the graphite cylinder. A folded sheet of paper was placed between the lead and borated polyethylene blocks to prevent lead contamination. This object was slightly raised in the field of view by a thin aluminum block that was placed on top of the wooden stand.

Another radiography object, "Object 2", was a stainless steel cylinder with a larger, disk-shaped flange (1.12 in thick) on each end, yielding a total height of 6.24 in. This object contains molybdenum, nylon, polypropylene, stainless steel, gold-coated stainless steel, and tungsten. Object 2 was raised in the camera's field of view by a roll of duct tape and a thin aluminum sheet on the wooden stand. A diagram of Object 2 with dimensions and material locations can be seen in Figure 5.17, and a photograph can be seen in Figure 5.16.

"Object 3", the third radiography object, was a 3 in diameter tungsten sphere with three boreholes: two of 1 cm diameter and 3 cm depth equidistant from a central, deeper borehole of 2 cm diameter and 6 cm depth. The sphere was placed in a thick piece of foam to prevent it from rolling off the wooden stand and hurting someone. A photograph of Object 3 can be seen in Figure 5.16.

5.2.4 Scatter Evaluation

With general experimental set-up completed, evaluation of FP15R scatter was conducted to determine its impact on dose to the ICCD camera and to personnel. To generate a scatter field similar to what would be seen during imaging, the tungsten

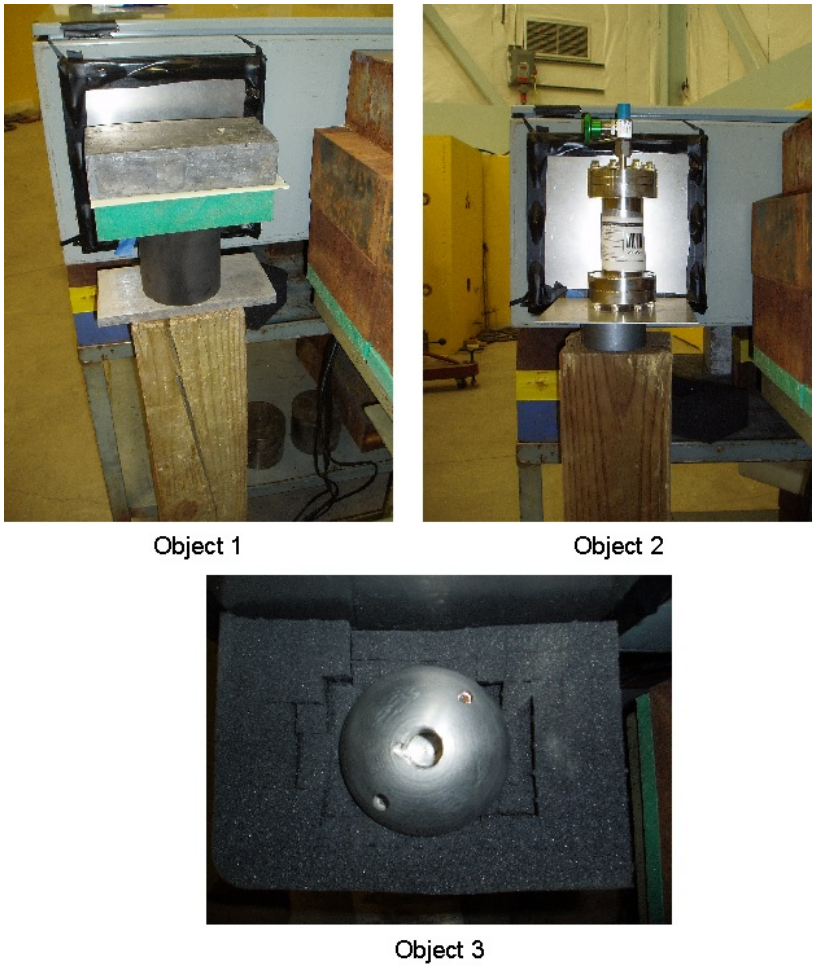


Figure 5.16: Photographs of Object 1, Object 2, and Object 3, the radiography objects that were imaged during the FP15R experiment, as placed in front of the scintillator.

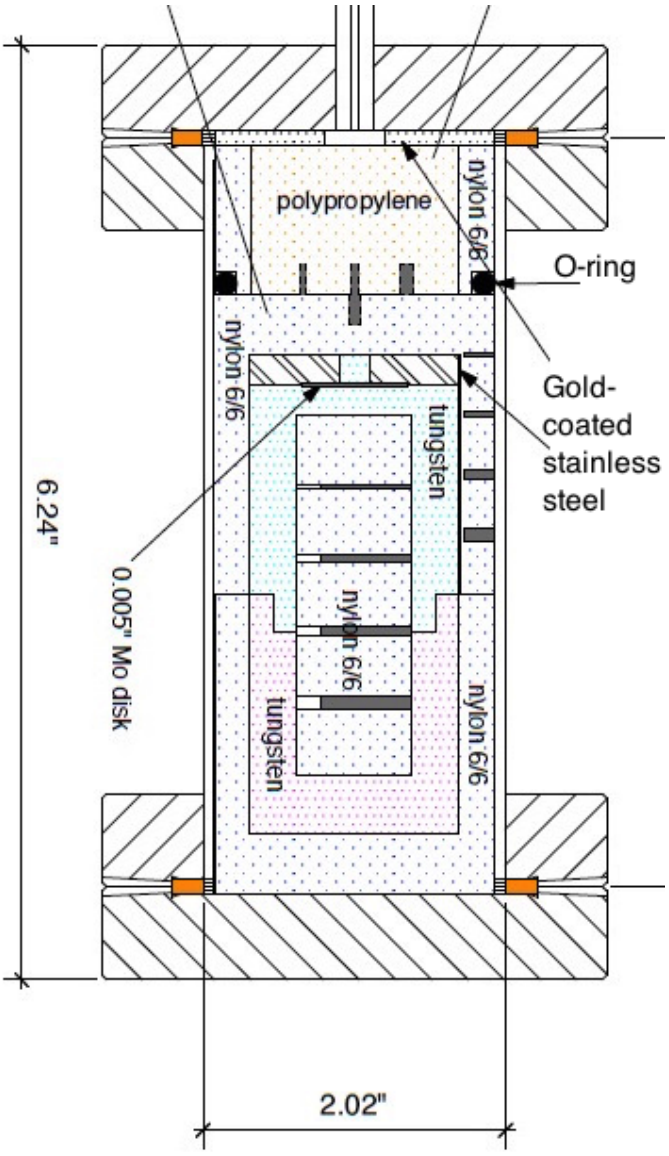


Figure 5.17: Diagram of Object 2, shown here in the orientation used for radiography. A valve is fitted to the object (not shown) and is located at the top of the object. The diagonal lines indicate stainless steel.

sphere was placed on the wooden stand in front of the scintillator. Object 3 was selected because it was made of dense tungsten and would therefore be the largest scatterer of the three objects.

The beam shutter was then opened to take dose measurements outside of the flight path where personnel would be operating the camera remotely. The dose at the location of the control equipment was found to be nearly 5 mR/hr, so the equipment was moved to a new location with lower dose in order to keep personnel dose as low as reasonably achievable (ALARA). This equipment relocation is indicated in Figure 5.9.

While the beam shutter was open, scatter to the camera was also examined. It was found that the scatter hitting the CCD chip was quite large, so the light-tight box was moved and shielding was reconfigured until scatter (and thus dose to the camera) was minimized. Image quality also improved with less scatter into the CCD chip.

5.2.5 Time-of-Flight Scan

Once it was determined that the camera was adequately shielded and ALARA principles had been applied to protect personnel, the next step in the experimental process was to determine the true time of arrival of the spallation pulse at the scintillator. According to time-of-flight principles, the spallation photons arrive at the scintillator first, followed by neutrons of decreasing energy. Therefore, for the purposes of TOF, the arrival time of photons at the scintillator is considered to be the start of the FP15R pulse.

As stated previously, the accelerator trigger signal had unknown time delays (δt), so that the arrival time of the trigger signal at the delay generator (t) was not the same as the arrival time of the photons at the scintillator (T_0), such that $t + \delta t = T_0$ and T_0 is the true start of the pulse if δt is the difference in arrival times.

To find δt, a scan in time of the beam was conducted according to the following general process. Object 2 was placed on the sample stand in front of the scintillator

as a point of reference, with the object partially in the beam so as to not fully block the beam. Two-inch collimation was added to the beam to reduce unnecessary dose to the camera during this process (Figure 5.4). The delay added to the trigger signal by the delay generator was varied in time so that radiographs could be generated with incremental sections of the pulse. Changes in average scintillator brightness as a function of added delay were noted, with a peak in brightness corresponding to T_0 because photons generate more light in the scintillator than scattered protons [65].

This general process was applied as follows. Initially, the delay generator was set to add a delay of 0 ns to the trigger signal, and an image (comprised of 50 frames averaged together) was obtained with a camera gate width of 50 ns. The delay was increased to 50 ns, and again a radiograph was taken with a 50 ns time gate. This process was repeated, incrementally increasing the delay by 50 ns, until the entire 1784 ns wide neutron pulse had been covered.

Next, for each image, a standardized region of interest (ROI) was selected in LightField, which computed an average intensity, $\bar{I}$, for the ROI. $\bar{I}$ was then plotted as a function of time to determine the peak in brightness and thus time of arrival of the gamma flash, T_0. Figure 5.18 shows the initial time-of-flight scan with the peak image brightness occurring from approximately 600 to 750 ns.

The process outlined in the previous two paragraphs was repeated with 25 ns time gates and from a range in time of 650 to 950 ns that encompassed the peak in brightness seen with the 50 ns time gates. This allowed for higher time resolution around the peak in intensity seen in Figure 5.18. The 25 ns radiographs showed a peak in average intensity between 705 ns to 755 ns, so this region was focused on in subsequent 10 ns time gate images to further improve time resolution in the estimate of T_0. It was thus seen that the peak average intensity occurs in the 715 ns to 725 ns time bin, with this time bin assumed to contain the majority of the spallation photons and thus bound T_0. The 25 ns and 10 ns average intensity plots can be seen in Figure 5.19, with the 50 ns average intensity plot shown for reference.

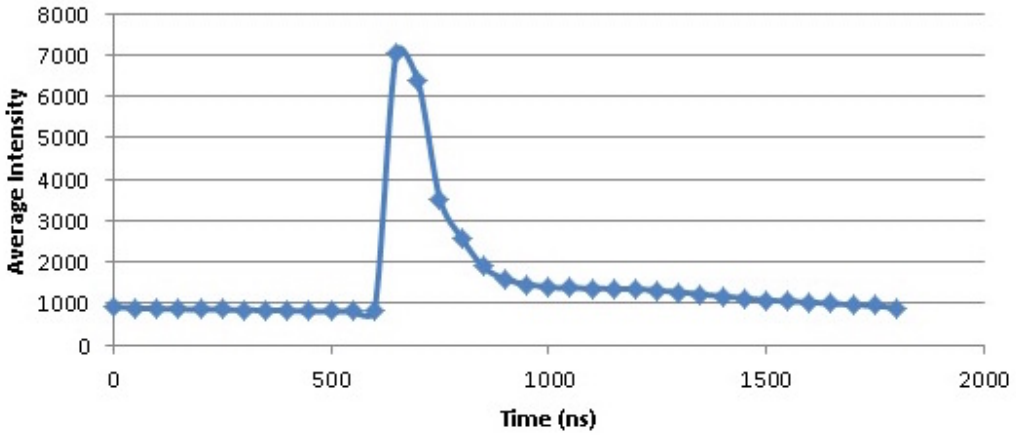


Figure 5.18: Initial time-of-flight scan results taken with 50 ns gate widths. The peak in average intensity, and thus arrival of photons at the scintillator, occurs between 600 to 750 ns.

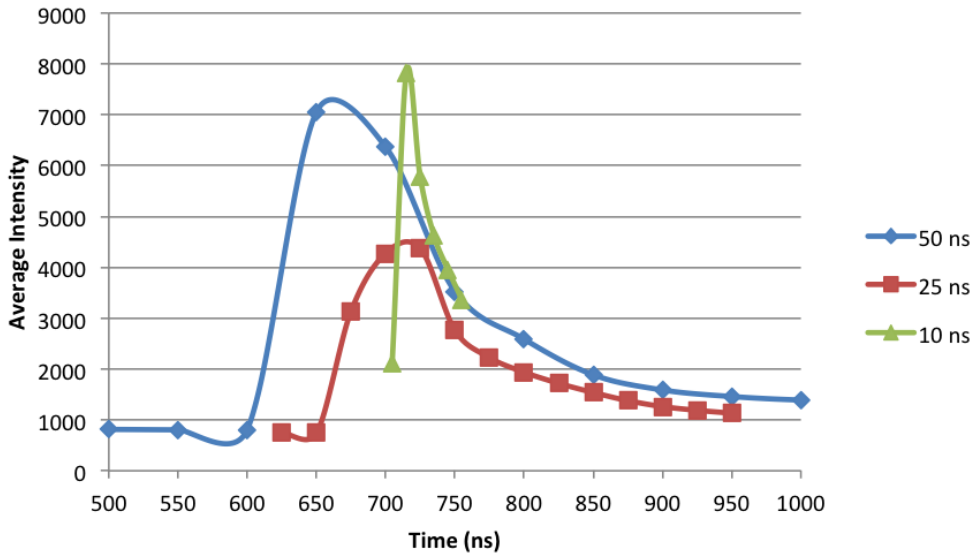


Figure 5.19: Initial time-of-flight scan with a gate width of 50 ns shown for reference, as well as increasingly narrow time-of-flight scans of gate widths of 25 ns and 10 ns around the previous peak in intensity. It was found that the peak in intensity, attributable to photons, occurs between 715 and 725 ns.

To determine consistency between pulses, radiographs were taken at the pulse endpoints of 0 and 1784 ns with gate widths of 50 ns. The 100 frames were combined to form one final frame using the median pixel values. It was found that the average intensity for a ROI spanning the entire image was approximately the same for both images ($\bar{I}_0 = 708.2$ vs. $\bar{I}_{1784} = 710.9$) (Figure 5.20). The values of $\bar{I}$ lie well within 1σ of each other ($1\sigma = \sqrt{708.2} = 26.6$), which indicates that the neutron spectrum is stable from pulse to pulse.

5.2.6 Radiography Data

Overview

With FP15R timing determined, the remaining time was spent radiographing Objects 1, 2, and 3. Time delays and camera gate widths were varied to obtain radiographs at different energies and with different particles. Flatfield images (i.e., beam on and camera intensifier on, but no object present) were also generated for image processing. The flatfield, I_0, images were taken for each time gate, particle type, and delay, so that they represented the same integration time and same portion of the polyenergetic pulse, thus allowing for the flatfield contribution to be divided out for radiograph normalization.

Radiograph data were processed according to the following procedure that converted grayscale pixel values to attenuation values, σt. This procedure was based on Equation 1.1 from Chapter 1, which is rewritten here as solved for σt, or the total probability of interaction, σ, for a neutron traveling along path, t:

$$\sigma t = -\ln\left(\frac{I(x)}{I_0}\right), \tag{5.8}$$

Data processing used ImageJ freeware, one of the only programs that can read Princeton Instrument's *.spe* file format. The software was used to average together the multiple frames taken of the radiography object, resulting in an average

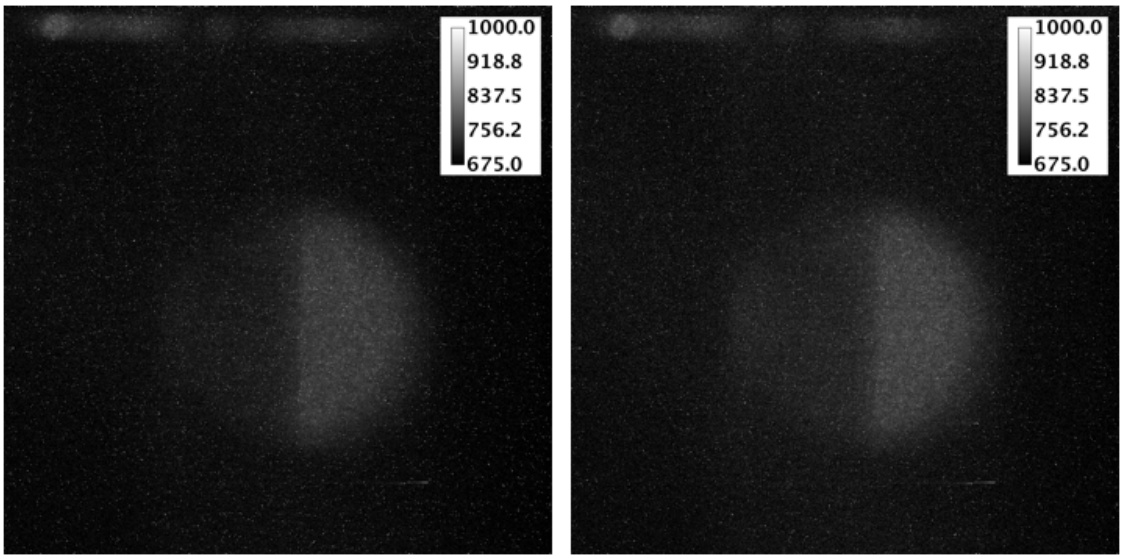


Figure 5.20: Radiographs taken with added time delays of 0 ns (left) and 1784 ns (right) are shown to have approximately equal intensities, which signifies the LANSCE beam is relatively stable from pulse to pulse.

$I(x)$ radiograph. The resultant image was then divided by a similarly-averaged corresponding flatfield image in order to normalize the pixel values and address the variation in light intensity across the camera field of view that results from a non-uniform source. Finally, a natural *log* filter was applied to the radiograph, and values were multiplied by -1 to finish the conversion of pixel data to σt. Because results were multiplied by -1, dense and/or low-flux regions appear bright in the radiographs, while high-flux and/or low-density regions appear dark .

There were three goals for this series of experiments, with the first being to demonstrate that the ICCD camera was capable of generating neutron radiographs and that its electronics could withstand a high-energy, high-flux radiation field. The second goal was to demonstrate partial scatter rejection (again, not full scatter rejection because that would require a monoenergetic beam). The third goal was to qualitatively determine the effect of neutron energy on image contrast, which is directly related to the neutron interaction cross-section at that energy, and to see whether future system designs could identify materials from variations in contrast. Additionally, it was necessary to determine how TiGReSSE could be improved for future use.

Object 1: Lead and Borated Polyethylene Blocks with Graphite Cylinder

Radiographs of Object 1 were generated first once the timing measurements had been completed. An aluminum plate was placed on top of the wooden sample stand in order to make the stand slightly taller and thus ensure Object 1 was in the camera's field-of-view. No collimation was used in the beam port, which resulted in an 8 *in* beam spot at the scintillator.

A series of four images were taken, each with a corresponding flatfield image. Table 5.2 shows the settings for the four radiographs and four flatfields, with the time gating also illustrated in Figure 5.21 on the time-of-flight scan plots to enable visualization of the time gating procedure. The delays, generated by the appropriately-named delay generator, are greater than the micropulse period of

Table 5.2: Properties of the four Object 1 radiographs, including the particle type, particle energy, added signal delay, camera gate width, and the number of integrated pulses per frame.

Particle Type	Energy (MeV)	Delay (ns)	Gate Width (ns)	Pulses per Frame
Neutron	10.0 to ∼600	2529.0	456.5	6.00×10^5
	2.5 to 10.0	2985.5	582.5	3.00×10^5
	∼0.1 to 10.0	2985.5	1287.5	1.25×10^5
Photon	All	715.0	10.0	6.00×10^5

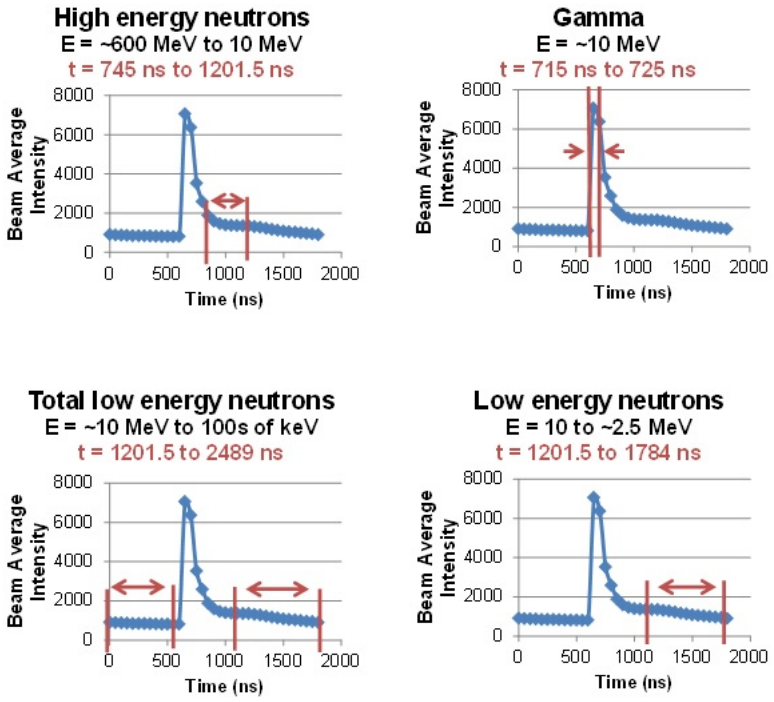


Figure 5.21: Time gating shown on the time-of-flight scan for the four radiographs taken of Object 1: 10 to ∼600 MeV neutrons (top left), ∼0.1 to 10 MeV neutrons (bottom left), 2.5 to 10 MeV neutrons (bottom right), and photons (top right).

1784 ns because the camera triggers off the previous pulse, making larger delays necessary.

The four post-processed radiographs of Object 1 can be seen in Figures 5.22 through 5.25. A quantity of 94 frames were processed for each image, with the frames averaged together to yield better image statistics. (Note: 100 frames were taken for all energy bins except for the 10 to ~600 MeV bin, which, due to a mistake during imaging, only had 94 saved frames. This meant that the other three time gates used 94 of the 100 frames for consistency). Both sources of gain were used, with the intensifier set to a gain of 80 and the ADC set to a gain of 50. It should be noted that any radiographs that were generated with the spallation photons do not represent traditional x-ray radiographs, simply because the spallation photons are low in flux in LANSCE when compared to a bremmstrahlung x-ray source. Rather, the spallation photon radiographs represent signal that may be rejected with TOF methods in order to lower noise and improve image quality.

Object 2: Tungsten, Stainless Steel, and Polypropylene Cylinder

Radiographs of Object 2 were generated following those of Object 1. Along with the four time gates used for Object 1, two additional time gates were used to generate a total of six radiographs of Object 2. Corresponding flatfield radiographs were also taken for the two additional time gates, with the four flatfields generated for Object 1 re-used here. Multiplicative scaling was applied if the number of accumulations per frame differed. Particle energies and equipment settings are shown in Table 5.3. For this series of images, 100 frames were taken for each time gate (again, to average them together and improve statistics), and all other equipment settings remained the same as those used for Object 1. No collimation was used in the beam pipe, which resulted in an 8 in beam spot at the scintillator. The six post-processed radiographs of Object 2 can be seen in Figures 5.26 through 5.31.

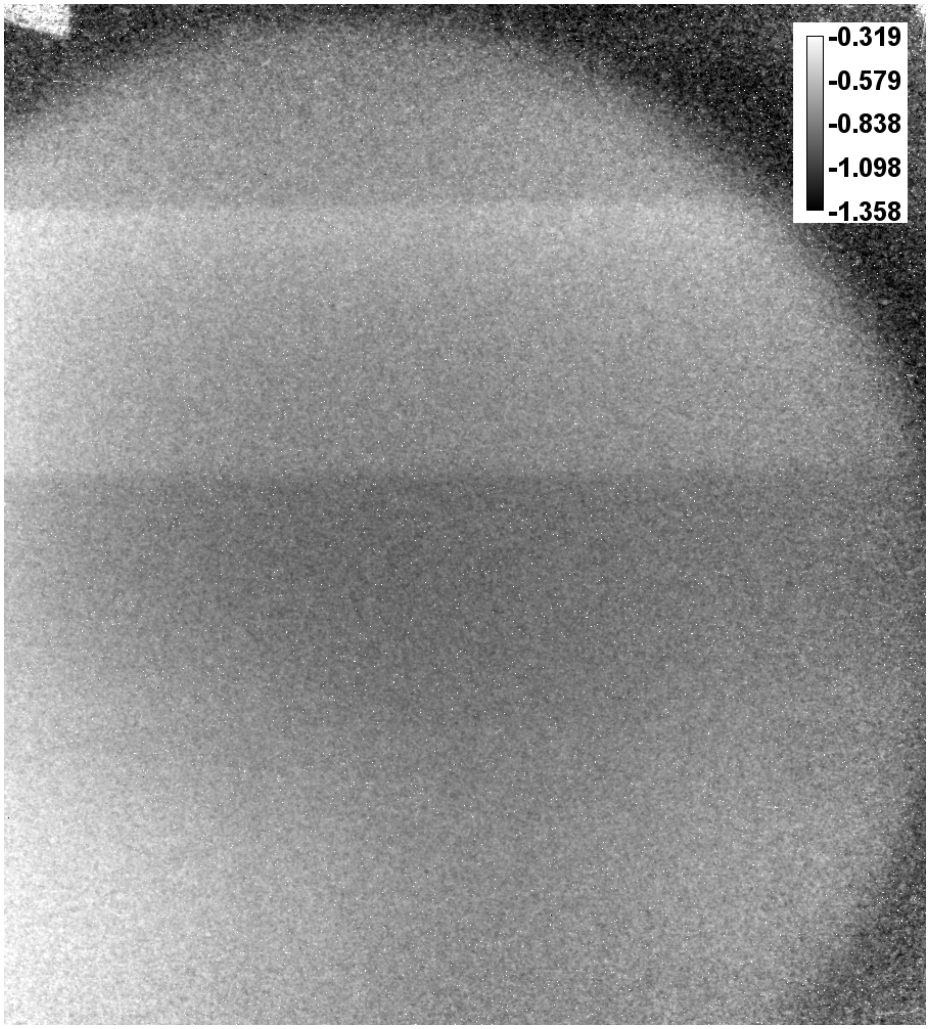


Figure 5.22: Spallation photon radiograph of Object 1. Note that the beam forms a circle on the scintillator around Object 1.

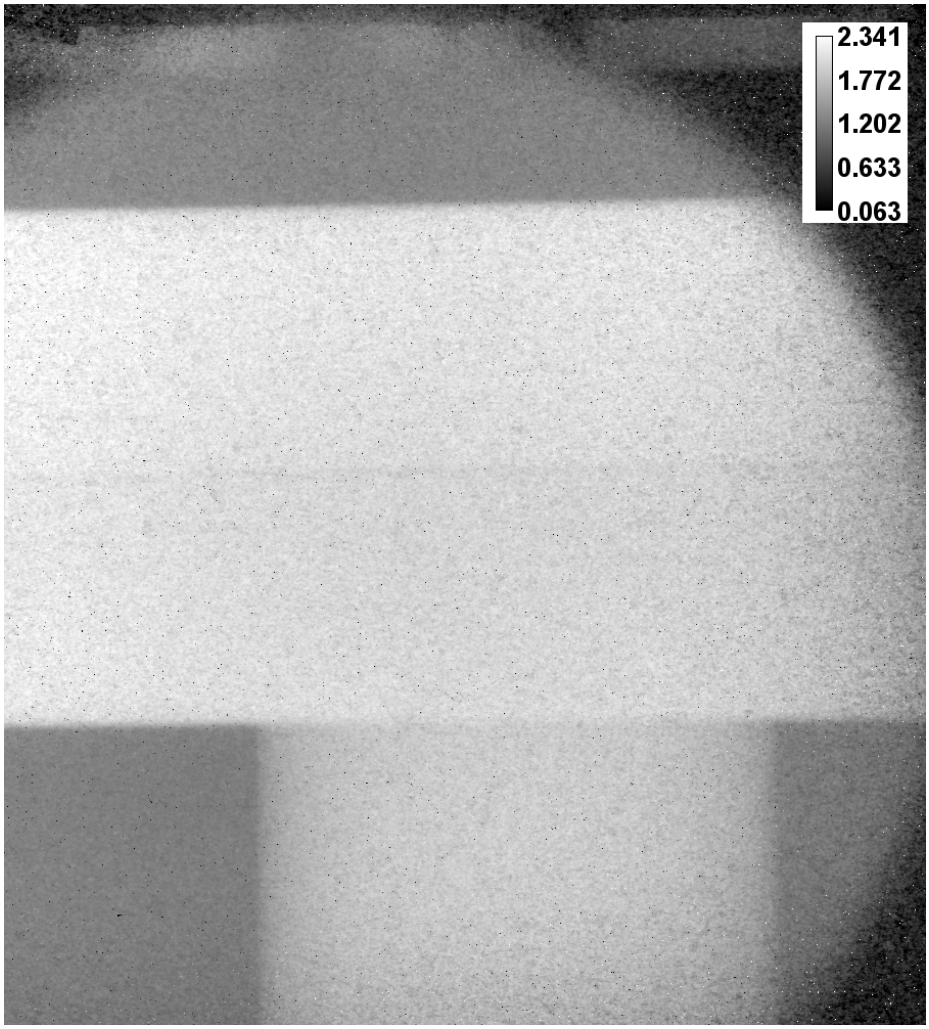


Figure 5.23: High-energy neutron radiograph of Object 1 taken with 10 to 600 MeV neutrons. Note that the beam forms a circle on the scintillator around Object 1.

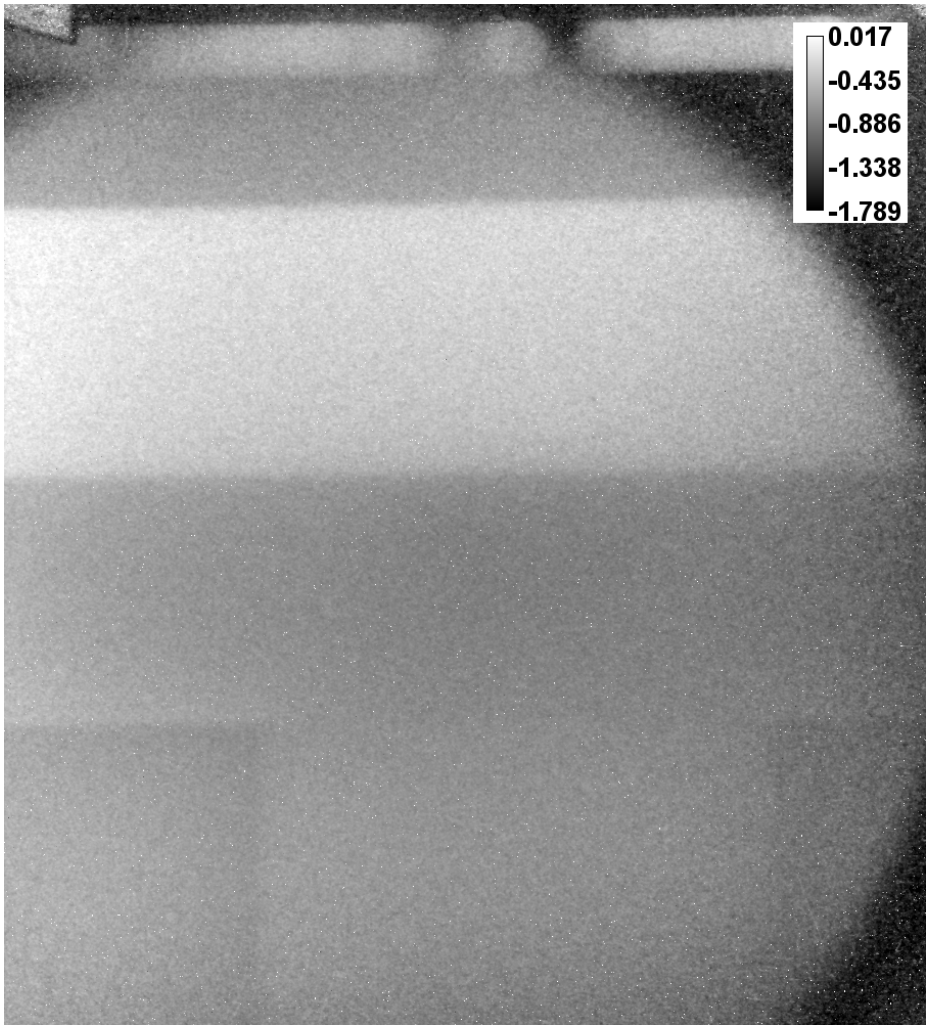


Figure 5.24: Mid-energy neutron radiograph of Object 1 taken with 2.5 to 10 MeV neutrons. Note that the beam forms a circle on the scintillator around Object 1.

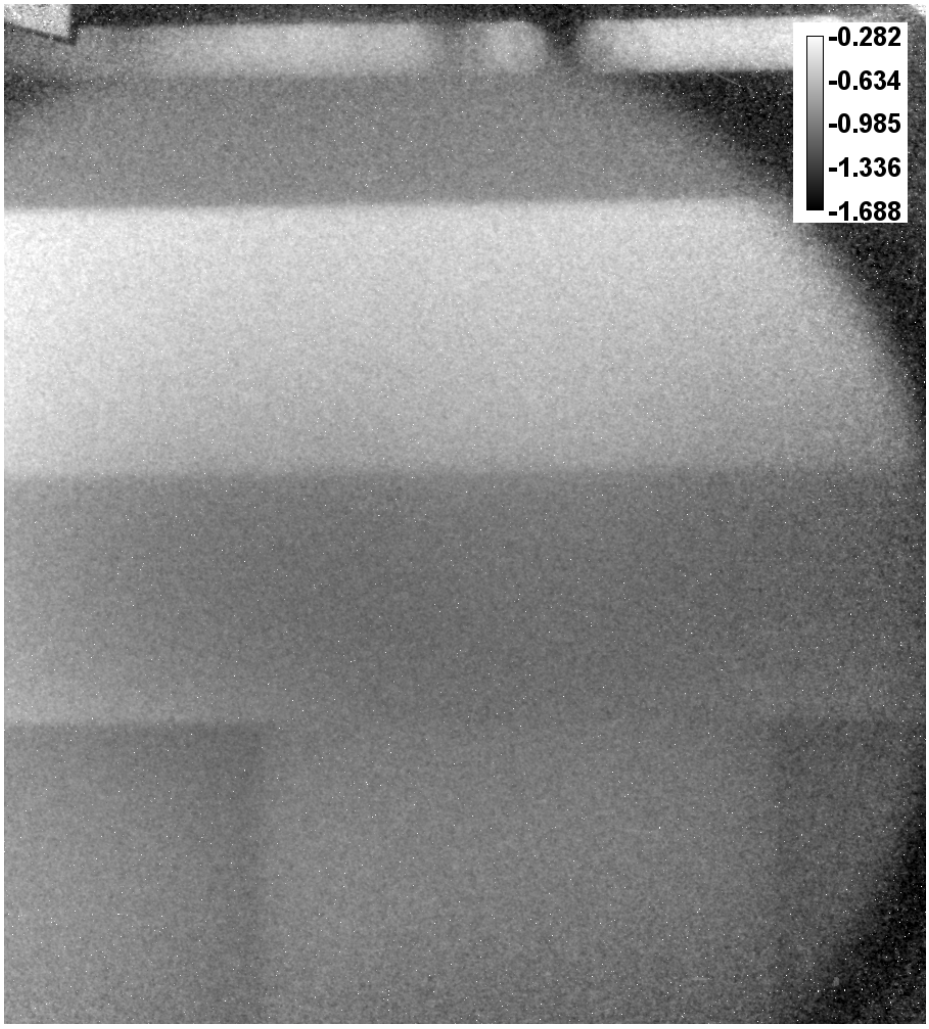


Figure 5.25: Low- and mid-energy neutron radiograph of Object 1 taken with ∼0.1 to 10 MeV neutrons. Note that the beam forms a circle on the scintillator around Object 1.

Table 5.3: Properties of the six Object 2 radiographs, including the particle type, particle energy, added signal delay, camera gate width, and the number of integrated pulses per frame.

Particle Type	Energy (MeV)	Delay (ns)	Gate Width (ns)	Pulses per Frame
Neutron	10.0 to ∼600	2529.0	456.5	6.00×10^5
	2.5 to 10.0	2985.5	582.5	3.00×10^5
	∼0.1 to 10.0	2985.5	1287.5	1.25×10^5
	∼0.1 to 2.5	0.0	705.0	3.00×10^5
Photon	All	715.0	10.0	6.00×10^5
Both	All	0.0	1700.0	1.25×10^5

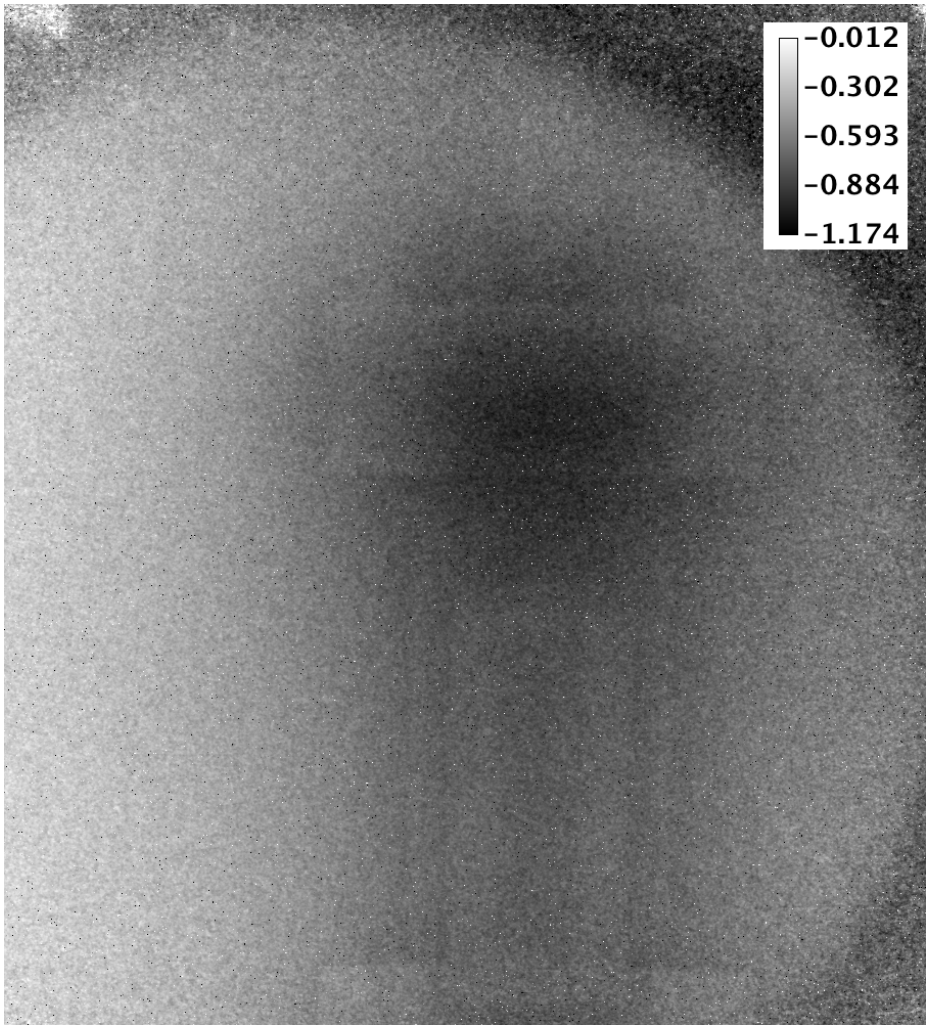


Figure 5.26: Spallation photon radiograph of Object 2. Note that the beam forms a circle on the scintillator around Object 2.

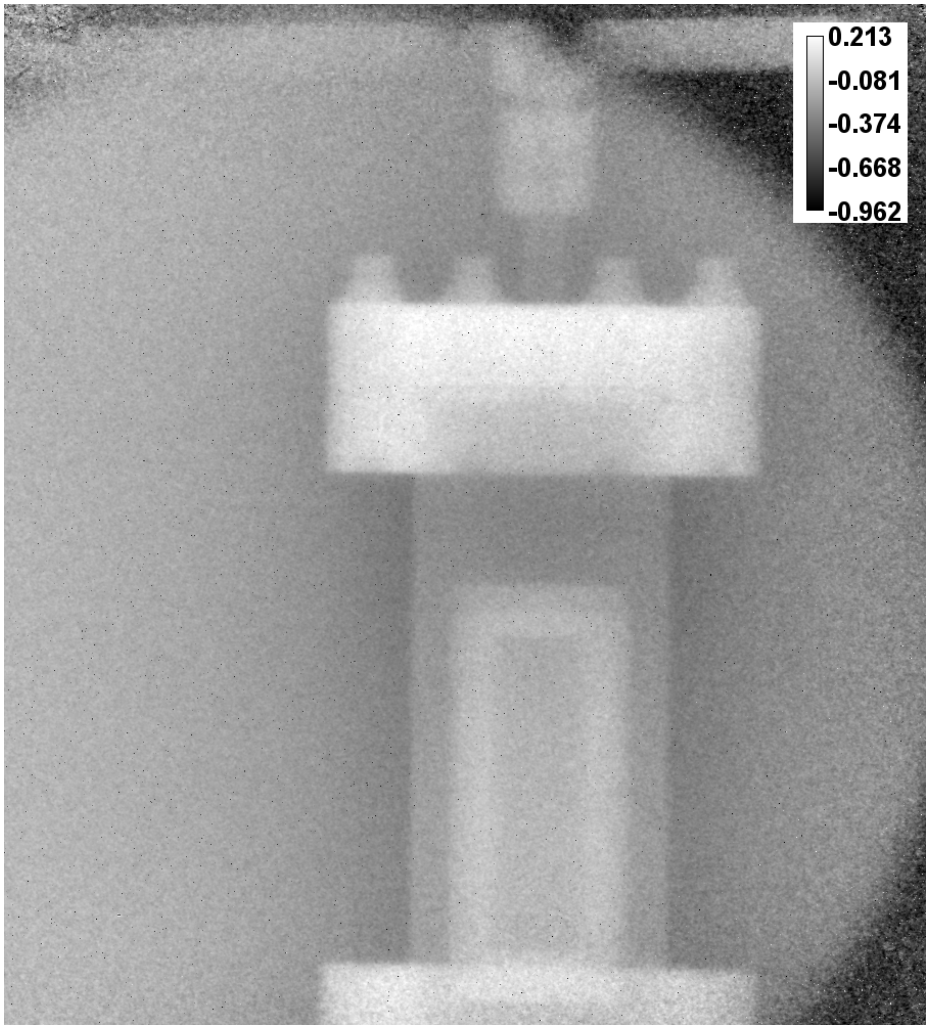


Figure 5.27: High-energy neutron radiograph of Object 2 with 10 to 600 MeV neutrons. Note that the beam forms a circle on the scintillator around Object 2.

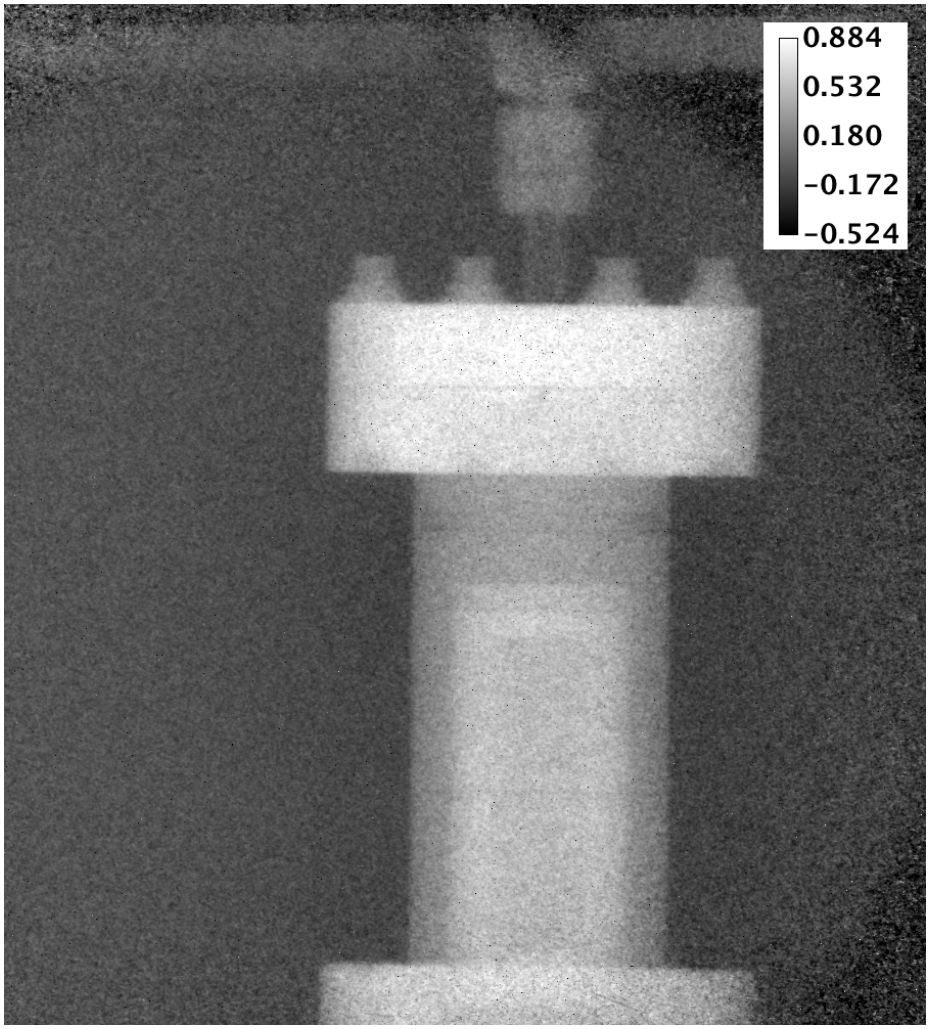


Figure 5.28: Mid-energy neutron radiograph of Object 2 taken with 2.5 to 10 MeV neutrons. Note that the beam forms a circle on the scintillator around Object 2.

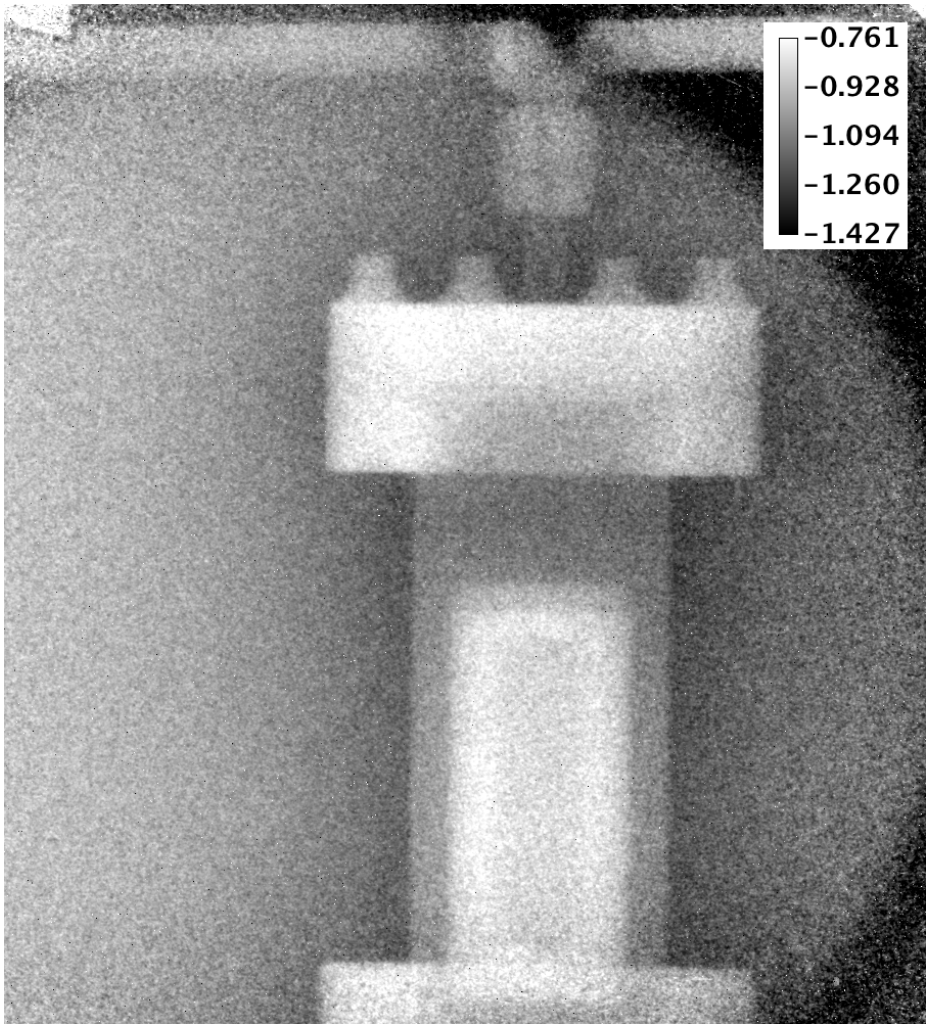


Figure 5.29: Low- and mid-energy neutron radiograph of Object 2 taken with ∼0.1 to 10 MeV neutrons. Note that the beam forms a circle on the scintillator around Object 2.

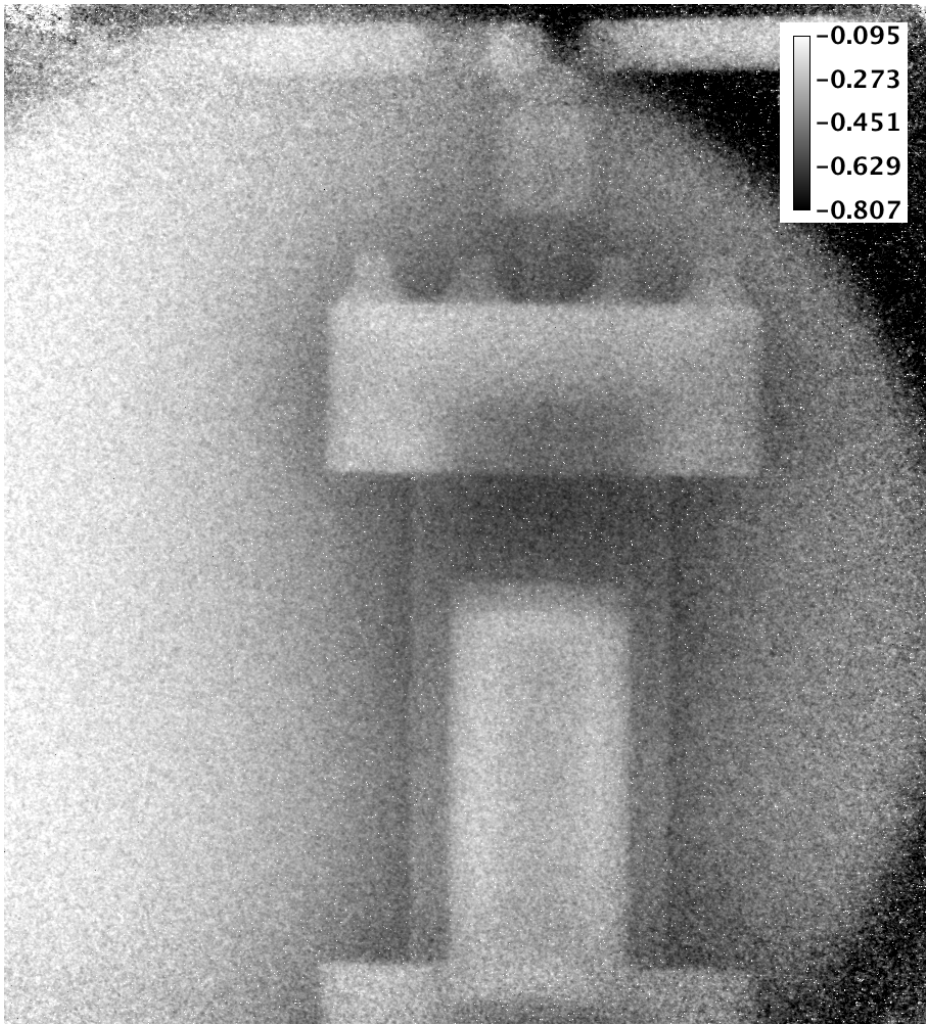


Figure 5.30: Low-energy neutron radiograph of Object 2 taken with ∼0.1 to 2.5 MeV neutrons. Note that the beam forms a circle on the scintillator around Object 2.

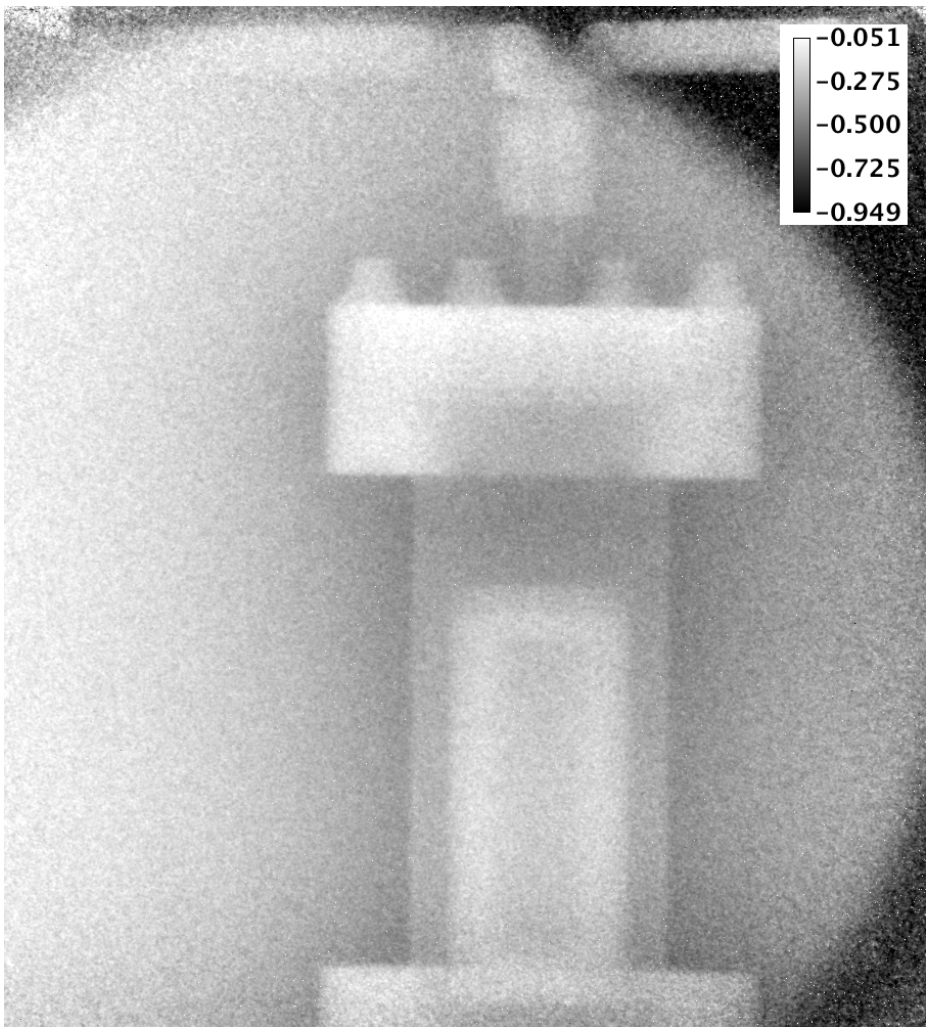


Figure 5.31: Radiograph of Object 2 using the total LANSCE spectrum (photons and neutrons). This radiograph approximates a traditional neutron radiograph that does not use time gating to reject signal. Note that the beam forms a circle on the scintillator around Object 2.

Object 3: Tungsten Sphere

Radiographs of Object 3 were generated last. Three time gates were used to image the tungsten sphere: 10 to 600 MeV, ~0.1 to 2.5 MeV neutrons, and spallation photons (Table 5.4). Object 3 was smaller than the other two objects, so the beam diameter was decreased to 4 *in* at the scintillator plane using the 2 *in* collimators. The beam spot before and after collimation can be seen in Figure 5.32 as the gray circular area surrounding Object 3. While the beam diameter was still bigger than the object even with the 2 *in* collimators, most of the direct beam was cropped out of the radiograph during post-processing to prevent contrast ranges from being skewed. For this series of images, 100 frames were taken, and camera gain settings remained the same. Corresponding flatfield images were also taken. Post-processed radiographs can be seen in Figures 5.33 through 5.35.

5.2.7 Evaluation of Radiography Data

Partial Scatter Rejection

As stated previously in this chapter, total scatter rejection (while understanding that small angle scatter most likely will not be rejected) cannot be demonstrated at LANSCE because it is a polyenergetic beam, and direct neutrons of low-energy arrive in the same time bin as scattered neutrons of high-energy. However, partial scatter rejection can be conducted for energies below a given range, allowing for some signal rejection and therefore some improvement in the signal-to-noise ratio.

Partial scatter rejection was most visibly demonstrated with Object 2. Some of the neutron radiographs of Object 2 appear to show a glow surrounding the cylinder (e.g., the ~0.1 to 2.5 MeV and ~0.1 to 10 MeV time gates shown in Figures 5.30 and 5.29, respectively). At these low energies, neutrons scatter off Object 2 and into the scintillator, causing this apparent glow. However, by gating in time so that the radiograph is taken for higher energies (e.g., the 2.5 to 10 MeV and 10 to 600 MeV neutron radiographs shown in Figures 5.28 and 5.27, respectively),

Table 5.4: Properties of the three Object 3 radiographs, including the particle type, particle energy, added signal delay, camera gate width, and the number of integrated pulses per frame.

Particle Type	Energy (MeV)	Delay (ns)	Gate Width (ns)	Pulses per Frame
	10.0 to $\sim$600	2529.0	456.5	6.00×10^5
Neutron	2.5 to 10.0	2985.5	582.5	3.00×10^5
Photon	All	715.0	10.0	6.00×10^5

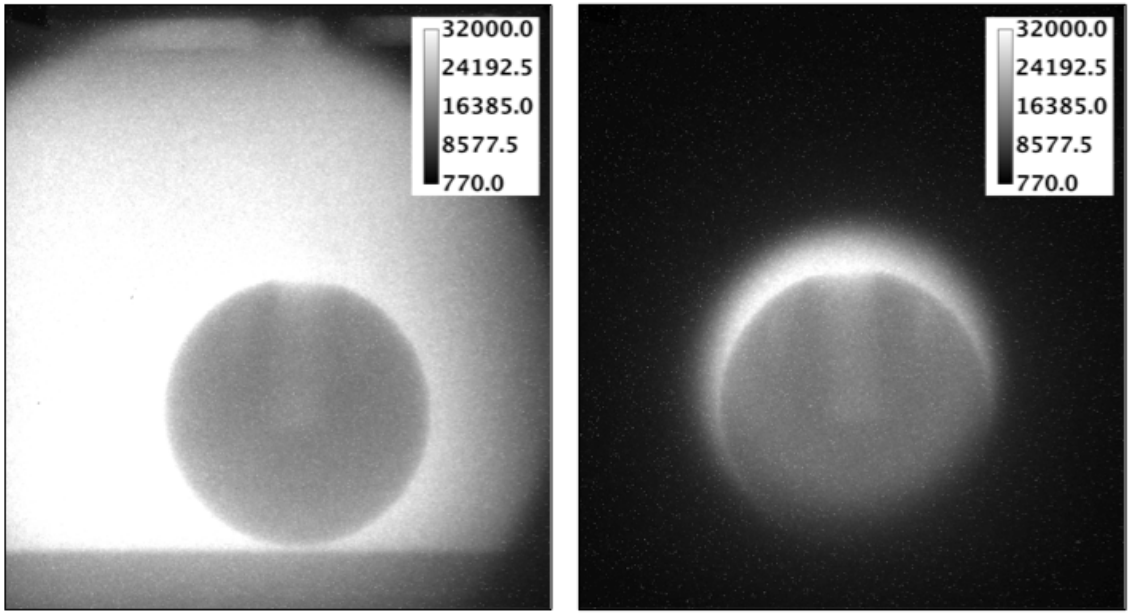


Figure 5.32: Radiographs of Object 3 without collimation (left) and with 2 *in* collimation (right), showing that collimation reduces scatter and improves feature visibility. Radiographs were generated with 10 to 600 MeV neutrons. Note that the beam forms a circle on the scintillator around Object 3, and that this circle shrinks with the 2 *in* collimation.

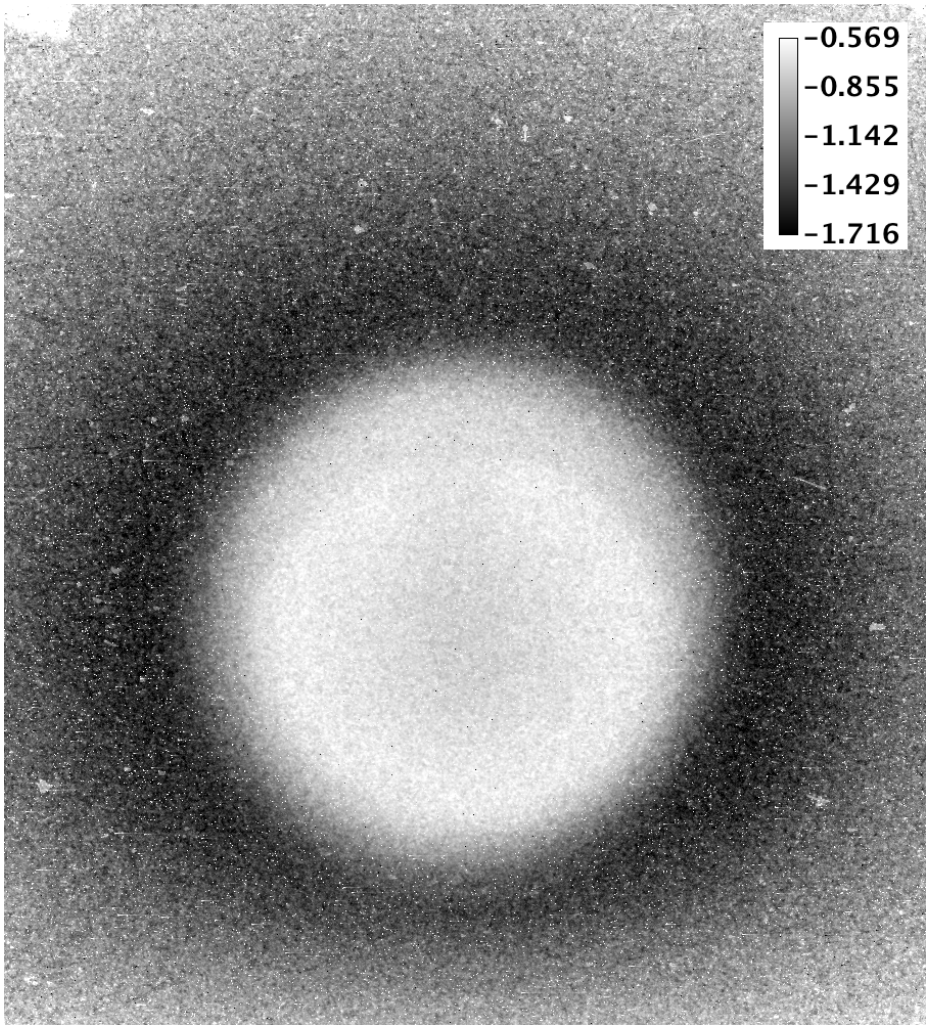


Figure 5.33: Spallation photon radiograph of Object 3. Note that the beam forms a circle on the scintillator around Object 3.

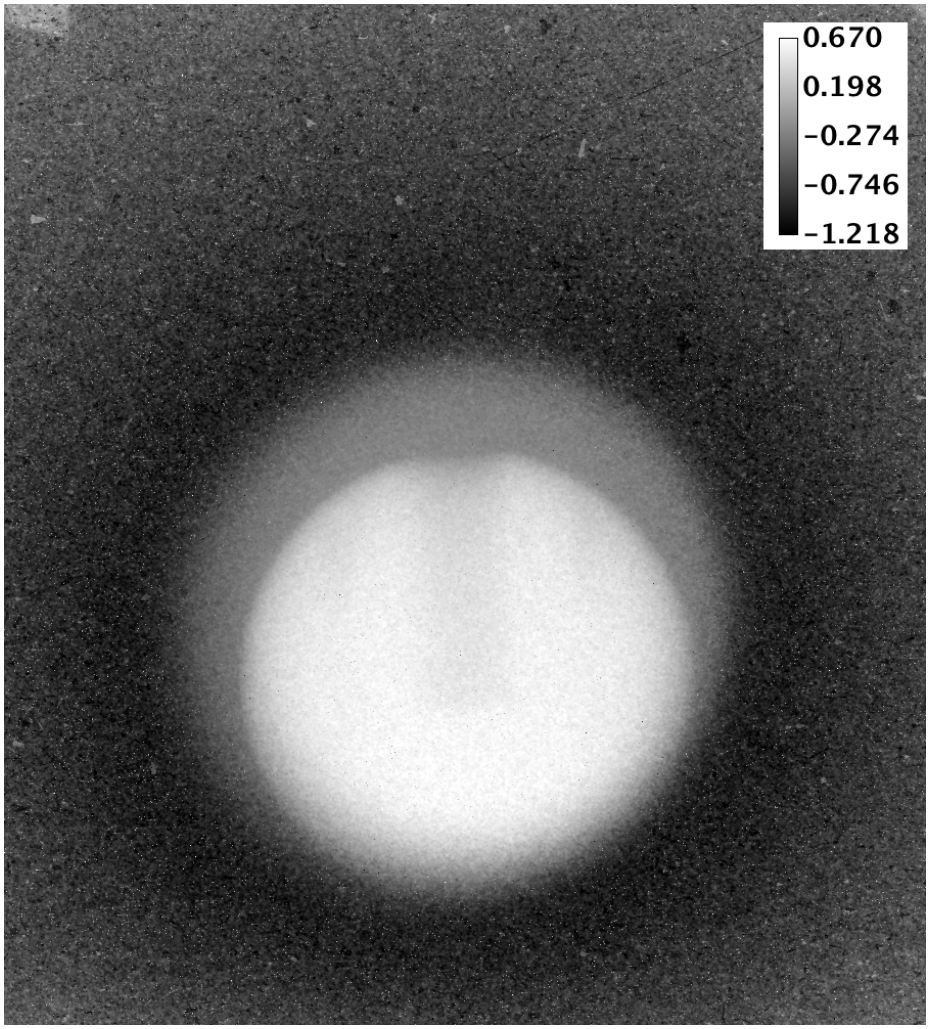


Figure 5.34: High-energy neutron radiograph of Object 3 taken with 10 to 600 MeV neutrons. Note that the beam forms a circle on the scintillator around Object 3.

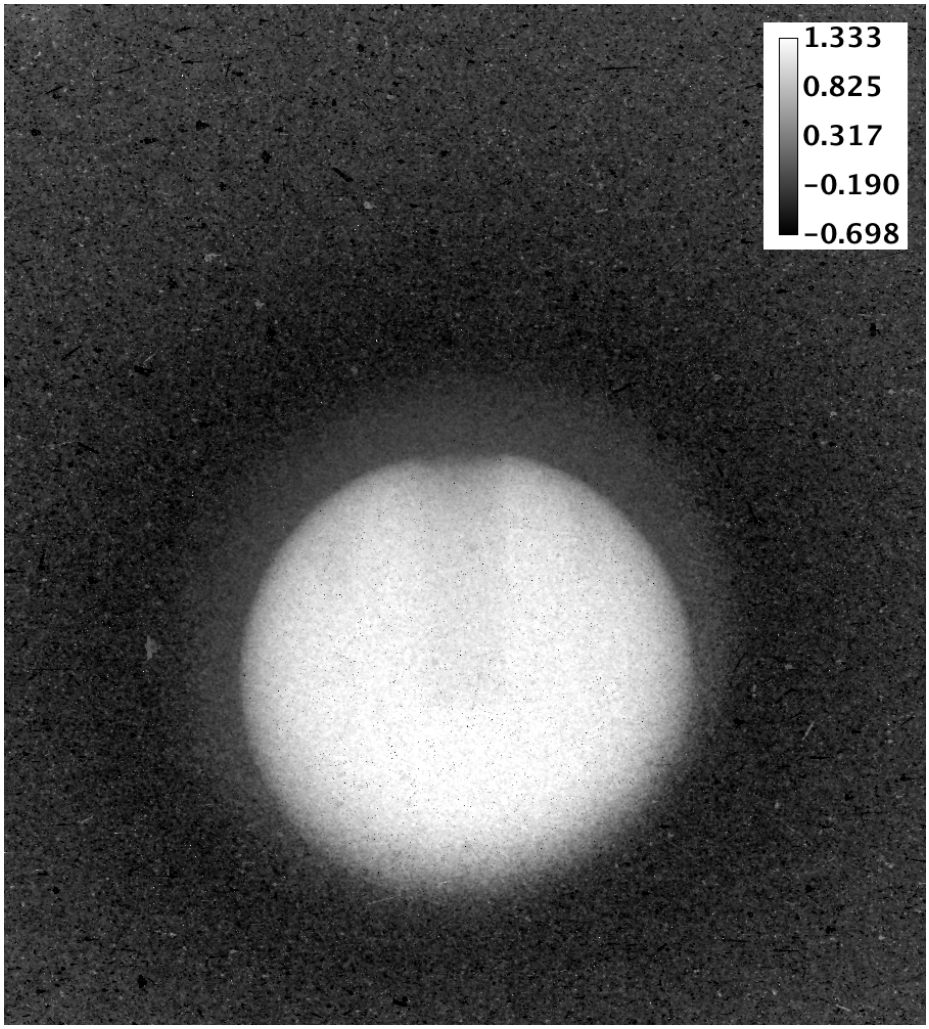


Figure 5.35: Mid-energy neutron radiograph of Object 3 taken with 2.5 to 10 MeV neutrons. Note that the beam forms a circle on the scintillator around Object 3.

the signal from low-energy scatter is rejected and the glow is nearly eliminated. Moreover, as one moves to higher energy bins within the LANSCE spectrum, downscatter contributes less to the total signal within that bin and thus scatter becomes increasingly diminished at upper LANSCE energies. Therefore, TiGReSSE was successfully used to partially reject scatter and improve image quality. With a monoenergetic source, TiGReSSE would only be more successful at rejecting scatter, since downscatter cannot be totally eliminated with a polyenergetic beam.

It should be noted that no glow was seen in the radiographs of Objects 1 and 3. Object 1 was composed of much thicker material, so scatter was most likely re-absorbed. Object 3 has no discernible glow because the incident neutron beam was much larger than the object and therefore masks scatter from the object that would otherwise appear as a glow.

Similar to partial scatter rejection is the idea that TiGReSSE was successfully used to reject any signal not of interest. In the case of FP15R, the photon signal is weak and does not provide particularly useful information. For Object 1 and 2, general object features could be seen with the spallation photons, but for Object 3, the spallation photon signal did not reveal any internal features other than a slight, non-specific increase in brightness where the central hole was located. Thus, by gating in time, for example, from 10 to 600 MeV, the weak spallation photon signal was rejected, as was the low-energy direct and scattered neutrons. Since the spallation photons and low-energy neutrons simply increase noise in the radiograph, rejecting noisy signal leads to more crisp images (compare the 10 to 600 MeV time gate in Figure 5.27 to the total spectrum time gate in Figure 5.31). Time gating of a polyenergetic beam to reject any signal not of interest, not just scatter, can thus be thought of as a more general application of TiGReSSE for NDA.

Energy Selection for Contrast Variation

Changing the time gate to generate radiographs with different energies and source particles was seen to have two interesting effects. First, the radiograph energy bin

was seen to affect whether internal features were visible in the image. For all three objects, some features were visible in one or two time gates, but not others. This is the result of energy-dependent changes in contrast that cause features to have nearly the same contrast as their surrounding material, or of additional noise that is present in that time bin (i.e., scatter, activation products, and so on). Taking Object 1 as an example, the folded sheet of paper between the lead and borated polyethylene blocks is visible, but only in the neutron energy range of 10 to 600 MeV (Figure 5.23). The other three radiographs are thus not using the correct energy to see the paper feature in Object 1.

Calculations were conducted to support this claim that the folded sheet of paper (thickness of 4.0 mil, or 101.6 μm) could be visible in radiographs generated by TiGReSSE. At a source-to-detector distance of 23.7 m and an object-to-detector distance of 13.91 cm, the object magnification is $M = 1.012$ (refer to Equation 1.9). Thus, the sheet of paper is magnified to a thickness of 4.05 mil (102.79 μm). The effective pixel size, or what portion of the detector is seen by a single camera pixel, is equal to the length of one side of the scintillator (8.0 in) divided by the number of pixels on one side of the CCD chip (1024 pixels). The effective pixel size is found to be 7.8 mil (198.0 μm), or nearly twice the thickness of the sheet of paper. In other words, the sheet of paper is half of the effective pixel size and thus would only be projected onto half of a camera pixel.

The sheet of paper is still visible, however, because Object 1 was not perfectly aligned with the beam and the scintillator, and may not have been perfectly parallel to the floor. Examination of the radiographs of Object 1 show that the object is at a slight angle to the vertical, and that the right side of the object appears larger than the left side which indicates different magnification and thus a non-uniform distance between the object and the scintillator. If Object 1 were tilted, it is possible that the sheet of paper would cover more pixels and appear larger than what was calculated. Additional causes could be blurring effects in the scintillator and the larger overall gap between the lead and borated polyethylene blocks.

As further evidence, an averaged vertical line-out was taken across the paper region in the 10 to 600 MeV neutron radiograph of Object 1 to quantify how well the sheet of paper was visible. First, the radiograph was rotated 0.9° clockwise from the vertical in an attempt to straighten the object; this step is necessary to reduce blur that would be introduced by the line-out process, not by the radiography system. The vertical line-out was next taken across a region, not a single column of pixels as is perhaps more traditional, so that each row of pixels within the region was averaged to a single value, forming a one-dimensional column vector. This can be thought of as collapsing a two-dimensional region into a one-dimensional vertical line. By averaging the values, the effect of stars and other noise in the image is greatly reduced. The line-out region on the rotated image can be seen in Figure 5.36. Note that the selected region does not extend all the way across the lead and borated polyethylene blocks in order to limit non-uniform beam effects that are visible on the right side of the image.

The averaged vertical line-out for the 10 to 600 MeV neutron radiograph shows a dip at Pixel 210 associated with the sheet of the paper, which corroborates the calculations outlined earlier in this section (Figure 5.37). An averaged vertical line-out for the same region in the 2.5 to 10 MeV neutron radiograph does not show such a dip, indicating that the sheet of paper is not visible at this lower energy range (Figure 5.38). While not shown here, similar results were found for the other two radiographs of Object 1, indicating that the 10 to 600 MeV neutron radiograph is indeed the only energy range of those tested that shows the paper feature.

Like Object 1, some features in Object 2 are visible at one energy range but not the others. Three features can only be seen in the neutron energy range of 2.5 to 10 MeV. This optimal source energy is lower than that of Object 1, demonstrating that one energy range is not equally beneficial for all objects. A polyenergetic beam thus has benefits even if it cannot allow for total scatter rejection by allowing multiple objects, which potentially have very different energy requirements, to be imaged by the same source.

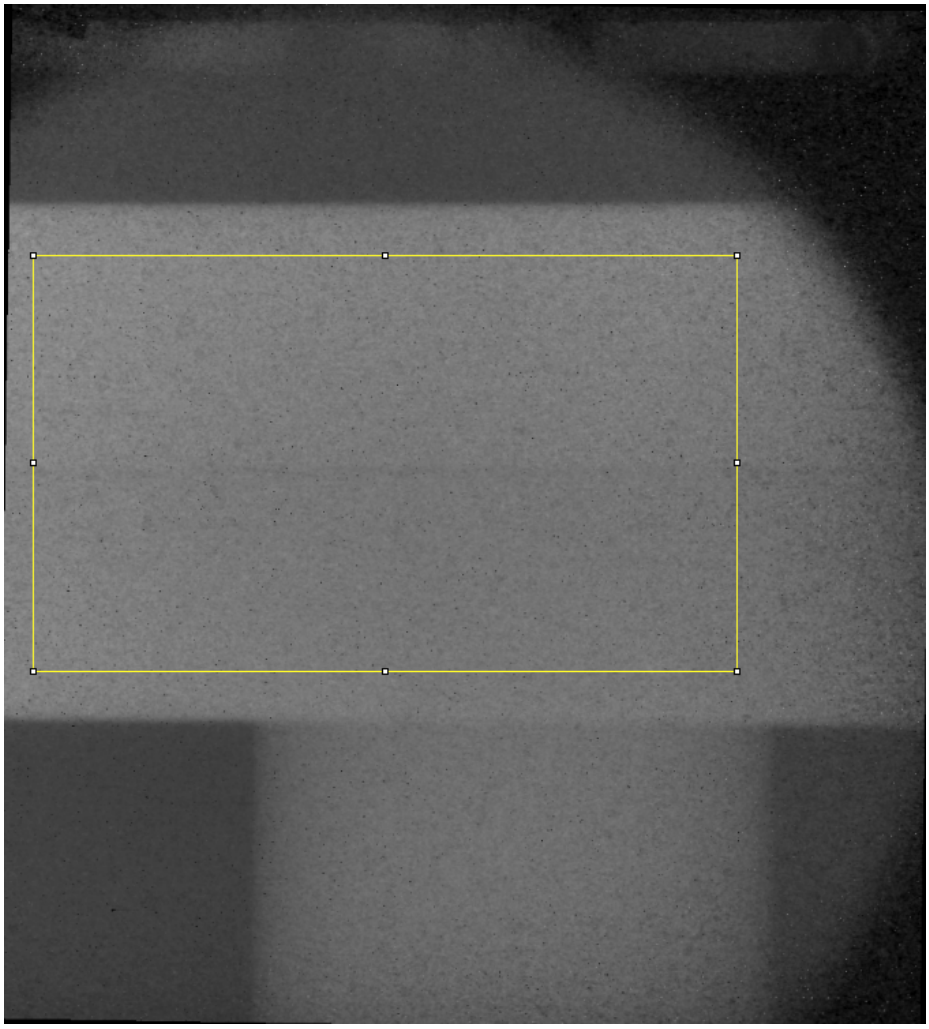


Figure 5.36: The 10 to 600 MeV neutron radiograph of Object 1 after it has been rotated 0.9° clockwise. The region of interest that was used to determine the averaged vertical line-out is shown in yellow.

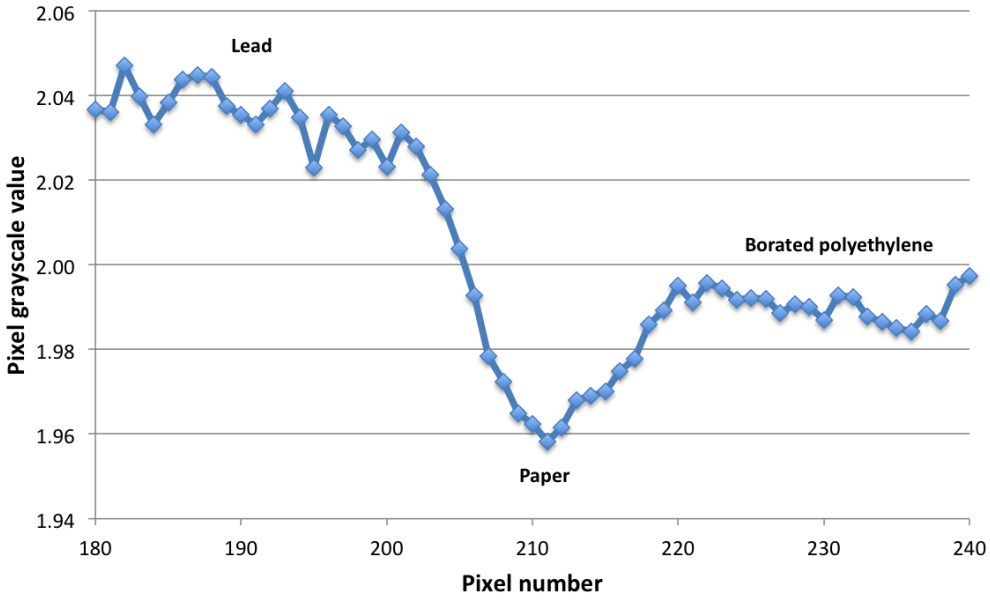


Figure 5.37: Averaged vertical line-out across the high-energy (i.e., 10 to 600 MeV) neutron radiograph of Object 1. The dip at Pixel 210 indicates the sheet of paper is visible.

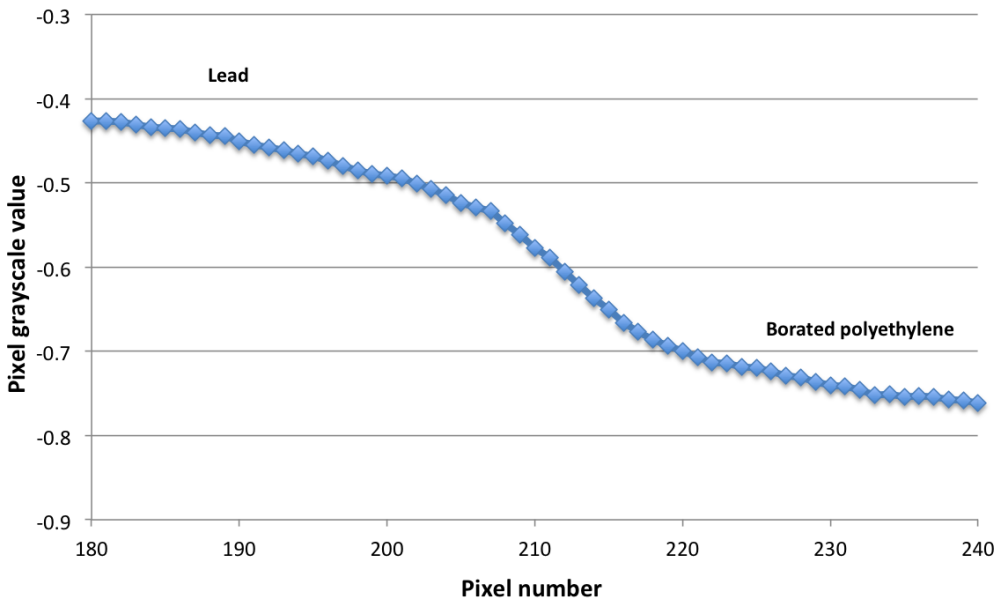


Figure 5.38: Averaged vertical line-out across the mid-energy (i.e., 2.5 to 10 MeV) neutron radiograph of Object 1. Note there is no dip at Pixel 210 and thus the sheet of paper is not visible at this energy range.

Averaged line-outs were generated to illustrated these conclusions. The Object 2 radiographs were rotated 0.9° counterclockwise to straighten the object. A region was selected around each of the three features (referred to by their relative location in the cylinder as "top", "middle", and "bottom"), and an averaged vertical line-out was generated for each region using the same method as that for Object 1 (Figure 5.39). Figures 5.40 through 5.42 show the line-outs for these three regions in the 2.5 to 10 MeV neutron radiograph. For comparison, averaged vertical line-outs for these three regions were also generated for the ∼0.1 to 10 MeV radiograph. The middle feature appears to be the hollow O-ring shown in Figure 5.17 because the contrast has two peaks which indicate the tube boundaries. Features in the three line-outs are indicated by arrows.

Varying the time gate to change the interrogation particle energy was also seen to vary contrast in the radiographs of Object 3. The three holes in Object 3 are visible in both the 10 to 600 MeV and 2.5 to 10 MeV neutron energy bins, with the range in contrast being greater for the higher energy bin (Figures 5.34 and 5.35, respectively). The photon bin, however, does not reveal any features to the naked eye, but rather an unspecific decrease in density in the center of the sphere, a fact which is thought to be a result of the low photon flux in the narrow time bin (only 10 ns) and not necessarily because the particles are photons. Thus, for Object 3, the best time bin of those studied was 10 to 600 MeV because features are most evident.

Quantitative analysis of the Object 3 radiographs was conducted in the same manner as that for Objects 1 and 2. A region was selected in the radiograph in order to generate an averaged line-out (Figure 5.43). The line-out for Object 3 differs from those for Objects 1 and 2 because it averaged pixel columns, instead of rows, to generate an averaged horizontal line-out. The radiograph was rotated 1.5° clockwise to align feature edges with the vertical. Figure 5.44 shows the averaged horizontal line-out for the three radiographs of Object 3: 10 to 600 MeV neutrons, 2.5 to 10 MeV neutrons, and photons. As can be seen in Figure 5.44, the photon radiograph does not indicate the presence of the two smaller holes located on either side of the central

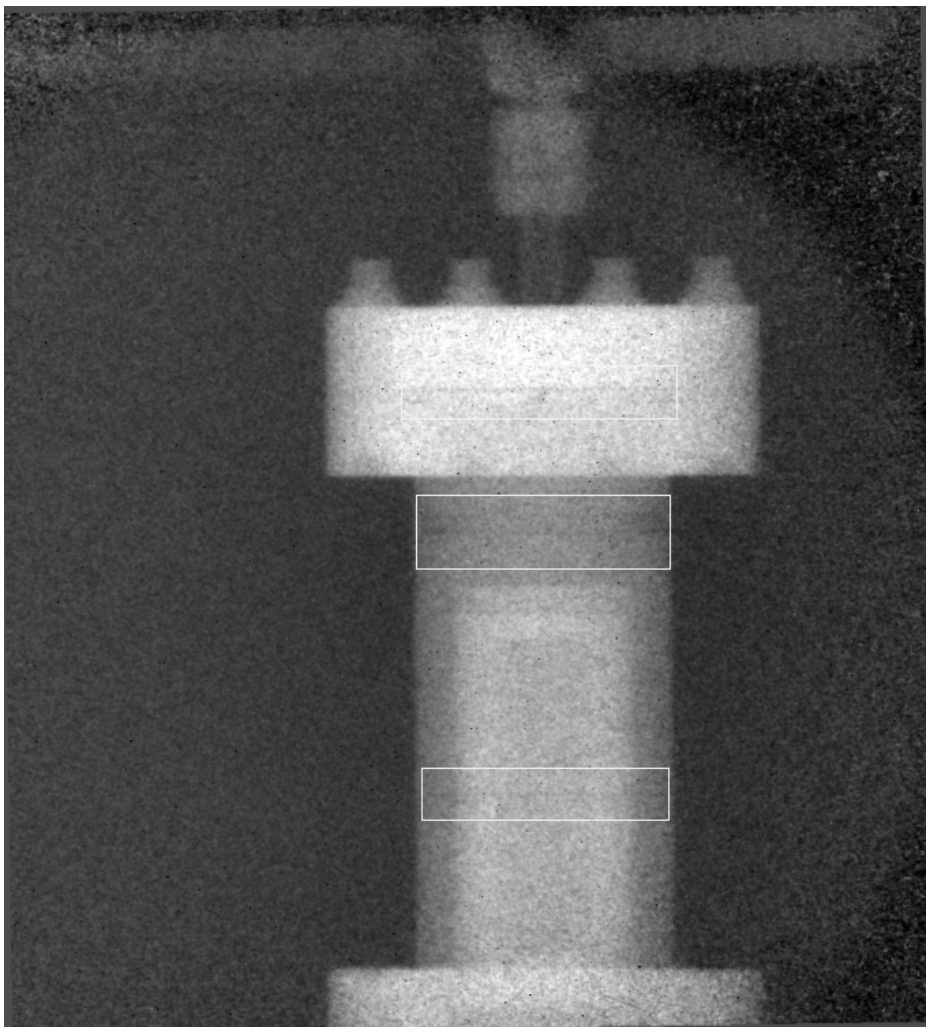


Figure 5.39: An averaged vertical line-out was generated for each of the three regions shown on Object 2 (white) to illustrate that features can be seen only with the 2.5 to 10 MeV time gate. The radiograph shown here was taken with 2.5 to 10 MeV neutrons and has been rotated 0.9° counter-clockwise.

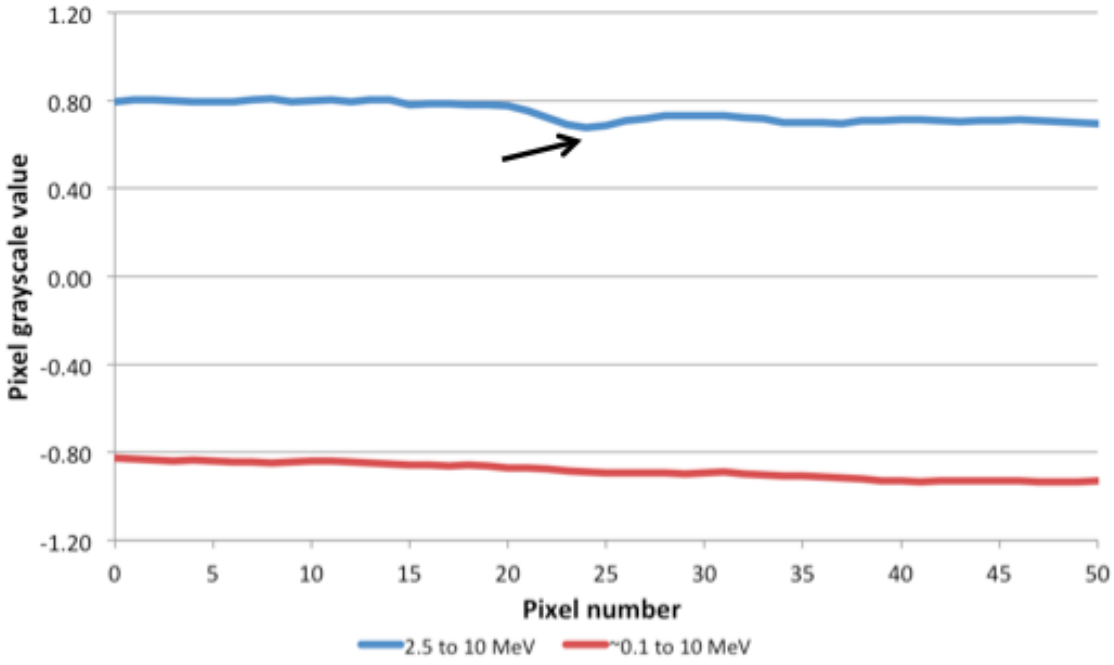


Figure 5.40: Averaged vertical line-out for the top feature in radiographs of Object 2 taken with 2.5 to 10 MeV and ∼0.1 to 10 MeV neutrons. The peak of interest is indicated by an arrow and is only visible with 2.5 to 10 MeV neutrons.

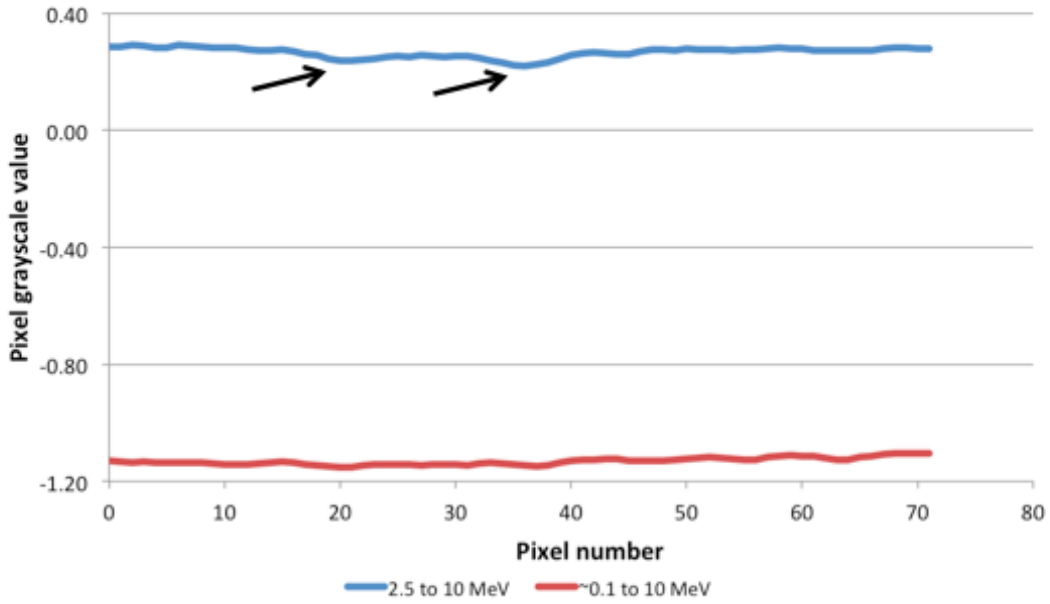


Figure 5.41: Averaged vertical line-out for the middle feature in radiographs of Object 2 taken with 2.5 to 10 MeV and ~0.1 to 10 MeV neutrons. The peaks of interest are indicated by an arrow and are only visible with 2.5 to 10 MeV neutrons.

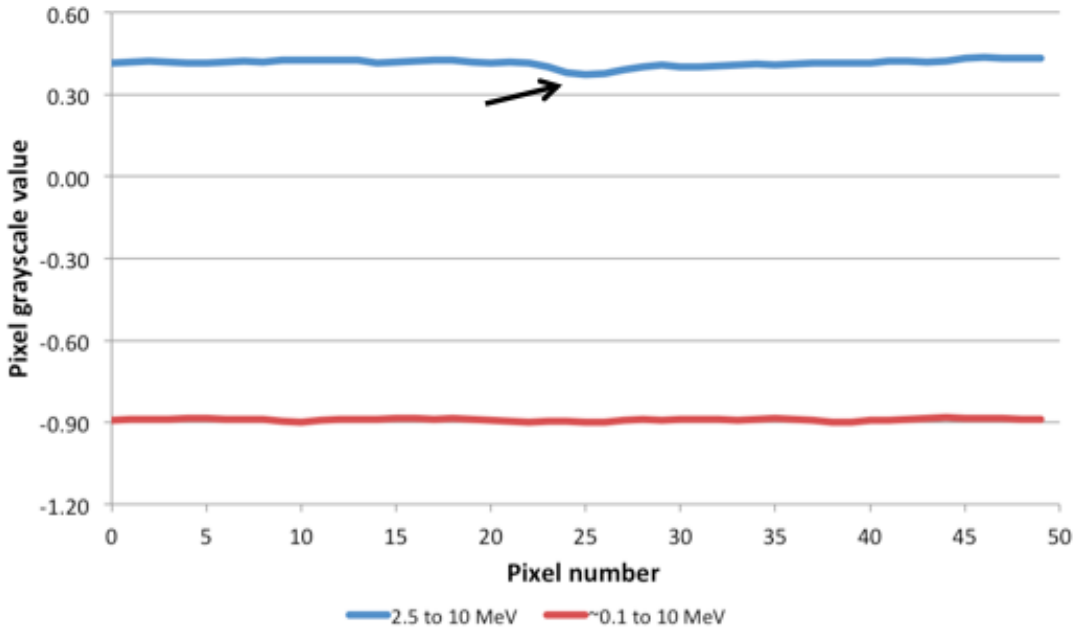


Figure 5.42: Averaged vertical line-out for the bottom feature in radiographs of Object 2 taken with 2.5 to 10 MeV and ~0.1 to 10 MeV neutrons. The peak of interest is indicated by an arrow and is only visible with 2.5 to 10 MeV neutrons.

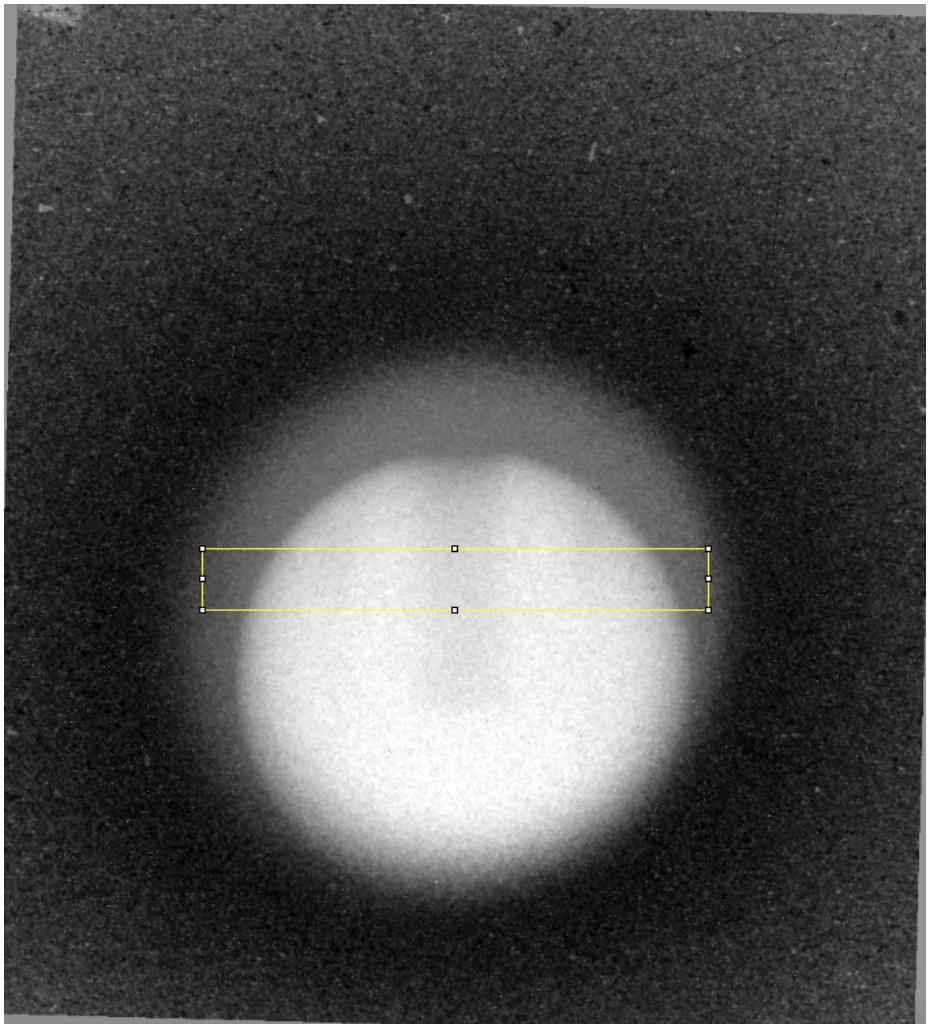


Figure 5.43: An averaged horizontal line-out was generated for a region spanning the three holes in Object 3 (yellow). The radiograph of Object 3 shown here was taken with 10 to 600 MeV neutrons and has been rotated 1.5° clockwise.

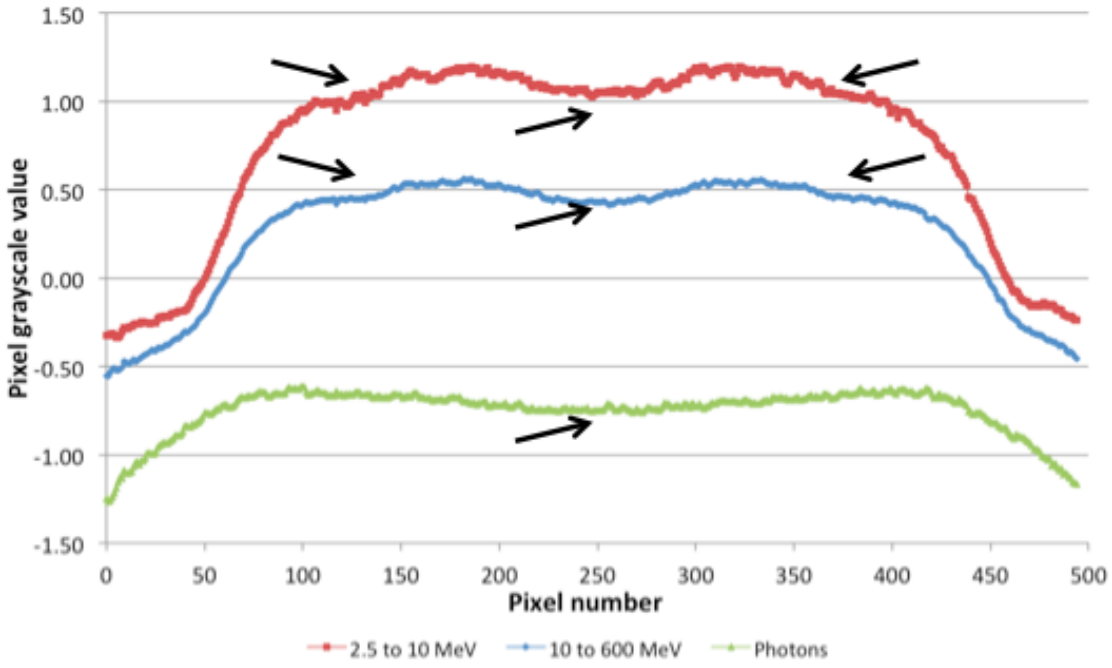


Figure 5.44: Averaged horizontal line-out for radiographs of Object 3 taken with 10 to 600 MeV, 2.5 to 10 MeV, and the photon time gate. The peaks of interest are indicated by an arrow.

hole, with only a shallow dip for the central hole, while the two neutron time gates show all three interior holes.

Having found that incident source energy affects whether features will be seen during NDA, and that this optimal energy varies between objects, subsequent work was conducted to evaluate the contrast values themselves. Did the pixel values for a given material in the experimental radiographs match neutron cross-section data such that the pixels were representative of σt? Also, did the contrast change with energy in the same way that the neutron cross-section changes with energy? To answer these questions, a study was conducted for Object 1 to compare transmission values (i.e., I/I_0) from the experiment to simulated and theoretical transmission values. Object 1 was selected because it is a rather simple configuration that allows for such a comparison, and it was assumed that, if Object 1 met expectations, then the other more complicated objects would also.

The first step in this analysis was to again post-process the experimental radiographs of Object 1. To obtain I/I_0 pixel values, the experimental radiograph of Object 1 was simply divided by the experimental flatfield image. A median filter with a pixel radius of 1.0 was then applied to reduce the effect of stars in the image, with both the flatfield and radiograph generated by averaging 94 frames together. As a reminder, the neutron energy ranges for these three radiographs were ~0.1 to 10 MeV, 2.5 to 10 MeV, and 10 to 600 MeV (Figure 5.45). Finally, average experimental I/I_0 values were found for the ROIs shown in Figure 5.46.

The next step of the study was to determine theoretical transmission values for comparison to the experimental data. A simple equation to determine the theoretical I/I_0 values is found by restating Equation 5.8 such that

$$I/I_0 = e^{-\Sigma t}, \tag{5.9}$$

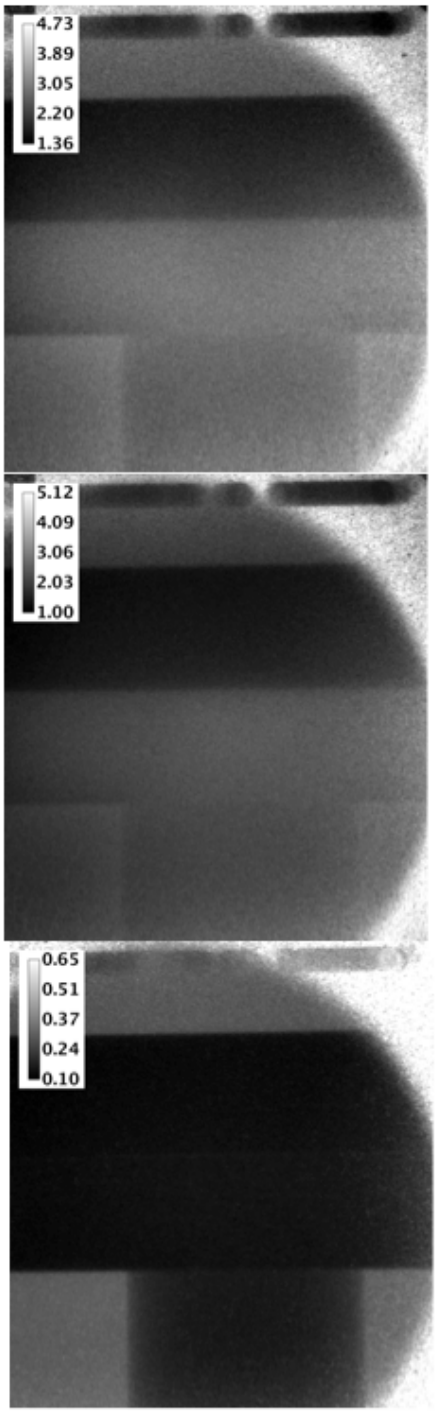


Figure 5.45: Transmission images (I/I_0) of Object 1 in FP15R generated with ∼0.1 to 10 MeV (top), 2.5 to 10 MeV (middle), and 10 to 600 MeV (bottom) neutrons.

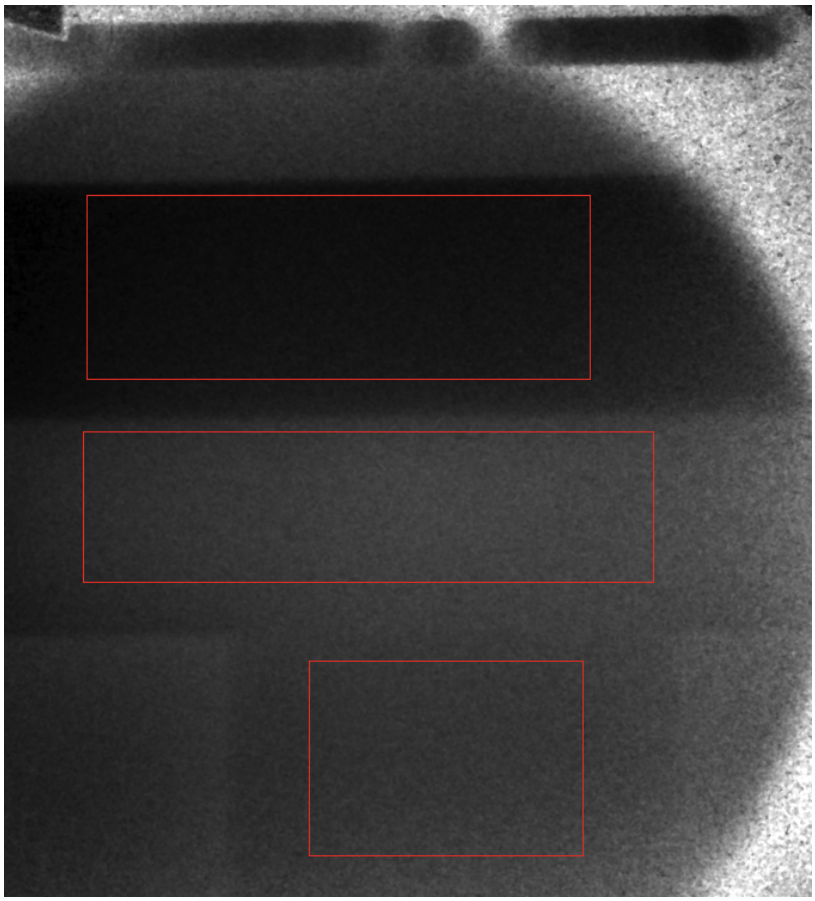


Figure 5.46: ROIs (red) used to find average I/I_0 values in lead (top), borated polyethylene (middle), and graphite (bottom). The ROIs are shown on the 2.5 to 10 MeV radiograph of Object 1.

where Σ is the macroscopic cross-section that is found from the microscopic cross-section, σ, according to

$$\Sigma = \frac{\rho N_A \sigma}{A}, \tag{5.10}$$

where ρ is the density (g/cm^3), N_A is Avogadro's number (mol^{-1}), and A is the mass number (g/mol) [69]. The units of Σ can be converted to cm^{-1} by multiplying by 1×10^{-24} cm^2/b. Note that this equation does not take into account any other effects that would be summed into an experimental image, such as scatter or activation products, nor any system effects, like detector efficiency or electronic noise.

To apply Equation 5.9, ENDF-B/VII.1 total neutron microscopic cross-section data was selected for energies that approximate the three experimental energy bins: 1.0, 2.5, 5.0, 10.0 20.0, 40.0, and 100.0 MeV [52]. (Data for energies above 100 MeV could not be found for all materials and was could not be used.) Isotopes employed to find material total cross-sections were ^1H, ^{10}B, and ^{12}C for the borated polyethylene block (combined according to percent composition specifications in Reference [70]); ^{12}C for the graphite cylinder; and ^{207}Pb for the lead block.

An average $\Sigma_{t,avg}$ was then calculated for each energy bin; for example, the 10 to 600 MeV energy range averaged Σ_t data for 10.0, 20.0, 40.0, and 100.0 MeV neutrons. (This assumed an equal probability for each neutron energy, which is not true for the LANCE beam, but with the beam profile unknown, a better assumption could not be made.) With material thickness, t, also known for Object 1 (see Section 5.2.3), I/I_0 could then be calculated by assuming that the original source strength, I, was equal to 1.

It was seen that calculated average I/I_0 values for the three materials and the three energy bins did not match that of the experimental data (Table 5.5). It was expected that the two data sets would be nearly the same because both results were normalized to the number of incident particles. However, some interesting differences were seen between the two data sets. Theory predicted that borated polyethylene was the least attenuating material (i.e., largest I/I_0 value), followed by graphite, with lead

Table 5.5: Experimental and calculated transmission data for three of the neutron energy bins used to radiograph Object 1, composed of borated polyethylene ("b-poly"), graphite, and lead. I/I_0 values larger than 1.0 indicate net particle birth, whereas values less than 1.0 indicate net particle attenuation.

Material	Data Source	$\sim$0.1 to 10 MeV I/I_0	2.5 to 10 MeV I/I_0	10 to 600 MeV I/I_0
B-poly	Experimental	2.86	2.32	0.14
	Calculated	0.54	0.61	0.71
Graphite	Experimental	2.74	2.23	0.16
	Calculated	0.35	0.41	0.50
Lead	Experimental	1.84	1.36	0.13
	Calculated	0.13	0.12	0.19

being the most attenuating material of the three materials radiographed. While this was true for the ∼0.1 to 10 MeV and 2.5 to 10 MeV experimental data, graphite was less attenuating than borated polyethylene in the 10 to 600 MeV radiograph, with lead as the most attenuating material. Additionally, the ∼0.1 to 10 MeV and 2.5 to 10 MeV experimental data showed that its materials had net particle birth, not net particle attenuation like what is to be expected and what was seen in the 10 to 600 MeV energy bin.

Additionally, relative changes in material contrast as a function of energy did not match between calculated and experimental results. For all three materials, the experimental average I/I_0 is seen to decrease with increasing energy, whereas theory shows that transmission should increase. This trend in the experimental results is believed to be a result of decreasing scintillator efficiency as a function of increasing energy, which is not accounted for in the calculations. However, this difference between the experimental and calculated results (i.e., the efficiency, which is found by dividing the experimental by the calculated data) is not constant for the three materials in a given energy bin, which indicates there are other factors at play.

Further work was therefore necessary to determine why calculated data does not match experimental data, either for all material contrasts in a given energy bin (to answer the questions "why does pixel data not represent σt?" and "why do some radiographs show net particle birth?") or for a given material contrast in all energy bins (to answer the question "why does material contrast change with energy in a manner different from what was predicted?"). To answer all three questions, it was necessary to re-examine cross-section data, but this time, the components of σ_t (e.g., scatter cross-section, absorption cross-section, and so on) were of interest. The most likely answer to these three questions is the generation of secondary particles that were being detected in the scintillator during the experiment, thus causing differences between experimental and calculated data, net particle birth in some energy bins, and a detector efficiency that varies by material in a given energy bin.

It was found that ^{207}Pb has rather large cross-sections for inelastic scatter, represented as (n, n^*), for incident neutron energies greater above 1 MeV, as well as for $(n, 2n)$ reactions above 6.77 MeV (Figure 5.47). This indicates that net birth of neutrons and photons occurs in lead for almost all of the neutron energies present in the FP15R beam. As for borated polyethylene and graphite, $(n, 2n)$ is only possible for the oxygen component in borated polyethylene and for neutrons above 9.99 MeV in energy. Inelastic scatter is possible for these two materials, but is a much lower value than that of lead (Figures 5.48 and 5.49). Thus, graphite and borated polyethylene can also generate additional neutrons for the three experimental radiograph energy bins.

This cross-section data explains why the ~0.1 to 10 MeV and 2.5 to 10 MeV experimental data shows net particle birth in all three materials. It is believed that there is no net particle birth in the 10 to 600 MeV energy bin because detector efficiency is too low, but additional study will need to be completed. It is also thought that graphite appears to be less attenuating than borated polyethylene for 10 to 600 MeV neutrons, when the opposite is true for neutrons below 10 MeV, because graphite has a higher density and thus more $(n, 2n)$ and inelastic scattering reactions are feasible. This data also explains why the efficiency varies for a material in a given energy bin: some materials generate more particle births than others.

An additional cause of the difference between the experimental and calculated data is the fact that the calculations assume no scatter is present, whereas the experimental data contains scatter because only partial scatter rejection is accomplished in a polyenergetic beam such as LANSCE. Thus, contrast values are shifted to higher values in the energy bins that contain large amounts of downscatter: ~0.1 to 10 MeV and 2.5 to 10 MeV radiographs. The former energy bin contains more scatter because it has a lower endpoint energy, and it also is seen to have the highest amount of net particle birth (i.e., largest average I/I_0). Thus, downscatter is another effect captured in the experimental data, but not the calculations.

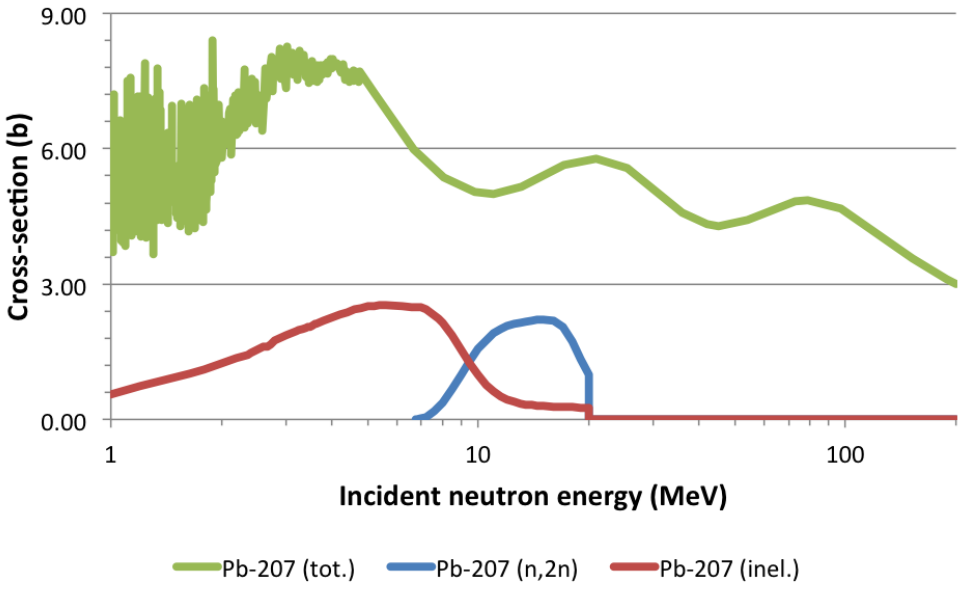


Figure 5.47: The inelastic ("inel."), total ("tot."), and $(n, 2n)$ ENDF/B-VII.1 microscopic cross-sections for ^{207}Pb [52].

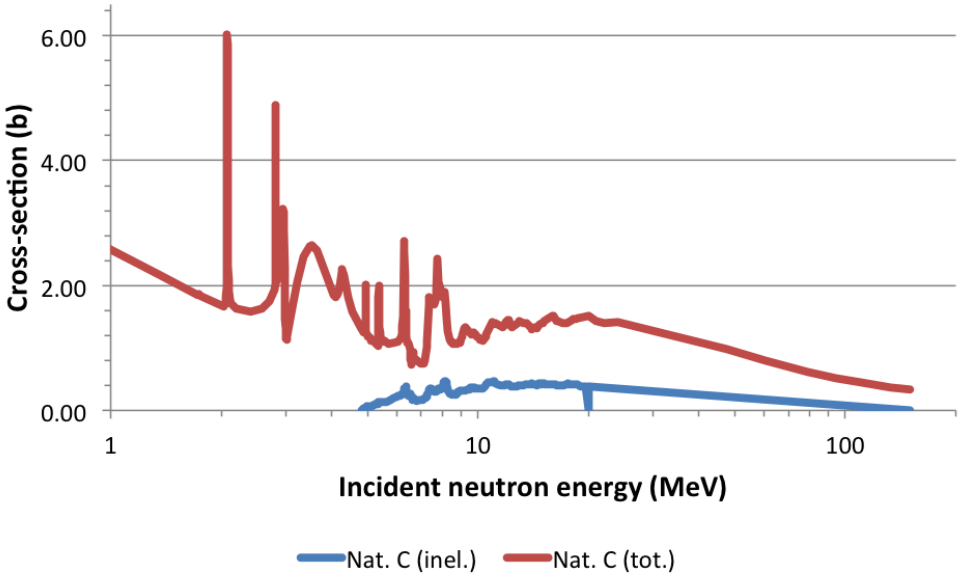


Figure 5.48: The inelastic ("inel.") and total ("tot.") ENDF/B-VII.1 microscopic cross-sections for graphite (natural carbon, or "nat. C") [52].

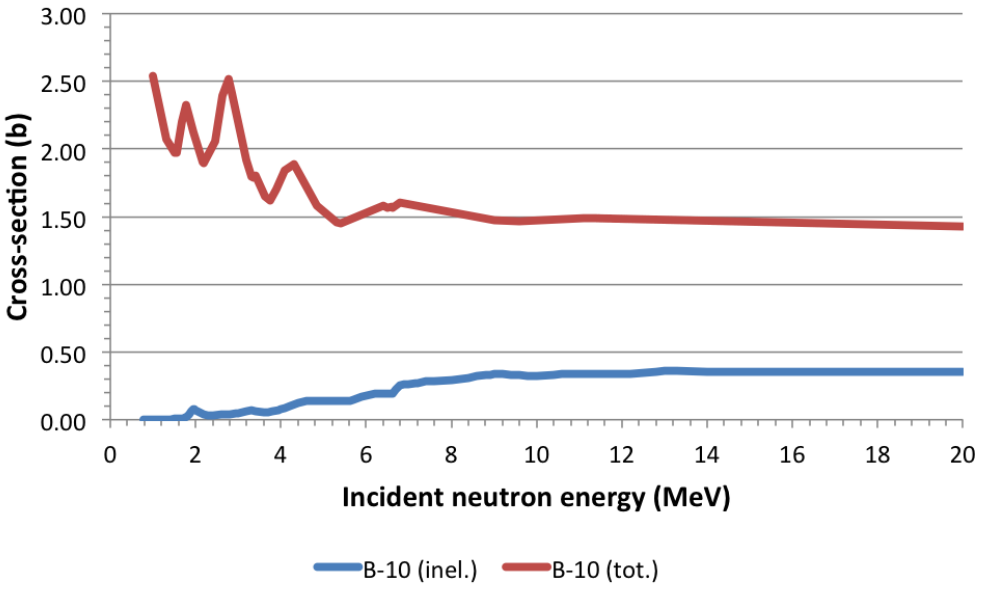


Figure 5.49: The inelastic ("inel.") and total ("tot.") ENDF/B-VII.1 microscopic cross-sections for ^{10}B ("B-10"), which is used as a dopant in polyethylene to better absorb thermal neutrons [52].

As a final attempt to understand the contrast values as a function of incident neutron energy as well as material, MCNP6 simulations were conducted to simulate radiography of Object 1 in FP15R. Simulations could account for secondary particles that cause experimental I/I_0 values to differ from theory, but not for downscatter in the beam, and thus do a better job of matching experimental data than was possible with the theoretical model.

A very simple geometry was simulated: Object 1 was placed in air and in front of the 5 mm EJ-212 scintillator. The source was simulated as a simple disk source 10 cm from the centerline of Object 1. 5×10^7 neutrons were simulated. The source used an experimental source spectrum from FP30L, provided by J. Hunter, and should be an approximate match to the spectrum seen in FP15R. It should be noted that the FP30L spectrum also did not account for neutrons of energy below 1.38 MeV, so lower FP15R energies were unaccounted for in the simulations of the $\sim$0.1 to 10 MeV radiograph. The source spectrum was then truncated, with the probabilities of neutron energies re-normalized, to reflect a given energy range (i.e., 10 to 600 MeV).

No floor, walls, light-tight box, or other components were simulated, but future simulations should include these items to obtain a more accurate scatter field (although the source will not scatter much in the current simulations because it is monodirectional onto the scintillator). Current simulations thus only include scatter within the object, within the scintillator, and from air into either the object and/or the scintillator.

The detector was simulated as 100% efficient at all neutron energies, and an FMESH tally with pixels 0.05 cm on an edge was placed over its its volume. The FMESH tally was used to simulate direct, as well as direct plus scatter, neutron radiographs; direct plus scatter secondary photon radiographs were also generated. A total simulated radiograph was created during post-processing by summing the neutron and photon direct plus scatter results. Corresponding flatfield radiographs were next generated by removing Object 1 from the input deck geometry and re-running the simulation, with a total direct plus scatter flatfield image also formed

in post-processing. To find simulated I/I_0 values, the simulated total radiograph (i.e., neutron plus photon) was divided by the simulated total flatfield (Figure 5.50). Again, ROIs were used to find an average I/I_0 for the three materials (Figure 5.51).

Much like the theoretical calculations, the simulated total I/I_0 data also did not exactly match the experimental data. This difference can be attributed to using a source spectrum from another flight path; missing sources of scatter in the simulations (e.g., from the surrounding environment and the beam downscatter); and lack of detector efficiency data in the simulations (Table 5.6). For example, the simulations only showed net particle birth in the 10 to 600 MeV total radiograph, while the experimental data showed net particle birth in the $\sim$0.1 to 10 MeV and 2.5 to 10 MeV radiographs. This can be explained by a lack of downscatter in the $\sim$0.1 to 10 MeV and 2.5 to 10 MeV simulated radiographs and also missing detector efficiency data that would cause net death in the 10 to 600 MeV simulated radiograph.

Additionally, simulations showed increased transmission as a function of energy like the theoretical model showed, which does not match the decreased transmission seen in the experimental data. This is explained by the lack of detector efficiency in the MCNP6 model and no or reduced scatter in the calculated and simulated data, respectively. It is expected that adding detector efficiency data and scatter sources would improve this result so that simulations would match experiments.

Finally, while simulations of the 10 to 600 MeV total radiograph showed relative material contrasts correctly according to theory, they did not match the experimental data (which showed graphite being less attenuating than borated polyethylene). Moreover, the two lower-energy radiographs (both simulated and experimental) showed just the opposite, and differences in contrast between materials was much less in the simulations than in the experimental data. This effect is also most likely caused by the lack of downscatter in the beam line.

Although the simulated radiographs did not look as similar to the experimental data as was hoped, several key observations were made with respect to secondary particles. Within the MCNP6 output are a number of tables that track particles as

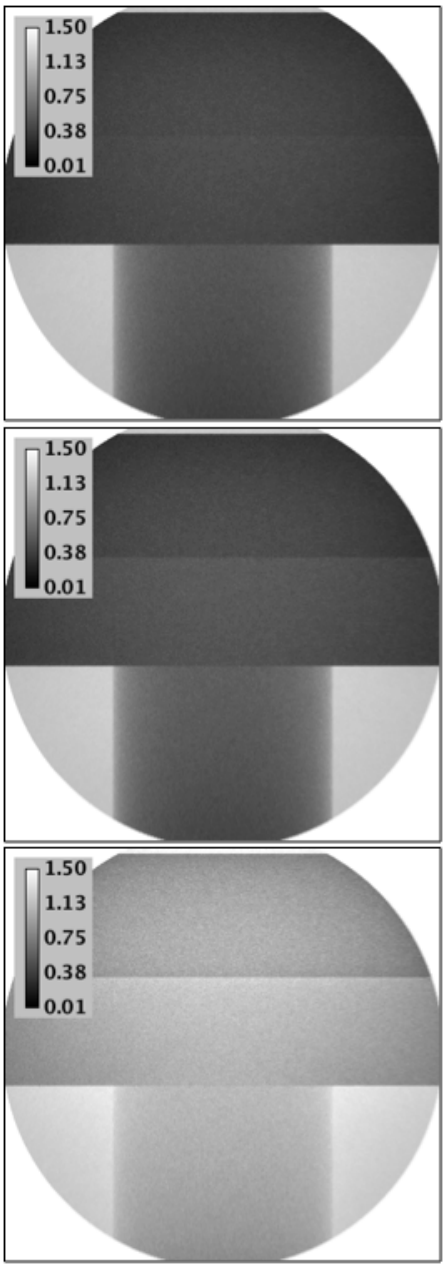


Figure 5.50: Simulated total (i.e., direct plus scatter) neutron radiographs of Object 1 in FP15R using MCNP6 FMESH tallies. These three radiographs are set to the same contrast levels. Top: Simulated ∼0.1 to 10 MeV total neutron radiograph. Middle: Simulated 2.5 to 10 MeV total neutron radiograph. Bottom: Simulated 10 to 600 MeV total neutron radiograph.

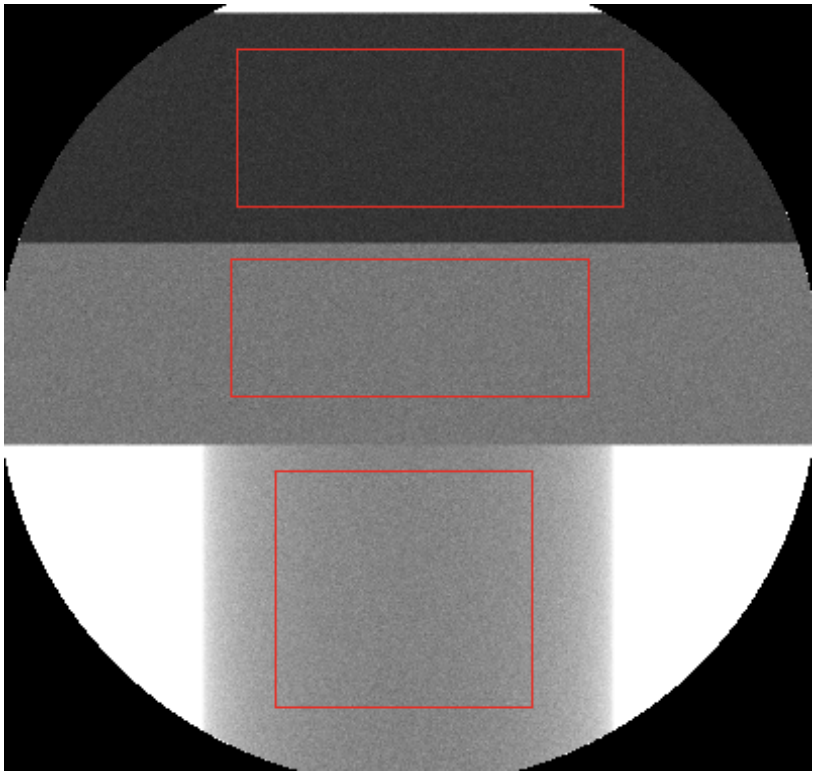


Figure 5.51: ROIs (red) used to find average simulated I/I_0 values in lead (top), borated polyethylene (middle), and graphite (bottom). The ROIs are shown on the 10 to 600 MeV simulated neutron radiograph of Object 1.

Table 5.6: Experimental and simulated transmission data for three of the neutron energy bins used to radiograph Object 1, composed of borated polyethylene ("b-poly"), graphite, and lead. I/I_0 values larger than 1.0 indicate net particle birth, whereas values less than 1.0 indicate net particle attenuation.

Material	Data Source	$\sim$0.1 to 10 MeV I/I_0	2.5 to 10 MeV I/I_0	10 to 600 MeV I/I_0
B-poly	Experimental	2.86	2.32	0.14
	Simulated	0.45	0.52	1.11
Graphite	Experimental	2.74	2.23	0.16
	Simulated	0.49	0.53	1.01
Lead	Experimental	1.84	1.36	0.13
	Simulated	0.41	0.42	0.99

a whole that are useful to determine what types of particles are being born, as well as how many and their location. The first such table showed that (n, xn) reactions (where x is the multiplicative number of neutrons) do not occur in air, but do occur in Object 1. For the ~0.1 to 10 MeV and 2.5 to 10 MeV energy bins, (n, xn) reactions only occur in very small numbers in ^{207}Pb. In the 10 to 600 MeV energy bin, however, all materials undergo the (n, xn) reaction, with ^{207}Pb being the largest contributor. Furthermore, in the 10 to 600 MeV radiograph, the number of neutrons generated from the (n, xn) reaction almost doubles the neutron source strength, from 5×10^7 simulated particles to 9.5×10^7! Thus, this reaction is non-trivial, particularly at upper LANSCE energies, and can explain why calculations do not match experimental data.

Next, secondary photons were examined. The (n, γ) reaction was seen to be large at all incident neutron energies and was approximately 50% of the incident neutron source strength. It was seen that ^{207}Pb was the largest contributor, with approximately 10% of this number generated in the air. Other smaller sources of photons were x-ray fluorescence, which only occurred in Object 1, and photon annihilation, which occurred in very small numbers in both the air and Object 1. These secondary photons, found to be non-trivial were unaccounted for in the calculated I/I_0 values, likely adding to the differences seen between the data sets.

To further illustrate the amount of secondary neutrons and photons generated, which were not incorporated into the I/I_0 calculations, two plots were created (Figure 5.52). These plots show that, while the photon production is nearly constant as the neutron energy increases, the production of neutrons has a large jump for the 10 to 600 MeV energy range.

A final interesting observation from the simulations resulted from a comparison of the direct I/I_0 values for the three energy bins of interest (Figure 5.53). With no scatter, no secondary particles (i.e., photons) are generated which have been shown to skew results. As a result, direct radiographs should nearly match the calculated data, as both the simulated and calculated data ignore scintillator efficiency and scatter,

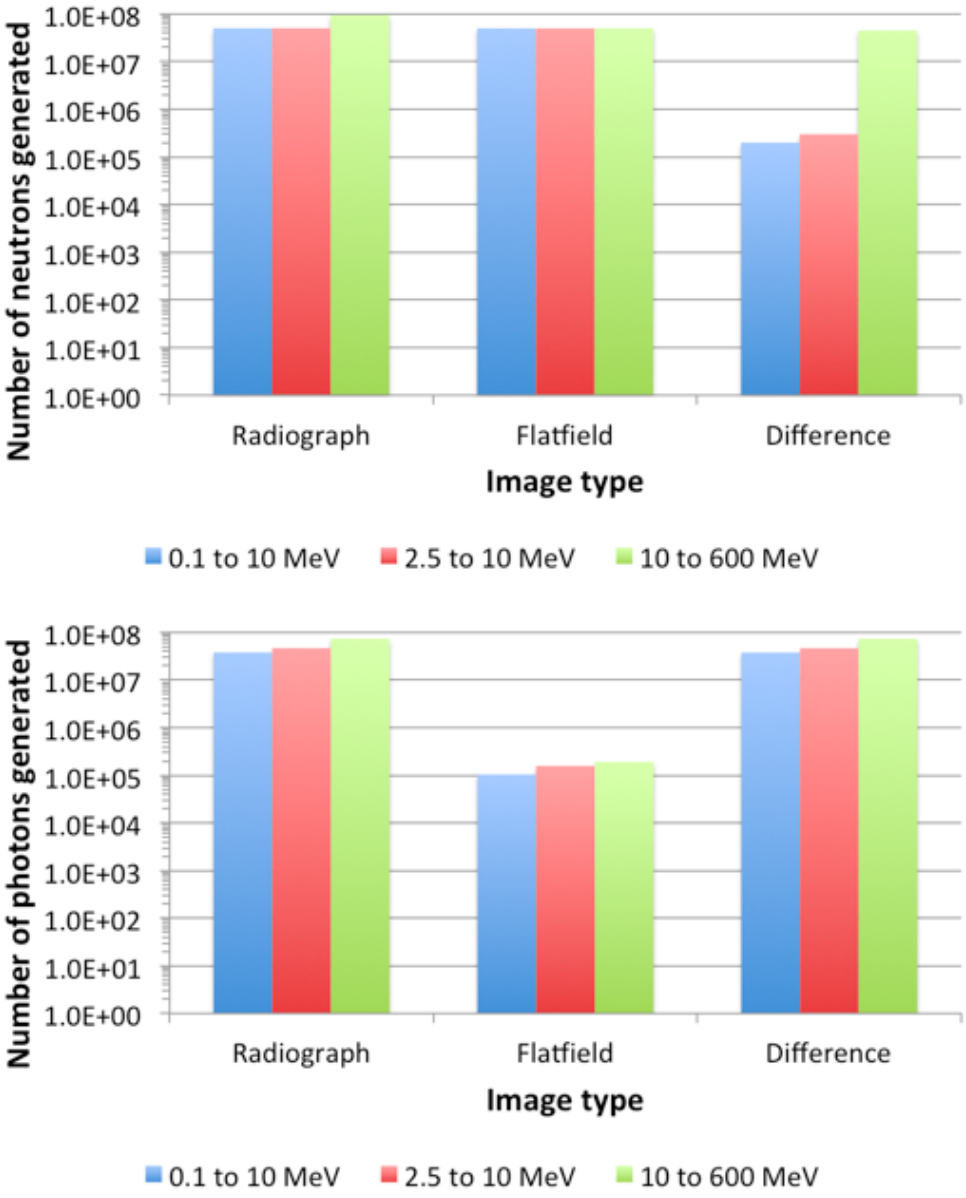


Figure 5.52: Simulations of FP15R total radiographs of Object 1, as well as simulations of corresponding flatfield images, allowed for determination of the number of secondary particles generated in each image type. The difference in secondary particles between the image types indicates the number of secondary particles born in the radiography object. Top: The number of secondary neutrons generated via the (n, xn) reaction. Bottom: The number of secondary photons generated via (n, γ), x-ray fluorescence, and photon annihilation reactions.

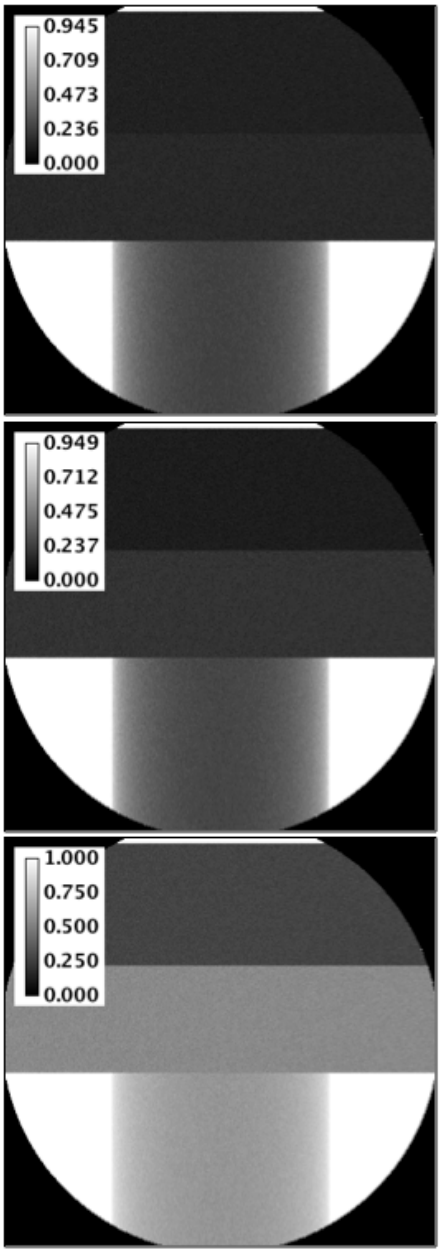


Figure 5.53: Simulated direct radiographs of Object 1 in FP15R using MCNP6 FMESH tallies. These three radiographs, set to different contrast levels, do not include secondary particles or scatter. Top: Simulated ∼0.1 to 10 MeV direct neutron radiograph. Middle: Simulated 2.5 to 10 MeV direct neutron radiograph. Bottom: Simulated 10 to 600 MeV direct neutron radiograph.

and are a better representation of what one would see with TiGReSSE if using a monoenergetic source without downscatter.

Average I/I_0 values were taken for the same ROIs shown in Figure 5.51 and compared to the calculated values (Table 5.7). As expected, the direct simulated data perfectly mirrored the calculations, with even a slight dip in the transmission for lead in the 2.5 to 10 MeV energy bin that matches a dip seen in the calculations. Additionally, transmission increased as a function of energy, and decreased as a function of density, as expected. Slight differences in the values between the two data sets can be attributed to the use of actual cross-section data in the simulated direct data, whereas calculated data used averaged cross-sections for the given energy range which is less accurate.

Thus, the contrast differences between calculations and the simulated total (direct and scatter) radiographs, as well as between calculations and experimental data, appear to be mainly the result of scatter and secondary particles that are not accounted for in either the theoretical or computational models. This is because these differences almost entirely disappear when simulated direct radiographs are compared to theory. It is therefore very important to match simulations to experimental conditions to minimize differences and enable a fair comparison of the two data sets, and future work should expand these models to include more sources of scatter and thus allow for better analysis of experimental data. Detector efficiency should also be employed to further improve future analysis. It is expected that Object 2 and 3 would also follow this pattern, and future work could also compare these objects to theory and simulation.

It should be stated, however, that even though the pixel values did not match theory, two regions of the same material had the same contrast levels in a given radiograph. Thus, experimental values for σt could be determined and used for material identification, even if those values did not match theoretical values. It is

Table 5.7: Calculated and simulated direct transmission data three of the neutron energy bins used to radiograph Object 1, composed of borated polyethylene ("b-poly"), graphite, and lead. Note that I/I_0 values larger than 1.0 indicate net particle birth, whereas values less than 1.0 indicate net particle attenuation.

Material	Data Source	$\sim$0.1 to 10 MeV I/I_0	2.5 to 10 MeV I/I_0	10 to 600 MeV I/I_0
B-poly	Calculated	0.54	0.61	0.71
	Simulated	0.15	0.19	0.54
Graphite	Calculated	0.35	0.41	0.50
	Simulated	0.27	0.29	0.61
Lead	Calculated	0.13	0.12	0.19
	Simulated	0.12	0.12	0.27

therefore still highly probable that TiGReSSE can be used to identify materials in an experimental setting.

5.2.8 Discussion of System Performance

Beam Operation

Operating the beam was a fairly time-consuming process. Access was controlled to the flight path, and a multi-step procedure had to be conducted prior to opening the beam shutter (Figure 5.54). The shutter also opened and closed fairly slowly, taking several minutes to move. Thus, swapping out samples or removing samples to generate flatfield images, which required closing the beam shutter, removing or replacing samples, and re-opening the beam shutter, could be time-consuming.

Imaging Times

The radiography process was lengthy, partially because every radiograph required additional images for post-processing (e.g., flatfield images). Given the short amount of time at LANSCE, images were taken in 36 min or less in order to get as much data as possible. Imaging times directly depended on the gate width and the section of the spectrum being used for imaging, since these two factors directly impacted the amount of flux available for radiograph generation. For example, imaging with a 10 ns gate to obtain the gamma signal needed 6.0×10^5 accumulations per frame and took 36 min, whereas an image with the entire pulse (a gate of 1784 ns) required 1.25×10^5 accumulations per frame and took 6 min due to a wider time gate. In later experiments, longer measurement times will be conducted in order to obtain better statistics and thus clearer images with better contrast and resolution.

Effect of Camera Temperature on Resolution

As stated previously in this chapter, the D-T generator radiography experiment that failed to produce radiographs led to the purchase and installation of a liquid chiller



Figure 5.54: Photograph of the controlled access door to FP15R. The position of the shutter here is closed, as indicated by the glowing lights above the door.

for the camera. During the week at LANSCE, the chiller had no problem keeping the camera at the recommended operating temperature of -20 °C, and not once did the camera overheat in the box like was common prior to installing the chiller. This was particularly important since the camera was on and running at one point for about 24 hours.

The ability to maintain this low temperature meant generating lower noise, higher resolution images. As can be seen in Figure 5.55, one image of the Siemens star pattern was taken at the recommended operating temperature of -20 °C and another at a higher temperature of -10 °C, with both images set to the same contrast level. The Siemens pattern was illuminated with the pulsed LED laser, and each image averaged together 75 frames to achieve better statistics. Note that the images in Figure 5.55 are not attenuation plots like the other radiographs in this chapter since they are not transmission radiographs and a flatfield image could not be generated. Thus, contrast levels indicate the opposite of what they indicated for the neutron radiographs: larger grayscale values indicate a brighter image.

When set to the same contrast scale, the image taken at -20 °C is sharper and brighter than the image taken at -10 °C (Figure 5.55). Quantitatively, this is evidenced by the line-out plot in Figure 5.56 that shows the range of pixel grayscale values increases when the temperature of the camera is reduced. An example of the line-out placement is also shown in Figure 5.56. Thus, cooling the camera reduces noise and provides better radiographs with greater range in contrast.

Scatter Field

Scatter in the beam line was a much larger problem than previously anticipated. An example of stars and tracks can be seen in Figure 5.57, which shows one of the frames of a radiograph taken of Object 1 with 2.5 to 10 MeV neutrons. High-energy neutrons approaching energies of 600 MeV are difficult to moderate and shield, and so they easily penetrated camera shielding and deposited dose on the silicon CCD chip as "stars" (very bright pixels where the neutron deposited all of its energy)

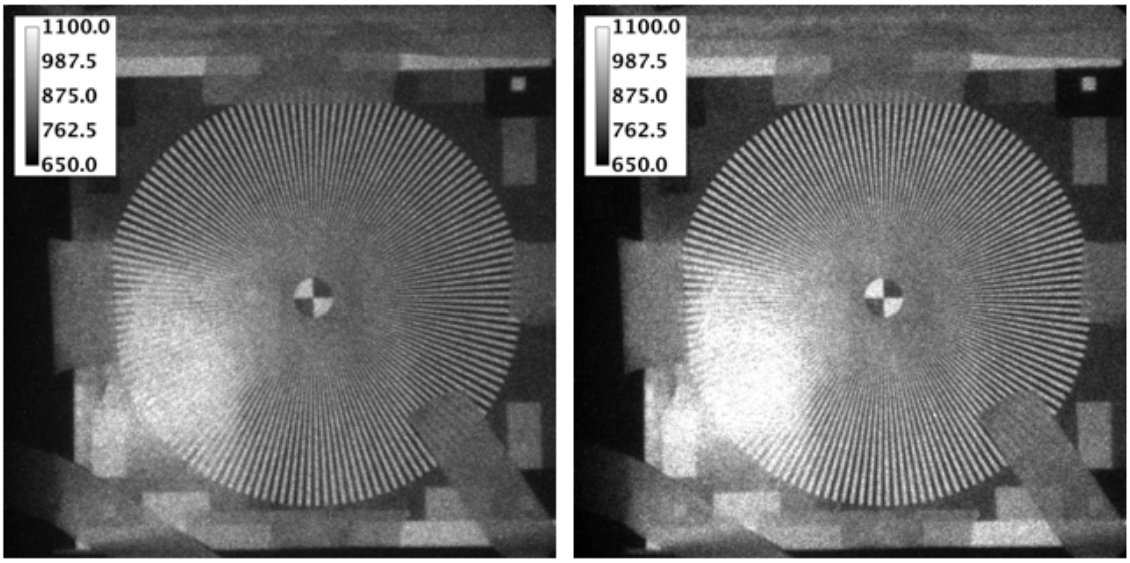


Figure 5.55: Two radiographs of the Siemens star pattern, one taken at a temperature of -10 °C (left) and one taken at a temperature of -20 °C (right). Both radiographs are set to the same contrast range to compare the effect of temperature on noise.

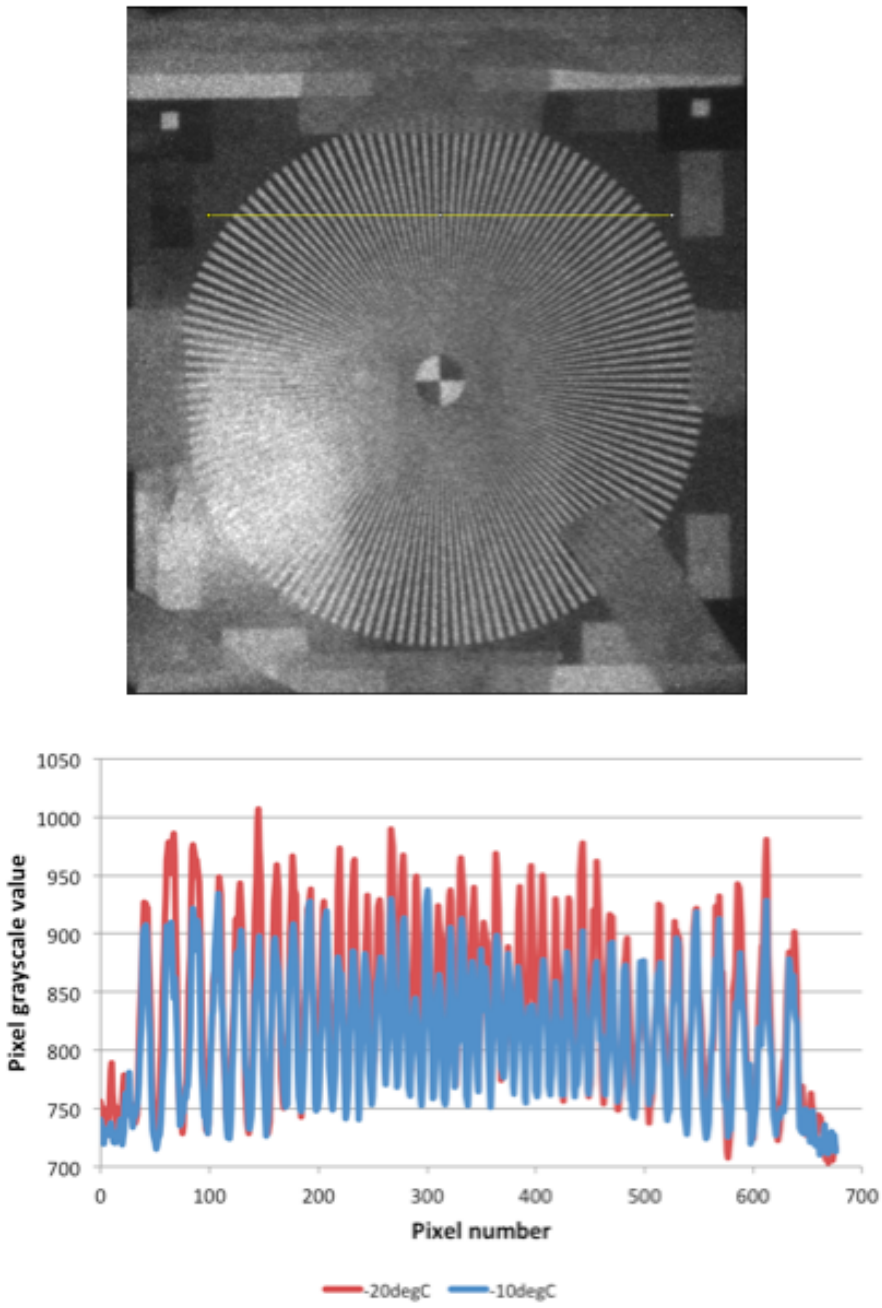


Figure 5.56: Line-outs of the Siemens star pattern as a function of camera operating temperature. Top: Line-out location indicated by the yellow line and demonstrated on the -20 °C image. Bottom: Line-out values plotted for both the -10 °C and -20 °C images.

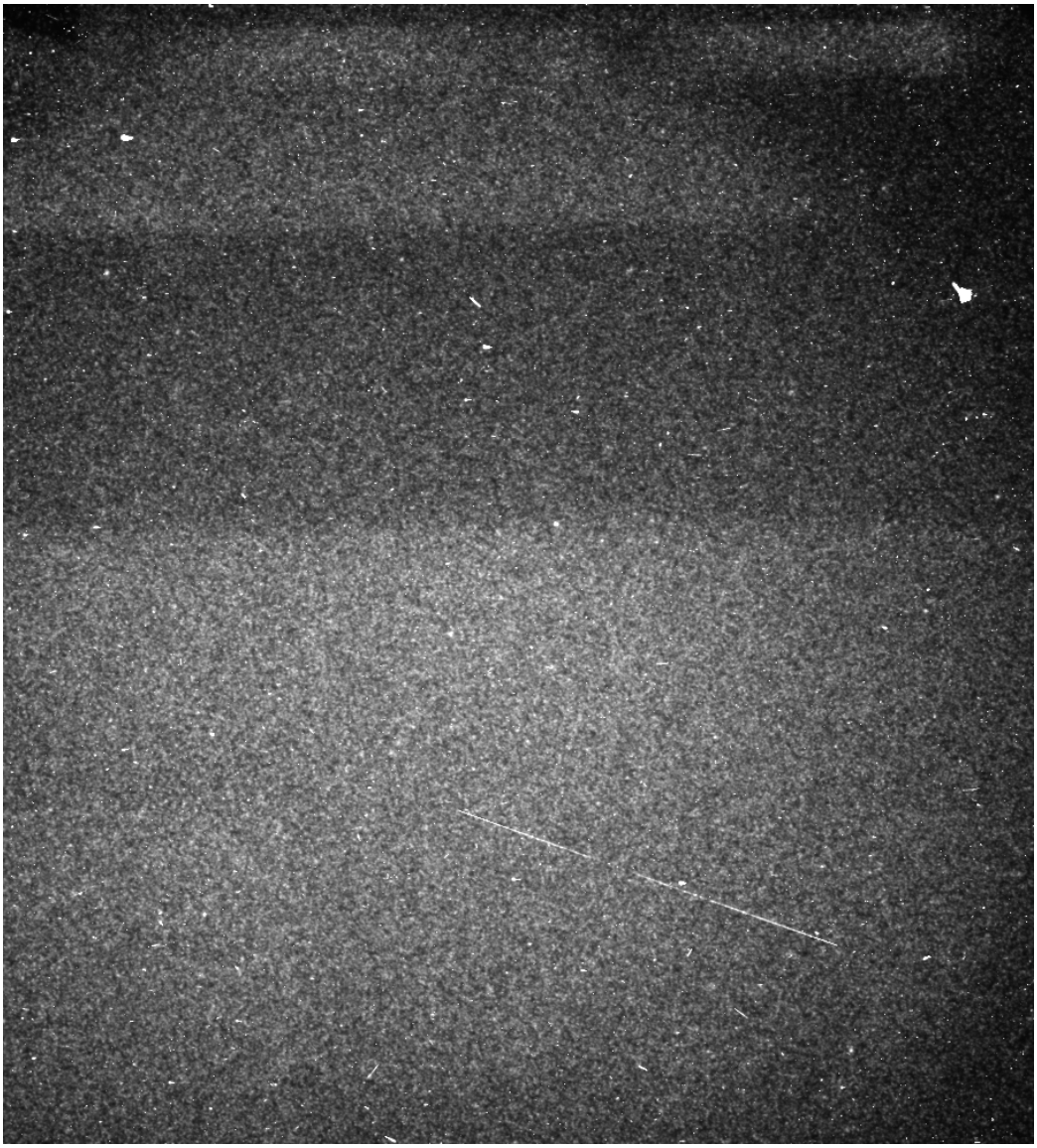


Figure 5.57: Example of stars and tracks in one of the frames taken of Object 1 with 2.5 to 10 MeV neutrons.

or as "tracks" where the neutron traveled across multiple pixels. The phosphor is less sensitive because it is gated on and off to conduct time gating; the CCD chip, however, is always on and thus much more sensitive to scatter.

There were many sources of scatter within the beam line. The neutrons scattered from the concrete shielding blocks that comprised the beam line, as well as the concrete floor, resulting in a large scatter field. Other components in the beam line, such as equipment from other experiments, were also sources of scatter. Additional sources of scatter and noise are the photons from the spallation target and the secondary photons resulting from material activation, as well as cosmic muons. There is also the possibility that, even with a magnetic sweeper above the beam line to capture charged particles, high-energy spallation particles like protons and electrons could escape, reach the camera, and form stars in the radiographs. Inside the light-tight box, scattering off the mirror was examined. The mirror was removed and a background image was taken to see if scatter to the camera decreased, but no change could be detected.

Not only was the scatter worrisome for the lifetime of the CCD chip and the camera electronics, but the stars in the radiographs reduced the amount of gain that could be used on the camera. This is because increasing the gain amplifies the star effect that then skews the perceived contrast range in the image so that other areas artificially appear very dark, which masks internal features. With stars limiting the useful range of gain, radiographs take longer to generate because the low light from neutrons impinging on the scintillator cannot be amplified. Lower light levels require more pulses to be integrated on the CCD chip to achieve the same level of light, thus increasing the amount of dose to the camera and the radiography object.

While it is true that stars can be partially removed with an averaging filter during image post-processing, this type of filter introduces a blurring factor that decreases resolution. It is also very difficult to subtract this form of background since it is random, and so often the stars remain in the image even after post-processing.

Therefore, an improved shielding design is necessary to obtain better quality images, with a study on developing specialized shielding for TiGReSSE detailed in Chapter 7.

Flatfield Images

As stated earlier in this chapter, the flatfield image, or image of the beam incident on the scintillator with no radiography object present, is taken so that it can be divided out of the radiograph and normalize the radiography data. Inspection of the six flatfield images taken in FP15R (e.g., full spectrum, photon, and neutrons varying in energy from 2.5 to 10 MeV, 10 to 600 MeV, 2.5 MeV and below, and 10 MeV and below) revealed that the beam intensity was not uniform. A non-uniform beam reduces image quality, even though its effects are divided out, because the flux varies across the object being imaged. This results in variations in scatter and transmission for identical material regions, which causes the signal-to-noise ratio to vary in a nonuniform way. Therefore, an ideal beam would have a perfectly uniform beam shape, but all beams have some degree of non-uniformity.

The non-uniformity of the FP15R beam was quantified by taking a line-out across the center of each of the six flatfield images after the 100 flatfield frames had been averaged together. The line-out results in each energy bin were then normalized to the total number of integrated pulses in that energy bin. The line used to generate the line-out, as well as a plot of the six line-outs, can be seen in Figure 5.58. The beam drops in strength for all six flatfields as one moves to the right in the flatfield image, which is what was seen visually in the flatfield images.

Another observation from the plot in Figure 5.58 is that the flatfield intensity is greatest for the full spectrum image. This makes sense when one remembers this energy bin is integrating the entire pulse and not certain energies. The 10 MeV and below-energy bin was second-highest in intensity, which is where the majority of the LANSCE flux can be found. The other neutron bins similarly follow the flux level in their energy bin. The lowest intensity time bin was seen to be the photon bin, which explains why photon radiographs were of such poor quality.

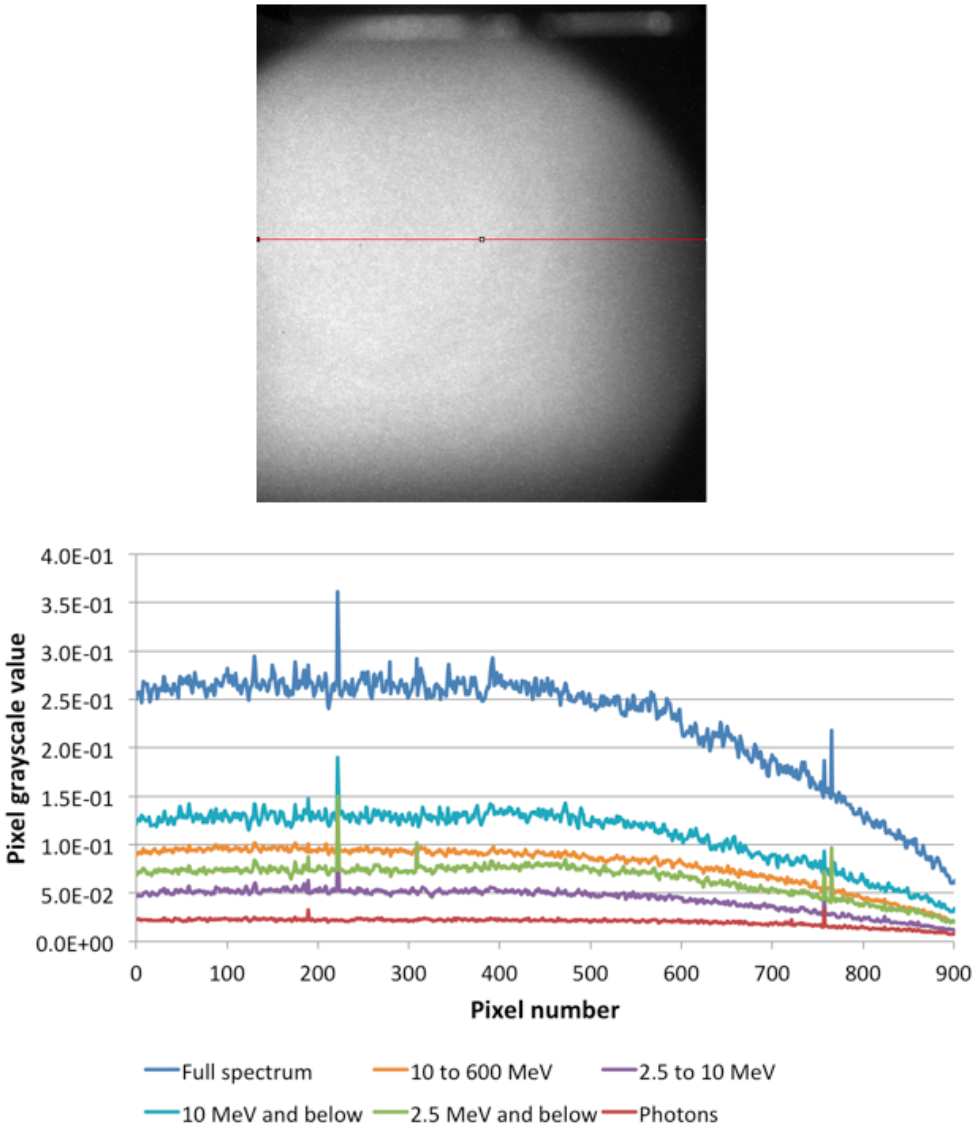


Figure 5.58: Top: Example of the line-out used to quantify FP15R beam non-uniformity. The line is shown on the full spectrum flatfield. Bottom: Line-outs for the six flatfield images taken in FP15R. Pixel grayscale values were normalized to the number of total pulse accumulations in each energy bin.

As a final comment, large peaks can be seen in the flatfield line-outs. Those that occur in the same location are most likely the result of a dead pixel caused by electronic damage from the high-energy particles in FP15R, whereas those that occur in random positions are the result of stars in the image.

5.3 Conclusions

TiGReSSE was successfully tested with neutron sources. Experiments with a D-T source showed that geometric light loss is a limiting factor for image quality, as is camera temperature. The latter problem was addressed by buying a liquid chiller to keep the camera cool and reduce electronic noise, whereas the former problem cannot be addressed with current system parameters. Perhaps future system designs will incorporate fiberoptic coupling to limit light loss.

FP15R experiments showed that the ICCD camera can successfully radiograph objects in a high-energy, high-flux environment. Gating in time using TOF methods was also shown to be successful, and covered a range of neutron energies from $\sim$0.1 to 600 MeV. Partial scatter rejection was demonstrated by eliminating scatter from the object, as well as undesired parts of the LANSCE spectrum, but a monoenergetic source will be needed to show full scatter rejection. Scatter was seen to be a large problem, reducing image quality due to stars on the ICCD chip and decreased contrast resolution that masked features within the radiography objects. Thus, future experiments will need to improve the camera shielding to protect the ICCD chip and will also need to reduce scatter within the flight path.

It was also shown at LANSCE that features may be visible at one energy but not another, and that the optimal energy varies among radiography objects. Thus, a monoenergetic source with a spallation target would allow full scatter rejection in some radiographs and energy selection in others.

Chapter 6

System Properties

This chapter provides an in-depth discussion of system properties that are necessary to understand the capabilities and limitations of the radiography system, TiGReSSE. The first such property discussed here is the plastic scintillator efficiency, which was determined via MCNP6 simulations. This work will enable an understanding of how the LANSCE beam is used for radiography, and whether certain energies are undesirable from a detector efficiency standpoint.

Another important system property studied in this section is image contrast resolution. The contrast resolution was found experimentally and provides an idea of what feature size is resolvable at the scintillator plane. This experiment used line pairs to determine the limiting resolution, according to the method outlined in Section 1.3.1.

6.1 Scintillator Properties

6.1.1 Theory: Fast Neutrons and Plastic Converters

As stated in Chapter 1, fast neutrons are mainly detected via proton scattering reactions in the detector material. These scattered protons then travel through the

scintillator, losing energy along the way. This energy is converted into visible light, which, in this case, is detected by the ICCD camera to form an image.

To maximize the (n, p) scattering reaction, low-Z scintillators (in particular, plastic scintillators) are typically used for fast neutron radiography because they are high in hydrogen content. Hydrogen is desirable because it is able to absorb all of a neutron's incident energy in a head-on collision. Thus, neutrons are better stopped in the low-Z material, and impart more of their incident energy to the scintillator, which increases the likelihood and intensity of counts and improves detection efficiency.

The average proton "range", or distance traveled, and the corresponding energy deposited in the scintillator are therefore important values to understand when estimating a given scintillator's fast neutron detection efficiency. Because protons are positively charged and electrons in the scintillator material are negatively charged, protons experience a number of deflections along their path through the scintillator. This leads to fluctuations in proton range, as well as energy deposited in the screen. Therefore, average values are often cited, with the continuous slowing-down approximation (CSDA) typically being used to approximate the average energy loss in the screen [69].

The CSDA assumes the proton slows continuously through the material, with an average energy loss per differential path length. Proton range and energy loss are thus often "stepped through" analytically (or with physics codes) by transporting the particle a small distance and calculating the energy loss across that distance, and then repeating that calculation until the proton is absorbed or leaves the material. This averaging calculation obviously ignores the variation in energy transfer from the neutrons to the protons, which is dependent on scattering angles, and also the energy transfer from neutrons to the carbon atoms present in plastic, which at high neutron energies is not negligible [69].

As for other charged particles (e.g., alpha particles), their range is approximately related to the proton range by m/z^2 if they have the same initial speed and are traveling through the same material, where m is the particle mass and z is the particle

charge. Using this rule, a 1 MeV alpha particle has approximately one-quarter of the range of a 1 MeV proton in a given material. A second rule applies for particles of the same speed but traveling through different materials. In such a case, CSDA ranges are related by $(m/z^2)\,(Z/A)$, where Z and A are the isotope's atomic number and atomic mass, respectively [69].

Semi-*log* plots of the CSDA range for proton and alpha particles in aluminum, vinyltoluene-based (VT-based) plastic scintillator, silicon, and air can be seen in Figures 6.1 and 6.2, respectively [71, 72]. Silicon represents the ICCD chip, and the VT-based scintillator approximates EJ-212. Aluminum and air were selected for comparison. CSDA values shown are for an 800 MeV incident neutron, which is the upper energy limit for the LANSCE beam. Such an incident neutron can give up to all of its energy to a proton (the proton has mass equal to that of a neutron), resulting in an 800 MeV proton, but only up to 64% of its energy to an alpha (resulting in a 512 MeV alpha particle). The x-axis of both plots therefore represents the range of energies that can be given by an 800 MeV neutron to an alpha or proton in the LANSCE beam line.

These plots show that an 800 MeV proton can travel approximately 247 cm in the VT-based scintillator material, and a 512 MeV alpha can travel approximately 24 cm in the same material. Both of these CSDA ranges are many times greater than the TiGReSSE scintillator thickness of 5 mm. The VT-based scintillator data shows (using linear interpolation of the data plotted in Figure 6.1) that 21.3 MeV neutrons have a range of 5 mm, the thickness of the EJ-212 scintillator used in TiGReSSE. A 2 mm screen (more desirable than a 5 mm scintillator due to reduced blur) of the same material would stop protons of energy up to 17.7 MeV and thus would sacrifice detection efficiency. These two energies are much less than the LANSCE endpoint energy, and thus simulations will need to be conducted to determine how many neutrons above 17.7 MeV and 21.3 MeV are actually being detected.

Silicon, with a greater mass and therefore larger electron density, has a smaller CSDA range than the VT-based scintillator material, which indicates that silicon is

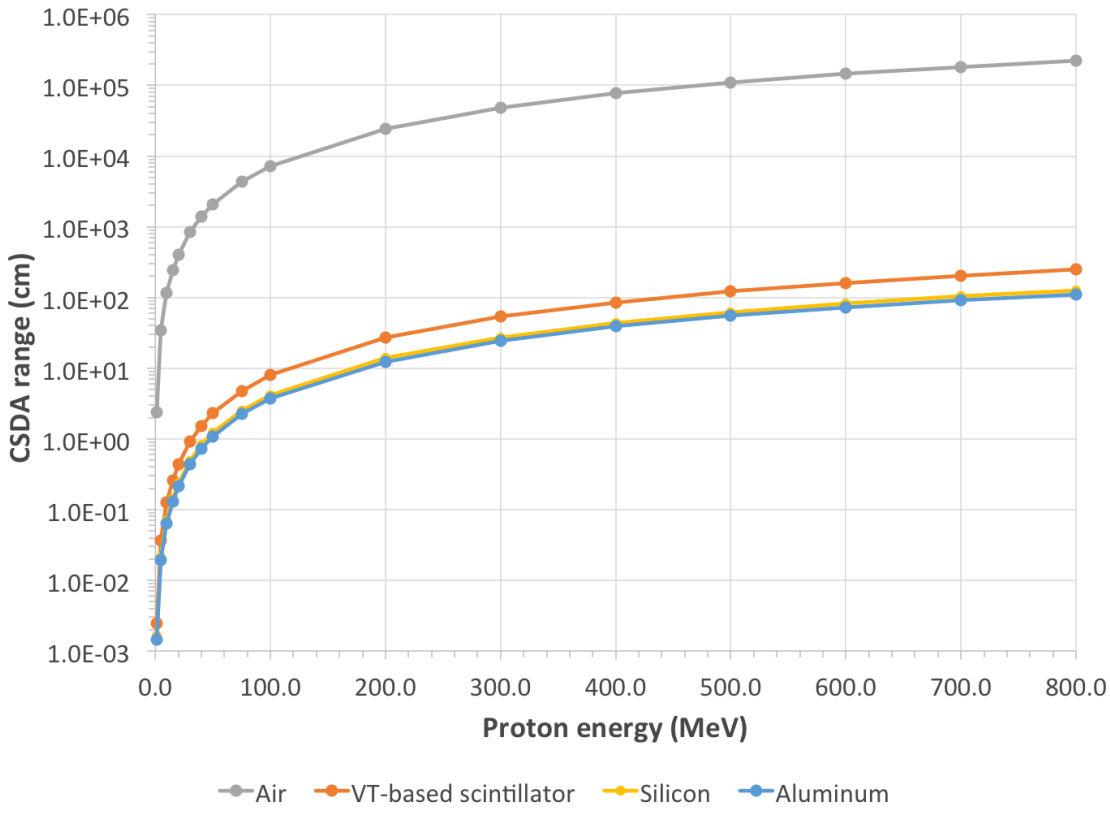


Figure 6.1: Semi-*log* plot of the proton CSDA range for a neutron of 800 MeV incident on various materials, taken from the NIST PSTAR database [71].

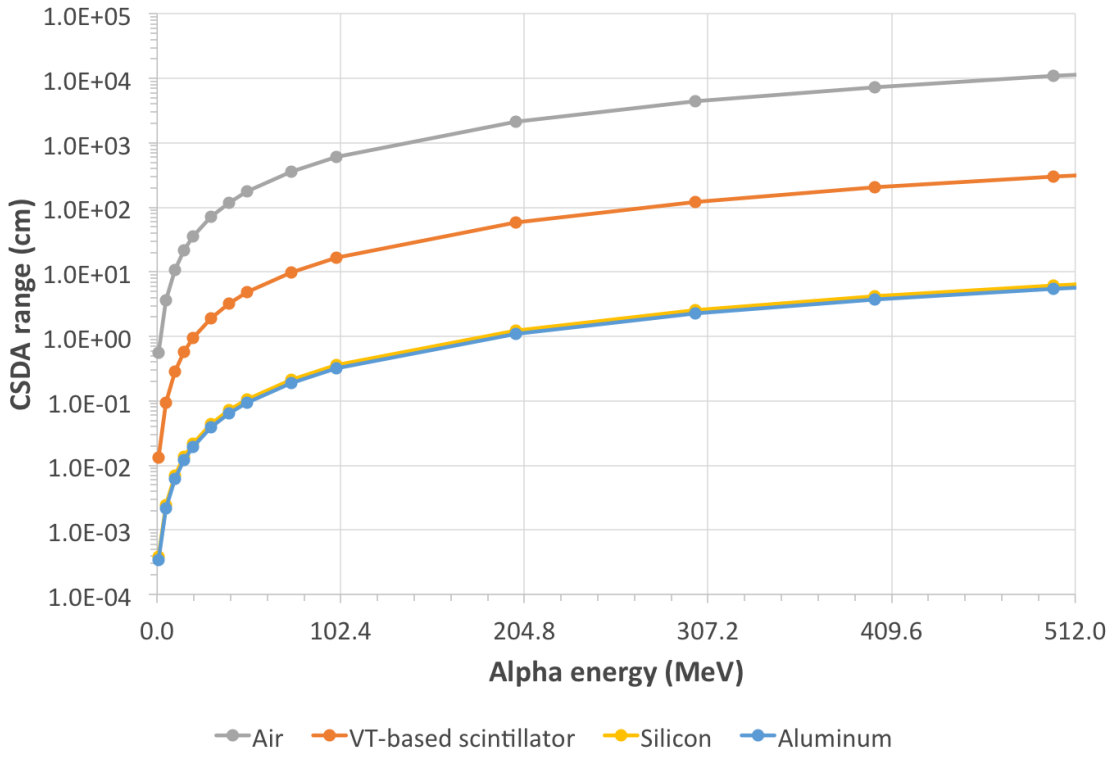


Figure 6.2: Semi-*log* plot of the alpha CSDA range for a neutron of 800 MeV incident on various materials, taken from the NIST ASTAR database [72].

better at stopping protons and alphas. This fact explain why, although the ICCD chip is thin, it can get high-energy hits that create stars in the radiographs and why these hits can be so damaging to electronics. This data illustrates why shielding the ICCD camera is very important for image quality and system longevity.

In summary, protons and alphas scattered at the energies seen in LANSCE travel surprisingly large distances and have non-trivial affects on TiGReSSE. It is important to characterize the EJ-212 efficiency at high neutron (and thus high proton) energies to determine how TiGReSSE behaves in the LANSCE beam lines.

6.1.2 MCNP6 Simulations of Detector Efficiency

Intrinsic detector efficiency depends on a number of variables, including the incident neutron energy, scintillator thickness, and the resultant light output [34]. The first dependency is important to determine because the efficiency impacts the choice of neutron source energy for use with TiGReSSE. Camera noise remains constant, so if fewer neutrons are detected above a given energy because of reduced scintillator efficiency, the signal-to-noise ratio will degrade. There will eventually be an upper source energy limit where the light output is no longer distinguishable from the noise, and it is important to determine what this limit is for TiGReSSE.

It is also necessary to determine the effect of scintillator thickness on efficiency. If TiGReSSE were to use a thinner converter screen to reduce spatial blur, it was unknown by how much the light output would be reduced. This relationship is important for time-of-flight imaging to determine the optimal screen thickness to maximize efficiency but also minimize blur.

MCNP6 simulations were conducted to determine the detector efficiency because most neutron cross section data has only been experimentally determined for neutron energies up to $\sim$20 MeV. As a result, the efficiency could not be analytically determined for upper LANSCE energies, but MCNP6 could computationally model high-energy (n, p) scattering reactions in the EJ-212 scintillator. Two screen

thicknesses were simulated, 2 mm and 5 mm, because these thicknesses are respectively the thinnest and thickest screens purchased for use with TiGReSSE, and thus bound the problem. The scintillator face was simulated to be the same size as that used in TiGReSSE, or 20.32 $\times$ 20.32 cm^2.

The simulations employed a combination of F6 and F8 tallies (energy deposition and pulse height tallies, respectively) to simulate the light output of the EJ-212 scintillator. The F6 tally was used to convert deposited proton energy (MeV) to deposited photon energy ($MeVee$) via a conversion table. This conversion table, described in more detail in the following paragraph, is employed in place of the low-energy photon physics models that do not exist in MCNP6. The F8 tally subsequently histograms the F6 results into a differential pulse height distribution (PHD) [34, 73]. The average of the histogram values, multiplied by the number of photons generated per $MeVee$ deposited ($\epsilon = 1\times10^4$), represents the average total light output generated by a neutron at a particular energy and for a particular screen geometry. Individually, these two tallies are traditionally not used for incident neutrons, but by using these two tallies in concert and inserting appropriate $MeV/MeVee$ energy conversion values into the F6 tally, the deposited photon energy could be tallied into a histogram with the F8 tally.

The conversion tables for NE-102A (a detector material analogous to EJ-212) were provided by E. McKigney of Los Alamos National Laboratory and cover a range of proton energies from 0.02 to 14.18 MeV. Some of the conversion data is shown in Table 6.1. The F6 tally uses the derivative of this data with respect to energy, so the slope was found by

$$Slope = \frac{CF_i - CF_{i-1}}{E_i - E_{i-1}}, \tag{6.1}$$

where CF is the conversion factor ($MeVee/MeV$), E is the proton energy (MeV), and i and $i-1$ represent the data index. The derivative could be approximated by the slope equation because, when plotted against energy, the conversion factor was found to be nearly linear with an R^2 value of 0.9916.

Table 6.1: Values used with MCNP6 F6 tally to convert from deposited proton energy (MeV) to generated photon energy ($MeVee$) and thus simulate EJ-212 efficiency.

Deposited Proton Energy (MeV)	Conversion Factor ($MeVee/MeV$)
0.0	0.0
2.0×10^{-2}	0.1640590
6.0×10^{-2}	0.1280335
0.1	0.1372980
0.2	0.1661625
0.3	0.1939000
0.4	0.2171275
0.5	0.2370575
0.6	0.2546500
0.7	0.2705500
0.8	0.2851250
0.9	0.2986250
1.0	0.3119500
1.5	0.3653750
2.0	0.4100750
3.0	0.4755000
4.0	0.5240000
5.0	0.5627500
6.0	0.5945000
7.0	0.6215000
8.0	0.6442500
9.0	0.6645000
10.0	0.6822500
11.0	0.6982500
12.0	0.7125000
13.0	0.7252500
14.0	0.7367500
14.2 or greater	0.7387500

The NE-102A CF values ended at 14.18 MeV, so CF had to be linearly extrapolated for proton energies above this point. It was found that the slope of the conversion factor becomes constant between 14.16 and 14.18 MeV, and so this value of 0.73875 was used for protons of any energy above 14.2 MeV. MCNP6 then linearly interpolated between these values during the simulations if a proton energy was between CF bin points, which is thought to be accurate because of the aforementioned R^2 value.

To determine the effect of incident neutron energy on detector efficiency, eleven monoenergetic sources of varying energy were simulated. The monoenergetic neutron sources were selected to represent LANSCE energies, as well as the proposed LLNL boosted D-D source and a D-T generator: 0.5, 0.76, 1, 2, 5 10, 14, 20, 40, 100, and 200 MeV. Thus, a recommendation could be made as to the source energy that should be used with TiGReSSE.

6.1.3 Simulation Results

As expected from the discussion in Section 6.1.1, the simulation statistics greatly worsened for the 2 mm screen above 14 MeV and, for the 5 mm screen, above 20 MeV. This is because, on average, protons are so energetic that they are leaving the screen before depositing all of their energy. Thus, above the 20 MeV energy bin, simulations did not converge.

For example, in simulations of the 2 mm scintillator, 1×10^8 0.5 MeV neutrons converged an answer with the highest histogram bin error of 0.11%, whereas almost 30×10^8 20 MeV neutrons converged an answer with the highest histogram bin error of 11%. Thus, comparing the two energies, the number of simulated particles increased 30 times, and the error was still 100 times greater than the 0.5 MeV neutron energy. Higher energies were shown to likely require trillions of simulated neutrons to converge answers (80 billion simulated particles were run in some cases, with no convergence achieved) because most neutrons do not interact in the scintillator, and

most protons will exit the scintillator before depositing even a fraction of their energy. Although a variance reduction technique was tested that forced neutron collision in the scintillator, it was found that the deposited proton energy was artificially increased and simulations were no longer valid.

As a result, pulse height distributions were only successfully generated for energies below 20 MeV where convergence occurred (Figure 6.3). Although shown as a curve, the PHD is truly a histogram, where each point represents the number of photons generated per incident neutron for energies ranging from the given energy on the x-axis, E_i, to the energy to its immediate left (E_{i-1}). This explains why the PHD is seen to start from varying locations. Because the bin structure was varied in the simulations to wider bin widths as the incident neutron energy increased, the leftmost point on each curve represents the total number of photons from 0 MeV to that particular energy. This was necessary to reduce the number of bins for higher energies. To address this fact, values shown are normalized to the histogram bin width.

These PHD curves show that an increase in neutron energy causes a decrease in the light output of the scintillator. Additionally, one can see that neutrons generate photons with energy less than the incident neutron energy. This is because protons from the (n, p) reaction are less efficient at generating photons in the scintillator than incident photons would be. Additionally, it is shown that, as expected, the 5 mm scintillator has a higher efficiency than the 2 mm scintillator due to its increased thickness.

An average photon light output was found for each PHD curve and for each scintillator thickness. Trendlines were fit to the data to predict the total light output as a function of energy and thus allow the estimation of total light output for incident neutron energies above 20 MeV. The total light output, N, for the 2 mm scintillator is approximated by the trendline equation (with $R^2 = 0.99909$)

$$N = 1066.8E^{-2.013}, \tag{6.2}$$

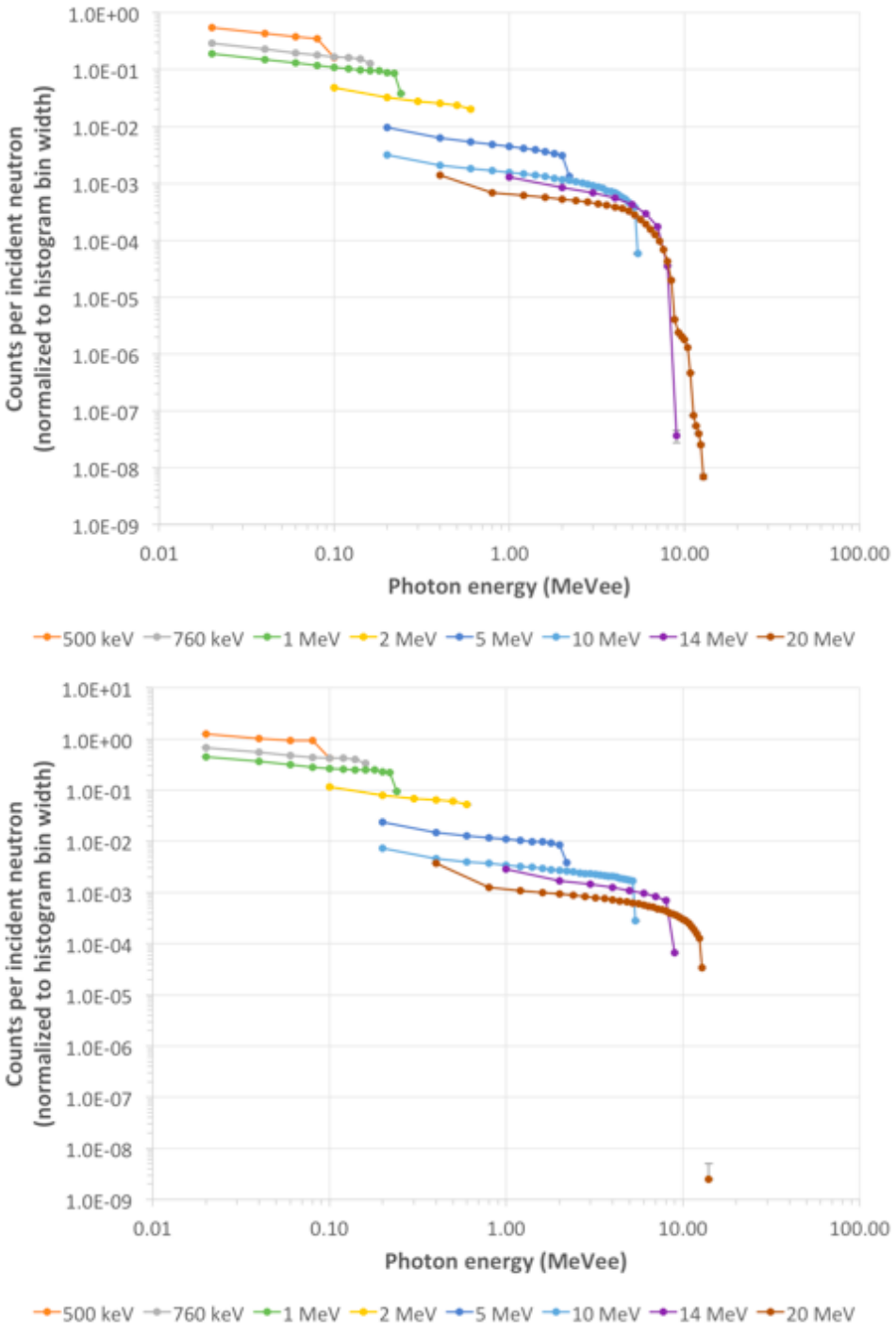


Figure 6.3: Simulated pulse height distributions for monoenergetic neutrons incident on EJ-212, ranging in energy from 500 keV to 20 MeV. The scintillator thickness was either 2 mm (top) or 5 mm (bottom), and had a face 20.32 $\times$ 20.32 cm^2 in area. MCNP6 relative error is indicated.

where E is the incident neutron energy. Similarly, N for the 5 mm scintillator is approximated by the trendline equation

$$N = 2632.4E^{-1.999}, \tag{6.3}$$

with $R^2 = 0.99912$. A plot of the average light output data can be seen in Figure 6.4.

Using Equations 6.2 and 6.3, the average light output was calculated for neutrons up to 750 MeV in energy (Figure 6.5). With this information, the approximate number of photons actually reaching the CCD chip per pixel, as a function of incident neutron energy, was calculated for FP15R and Flight Path 60 Right ("FP60R", another LANSCE beam line used for additional experiments detailed in Chapter 9; note that a new Generation II TiGReSSE geometry was tested in FP60R that placed the camera further from the scintillator when compared to the original Generation I design detailed in Chapters 4 and 5) geometries.

For the FP15R configuration that had the camera at an effective distance of 0.8 m from the scintillator, only 1 out of 1.64×10^4 photons that are emitted by the scintillator actually reach the camera lens due to geometric losses. For the FP60R configuration, the scintillator-camera distance increased to 1.0275 m and so the geometric losses also increased such that only 1 out of 2.70×10^4 photons reach the lens. Once entering the lens, the quantum efficiency of the photocathode is ~13% for light with wavelength of 423 nm (i.e., the maximum emission wavelength of EJ-212) [53, 55]. Based on camera characteristics, it is believed that the PI-Max4 uses a Hamamatsu three-stage microchannel plate (or a similar product) which yields, on average, 10^3 multiplication of electrons [74]. The P47 phosphor, used in the PI-Max4 because of its fast decay times, yields approximately 296 photons per electron when used with an 8 kV voltage such as that in the PI-Max4 camera [55, 75].

At a distance of 30 m from the target in the FP30L beam line at LANSCE, there are $\sim 1 \times 10^8$ neutrons per second, with a probability of emission associated with each neutron energy (note: the LANSCE FP30L measured source data was provided

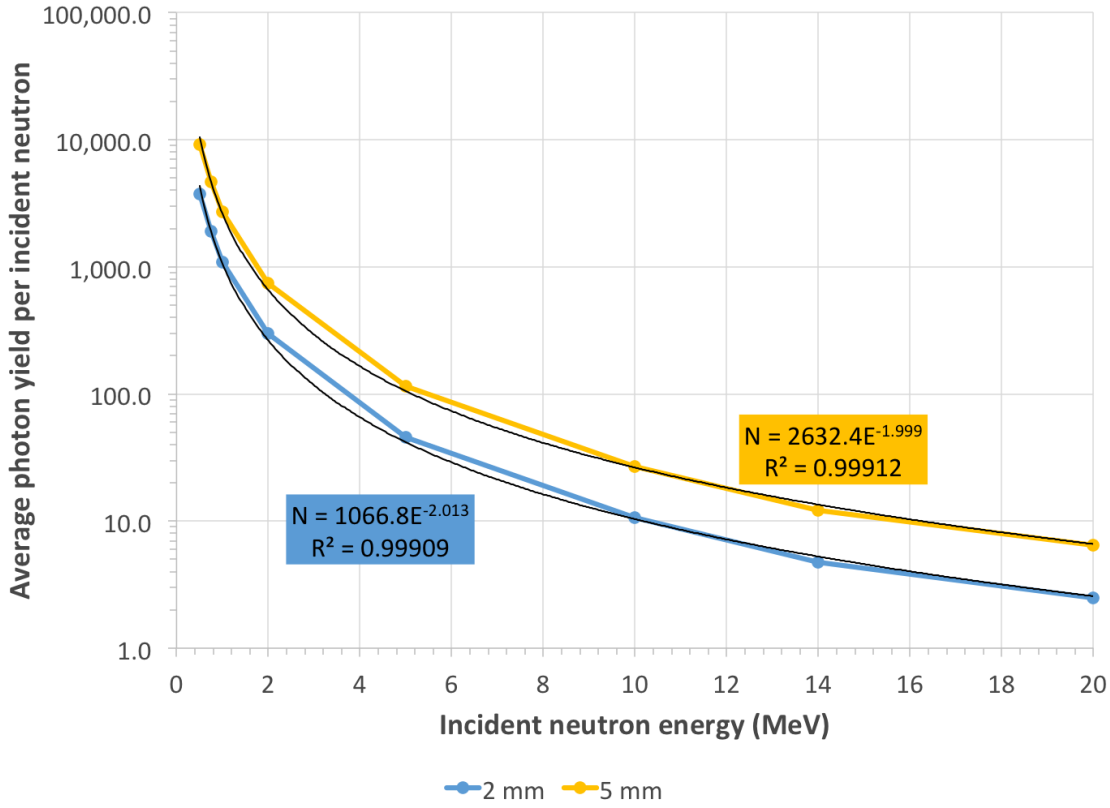


Figure 6.4: Power trendlines fit to the average light output data for monoenergetic neutrons incident on a 2 mm or 5 mm EJ-212 scintillator with face 20.32 $\times$ 20.32 cm^2 in area. Neutron energies range from 500 keV to 20 MeV. Trendline equations and corresponding R^2 values are indicated on the plot. MCNP6 relative error is so small that is does not appear on the plot.

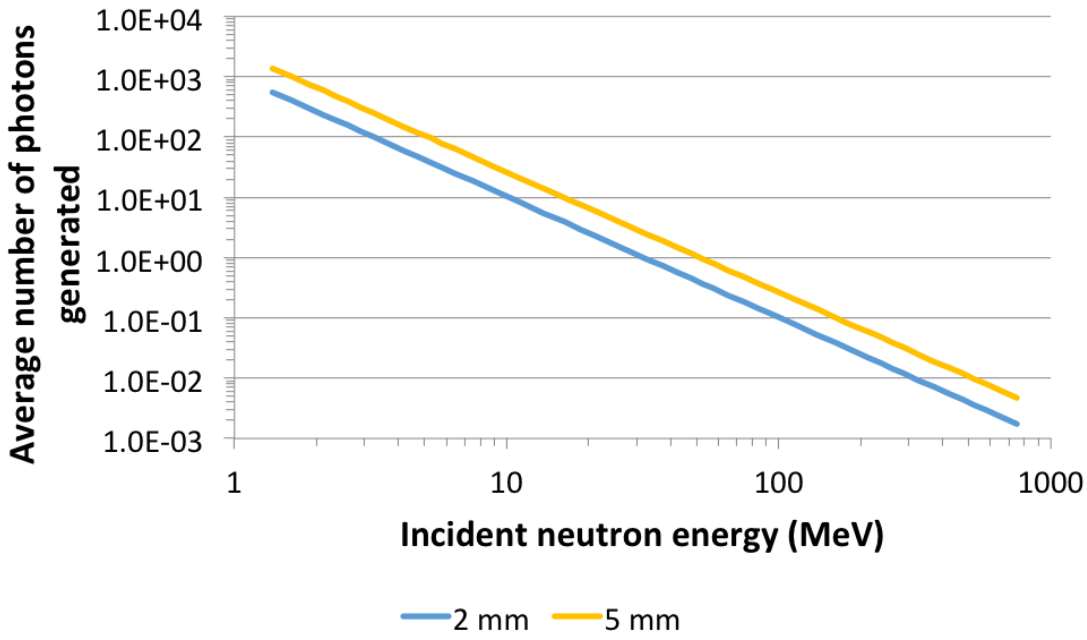


Figure 6.5: *Log* plot of the average light output for neutrons incident on EJ-212 of 2 mm or 5 mm thickness.

by J. Hunter). Thus, applying the FP30L data along with the assumptions listed in the previous paragraph, plots were generated of the average number of photons per pixel for the Generation I (i.e., FP15R) and II (i.e., FP60R) designs (Figure 6.6). The PI-Max4 literature states that dark current is 2.5 electrons per pixel per second [55]. Thus, it was assumed that a given neutron energy would be "detectable" if it generates a number of photons per pixel per second that is at least 3.0×10^{-2} at the CCD chip, a value that is just larger than the dark current value.

The incident neutron energy above which neutrons are no longer detectable by TiGReSSE is listed in Table 6.2 for 2 mm and 5 mm EJ-212 screens and for Generation I and II configurations. As expected, the detection limit decreased as the distance between the scintillator and the camera increased, or as the scintillator became thinner. More importantly, commercial sources with 10^8 neutrons per second incident on the scintillator fall well below this detection limit.

However, what of commercial sources with lower flux levels? If the source strength is reduced by a factor of 100 to 10^6 neutrons per second, the detection limit is drastically reduced (Table 6.3). In fact, if the source is reduced further to 10^4 neutrons per second, 10 or 14 MeV sources are no longer detectable with TiGReSSE in either of the Generation I or II configurations. This fact is corroborated by the D-T experiment and subsequent analysis in Section 5.1.2, which showed that only 2.01×10^4 neutrons per pulse of the 14 MeV source reached the scintillator and that this level of flux was not detectable above camera noise levels. Therefore, special care must be taken to ensure that the source flux is large enough to overcome reduced efficiency at increased neutron energies.

As a final note, the calculations shown here may be improved by using FP15R and FP60R measured spectra (as opposed to FP30L), but the exercise shows that screen thickness does limit what neutron energies are feasibly detected with TiGReSSE. It does appear, however, that the 5 mm scintillator can be replaced by a 2 mm scintillator to minimize blur while still capturing the majority of the LANSCE

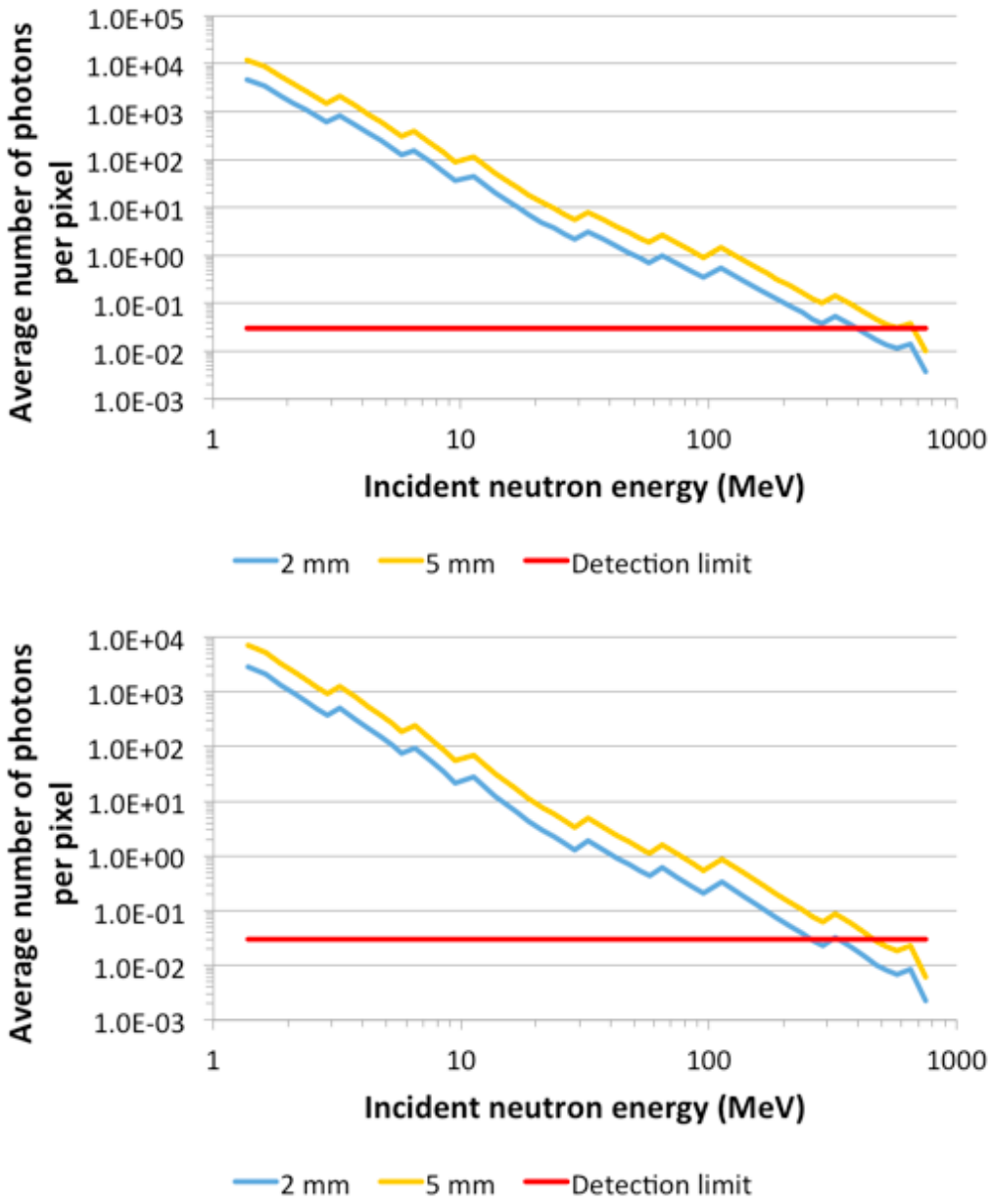


Figure 6.6: *Log* plot of the average number of photons per pixel reaching the CCD chip as a function of incident neutron energy and EJ-212 thickness. The detection limit of 3.0×10^2 photons per pixel per second is shown in red, with values below this red line not detected by TiGReSSE. The top plot is for the Generation I design used in FP15R, whereas the bottom plot is for the Generation II design used in FP60R.

Table 6.2: Upper detectable neutron energy for 2 mm and 5 mm EJ-212 screens and for Generation I and II system designs.

TiGReSSE Configuration	Screen Thickness (mm)	Energy (MeV)
I	2	398.0
	5	673.0
II	2	258.4
	5	463.0

Table 6.3: Upper detectable neutron energy for 2 mm and 5 mm EJ-212 screens and for Generation I and II system designs, if the source strength is reduced to 10^6 neutrons per second.

TiGReSSE Configuration	Screen Thickness (mm)	Energy (MeV)
I	2	25.5
	5	47.8
II	2	21.2
	5	39.2

spectrum and all fast commercial sources. Experimental studies should be conducted to validate these results.

6.2 Limiting Contrast Resolution

6.2.1 Overview

The MTF, as explained in Chapter 1, is a representation of the contrast resolution of an optical imaging system, and provides information on how well the imaging system (in this case, the camera, lens, and mirror) can distinguish between very small variations in grayscale. Thus, the MTF provides information on what levels of contrast can be distinguished by the imaging system.

Typically, the MTF is tested using a light source and a test pattern imprinted on glass, along with the imaging system being studied. The test patterns and light sources come in many styles, with Edmund Optics Models 85276 and 83874 used here, respectively. An image of the test pattern used in this study is shown in Figure 6.7, with an image of the light source shown in Figure 6.8. The pattern used in this study has 26 sets of five lines that spiral toward the center of the pattern. This is to keep the sets of line pairs centered and thus limit the effect of non-uniform light intensity. Each set of lines gets smaller in width and spacing, and therefore increase in spatial frequency, as one moves in a counter-clockwise position around the test pattern. The number above each set of lines is equal to the spatial frequency of that set (measured in line pairs (lp) per mm). For example, a spatial frequency of f =1.25 lp/mm shown in Figure 6.7 equates to a line spacing of $1/f$, or 0.8 mm.

Figure 6.9 illustrates this blurring effect that increases as the sets of lines get thinner and closer together. The five black lines represent a grayscale value of 0, with the four equally-spaced white lines representing a grayscale value of 1. These black and white lines therefore represent a square wave input, varying from 0 to 1 and back to 0. The imaging system, however, has some characteristic blurring from optical

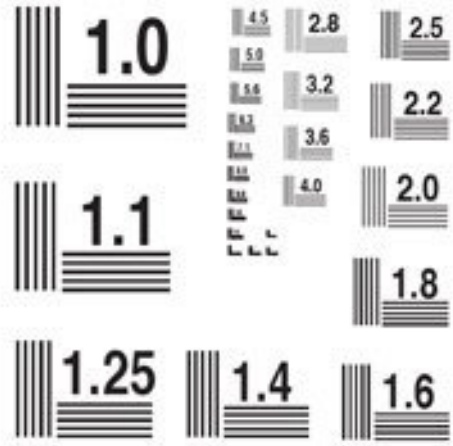


Figure 6.7: Illustration of the test pattern used in the MTF experiment [76].



Figure 6.8: Photograph of the light source used in the MTF experiment [77].

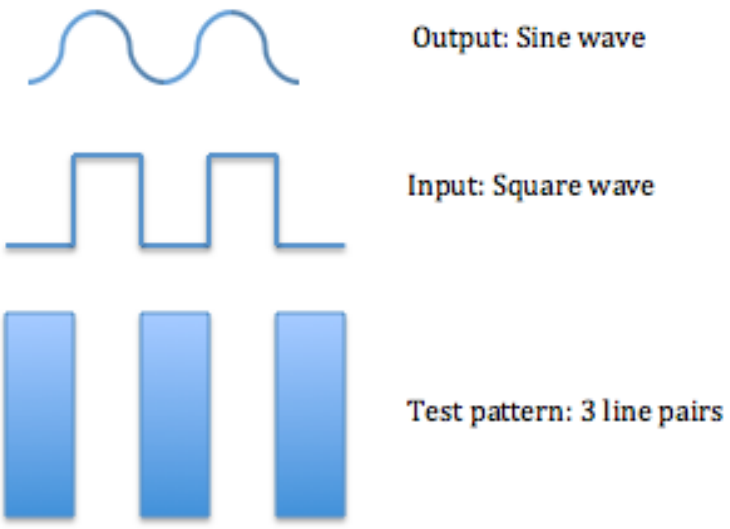


Figure 6.9: Bottom: An input stimulus of three line pairs, such as those in a line pair test pattern, is used to find the MTF of a system. Middle: A perfect system images the line pairs as a square wave. Top: A real-world system adds blur that rounds edges and reduces amplitude. The MTF represents such blur and determines the limiting contrast resolution of an optical system.

interference that rounds the edges of the square input and results in a sinusoidal image of the square wave input.

As the spatial frequency increases, the optical interference also increases and the difference in grayscale between the output's maximum and minimum values decreases (i.e., the range in amplitude between the valleys and the peaks of the sinusoidal output). This is seen by the imaging system as a decrease in contrast resolution because white is no longer 1 and black is no longer 0; values are now some intermediate level of gray. At a certain spatial frequency, the white and black line pairs are no longer distinguishable and appear nearly the same grayscale value. This spatial frequency indicates the MTF limit of the system.

The MTF can be calculated with the image of the test pattern by first taking a line-out across a set of lines pairs at a given spatial frequency. This line-out creates a plot of the pixel grayscale values along the line's length. Peaks (which correspond to the white lines) and valleys (which correspond to the black lines) in the line-out can thus be identified, and average minimum (A_{min}) and maximum (A_{max}) values can be determined for that spatial frequency. A_{min} and A_{max} will not be the respective original square wave input values of 0 and 1 due to optical interference. Therefore, true white and true black values must be determined to benchmark the changes in white and black that result from increasing spatial frequency. A line-out across a white part of the image can be used to determine the average white (A_{white}), or overall maximum, value; a similar line-out across a black part of the image can thus determine the average black (A_{black}), or overall minimum, value. Line-outs are taken for line pairs up to the limiting spatial frequency when peaks and valleys are no longer distinguishable.

Once the A_{min}, A_{max}, A_{white}, and A_{black} values are found from the experimental image, the MTF can be calculated using the next three equations. First, the modulation depth ($C(f)$), or the ability to resolve grayscale values as a function of spatial frequency, is found according to Equation 1.7 in Chapter 1, shown here

with slightly different variables:

$$C(f) = \frac{A_{max} - A_{min}}{A_{max} + A_{min}} \tag{6.4}$$

Second, the modulation depth for the average white and black values (i.e., the square wave input), $C(0)$, and therefore for an ideal system is similarly found according to Reference [78] by

$$C(0) = \frac{A_{white} - A_{black}}{A_{white} + A_{black}} \tag{6.5}$$

Third, the MTF for a given spatial frequency is thus found by

$$MTF(f) = \frac{\pi}{2}\frac{C(f)}{C(0)}, \tag{6.6}$$

where the $\frac{\pi}{2}$ term is used for circular apertures such as those in the lens used with TiGReSSE (note: a square aperture would use $\frac{\pi}{4}$ instead) [16]. Plotting $MTF(f)$ as a function of spatial frequency thus creates the MTF curve for a given system and allows for evaluations of the system's contrast resolution to be made.

6.2.2 Experimental Set-up

The MTF experimental set-up was selected to match as closely as possible to the settings used in FP15R and detailed in Chapter 5. The same delay generator, pulser, oscilloscope, camera, lens, mirror, and chiller were used as those detailed in Chapter 4. Aperture sizes were varied to determine the effect of lens speed and depth of field on the MTF. Aperture sizes studied were $f/2$ (the FP15R setting) and $f/4$, which lets in less light but has a larger depth of field.

To set up the experiment, first the scintillator and scintillator holder in the light-tight box were removed. The glass test pattern was affixed to the light source to provide illumination of the pattern, and the light source was then placed in the void where the scintillator had been (Figure 6.10). Tape was placed between the back of the test pattern and the light source to act as a spacer between the light source and

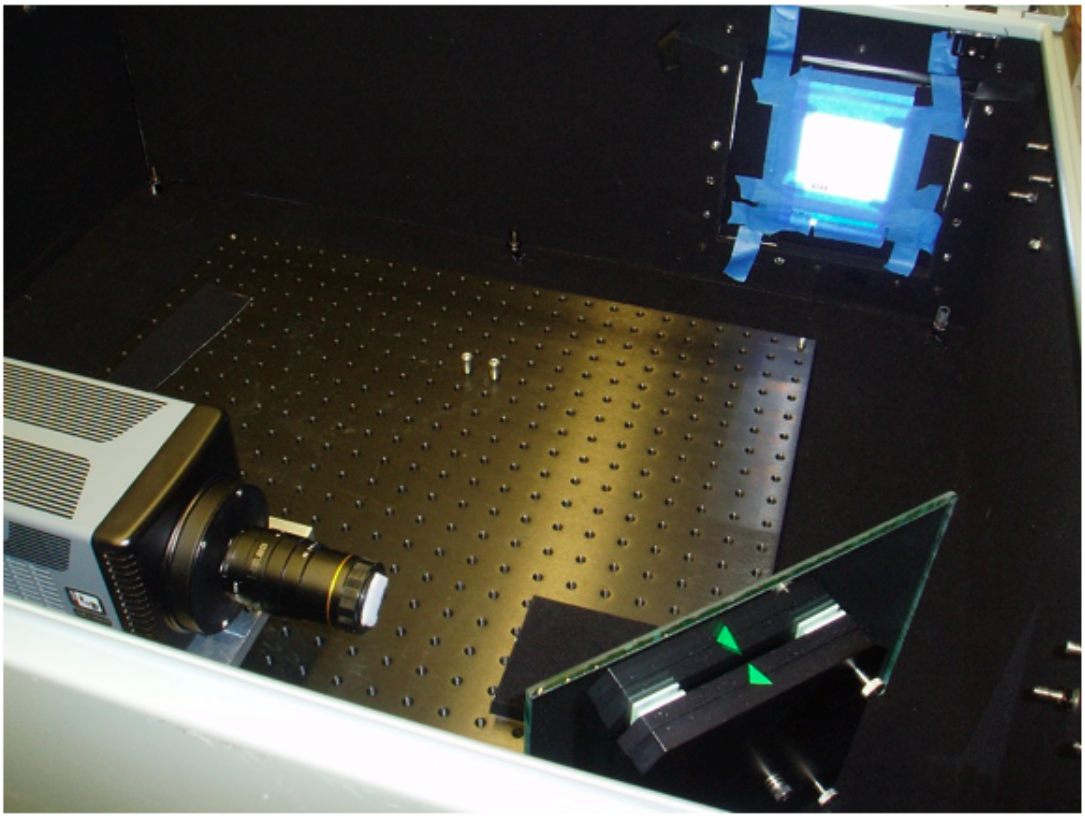


Figure 6.10: Photograph of the experimental set-up to determine the contrast resolution of the system. The light source and test pattern were placed where the scintillator is typically located, while the camera and mirror remained in the same position as that in FP15R. Blue tape was used to affix the test pattern to the light source.

the glass. This was necessary to prevent the formation of Newton's rings, or circular optical interference patterns on the glass, which would degrade MTF measurement quality. Best attempts were made to place the test pattern at the same focal point as the scintillator.

The test pattern used was the Edmund Optics ISO Resolution Test Chart No. 2 (Figure 6.11). It measures $101.6 \times 101.6 \times 1.5\ mm^3$, with spatial frequency ranging from 1 to 180 lp/mm. The pattern is made from chromium that was vacuum deposited on soda lime float glass. The visible light source (Figure 6.8) used is also produced by Edmund Optics, and is $12 \times 7.5 \times 0.75\ in^3$ in size. The active area is smaller, measuring $5.75 \times 10\ in^2$. The light is emitted by a white LED, and has a variation in light intensity of $\pm 5\%$. This variation across the light plane was larger than expected, and actually was visible to the naked eye. Additionally, the intensity of the light source varied in time. Thus, multiple frames of each image were taken and averaged together to minimize the time dependence of this experiment, but it is possible that this light source (which had been advertised as very stable) did introduce some error into the experiment.

6.2.3 Experimental Procedure

The first step of the experiment was to ensure the test pattern was indeed placed at the focal point of the lens, which would have been the focal point during FP15R measurements. A "before" image was taken with the lens aperture at its FP15R setting of $f/2$, the intensifier turned off (the light source was very bright), and the gain set to 50 (Figure 6.12). The camera gate width was 750 ns, and the camera took 150 frames that were later averaged together in post-processing. The camera was triggered by the waveform generator.

The second step was to generate an "after" image for comparison to ensure the test pattern was located at the scintillator plane (Figure 6.13). The lens was adjusted until the test pattern came into best focus; this aperture setting was found to be the

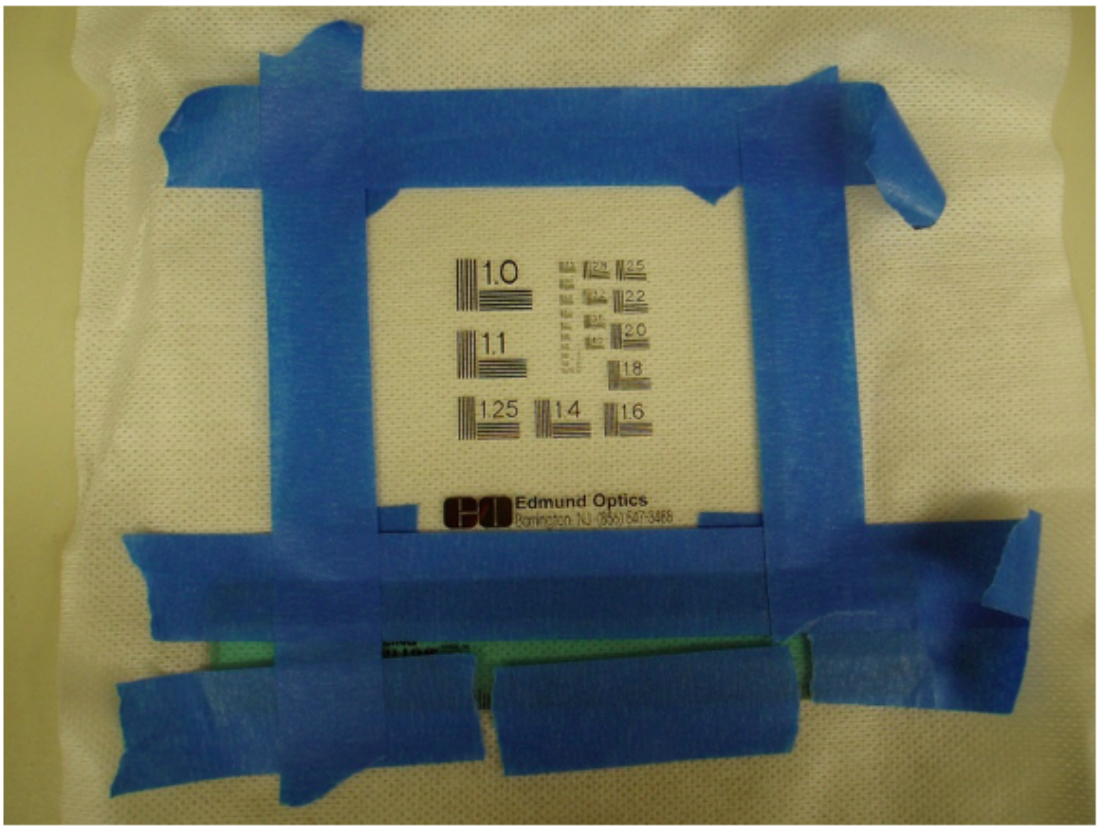


Figure 6.11: Photograph of the test pattern used in the MTF experiment, along with the blue tape used to affix the test pattern to the light source.

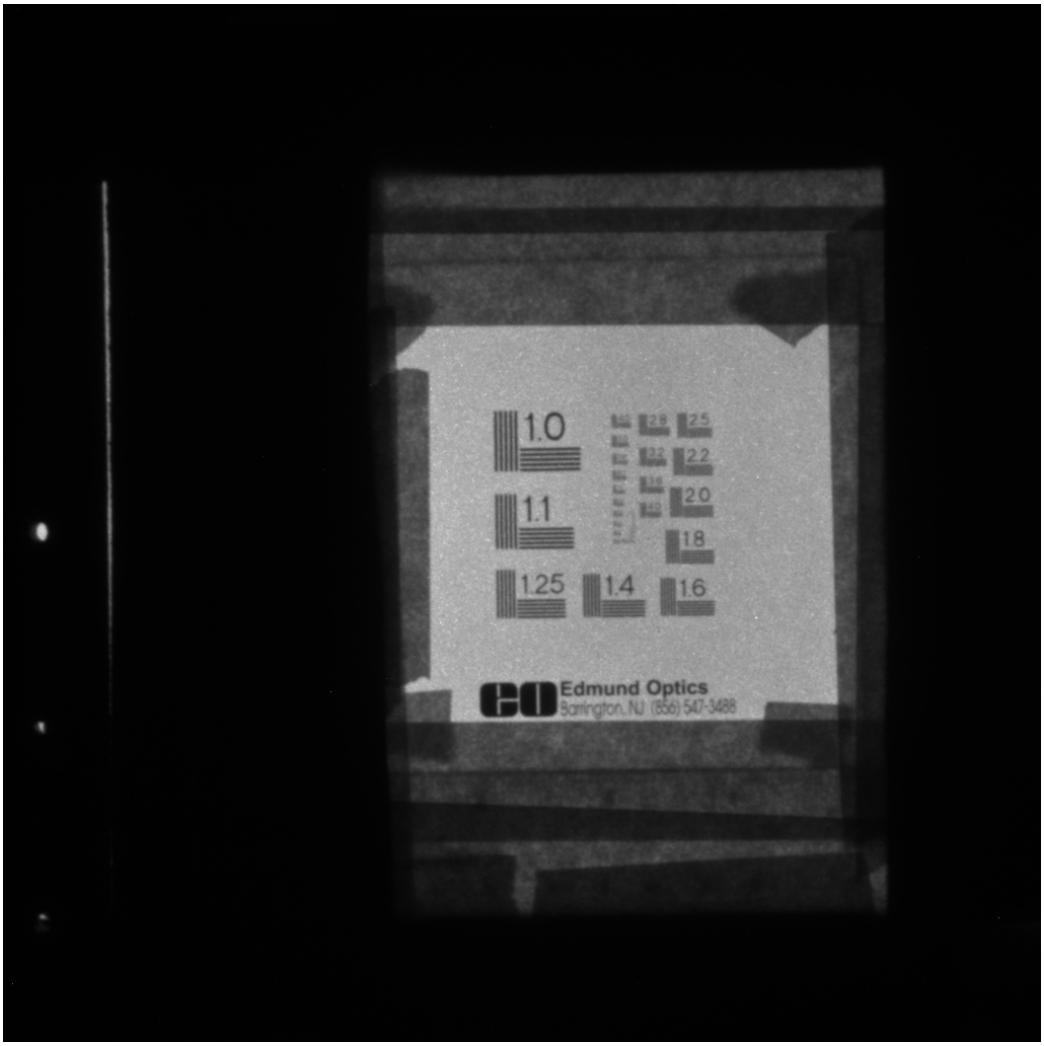


Figure 6.12: Averaged image taken of the test pattern prior to adjusting the lens focus.

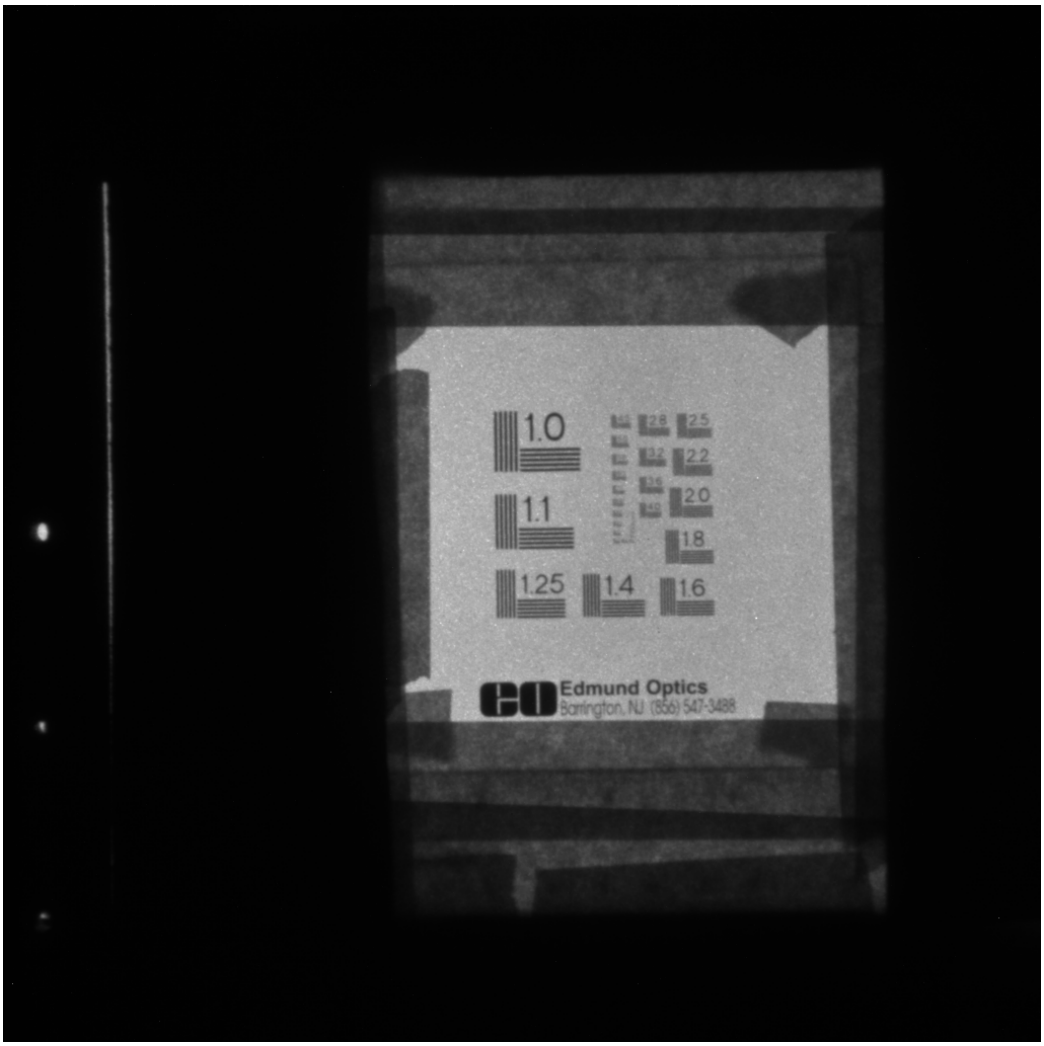


Figure 6.13: Averaged image taken of the test pattern after adjusting the lens focus.

same as that used in LANSCE, indicating that the test pattern was at the focal point used in LANSCE experiments.

Next, the test pattern was removed from the front of the light source to allow a flatfield image to be taken. This type of image captures the variation in the light source intensity, which was seen to decrease in intensity from left to right from the camera's viewpoint. The intensifier was turned on and set to 80. The camera took 150 frames, again to average them together. The gate width used was 456.5 ns, which was the gate width used at LANSCE to image with neutrons of energy from 10 to 600 MeV.

Subsequently, the test pattern was re-attached to the face of the light source and an image with the same settings was taken to determine the MTF with a lens aperture of $f/2$. The aperture was then decreased to $f/4$, and an image of the test pattern was taken using the same settings. The test pattern was then removed and another flatfield image was taken with the new aperture size.

6.2.4 Data Processing and Results

Data processing used ImageJ freeware, one of the only programs that can read Princeton Instrument's *.spe* file format, and is the same software that was used to process images in Chapter 5. The software was used to average together the 150 frames taken of the $f/2$ test pattern; this was also done for the corresponding $f/2$ flatfield image. The test pattern image was then divided by the flatfield image in order to normalize the pixel values and address the variation in light intensity. These steps were then repeated for the $f/4$ test pattern and flatfield images. The resultant cropped images can be seen in Figures 6.14 and 6.15. Images taken with an aperture of $f/4$ are darker (lower in intensity) because the aperture is smaller and less light enters the camera.

Line-outs were then taken for spatial frequencies up to and including 2.2 lp/mm and were taken for both the horizontal and vertical line pairs on the test pattern.

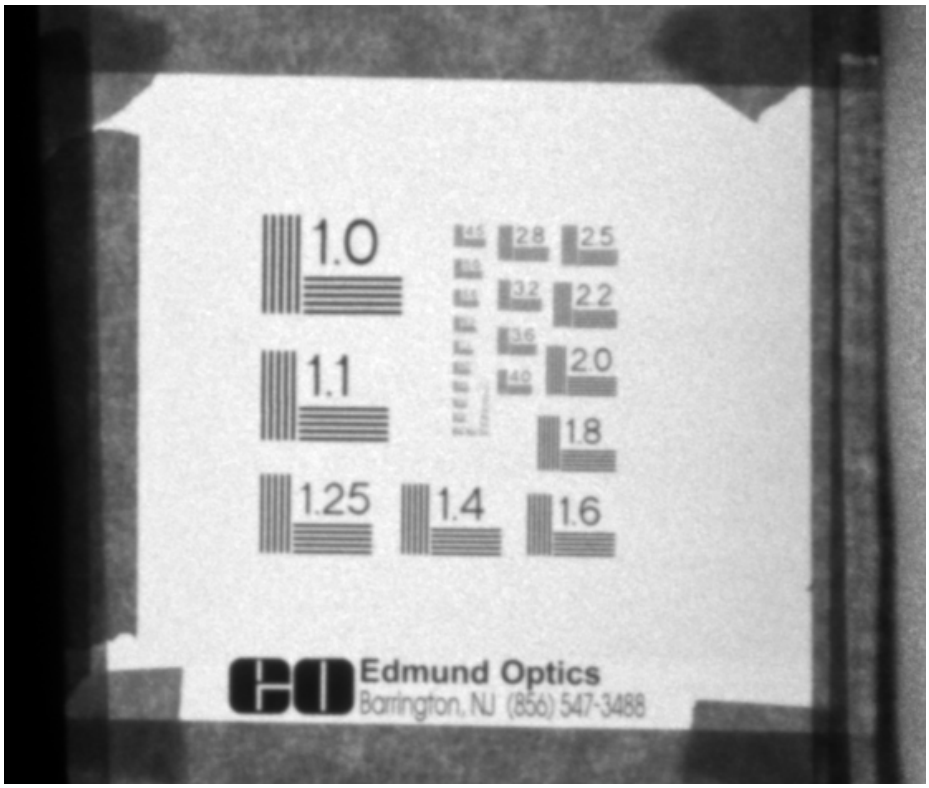


Figure 6.14: Post-processed cropped image of the test pattern at $f/2$.

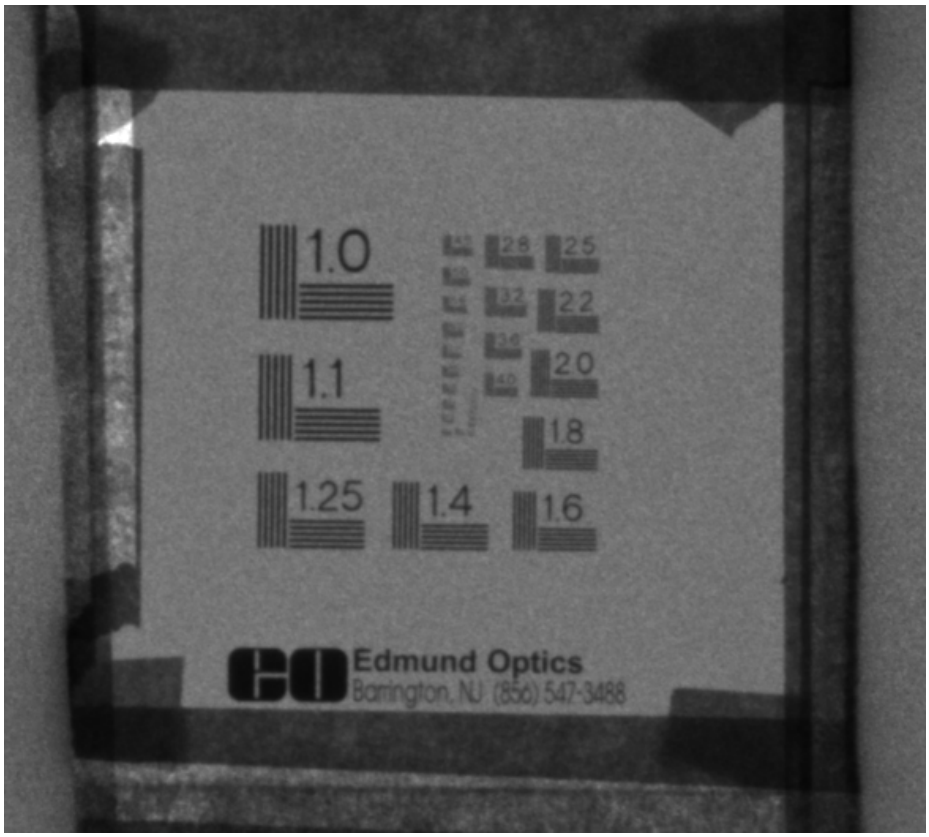


Figure 6.15: Post-processed cropped image of the test pattern at $f/4$.

(Horizontal and vertical line-outs were taken in case one of the two directions aligned with pixels within the CCD chip and caused distortion.) An example of the slight differences between horizontal and vertical line-outs can be seen in Figure 6.16, for an image taken of the 1.0 lp/mm spatial frequency and with an aperture of $f/2$.

For each line-out up to and including 2.0 lp/mm, there were 4 peaks and 5 valleys. The valleys correspond to the five dark lines on the test pattern surface, and the peaks correspond to the four white lines. Due to optical interference, the peaks are not as bright as the white space surrounding the five bars, and so they are at a lower height than the edges of the line-out (for example, Figure 6.16). For 2.2 lp/mm at both aperture settings, only 2 to 3 peaks were distinguishable, and so this frequency was determined to be unresolvable by the system (Figure 6.17). As expected, the difference between the peaks and valleys decreases as the frequency and the optical interference increase.

For a given spatial frequency and a given line-out direction (horizontal or vertical), the four A_{max} grayscale values were averaged together, as were the five A_{min} grayscale values. The average A_{min} and A_{max} values for the horizontal and vertical line-outs were then averaged together to yield overall average A_{min} and A_{max} values for a given spatial frequency; thus, slight differences between the horizontal and vertical line-outs were addressed. These overall average values were then with Equation 6.4.

Similarly, the average white level was found by taking a vertical line-out in the center of the test pattern between the line pairs and a horizontal line-out across the top of the image (and thus addressing the horizontal variation in light intensity). Because there are not true peaks and valleys (simply variation as a result of noise), all values along the line-out were averaged together, with vertical and horizontal average values then being averaged together to yield an overall average A_{white}. A similar process was conducted to determine an overall average A_{black}, with horizontal and vertical line-outs taken within the opaque "O" in the "EO" logo at the bottom of the test pattern. Results are plotted in Figure 6.18 and listed in Table 6.4 that

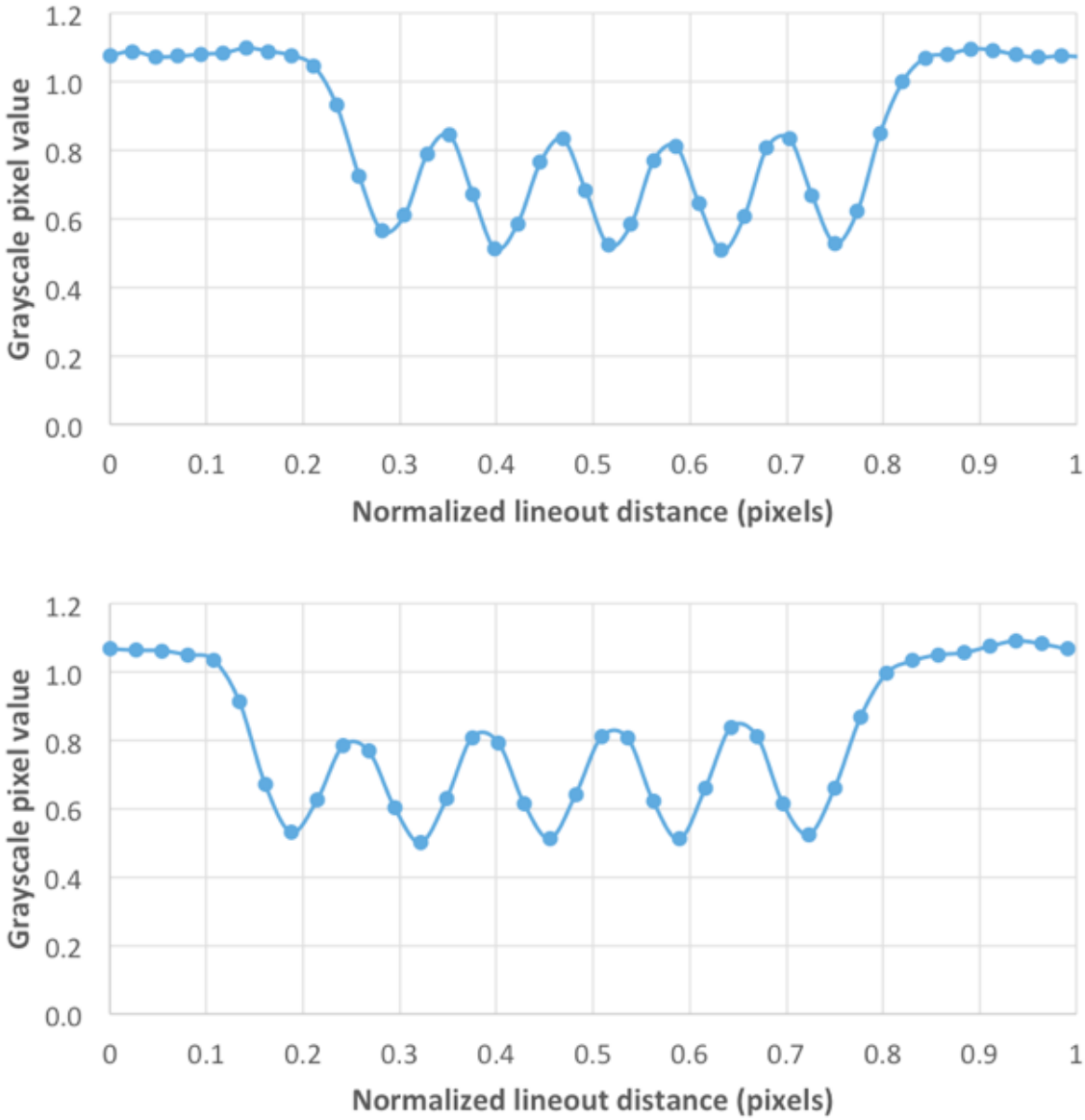


Figure 6.16: Vertical line-out (top) and horizontal line-out (bottom) for a frequency of 1.0 lp/mm and aperture of $f/2$.

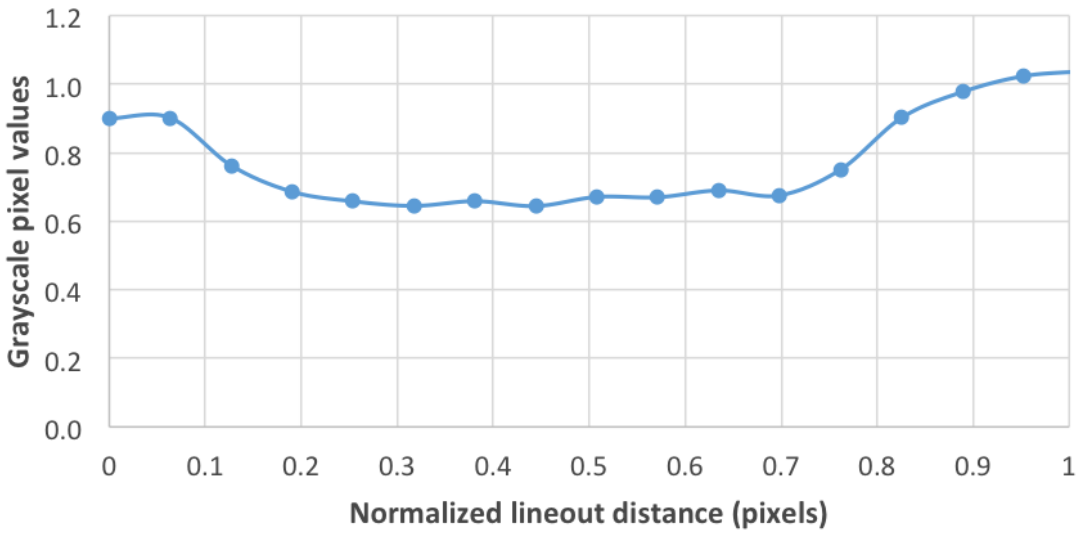


Figure 6.17: Vertical line-out for a frequency of 2.2 lp/mm and aperture of $f/2$. Note that the peaks and valleys are virtually indistinguishable.

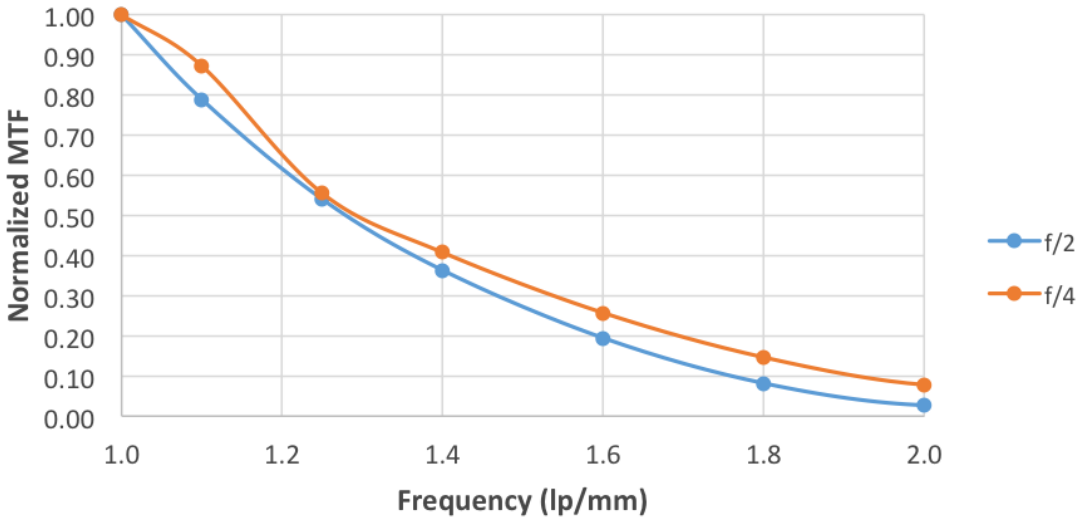


Figure 6.18: Plot of the normalized MTF at the imaging plane for apertures of $f/2$ and $f/4$.

Table 6.4: Normalized MTF values for apertures of $f/2$ and $f/4$.

Spatial Frequency (lp/mm)	$f/2$ MTF	$f/4$ MTF
1.00	1.00	1.00
1.10	0.79	0.54
1.25	0.54	0.55
1.40	0.36	0.41
1.60	0.19	0.26
1.80	0.08	0.15
2.00	0.03	0.08

were generated with Equations 6.5 and 6.6 to determine the MTF as a function of spatial frequency.

6.2.5 Conclusions

The resolution measurements show, for both $f/2$ and $f/4$ aperture sizes, that the limiting spatial frequency is $f = 2\ lp/mm$. This corresponds to a feature size of $1/f$, or $0.5\ mm$, which indicates the approximate size of features at the scintillator plane (not within the object!) that can be seen with this camera. Additionally, making the aperture smaller by going from $f/2$ to $f/4$ was seen to have a small effect in improving the MTF. This can be attributed to the larger depth of field that brings more of the test pattern into focus and yields better results. However, having a larger aperture was not seen to greatly reduce system resolution and, at this point in time, the increase in speed of exposure with an $f/2$ lens setting is more important than the slight increase in contrast resolution with an $f/4$ lens setting.

Because this is a neutron radiography system, the limiting spatial frequency at the scintillator plane may actually be different than $2\ lp/mm$ due to neutron scattering within the object (prior to interacting in the scintillator) and the scintillator itself. Such scattering makes dark areas in the image appear brighter and thus decreases contrast resolution. Future experiments should be done in the LANSCE beam line to determine the spatial resolution in a neutron beam. Two scintillators can be used to sandwich the test pattern so the test pattern is located at the center of the $5\ mm$ scintillator plane where the lens is focused, and time gates can be varied to determine how contrast resolution varies with incident neutron energy. This is an interesting avenue for exploration in future work.

Finally, the light source could have caused error in this measurement. The light intensity was seen to vary across the source surface, and best efforts were taken to address this issue (e.g., dividing out the flatfield). Additionally, it is possible the lens was not set to its best focus; at $f/2$, the lens is very tricky to focus because

of the shallow depth-of-field. This could mean that higher spatial frequencies could be resolved if somehow the lens was not at its optimal focus during this experiment. However, its focus was seen to be the same as that used in FP15R, so results are representative of past experiments outlined in Chapter 5. Future work could be done to verify this experiment with a more stable light source.

Chapter 7

Shielding Studies

This chapter discusses a parameter study conducted to determine the type(s) and quantity(ies) of shielding material necessary for additional experiments at LANSCE. Scatter was seen to be a significant problem in FP15R, both in reducing radiograph quality and in increasing dose to the camera electronics. Therefore, it was necessary to redesign the shielding, both internal and external to the light-tight box, to improve image contrast and extend the lifetime of the camera.

The study consisted of MCNP6 simulations of the FP15R experimental set-up detailed in Chapter 5. The spectrum data was provided by J. Hunter of Los Alamos National Laboratory, who experimentally measured the flux as a function of energy in FP30L, and thus approximately represents the source spectrum in FP15R. Although future experiments will possibly occur in other LANSCE beam lines, FP15R was very well characterized, which led to easier and more accurate shielding simulations. This chapter will begin with the theory of designing neutron and photon shielding, followed by the design parameters studied and the final recommended design.

7.1 Theory

Several principles that underpin the theory and process of developing shielding to protect against ionizing radiation are outlined in this section, all taken from Shultis

and Faw's definitive text, *Radiation Shielding* [69]. First, the shielding process differs among photon sources, neutron sources, and mixed (photon and neutron) sources. In this instance, "source" implies not only an active interrogation source (e.g., LANSCE), but also all other sources of ionizing radiation present during the measurement (e.g., background radiation, activation products, scatter fields, and so on). Thus, shielding must be designed for each application at hand because it is dependent on source type, energy, flux, and other system-dependent variables.

Differences in shielding design are a function of differences in energy loss mechanisms among particles. For instance, photons and neutrons lose energy via different mechanisms. As outlined in Chapter 1, fast neutrons primarily lose their energy via the scattering interaction, which is generally elastic scattering, but at higher energies, inelastic scatter is also possible. Unlike elastic scatter, inelastic scatter causes the target atom to remain in an excited state until it decays and emits secondary particles. When the excited nuclei decay, they typically emit one or more high-energy gammas approximately 1 ps after absorption. These photons are usually emitted near the outer edges of the shield material, and thus can be difficult to shield and, depending on the situation, may be just as damaging as the incident neutron. The (n, γ) reaction also turns a neutron source into a mixed source, which is more difficult to address than a pure neutron source.

To minimize the (n, γ) reaction, neutron shield materials are often chosen so that they have high cross sections for charged particle reactions and not for gamma reactions. Typically, these materials are ^{6}Li and ^{10}B, which are selected for their large (n, α) cross sections. Alpha particles are easier to shield because they travel much shorter distances than gammas due to their charge.

Above neutron energies of 8 MeV, multiple particle reactions also become possible, such as $(n, 2n)$ and $(n, n+p)$ reactions. Thus, shielding at LANSCE energies is much more difficult than low energy neutron sources because secondary particles must also be shielded in addition to the (n, γ) reaction described in the previous paragraph. High-energy neutrons also require much more shielding material than low energy

neutrons because it takes many more scatters to slow down a fast neutron than a slow neutron. This means that shielding can get quite bulky and heavy, and so other engineering considerations may need to be taken into account (e.g., weight-rated tables may be necessary to support the material).

As for photons, the cross section reactions vary as a function of energy. For high-energy photons (above approximately 1 MeV), pair production is the dominant effect, whereas photons with energy below 1 MeV can lose energy by coherent or incoherent scattering with electrons or through the photoelectric effect. Thus, while low-Z shielding materials are selected for neutrons to increase the likelihood of scatter, high-Z shielding materials are used for photons because they are slowed by the presence of electrons and the number of electrons is proportional to Z.

7.2 Simulated Case Studies

7.2.1 Overview of Simulations

As stated in the beginning of this chapter, a number of shielding case studies were simulated using MCNP6 to determine the best design to protect the camera against the FP15R spectrum. In general, the best design would limit particle flux through the camera body and, as a result, through the sensitive electronics and pixellated silicon chip. Particles tracked in this study included neutrons, photons, protons, deuterons, tritons, and alphas. The deuteron and triton flux was found to be so low as to be statistically insignificant and thus virtually nonexistent, so these particles are not mentioned for the remainder of this chapter. Alpha flux was also extremely low and thus the MCNP-calculated error was higher than for protons, photons, and neutrons, but the results are included here because they did carry enough energy to damage the silicon chip even if there were fewer of them. Each simulation ran 50×10^6 neutrons.

The particle current was tracked as it entered each surface of the camera volume; the current through each surface was totaled by MCNP6 to generate a total current

through the camera. Only current entering the volume was tallied; while some particles will obviously leave the camera volume without interfering with the smaller chip, this allowed for a conservative design strategy that assumed all particles entering the camera hit the silicon chip.

This current was binned by energy from 0 to 800 MeV to determine the relative effect of shielding design on the energy of the particles entering the camera volume. This was important because high-energy particles have the potential to be more damaging than low energy particles. Thus, a design that reduces low energy flux but not high-energy flux is not necessarily a useful design. For the purposes of this case study, particles below 1 MeV were assumed to be non-damaging to the silicon chip (based upon conversations with D. Mayo of Los Alamos National Laboratory who has worked at LANSCE), so reductions to this area of the spectrum were considered welcome but not essential to shielding design. Current was not binned in time because scatter is integrated on the silicon chip for the length of the pulse.

Cell flagging was also conducted to determine what cell(s) a given particle traveled through before entering the camera volume and whether a component of TiGReSSE or the beam line was causing large scatter fields that should be addressed (note: a "cell" in MCNP6 is a volume defined by one or more surfaces). Flagged cells included the beam pipe, beam line walls and floor, light-tight box, mirror, scintillator, shielding materials, and radiography object (simulated as the tungsten sphere described in Section 5.2.3). Cell flagging does not inform the particle's origin, but rather whether it passed through a given cell on its path to the camera volume. Thus, a particle may contribute to several flagged cells.

7.2.2 Simulated Geometry

The FP15R simulations attempted to be as accurate as possible with respect to beam line geometry. Thick concrete floors and walls were simulated, as well as the steel beam pipe protruding from the wall. The beam pipe is the reference point for

direction, so, for example, the right wall is the wall that would be on the right side of the beam line from the beam pipe's perspective. The source, modeled as a flat disk the width of the inner beam pipe (10.16 cm), was placed at the back of the beam pipe and angled to provide an 8 in spot size like that seen in previous experiments (Figure 7.1).

The disk source was placed at the back of the beam pipe to allow for neutron interactions in the concrete wall and the beam pipe, thus generating secondary particles that may increase dose to the camera volume and are more representative of the scatter fields seen in FP15R experiments. Such source placement therefore allows for conservative shielding design. While using a disk source with the measured FP30L spectrum is not as accurate as modeling the 800 MeV protons incident on the tungsten target, simulating the source in this manner allowed for faster runs which was necessary to meet experimental deadlines for purchasing shielding material.

Beam line walls were simulated as concrete 1 m thick and 10 ft tall. The concrete floor was simulated as 250 cm thick. The back wall (i.e., the wall facing the beam pipe wall) was placed 20 ft from the center of the light-tight box. The left wall was 500 cm from the left edge of the light-tight box, and the right wall was 68 cm from the right wall (the wall-to-box distances were measured during experiments in January 2015).

The steel light-tight box and its contents (ICCD, mirror, scintillator, scintillator holder) were measured and simulated exactly. The light-tight box was placed in the beam line at the same height and location as in the experiments in Chapter 5. The scintillator stuck out 1.5 cm from the front of the light-tight box and was 5 mm thick. The centerline of the tungsten sphere from previous experiments was 8 cm from the front of the scintillator, and the tungsten sphere was centered on the scintillator. The tungsten sphere was modeled as a solid without the three holes in order to increase the scatter off the object and into the light-tight box, again leading to conservative shielding design. The aluminum scintillator holder was assumed to be 1 cm thick. The light-tight box was assumed to have walls 0.5 cm thick and composed of steel

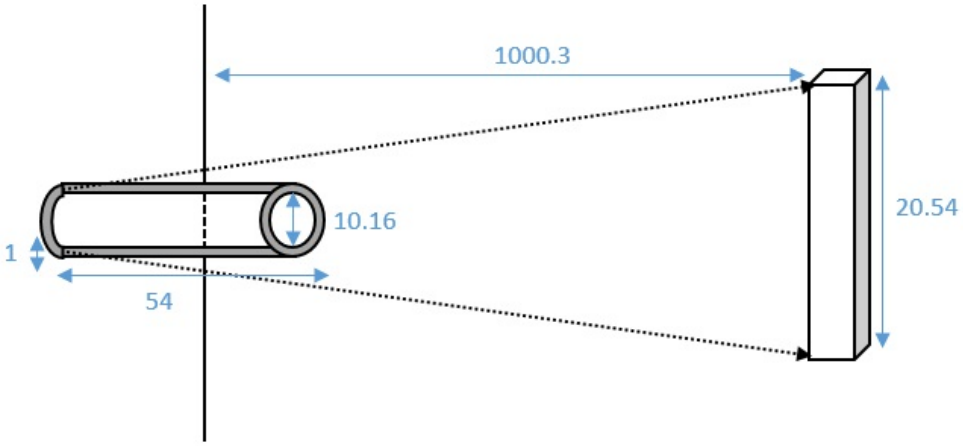


Figure 7.1: Diagram of the beam pipe and scintillator, designed in MCNP6 simulations to approximate experimental conditions. The source was angled to provide an 8 *in* spot size on the front face of the scintillator. Dimensions are in *cm* and are not to scale.

(approximated in the simulations as ^{56}Fe). Not-to-scale diagrams of the system geometry can be seen in Figures 5.11 and 5.12.

When possible, material composition data was taken from the National Institute of Science and Technology (NIST) databases. The tungsten sphere was modeled as pure ^{184}W since its atomic composition was unknown. The mirror was modeled as plate glass, and the camera was modeled as a void. Borated polyethylene ("B-poly"; 5 $wt\%$ ^{10}B) and lithiated polyethylene ("Li-poly"; 7.5 $wt\%$ ^{6}Li) were simulated to match material properties provided by Shieldwerx, who is the manufacturer of shielding purchased for the experiments outlined in Chapters 5 and 9 [70]. These forms of polyethylene are better at scavenging neutrons than regular polyethylene. While Li-poly is worse at absorbing low-energy neutrons than B-poly, it does not emit approximately 500 keV gammas like B-poly.

Support tables for shielding and the light-tight box were not simulated because of their unknown sizes and complicated geometry. Concrete shielding placed below the camera, which was used in the January 2015 experiments, was also not simulated in order to isolate the effect of shielding outside the light-tight box next to the scintillator. FP15R's ceiling was not simulated because it is a thin corrugated warehouse-style roof located very high above the experiment, so its impact on shielding design would be very small. The wooden stand used in January 2015 to support the object was also not simulated. Additionally, other components and objects that were present in the beam line (e.g., J. Hunter's equipment and other equipment in the beam line) were not simulated, even though they do contribute to scatter, because their locations, sizes, and compositions were unknown. The beam dump in the back wall was also not simulated (this is a conservative assumption because lack of a beam dump increases scatter from the back wall). Finally, aluminum mounts for the mirror and camera, as well as the optical board in the bottom of the light-tight box, were not simulated.

7.2.3 Shielding Configurations

Three baseline configurations were simulated to serve as benchmarks for the eighteen case studies simulated. The baseline configuration names and their descriptions are as follows:

- "No object, no shield": Neither the tungsten sphere nor shielding (internal or external) were simulated. Only the concrete walls and floor, the light-tight box and its contents, and the beam pipe were simulated.
- "No shield": Similar to the above configuration, but the tungsten sphere was now added in front of the scintillator. Comparing this configuration to "No object, no shield" would allow the object's scatter field to be isolated.
- "LANSCE": This configuration approximated the FP15R experiment detailed in Chapter 5 and included the tungsten sphere, 5 cm of polyethylene shielding around the camera within the light-tight box, and steel shielding outside of the light-tight box. This configuration also served as a baseline against which new configurations could be compared.

Each of the eighteen simulated configurations was designed to test shielding material, shielding geometry, or shielding location. The names of these configurations and their descriptions are listed below:

- "Configuration 0": Like "LANSCE", but the external steel shielding thickness was doubled (4 ft vs. 2 ft) to isolate the effect of steel thickness on current through the camera volume.
- "Configuration 00": Like "LANSCE", but with polyethylene shielding placed above, below, to the right, and to the left of the light-tight box to see if additional external shielding will reduce flux through the camera volume.
- "Configuration 000": Like "Configuration 00", but instead of external polyethylene, concrete was used as external shielding.

- "Configuration 1": Like "LANSCE", but 3 *cm* of lead was added inside the light-tight box between the polyethylene and the camera. Lead of the same thickness was also added behind the external steel shielding, slightly reducing the thickness of the steel.

- "Configuration 2": Like "Configuration 1", but the lead and polyethylene changed locations so the polyethylene was now between the lead and the camera.

- "Configuration 3": Like "Configuration 1", but the polyethylene inside the light-tight box was replaced with steel.

- "Configuration 4": Like "LANSCE", but with Li-poly instead of regular polyethylene inside the light-tight box.

- "Configuration 5": Like "Configuration 4", but also with external polyethylene shielding (like "Configuration 00").

- "Configuration 6": Like "Configuration 5", but now with twice the thickness of external steel shielding (like "Configuration 0").

- "Configuration 7": Like "LANSCE", but with B-poly instead of regular polyethylene inside the light-tight box.

- "Configuration 8": Like "Configuration 7", but also with a 3 *cm* aluminum sheet between the B-poly and camera to attenuate gammas and protons.

- "Configuration 9": Like "Configuration 8", with the addition of external polyethylene shielding (like "Configuration 00").

- "Configuration 10": Like "Configuration 1", with lead replaced by copper.

- "Configuration 11": Like "Configuration 1", with lead replaced by nickel.

- "Configuration 12": Like "Configuration 1", with lead replaced by tungsten.

- "Configuration 13": Like "LANSCE", but with reactor-grade graphite as the external shielding material instead of steel.
- "Configuration 14": Like "Configuration 1", but with Li-poly instead of regular polyethylene inside the light-tight box and lead behind the external steel shielding (like "Configuration 1").
- "Configuration 15": Like "Configuration 14", but with no lead behind the external steel shielding.
- "Configuration 16": Like "Configuration 15", but with bismuth inside the light-tight box instead of lead to possibly reduce the amount of gammas emitted by (n,γ) reactions in lead (bismuth does not have a cross-section for this reaction).

7.2.4 Results

As stated previously in this chapter, a number of shielding configurations were simulated to determine how best to limit current through the camera volume, and by extension, through the CCD chip. A brief explanation of subsequent plots is included here for brevity.

Each configuration is given its own unique color in plots for ease of reference. Plotted values supporting each conclusion are on a per pulse basis, meaning that a given particle current generated by MCNP6 is normalized to the number of neutron source particles and that the values plotted have been multiplied by the approximate number of neutrons in a given LANSCE pulse. Two plots were generated for each study. First, surface current plots were generated that show the current through a given camera surface, with the point of reference for surface labeling from the beam pipe's point of view. Second, the energy distribution of a given particle current is shown in a *log-log* plot to provide a sense of scale for the upper energies. Caution should be used, however, when examining *log-log* plots because the variation in particle fluence between configurations appears reduced in a *log-log* plot.

Baseline Results

The results from "No object, no shield", "No shield", and "LANSCE" serve as a baseline for the shielding designs explored in this chapter. It was seen in the simulations, as it was during the FP15R experiments at LANSCE, that adding a radiography object increased scatter into the camera volume, in particular low-energy neutrons and photons. Moreover, the tungsten object creates a marked increase in secondary photon current, and thus "No shield" and "LANSCE" have much higher total photon currents than "No object, no shield". This underscores the fact that time-of-flight neutron radiography is necessary to reject scatter from the radiography object, as well as the fact that shielding between the object and the camera is a necessity to protect the ICCD camera.

A final conclusion from the three baseline studies is that, overall, the addition of internal and external shielding reduces current through the camera volume, and that the large amount of steel in the "LANSCE" shielding design reduces high-energy current through the camera volume. Results can be seen in Figures 7.2 through 7.5.

Study One

The first study compared the shielding ability of external polyethylene ("Configuration 00") to external concrete ("Configuration 000"). This study took the "LANSCE" configuration and added the material in question around all sides of the light-tight box except the side with external steel. Each of the five sides had 5263.5 cm^3 of material (either concrete or polyethylene) beside it. It was hypothesized that additional hydrogenous material around the light-tight box would reduce scatter into the camera volume from the beam line walls and floor. The results of Study One can be seen in Figures 7.6 through 7.9.

This study found that external polyethylene is only slightly better for shielding neutrons than external concrete. Alphas and protons respond approximately the same to both materials. Gammas are slightly better shielded by concrete, which is

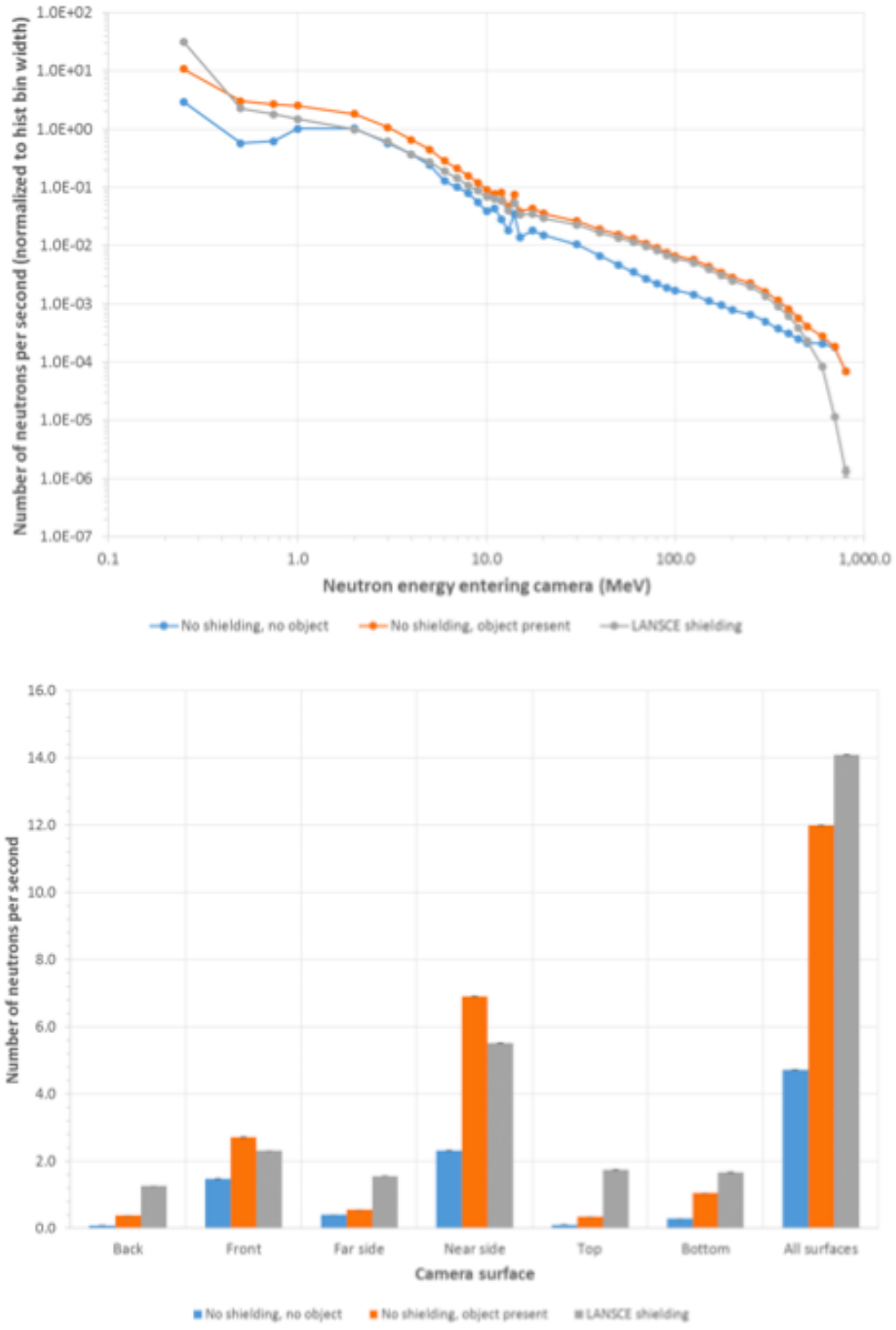


Figure 7.2: Baseline energy distribution (top) and surface current (bottom) for neutrons entering the camera body and for "No object, no shield", "No shield", and "LANSCE".

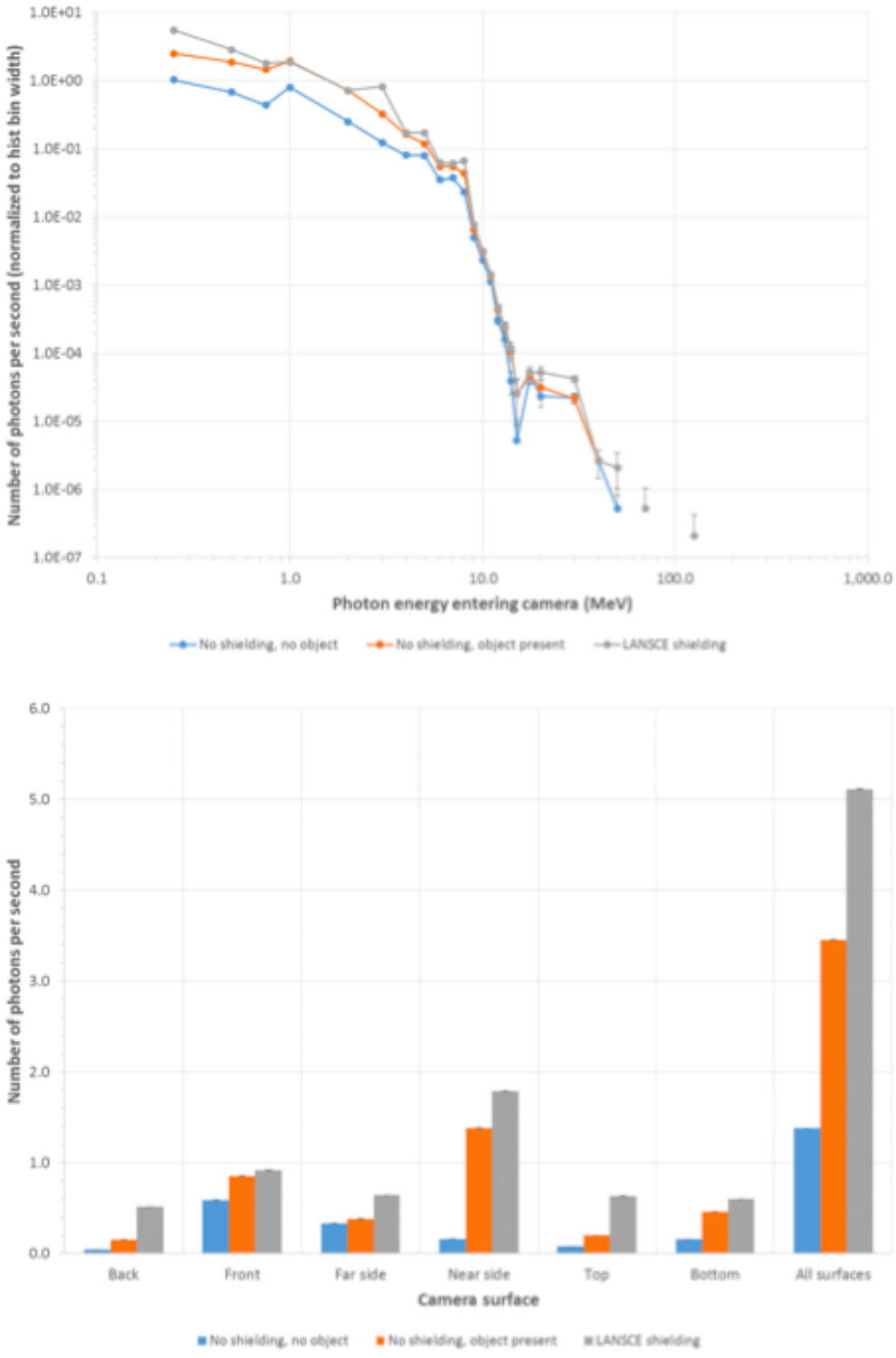


Figure 7.3: Baseline energy distribution (top) and surface current (bottom) for photons entering the camera body and for "No object, no shield", "No shield", and "LANSCE".

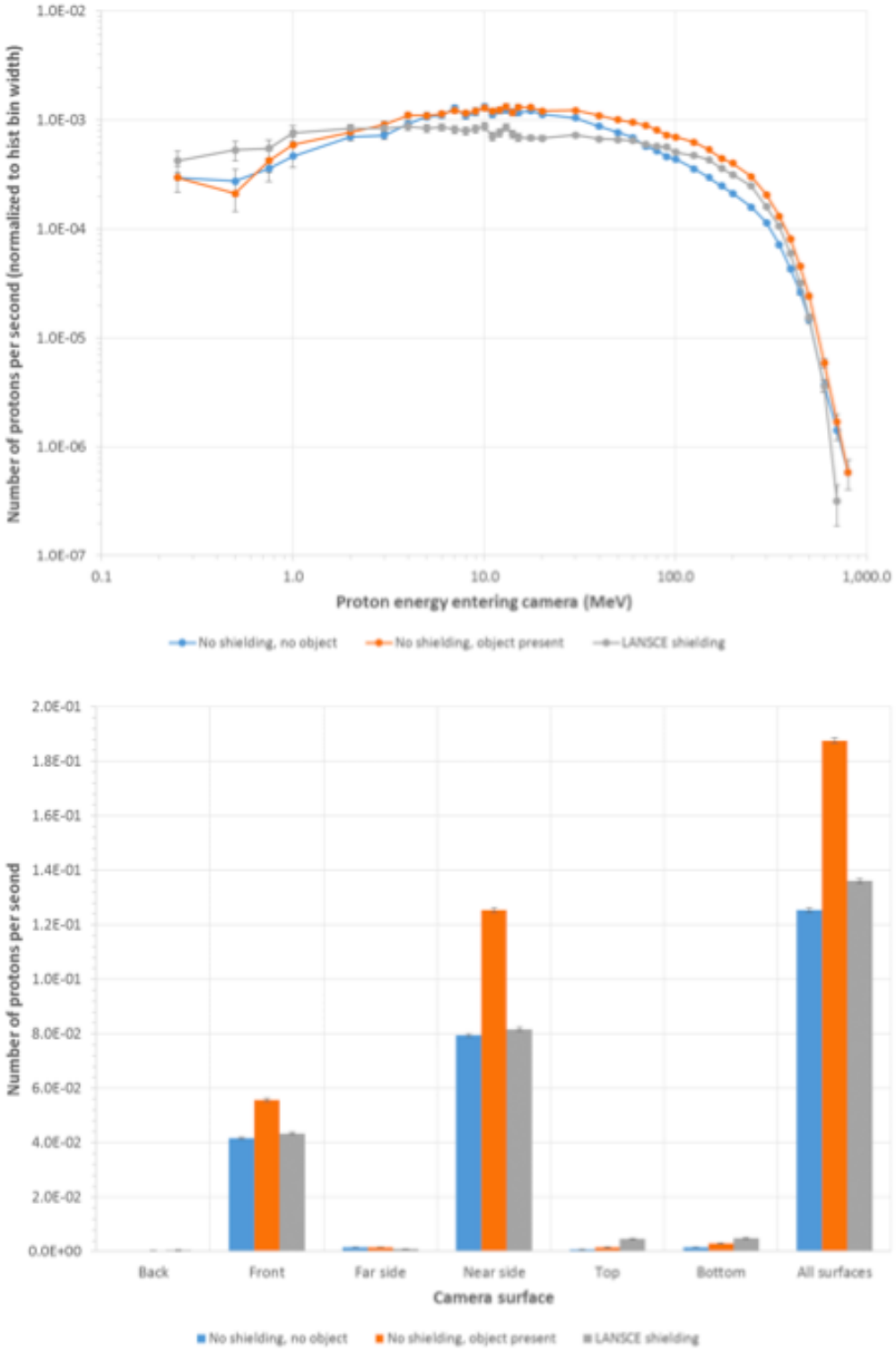


Figure 7.4: Baseline energy distribution (top) and surface current (bottom) for protons entering the camera body and for "No object, no shield", "No shield", and "LANSCE".



Figure 7.5: Baseline energy distribution (top) and surface current (bottom) for alphas entering the camera body and for "No object, no shield", "No shield", and "LANSCE".

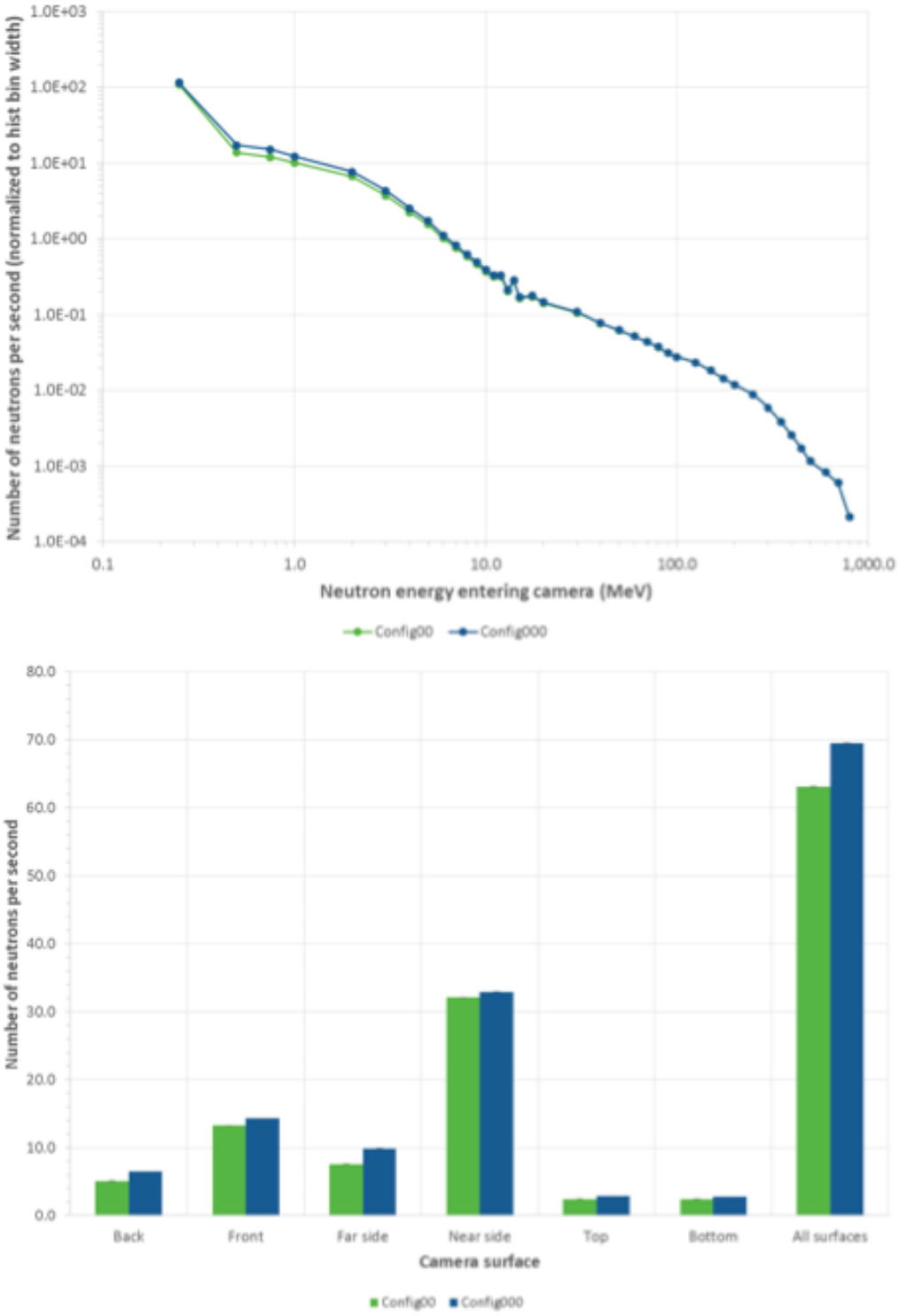


Figure 7.6: Energy distribution (top) and surface current (bottom) for neutrons entering the camera body and for Configurations 00 and 000.

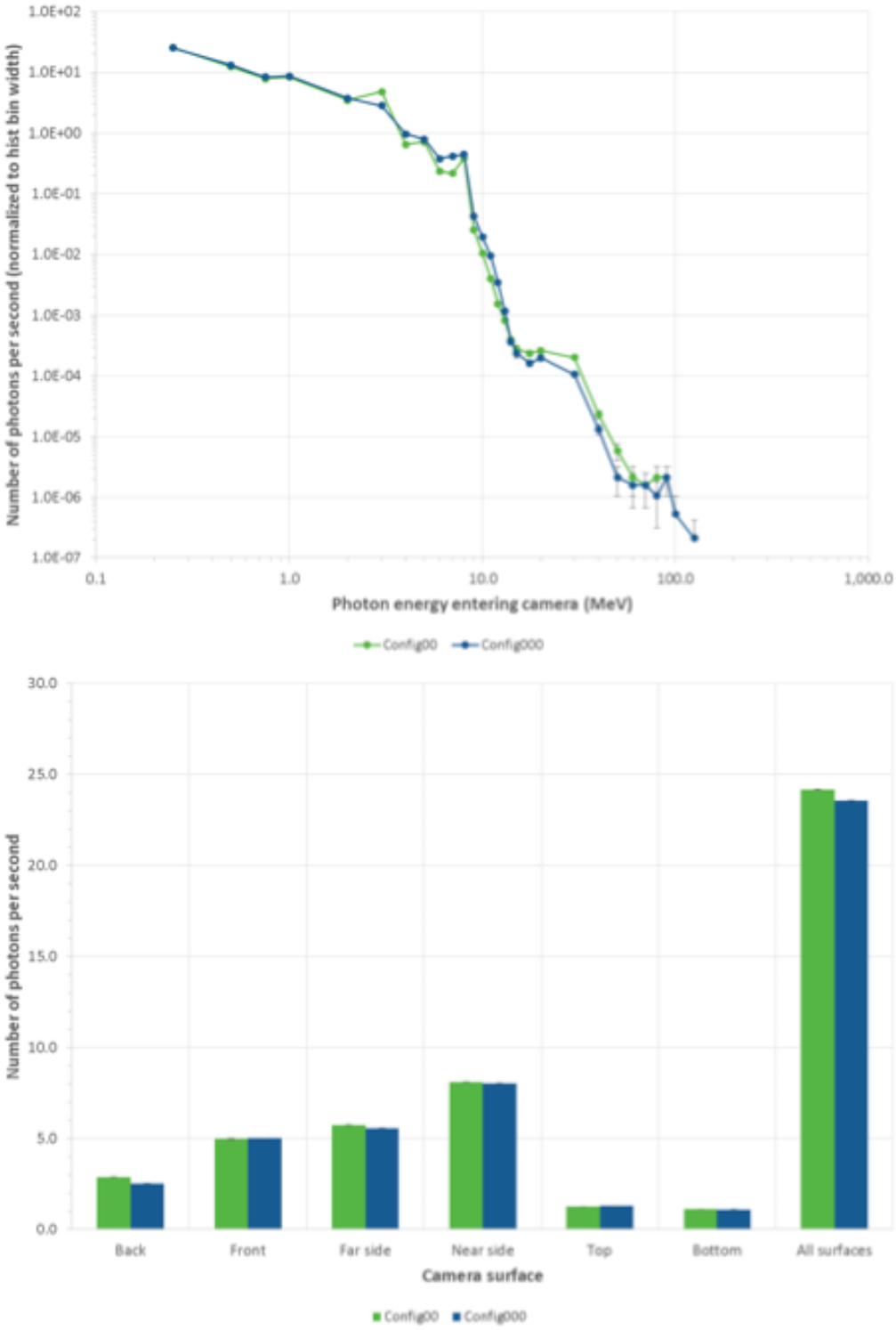


Figure 7.7: Energy distribution (top) and surface current (bottom) for photons entering the camera body and for Configurations 00 and 000.

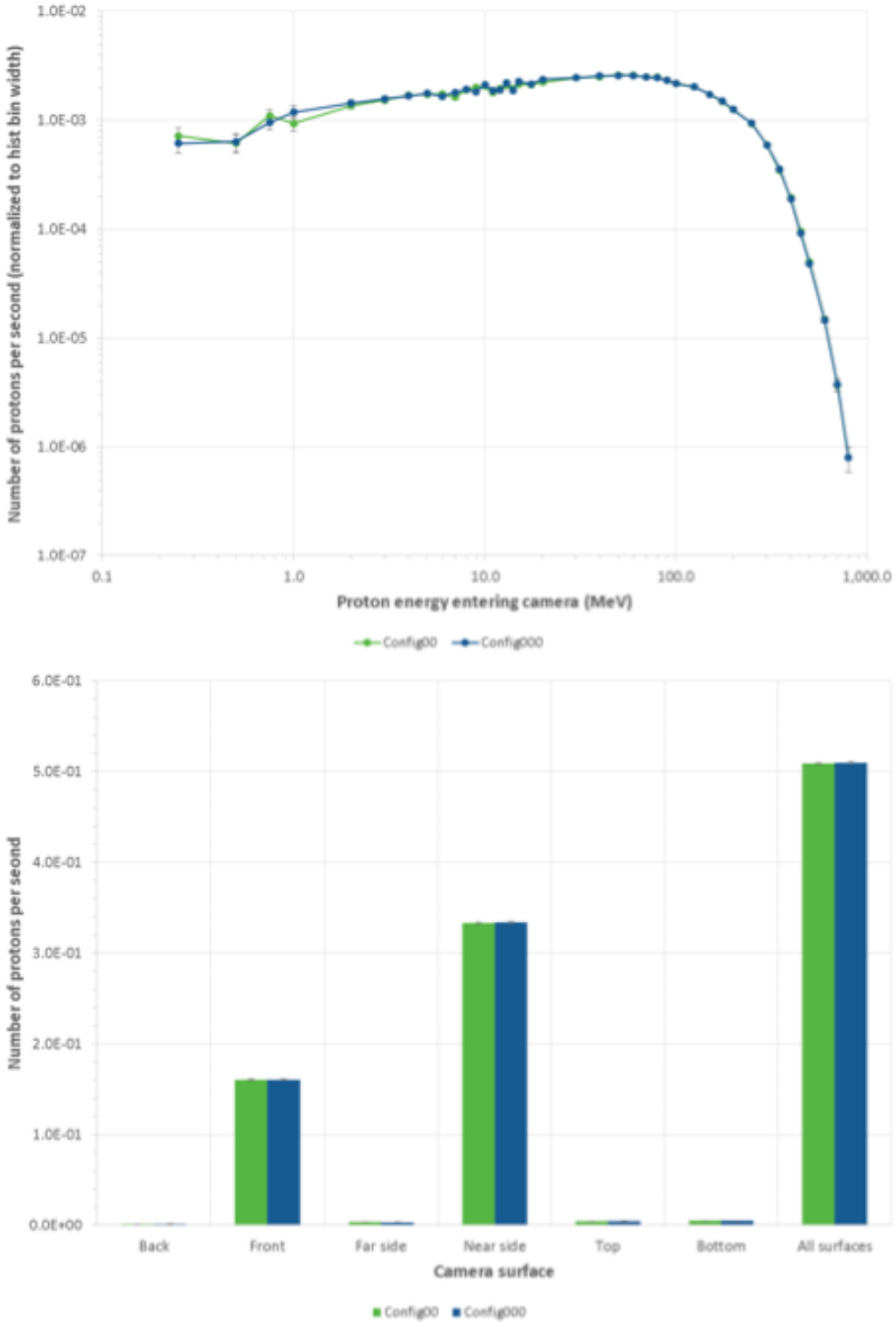


Figure 7.8: Energy distribution (top) and surface current (bottom) for protons entering the camera body and for Configurations 00 and 000.

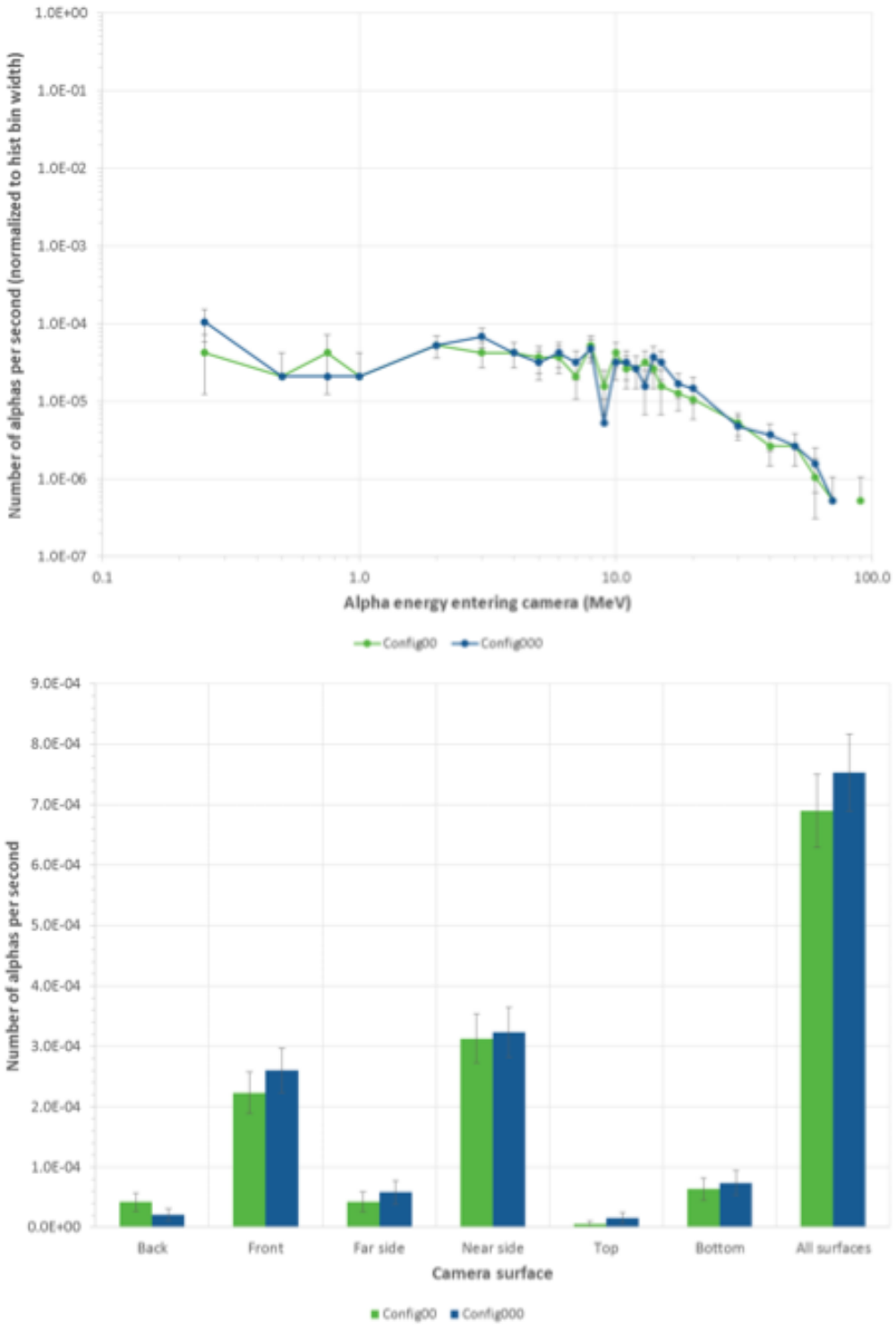


Figure 7.9: Energy distribution (top) and surface current (bottom) for alphas entering the camera body and for Configurations 00 and 000.

attributable to the presence of higher-Z elements (e.g., ^{23}Na) that are not present in polyethylene. External polyethylene is the better choice, however, because it reduces neutrons in the 1 to 10 MeV range more than concrete reduces photons in the same energy range, thereby better reducing overall current.

Study Two

The second study examined the impact of shielding internal to the light-tight box. Simulation results for "Configuration 1" and "Configuration 3" were compared to see whether it is better to surround the camera with polyethylene and lead or with steel and lead, respectively. In both cases, lead of 3 cm thickness was placed between the shielding material in question and the camera. The polyethylene and steel were 5 cm thick. Lead of 5 cm thickness was also placed behind the external steel shielding in both configurations.

Results showed that, overall, "Configuration 1" is better if it is assumed that neutrons with energy less than 1 MeV are not damaging to the silicon chip inside the camera (Figures 7.10 through 7.13). While "Configuration 3" reduced the neutron current for energies below 500 keV (and had a lower total neutron current as a result), "Configuration 1" reduced the neutron current for energies between 500 keV and approximately 5 MeV. These higher energy neutrons have a much greater potential to damage the CCD chip, so polyethylene is preferable for shielding neutrons for the material thicknesses studied here. Moreover, polyethylene weighs significantly less than steel, making it more desirable from an engineering and safety standpoint, and also costs less.

As for the other particles, "Configuration 1" reduced photons with energy below 10 MeV more than "Configuration 3". In contrast, the proton current is higher (approximately double) for "Configuration 1" than for "Configuration 3". This is not particularly worrisome because the proton current is much lower than the neutron or photon current over the same range of energies. For example, there is approximately

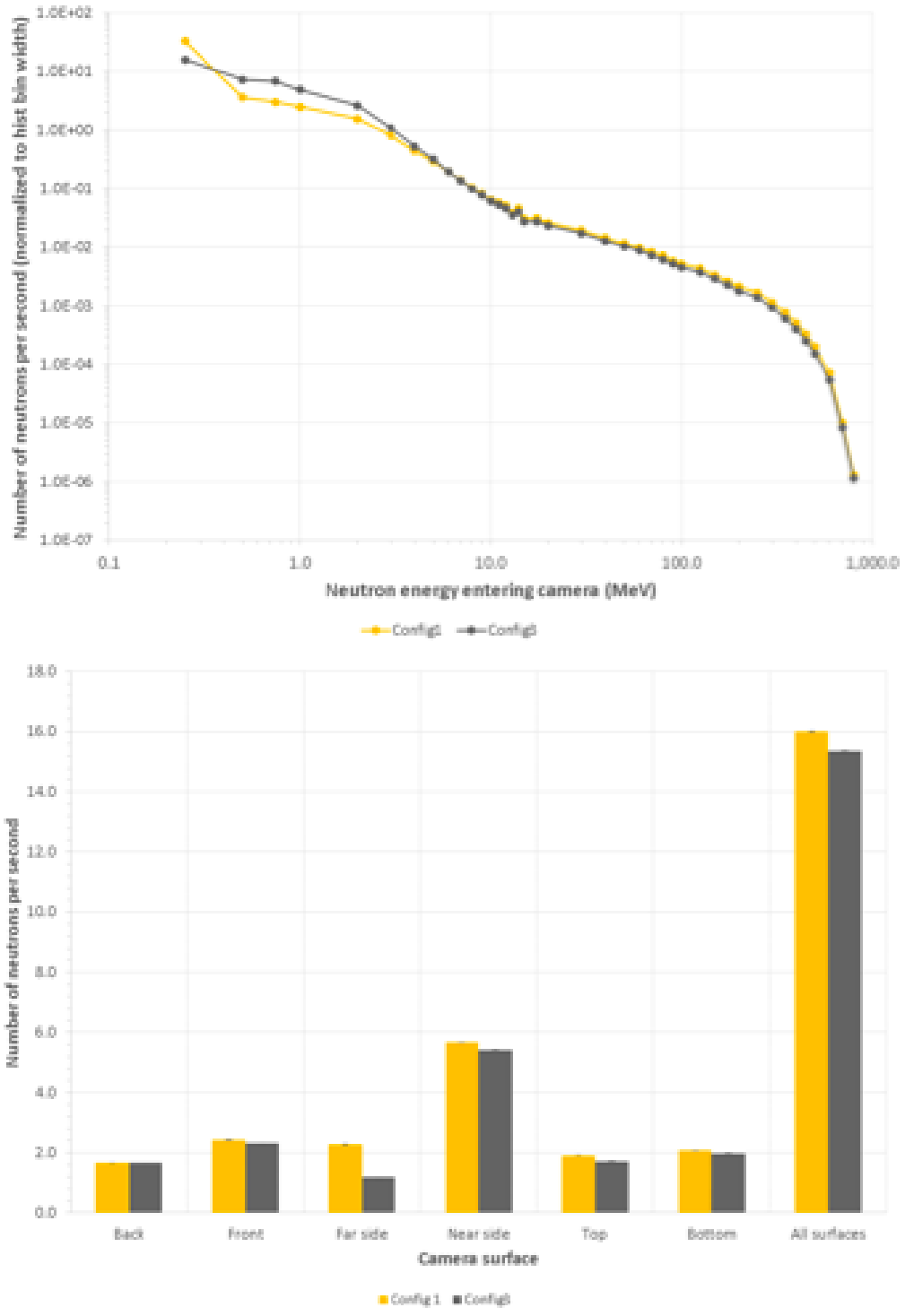


Figure 7.10: Energy distribution (top) and surface current (bottom) for neutrons entering the camera body and for Configurations 1 and 3.

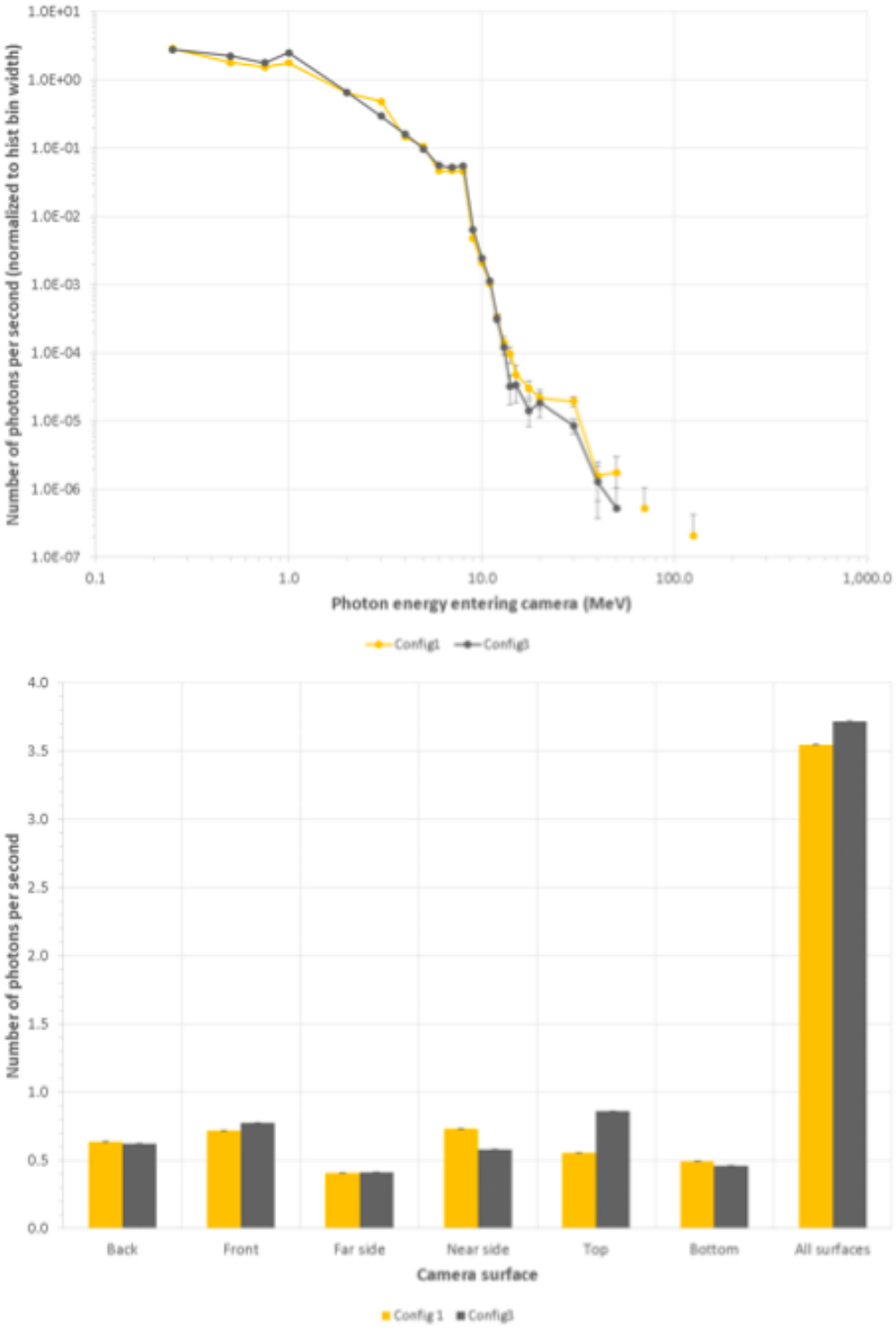


Figure 7.11: Energy distribution (top) and surface current (bottom) for photons entering the camera body and for Configurations 1 and 3.

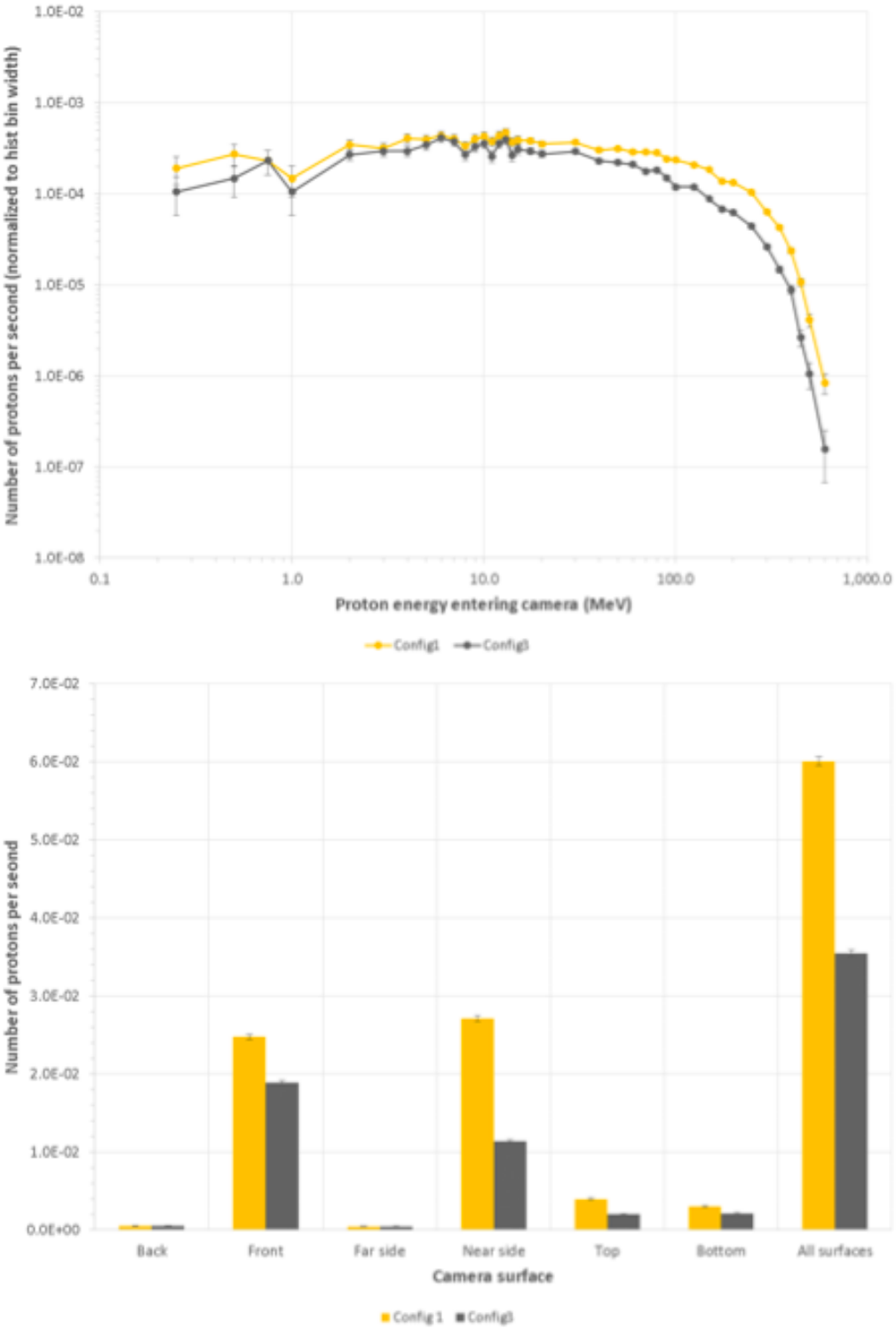


Figure 7.12: Energy distribution (top) and surface current (bottom) for protons entering the camera body and for Configurations 1 and 3.

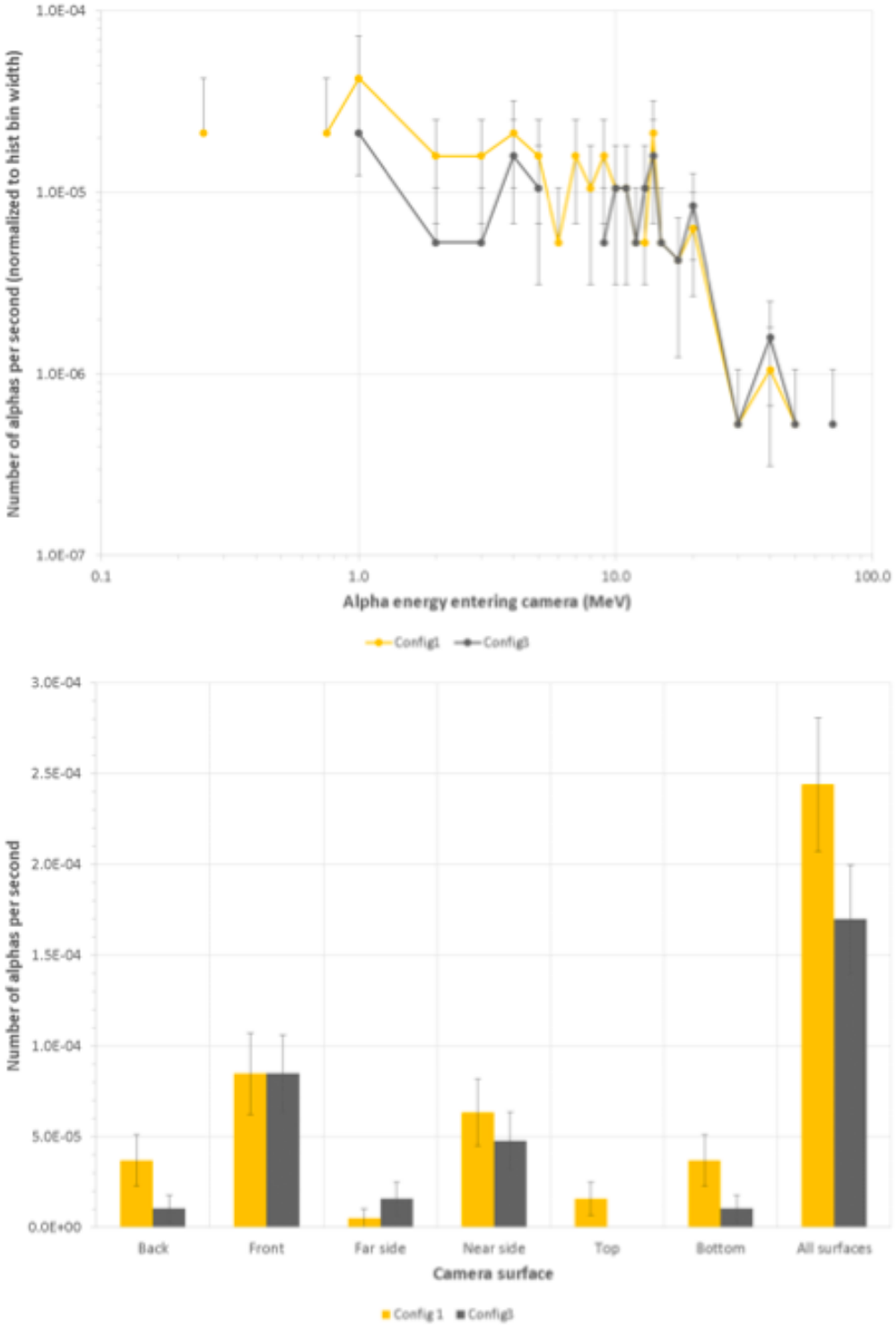


Figure 7.13: Energy distribution (top) and surface current (bottom) for alphas entering the camera body and for Configurations 1 and 3.

1 proton for every 267 neutrons for "Configuration 1", making the increased proton current for "Configuration 1" an essentially negligible effect.

Finally, the alpha current is approximately the same for the two configurations, with data falling within error bars for the two configurations. Thus, taking all of these results into account, "Configuration 1" is better than "Configuration 3" because it has reduced neutron and photon current in the damaging energy ranges and its increased proton current is negligible.

Study Three

Related to Study Two is the question of whether it is better to place lead between the polyethylene and the camera ("Configuration 1"), or to place polyethylene between the lead and the camera ("Configuration 2"). It was thought that one configuration may have fewer secondary particles than the other. The lead was 3 *cm* thick and the polyethylene was 5 *cm* thick.

It was found that "Configuration 1" is better than "Configuration 2" (Figures 7.14 through 7.17). The neutron, photon, and alpha currents are approximately the same, but the proton current is much less for "Configuration 1" (in some places, it is 25% of the "Configuration 2" proton current). While proton current is much smaller in magnitude than the neutron or photon currents, in this case it is used as the deciding factor on geometry because it is the only difference between the two configurations. Thus, it is better to place the high-Z shielding behind the low-Z shielding such as in "Configuration 1".

Study Four

This study was conducted to determine the best high-Z material for shielding the camera: lead ("Configuration 1"), copper ("Configuration 10"), nickel ("Configuration 11"), or tungsten ("Configuration 12"). The high-Z material was placed between the polyethylene shielding and the camera. A sheet of high-Z material (5 *cm* thick)

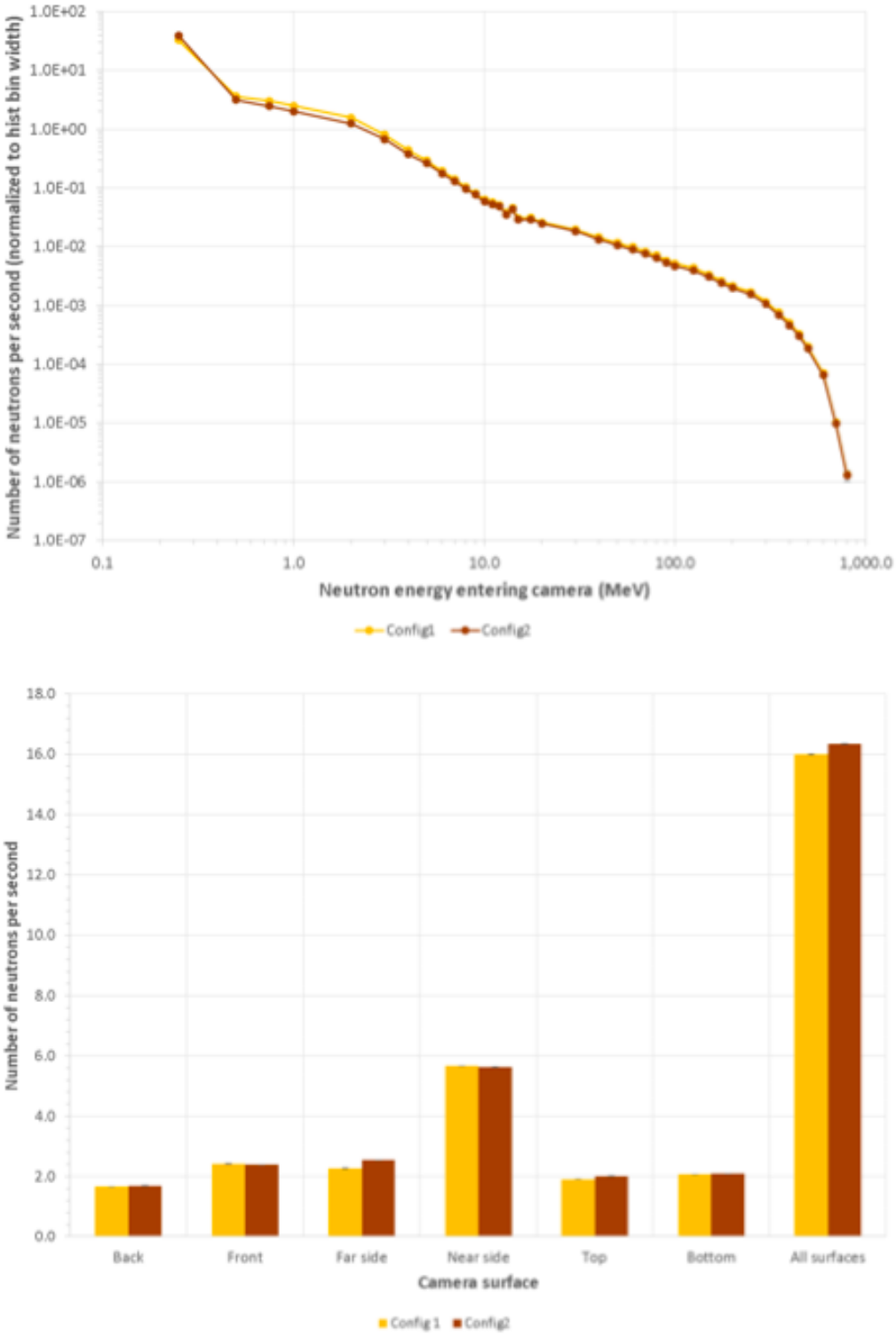


Figure 7.14: Energy distribution (top) and surface current (bottom) for neutrons entering the camera body and for Configurations 1 and 2.

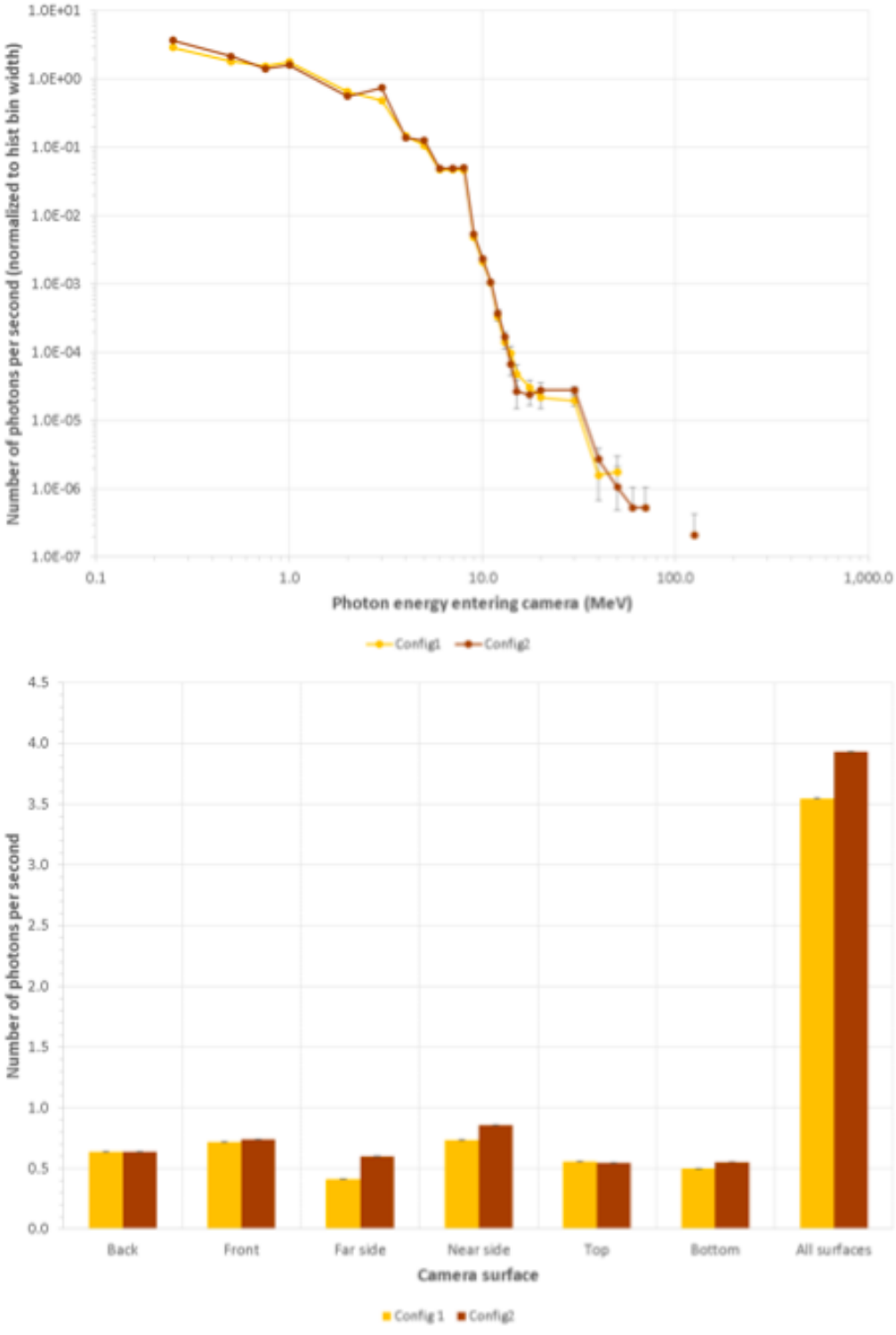


Figure 7.15: Energy distribution (top) and surface current (bottom) for photons entering the camera body and for Configurations 1 and 2.

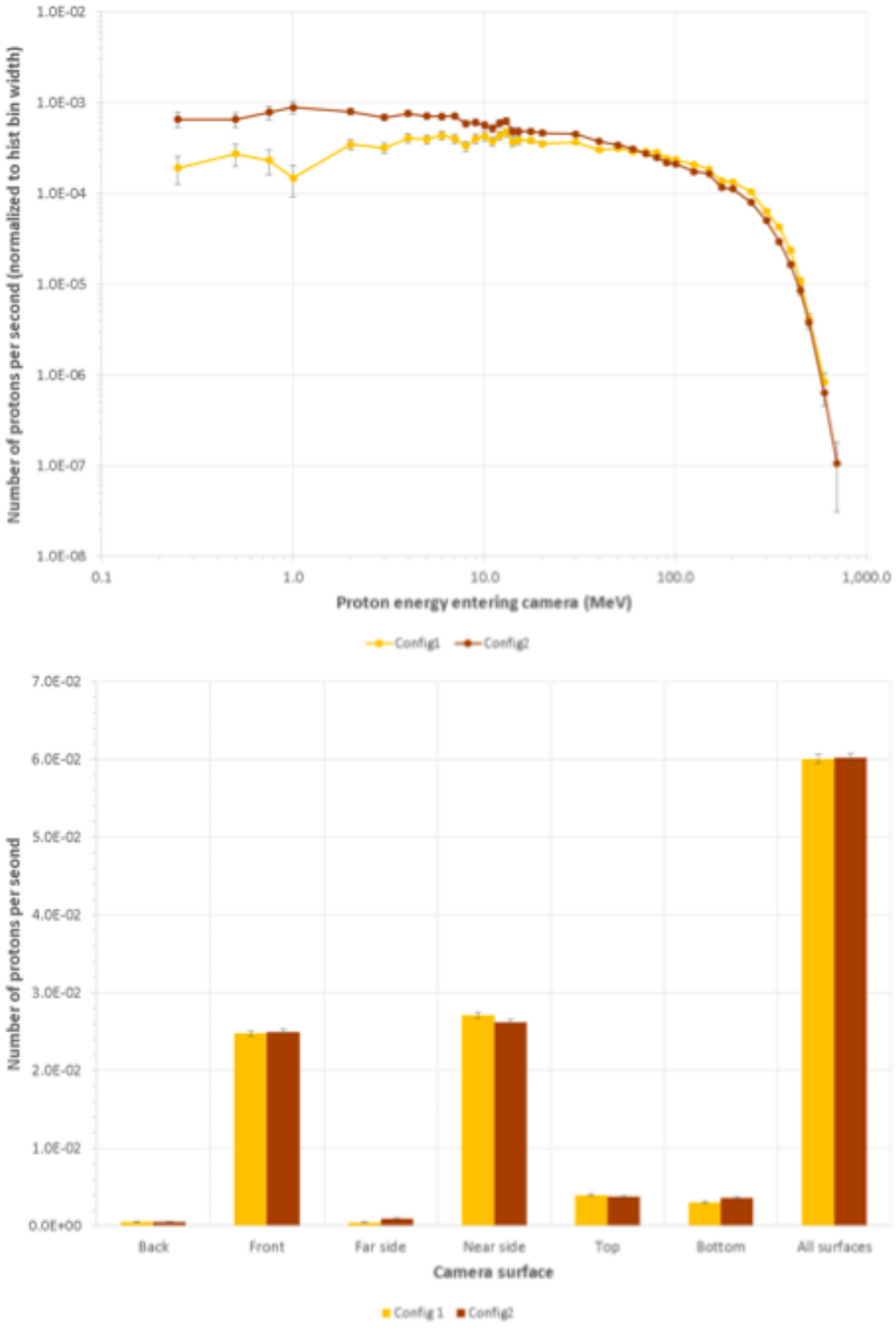


Figure 7.16: Energy distribution (top) and surface current (bottom) for protons entering the camera body and for Configurations 1 and 2.

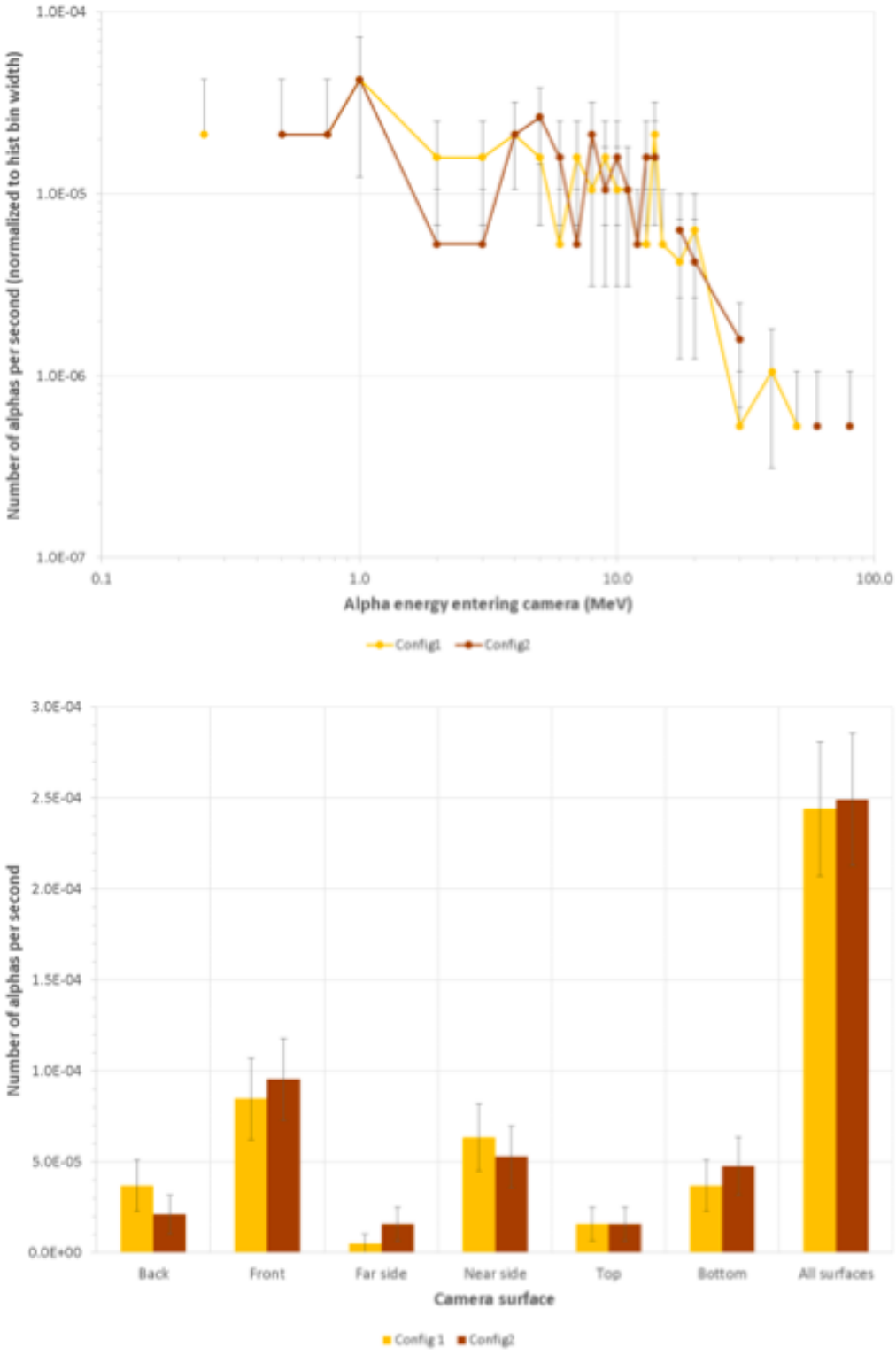


Figure 7.17: Energy distribution (top) and surface current (bottom) for alphas entering the camera body and for Configurations 1 and 2.

was also placed behind the steel to determine if it would reduce (n,γ) current from the steel. The high-Z material was 3 cm thick and the polyethylene was 5 cm thick. All four configurations were compared to the "LANSCE" baseline, which did not use a high-Z material either inside or outside of the light-tight box, to isolate the effect of using a high-Z shielding material.

It was determined from Figures 7.18 through 7.21 that the optimal high-Z material varies according to which type of particle current one is aiming to reduce. The neutron current was best reduced by nickel, with 500 keV neutron current approximately 60% of that for tungsten. Above approximately 2 MeV, however, all high-Z materials shield neutrons more or less equally. The proton, photon, and alpha currents were best reduced by lead, followed by tungsten, for energies below approximately 1 MeV. Lead had approximately a 43% lower 500 keV proton current than "LANSCE", which had the highest proton current at 500 keV. For photons, the high-Z materials studied have the same shielding effect for photon energies above approximately 3 MeV.

For all materials studied, the presence of a high-Z material greatly reduced the total proton current when compared to the "LANSCE" configuration. This is important for developing the shielding design because the addition of high-Z material increases the likelihood that protons are stopped before they deposit energy on the silicon chip. Thus, high-Z material use is recommended, with lead selected as the material of choice because it has a greater impact on photons than nickel has on neutrons.

Study Five

The fifth study compared steel ("LANSCE") to reactor-grade graphite ("Configuration 13") in order to determine which is a better shielding material to place external to the light-tight box. It was found that both materials have approximately the same effect on the four particle types studied in this series of simulations (Figures 7.22 through 7.25). It is recommended that the external shield material, therefore, take into account cost and weight considerations, since one material does not have a

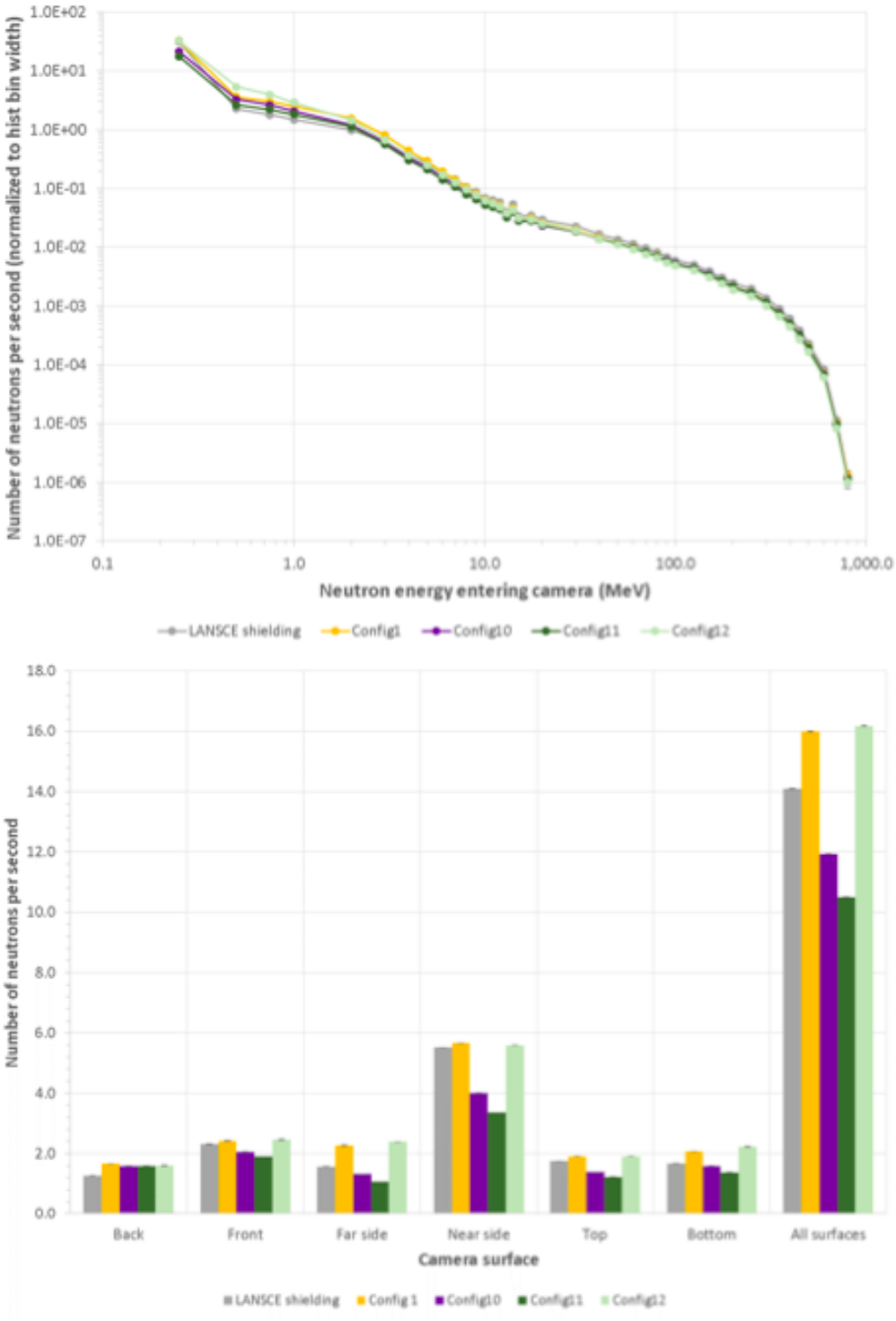


Figure 7.18: Energy distribution (top) and surface current (bottom) for neutrons entering the camera body and for Configurations 1, 10, 11, and 12 as compared to the LANSCE set-up.

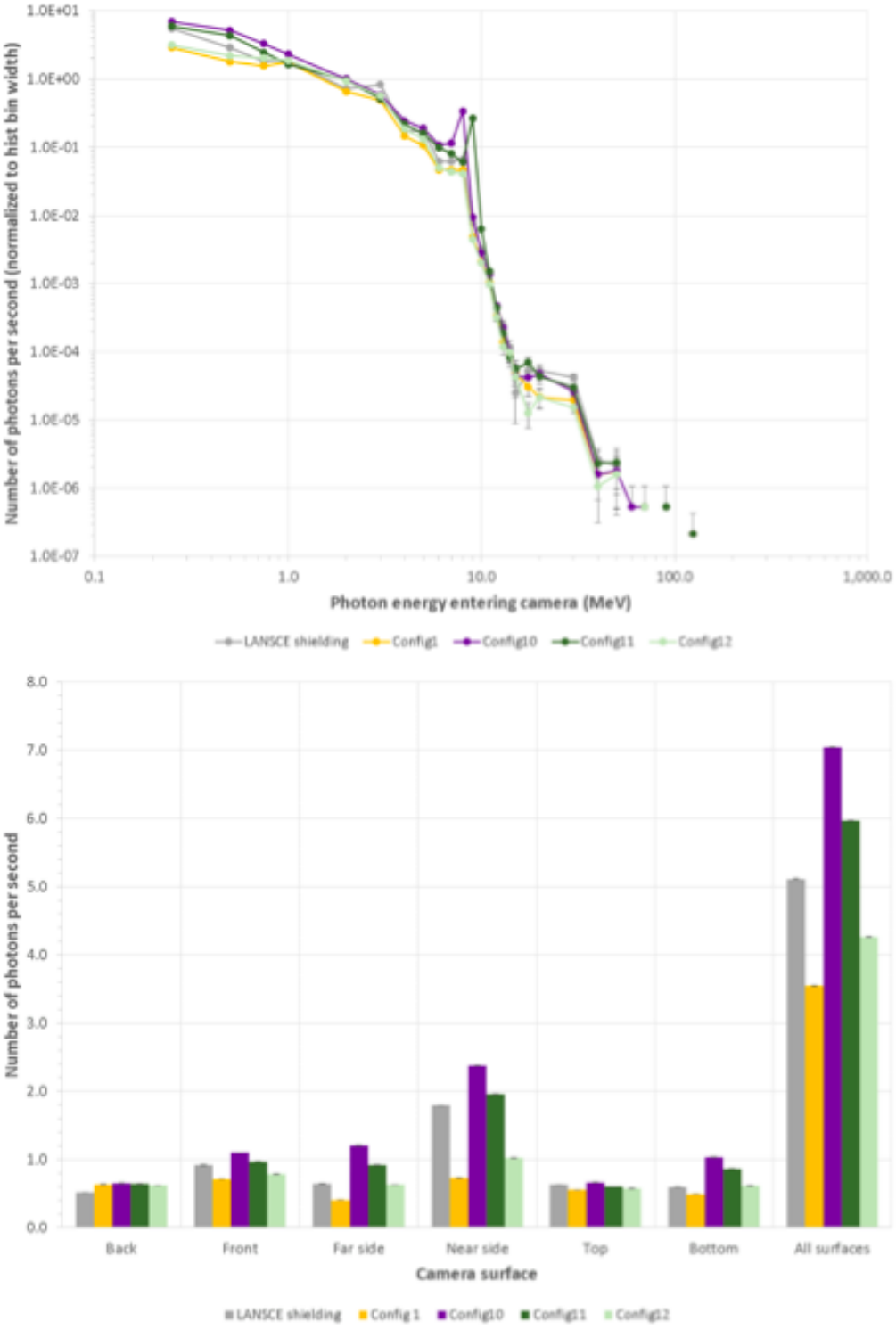


Figure 7.19: Energy distribution (top) and surface current (bottom) for photons entering the camera body and for Configurations 1, 10, 11, and 12 as compared to the LANSCE set-up.

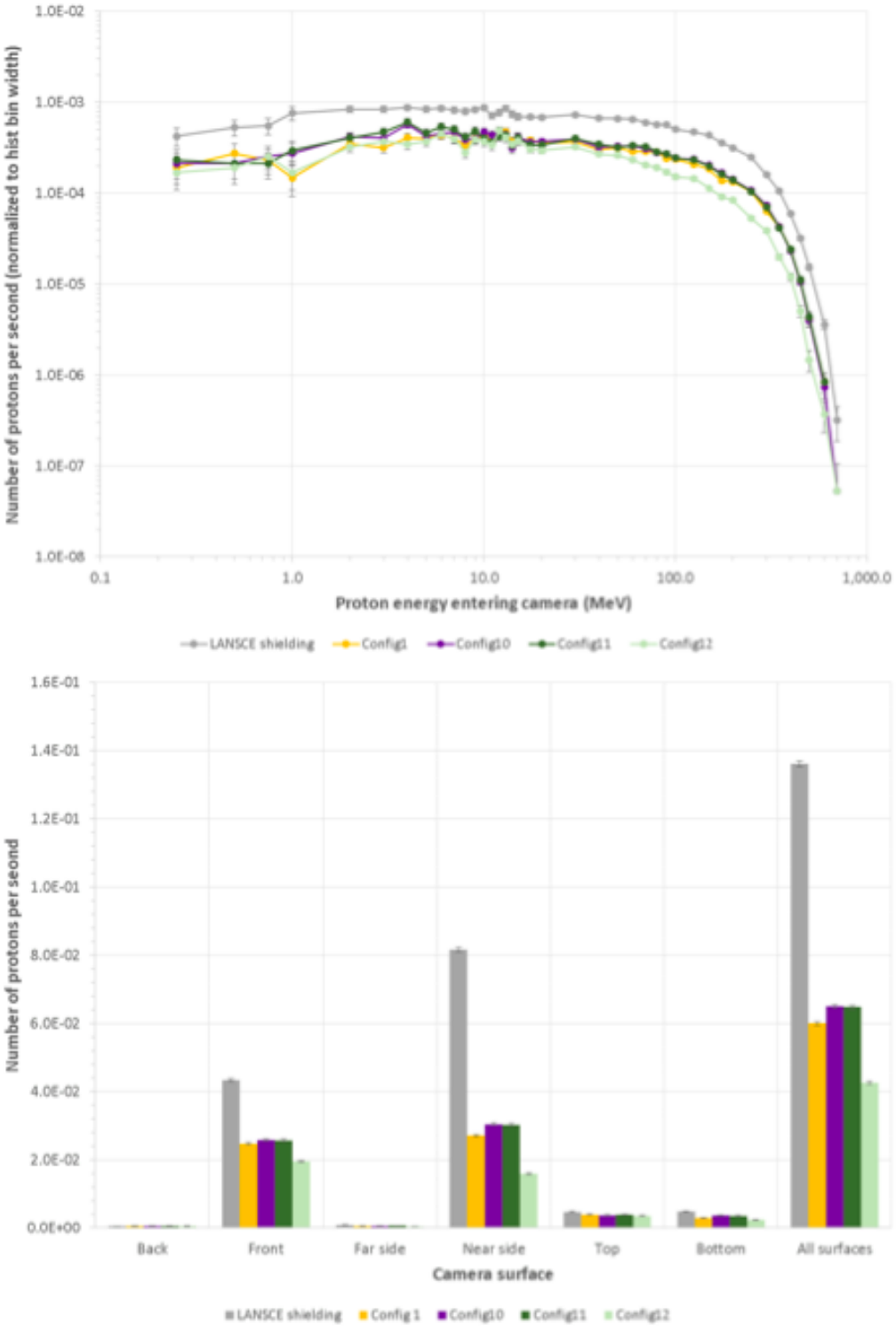


Figure 7.20: Energy distribution (top) and surface current (bottom) for protons entering the camera body and for Configurations 1, 10, 11, and 12 as compared to the LANSCE set-up.



Figure 7.21: Energy distribution (top) and surface current (bottom) for alphas entering the camera body and for Configurations 1, 10, 11, and 12 as compared to the LANSCE set-up.

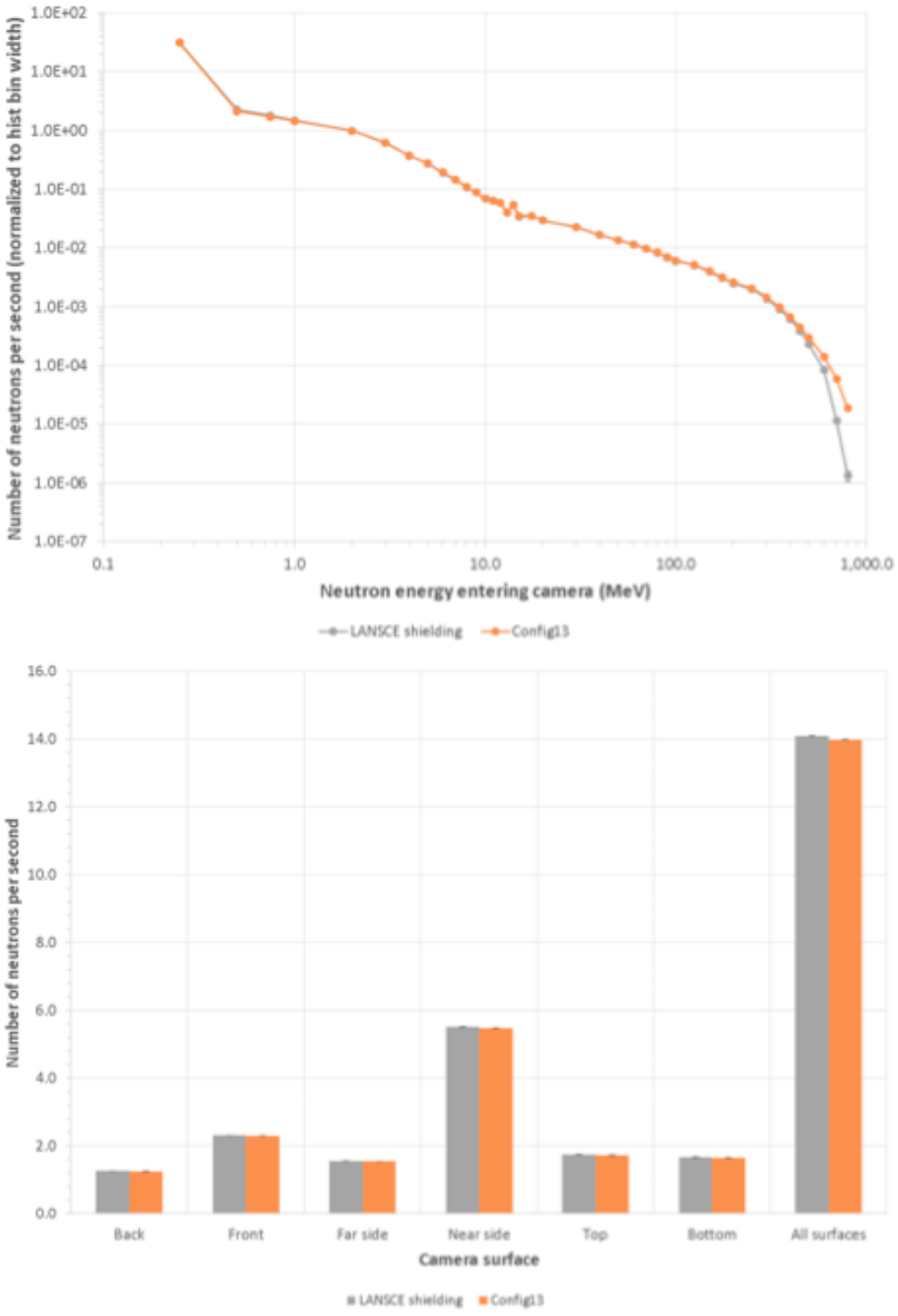


Figure 7.22: Energy distribution (top) and surface current (bottom) for neutrons entering the camera body and for Configuration 13 as compared to the LANSCE set-up.

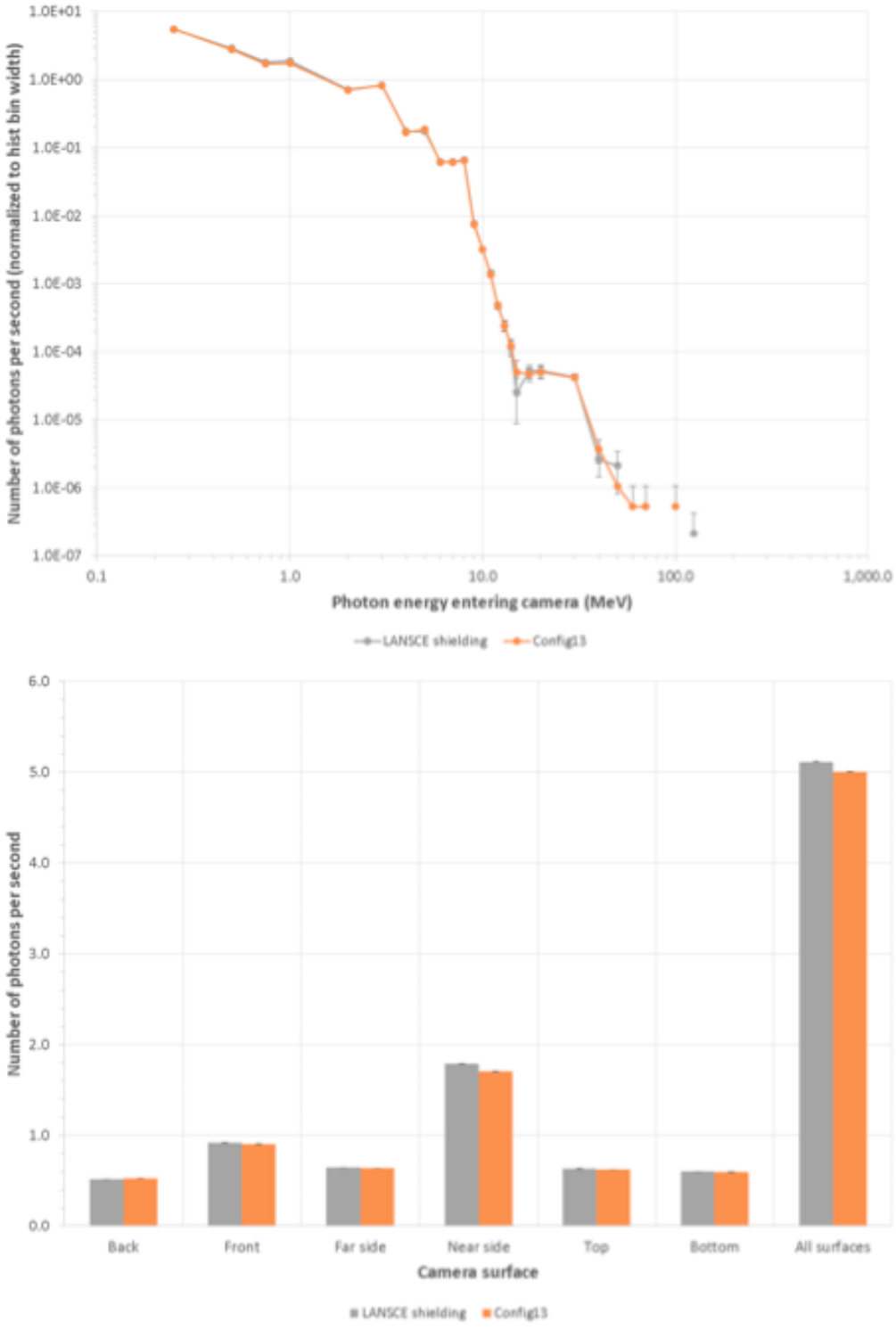


Figure 7.23: Energy distribution (top) and surface current (bottom) for photons entering the camera body and for Configuration 13 as compared to the LANSCE set-up.

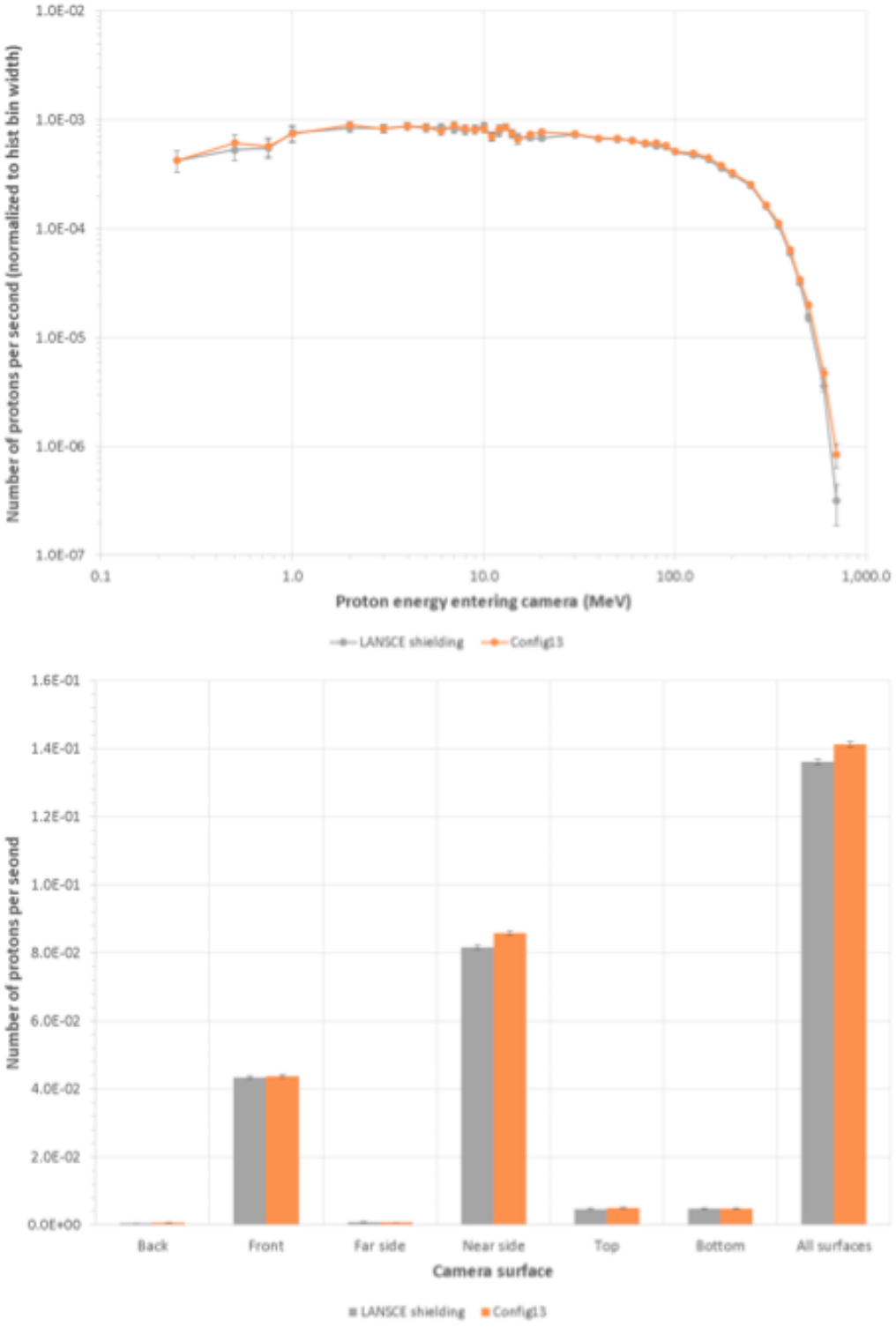


Figure 7.24: Energy distribution (top) and surface current (bottom) for protons entering the camera body and for Configuration 13 as compared to the LANSCE set-up.

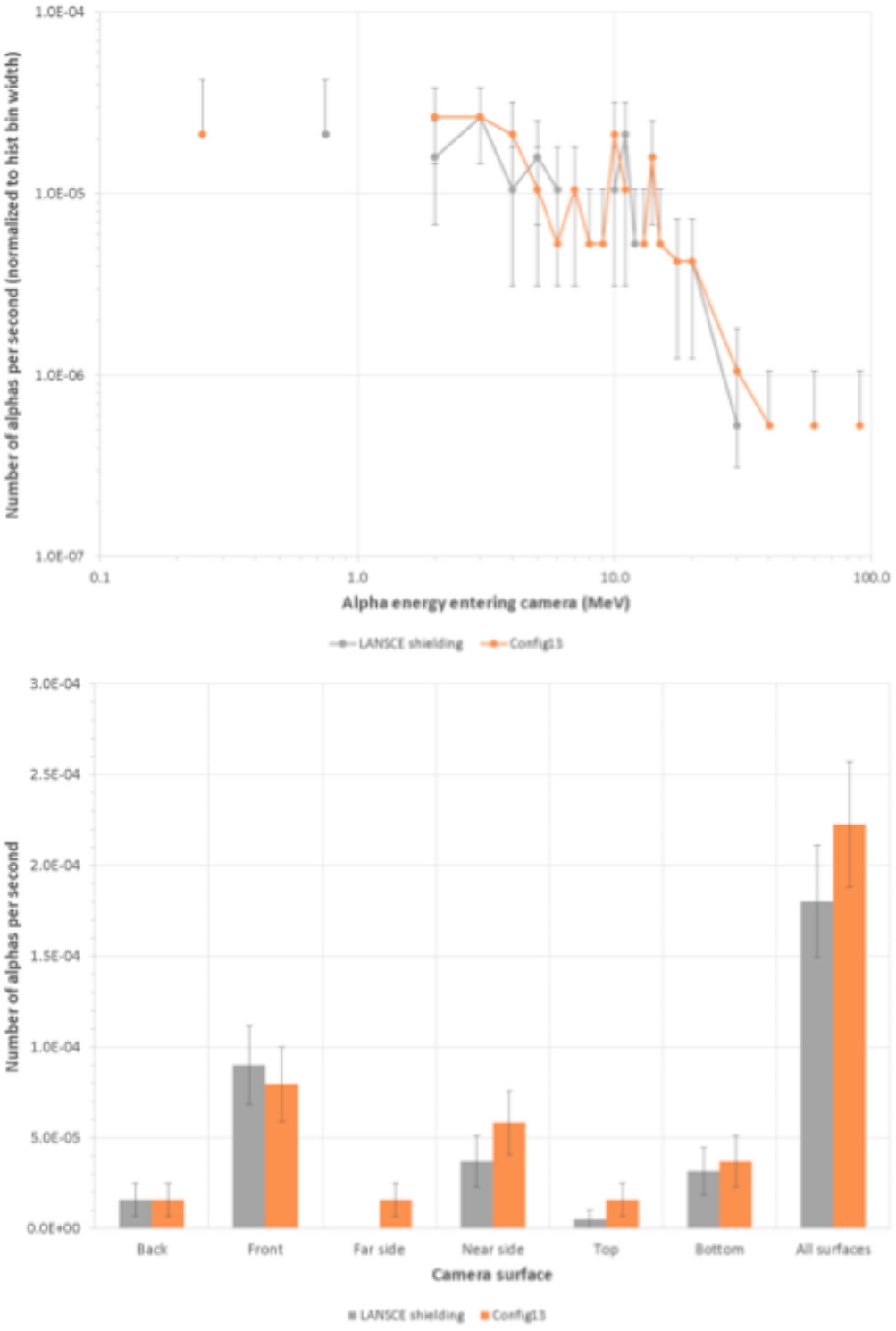


Figure 7.25: Energy distribution (top) and surface current (bottom) for alphas entering the camera body and for Configuration 13 as compared to the LANSCE set-up.

marked shielding advantage over the other. It should also be considered that LANSCE already has a large supply of steel available for experimental use. For this reason, steel is optimal when compared to graphite because it is cheaper, albeit heavier, and additional material procurement would be unnecessary.

Study Six

This particular study examined whether it was necessary to use more external steel shielding than was used in the FP15R experiments. Thus, Study Six compared "LANSCE" (which used 2 ft of steel) to "Configuration 0" (which used 4 ft of steel).

The results showed that doubling the thickness of external steel shielding from 2 ft to 4 ft made almost no difference in the total particle current through the camera volume (Figures 7.26 through 7.29). While current in the upper neutron energies was slightly reduced (above approximately 100 MeV), the difference was so small that it would not be worth the added cost or weight to use additional external steel shielding. Thus, 2 ft of steel is sufficient to shield the camera volume.

Study Seven

This study examined whether it was better to use polyethylene ("LANSCE"), Li-poly ("Configuration 4"), or B-poly ("Configuration 7") as the low-Z shielding material inside the light-tight box. In all cases, the shielding materials were 5 cm thick. It was found that the material choice depends on which type of particle current one wanted to limit.

Of the materials studied, B-poly is the best material at reducing total neutron current, particularly because it is the best at absorbing thermal neutrons, thus reducing total neutron current by approximately 25% when compared with polyethylene. Li-poly total neutron current was seen to be lower than that of polyethylene, but not as low as B-poly. This is because the lithium dopant is better at scavenging neutrons

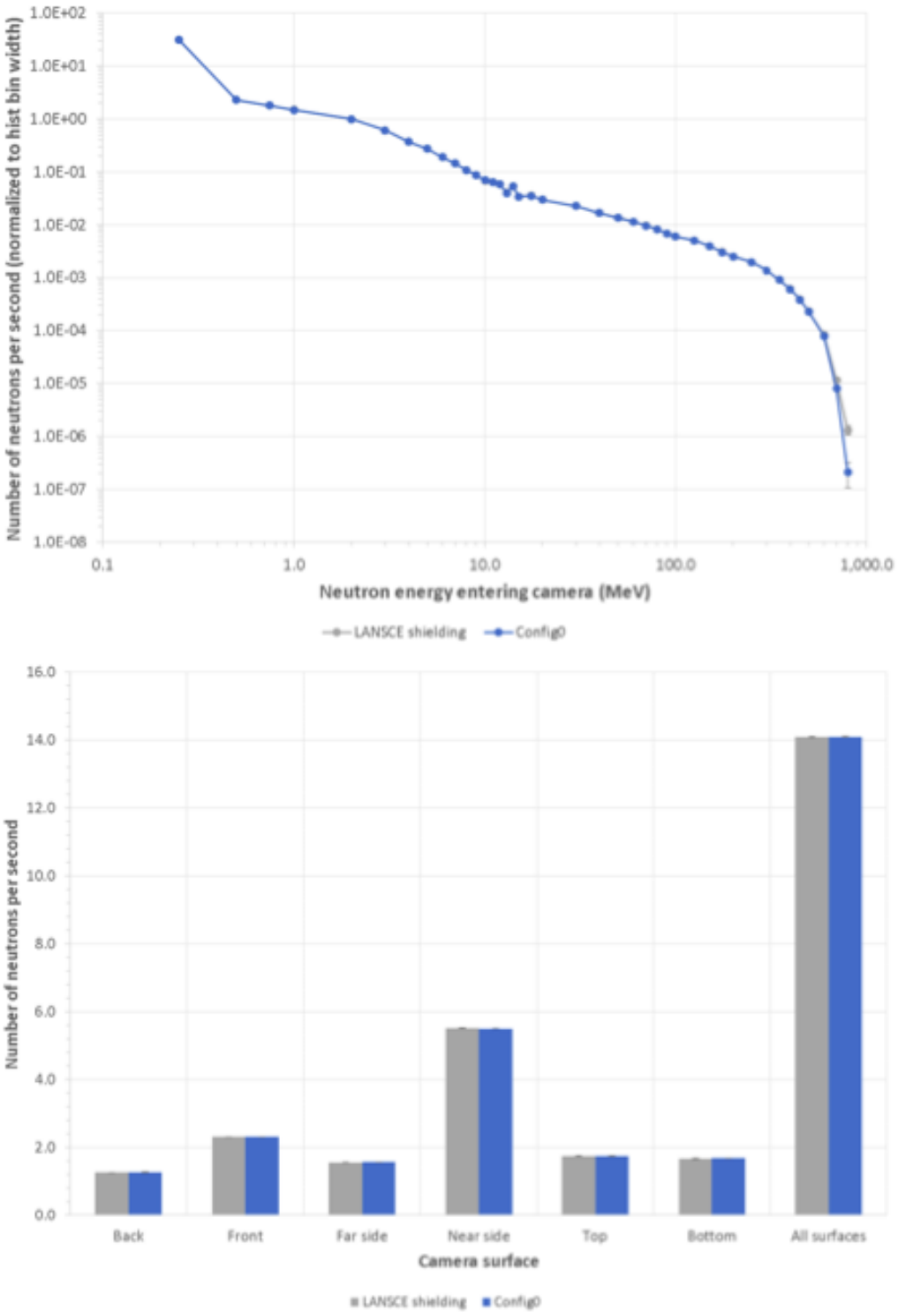


Figure 7.26: Energy distribution (top) and surface current (bottom) for neutrons entering the camera body and for Configuration 0 as compared to the LANSCE set-up.

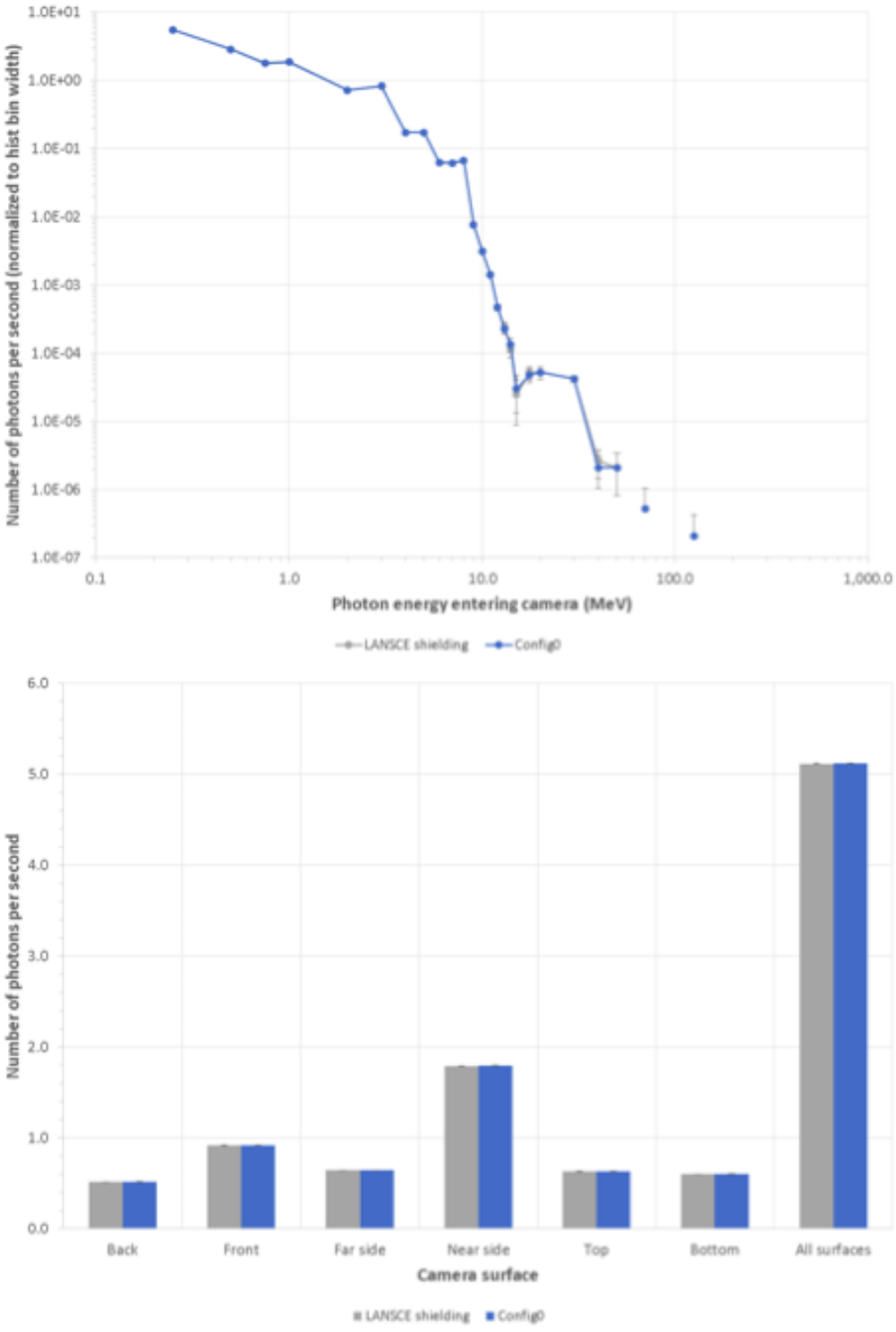


Figure 7.27: Energy distribution (top) and surface current (bottom) for photons entering the camera body and for Configuration 0 as compared to the LANSCE set-up.

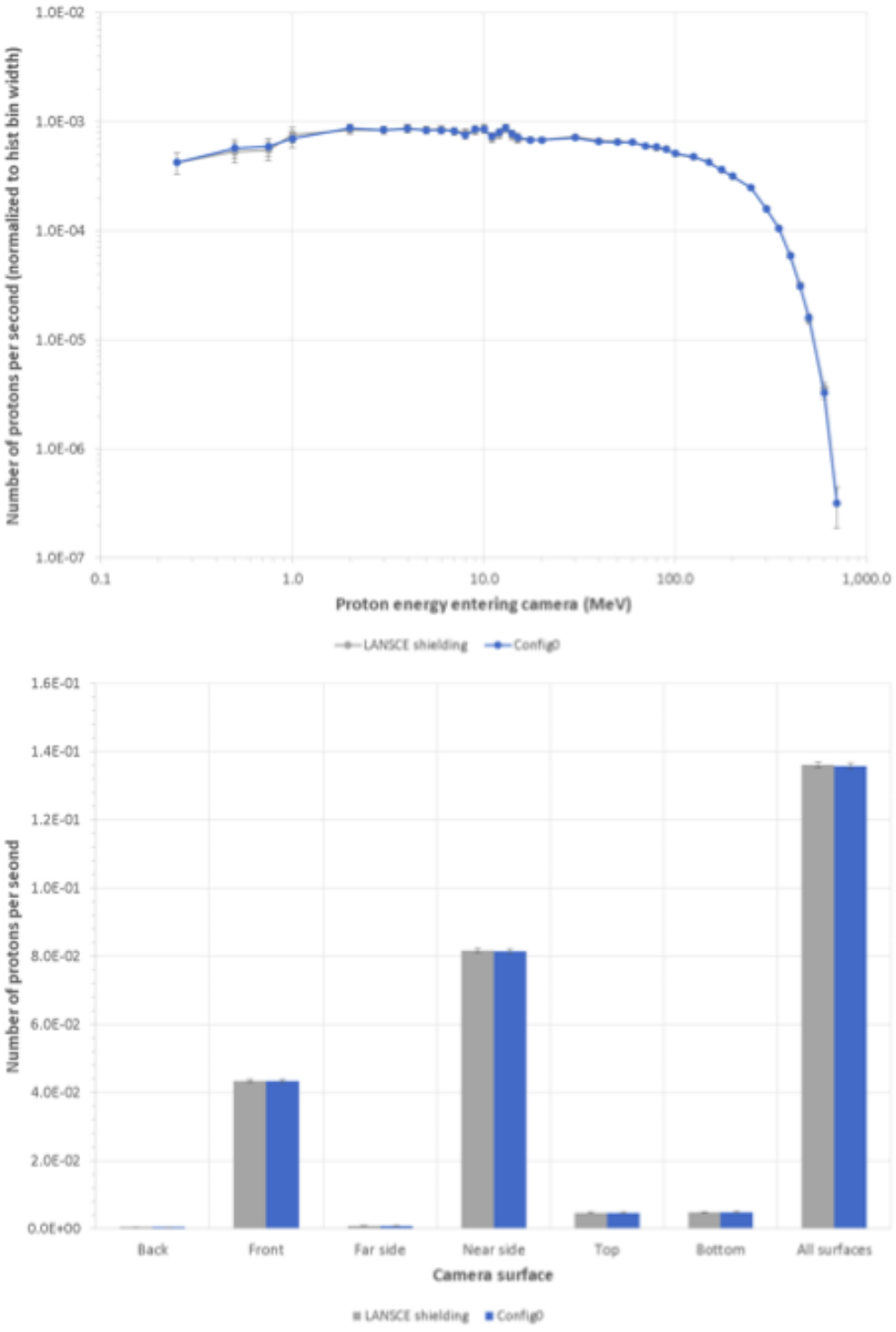


Figure 7.28: Energy distribution (top) and surface current (bottom) for protons entering the camera body and for Configuration 0 as compared to the LANSCE set-up.

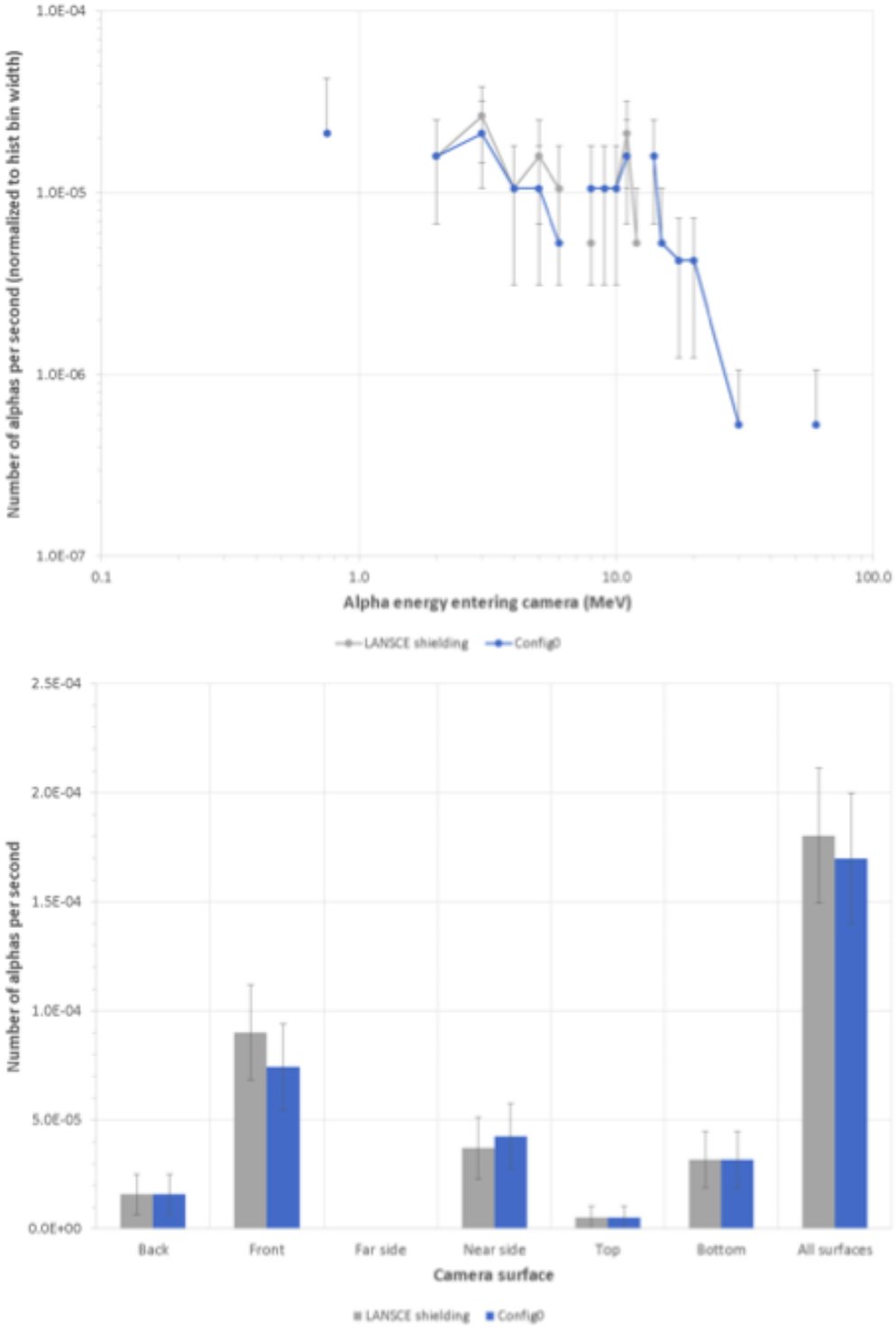


Figure 7.29: Energy distribution (top) and surface current (bottom) for alphas entering the camera body and for Configuration 0 as compared to the LANSCE set-up.

than no dopant at all (i.e., polyethylene), but is not as good of a dopant as boron due to its comparatively lower neutron cross-section for thermal neutrons. However, above 1 MeV, the three materials shield neutrons approximately equally.

Interestingly, the proton current through the camera volume was seen to be approximately equal for Li-poly and B-poly plastics, with polyethylene having a slightly higher current than the other two materials. In contrast, the alpha current was lowest for regular polyethylene (but not by much).

As for the gamma current, Li-poly has ∼60% of the gamma current of B-poly due to having no (n,γ) cross-section. Moreover, because gammas are potentially more damaging to the CCD chip than thermal neutrons, Li-poly is a better shield material to be inside the light-tight box. In other words, it is better in this case to reduce the photon current with Li-poly than to reduce the thermal neutron current with B-poly. These results can be seen in Figures 7.30 through 7.33.

Study Eight

Study Eight examined the effect of modifying "Configuration 7" by adding a thin sheet of aluminum between the B-poly and the camera ("Configuration 8"). It was thought that the aluminum plate would reduce the photon current resulting from the (n,γ) reaction in the B-poly, while still reaping the benefit of reduced neutron current that B-poly provides. If true, B-poly plus aluminum could be more desirable than Li-poly ("Configuration 4") inside the light-tight box. The aluminum was simulated as 3 cm thick, and the B-poly and Li-Poly were simulated as 5 cm thick.

While the addition of the aluminum sheet reduced the photon current between the energies of 500 keV and 1 MeV when compared to "Configuration 7" values, the "Configuration 8" photon current increased for energies below 500 keV. This can be attributed to neutron capture by the aluminum sheet, which caused the total photon current to actually increase when compared to "Configuration 7". In either case, however, Li-poly still had the lowest total photon current (4.5 photons per second with "Configuration 4", vs. approximately 7.5 photons per second with "Configuration 8").

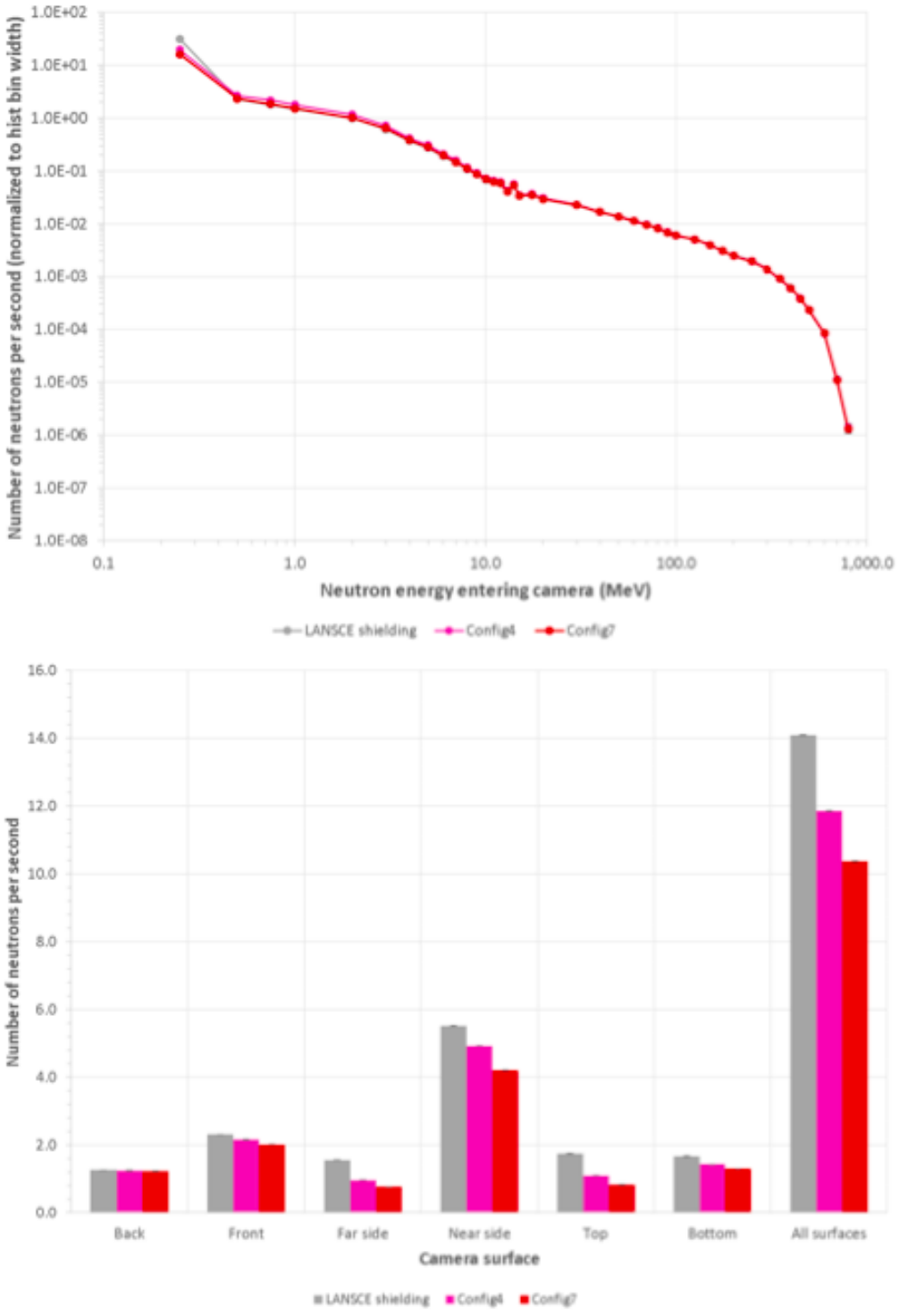


Figure 7.30: Energy distribution (top) and surface current (bottom) for neutrons entering the camera body and for Configurations 4 and 7 as compared to the LANSCE set-up.

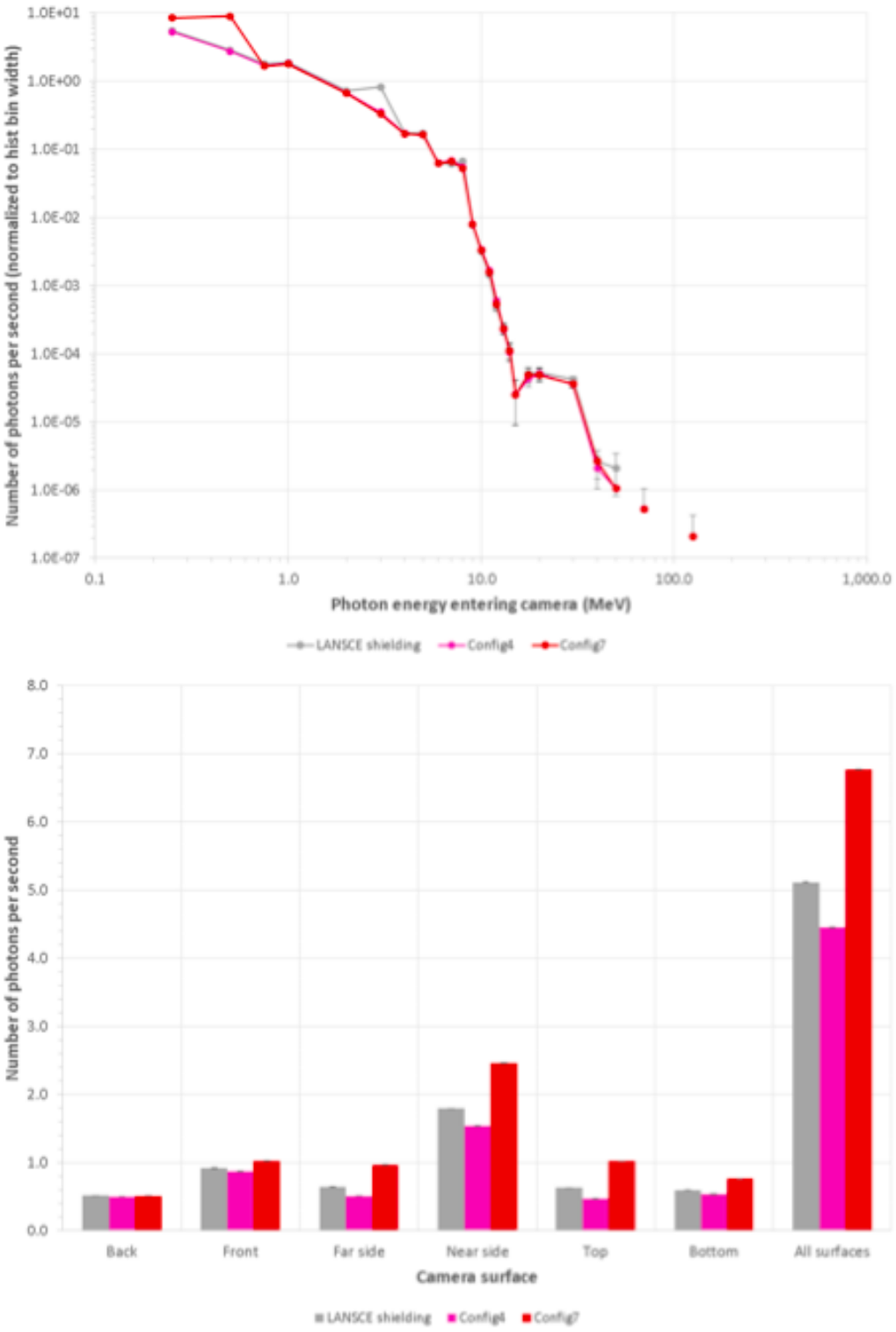


Figure 7.31: Energy distribution (top) and surface current (bottom) for photons entering the camera body and for Configurations 4 and 7 as compared to the LANSCE set-up.

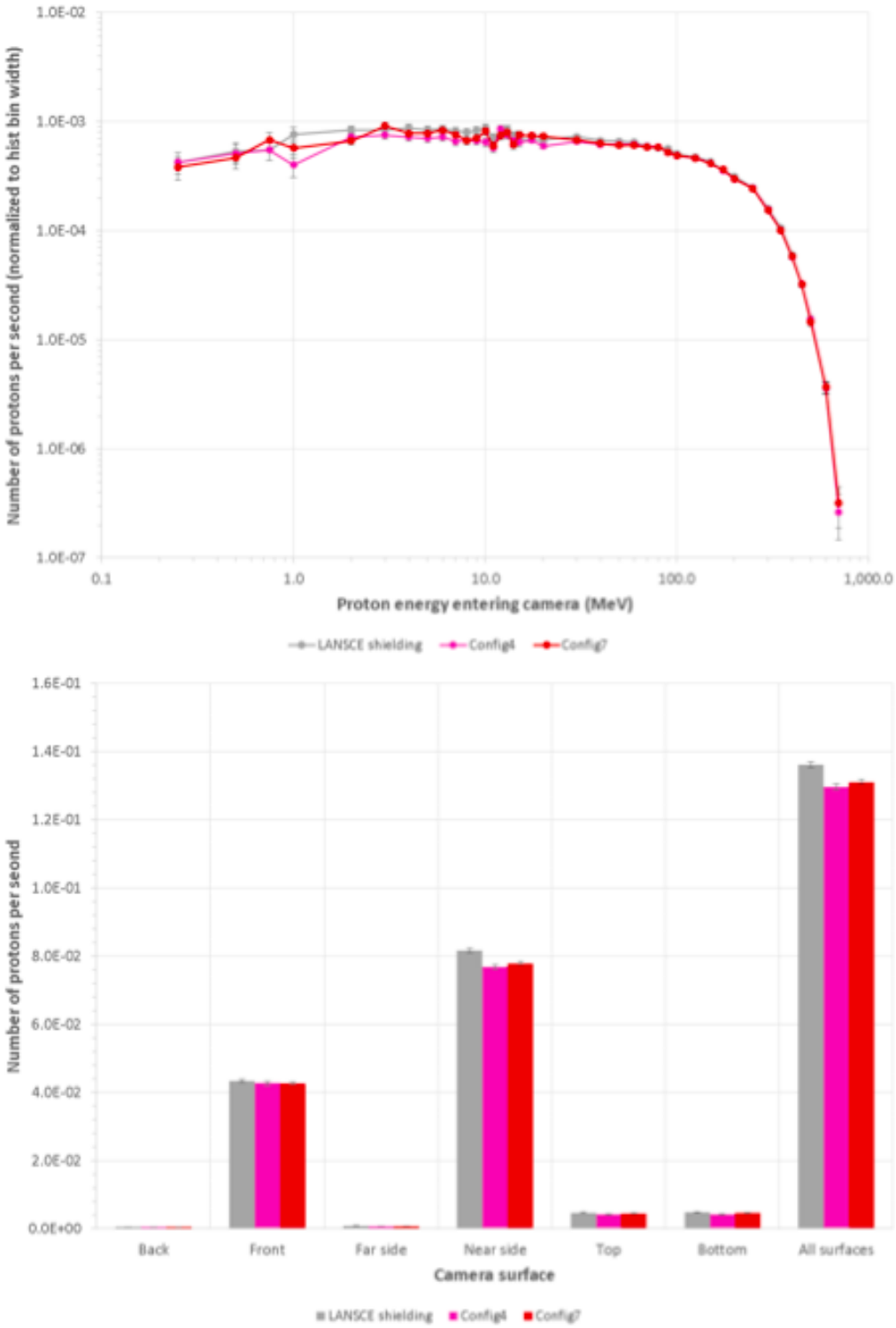


Figure 7.32: Energy distribution (top) and surface current (bottom) for protons entering the camera body and for Configurations 4 and 7 as compared to the LANSCE set-up.

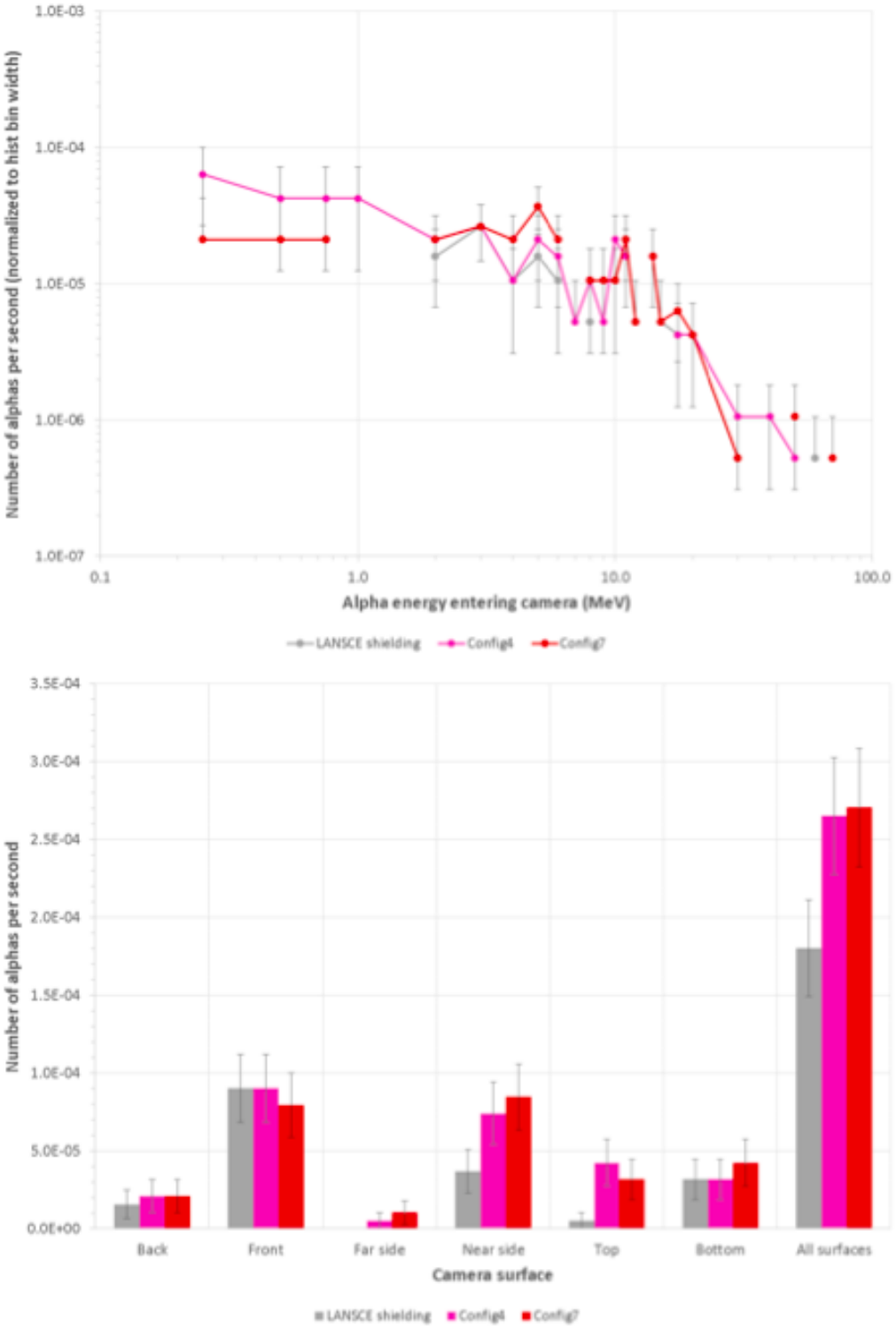


Figure 7.33: Energy distribution (top) and surface current (bottom) for alphas entering the camera body and for Configurations 4 and 7 as compared to the LANSCE set-up.

Interestingly, the total neutron current also increased when adding an aluminum sheet to "Configuration 7", causing it to match "Configuration 4" levels. This is believed to be a result of activation of the aluminum, since the thickness of the polyethylene remained constant. The aluminum sheet did reduce total proton current, however, by about 25% when compared to the other two configurations. While this is a good way to reduce energetic protons from hitting the CCD chip, the increased gamma current is worrisome enough that adding the aluminum is not recommended (due to the greater amount of photons than protons). These results can be seen in Figures 7.34 through 7.37.

Study Nine

Study Nine is similar to Study One except that, instead of comparing concrete and polyethylene shielding abilities, this study was conducted to determine whether external low-Z shielding decreased the current through the camera volume. Configurations studied include "LANSCE" (external steel and internal polyethylene shielding), "Configuration 00" (like "LANSCE" but also with external polyethylene placed around the light-tight box), "Configuration 5" (like "Configuration 00" but with Li-poly inside the light-tight box), and "Configuration 9" (like "Configuration 00" but with B-poly inside the light-tight box).

It was found that, in all cases, placing polyethylene shielding around the light-tight box increases current through the camera volume (Figures 7.38 through 7.41). This is a result of the low-Z material scattering particles into the light-tight box that would have otherwise missed the box. For all four particle types studied, "LANSCE" had significantly less total current (approximately 25% in all cases) than the other three configurations. There appears to be no reason to add polyethylene around the light-tight box unless there is a very large scatterer in the beam line that is more worrisome than scattering direct beam into the box (which is unlikely and is not accounted for in these simulations).

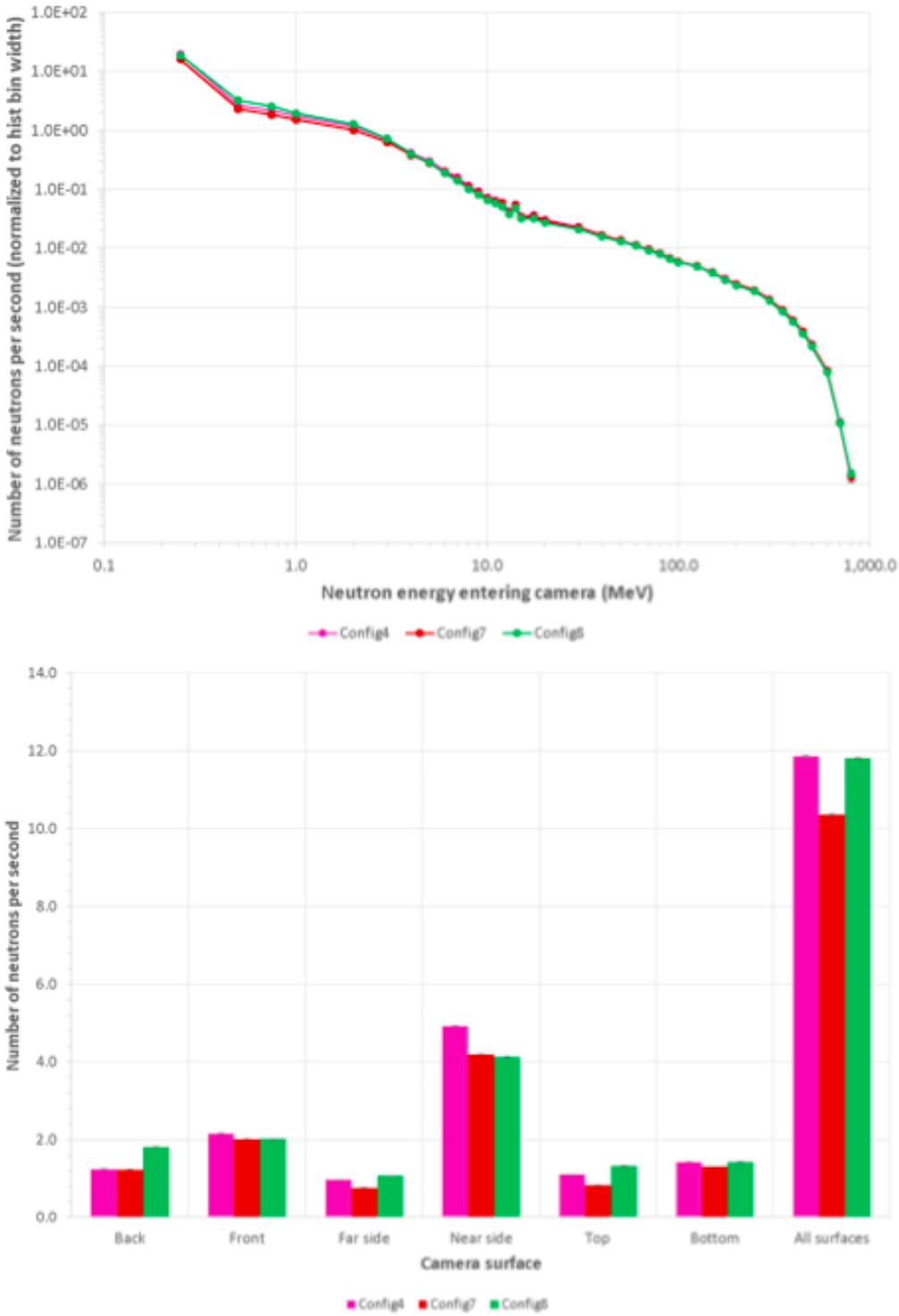


Figure 7.34: Energy distribution (top) and surface current (bottom) for neutrons entering the camera body and for Configurations 4, 7, and 8.

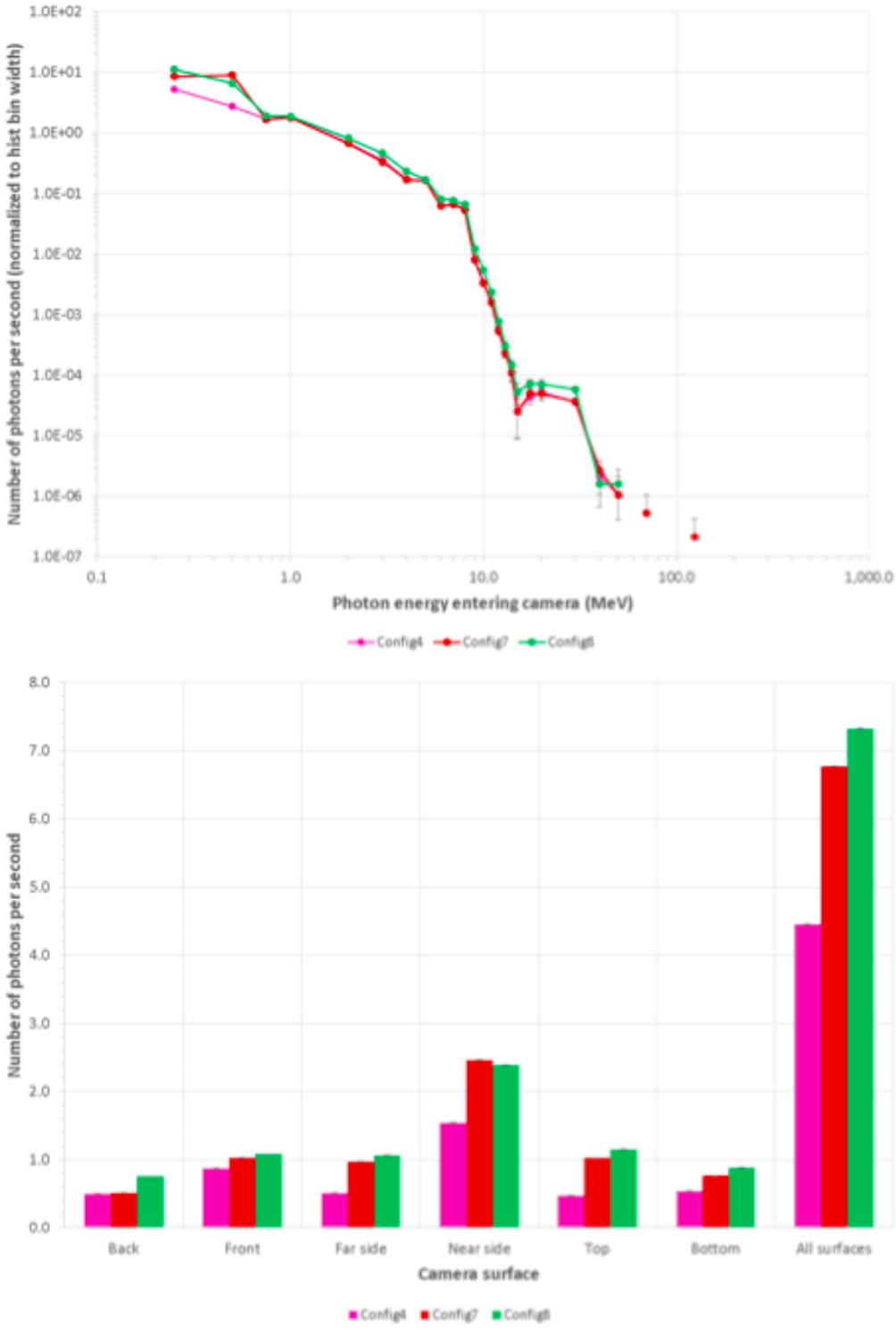


Figure 7.35: Energy distribution (top) and surface current (bottom) for photons entering the camera body and for Configurations 4, 7, and 8.

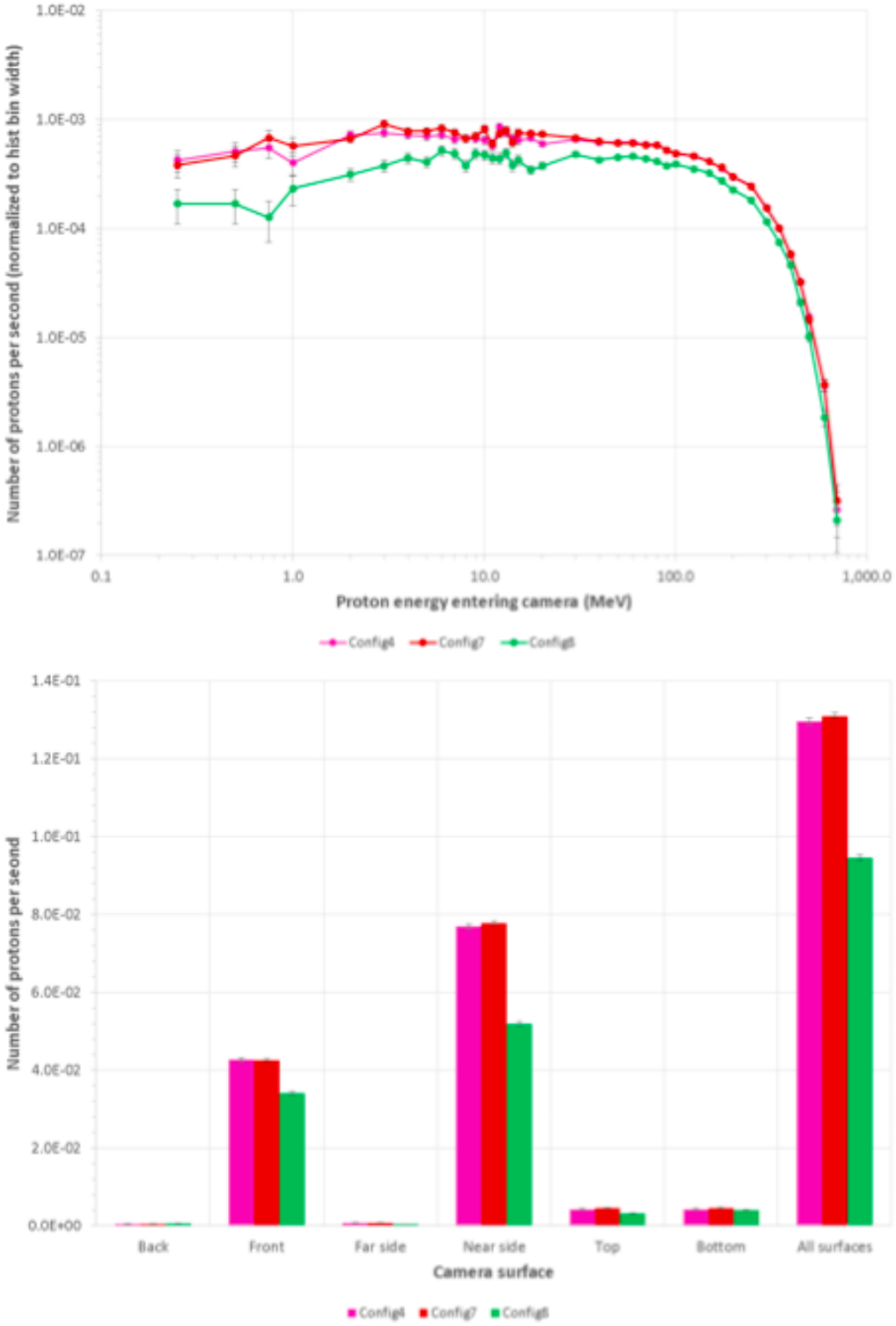


Figure 7.36: Energy distribution (top) and surface current (bottom) for protons entering the camera body and for Configurations 4, 7, and 8.



Figure 7.37: Energy distribution (top) and surface current (bottom) for alphas entering the camera body and for Configurations 4, 7, and 8.

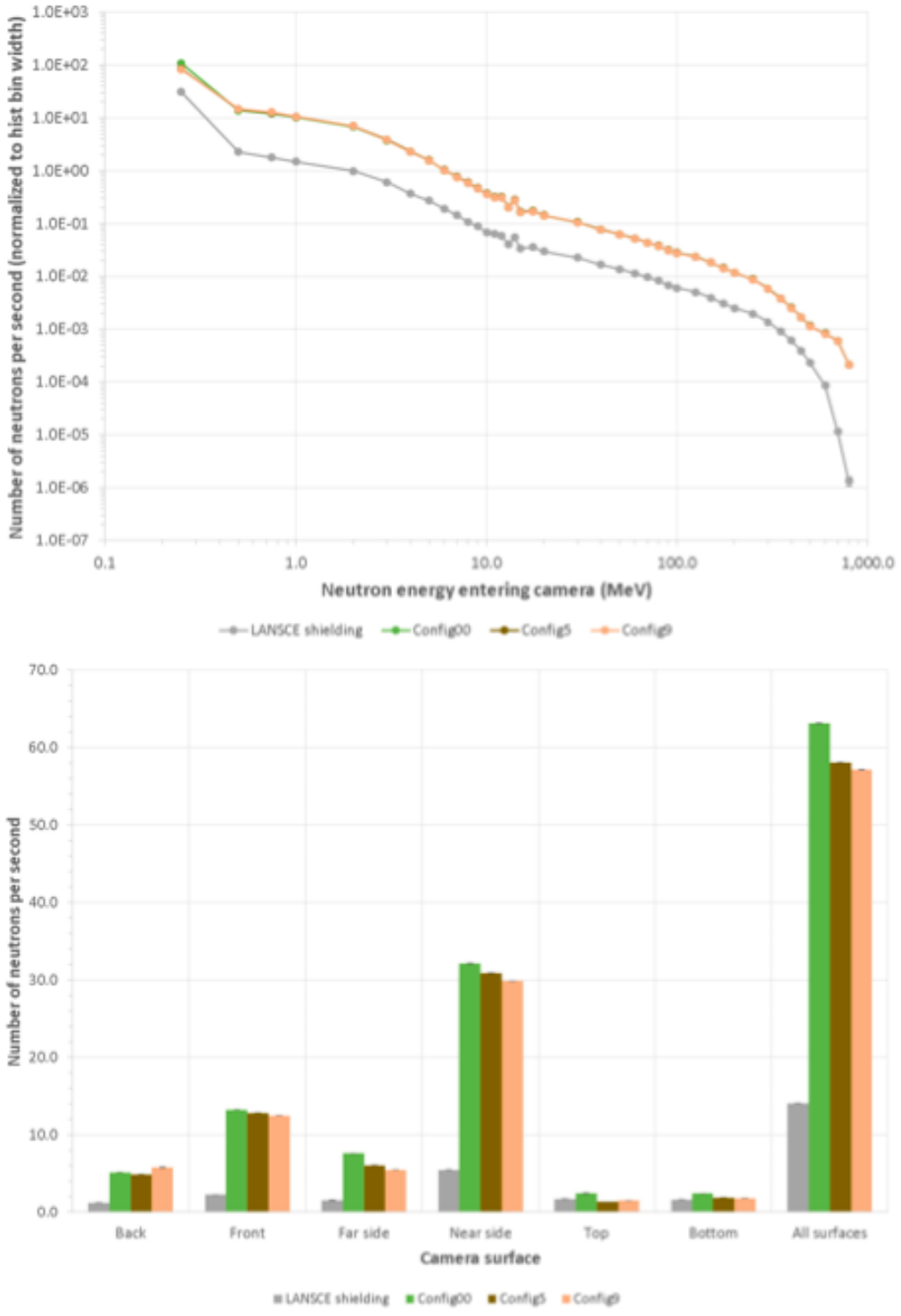


Figure 7.38: Energy distribution (top) and surface current (bottom) for neutrons entering the camera body and for Configurations 00, 5, and 9 as compared to the LANSCE set-up.

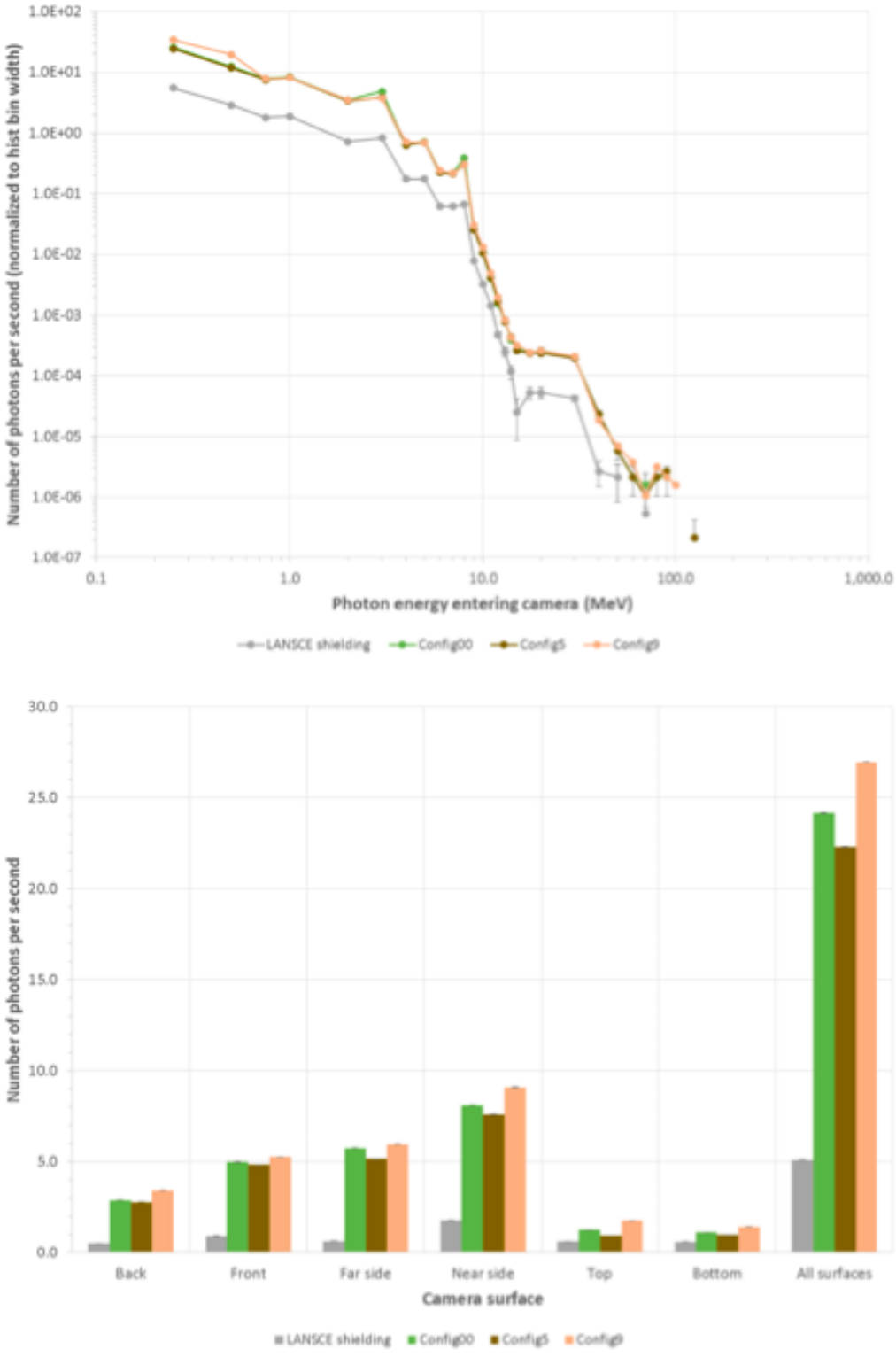


Figure 7.39: Energy distribution (top) and surface current (bottom) for photons entering the camera body and for Configurations 00, 5, and 9 as compared to the LANSCE set-up.

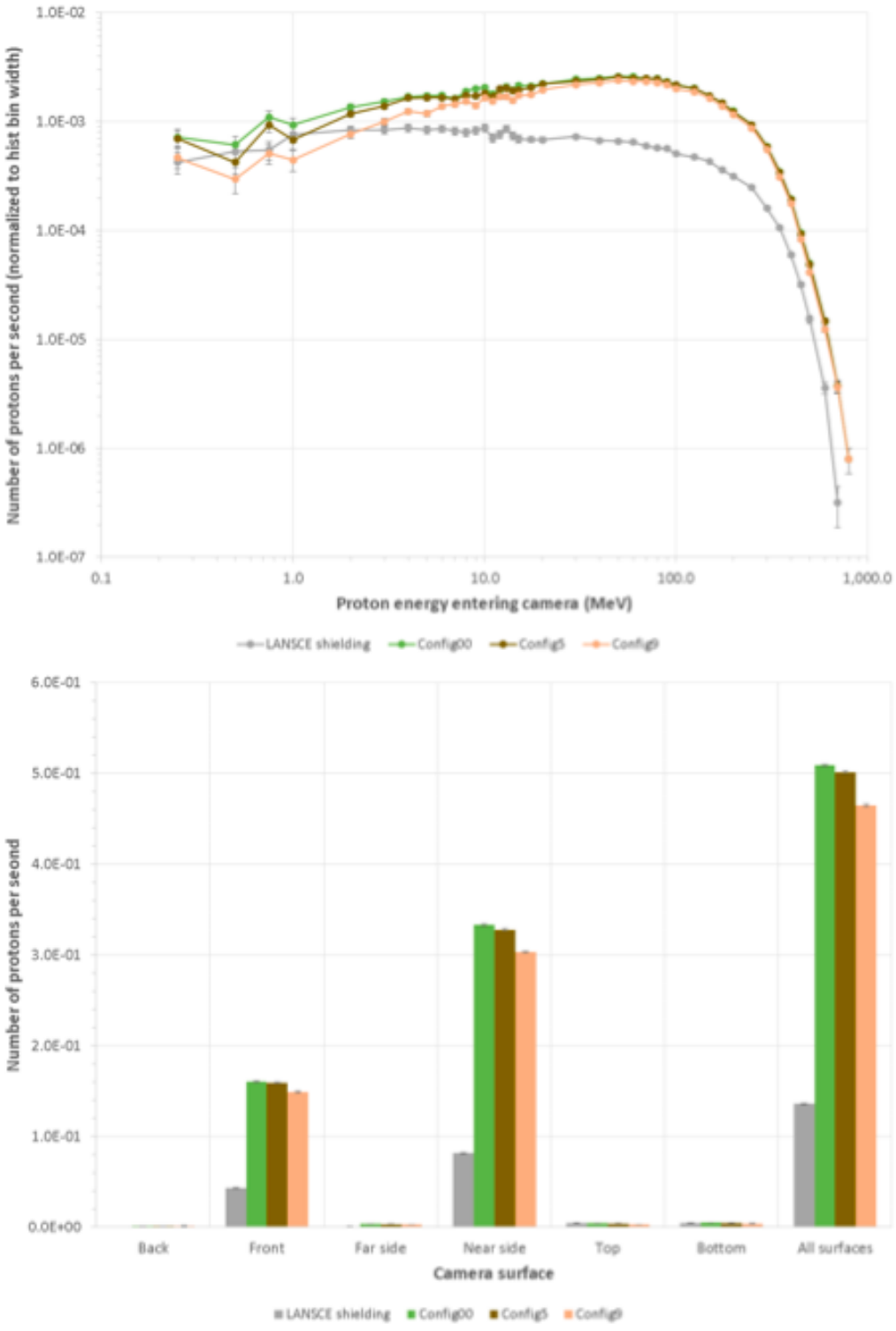


Figure 7.40: Energy distribution (top) and surface current (bottom) for protons entering the camera body and for Configurations 00, 5, and 9 as compared to the LANSCE set-up.

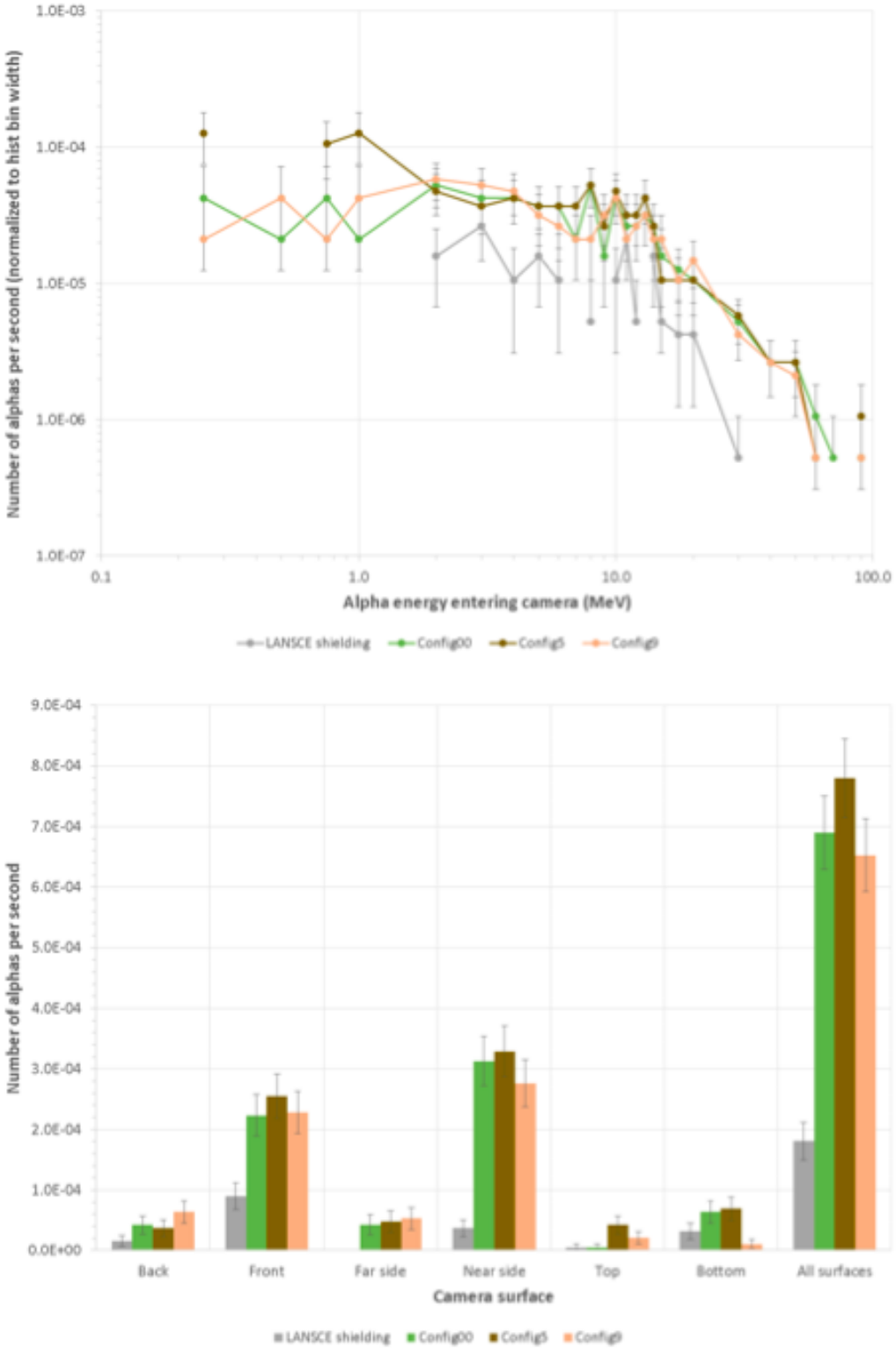


Figure 7.41: Energy distribution (top) and surface current (bottom) for alphas entering the camera body and for Configurations 00, 5, and 9 as compared to the LANSCE set-up.

Study Ten

In further support of the conclusions of Study Six, Seven, and Nine, this study examined whether a better shielding design consisted of Li-poly internally and 2 ft of steel externally ("Configuration 4"), "Configuration 4" plus external polyethylene ("Configuration 5"), or "Configuration 4" with 4 ft of external steel ("Configuration 6"). Results showed that, as expected, "Configuration 4" had the lowest neutron current of the three configurations (approximately 25% or less).

Interestingly, "Configuration 5" and "Configuration 6" had nearly identical current profiles for neutrons, protons, photons, and alphas, meaning that the external steel can be just as much of a scatterer as external polyethylene. Thus, Study Ten shows that care must be taken with shielding placed external to the light-tight box and that in most cases, as was found in Study Nine, external shielding can hurt more than it helps. Relevant plots for these three configurations can be seen in Figures 7.42 through 7.45.

Study Eleven

Study Eleven was conducted to determine whether it is better to have lead inside the light-tight box between the Li-poly shielding and camera ("Configuration 15"), or if it is better to also add lead behind the external steel shield so that it is both internal and external to the light-tight box ("Configuration 14"). It was found, like in Study Four, that placing lead behind the external steel shielding did not significantly reduce the current for any of the four particles studied (Figures 7.46 through 7.49). Neutron current was particularly unaffected by adding lead behind the steel shielding. Thus, for weight, cost, and safety considerations, it is better to limit the use of lead to inside the light-tight box.

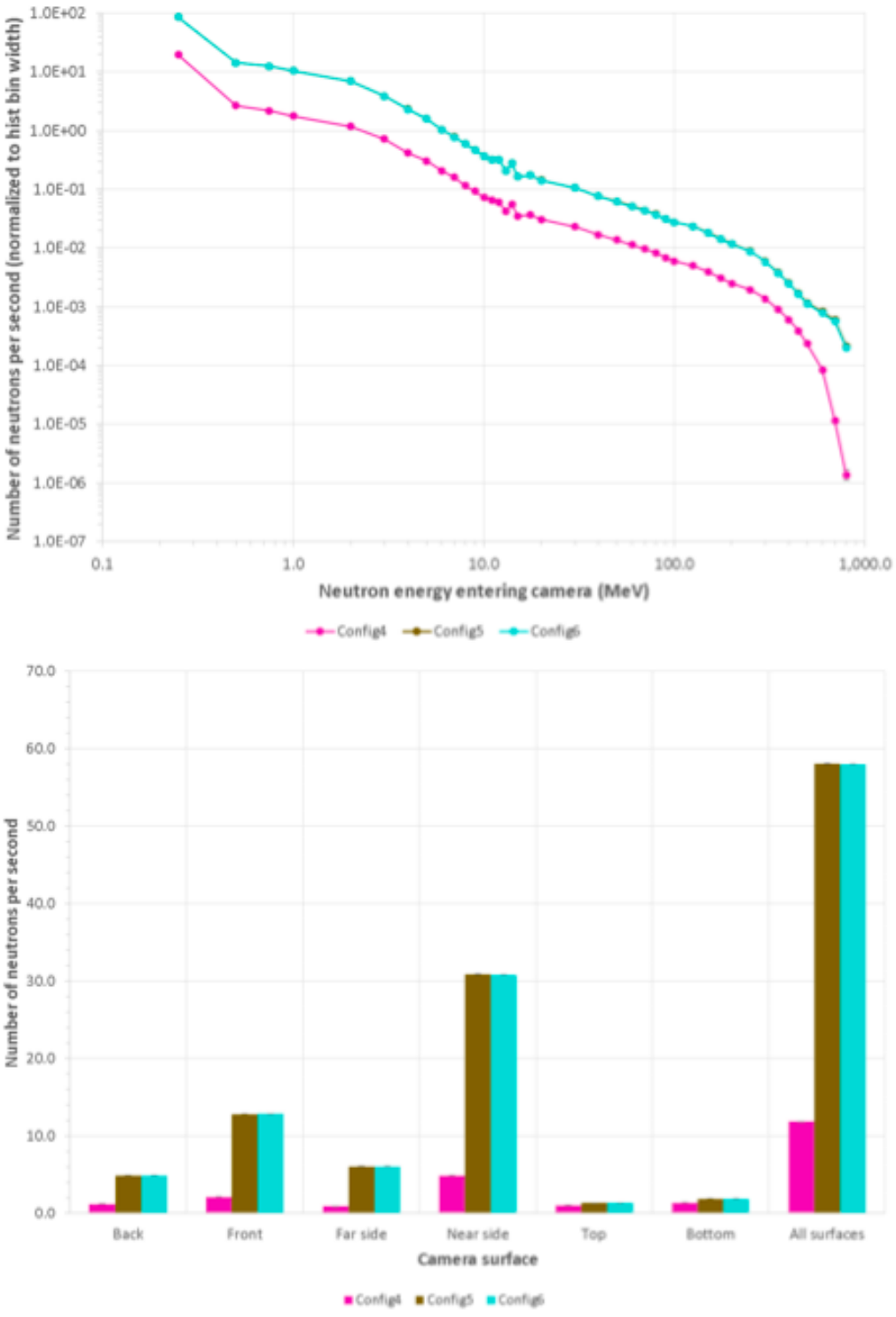


Figure 7.42: Energy distribution (top) and surface current (bottom) for neutrons entering the camera body and for Configurations 4, 5, and 6.

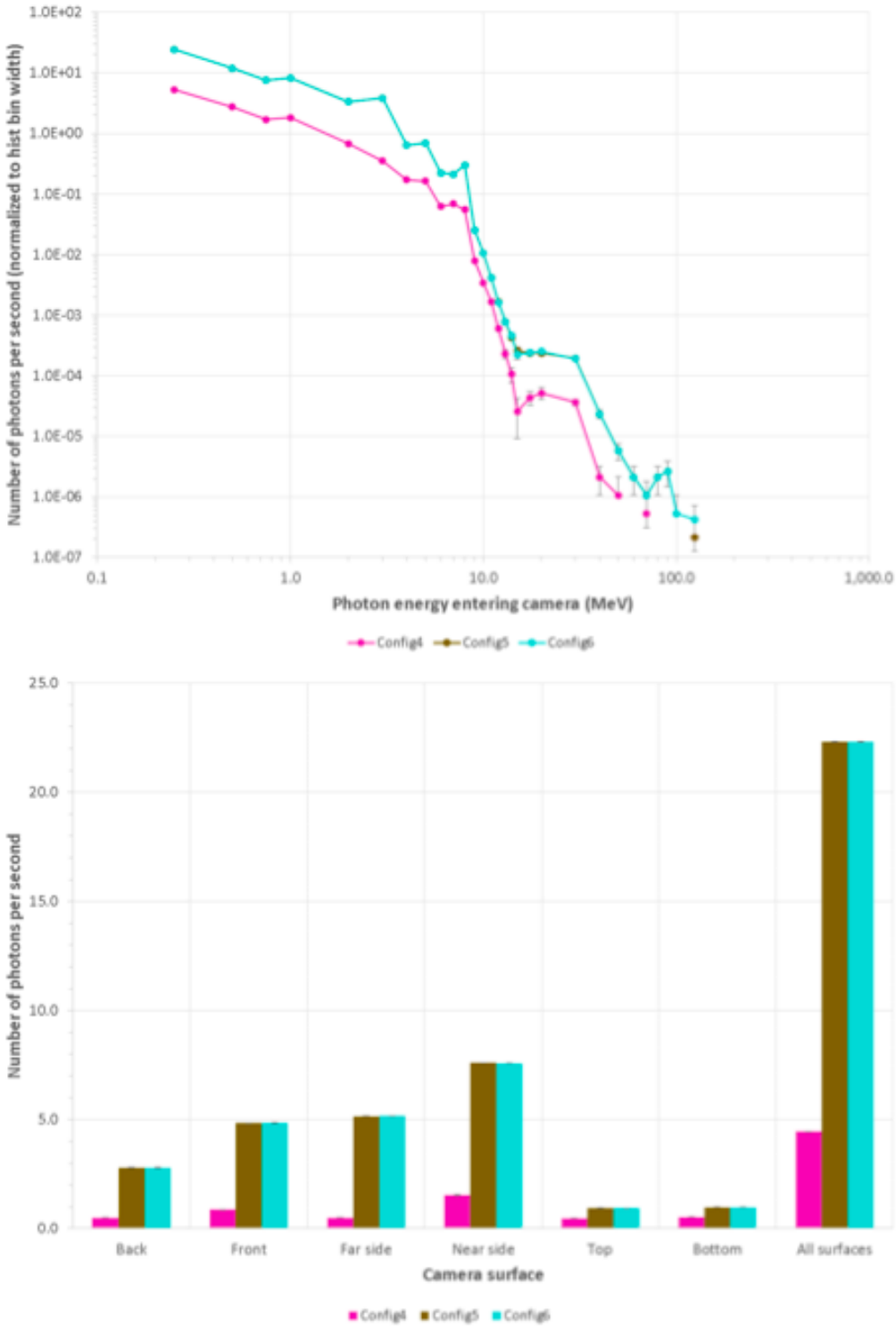


Figure 7.43: Energy distribution (top) and surface current (bottom) for photons entering the camera body and for Configurations 4, 5, and 6.

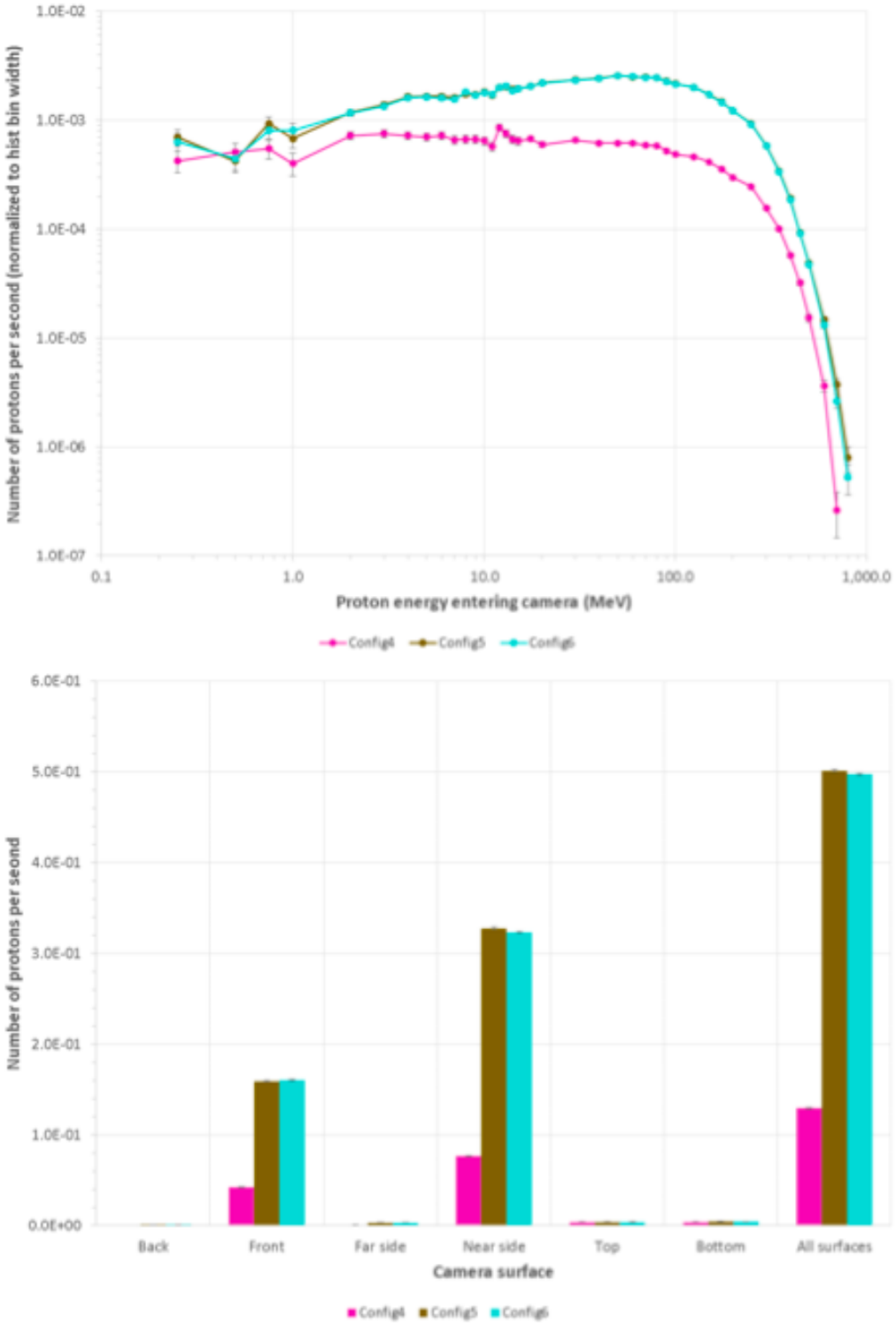


Figure 7.44: Energy distribution (top) and surface current (bottom) for protons entering the camera body and for Configurations 4, 5, and 6.

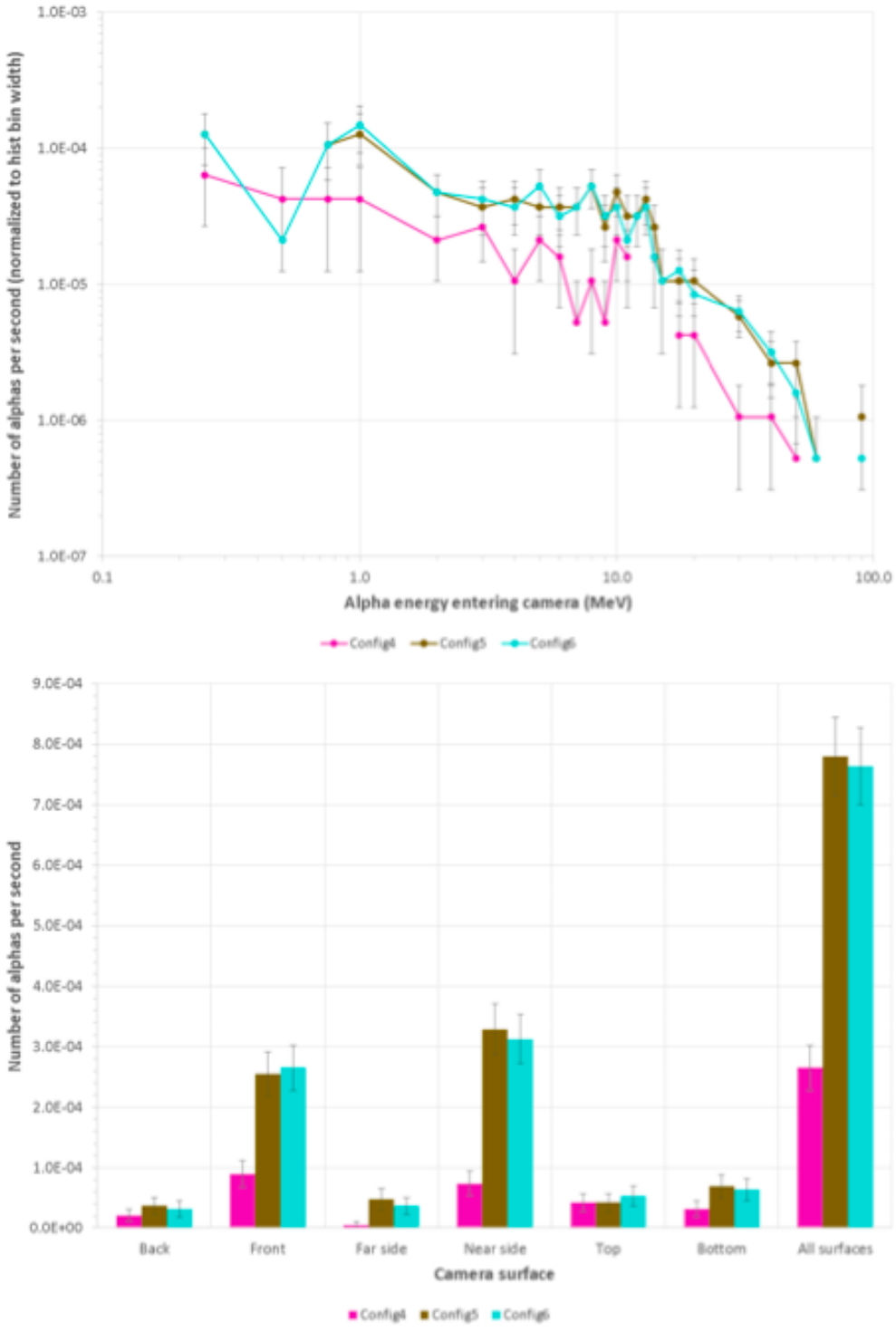


Figure 7.45: Energy distribution (top) and surface current (bottom) for alphas entering the camera body and for Configurations 4, 5, and 6.

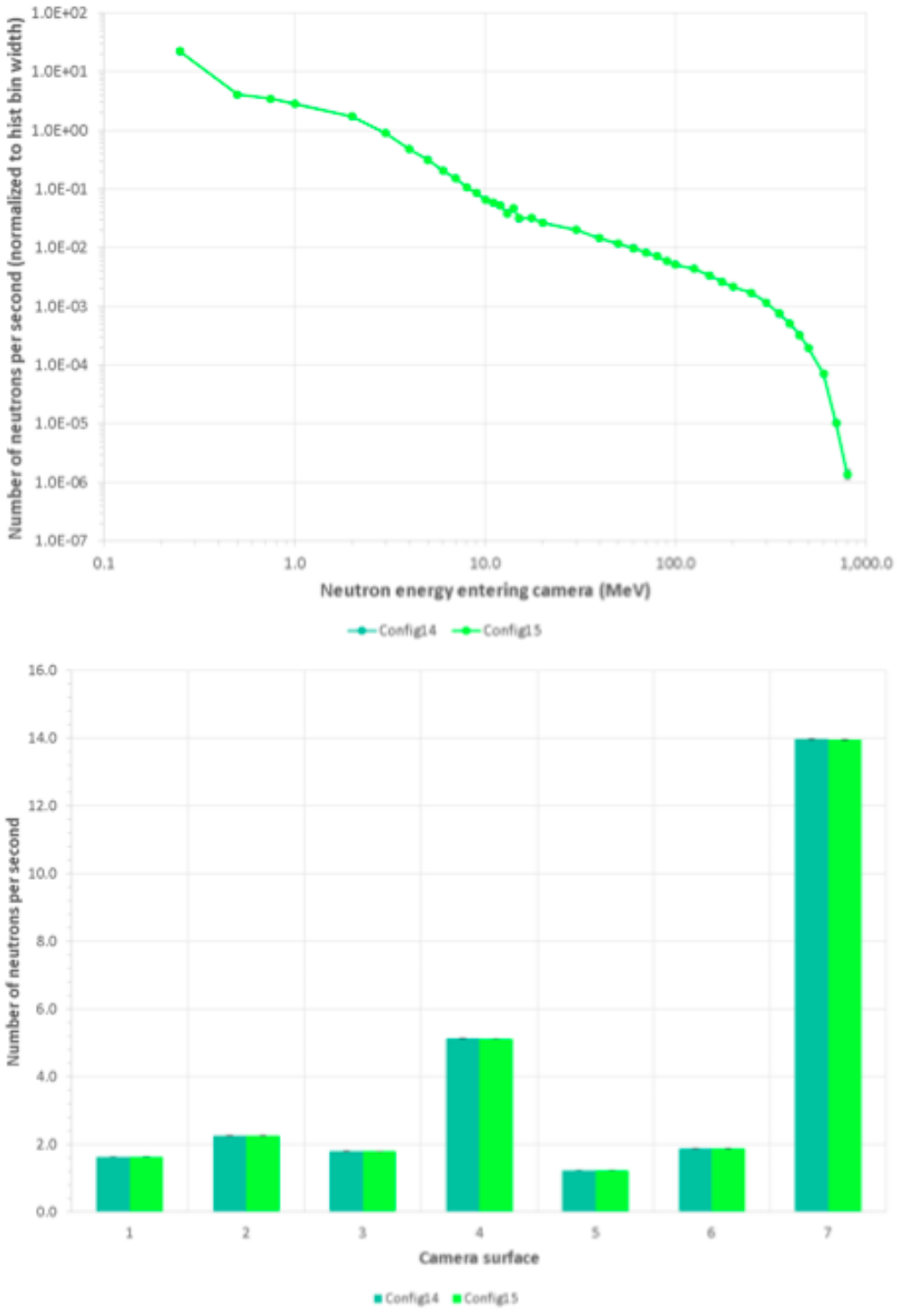


Figure 7.46: Energy distribution (top) and surface current (bottom) for neutrons entering the camera body and for Configurations 14 and 15.

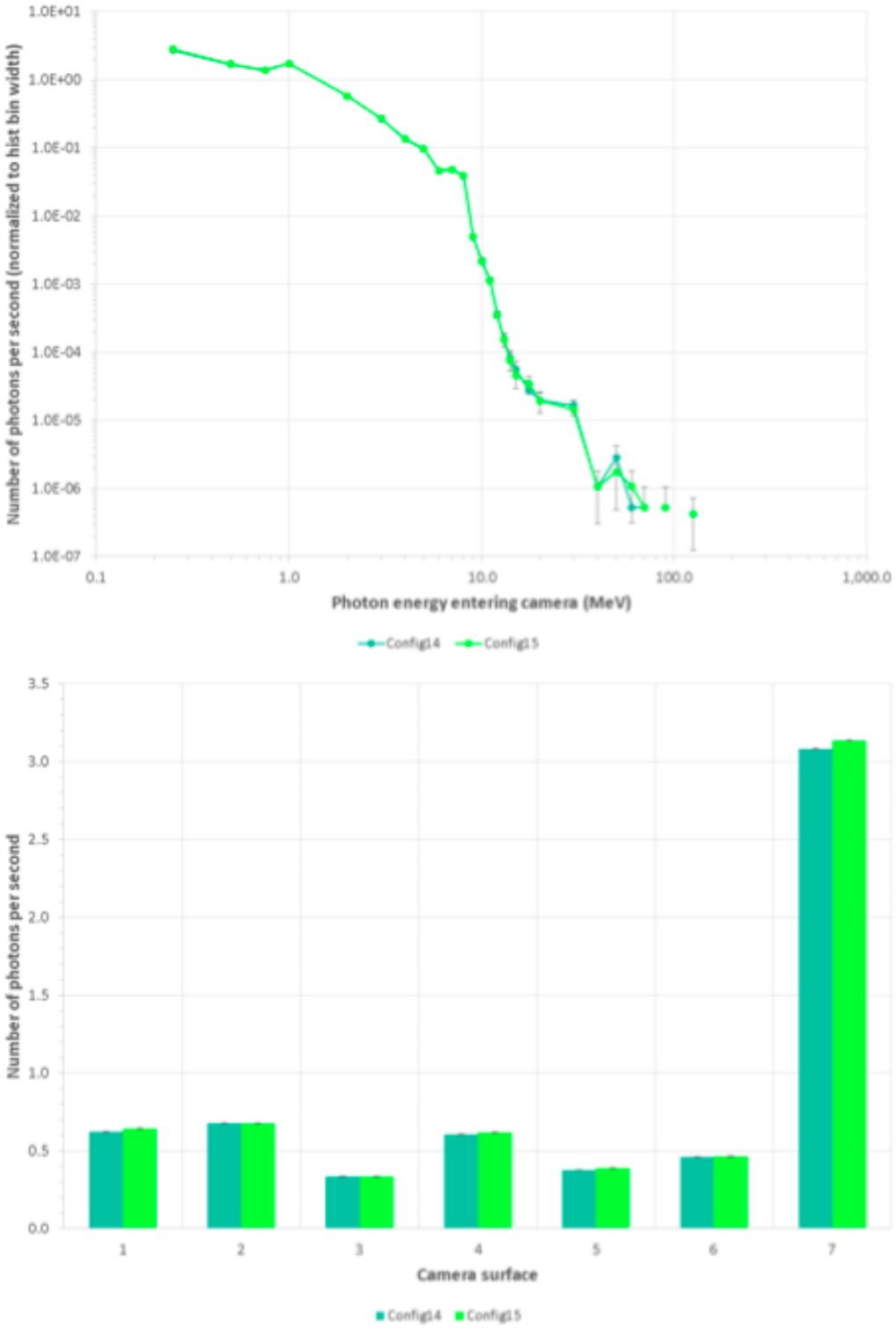


Figure 7.47: Energy distribution (top) and surface current (bottom) for photons entering the camera body and for Configurations 14 and 15.

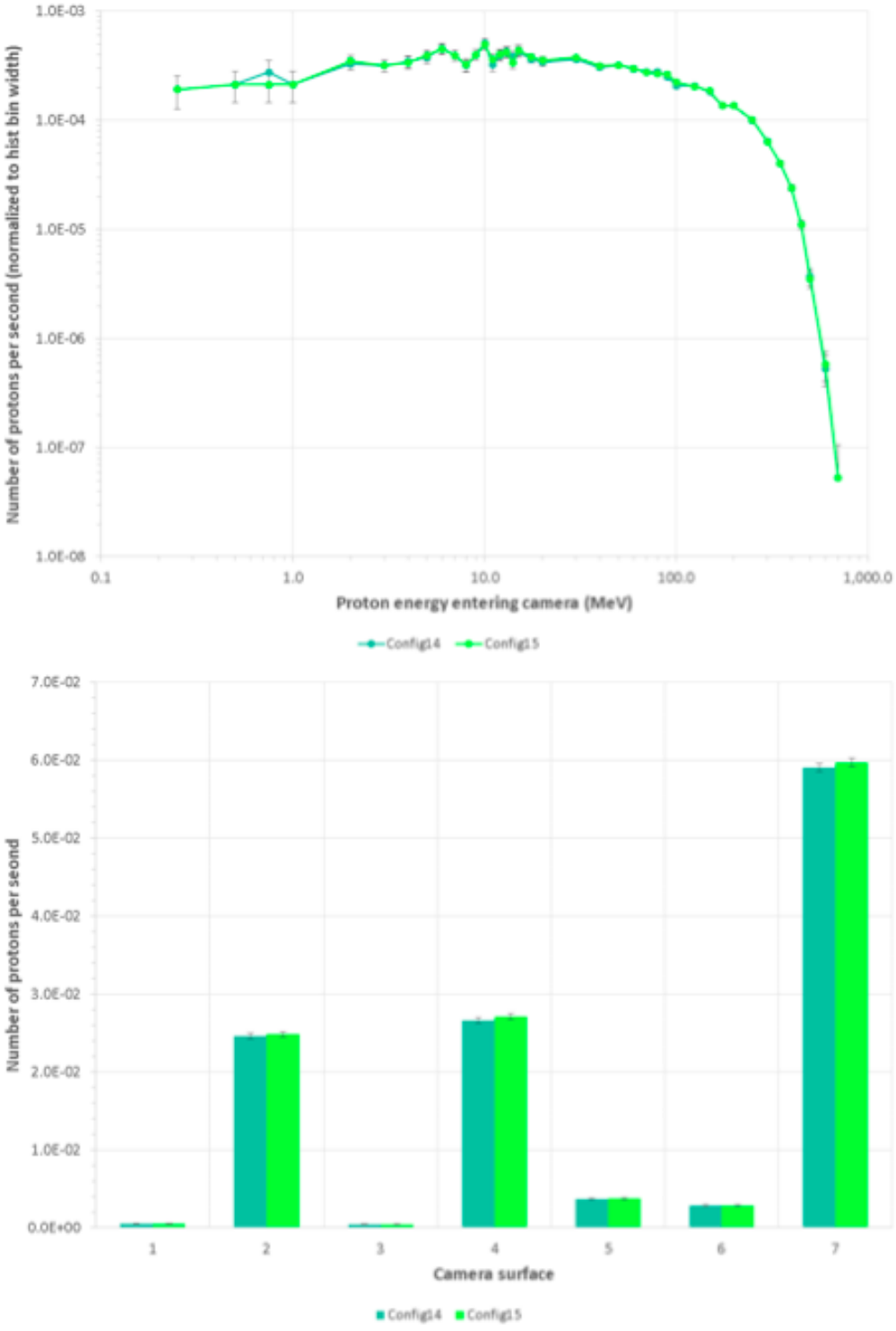


Figure 7.48: Energy distribution (top) and surface current (bottom) for protons entering the camera body and for Configurations 14 and 15.

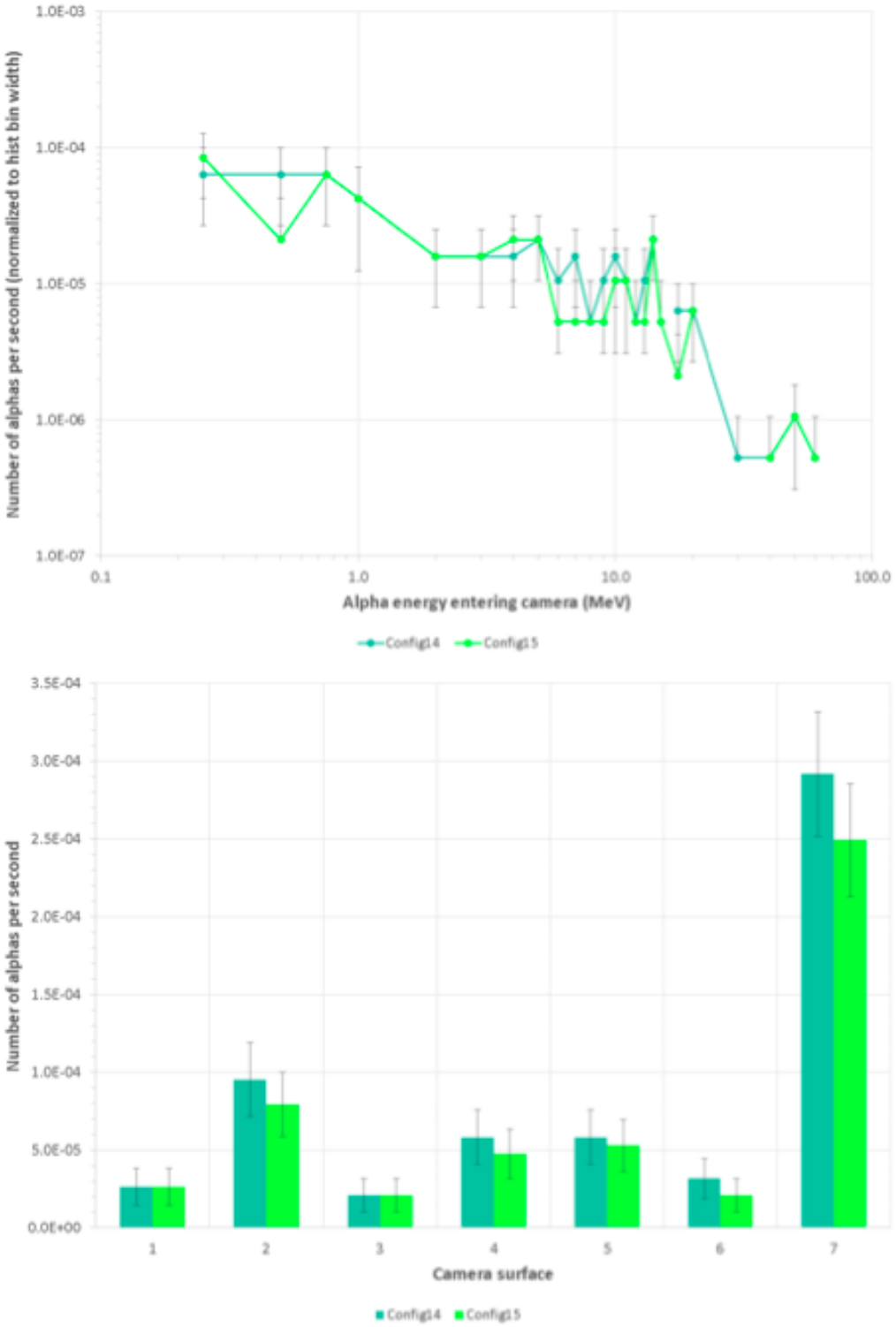


Figure 7.49: Energy distribution (top) and surface current (bottom) for alphas entering the camera body and for Configurations 14 and 15.

Study Twelve

It was thought that perhaps bismuth would be a better internal shield ("Configuration 16") than lead ("Configuration 15") when combined with Li-poly. Study Twelve showed that, while bismuth reduces neutron and gamma currents slightly when compared to lead (particularly the 1 MeV gammas that are seen with Li-poly), the high-energy proton current is elevated by using bismuth instead of lead (Figures 7.50 through 7.53). This is worrisome because, as stated before, protons are more damaging to the ICCD chip than photons of the same energy. Thus, bismuth is not recommended for this high-energy application.

Study Thirteen

The final study, Study Thirteen, was conducted to isolate the best overall design from the configurations simulated and to determine if it was indeed better than the previous design used in FP15R ("LANSCE"). It was found that, overall, the best design is "Configuration 15" (Figures 7.54 through 7.57). First, this configuration does not use external polyethylene shielding, which scatters particles into the light-tight box. Second, "Configuration 15" uses external steel shielding, which is best for reducing high-energy neutron current when compared to concrete or graphite, and only needs to be 2 ft thick. Next, this design uses Li-poly, which does not have the gamma output of B-poly, but is almost as good at attenuating neutrons as B-poly. Finally, lead placed between the Li-poly and the camera reduces the photon and proton current, which is beneficial for protecting the ICCD chip.

When compared to "LANSCE" particle current levels, "Configuration 15" is better (Figures 7.58 through 7.61). While "Configuration 15" has slightly higher thermal neutron current, this is not a potential source of immediate damage to the ICCD chip, and the total neutron current is reduced by "Configuration 15" when compared to "LANSCE". Greater reductions are seen in the total photon and proton current when using "Configuration 15" instead of "LANSCE", with both types of

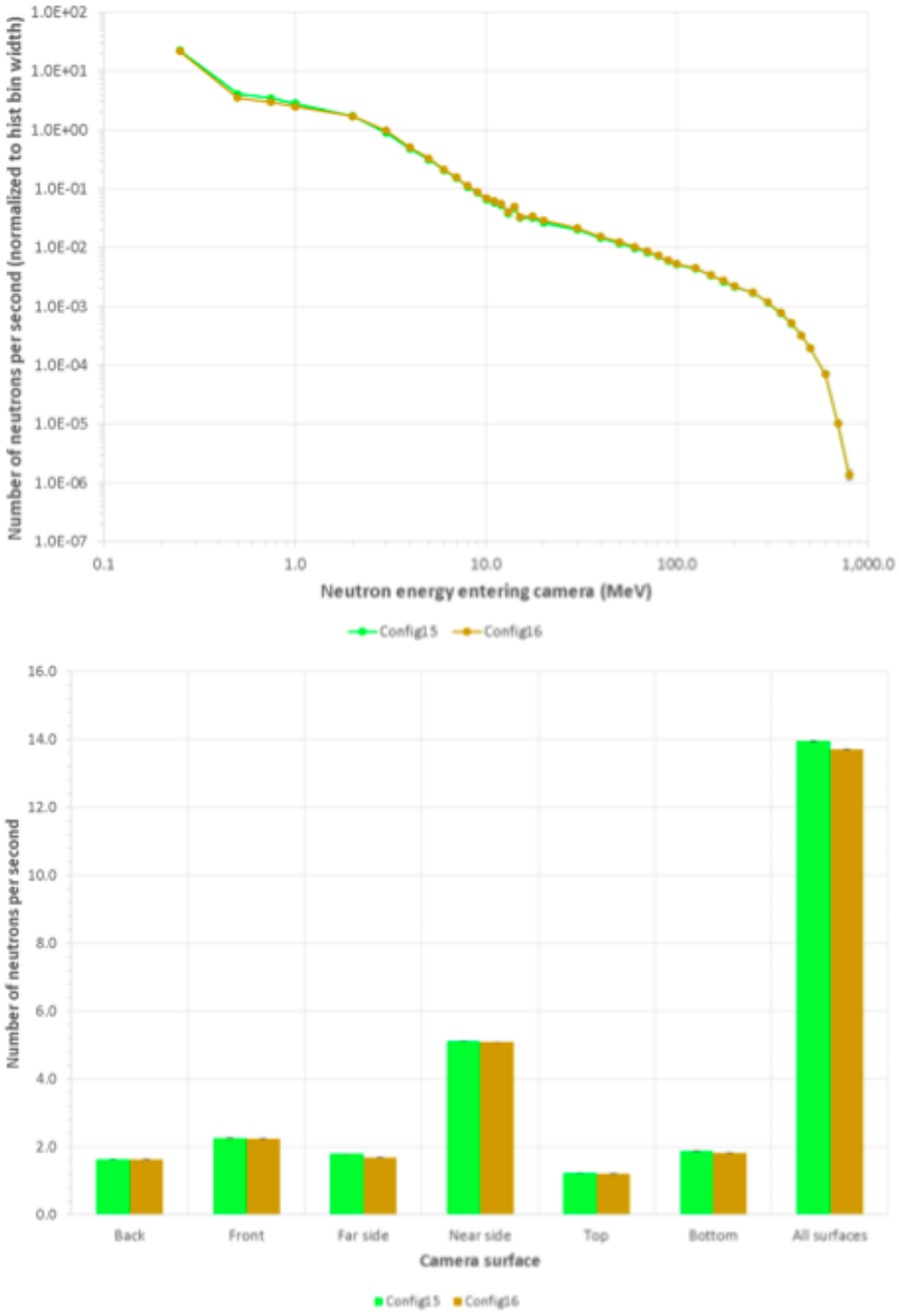


Figure 7.50: Energy distribution (top) and surface current (bottom) for neutrons entering the camera body and for Configurations 15 and 16.

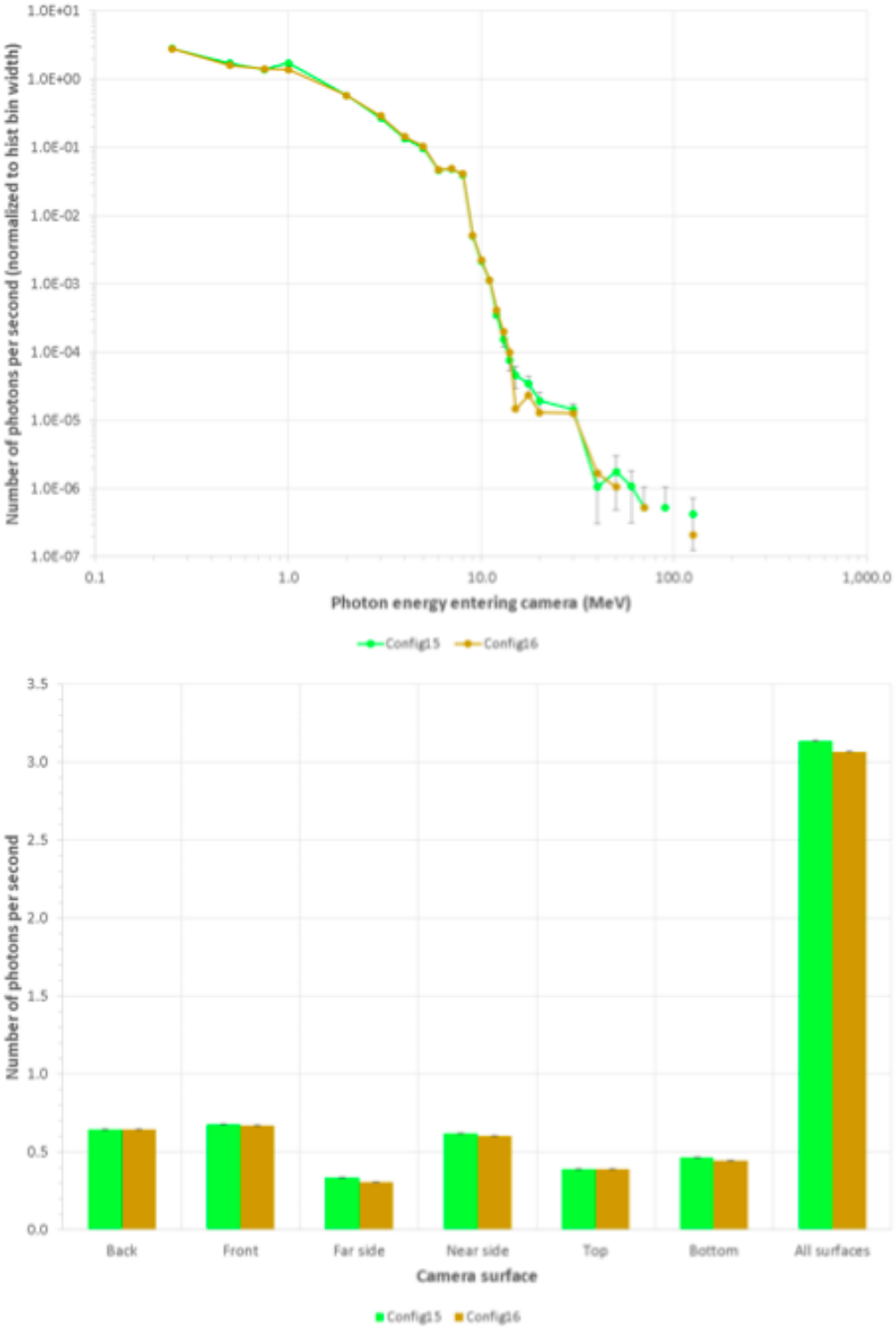


Figure 7.51: Energy distribution (top) and surface current (bottom) for photons entering the camera body and for Configurations 15 and 16.

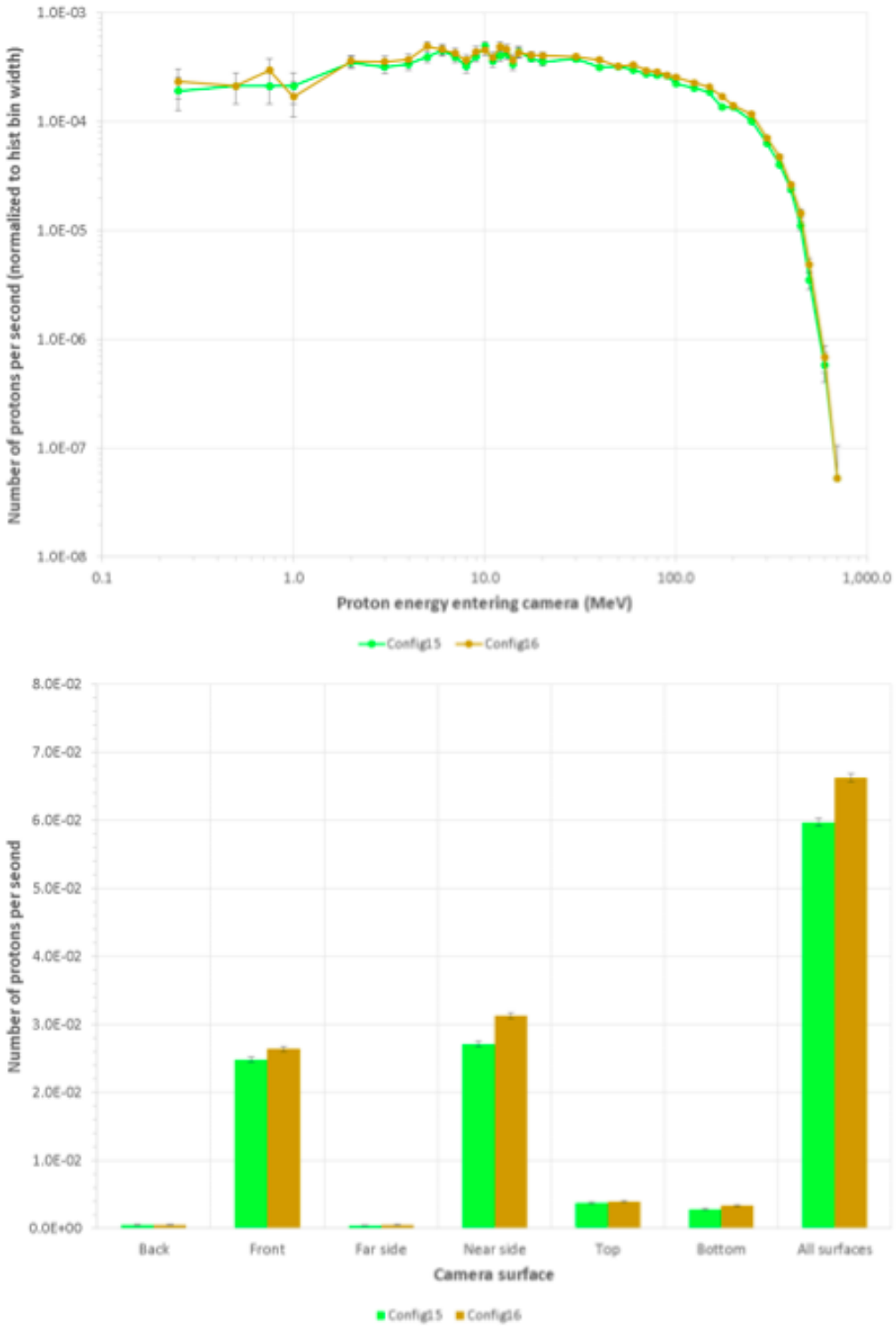


Figure 7.52: Energy distribution (top) and surface current (bottom) for protons entering the camera body and for Configurations 15 and 16.



Figure 7.53: Energy distribution (top) and surface current (bottom) for alphas entering the camera body and for Configurations 15 and 16.

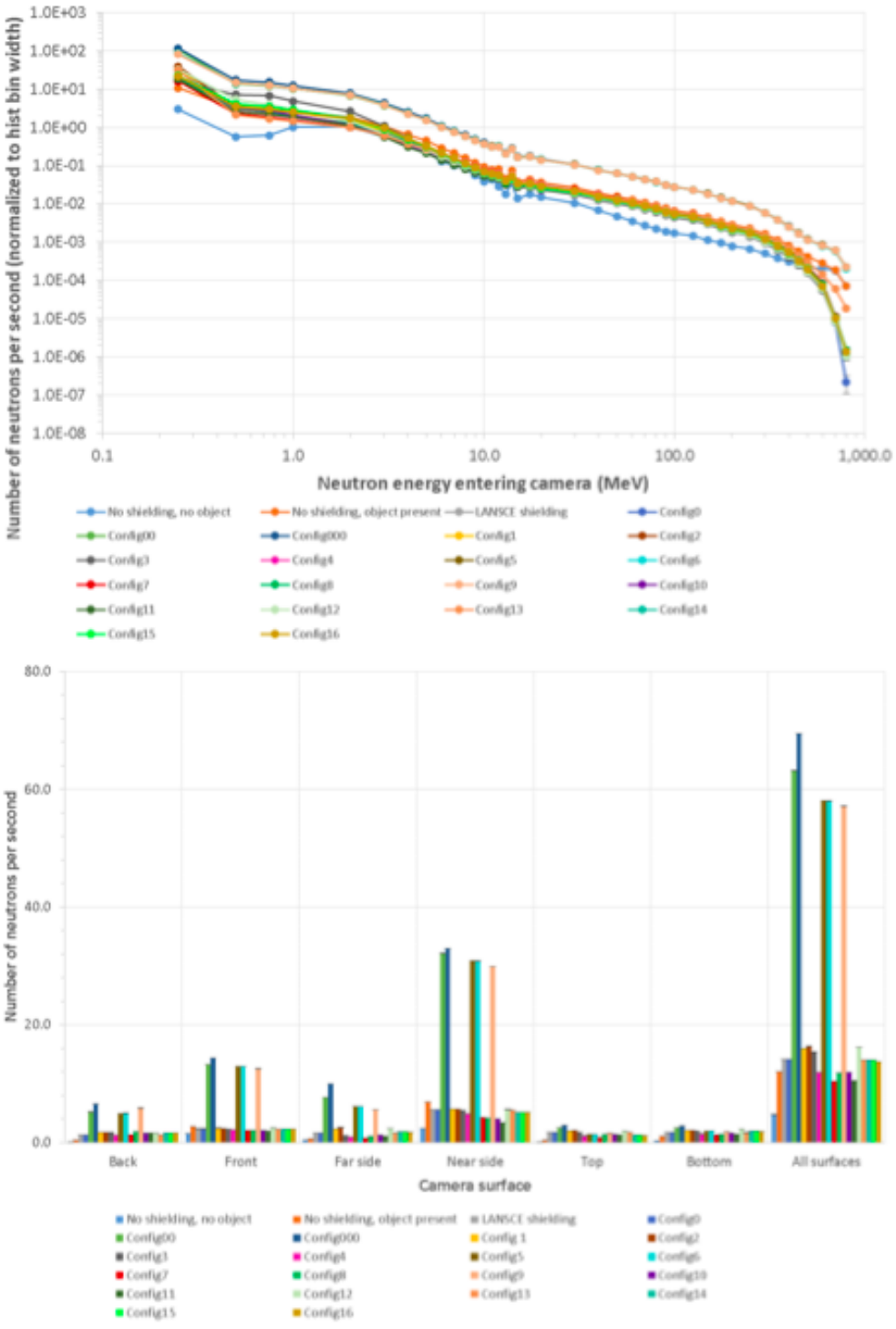


Figure 7.54: Energy distribution (top) and surface current (bottom) for neutrons entering the camera body and for all configurations simulated.

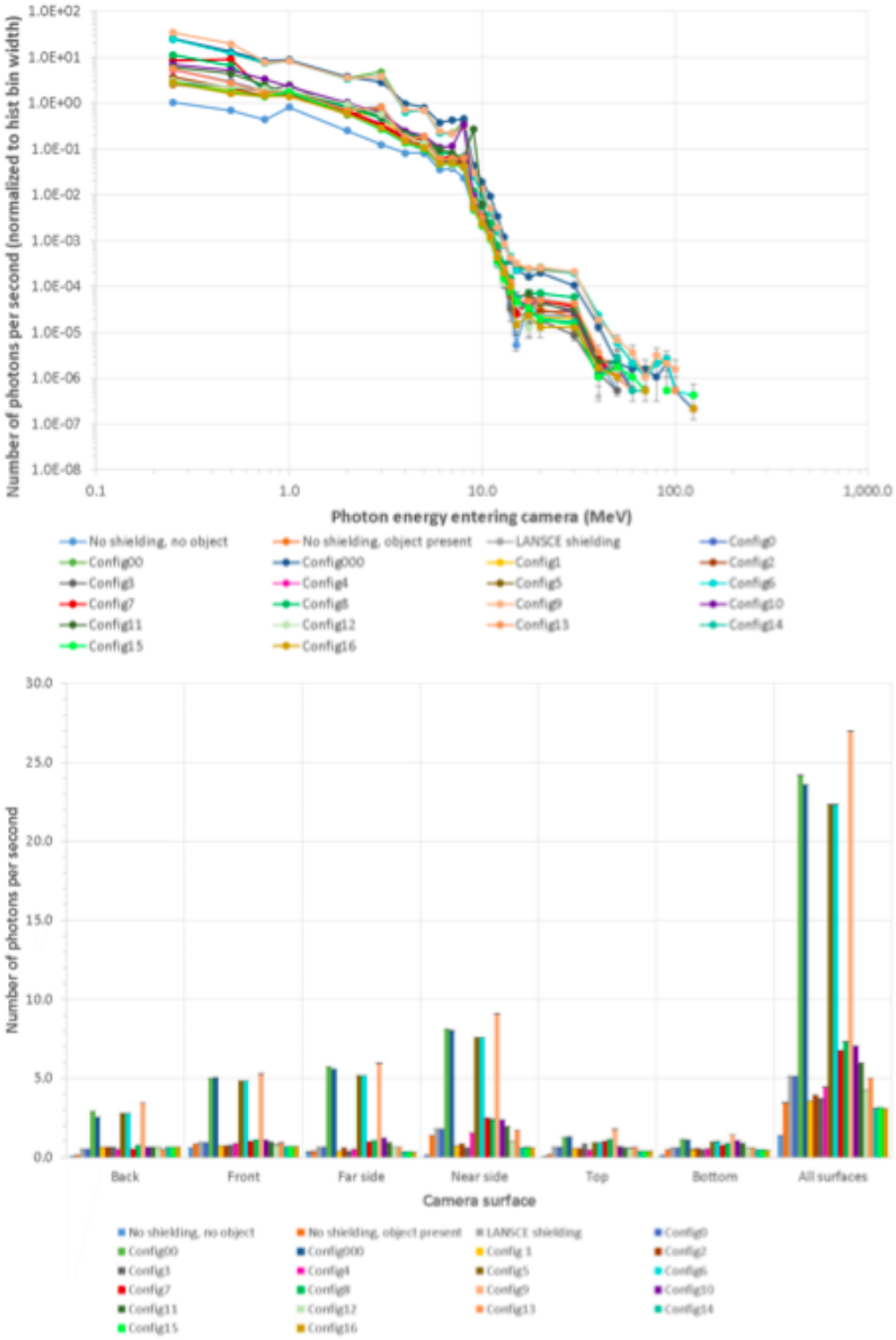


Figure 7.55: Energy distribution (top) and surface current (bottom) for photons entering the camera body and for all configurations simulated.

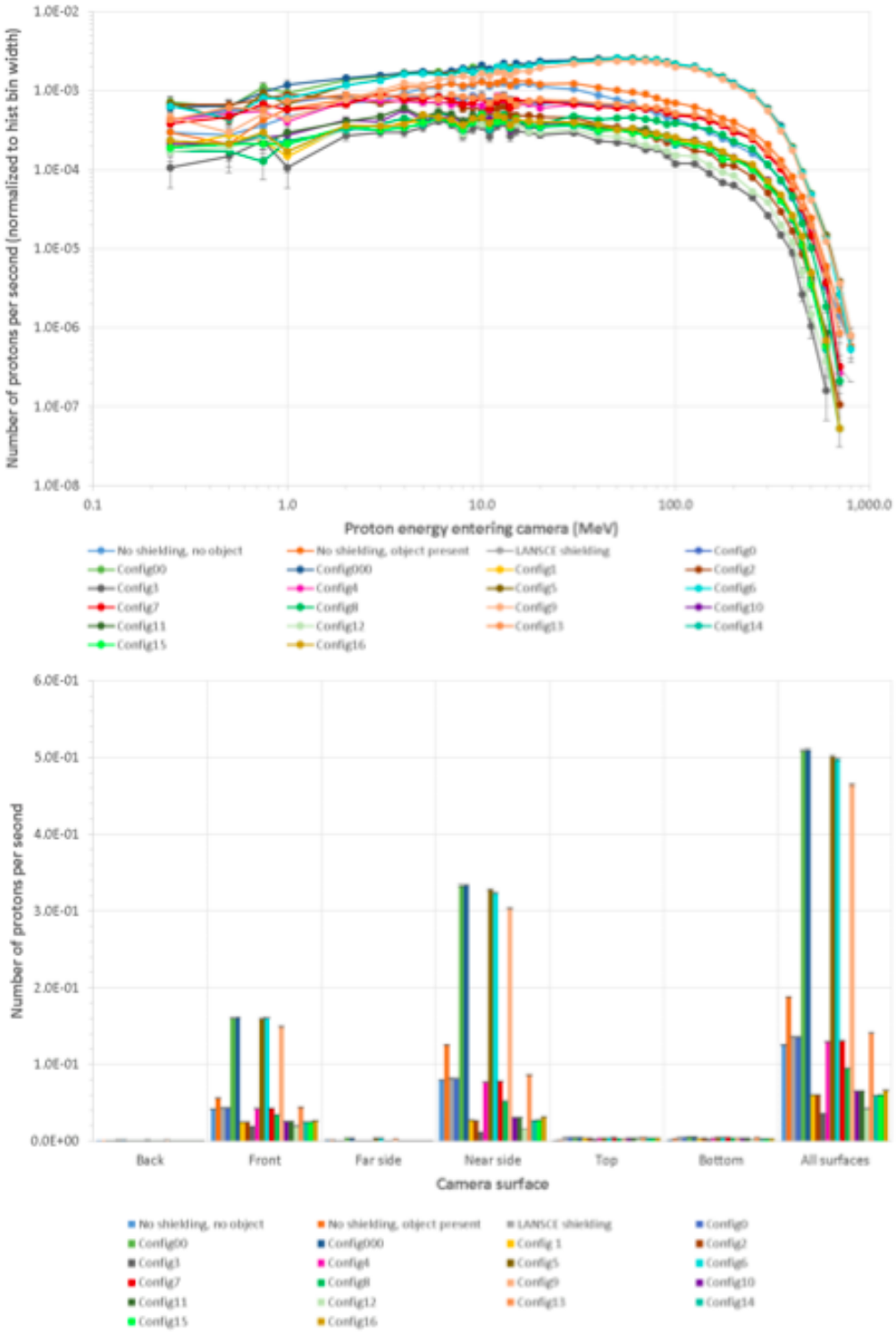


Figure 7.56: Energy distribution (top) and surface current (bottom) for protons entering the camera body and for all configurations simulated.



Figure 7.57: Energy distribution (top) and surface current (bottom) for alphas entering the camera body and for all configurations simulated.

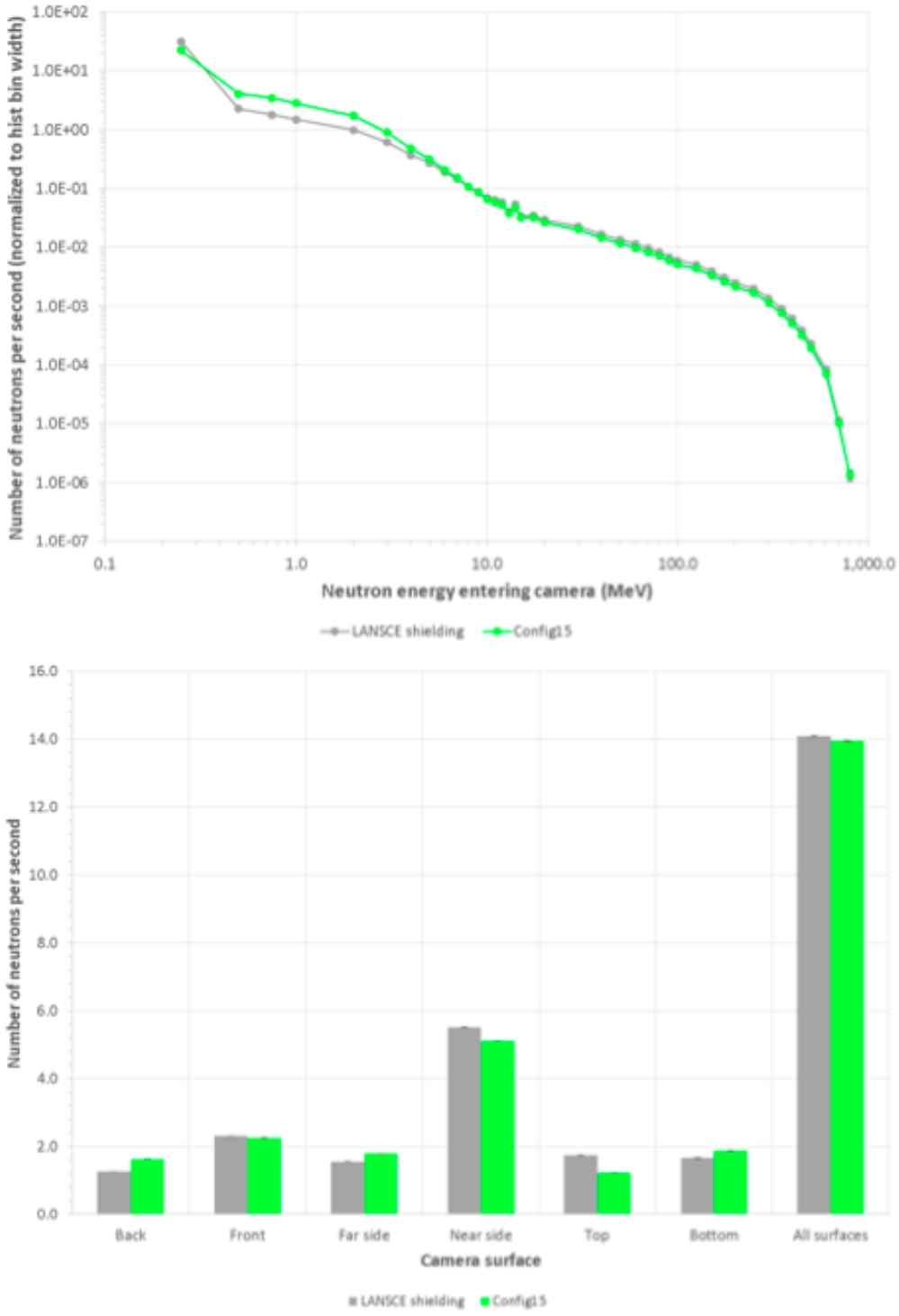


Figure 7.58: Energy distribution (top) and surface current (bottom) for neutrons entering the camera body and for Configuration 15 as compared to the LANSCE set-up.

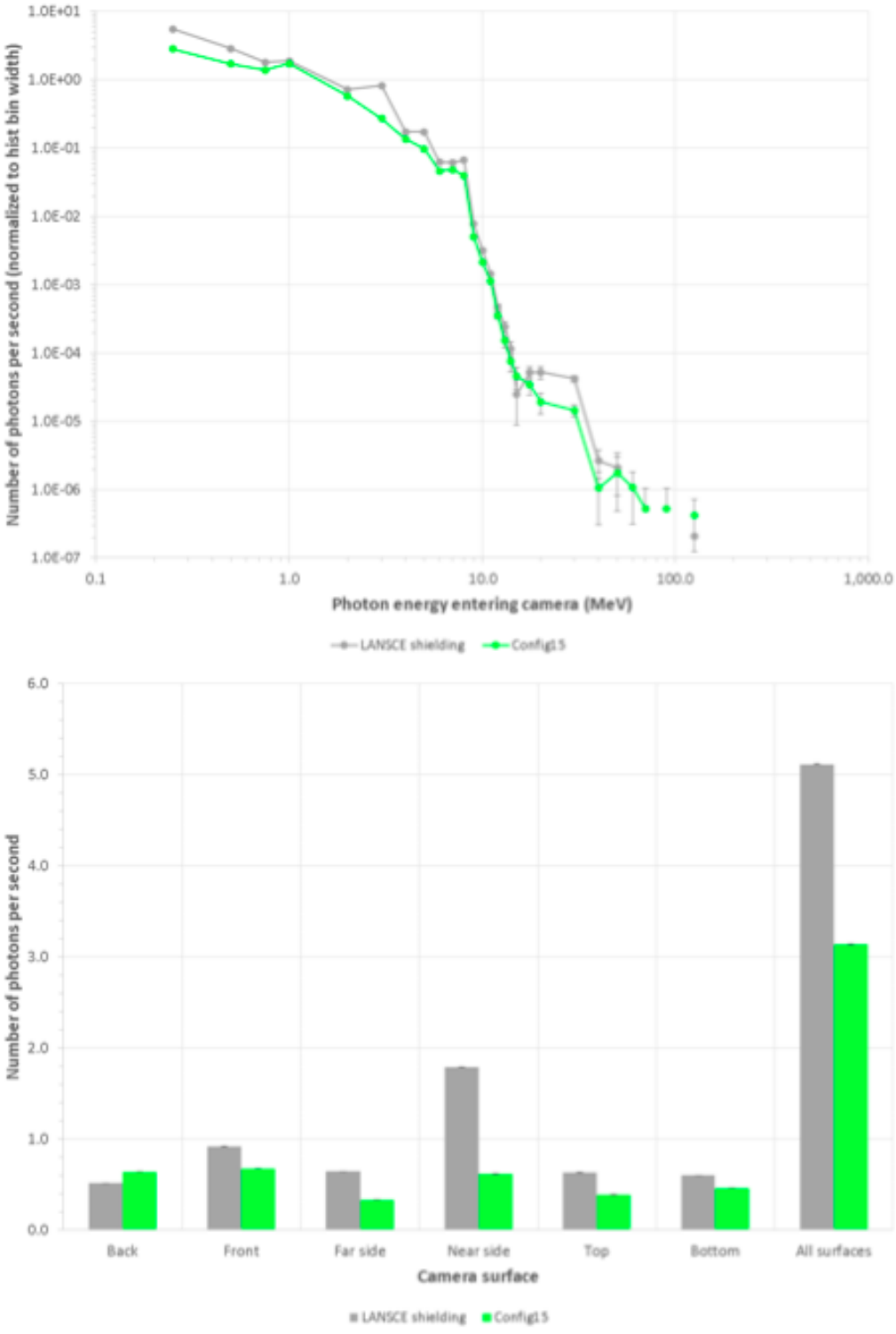


Figure 7.59: Energy distribution (top) and surface current (bottom) for photons entering the camera body and for Configuration 15 as compared to the LANSCE set-up.

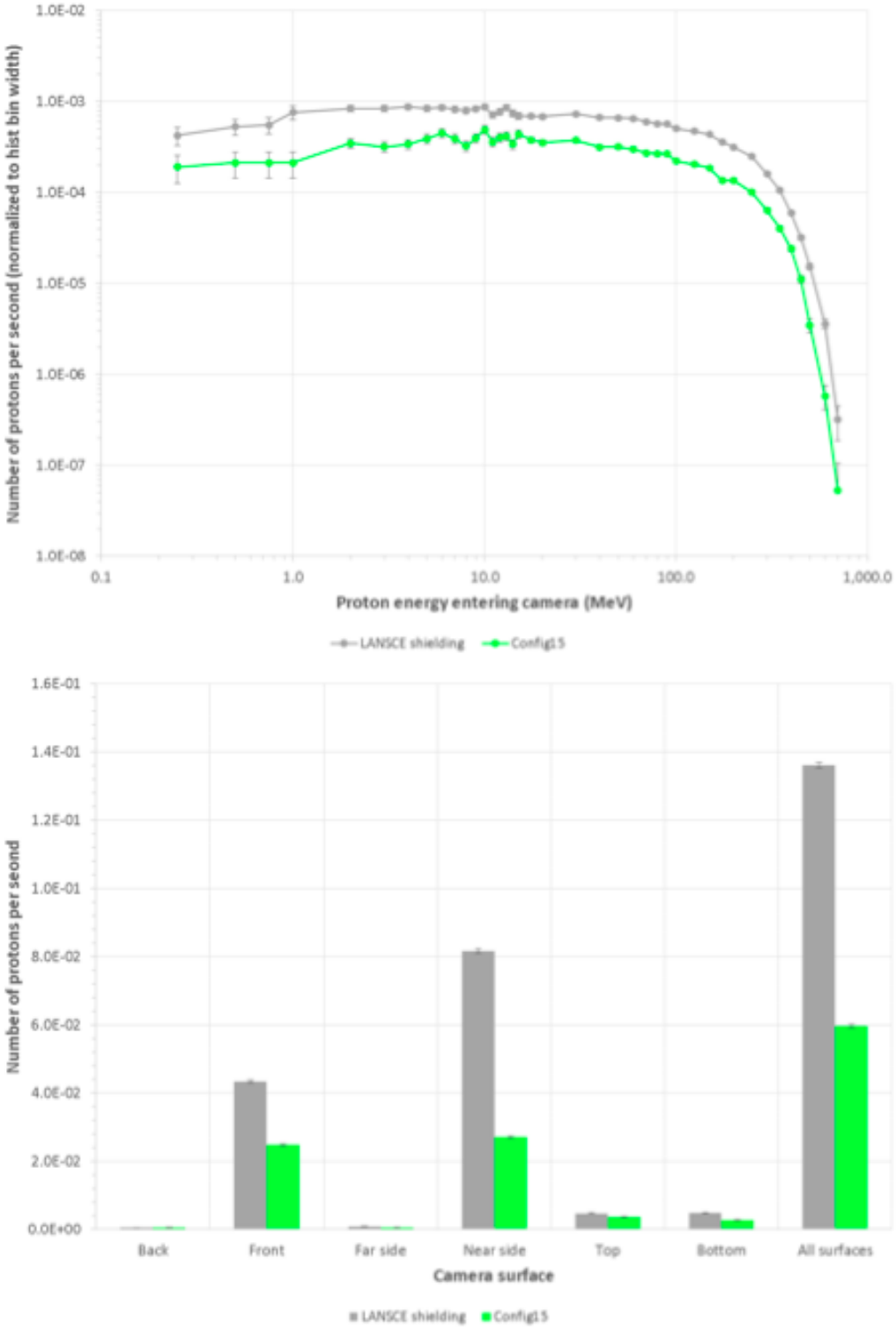


Figure 7.60: Energy distribution (top) and surface current (bottom) for protons entering the camera body and for Configuration 15 as compared to the LANSCE set-up.



Figure 7.61: Energy distribution (top) and surface current (bottom) for alphas entering the camera body and for Configuration 15 as compared to the LANSCE set-up.

current approximately cut in half. The alpha current is within error bars, so it is approximately the same for both designs. Therefore, by switching to "Configuration 15", the camera will be better protected from the beam and its secondary particles than it was in FP15R.

7.2.5 Source of Scatter and Secondary Particles

One final study conducted for the experimental shielding design was to determine the origin(s) of the particles entering the camera volume, thereby pinpointing major sources of flux so they might be addressed. Two quantities were simulated: the flux through a given volume (normalized to volume), and the number of particles born in a given volume (not normalized to volume). The first value gives an idea of how much scatter is entering a volume, whereas the second value provides information on which volumes create the most secondary particles.

For both quantities, the particles eventually had to enter the camera volume and thus do not represent total flux and total birth numbers. Volumes examined typically included the walls, the floor, the external shielding, the internal shielding, the tungsten radiography object, the mirror, and the beam pipe, and were obviously dependent on the shielding design in question. To be concise, only "LANSCE" and "Configuration 15" designs will be discussed.

Flux Levels

The simulated flux values for the LANSCE shielding design showed that, for all four particle types, the majority of flux entering the camera volume passed through the internal polyethylene shielding first. This makes intuitive sense, since the internal polyethylene surrounds the camera, and most particles will have to enter the polyethylene volume to reach the camera. The three volumes with the largest flux values are shown in Table 7.1 for each of the four particles tracked.

Table 7.1: The three volumes with the largest "LANSCE" flux values for neutrons, photons, protons, and alphas. Here, NPS is the number of particles simulated, and flux values shown are normalized to this value.

Particle Type	Location	Flux/NPS ($\#/cm^3$/NPS)	Relative Error (%)
Neutron	Internal poly.	7.22×10^{-11}	0.09
	W Object	6.43×10^{-11}	0.10
	Floor	1.39×10^{-11}	0.23
Photon	Internal poly.	2.38×10^{-11}	0.16
	W Object	2.26×10^{-11}	0.17
	Mirror	5.49×10^{-12}	0.33
Proton	Internal poly.	8.27×10^{-13}	0.73
	W Object	6.42×10^{-13}	0.84
	Mirror	7.99×10^{-14}	2.86
Alpha	Internal poly.	1.63×10^{-15}	17.1
	External steel	1.14×10^{-15}	19.1
	Object	1.14×10^{-15}	19.1

The "Configuration 15" simulations showed a similar trend, with the majority of the flux for neutrons, protons, and alphas traversing the internal shielding (both lead and Li-poly). This design deviated from "LANSCE", however, with the majority of photon flux occurring in the tungsten object. This is because, with gamma-generating polyethylene replaced by Li-poly, the tungsten radiography object is now the largest photon source in the simulations. Table 7.2 shows the three volumes with the largest flux values for the four particle types studied in this chapter.

Comparing the values listed in Tables 7.1 and 7.2 shows that, while the volumes with the highest flux remain relatively the same for all four particles and both shielding designs, the flux values are generally reduced by switching to the "Configuration 15" design. Alpha flux is reduced by an order of magnitude by the new design, and the highest neutron, photon, and proton flux values for "Configuration 15" are below those of "LANSCE". This comparison leads further credence to the "Configuration 15" shielding design.

Sources of Secondary Particles

The majority of particles, as one would expect, enter the camera volume through the front surface (i.e., the side with the lens) and the side nearest to the beam pipe. These are the two surfaces nearest to the source, and so it follows that they would see the highest current. Thus, although simulations had equal amounts of lead and Li-poly surrounding the camera, it may be desirable to place more of the shielding on the side nearest the beam and around the lens of the camera (without blocking the field of view) and thus better shield problem areas. This slight change in the shielding design would have the added benefit of pushing the camera away from the beam within the light-tight box, and thus takes advantage of geometry to reduce flux.

The simulations also described the energy of photons resulting from the (n, γ) reaction in the various materials represented in the problem. A histogram provided by MCNP6 binned the number of photons generated by energy. When normalized to bin width, two conclusions can be drawn from the histogram. First, "LANSCE"

Table 7.2: The three volumes with the largest "Configuration 15" flux values for neutrons, photons, protons, and alphas. Here, NPS is the number of particles simulated, and flux values shown are normalized to this value.

Particle Type	Location	Flux/NPS ($\#/cm^3$/NPS)	Relative Error (%)
Neutron	Internal Lead	6.76×10^{-11}	0.12
	Internal Li-poly	6.39×10^{-11}	0.12
	W Object	6.23×10^{-11}	0.12
Photon	W Object	1.59×10^{-11}	0.21
	Internal Lead	1.49×10^{-11}	0.22
	Internal Li-poly	1.46×10^{-11}	0.23
Proton	Internal Li-poly	2.55×10^{-13}	1.03
	Internal Lead	2.53×10^{-13}	1.03
	W Object	2.09×10^{-13}	1.11
Alpha	Internal Lead	7.29×10^{-16}	1.71
	Internal Li-poly	7.28×10^{-16}	1.71
	W Object	6.54×10^{-16}	1.79

and "Configuration 15" have nearly identical histograms. "Configuration 15" has a slightly higher amount of low-energy gammas (less than 1 MeV), but a slightly lower amount of high-energy gammas, when compared to "LANSCE". This demonstrates that "Configuration 15" is better at shielding high-energy photons, which is desirable.

Second, the peak number of gammas emitted via the (n, γ) reaction occurs in the 0.1 to 0.5 MeV energy bin, and are most likely due to the high-Z shielding within the light-tight box. Additionally, gammas above 9 MeV are negligible in number (Figures 7.62 and 7.63). Note that the numbers shown in these plots are not normalized to the number of particles simulated (NPS) and so are much higher in value than other plots in this chapter.

The final result taken from the MCNP6 simulations is the number of particles created in a given volume, from reactions such as the (n, γ) reaction described in the preceding paragraphs. The quantity of a given particle (e.g., neutron, photon, proton, and alpha) that exited a volume was subtracted from the number of that same particle that entered. If more particles exited than entered, that meant an overall particle death in that volume, thus yielding a positive number. If the opposite were true and more particles entered than exited, the result was negative and indicated that there was net particle birth in that volume. Therefore, the largest birth and death volumes could be found.

All volumes simulated in the shielding problems were examined. For all four particle types, the top three birth and death volumes (excluding the camera volume, which was set to neither create nor absorb particles and simply record the number entering) are listed in Tables 7.3 and 7.4 below. It should be noted that, unlike the flux values described in Tables 7.1 and 7.2, these values are not normalized to volume and as such represent the overall total.

Comparing Tables 7.3 and 7.4 shows that the two designs are almost identical. The top three volumes for both particle birth and death are the same for both designs, with numbers only varying slightly. Unfortunately, none of these volumes can be altered to reduce particle birth because they are part of the beam line or TiGReSSE.

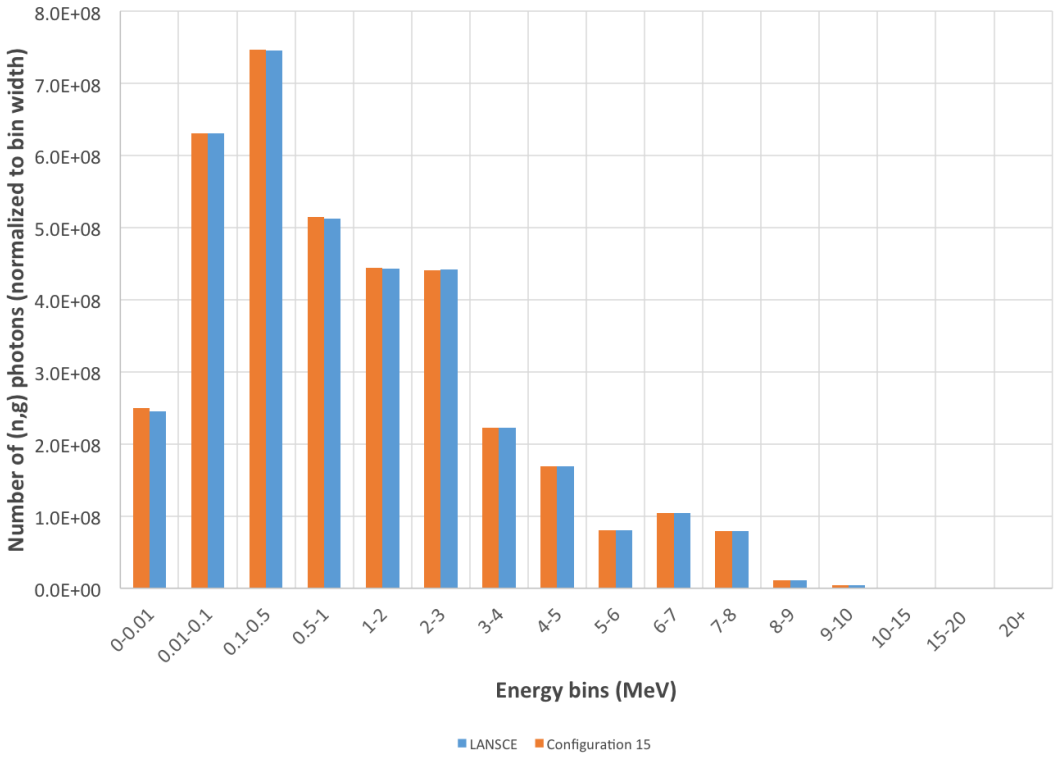


Figure 7.62: Histogram of the (n, γ) reaction for "Configuration 15" and "LANSCE" shielding designs. The number of secondary gammas is not normalized to the number of particles simulated.

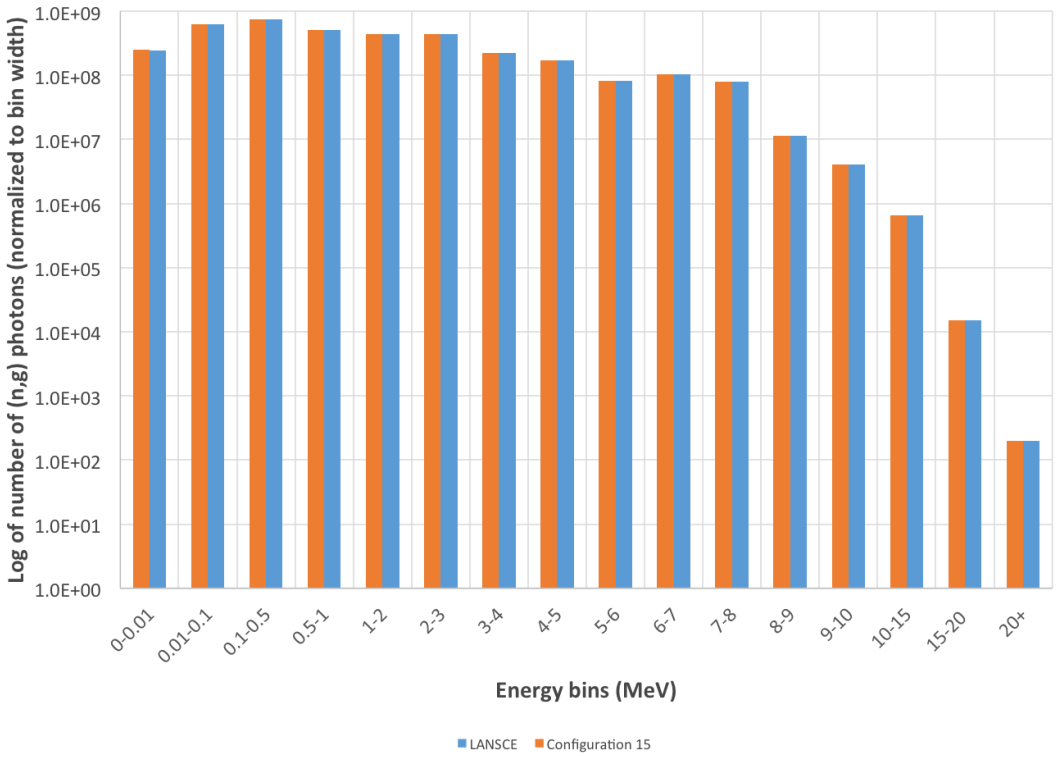


Figure 7.63: Semi-*log* histogram of the (n, γ) reaction for "Configuration 15" and "LANSCE" shielding designs. The number of secondary gammas is not normalized to the number of particles simulated.

Table 7.3: The three largest sources of particle births and deaths for the "LANSCE" configuration. Here, NPS is the number of particles simulated, and values shown are normalized to this value but not to cell volume. MCNP6 does not generate error for these values. Note that for alpha particles, there are no net births, only net deaths.

Particle Type	Net Reaction	Location	Number/NPS
Neutron	Birth	W Object	-2.30 × 10^{-6}
		Beam Pipe	-1.32 × 10^{-6}
		Light-tight Box	-3.34 × 10^{-8}
	Death	Beam Pipe Wall	1.46 × 10^{-6}
		Floor	8.05 × 10^{-7}
		Back Wall	7.88 × 10^{-7}
Photon	Birth	Beam Pipe	-2.50 × 10^{-6}
		Back Wall	-9.08 × 10^{-7}
		W Object	-7.51 × 10^{-7}
	Death	Beam Pipe Wall	9.60 × 10^{-7}
		Floor	1.95 × 10^{-7}
		Right Wall	1.50 × 10^{-7}
Proton	Birth	Inner Beam Pipe	-3.27 × 10^{-11}
		—	—
		—	—
	Death	Back Wall	1.78 × 10^{-5}
		Beam Pipe Wall	1.46 × 10^{-5}
		Floor	7.42 × 10^{-6}
Alpha	Birth	—	—
		—	—
		—	—
	Death	Back Wall	1.79 × 10^{-6}
		Beam Pipe	7.59 × 10^{-7}
		Floor	2.53 × 10^{-7}

Table 7.4: The three largest sources of particle births and deaths for "Configuration 15". Here, NPS is the number of particles simulated, and values shown are normalized to this value. MCNP6 does not generate error for these values. Note that for alpha particles, there are no net births, only net deaths.

Particle Type	Net Reaction	Location	Number/NPS
Neutron	Birth	W Object	-2.30×10^{-6}
		Beam Pipe	-1.32×10^{-6}
		Light-tight Box	-3.44×10^{-8}
	Death	Beam Pipe Wall	1.46×10^{-6}
		Floor	8.06×10^{-7}
		Back Wall	7.88×10^{-7}
Photon	Birth	Beam Pipe	-2.50×10^{-6}
		Back Wall	-9.09×10^{-7}
		W Object	-7.51×10^{-7}
	Death	Beam Pipe Wall	9.60×10^{-7}
		Floor	1.92×10^{-7}
		Right Wall	1.50×10^{-7}
Proton	Birth	Inner Beam Pipe	-3.03×10^{-11}
		—	—
		—	—
	Death	Back Wall	1.78×10^{-5}
		Beam Pipe Wall	1.46×10^{-5}
		Floor	7.45×10^{-6}
Alpha	Birth	—	—
		—	—
		—	—
	Death	Back Wall	1.79×10^{-6}
		Beam Pipe Wall	7.59×10^{-7}
		Floor	2.53×10^{-7}

Essentially, one can only better collimate the beam to limit activation of the steel beam pipe.

It was interesting to see that no volume causes net birth of alpha particles, and that only one volume (the inside of the beam pipe, which is air) causes net birth of protons. This is because the range of alpha particles is extremely small, with protons having a slightly longer range. Air is enough to stop alphas, but not quite stop protons, in the geometries simulated. This is illustrated by referring to Figures 6.1 and 6.2 in Chapter 6.

7.3 Conclusions

To conclude, "Configuration 15" is the best shielding design studied in this chapter. It reduces neutron, photon, alpha, and proton current when compared to the "LANSCE" shielding design used for the experiments detailed in Chapter 5. Other findings showed that typically the greatest amount of flux entered through the front of the camera and the side of the camera closest to the beam. Shielding should be concentrated in these locations to best protect the ICCD chip.

Shielding material studies showed that concrete blocks have roughly the same shielding capabilities as polyethylene, as do graphite and steel, when placed externally to the light-tight box. Therefore, whatever is less costly and more freely available should be used in the shielding design. Li-poly is the best for shielding the camera against neutrons when placed inside the light-tight box because it does not emit 500 keV gammas like B-poly does. B-poly and aluminum was not a great option, with gamma flux actually increased, but aluminum did reduce the number of protons entering the camera volume.

Metals inside the light-tight box should be selected according to the desired effect and according to cost and weight considerations. Nickel, followed by copper, did the best job at reducing neutron flux. Tungsten and lead did the best job at reducing

photon, proton, and alpha flux, with photon fluence through the camera volume reduced by ∼25%.

Geometry studies showed that shielding (polyethylene or concrete) placed around the light-tight box was particularly harmful because they increased flux into the camera volume by scattering direct beam into the light-tight box. Additionally, doubling the thickness of external steel to 4 ft did not reduce the four particles' current beyond the levels that 2 ft provided.

Finally, it was found that the majority of birth sources of scatter are beam line components that can not be addressed by removal or replacement. The radiography object is also a non-trivial source of scatter into the camera volume. Thus, creating the best shielding design is of utmost priority, particularly to address scatter from the radiography object. The new design, "Configuration 15", should greatly improve image quality and protect the camera's electronics.

Future work in this area should determine a limiting dose rate to the camera and the related probability of losing pixel function. Such information can aid in any additional improvements to the shielding design recommended in this chapter, as well as provide an idea of camera lifetime.

Chapter 8

System Design Considerations

Other system design considerations must be studied to build the best possible version of TiGReSSE. This chapter focuses on design elements "outside the light-tight box", so to speak, and addresses the direct-to-scatter ratio, which measures the percent of signal that would be rejected by TiGReSSE if using TOF methods to conduct scatter rejection. This chapter will also discuss the dose expected to be deposited on the radiography object during NDA measurements.

8.1 Direct-to-Scatter Ratio

8.1.1 Overview

The direct-to-scatter ratio in radiography is similar to the signal-to-noise ratio in other detector applications. Both ratios provide information on how much signal is useful and how much is not, and whether the direct signal is large enough to be detected over the system noise. The direct-to-scatter ratio is dependent on the properties of the scintillator, the source, and the object being imaged. Thus, to determine the behavior of TiGReSSE, simulations of a representative object were conducted to estimate the direct-to-scatter ratio.

A spent nuclear fuel (SNF) cask was selected as a representative object because of its large size and the presence of both low-Z and high-Z materials, both of which are drivers for TiGReSSE design. A SNF cask is therefore very difficult to image and serves as a very hard problem that can provide an upper-limit bound of TiGReSSE's abilities. Additionally, with the uncertainty surrounding the use as a repository of Yucca Mountain, spent fuel casks are becoming more widely used in the United States, and NDA of these casks will most likely grow in importance to ensure spent fuel is properly protected from the public and the environment.

The fuel cask selected was the NAC-I28, which is currently licensed for storage purposes at the Surry power generating station in the United States and also for the transport of SNF [79]. The NAC-I28 is a right circular cylinder made of austenitic stainless steel, lead, and an unspecified borated material. This unknown material was assumed to be borated concrete because the cask is approved for transportation of SNF. The borated concrete, however, was simulated as concrete because material specifications could not be found for borated concrete. The cask was assumed to be empty of everything except air, thus representing the hypothetical situation of radiography of the cask prior to leaving the factory to ensure it was properly built. A diagram of the cask can be seen in Figure 8.1.

8.1.2 MCNP6 Simulations

MCNP6 simulations were conducted of the NAC-I28 using an FIR tally. This particular tally creates a rectangular projection of the object being imaged by having each event within the cask make some contribution to the voxellated grid at the image plane [47]. This tally was selected over the FMESH tally, which was used in previous chapters to form simulated images, because the FIR tally uses far less computer memory that would allow for smaller simulated pixels. The FIR tally also has inherent variance reduction that improves statistics (in other words, fewer

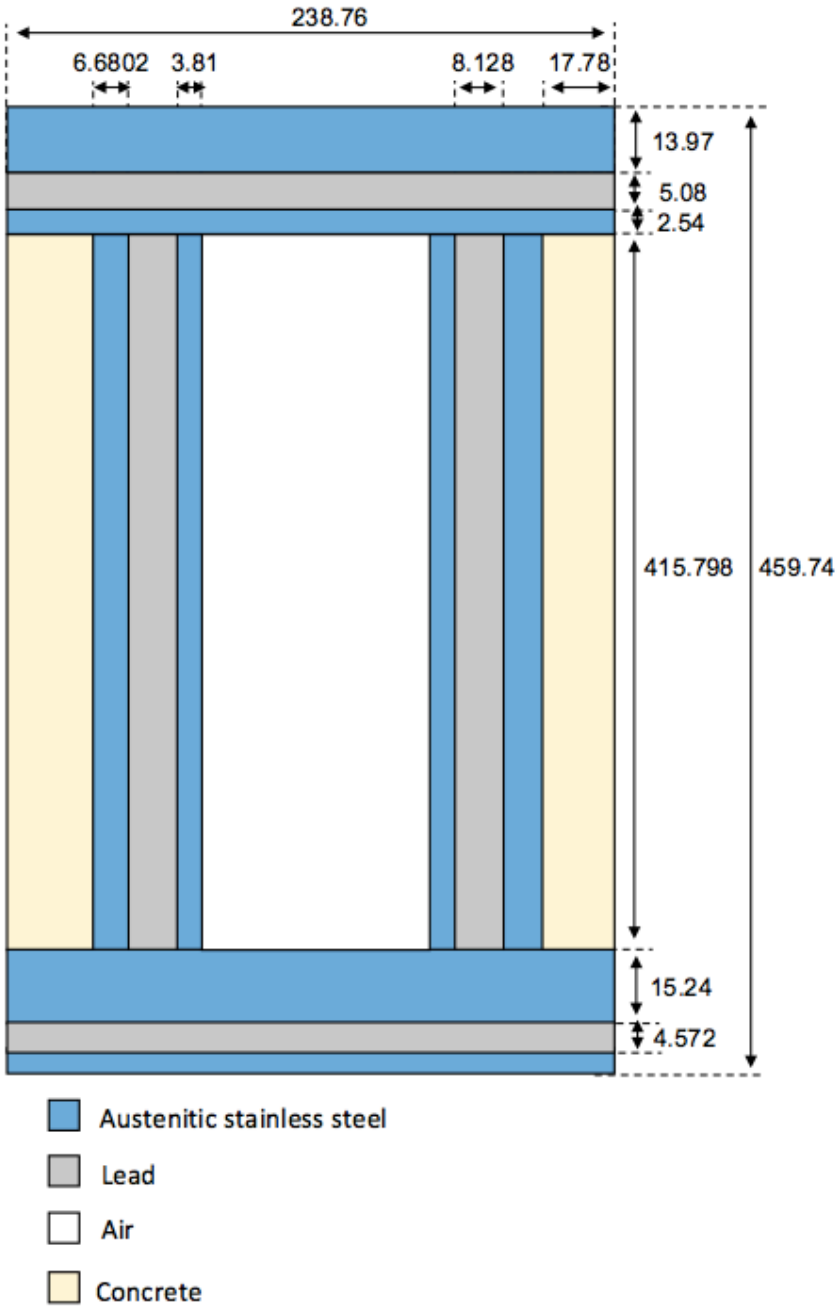


Figure 8.1: Diagram of the cylindrically symmetric NAC-I28 spent nuclear fuel cask, with dimensions in *cm* (not to scale).

particles need to be simulated). Using this tally, images from direct neutrons, as well as from direct and scattered neutrons, were generated.

The grid, assumed to be a perfect detector with 100% efficiency, used 240×480 pixels, with each pixel having a 1 cm^2 area. The number of simulated particles was 1×10^6, whereas the FMESH tally typically uses around 1×10^9 simulated particles. The SNF cask did not have added defects; rather, the idea of the simulations, besides evaluating the direct-to-scatter ratio for such an object, was to test whether gross features such as material boundaries could be seen in such a difficult radiography object.

Simulated monoenergetic neutron sources had energies of 10, 14, and 20 MeV. For comparison, bremsstrahlung x-ray sources with typical endpoint energies of 6 and 15 MeV were also simulated (x-ray source spectra were respectively provided by B. Temple and J. Hunter of LANL). The source was a disk source located 10 cm from the edge of the cask and with radius of 260 cm to ensure equal coverage of the cask. Radiographs are not shown with grayscale bars because the grayscale bar would cover cask features.

8.1.3 Simulated Radiograph Observations

An in-house LANL script was used to convert the simulated data into a text file that listed contrast values on a per pixel basis. ImageJ was then used to create images from these text files. These images were interesting for several reasons. First, the disk source, which is larger in diameter than the cask is wide, can be seen around the edges of the cask as a bright white area prior to post-processing and black after post-processing (dividing by the flatfield, taking the natural log of pixel values, and multiplying by -1 to convert pixel values to σt). The white (or black, if post-processed) edge around the SNF cask, however, skews the contrast levels within the cask and washes out internal features within the radiograph (Figure 8.2). Thus, cropping images helped ImageJ properly adjust contrast.

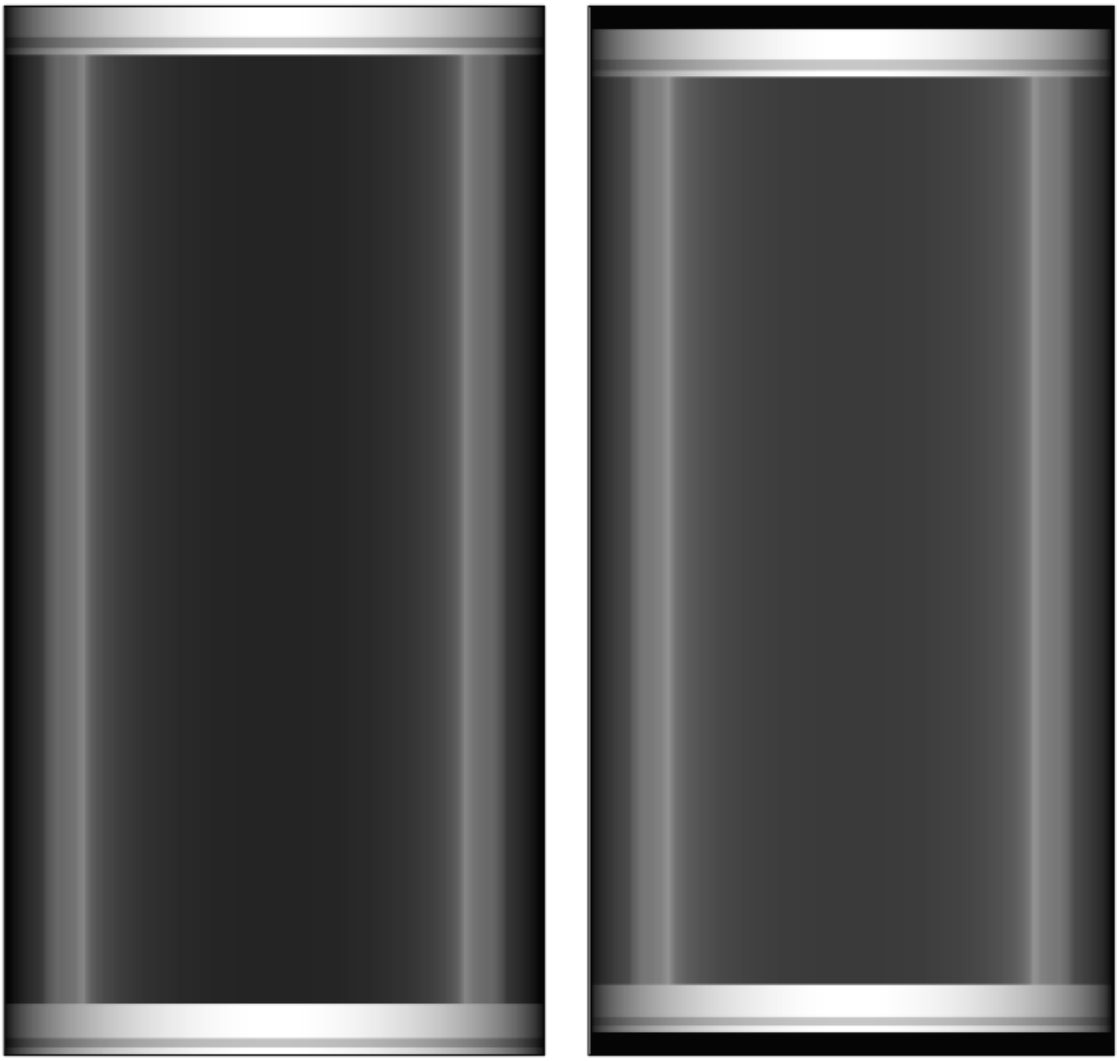


Figure 8.2: Simulated direct 14 MeV neutron radiographs of the NAC-I28 SNF cask, with one image cropped (left) and the other image the full size of the detector (right). Note that cropping the image to remove the beam area outside the edges of the cask increases the range of contrast within the cask (notice that the center of the cask now appears darker as a result of cropping).

8.1.4 Simulated Direct-to-Scatter Ratio Results

ImageJ was used to manipulate the simulated radiograph data. The direct radiograph (D) was subtracted from the total (direct plus scatter; T) radiograph to obtain net scatter data (S). ImageJ was then used to divide D by S, with the resultant image serving as a 2-D plot of the direct-to-scatter ratio for the particular source type and energy. The D/S image can be thought of as representing the amount of direct signal reaching the detector for a given pixel as compared to the amount of scatter in that same pixel. A pixel with a larger D/S ratio thus sees more direct signal than a pixel with a smaller D/S ratio, caused by that pixel viewing a more transmissible part of the object and/or receiving less scatter. As should be expected, D/S varies as a function of energy and the radiography object.

The D and T images themselves were also manipulated to provide attenuation plots according to Equation 1.1 and the procedure discussed in Chapter 5, with I equal to the pixel value and I_0 equal to the pure beam value (determined from pixels that counted direct beam outside the SNF cask region of the image). Thus, by using ImageJ to divide I by I_0, apply a natural *log* filter, and multiply by -1, a pixel value was then equal to σt (Figure 8.3). This conversion of the data is desirable because it represents the attenuation a particle would have as it passed through the object. It is important to note that, because the D and T images are multiplied by -1, they have an inverse grayscale than the D/S images. In other words, the D and T images have low-density regions appear dark and high-density regions appear light; D/S images are more intuitive, with the opposite scaling (Figure 8.4).

Several conclusions could be drawn from the D, T, and D/S images, with the first being that scatter completely masks the interior of the cask from being visible. This is because the scatter "fills in" dense regions of the image, reducing contrast from black and white to shades of gray and causing all regions to appear the same color. Rejecting the scatter, however, increases the contrast range so that material boundaries can be seen. This effect is evident in Figure 8.5, which compares D and T

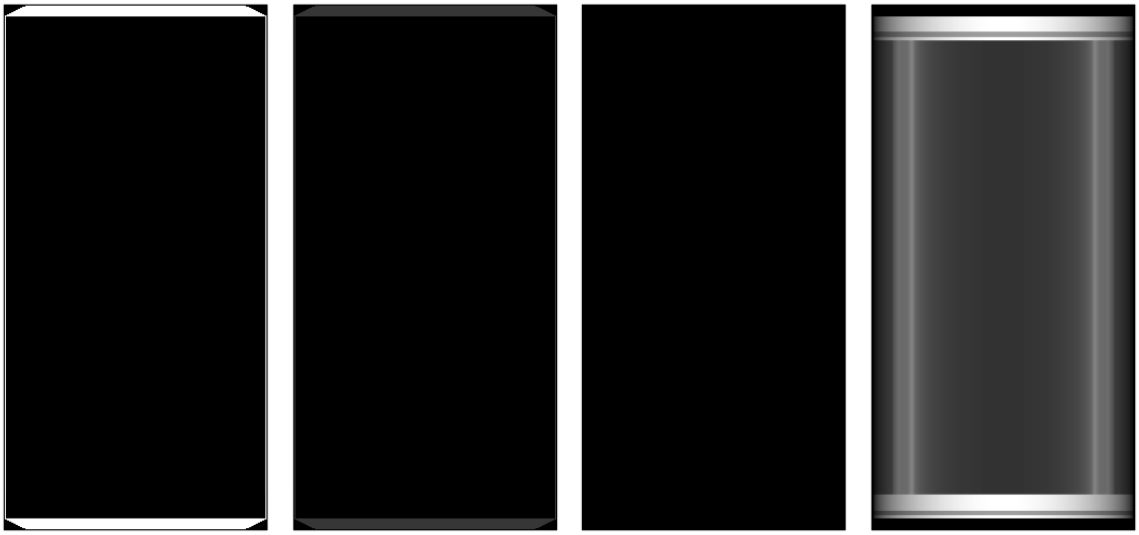


Figure 8.3: Simulated direct 10 MeV neutron radiographs of the NAC-I28 SNF cask, arranged according to the procedure to convert pixel grayscale values to areal density, σt. The direct data (left) is divided by the value of the beam incident on the detector (middle left), a natural log filter is applied (middle right), and the data is multiplied by -1 before image contrast is adjusted for optimal feature visibility (right).

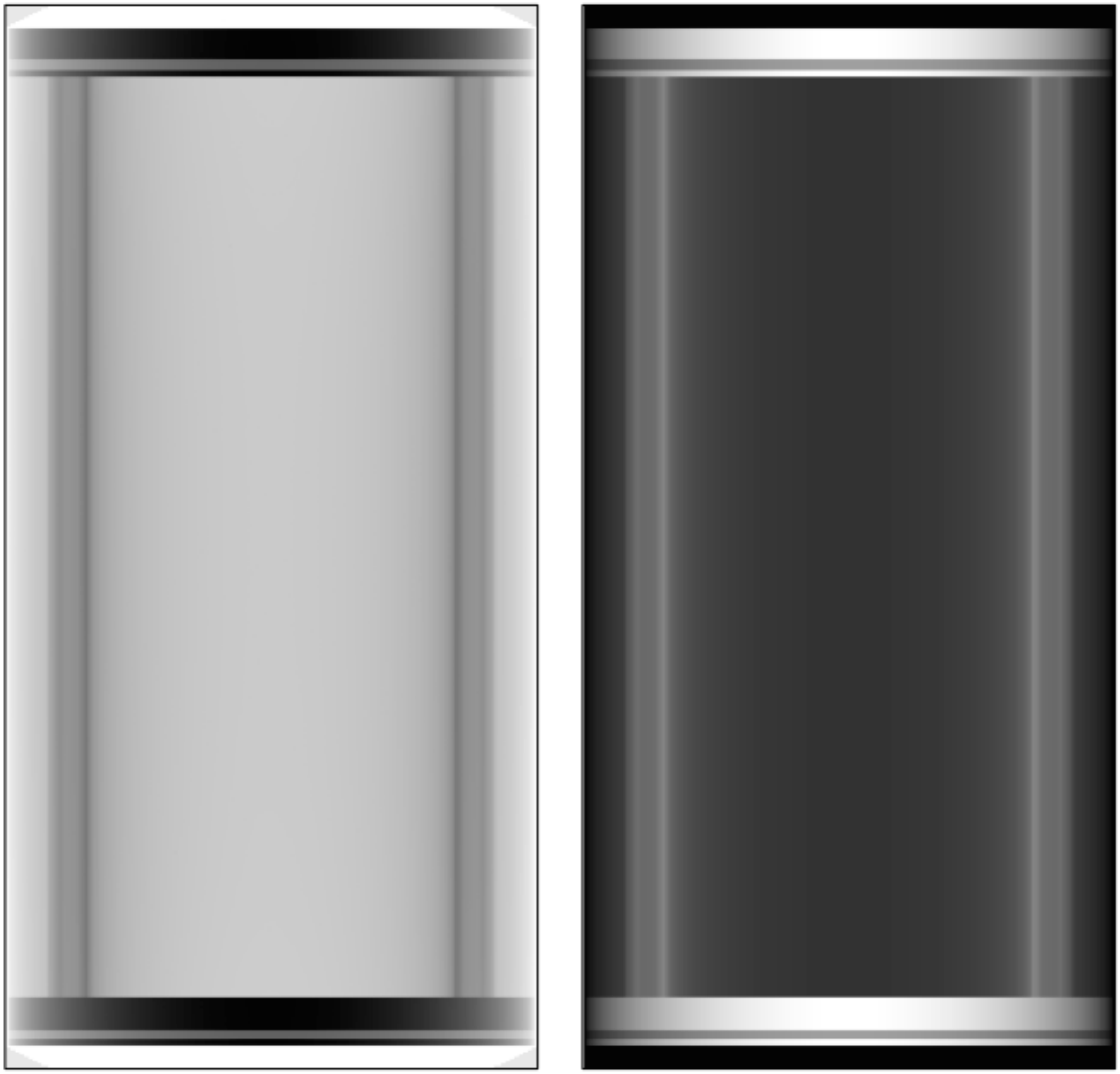


Figure 8.4: Comparison of a 10 MeV direct-to-scatter (D/S) neutron radiograph (left) to a 10 MeV direct (D) neutron radiograph (right). Note that the grayscale values are inverted because the D radiograph is multiplied by -1, and that the grayscale values differ slightly between the two radiographs because they represent different quantities.

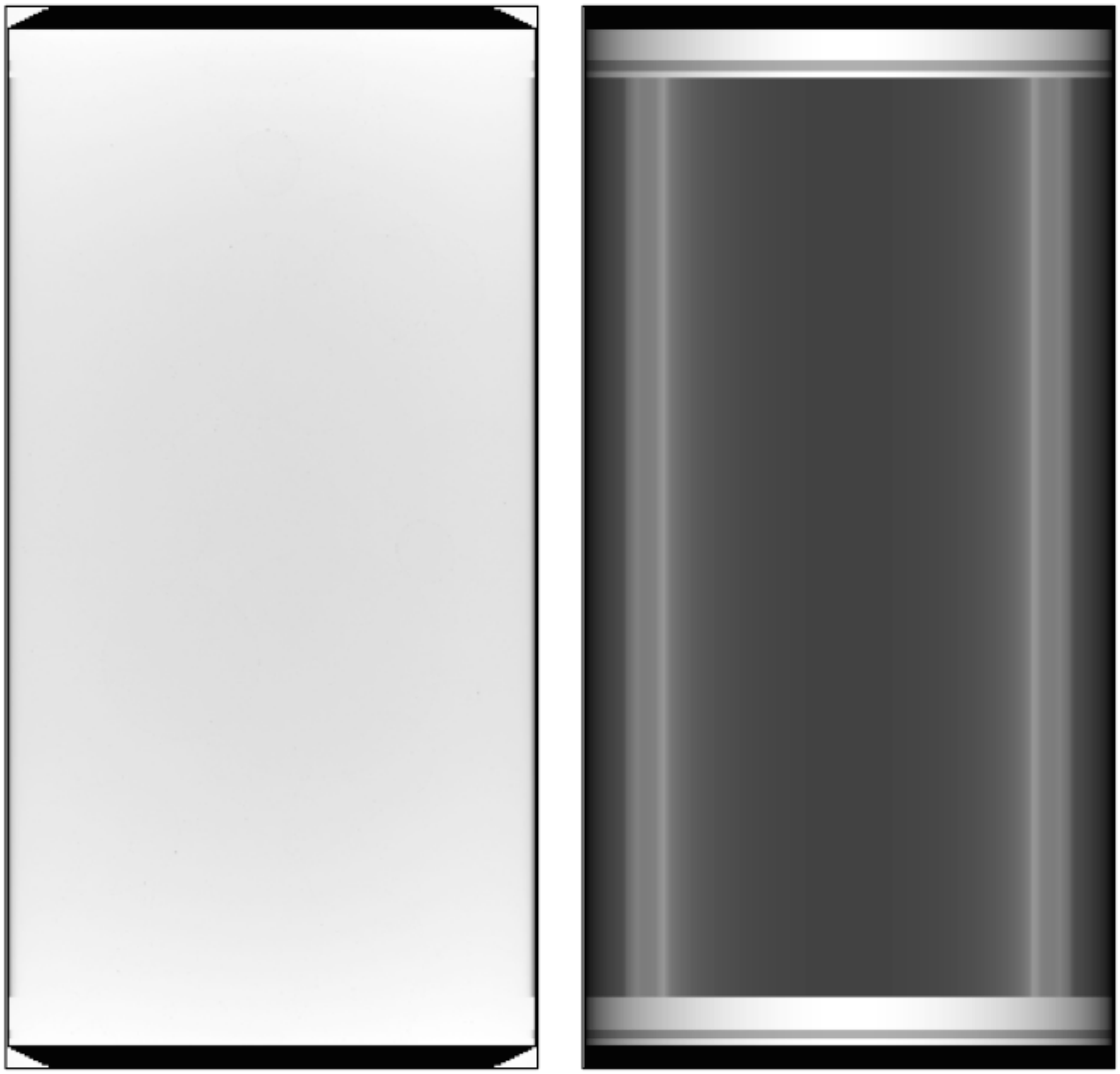


Figure 8.5: Simulated 10 MeV neutron radiographs of the NAC-I28 SNF cask, with the total (direct plus scatter; left) image compared to the direct (right) image.

images generated by a 10 MeV neutron source. This trend was seen for all energies simulated, not just the 10 MeV images shown here, and provides further evidence that using TIGReSSE for TOF scatter rejection is necessary when imaging large, dense objects.

Another conclusion from the D simulated radiographs is that x-rays (6 or 15 MeV) are less penetrating than neutrons (10, 14, or 20 MeV), as expected from theory (refer to Chapter 1). Figure 8.6 illustrates this by comparing 15 MeV x-rays to lower energy 10 MeV neutrons. The x-ray image appears to show that there is a large void in the lead regions of both SNF cask end caps. In actuality, no x-rays are able to penetrate the center of the lead region, which causes a perceived "void". An inspector might believe there is a large flaw in the SNF cask being tested. However, if the inspector were to use neutrons, the contrast remains constant across the lead regions and it is apparent that this cask does not have any defects. A related observation is that the x-ray contrast range is much smaller than that of the neutron radiograph, which is again a result of fewer x-rays penetrating the SNF cask than neutrons.

It should be noted that D x-ray radiographs are essentially only possible in simulations. This is because x-rays travel at the speed of light, and impractically large distances would be needed to conduct time-of-flight scatter rejection (since $TOF = distance/velocity$). In reality, a 15 MeV x-ray radiograph would look similar to the simulated T image in Figure 8.7, which provides no useful information. However, D x-ray images are included here for the sake of comparison.

Another conclusion that can be drawn from simulated radiographs of the NAC-I28 SNF cask is that increasing the particle energy increases transmission through the cask. This was seen with both x-ray and neutron D/S radiographs, where an increased D/S ratio indicates an increased amount of direct transmission through the cask. This is qualitatively seen as increased brightness and reduced contrast range in the radiographs, particularly in the lead regions of the cask. Figure 8.8 shows the neutron D/S radiographs for 10, 14, and 20 MeV, all of which are set to the same contrast range (grayscale values between -70 and 6 are included, with values

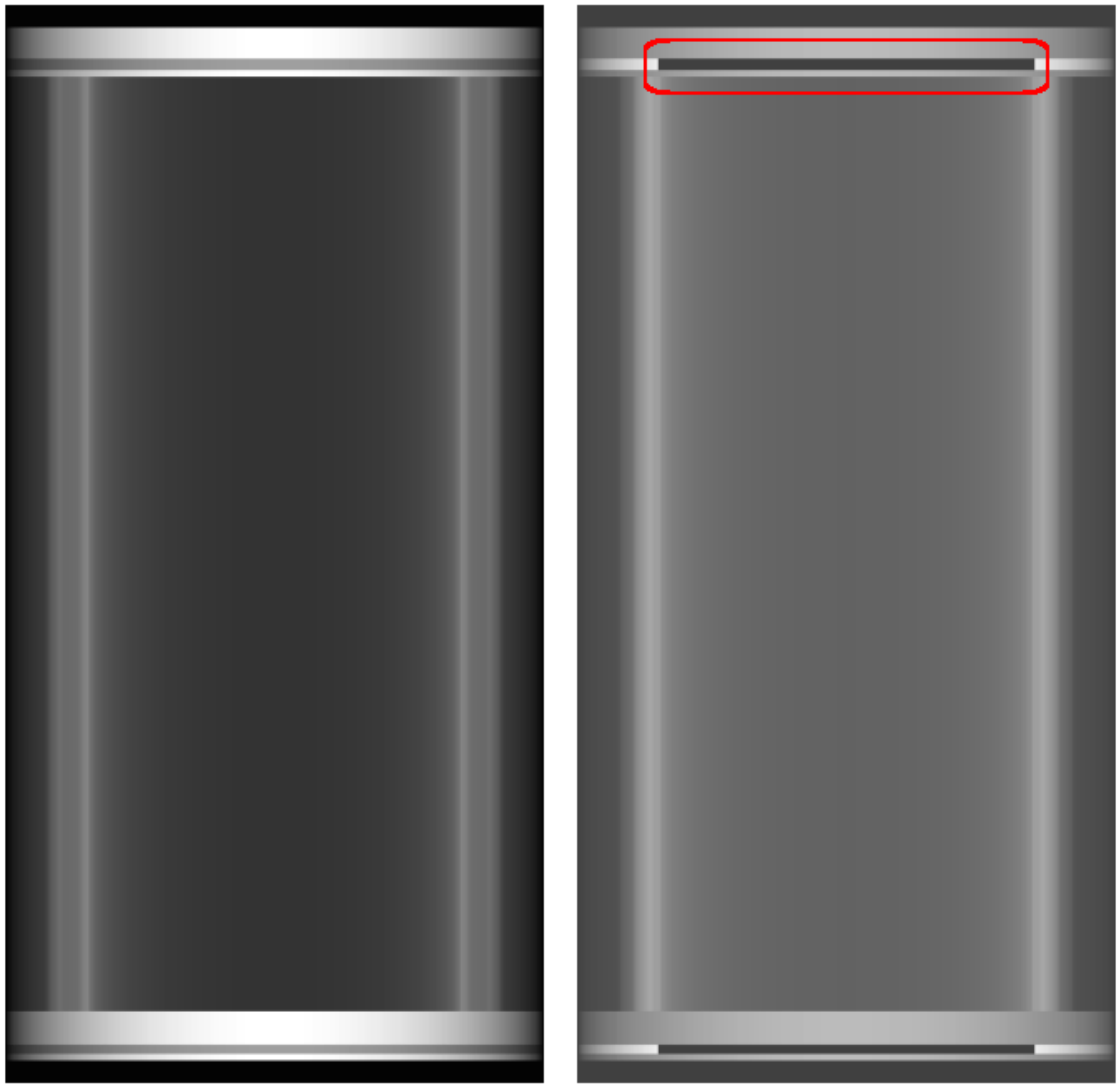


Figure 8.6: Simulated direct (D) radiographs of the NAC-I28 SNF cask, with the 10 MeV neutron radiograph (left) compared to the 15 MeV x-ray radiograph (right). The x-ray image appears to show a void (circled in red) that does not exist because x-rays, unlike fast neutrons, are unable to penetrate the thickest part of the lead.

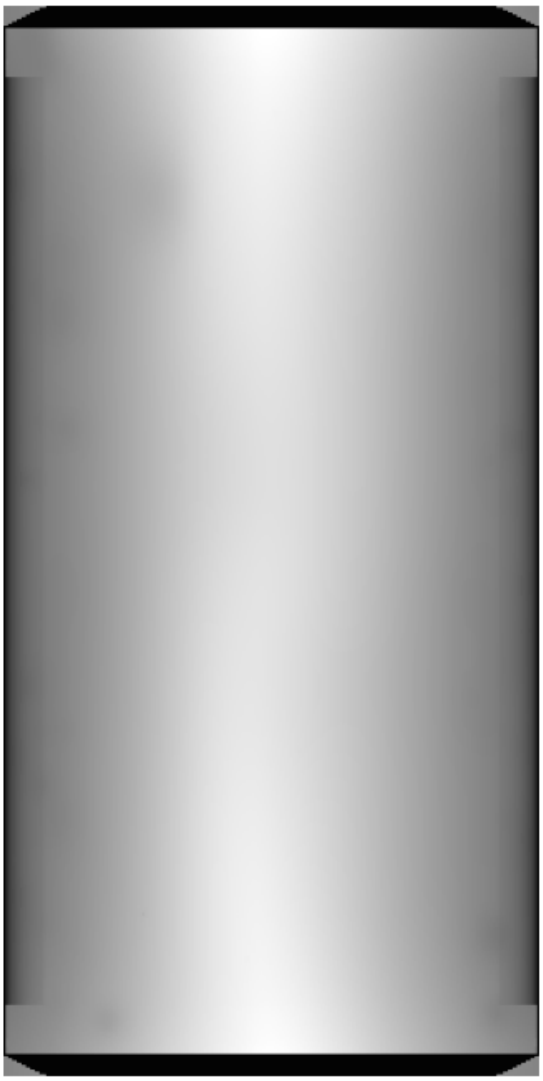


Figure 8.7: Simulated 15 MeV total (T) x-ray radiograph of the NAC-I28 SNF cask.

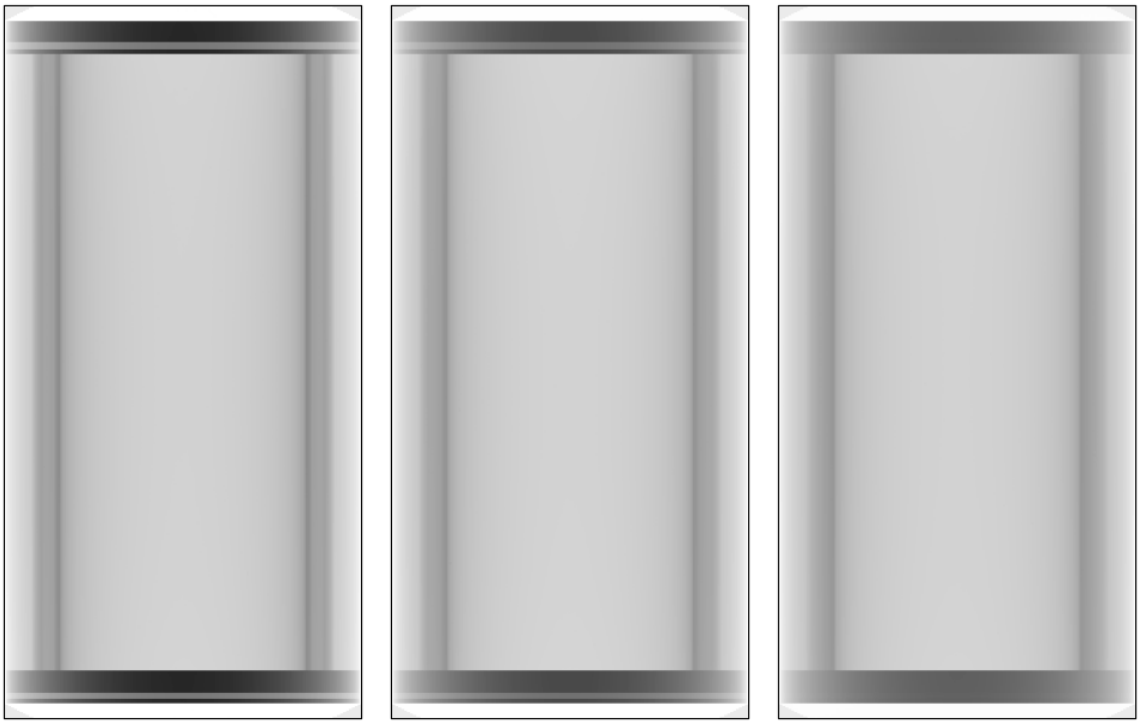


Figure 8.8: Simulated D/S neutron radiographs for 10 MeV (left), 14 MeV (center), and 20 MeV (right) monoenergetic neutrons. The three radiographs are set to the same logarithmic contrast range, [-70,6].

outside this range excluded). Figure 8.9 similarly shows D/S x-ray radiographs for 6 and 15 MeV, also set to the contrast range of [-70,6]. Both x-ray sources do not penetrate the lead region of the cask, with radiographs showing false voids. (Note that the range of [-70,6] is not the optimal range to see object features, since the optimal range varies from image to image; instead, the range of [-70,6] was selected simply to showcase how transmission increases as a function of source energy.)

Quantitatively, the increased transmission can be seen with line-outs across the D/S images. Line-outs were taken across the center of the object, both horizontally and vertically (Figures 8.10 and 8.11). The horizontal line-out equation was $y = 239$, with the vertical line-out equation being $x = 119$ (with the numbers shown here indicating pixel number, or half of the 480×240 pixels in the image, respectively). The pixel numbers selected as the line-out locations are not true halves, so to speak, because the pixel counter starts at 0. The ratios were not multiplied by -1 like the radiographs were in post-processing, so larger, more positive numbers indicate a better D/S ratio.

These D/S line-outs are interesting for three reasons. First, the curvature in the vertical line-out is not seen to the same degree in the horizontal line-out; thus, the horizontal line-out provides information that the cask is cylindrical. Therefore, the line-out shape can provide information on the general shape of the radiography object, such as a block versus a cylinder.

Second, while x-ray sources have a greater D/S ratio in the outer part of the object (i.e., the concrete region) and the center of the object (i.e., the air region) than neutron sources, thus indicating better transmission in these two regions, the x-ray D/S ratio is much lower than neutrons in the densest part of the cask: the lead and stainless steel regions. This is because thick, dense material regions attenuate neutrons much less than x-rays. Moreover, inspecting the horizontal line-out shows that increasing the neutron energy improves the D/S ratio in the dense regions of the SNF cask, particularly at material boundaries.

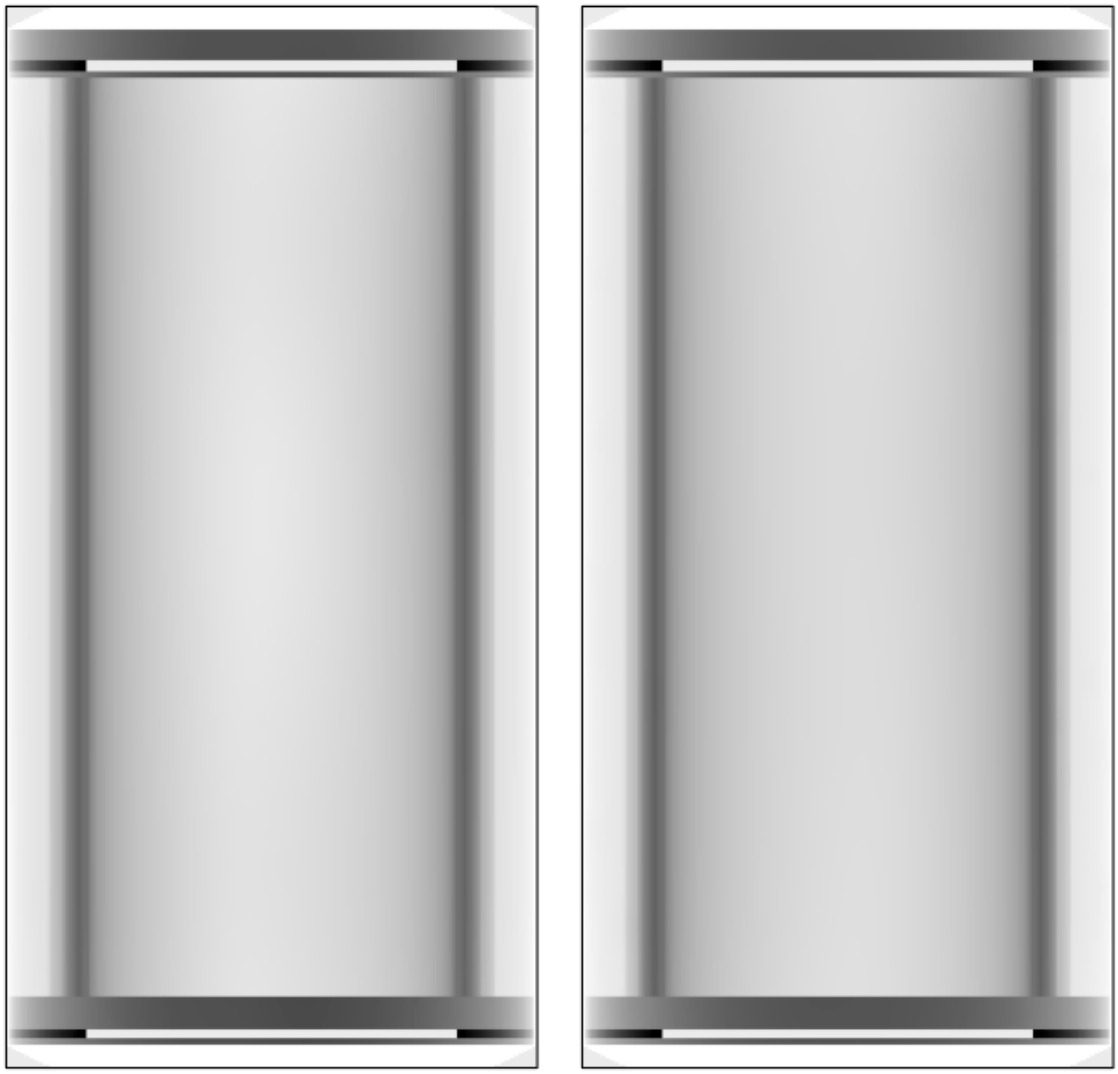


Figure 8.9: Simulated D/S x-ray radiographs for 6 MeV (left) and 15 MeV (right) bremsstrahlung x-rays. The two radiographs are set to the same contrast range, [-70,6].

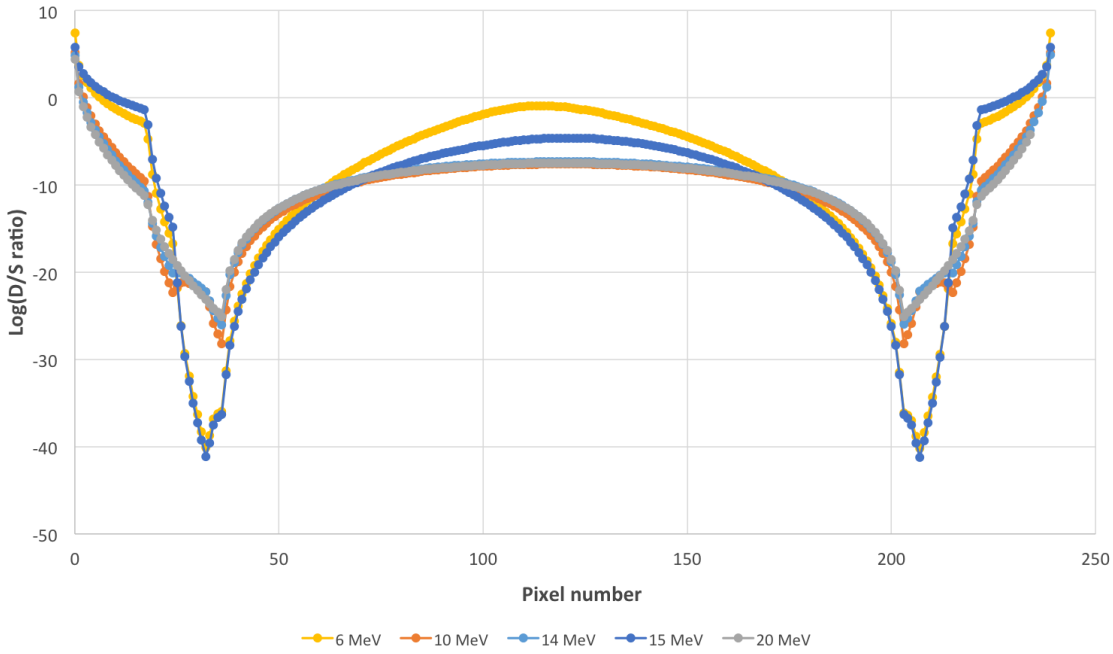


Figure 8.10: Plot of the horizontal line-out data for the simulated neutron (10, 14 and 20 MeV) and x-ray (6 and 15 MeV) D/S radiographs.

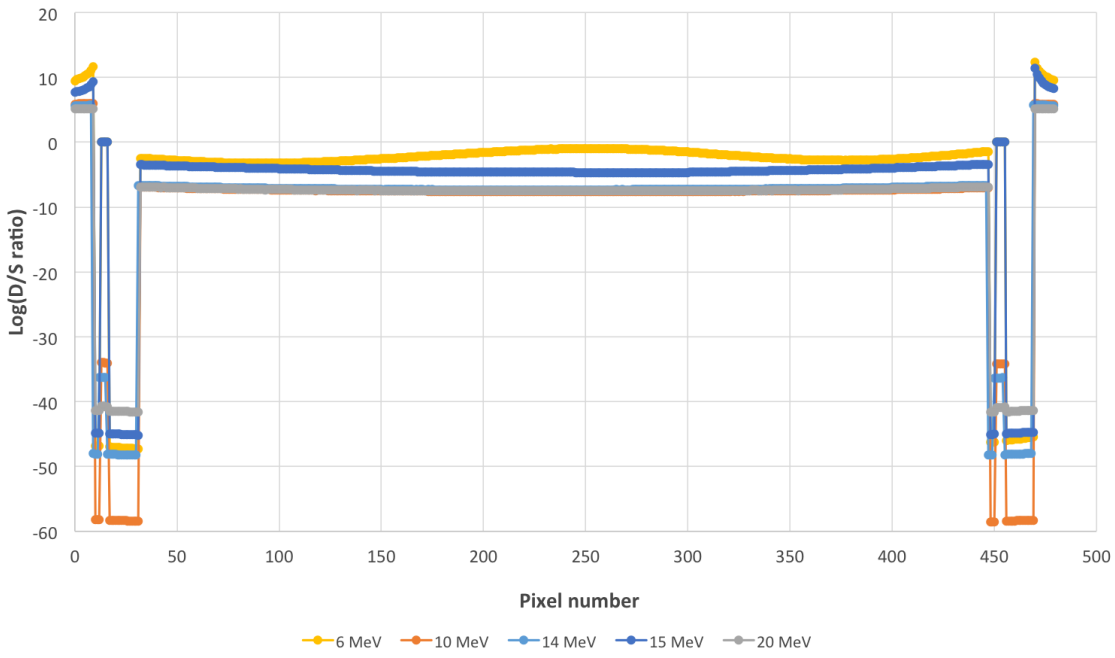


Figure 8.11: Plot of the vertical line-out data for the simulated neutron (10, 14 and 20 MeV) and x-ray (6 and 15 MeV) D/S radiographs, where Pixel 0 is the bottom of the radiograph.

Third, and possibly most importantly, region boundaries can be seen in the line-outs as changes in contrast and thus changes in slope. The horizontal line-outs of the 10 and 14 MeV neutron radiographs show all region boundaries, as do the 6 and 15 MeV x-ray radiographs (Figures 8.12 through 8.15, respectively).

The horizontal line-out of the 20 MeV neutron radiograph, however, only shows the concrete-outer stainless steel boundary and the outer stainless steel-air boundary; all other boundary details, such as the lead layer, are lost (Figures 8.16). This is because the lowest D/S ratio for 20 MeV is larger than that of the other neutron and x-ray sources modeled. This means that the range of available contrast is decreased for 20 MeV when compared with the lower-energy neutron sources studied here. Thus, for the SNF cask, the 10 or 14 MeV sources are better because material boundaries are more visible.

Material information can also be determined from the slope of the D/S line-out. For example, as seen in Figure 8.12, the two stainless steel regions have the same slope in the 10 MeV line-out. Additionally, the stainless steel slope differs from the air, concrete, and lead regions, each of which have their own distinct slope. This is also true for the simulated 14 MeV D/S line-out (but not for the 20 MeV plot, since the contrast range is too small to see all material boundaries).

Interestingly, the slope of the inner stainless steel region is concave for the neutron radiographs, but it is convex for the x-ray radiographs. This is believed to be a result of increased attenuation for x-rays as compared to neutrons, thus affecting the line-out slope differently. Moreover, the slope of the concrete region in the x-ray radiograph line-outs is much shallower than that in the neutron radiograph line-outs, indicating a higher D/S ratio since neutrons are more easily scattered by hydrogenous material; conversely, the slope of the lead region is much steeper for x-rays than for neutrons, again due to attenuation differences between the two particle types.

On a final note, line-outs were relatively constant in contrast regardless of where on the image the line-out was taken. A horizontal line-out was also taken at $y = 68$, and a vertical line-out at $x = 68$, and plotted against $y = 239$ and $x = 119$, respectively,

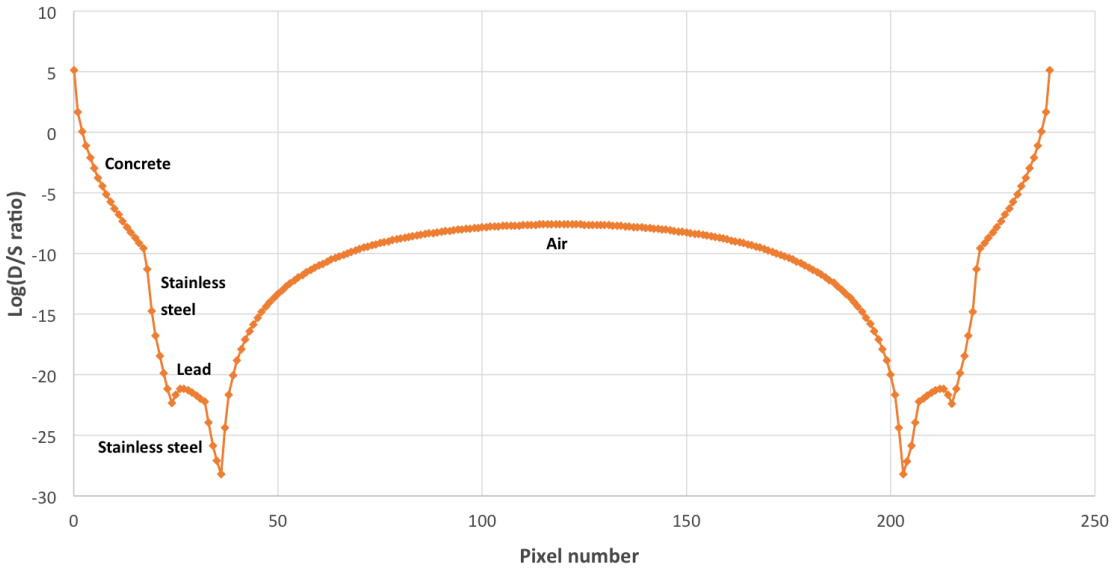


Figure 8.12: Plot of the horizontal line-out data for the simulated 10 MeV neutron radiograph, with all material boundaries visible.

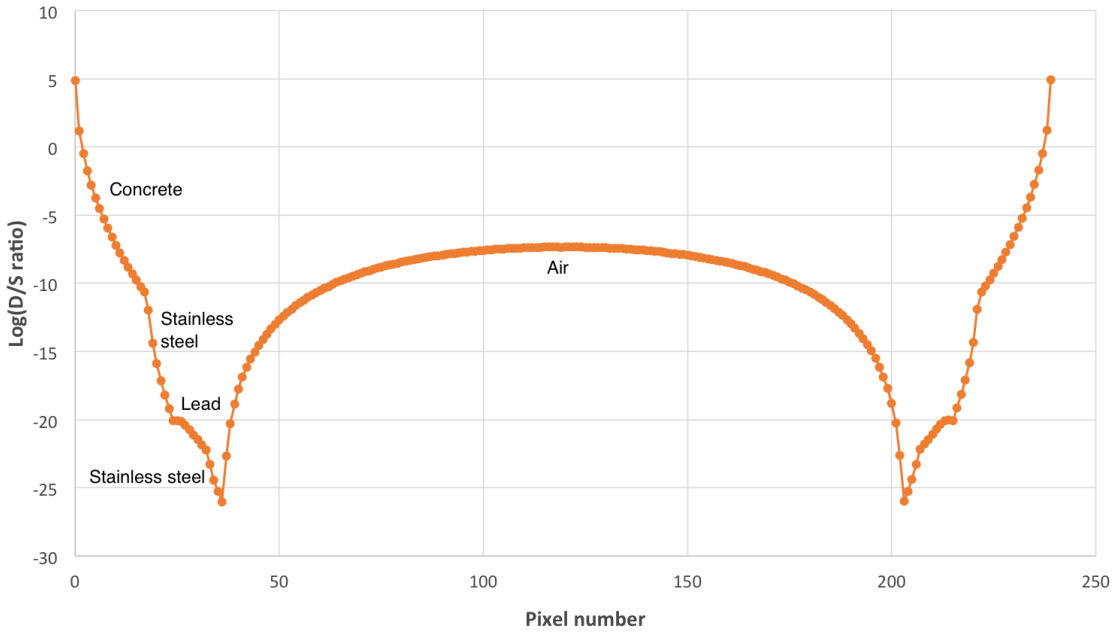


Figure 8.13: Plot of the horizontal line-out data for the simulated 14 MeV neutron radiograph, with all material boundaries visible.

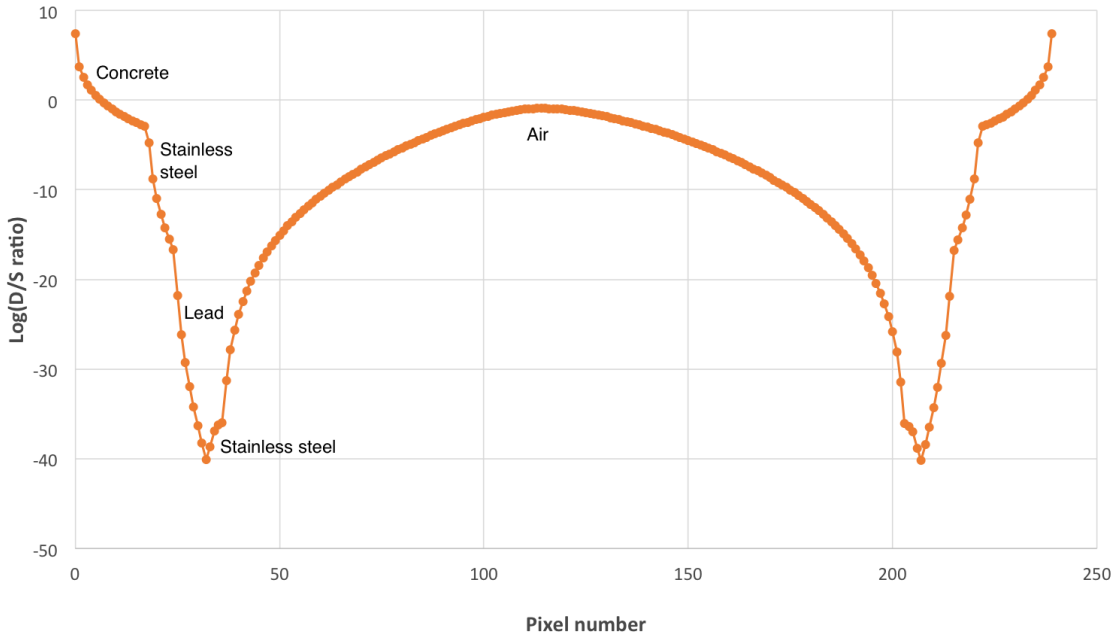


Figure 8.14: Plot of the horizontal line-out data for the simulated 6 MeV x-ray radiograph, with all material boundaries visible.

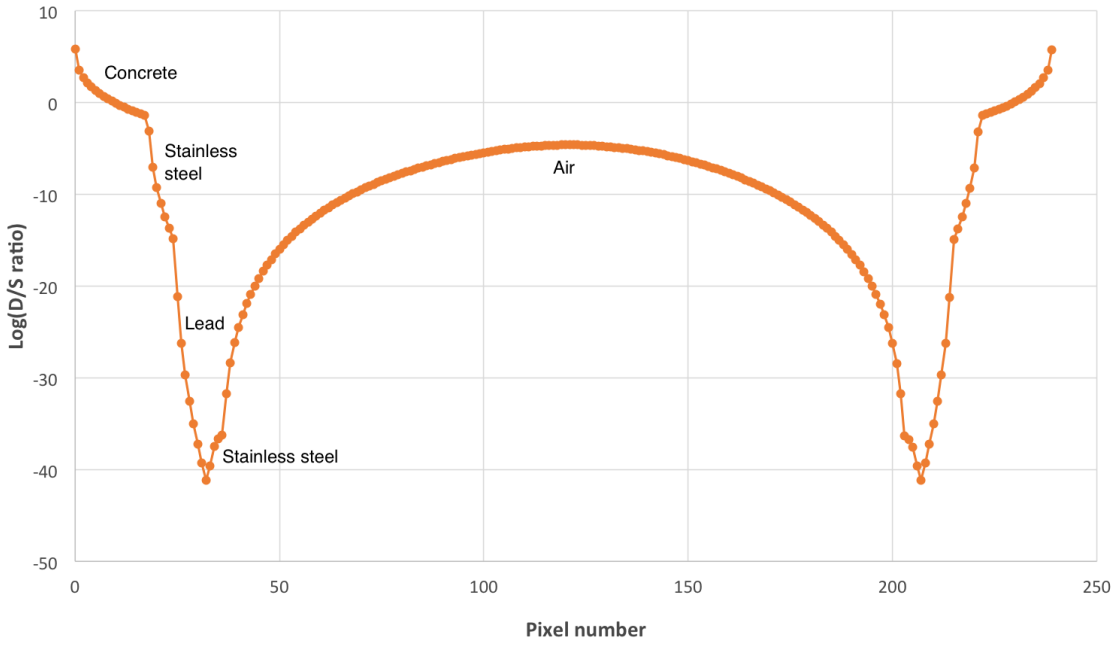


Figure 8.15: Plot of the horizontal line-out data for the simulated 15 MeV x-ray radiograph, with all material boundaries visible.

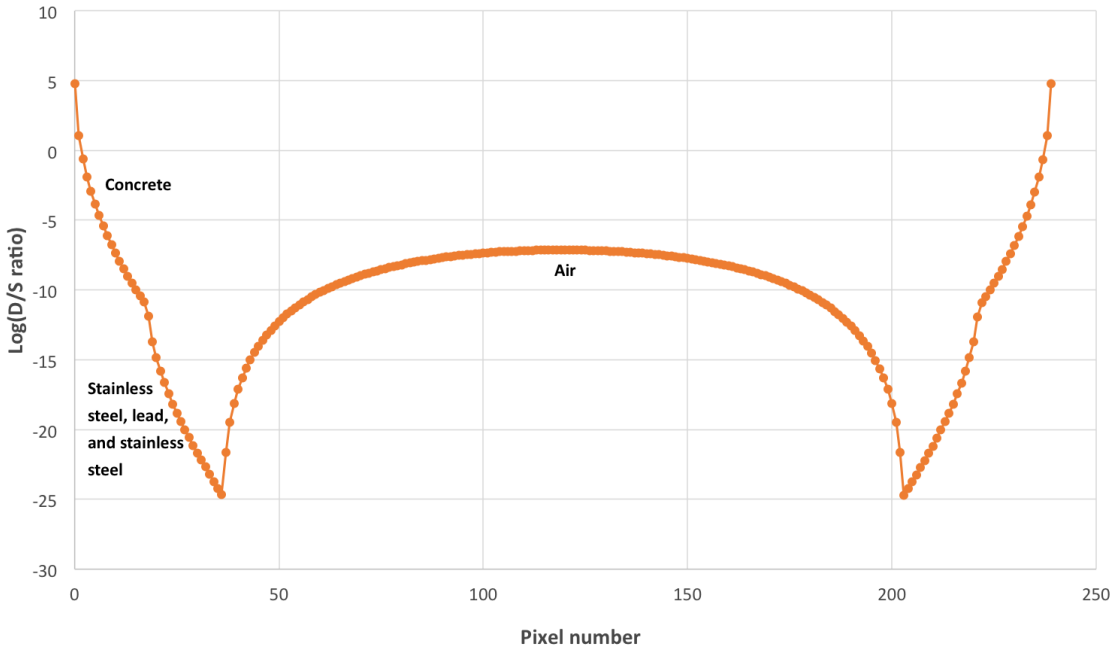


Figure 8.16: Plot of the horizontal line-out data for the simulated 20 MeV neutron radiograph, with only some material boundaries visible.

to see how line-out location affected visibility of features in the line-outs. For both the horizontal and vertical line-outs, D/S values varied slightly, but the material boundary changes were still visible. The D/S ratio varied more for the vertical line-outs due to the curvature in the object that causes the $x = 68$ line-out to see a thicker part of the cask than $x = 119$. Examples are shown in Figures 8.17 and 8.18 for a 10 MeV neutron source.

If one compares D images, which are manipulated so that pixel values are equal to areal density (σt) and are set to the optimal contrast level for that particular source energy (set using the "Auto" contrast algorithm within ImageJ), an interesting result is seen. As the neutron energy increases, the ability to see features with the "Auto" setting gets worse (Figure 8.19). This is because neutron attenuation decreases with energy, and contrast differences between areas of high and low attenuation became less distinct. Thus, if using the "Auto" setting, 10 MeV appears to be the best overall image because it easily penetrates the SNF cask but does not have the loss in contrast range that 14 and 20 MeV neutrons have.

However, it should be noted that contrast can be adjusted by a radiographer so that certain parts of the image are "washed out" in order to improve contrast in a certain region of interest. For example, by adjusting the contrast, the lid can be preferentially focused on in order to determine its components (Figure 8.20). Image manipulation is thus an important tool for radiographers to find defects or features.

8.2 Dose Delivered to the Radiography Object

8.2.1 Overview

Another MCNP6 study was conducted to determine the dose delivered, on a per source particle basis, to a representative cylindrical radiography object composed of tungsten and polyethylene. Such an object was designed to be thick and dense, and as such would be typical of an object requiring TiGReSSE for NDA. The object had

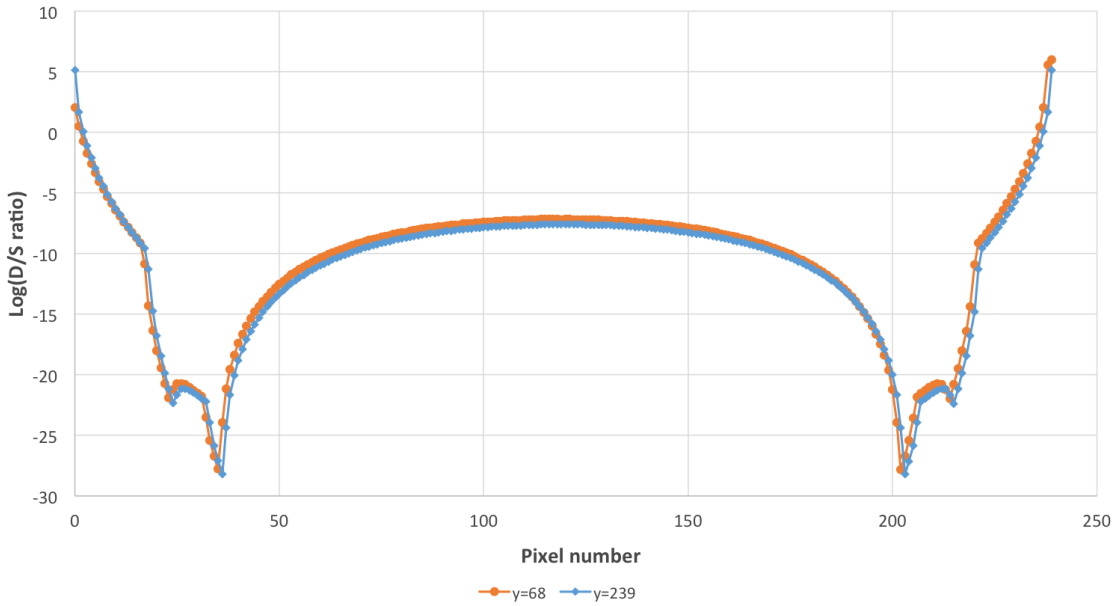


Figure 8.17: Horizontal line-outs were taken in two locations within the 10 MeV neutron radiograph of the SNF cask ($y = 68$ and $y = 239$) in order to determine the impact of the line-out location on the ability to find material boundaries.

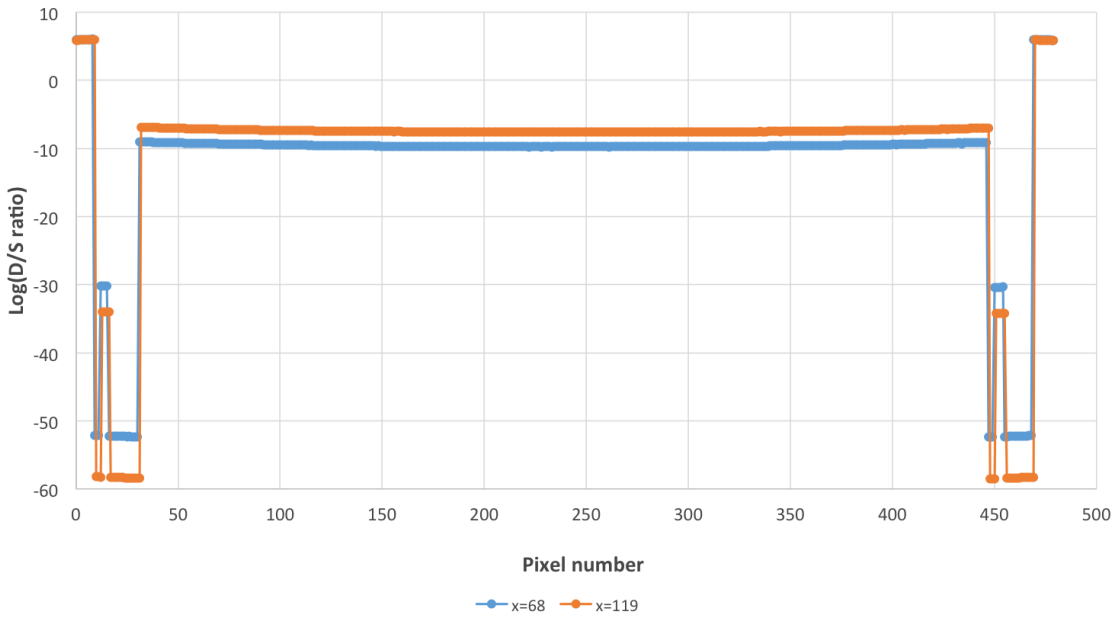


Figure 8.18: Vertical line-outs were taken in two locations within the 10 MeV neutron radiograph of the SNF cask ($x = 68$ and $x = 119$) in order to determine the impact of the line-out location on the ability to find material boundaries. Pixel 0 indicates the bottom of the cask.

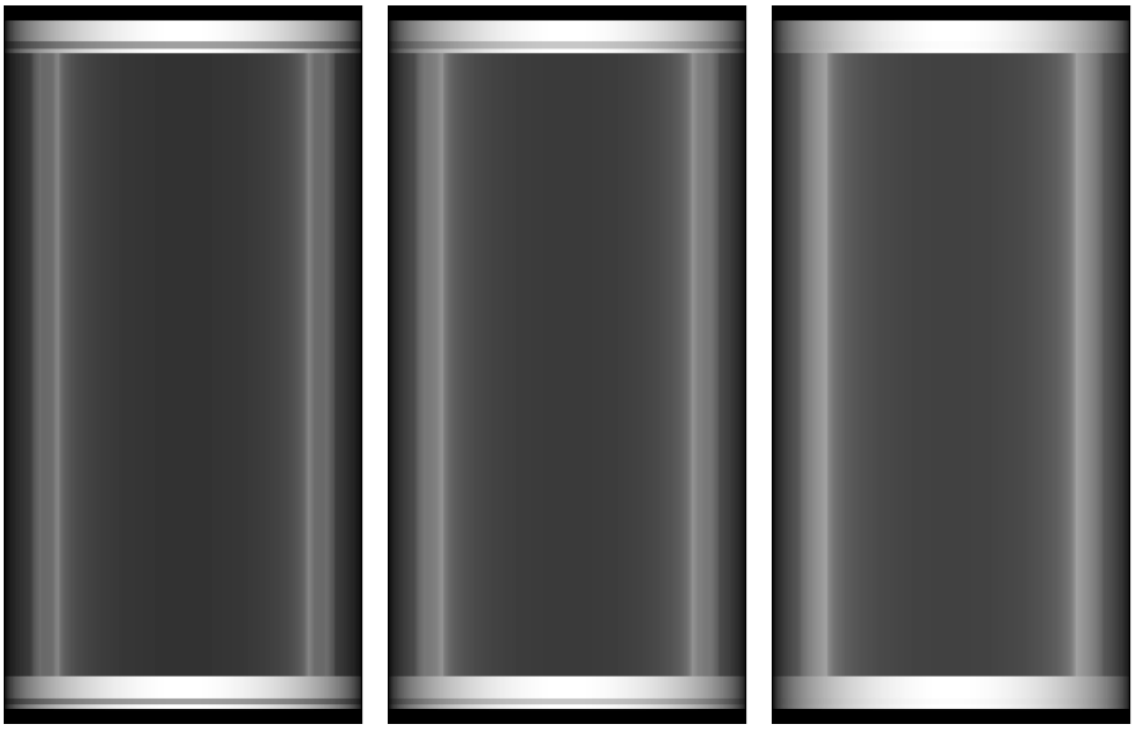


Figure 8.19: Simulated D neutron radiographs for 10 MeV (left), 14 MeV (center), and 20 MeV (right) neutrons. The three radiographs are set to different contrast ranges, which are determined to be optimal by an ImageJ "Auto" algorithm.

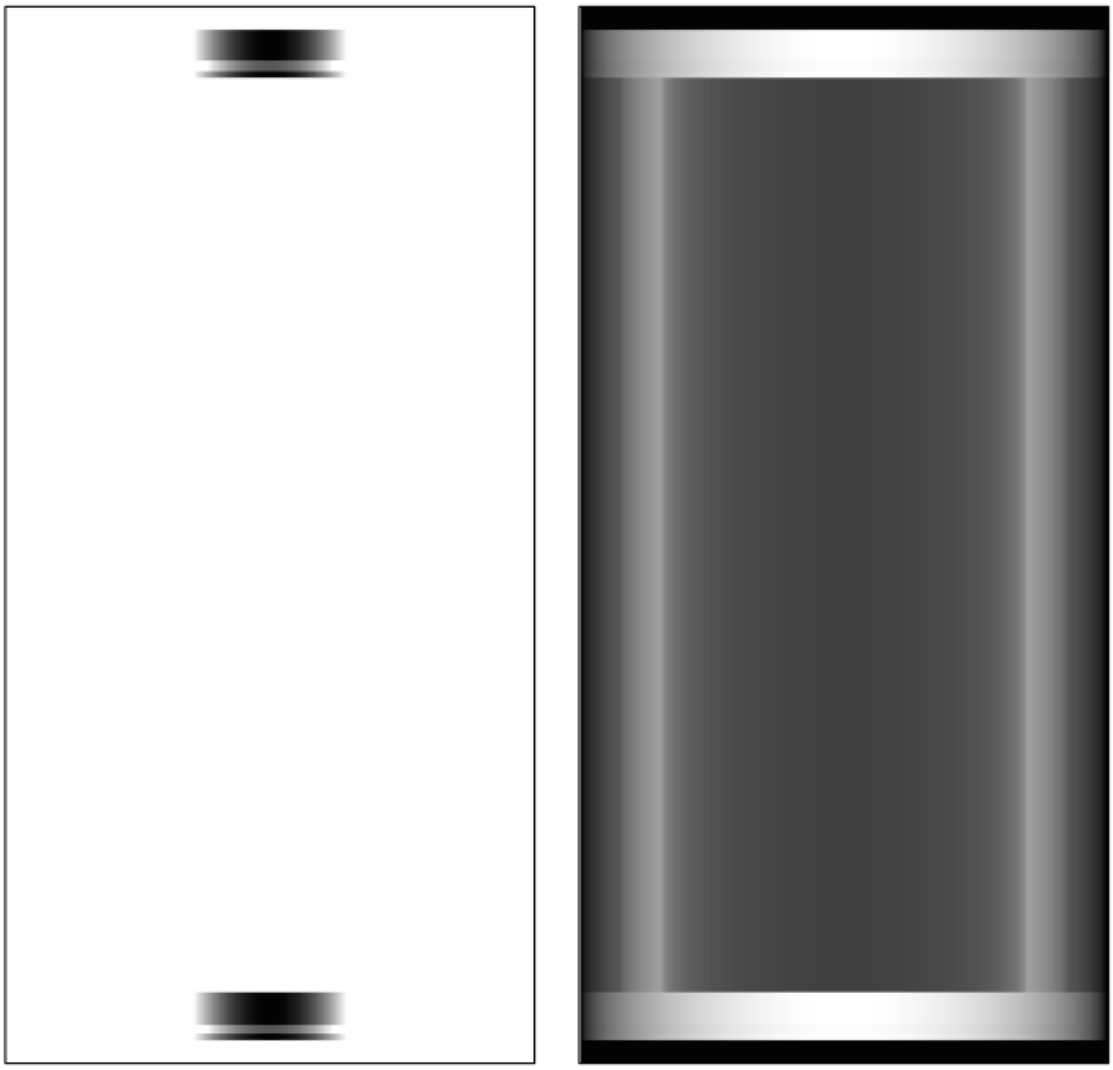


Figure 8.20: Two views of the 20 MeV simulated D neutron radiograph, one with a custom contrast setting (left) and one with the "Auto" contrast setting in ImageJ (right). Note that, while the "Auto" setting provides the most useful overall image, changing the contrast to a custom setting allows for features to be preferentially viewed while ignoring others and thus reveals features that may otherwise be hidden.

three cracks, modeled as rectangular prisms, and the cracks were varied in size to determine the effect of feature size on object dose; cracks were 1 cm, 5 mm, and 1 mm.

Dose varies as a function of particle type and energy, so multiple sources were simulated. For neutrons, monoenergetic sources of 10 MeV, 14 MeV, 20 MeV, 40 MeV were simulated, as well as the polyenergetic LANSCE spectrum. Bremsstrahlung x-ray sources were also simulated to compare to neutron sources, with endpoint energies of 6 MeV and 15 MeV.

This study simulated a perfectly efficient scintillator because the EJ-212 efficiency simulations were not completed by this time. Additionally, this study did not determine the number of source particles required to resolve features in a radiograph. Both of these variables affect the total dose delivered to the object because the scintillator efficiency varies with incident particle type and energy, as does the contrast within a radiograph. Future work will need to incorporate these two variables into the simulations in order to better determine the dose to the object. This study, however, provides a general idea of the amount of dose that TiGReSSE would deliver to a radiography object.

8.2.2 Simulation Description

A representative object was selected for this study. Low-Z material was placed inside of high-Z material, as this is a more challenging case for x-ray radiography (as compared to a high-Z material inside of a low-Z material). Cylindrical in shape, a polyethylene region (8 in diameter) was centered in a larger tungsten cylinder (12 in outer diameter). Both regions were 10 in tall. Three cracks were placed in the object, two full-length and one half-length in size. The full-length cracks were placed at the center of the polyethylene and on the polyethylene-tungsten border. The half-length crack was placed in the tungsten region. A not-to-scale diagram can be seen in Figure 8.21, with crack coordinates and object dimensions labelled.

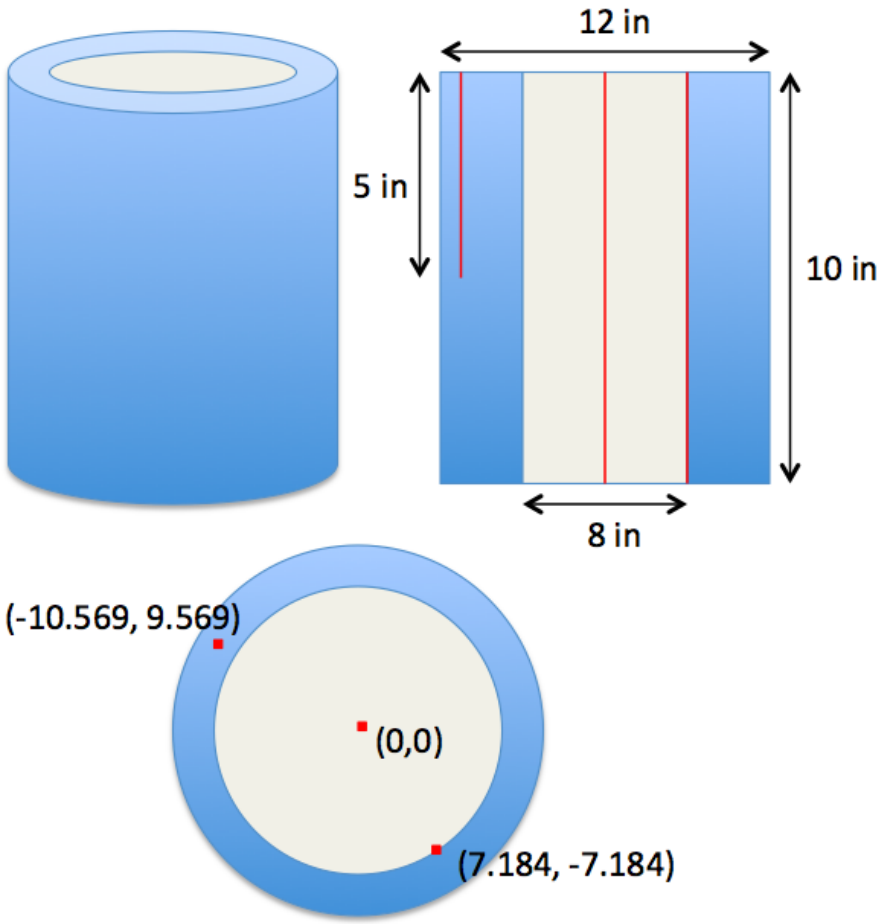


Figure 8.21: Not-to-scale diagram of the tungsten (blue) and polyethylene (beige) radiography object simulated in MCNP6 to estimate dose-to-object values. Cracks (red) are shown in their locations. Top left: External view of the object. Top right: Internal view of the center of the object, with full-length and half-length cracks shown. Bottom: View of the object from the top, with the crack coordinates listed.

The source was modeled to be the same geometry regardless of whether the source particles were neutrons or photons. The source and the object were placed in air, and the source was placed 20 cm from the object's centerline. The source was modeled as a pencil beam with a 30 cm diameter to ensure all areas of the object were equally exposed. This source diameter is possible at some LANSCE beam lines, so it is also a good approximation for experimental work, as well. The source was simulated with a strength of 5×10^8 particles.

An F6 tally was conducted to estimate the deposited energy within the object. Within the MCNP6 input deck, the F6 tally was multiplied by a factor of 1.6022×10^{-10} to convert the units from joules (J) to those of dose (Gy). The results of the F6 tally are volume-averaged, and thus dependent on the volume of the region being tallied, and are also normalized to the number of source particles simulated. The F6 tally was used in the polyethylene region, the tungsten region, and the total object, and, regardless of the source particle type, both photons and neutrons were tallied to study secondary (n, γ) and (γ, n) reactions.

8.2.3 Results and Conclusions

F6 tally results were multiplied by the associated volume to yield units of dose per source particle. Results are therefore independent of source strength and can be easily scaled if source properties are known. This is especially helpful for source design considerations. Additionally, normalizing dose to the source particle allows for scaling based on the number of source particles necessary to resolve features in a radiograph. For a feature of a given size and location within the radiography object, the source must have a flux large enough to overcome system noise; otherwise, contrast resolution is too poor to see the feature in the radiograph. The necessary flux is best determined experimentally, where the interdependence of properties of the source and TiGReSSE can be studied. Results can also be scaled by the EJ-212 efficiency for a given particle type and energy. This is left for future work.

Dose resulting from secondary particles was seen to differ according to the interrogation source. Neutron sources, via the (n, γ) reaction, deliver photon dose to the inner polyethylene region of the cylinder that is approximately one order of magnitude lower than the neutron dose. In comparison, the (γ, n) dose from the x-ray sources is zero for the polyethylene region, and photon dose to the polyethylene region is two orders of magnitude lower than that from the (n, γ) reaction. This indicates that neutrons cause more photon dose than photons themselves for the polyethylene region, most likely aided by the fact the most x-rays do not penetrate the thick tungsten. These results can be seen in Figure 8.22.

Similarly, dose from secondary particles in the tungsten region has no (γ, n) component, indicating that such a reaction does not occur in this object (Figure 8.23). The (n, γ) reaction also occurs in the tungsten region, but is much larger in value than in the polyethylene. This indicates that the photons are generated in the tungsten and travel into the polyethylene, attenuating along the way. Overall, dose is higher in the tungsten region because all of the source particles reach its outer edge, as opposed to the attenuated number that reach the outer border of the polyethylene region.

The fact that x-ray sources are penetrating the tungsten region in much lower numbers than the neutron sources is further evidenced by FMESH simulated radiographs. To simulate direct radiographs, the F6 tally was replaced by an FMESH tally in MCNP6. The FMESH tally used 1200 voxels along the x-axis (i.e, along the cylinder diameter) and 600 voxels along the y-axis (i.e., along the cylinder height). This provided a 0.1 mm resolution at the detector plane, which was 20 cm from the object centerline and facing the source.

Direct images are shown in Figure 8.24, which have no flatfield manipulation or otherwise. These radiographs show that the 14 MeV neutrons not only penetrate the object but also yield images of the tungsten-polyethylene boundary and two of the three cracks. On the other hand, the 15 MeV x-rays are hardly able to penetrate the object. By increasing the number of source particles, statistics would improve for both sources, but the neutron source strength would not need to be increased nearly

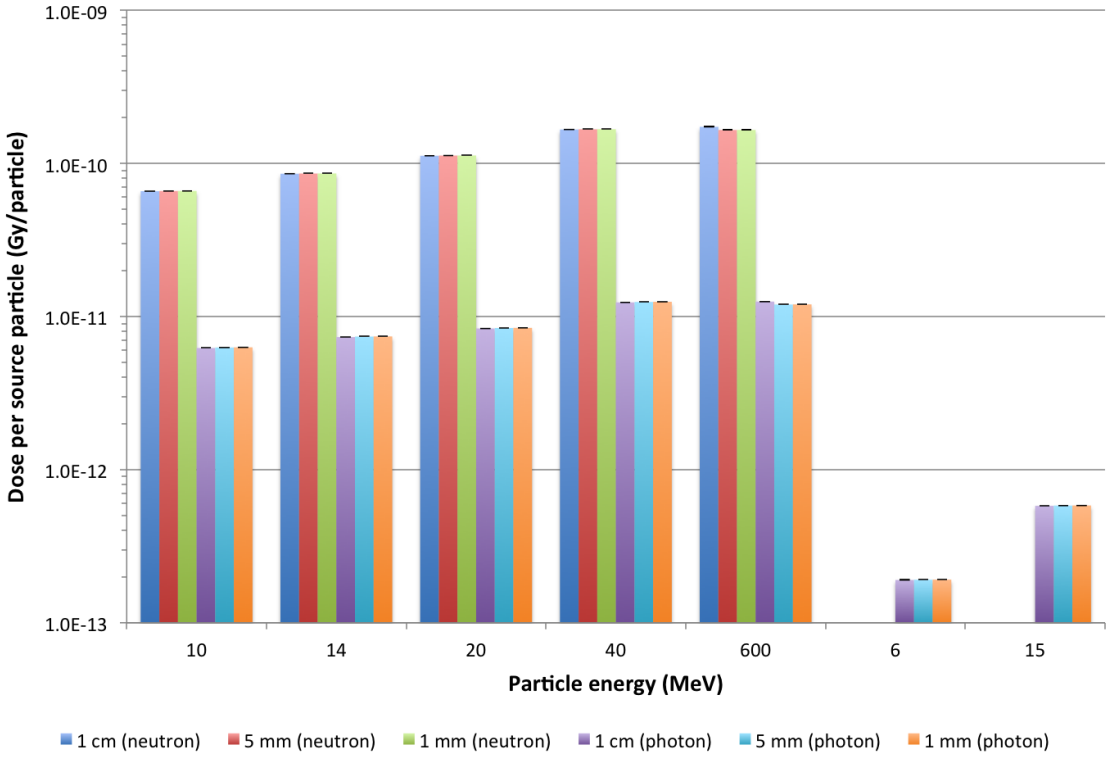


Figure 8.22: Dose per source particle that is delivered to the polyethylene region as a function of source type and energy, particle type delivering dose (neutron or photon), and crack size (1 cm, 5 mm, or 1 mm). Neutrons deliver neutron dose and, via the (n, γ) reaction, photon dose. X-rays deliver photon dose, with neutron dose via the (γ, n) reaction equal to zero for this radiography object. The polyenergetic sources (LANSCE, 6 MeV, and 15 MeV) are indicated by their endpoint energy. Error bars are indicated.

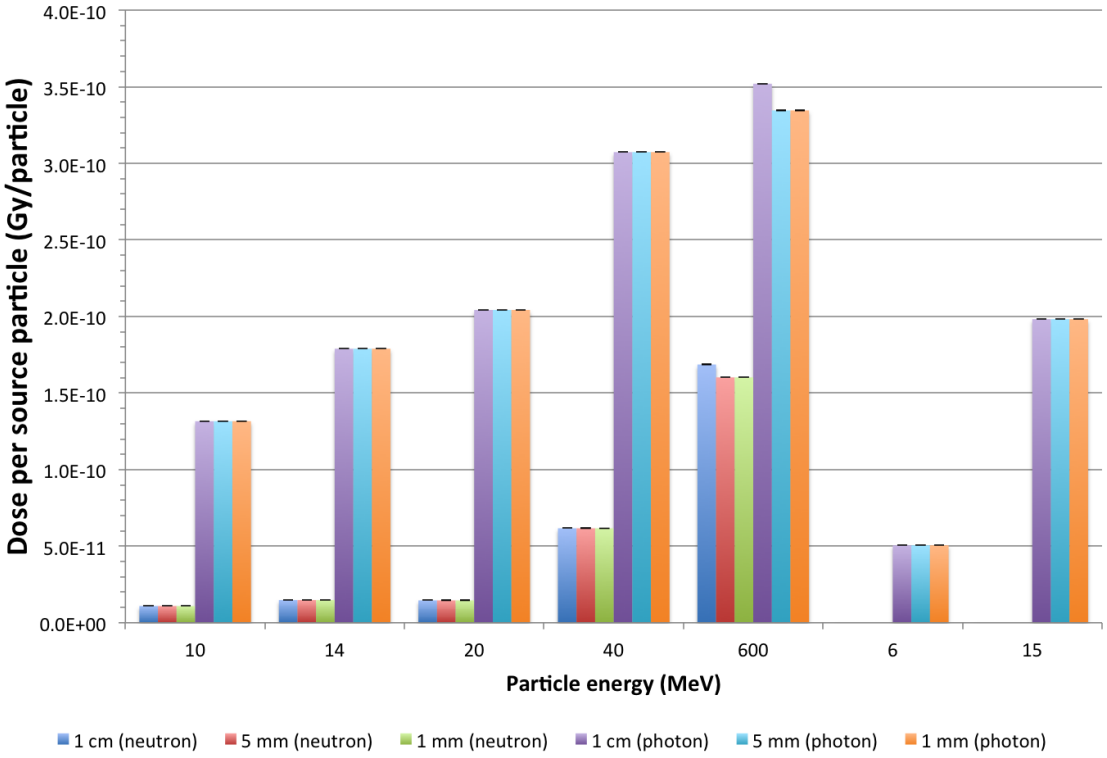


Figure 8.23: Dose per source particle that is delivered to the tungsten region as a function of source type and energy, particle type delivering dose (neutron or photon), and crack size (1 cm, 5 mm, or 1 mm). Neutrons deliver neutron dose and, via the (n, γ) reaction, photon dose. X-rays deliver photon dose, with neutron dose via the (γ, n) reaction equal to zero for this radiography object. The polyenergetic sources (LANSCE, 6 MeV, and 15 MeV) are indicated by their endpoint energy. Error bars are indicated.

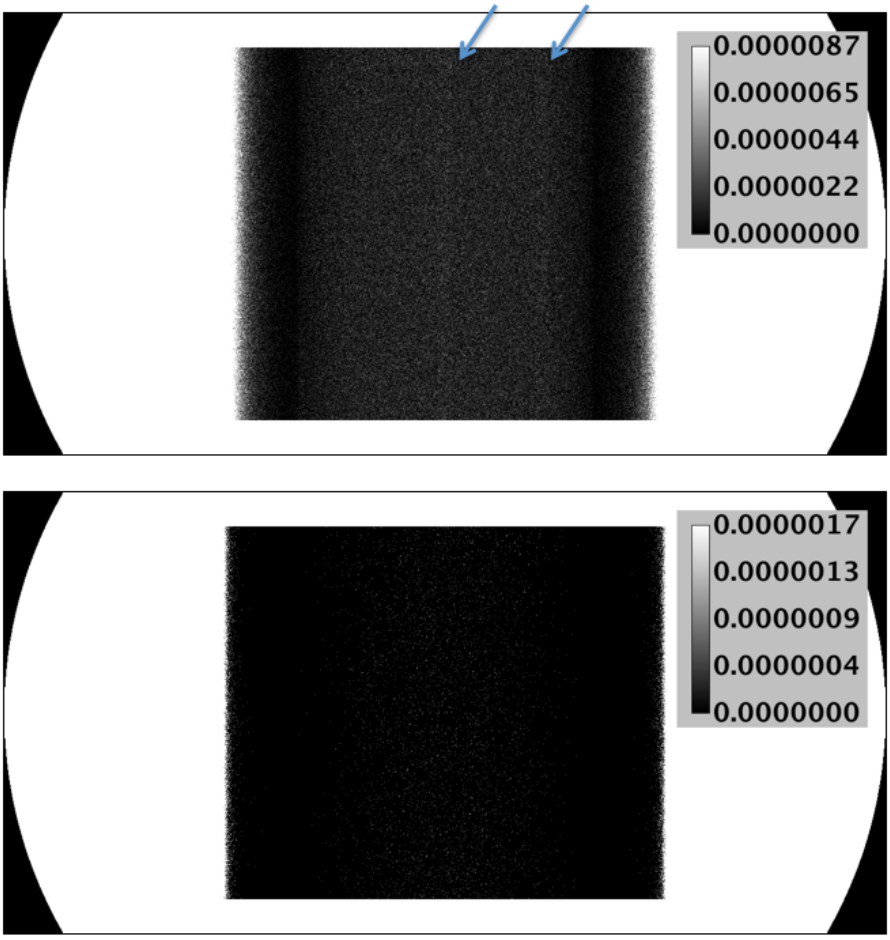


Figure 8.24: Simulated direct radiographs of the cylindrical object, generated by an MCNP6 FMESH tally. Source and geometry specifications remained the same as the MCNP6 F6 dose tally outlined in this section. The cylindrical object, composed of tungsten and polyethylene, has three 1 cm cracks. Top: Radiography source is 14 MeV neutrons. Note that the tungsten-polyethylene border and two of the three cracks are visible (indicated by arrows), with the third most likely in a contrast-stretched region. Bottom: Bremsstrahlung x-ray radiography source with a 15 MeV endpoint energy. Note that hardly any x-rays are penetrating the center, which is the thinnest (and therefore easiest) part of the object for x-rays to image, and that no cracks are visible.

as much as the x-ray source strength to clearly view all interior features. Thus, an x-ray source has the potential to deliver more dose to the radiography object than a neutron source because more x-rays are required to resolve the three cracks. (Note that the number of simulated particles was not selected for image quality but rather for good F6 tally statistics.)

The plot in Figure 8.25 shows the dose per source particle for the entire object as a function of source particle energy and type, as well as crack size. Examining this plot reveals that the photon dose is higher than the neutron dose, except for the LANSCE spectrum source, in which case they are about equal. Higher photon dose is driven by the (n, γ) reaction in the tungsten region, which is an important result; one cannot solely consider neutron dose from a neutron source when calculating dose-to-object values because the (n, γ) dose can actually exceed the dose from the incident source particle itself.

The fourth plot, shown in Figure 8.26, compares the total dose (neutron plus photon) in each region as a function of crack size and particle energy. This plot indicates the dose to the tungsten region is higher than that to the polyethylene region, due to unattenuated flux at the tungsten boundary and the high incidence of (n, γ) reactions. Additionally, crack size does not seem to affect the dose delivered to the object.

The final plot, Figure 8.27, shows dose per source particle to the entire radiography object as a function of crack size and particle energy. This plot is even more clear than the others that increasing particle energy increases the dose deposited per source particle, and that, overall, the change in size of the cracks does not appear to affect dose per source particle in a meaningful way. The only exception is the LANSCE energy spectrum, which shows a higher dose for the object with 1 *cm* cracks than the other two crack sizes. This is thought to be a result of activation of the air within the cracks.

Combining the conclusions from the final plot in Figure 8.27 with the direct radiographs in Figure 8.24, it becomes perhaps more obvious that neutrons and x-rays

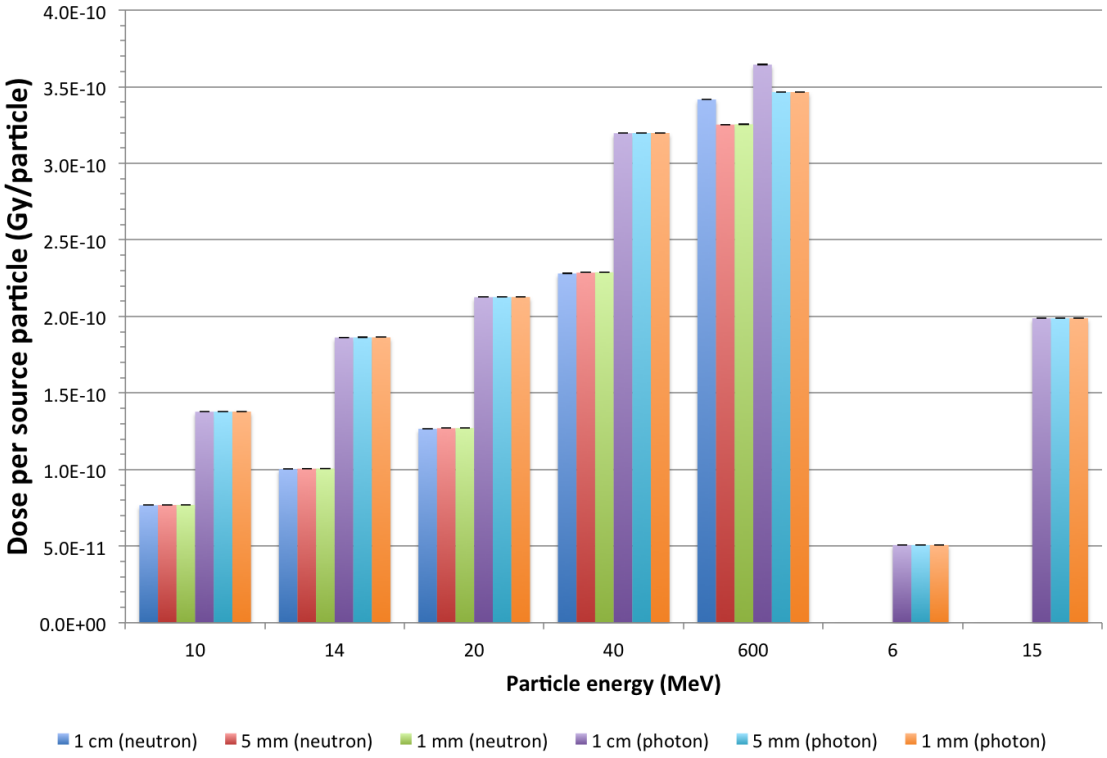


Figure 8.25: Dose per source particle that is delivered to the entire radiography object (tungsten plus polyethylene) as a function of source type and energy, particle type delivering dose (neutron or photon), and crack size (1 cm, 5 mm, or 1 mm). Neutrons deliver neutron dose and, via the (n, γ) reaction, photon dose. X-rays deliver photon dose, with neutron dose via the (γ, n) reaction equal to zero for this radiography object. The polyenergetic sources (LANSCE, 6 MeV, and 15 MeV) are indicated by their endpoint energy. Error bars are indicated.

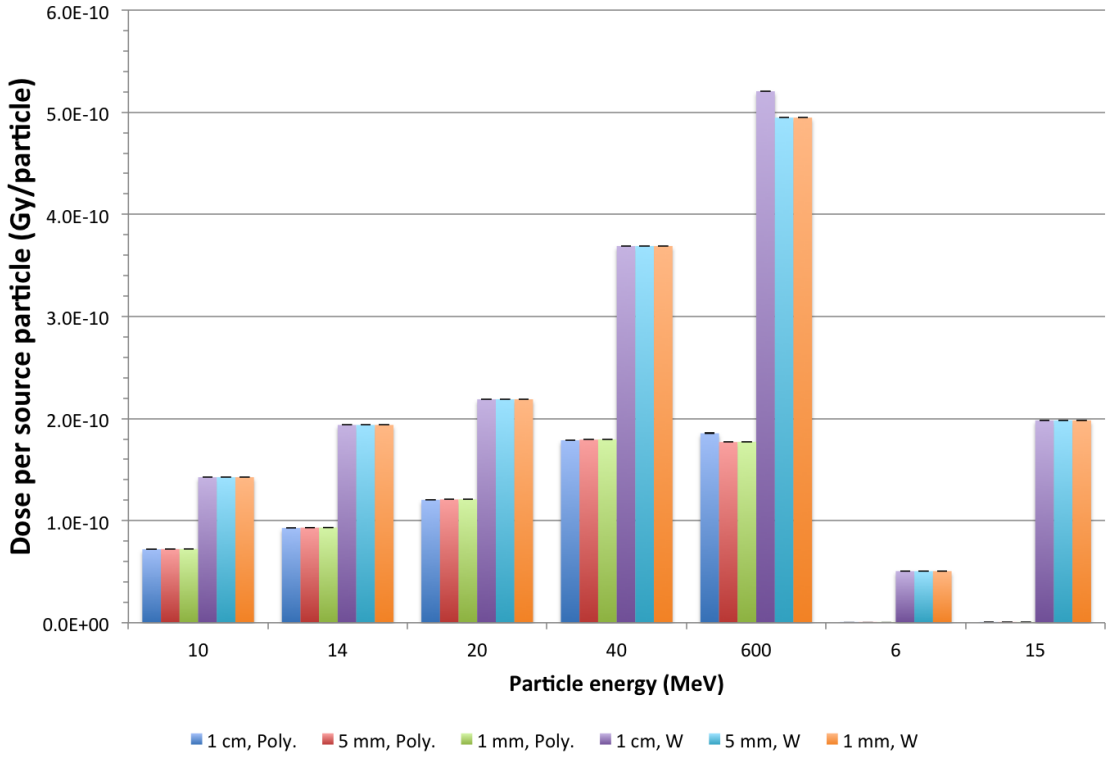


Figure 8.26: Total dose (neutron plus photon) per source particle that is delivered to each material region as a function of source type and energy, particle type delivering dose (neutron or photon), and crack size (1 cm, 5 mm, or 1 mm). Neutrons deliver neutron dose and, via the (n, γ) reaction, photon dose. X-rays deliver photon dose, with neutron dose via the (γ, n) reaction equal to zero for this radiography object. The polyenergetic sources (LANSCE, 6 MeV, and 15 MeV) are indicated by their endpoint energy. Error bars are indicated.

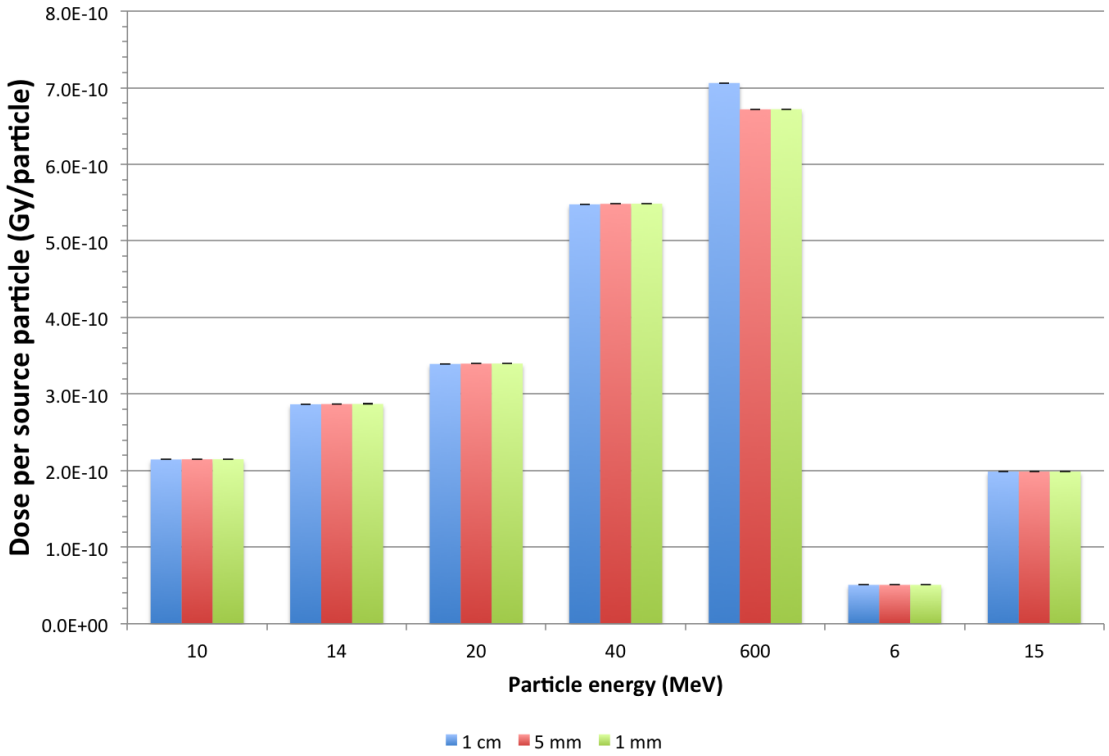


Figure 8.27: Total dose (neutron plus photon) per source particle that is delivered to the entire radiography object as a function of source energy and crack size (1 cm, 5 mm, or 1 mm). The polyenergetic sources (LANSCE, 6 MeV, and 15 MeV) are indicated by their endpoint energy. Error bars are indicated.

have very different mechanisms for depositing dose. While the total dose per source particle is higher for neutrons (again, driven by the (n, γ) reaction within tungsten), fewer neutrons are necessary to radiograph thick, dense objects such as the tungsten and polyethylene cylinder described here. If secondary particle reactions were to be ignored, 15 MeV x-rays would deliver twice the dose as 14 MeV neutrons; secondary particles are thus a large contributor to dose.

For these types of dense, high-Z objects, there is most likely less dose deposited by neutrons than x-rays when one considers the number of particles necessary to resolve features. Additional experimental or computational studies need to be completed to determine how detector efficiency and required image quality affect dose delivered to the object.

Chapter 9

Additional Neutron Radiography Testing

This chapter outlines additional experimental testing of the TiGReSSE neutron radiography system, conducted nearly a year after the experiments outlined in Chapter 5. Based on the results seen in FP15R, the camera was moved within the light-tight box to allow for better shielding of the camera that would reduce the number of stars in the radiographs and better preserve camera electronics.

An important difference between the experiments in Chapter 5 and this chapter is that the flight path changed from FP15R to Flight Path 60 Right (FP60R). FP60R is also to the right of the spallation target, but instead views the target at 60° and thus has a different energy spectrum (refer to Figure 5.3). The neutrons are shifted to lower energies, with a slightly lower endpoint energy and increased flux below $\sim$10 MeV. This is because FP60R does not receive as many forward-peaked spallation particles as FP15R, causing the spallation particles to have lower energies due to the principles of kinematics. The location of the new flight path with respect to the target is indicated in Figure 9.1.

Goals of this second series of experiments included conducting an energy scan to determine the true start of the pulse; testing the new shielding design, which was

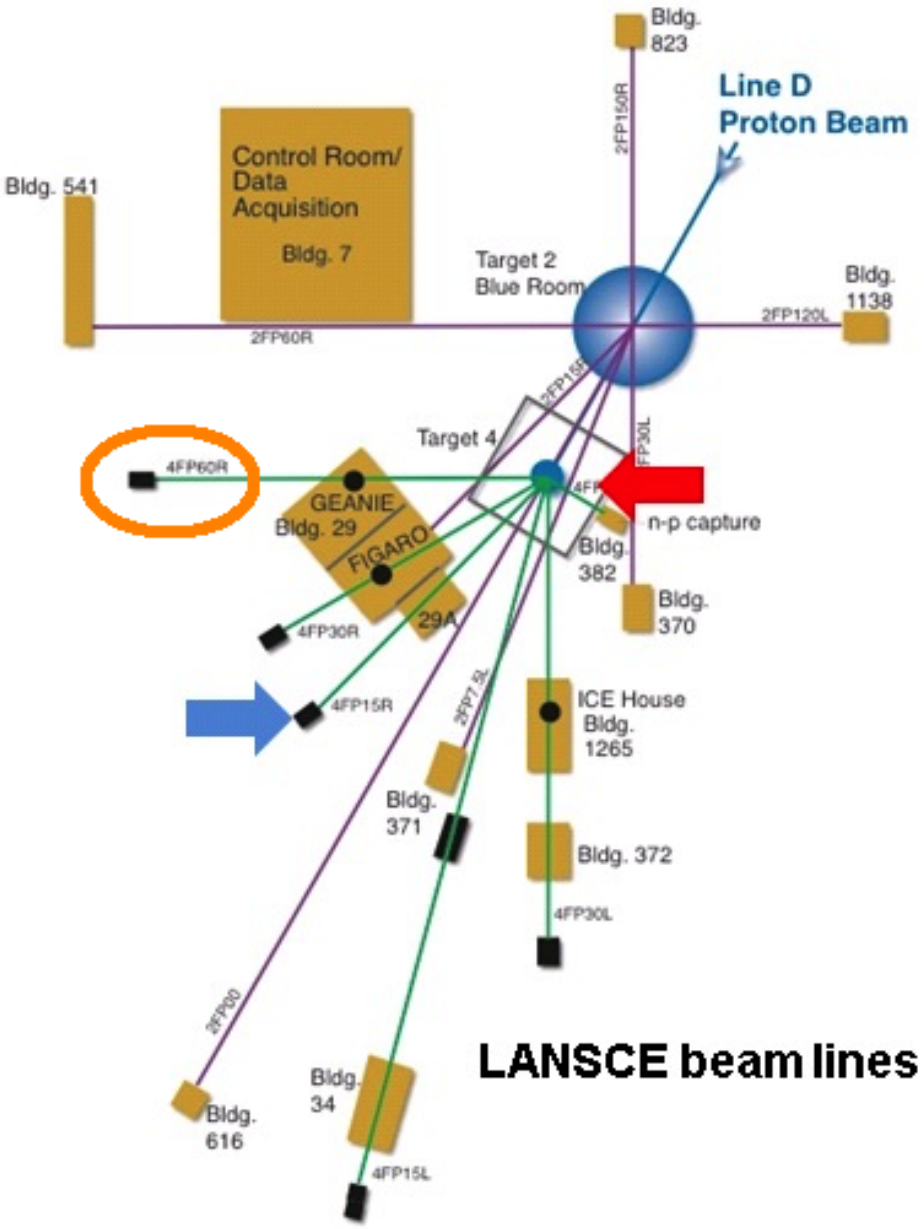


Figure 9.1: Diagram of LANSCE beam lines, with the red arrow pointing to Target 4 and the blue arrow pointing to FP15R. The new flight path, FP60R, is indicated by an orange oval [67].

outlined in Chapter 7, and a Generation II TiGReSSE design; generating radiographs for a longer period of integration time to improve statistics; radiographing interesting objects, some of which were imaged in FP15R; and comparing the effect of flight path properties (i.e., FP60R vs. FP15R) on image quality. Changing from FP15R to FP60R should benefit these studies because the beam diameter can be much wider in FP60R (a maximum of 11 in in FP60R, as compared to a maximum of 4 in in FP15R), which decreases exposure time due to increased flux. Additionally, there is less upstream clutter in FP60R than in FP15R, such as other experiment's equipment, which is expected to improve image quality by reducing scatter and activation products. Results from these experiments will further improve TiGReSSE system design.

9.1 Overview

9.1.1 FP60R Beam Description

Although the energy distribution of the FP60R spallation source is slightly lower than that of FP15R, the micropulse width remained the same (1784 ns), as did the macropulse period (625 μs). However, because FP60R views the target at a different angle (60° versus 15°) and at a different distance from the target (21.95 m from the target to the scintillator, as compared to 22.7 m in FP15R), the time-of-flight and relevant time bins are not the same. An accelerator trigger signal was provided in the same way that it was provided at FP15R, and was similarly used to trigger the camera.

The beam port was also different for FP60R. While also made of steel, the FP60R beam port was larger in diameter and could be operated with an inner diameter of up to 11 in. As a result, from a simple ratio of the areas, the FP60R flux has the potential to be approximately eight times higher than the FP15R flux. A cylindrical fission chamber was provided by LANSCE and attached to the front of the beam pipe

to record beam flux levels as a function of time, but because it did not work for almost the entire experiment, its output is not described in this chapter. A photograph of the beam pipe, the fission chamber, and its shielding wall can be seen in Figure 9.2, and a photograph of the front of the fission chamber can be seen in Figure 9.3. Note that there are holes in both the fission chamber and beam pipe, which will be seen in the radiographs in this chapter.

It was also seen that FP60R was better collimated than FP15R, preventing spallation particles from clipping the beam pipe and causing additional scatter, and most likely better aligned with the beam stop (a wall designed to prevent high dose to pedestrians outside the beam line). For all these reasons, dose in FP60R was much less to the scientists, even though they sat closer to the beam.

9.1.2 Flight Path Geometry

Compared to FP15R, FP60R has a much smaller flight path area to set up and monitor TiGReSSE equipment (Figure 9.4). With staff thus sitting closer to the beam pipe than in FP15R, a large magnetite concrete cave was constructed in FP60R to reduce dose to staff. The cave was placed around the area where the radiography object would be located since it is the largest potential source of scatter. Diagrams of the front and side views of the cave can be seen in Figures 9.5 and 9.6, respectively. Figure 9.7 shows the sliding block that is used to further protect staff from the direct beam. A photograph of the cave can be seen in Figure 9.8.

9.1.3 Experimental Set-up

Light-tight Box

TiGReSSE was placed into a new configuration for the measurements in FP60R so as to reduce scatter into the camera. An additional mirror was added and the camera was rotated, allowing for the addition of more shielding within the light-tight box (compare Figure 9.9 to Figure 5.11). This new Generation II design also increased



Figure 9.2: A photograph of the beam pipe, the fission chamber, and the concrete shielding blocks placed around it to reduce scatter and dose to personnel.

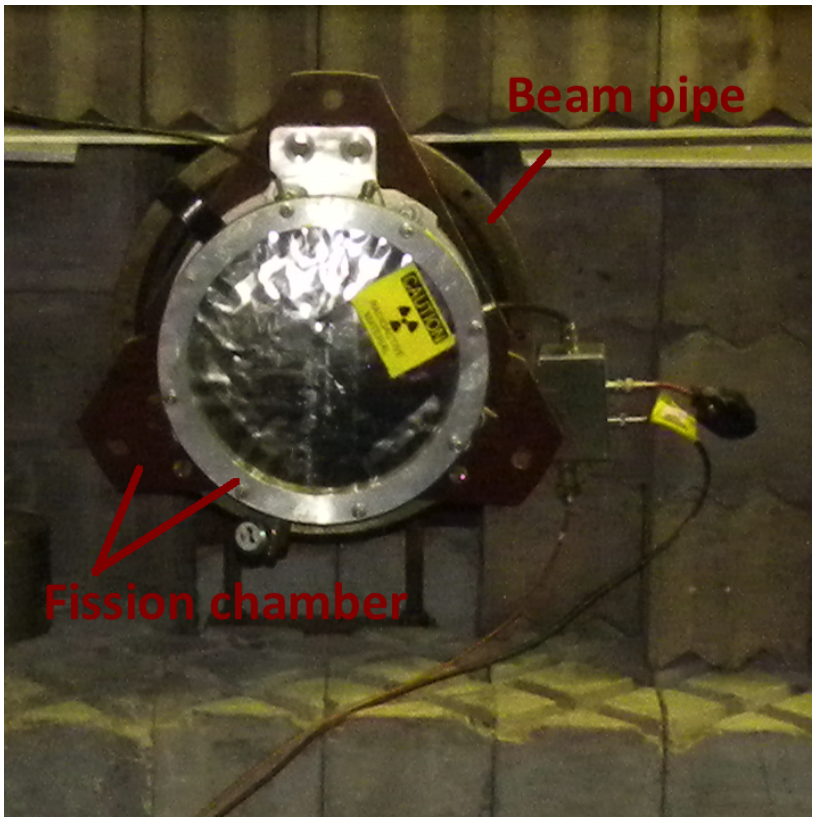


Figure 9.3: A photograph of front of the fission chamber, with its instrumentation and the beam pipe visible behind it. Note how the fission chamber has three large holes, one in each corner of its support, and that the beam pipe also has smaller holes along its edge.

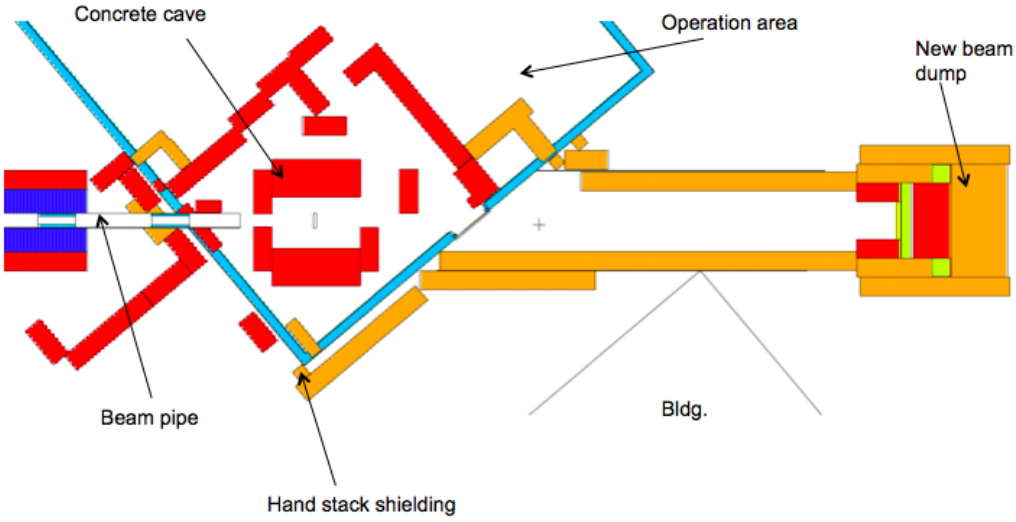


Figure 9.4: A not-to-scale diagram of FP60R. The FP60R building is shown in light blue, hand stack shielding (mostly concrete) is shown in yellow, and magnetite concrete is shown in red. The cave, beam pipe, beam dump (used to stop particles that would exit the flight path in order to protect workers), a neighboring building, and experimental operation area are indicated. This diagram was provided by R. Nelson of LANSCE.

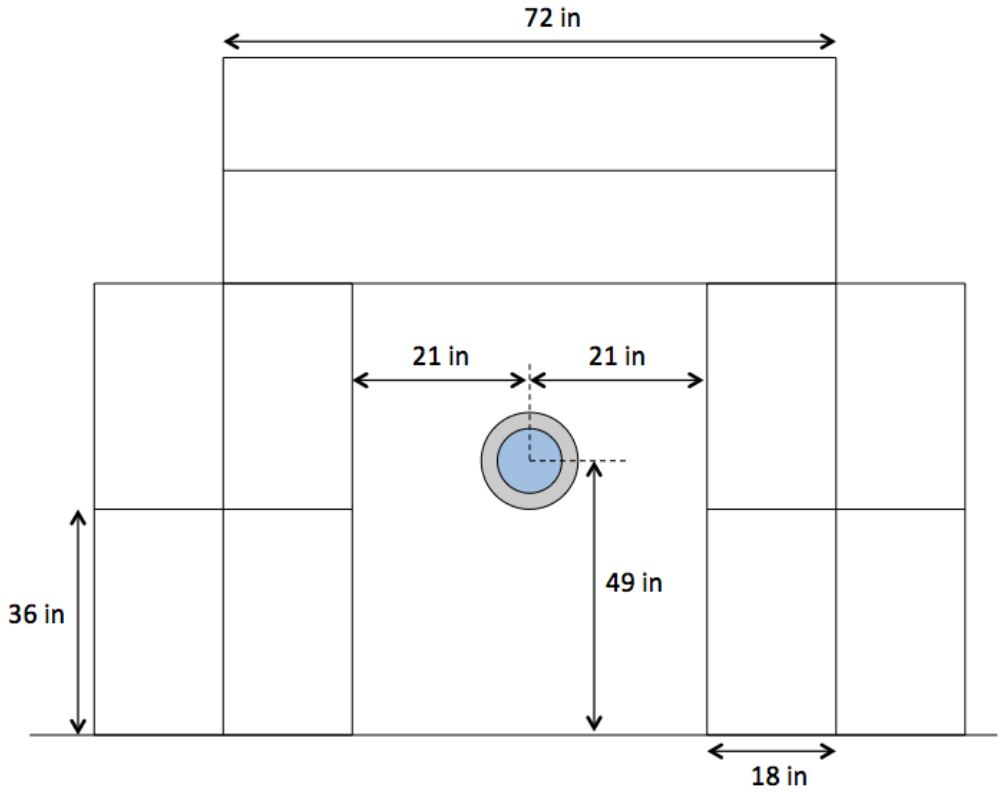


Figure 9.5: A not-to-scale diagram of the front view of the cave used to shield staff from scatter off of the radiography object. The beam pipe is shown in gray, and the fission chamber used to monitor beam flux is shown in blue. Concrete magnetite blocks (white) are of identical dimensions.

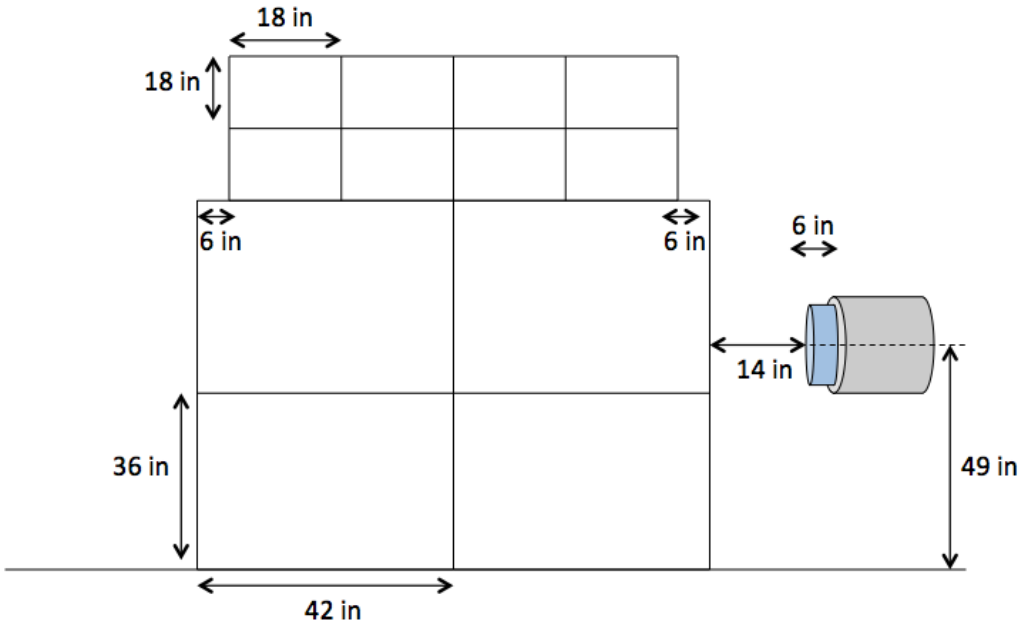


Figure 9.6: A not-to-scale diagram of the side view of the concrete cave used to shield staff from scatter off of the radiography object. The beam pipe is shown in gray, and the fission chamber used to monitor beam flux is shown in blue. Concrete magnetite blocks (white) are of the same dimensions.

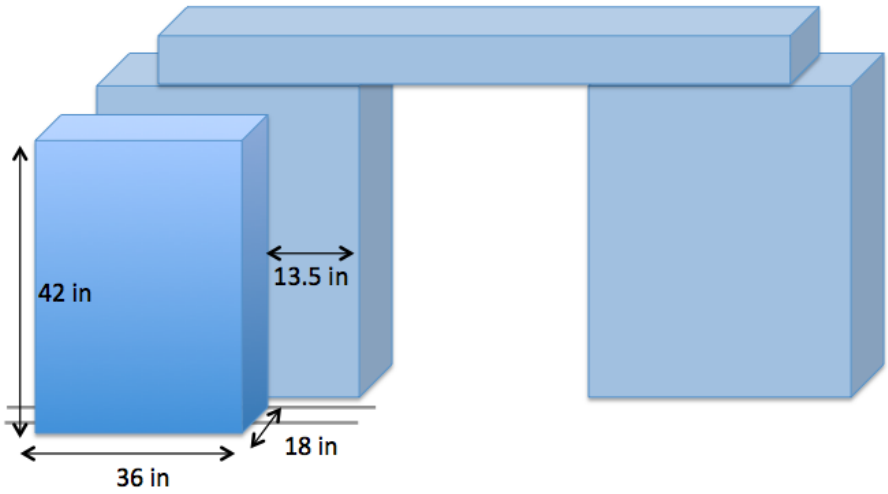


Figure 9.7: A not-to-scale diagram of the sliding concrete block that is used to protect staff walking outside of FP60R. The block is placed on rails (gray) so its position can be changed as needed. Note that there is no gap between the sliding block and the concrete cave behind it.

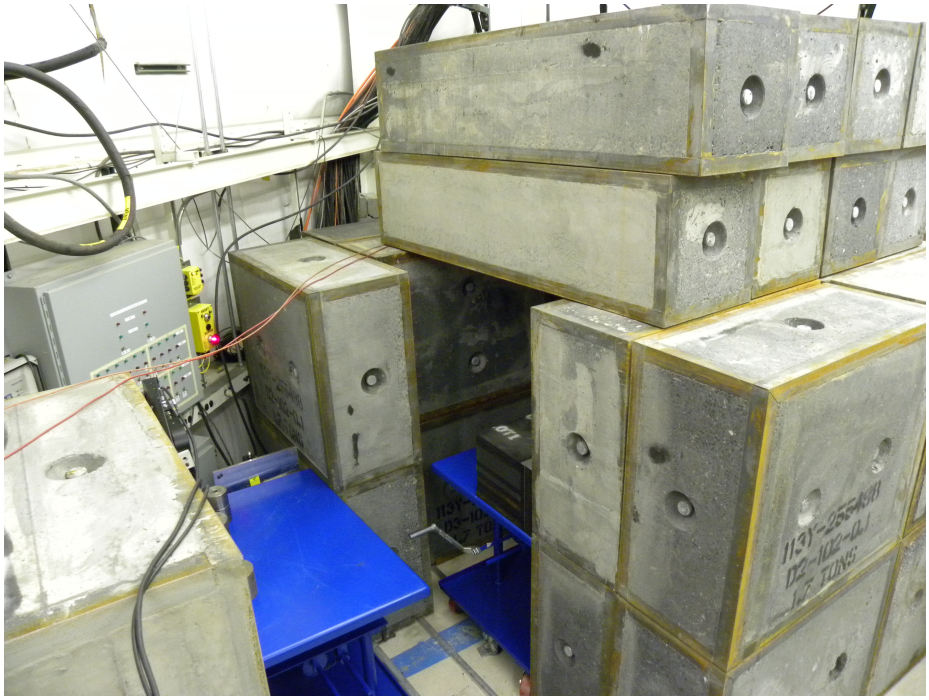


Figure 9.8: A photograph of the magnetite cave during set-up of the experiment. Note that a table is inside the cave for the purpose of supporting external shielding, and a second table to support the light-tight box is seen outside the cave but not yet in position.

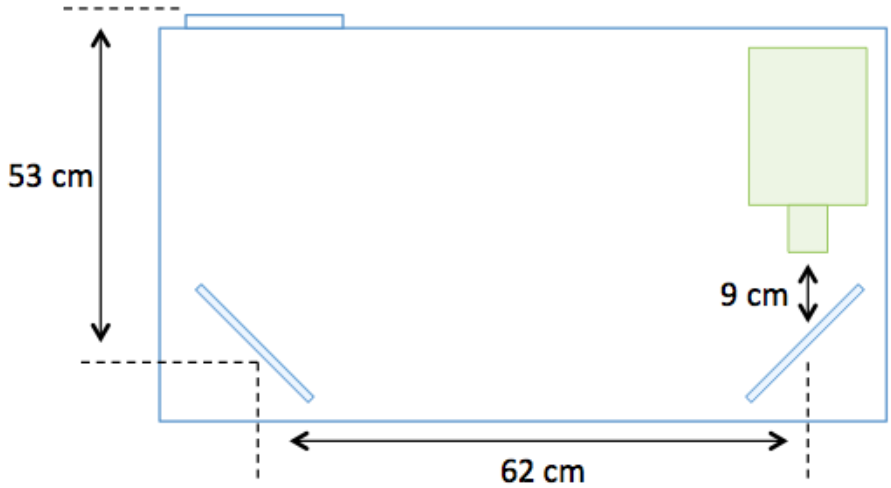


Figure 9.9: TiGReSSE was reconfigured for the experiments in FP60R. The light-tight box remained the same size, with overall dimensions of 76.2 cm × 91.4 cm × 32.8 cm.

protection of the camera by moving it farther from the direct beam. The light-tight box was placed on a table (Global Industrial Equipment, Model B53900) rated to support up to 2000 lb for safety reasons. The table top was 30 in by 42 in, and the table height could be adjusted with a hand crank. One of the team members, A. Madden, is shown with the light-tight box for a sense of scale (Figure 9.10). To remove dust that degrades image quality, the scintillator was cleaned with pressurized air and the mirrors were cleaned with a gel that, when dried, could be peeled off (Figure 9.11). This gel was painted onto the mirrors prior to placing shielding within the light-tight box to prevent shielding dust from getting on the mirror surface.

Shielding

A second, identical table was placed within the concrete cave to support the translation stage, radiography object, and external shielding for the camera. A translation stage (Newmark Systems, Inc., Model RH-8-100), weighing approximately 100 lb, was placed on the table top and used to support the radiography object as well as rotate and translate it. A diagram of the translation stage can be seen in Figure 9.12, with a photograph shown in Figure 9.13. A diagram of the light-tight box table, as well as the shielding and translation stage table, can be seen in Figure 9.14.

The two tables were placed flush to each other along the back wall of the concrete cave so that the external shielding was directly against the light-tight box. The light-tight box was placed on its table in such a way that the cave provided direct shielding for the camera and the external shielding protected the camera from scatter off the radiography object. The two tables were set to different heights to place the translation stage 1.5 in below the scintillator and reduce scatter from the bulky translation stage into the scintillator or camera.

External shielding was placed within the cave between the translation stage and light-tight box. Steel plates, measuring 2 in $\times$ 12 in $\times$ 1 in and weighing approximately 45 lb each, were stacked to cover the light-tight box from the edge of the concrete cave to the edge of the scintillator. In total, 36 plates were used to yield

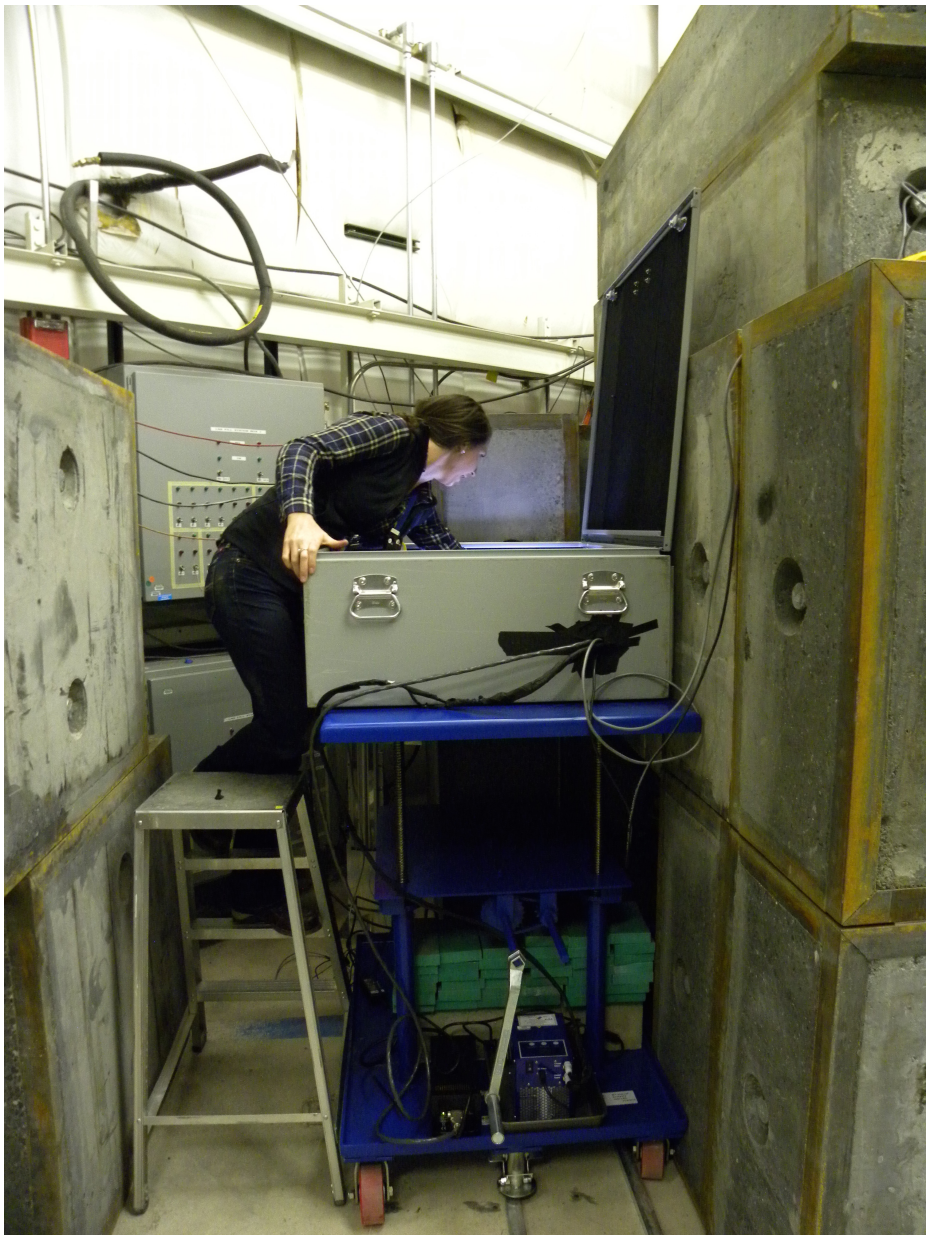


Figure 9.10: A photograph of one of the team members, A. Madden, with the light-tight box for a sense of scale.

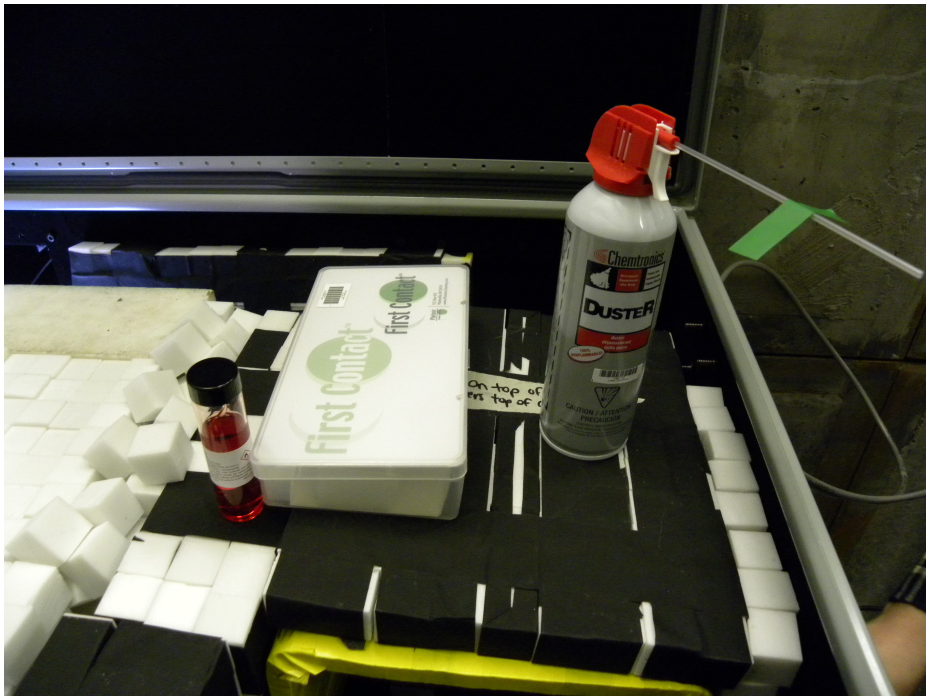


Figure 9.11: A photograph of the products used to clean the scintillator (right) and the mirrors (left) within the light-tight box.

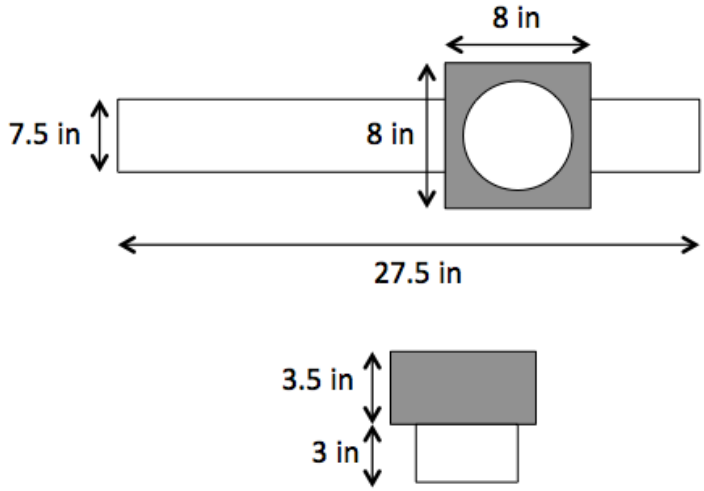


Figure 9.12: A not-to-scale diagram of the translation stage used to rotate and translate the radiography object. Top: Top view of the translation stage. The object is placed on the 8 in^2 plate, shown as dark gray. Bottom: Side view of the translation stage.

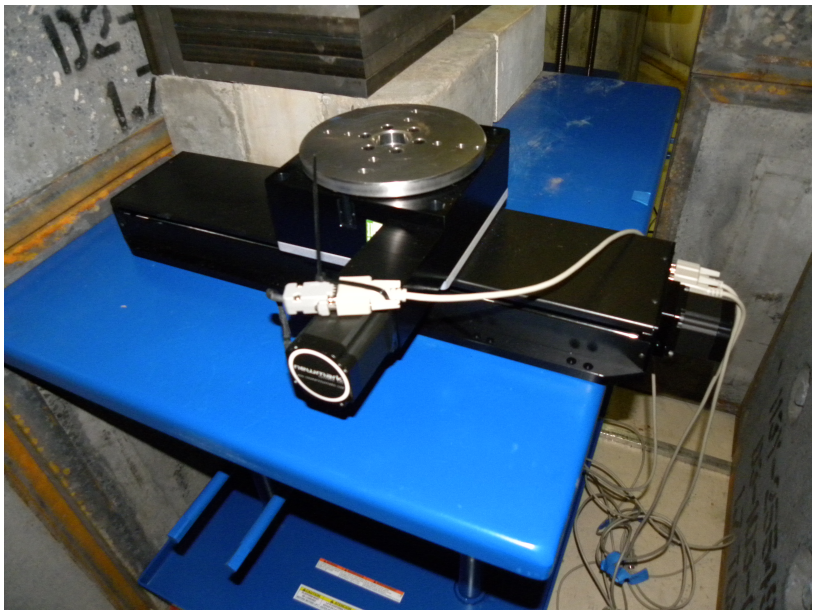


Figure 9.13: A photograph of the translation stage within the concrete cave.

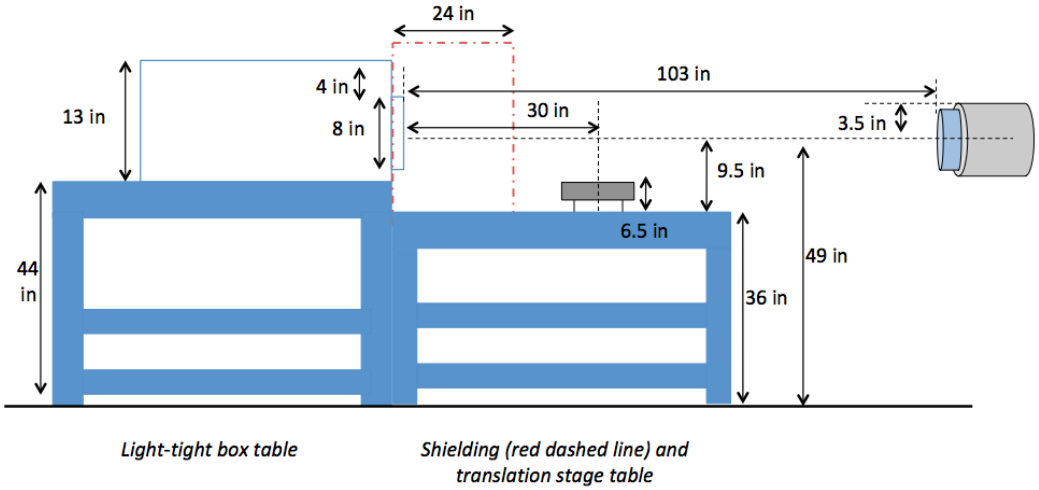


Figure 9.14: A not-to-scale diagram of the two tables used in the beam line, one for the light-tight box (left table) and one for the external shielding and translation stage (right table). The beam pipe is shown for reference. The right table was placed within the concrete cave (not shown), and both tables sat flush with the edge of the concrete cave. The shielding is shown as a red dashed line. The lower shelves on the left table were used to store the chiller and the camera power supply, which were shielded with borated polyethylene and concrete (not shown).

total dimensions of 15 in × 15 in × 24 in, which were shown in Chapter 7 to reduce fluence through the camera volume for steel thicknesses of 2 ft. To save weight, the steel blocks were raised in height by concrete blocks measuring 6 in × 6 in × 12 in. It is estimated that the total external shielding weighed 1680 lb. A diagram of the external shielding arrangement can be seen in Figure 9.15, and a photograph of the shielding set-up can be seen in Figure 9.16.

Shielding internal to the light-tight box was also necessary to reduce scatter into the camera volume that damages camera electronics and reduces image quality. The internal shielding was based on the "Configuration 15" shielding study outlined in Chapter 7. Lead and lithiated polyethylene, which had not been used in FP15R, were shown in MCNP6 simulations to reduce fluence through the camera volume. A 1 in thick piece of lead was bent to create a housing to place over the camera and its aluminum stand. The lead was a bit short and had to be supported by lithiated polyethylene blocks (Figure 9.17). Lithiated polyethylene sheets were placed directly next to the camera because, as seen in Chapter 7, this material yields fewer protons and photons than borated polyethylene or polyethylene. The remaining space in the light-tight box between the scintillator and the lithiated polyethylene was filled with polyethylene, borated polyethylene, and lithiated polyethylene. These three materials were placed rather randomly in order to fill the void within the box; there was a shortage of low-Z shielding material, and so all forms of polyethylene were used. A photograph of the shielding within the light-tight box can be seen in Figure 9.18.

Radiography Objects

A series of radiography objects were selected, including Object 2 that had been used in FP15R (refer to Section 5.2.3 for a detailed description and Figure 5.17 for a diagram). Object 2 was selected to compare FP60R behavior to that of FP15R, and also because it has many interesting features to radiograph.

A new radiography object was a polyethylene penetrameter with holes of various diameters and depths, hereafter referred to as the "penetrameter object". This object

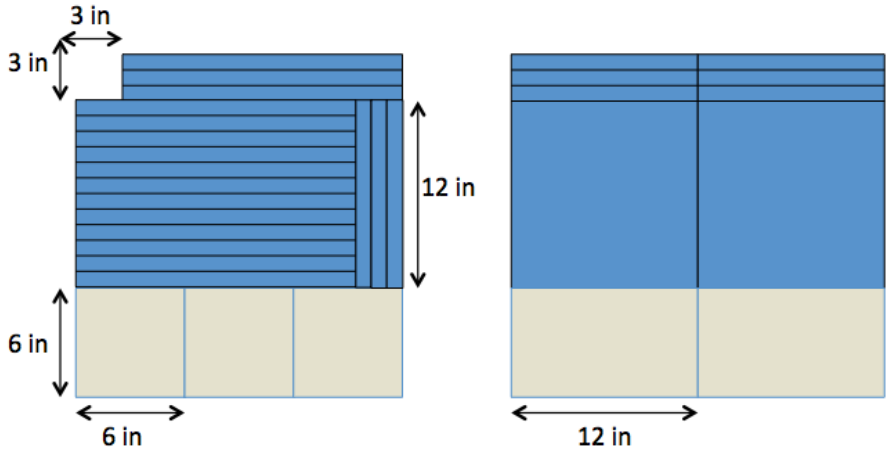


Figure 9.15: A not-to-scale diagram of the external shielding used to protect the camera from the direct beam. Steel plates (blue) were stacked on top of concrete blocks (beige) in order to get the steel shielding to the correct height while saving weight. Left: The shielding as viewed looking from the light-tight box toward the beam pipe. Right: Side view of the shielding.

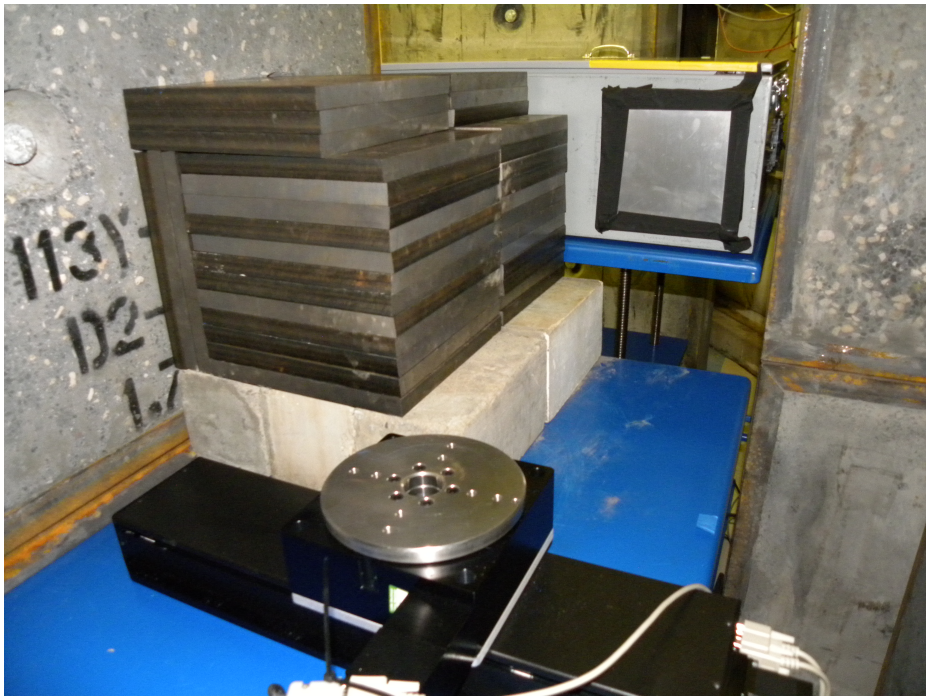


Figure 9.16: A photograph of the external shielding composed of steel plates and concrete blocks. The translation stage can be seen in the foreground, with the light-tight box in the background.

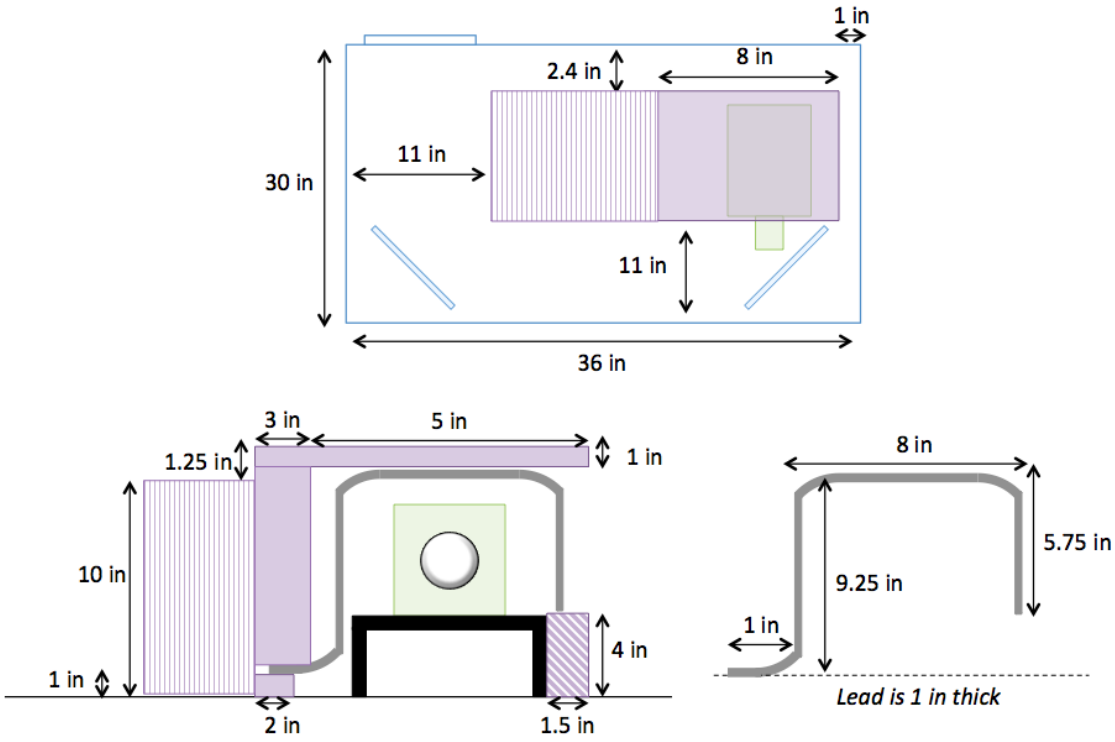


Figure 9.17: A not-to-scale diagram of the shielding placed within the light-tight box to protect the camera from the direct beam. Top: Shielding inside the light-tight box as viewed from above. Lithiated polyethylene is indicated by solid purple, and an assortment of polyethylene, borated polyethylene, and lithiated polyethylene blocks is indicated by vertical purple stripes. The camera, mirrors, and scintillator are shown for reference. Bottom left: Front view of the shielding within the light-tight box. Here, diagonal purple stripes indicate polyethylene. The camera and its stand are shown for reference. The lead shield, bent to wrap around the camera while leaving a gap between it and the camera, is shown as gray. Not shown is 1 *in* thick lithiated polyethylene placed between the wall of the light-tight box and the right side of the camera. Bottom right: Detailed diagram of the lead shield, which is also seen in the bottom left diagram. The lead shield is 1 *in* thick.



Figure 9.18: A photograph of the shielding within the light-tight box. The mirrors, light source (used for testing lens focus), and the scintillator (located where the light source reflection can be seen) are also visible. The camera lens and lens cap are visible beneath the bent lead shielding (which was covered in yellow tape to allow safe handling). On top of the lead, borated polyethylene blocks are held together with black tape, and an assortment of lithiated polyethylene, borated polyethylene, and polyethylene is seen to its left.

was borrowed from J. Hall of LLNL and serves the purpose of determining resolution at the object plane instead of the scintillator plane, as was done in Chapter 6. A penetrameter is useful for providing an idea of the smallest feature that is resolvable by an imaging system. A diagram showing penetrameter dimensions, as well as hole depths and diameters, was also provided by J. Hall, and can be seen in Figure 9.19.

Another object borrowed from LLNL was comprised of polyethylene and steel blocks held together by a frame composed of aluminum plates and screws. This object is interesting because it contains various cracks cut into the polyethylene (some rough, some smooth). The crack thicknesses can be varied by adjusting the screws in the aluminum frame. Figures 9.20 and 9.21 show a diagram and a photograph of the "crack test object", respectively, with the diagram provided by LLNL.

Finally, three one-inch-thick depleted uranium (DU) plates were provided by LANSCE for imaging. Two plates were in the shape of a semi-circle, with the third in the shape of a rectangle. When all three plates are stacked upright, the plates are 3 in thick in the center, and 1 in thick in the upper edges where the rectangular plate extends past the semi-circular plates. A hole of unknown, but identical, diameter is in all of the plates so that the holes line up when stacked appropriately, resulting in a circular region with no beam attenuation. The three plates were coated in an unknown metal that allowed for safe handling by LANSCE staff. A not-to-scale diagram of the plates can be seen in Figure 9.22.

9.2 System Performance Evaluations

Following the set-up of the experiment, the lens was focused at the center of the scintillator plane. In the Generation II design, a new lens was used with a larger maximum aperture size (i.e., $\sim f/1$ instead of $f/2$) in order to increase the signal-to-noise ratio by decreasing exposure time. The lens selected was a Bower 85 mm high speed cinematic lens.

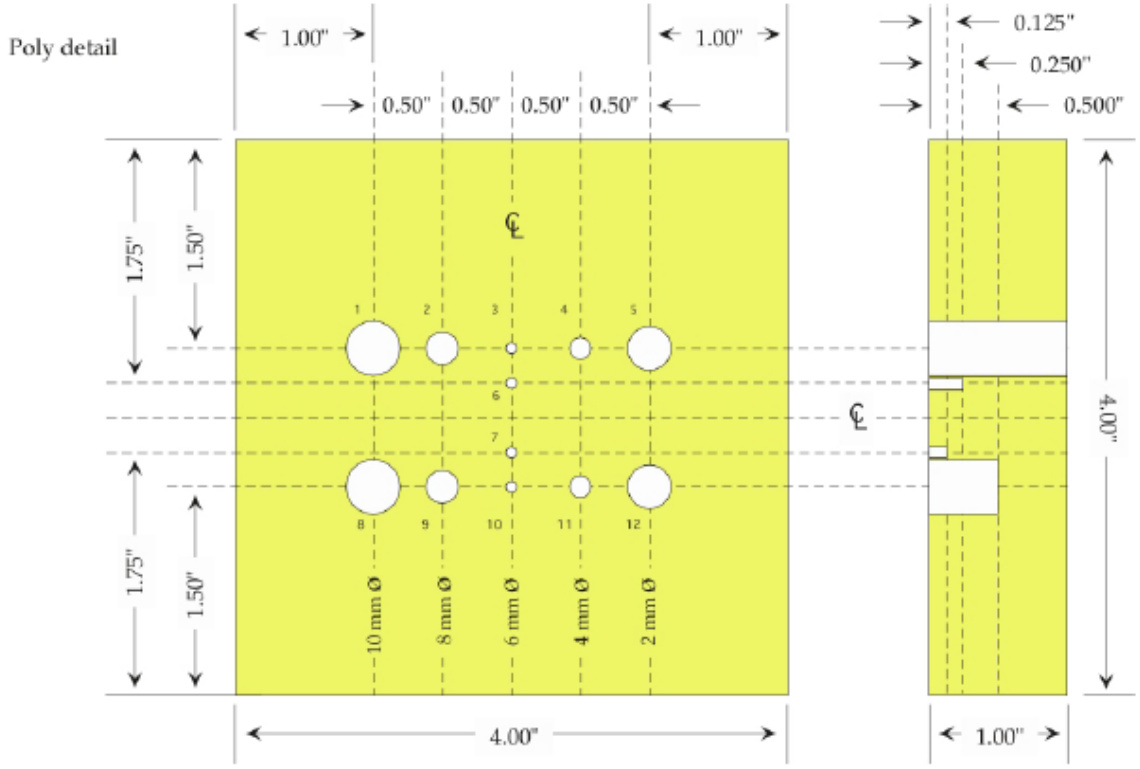


Figure 9.19: A diagram of the polyethylene penetrameter used to test system resolution at the object plane. Both the object and this diagram were provided by J. Hall of Lawrence Livermore National Laboratory.

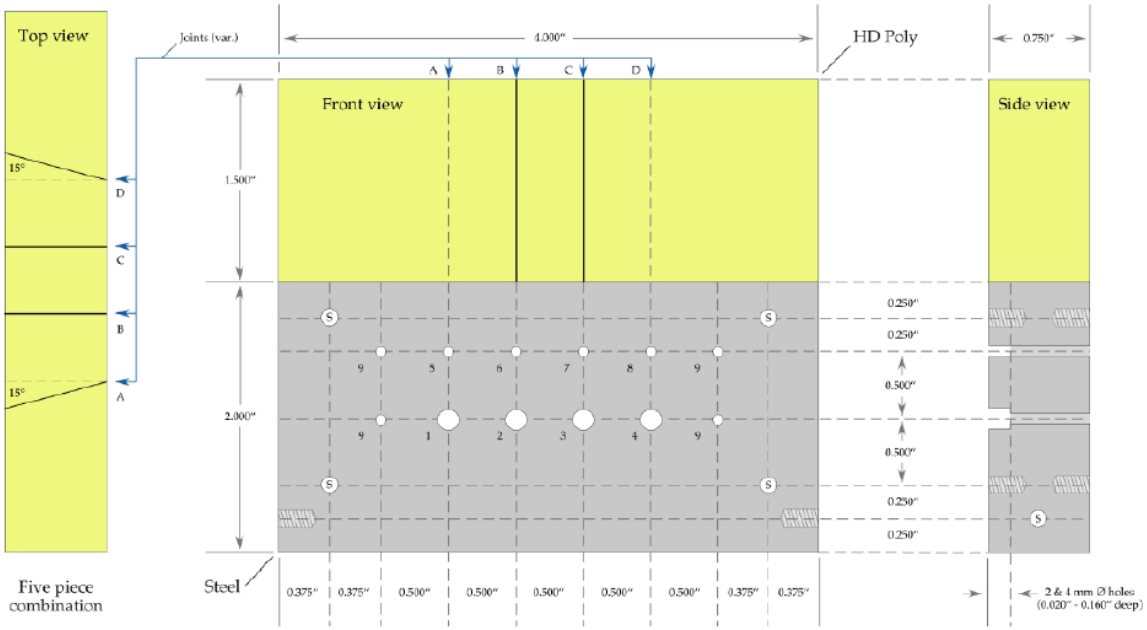


Figure 9.20: A diagram of the polyethylene (yellow) and steel (gray) crack test object used to determine system resolution at the object plane. Both the object and this diagram were provided by J. Hall of Lawrence Livermore National Laboratory.

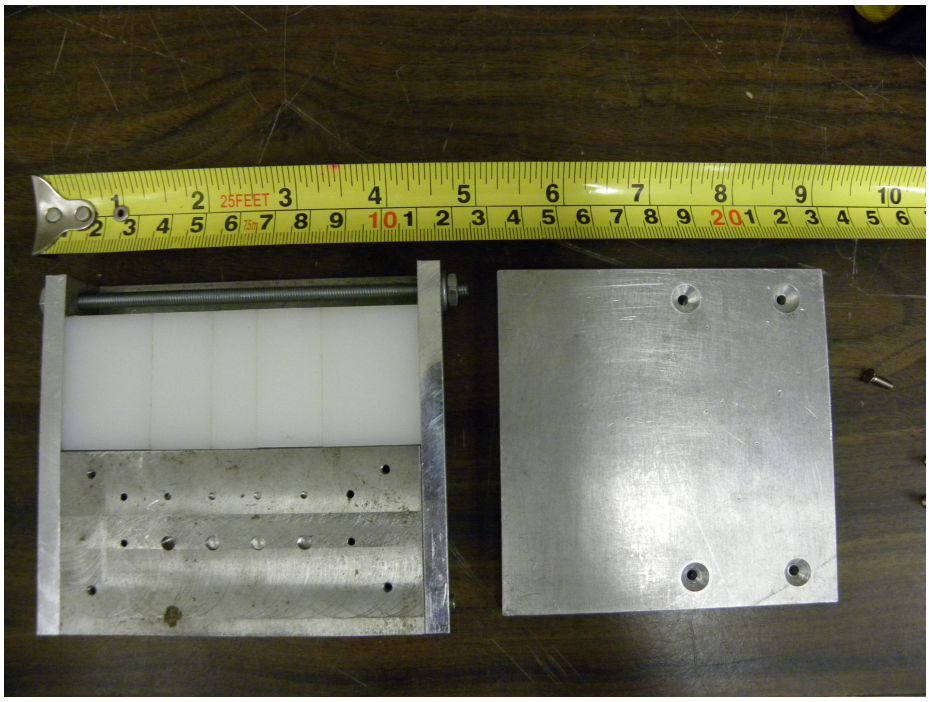


Figure 9.21: A photograph of the disassembled crack test object. A tape measure is shown for reference. Left: The interior of the crack test object showing the four cracks in the polyethylene and the holes of various depths and diameters in the steel. The various pieces are held together by an aluminum frame that can be tightened via the screw at the top of the frame in order to vary the crack spacing. Right: The front cover of the crack test object, made of aluminum, would be rotated 90° clockwise and attached via four screws.

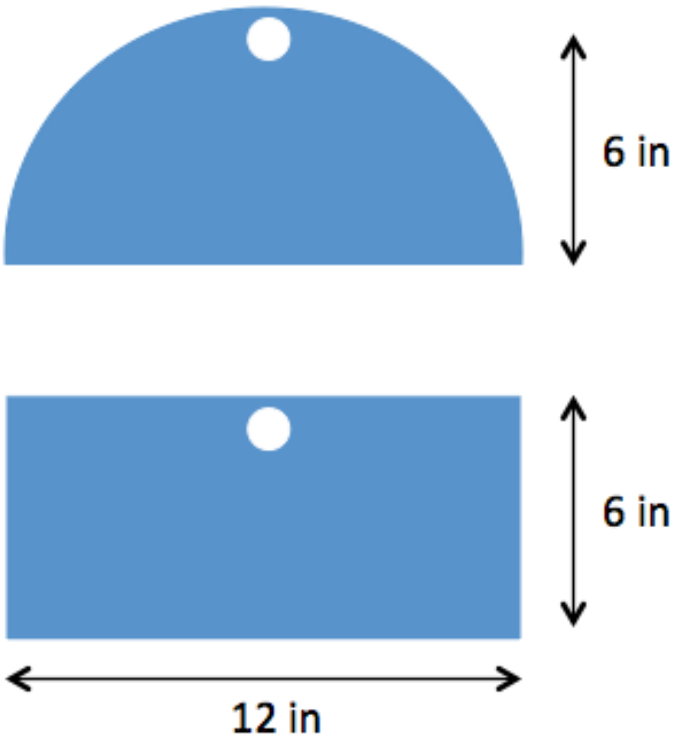


Figure 9.22: A diagram of the DU plates imaged in FP60R. Each plate has an identical hole of unknown diameter. Top: Two plates are shaped like the semi-circle depicted here. Bottom: One plate is shaped like the rectangle shown here.

A high-quality print-out of the Siemens star pattern was used to focus the lens, which had been used in FP15R for the same task. The pattern was taped to a piece of cardboard half the thickness of the scintillator (2.5 mm). The scintillator was removed and the cardboard was placed within the scintillator holder (Figure 9.23). This placed the pattern at the center of the scintillator plane, which would ensure blur was minimized. The lens focus was iteratively adjusted, taking images with the light source shown in Figure 9.23, until the pattern was determined to be at its best focus ($\sim f/1.3$). An image of the Siemens star at the system's best focus can be seen in Figure 9.24. A test for light leaks within the light-tight box was also conducted, with none being found.

Additionally, images using the light source were generated to ensure the new internal shielding design did not block the camera's field of view. Initially, the shielding was seen to partially block the mirror and thus the camera's field of view, so the shielding was shifted iteratively and evaluated by taking images with the light source until it was confirmed that the internal shielding was no longer in the field of view.

Then, the light source was removed from the light-tight box and the FP60R beam was used to evaluate shielding performance, with an image of the FP15R scatter serving as a benchmark. A fifty-frame radiograph was taken in FP60R with system settings matching those used in FP15R so that the two images could be compared to evaluate scatter: no object was in the field of view, the ADC and intensifier were scaled to 50, the time gate was 200 ns wide with a delay of 200 ns, the camera integrated 35,000 pulses per frame, and the lens cap was on the lens so that only stars on the CCD chip were imaged.

The scatter was seen to be drastically reduced for the FP60R configuration when compared to the FP15R configuration. A color scale had to be applied to the results, instead of the typical grayscale, so that scatter was more easily seen in the FP60R image. The scatter test results for FP15R and FP60R were set to the same contrast level for a fair comparison, and images can be seen in Figures 9.25 and

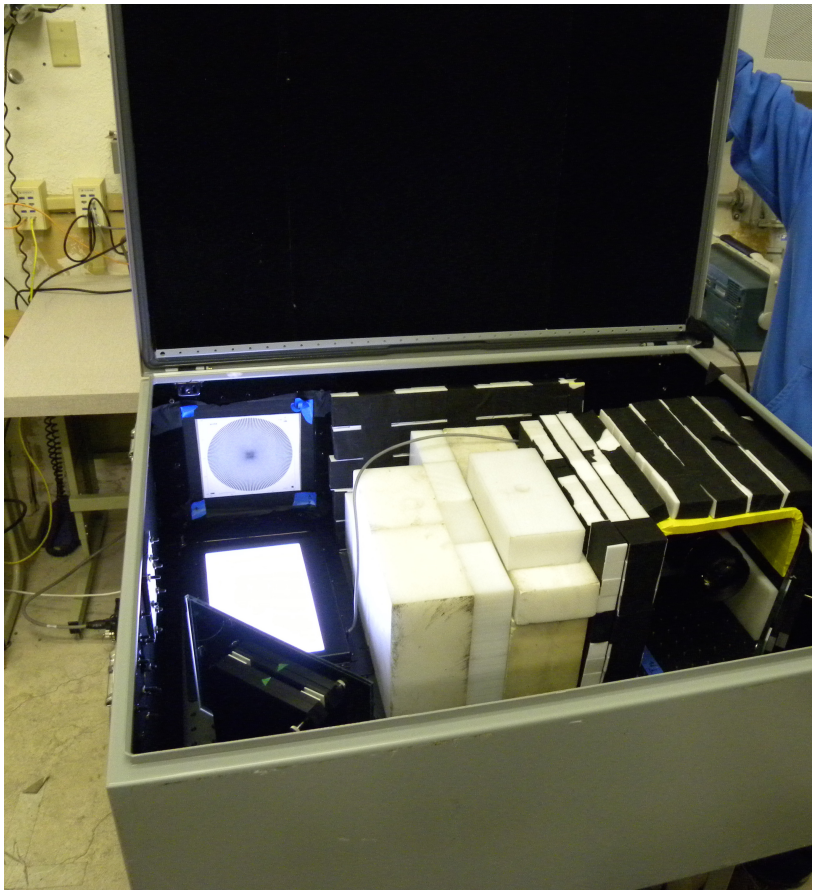


Figure 9.23: A photograph of the interior of the light-tight box, with the Siemens star pattern placed at the center of the scintillator plane. The light source used to illuminate the test pattern is also visible.

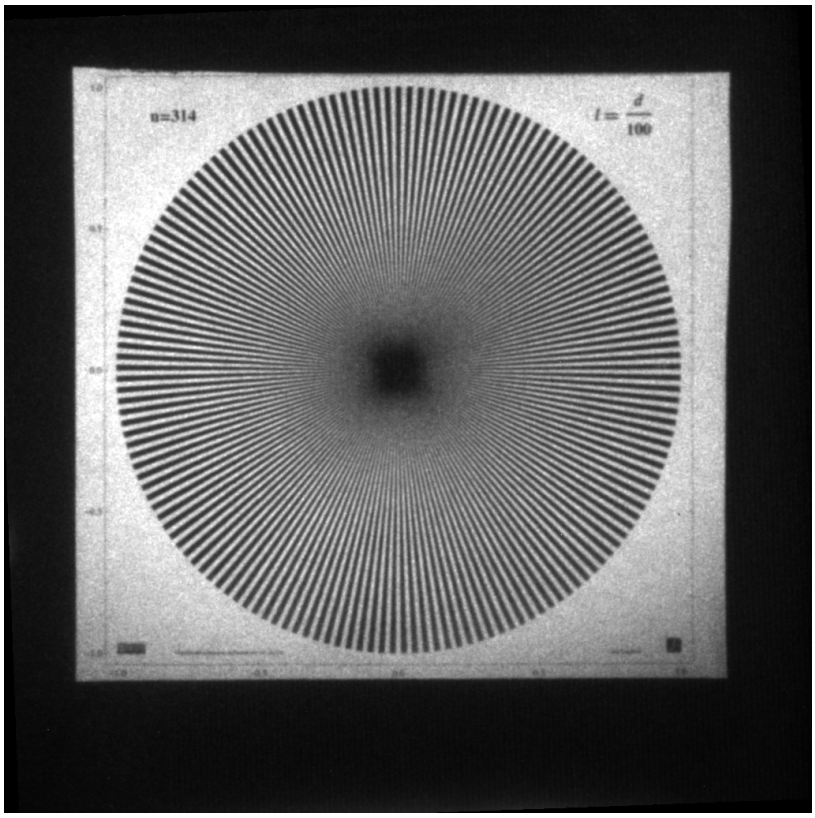


Figure 9.24: Image of the Siemens star pattern, located at the center of the scintillator plane, at the system's best focus.

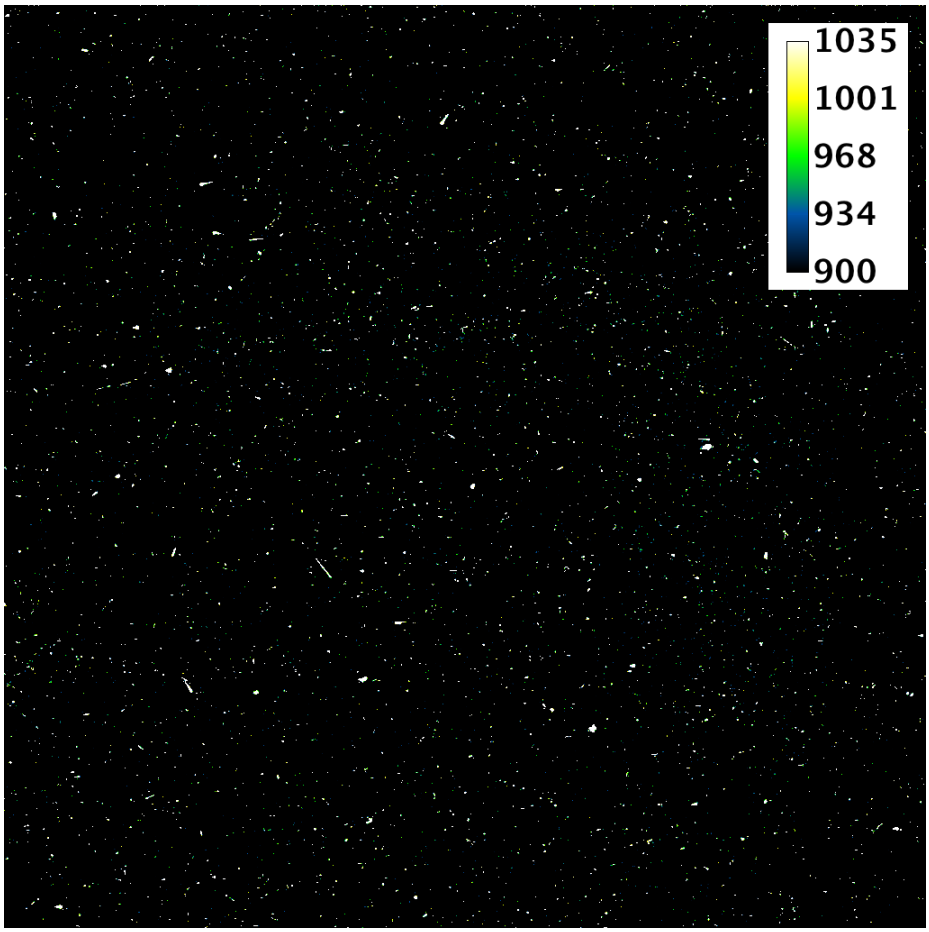


Figure 9.25: Scatter as seen by the camera with the FP15R configuration.

9.26, respectively. The average pixel value was seen to drop from 719.6 to 652.2, the mode value was reduced from 685.8 to 621.0, and the maximum value decreased from 1.5×10^4 to 7.4×10^3. This indicates that the number and intensity of stars in the image were greatly reduced by the new shielding design. A histogram of the two scatter radiographs can be seen in Figure 9.27.

As a final test of system set-up, J. Hunter, a LANL scientist working on a related neutron radiography project, placed his flat panel detector behind the light-tight box to measure the beam shape and location with respect to TiGReSSE's scintillator (Figure 9.28). This was done to see if the beam was centered on the scintillator and whether the beam was clipping the edge of the internal shielding, which would unnecessarily increase scatter into the camera volume. It was found that the beam spot measured 11 *in* by 7.5 *in*, indicating that the direct beam was being cropped in one direction by the shutter (located upstream of the beam pipe but after the tungsten spallation target). The light-tight box position and height were adjusted slightly to ensure the beam spot was centered on the scintillator, with the table holding the light-tight box being lowered 6 *cm* below the level shown in Figure 9.14.

9.3 Time-of-Flight Scan

With the system properly configured, the next step was to conduct a scan in time to determine when photons arrive at the scintillator, thus establishing the true start of the pulse, T_0, which occurs some time δt after the arrival of the accelerator trigger signal. The camera settings remained the same as during the scatter test outlined in Section 9.2, except that the number of accumulations was increased to 5×10^4.

The scan was conducted using the general procedure outlined in Section 5.2.5, but with slight differences intended to increase the speed of this process without sacrificing precision. First, the entire pulse was scanned in 200 *ns* time gates, much larger than the 50 *ns* initial time gates used in FP15R, to more quickly find the peak in the average intensity. Second, the average intensity, $\bar{I}$, which is plotted against

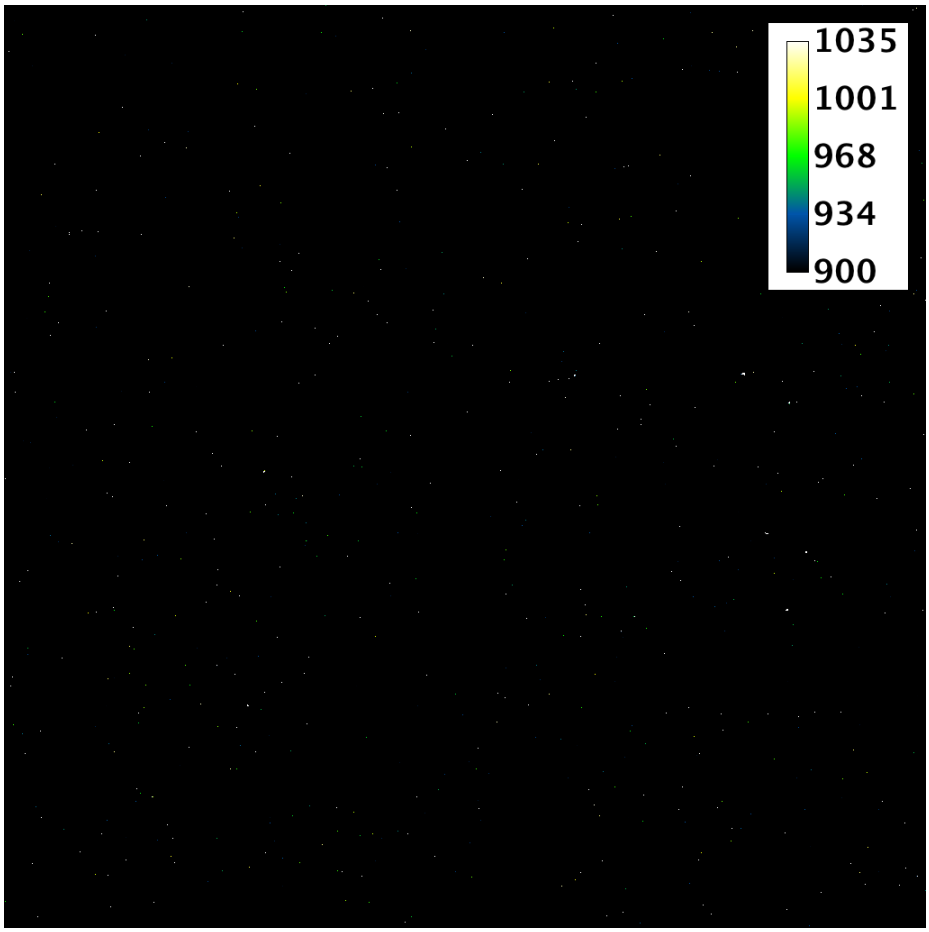


Figure 9.26: Scatter as seen by the camera with the FP60R configuration.

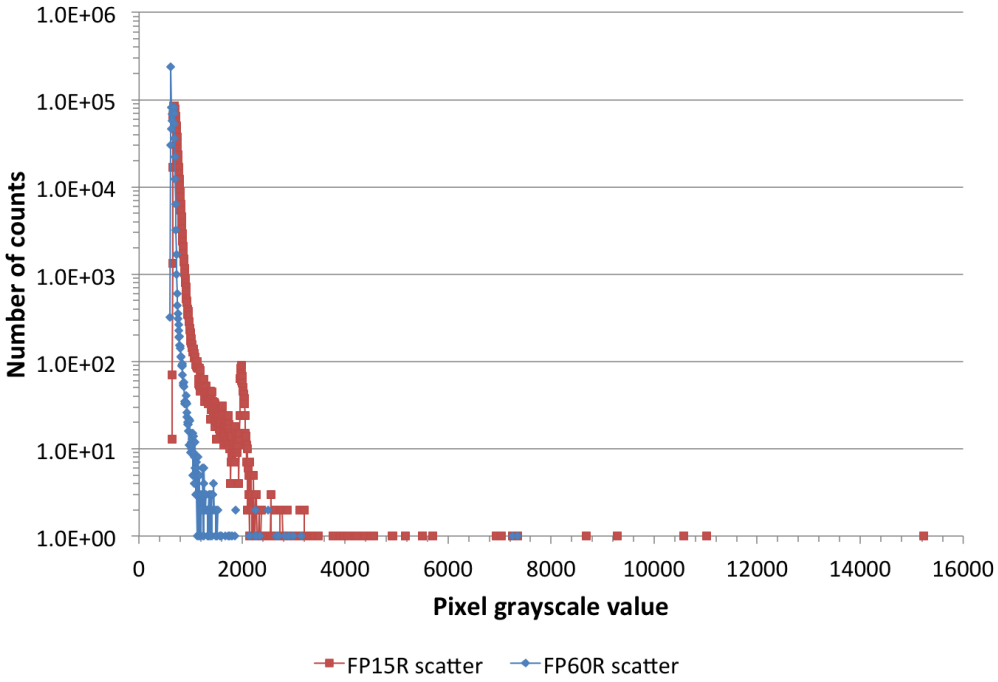


Figure 9.27: Histogram of the scatter seen in FP60R and FP15R, with the number and intensity of large pixel grayscale values (caused by stars) decreased in FP60R.



Figure 9.28: A photograph of the flat panel detector used to determine the true beam shape and location. This allowed for the light-tight box's position to be adjusted so that the scintillator was centered in the beam. The detector and its stand are visible behind the light-tight box.

time to find the peak in intensity that corresponds to the photon arrival time, was found for the entire radiograph instead of a small region of interest. This change was enacted to further increase the speed of this process because LightField had a direct method for calculating $\bar{I}$ for the entire radiograph, whereas the ROI had to be tediously drawn for each image during this process in FP15R.

After scanning the entire pulse with 200 ns time bins, the process was repeated over the peak boundaries of 800 and 1500 ns with a narrower time gate of 50 ns; between 900 and 1175 ns with a time gate of 25 ns; and between 950 and 1100 ns with a time gate of 10 ns. It was found that the photons arrive between 990 and 1000 ns after the trigger signal, or 275 ns after the FP15R results (Figure 9.29). This is a result of several factors, such as viewing the target at a different angle, moving the camera within the light-tight box so it was farther from the scintillator, being slightly closer to the tungsten spallation target, and different cabling to provide the trigger signal.

Relativistic calculations, based upon the FP60R time-of-flight scan results, were conducted to determine the time gates for particle types and energies of interest. These time gates were then used to generate the radiographs discussed in this chapter. The results are listed in Table 9.1.

Interestingly, the FP60R scans with time gates of width up to and including 50 ns showed two peaks. It was deduced that TiGReSSE can resolve the neutron and photon arrival times in FP60R, which was not seen in FP15R. The previous experiments only showed one large peak because poor image resolution blurred the two peaks together. It is believed that the ability to resolve both peaks was possible in FP60R because of reduced scatter. The shielding design was greatly improved and the beam was better collimated in FP60R. Also, TiGReSSE was the only equipment in the beam line, so scatter from other upstream experiments was not a problem. It should be noted that only one peak is visible in the FP60R 200 ns time gate results because the time gate was too broad to capture this behavior.

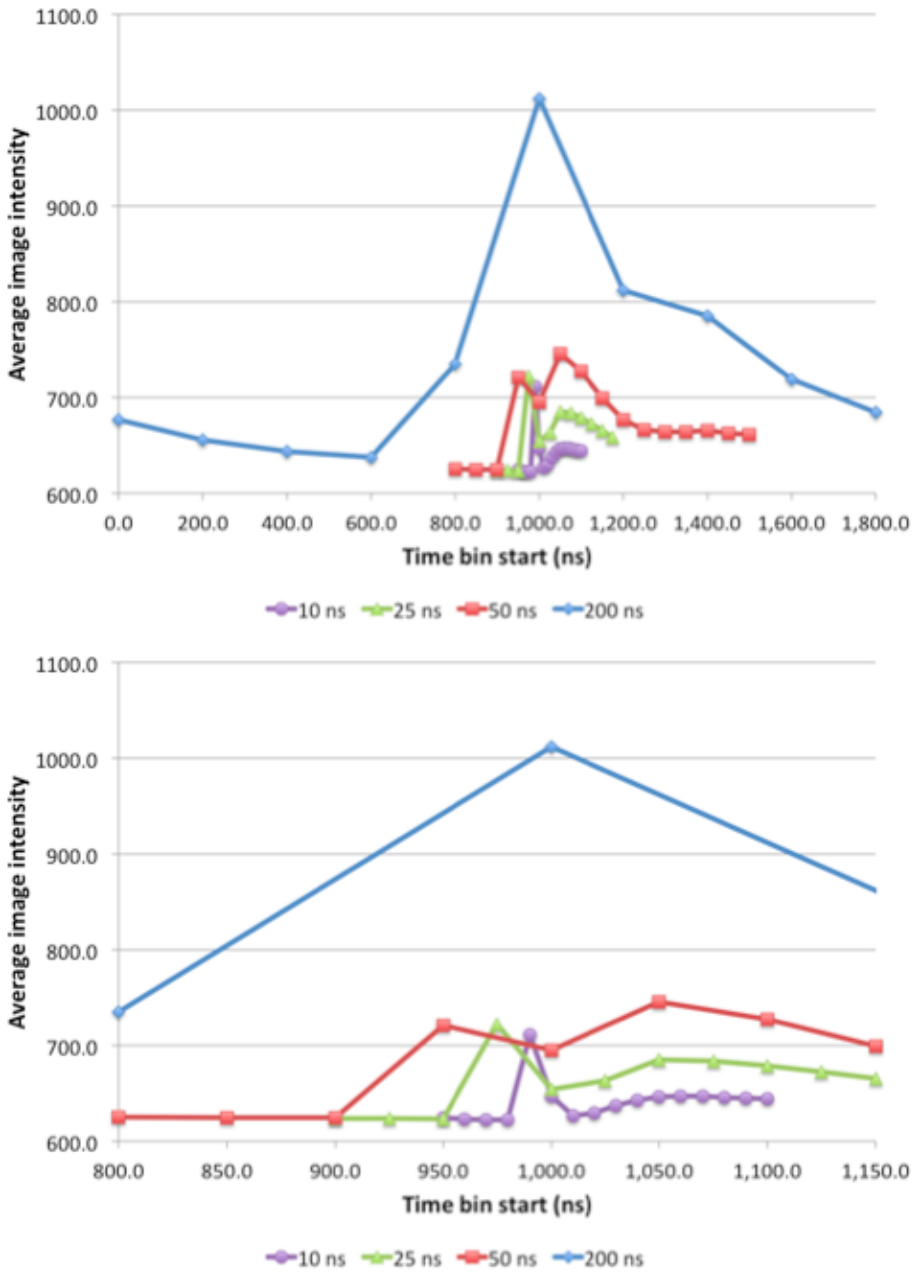


Figure 9.29: Top: Graph of the FP60R results for the time-of-flight scan, which plots average scintillator intensity as a function of time. Gate widths of 10 (purple), 25 (green), 50 (red), and 200 *ns* (blue) are shown. Bottom: A close-up view of the top plot so that the peaks for both photons and neutrons can be seen in the 50, 25, and 10 *ns* time gates (the 200 *ns* time gate was too broad in time to capture this behavior). The photons arrive between 990 and 1000 *ns*.

Table 9.1: FP60R TOF time gates for particles and energy ranges of interest.

Particle Type	Energy (MeV)	Average Energy (MeV)	Time Gate (ns)	Gate Width (ns)
Neutron	2 to 3	2.5	1816.7 to 2015.0	198.3
	8 to 12	10	1376.8 to 1475.3	98.6
	9 to 11	10	1396.2 to 1444.6	48.3
	12 to 16	14	1318.2 to 1376.8	58.6
	13 to 15	14	1330.6 to 1359.6	29.0
	50 to 70	60	1123.6 to 1155.6	32.0
Photon	—	—	990.0 to 1000.0	10.0

The experimental arrival times of the photons and high-energy neutrons, as plotted in Figure 9.29, were compared to calculations of their expected arrival times based on relativistic kinematics. The photon TOF could not be compared to theory because its window of arrival (990 to 1000 ns) is measured from the LANSCE trigger signal and can only be determined experimentally because signal delays from cable length and electronics are unknown. Assuming that the photon TOF is correct, the neutron peak is seen to occur from 1060 to 1070 ns, or 60 to 70 ns after the photon arrival window. The rising edge of the neutron peak occurs in the 1020 to 1030 ns time bin, or 20 to 30 ns after the photon arrival window. These two time bins approximately correspond to 147 to 177 MeV and 380 to 560 MeV neutrons, respectively.

These results seem valid when one considers that the peaks correspond to a peak in scintillator brightness as a function of time bin, and thus as a function of particle type and energy. The scintillator intensity peaks at a lower neutron energy than the rising edge, which may seem counter-intuitive except when one considers the larger source strength in the 1060 to 1070 ns time bin. In FP60R, the neutron spectrum is shifted to lower energies than what was seen in FP15R, which causes upper energy bins to have less flux than lower energy bins (refer to Figure 5.3). Combined with the fact that scintillator efficiency decreases with increasing neutron energy, the theoretical calculations appear correct and TiGReSSE is indeed resolving the arrival time of the photons and high-energy neutrons in FP60R.

9.3.1 Error in TOF Calculation

While the results shown in Table 9.1 were used to generate the radiographs that will be shown in this chapter, it was later discovered that there was a slight error in the spreadsheet used to calculate the TOF, which was carried through into determining the neutron time gates of interest. While neutron relativistic TOF was correctly calculated, the TOF with respect to the photon time of arrival was not. This is because the distance that the optical photons travel between the scintillator and

the camera was not updated to reflect the new FP60R TiGReSSE configuration. With the camera moved within the light-tight box, the effective distance between the scintillator and the camera increased from 1 m to 1.24 m, which caused the travel time for the optical photons to increase from 3 ns to 4.13 ns. Unfortunately, this error was not found until after beam time had ended.

This error resulted in TOF calculations being underestimated by 1.13 ns, meaning that time gates were opening earlier in time than was intended. Thus, slightly higher energies were being selected for radiographs than intended, with this effect being greater at higher energies because faster neutrons can travel a greater distance in 1.13 ns than slower neutrons. Note that the photon time gate was not affected because this particular time gate was found experimentally, not theoretically. The term "imagined energy" will refer to the radiograph energies the scientists thought they were using, which turned out to be incorrect, and the term "actual energy" will refer to the energy that was actually captured with the radiograph as a result of opening the camera shutter earlier than intended.

Corrective calculations were completed to determine what the neutron energy bins truly were, as well as whether this was a large enough effect to throw out data. Table 9.2 shows the results of this calculation. The left column is the energy bin that was desired, and the center column is the corresponding energy bin that was actually taken. The percent differences between the two energy endpoints is shown in the final column, with the left difference being for the lower energy endpoints and the right difference being for the higher energy endpoints.

The percent differences between the imagined energies and the actual energies does not become larger than 1 MeV until neutrons reach an imagined energy of $\sim$75 MeV. Differences between the imagined and actual energies rapidly grow above this energy, with an imagined energy of 600 MeV matching an actual energy of 635 MeV and yielding a difference of 35 MeV. A plot of the differences in energy between the imagined energy and the actual energy as function of the imagined energy is shown in Figure 9.30.

Table 9.2: Corrected FP60R time-of-flight time gates for neutron time gates of interest, showing what time gates were thought to have been used ("imagined energy") and those that were actually used ("actual energy") during experiments.

Imagined Energy (MeV)	Actual Energy (MeV)	Percent Difference (%)
2 to 3	2.004 to 3.008	4×10^{-3}; 8×10^{-3}
8 to 12	8.034 to 12.062	3.4×10^{-2}; 6.2×10^{-2}
9 to 11	9.040 to 11.055	4.0×10^{-2}; 5.5×10^{-2}
12 to 16	12.062 to 16.096	6.2×10^{-2}; 9.6×10^{-2}
13 to 15	13.070 to 15.087	7.0×10^{-2}; 8.7×10^{-2}
50 to 70	50.549 to 70.925	5.5×10^{-1}; 9.3×10^{-1}
10 to 600	10.047 to 634.746	4.7×10^{-1}; 5.47

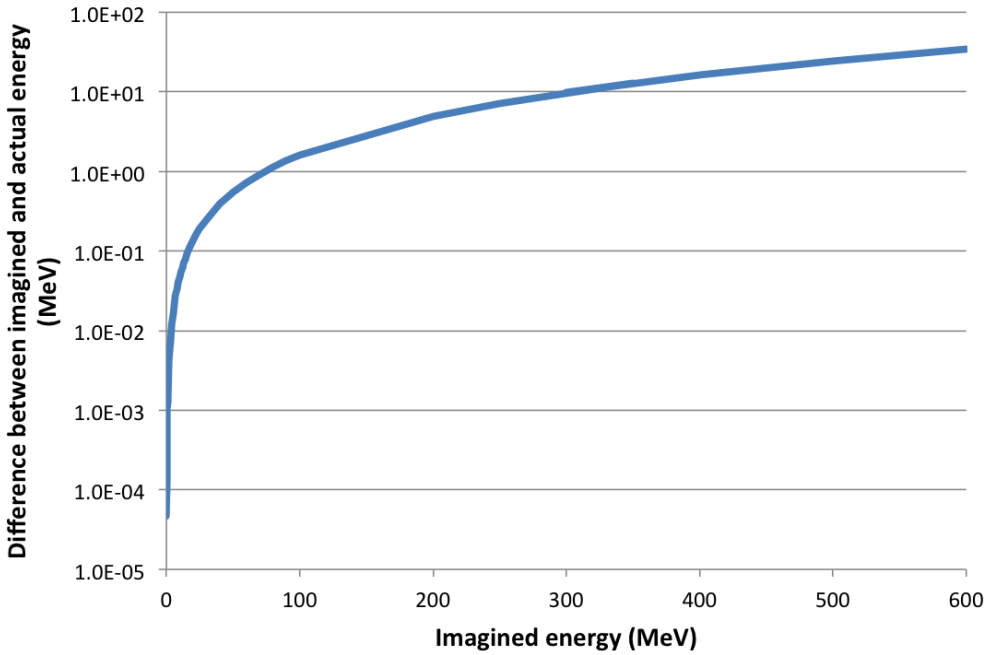


Figure 9.30: Semi-*log* plot of the difference, in MeV, between the imagined energy and the actual energy measured in FP60R.

Figure 9.31 shows a plot of the percent difference between the imagined energy and the actual energy as a function of the imagined energy. Percent errors did not rise above 1% until an imagined energy of ~45 MeV, with a percent difference of 1.3% for an imagined energy of 70 MeV. At worst, the 600 MeV imagined TOF underestimated the actual TOF by 5.47%.

Overall, the miscalculation of the TOF by 1.13 ns appears to have little effect on the data collected. Percent differences equal to approximately 1% are in the noise when one considers other uncertainties in the measurement, such as a 10 ns uncertainty for the time-of-arrival of the photons which arrive sometime between 990 and 1000 ns. Data, however, that include energy bins above 70 MeV are most likely unreliable. For example, an image of Object 2 from 10 to 600 MeV was taken in FP60R for comparison to a similar image taken in FP15R. This comparison will unfortunately not be entirely correct due to an error of 5.47% in the upper energy endpoint, but with almost no flux between 600 and 635 MeV, the effect is most likely small. Additional experiments would be necessary to determine this effect.

All other data listed in the following sections of this chapter will continue to use the imagined energy to describe the radiographs because the error is very small for most energy bins selected. The reader, however, may reference Table 9.2 for the actual energy used to generate radiographs in FP60R.

9.4 Description of Experiments

9.4.1 Optimal Source Energy

The first study was conducted to determine the best neutron source energy if a monoenergetic source were to be designed for use with TiGReSSE to accomplish total scatter rejection. Source energies were tested by selecting energy bins that averaged to the source energy of interest (EOI). Approximated sources included 2.5 MeV neutrons from a D-D reaction; 10 MeV neutrons from a boosted D-D reaction (as proposed by

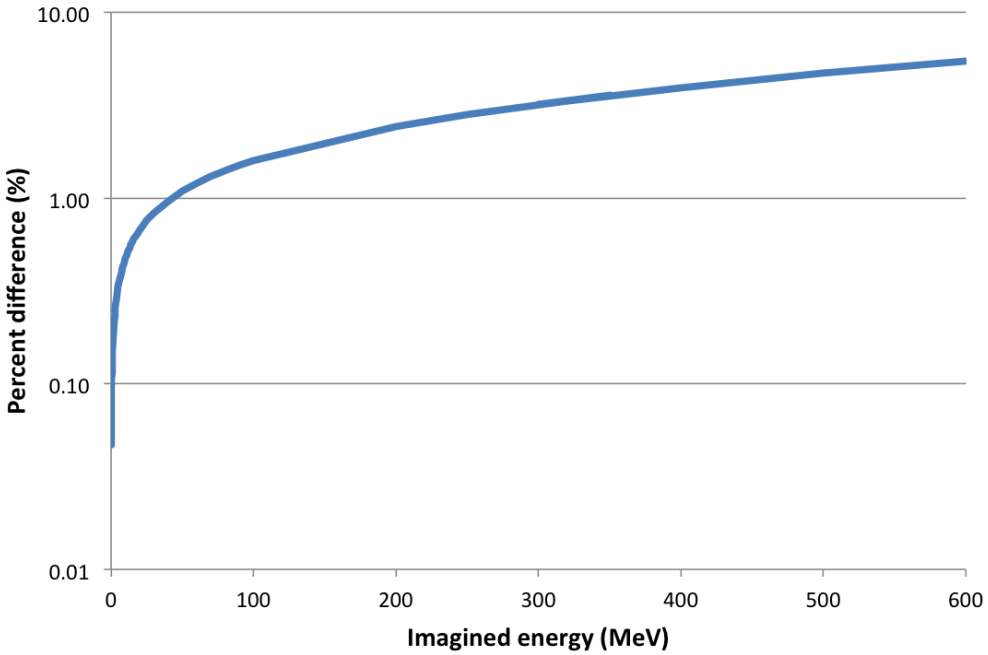


Figure 9.31: Semi-*log* plot of the percent difference between the imagined energy and the energy actually measured in FP60R.

LLNL and described in Section 4.1.2); 14 MeV neutrons from a D-T reaction; and 60 MeV neutrons from an adapted medical source. The reader, referring to Table 9.1, will notice the time gates used to approximate these energies.

The reader will also see that 10 MeV and 14 MeV EOIs were each approximated by two time gates, with the purpose of isolating the effect of time gate width on the study. A narrower time gate centered on the energy of interest more accurately approximates the EOI, but a narrower time gate has a lower signal-to-noise ratio. Thus, a narrower time gate may produce radiographs of poorer quality that do not necessarily represent the EOI because, as flux is reduced by narrowing the time gate, electronic noise stays relatively constant. Thus, radiographs with actual commercial sources may differ from the results obtained at LANSCE.

The object selected to radiograph for this study was Object 2, one of the three objects that had been previously radiographed in FP15R. Object 2 was placed on the translation stage at a distance of 31 in (78.7 cm) from the scintillator as measured from the object's centerline. Object 2 was raised in the field of view by a piece of thick foam (15 cm $\times$ 30 cm and 5 cm tall) that had been placed on top of two aluminum plates (8 cm $\times$ 15 cm and 2 cm tall) that were themselves on top of the translation stage. (Foam was used instead of polyethylene because it would cause less scatter into the camera volume and its field of view.) This set Object 2 to a height that placed the majority of the object in the camera's field of view. Object 2 was placed 22.5 in from the right concrete wall of the cave, if looking toward the scintillator. Time gates and associated energies can be seen in Table 9.3. For each of the five neutron radiographs generated in this study, 100 frames were taken, the ADC gain was set to 50, and the intensifier gain was set to 80. Corresponding flatfield images were taken, also with the same settings described here and in Table 9.3.

Table 9.3: Equipment settings for the five Object 2 neutron radiographs conducted to determine optimal source energy, including the neutron energy, added signal delay, camera gate width, and the number of integrated pulses per frame.

Energy (MeV)	Delay (ns)	Gate Width (ns)	Pulses per Frame
2 to 3	1816.70	198.30	6.00×10^5
8 to 12	1376.75	98.58	6.00×10^5
9 to 11	1396.23	48.35	6.00×10^5
12 to 16	1318.18	58.57	6.00×10^5
50 to 70	1123.58	32.01	6.00×10^5

9.4.2 Optimal Location for Radiography Object

A second study was completed to begin to understand how image quality is affected by the location of the radiography object. A balancing game must be played between placing the object as close to the scintillator as possible, thus improving spatial resolution by minimizing feature blur, and placing the object as far from the scintillator as possible, thus improving contrast resolution by minimizing scatter from the object into the scintillator's field of view. The optimal location of the object partially depends on the object characteristics, such as geometry and material composition, and thus is an object-dependent value. Some objects would have larger features where spatial resolution is less of a concern; the object could therefore be moved further from the scintillator to decrease scatter. Other objects are made of materials that do not scatter as much, and they could be placed closer to the screen to improve spatial resolution. Most objects, however, have small features and generate scatter, which makes finding the optimal distance tricky.

To illustrate this concept, two plots were generated of the theory behind these competing effects. For these calculations, it was assumed that the object is being radiographed in FP60R with a source-to-detector distance of 2119.5 *cm* (i.e., the distance between the target and the scintillator as stated in Section 9.1.1). The first plot in Figure 9.32 shows the object magnification as a function of the object-to-detector distance, while the second plot shows the percent of the radiography object's scatter that reaches the scintillator's field of view (which was assumed to be 180°). While the magnification is seen to be nearly linear with object-to-detector distance ($R^2 = 0.999$), the percent of scatter impinging on the screen drops rapidly with increasing distance until ~75 *cm*, when the effect begins to flatten out. Thus, the best region for balancing spatial and contrast resolution appears to be an object-to-detector distance between 75 and 100 *cm*. This region is shown in Figure 9.32 in yellow.

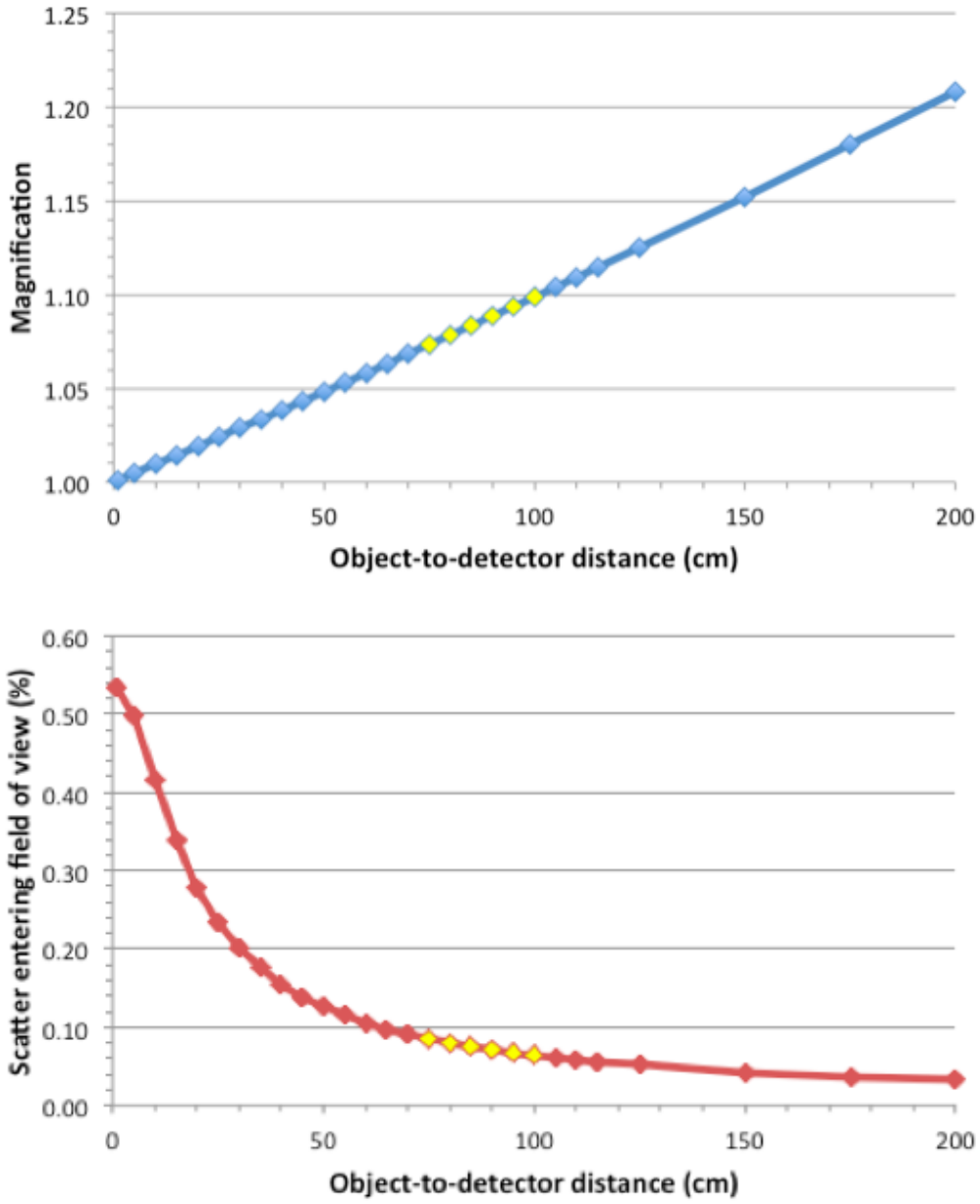


Figure 9.32: These two plots show the balance that must be struck between spatial and contrast resolution, with the best location for the object shown in yellow on both plots. Top: Plot of the magnification in FP60R as a function of object-to-detector distance. Bottom: Plot of the scintillator's field of view of the scatter off the radiography object.

This hypothesis was tested in FP60R by choosing two object-to-detector distances to radiograph Object 2. A neutron energy bin ranging from 100s of keV to 2.5 MeV were selected as the source because this energy bin contains a large amount of scatter, which is necessary for this study. First, the centerline of Object 2 was placed 78.7 cm from the scintillator on the translation stage, with the object set upon the foam and two aluminum plates, as described in Section 9.4.1 (Figure 9.33). After generating a radiograph, Object 2 was moved so that its centerline was 5.5 cm from the scintillator. The translation stage was too large to fit in the space between the steel shielding and the concrete cave, so the stage was replaced by three 2 in thick polyethylene blocks and three aluminum plates. Object 2 was again blocked up by the foam and two aluminum plates so that the material closest to Object 2 remained the same (Figure 9.34). Both radiographs took 50 frames, integrated 3.00×10^5 pulses per frame, and set the ADC to 50 and the intensifier to 80.

9.4.3 Comparison between FP60R and FP15R

Building upon the scatter studies outlined in Section 9.2, several radiographs of Object 2 were taken in FP60R with four of the energy bins that had been used in FP15R. Energy bins selected were 10 to 600 MeV; 2.5 MeV and below; the full spectrum; and spallation photons. The purpose of this study was to compare radiograph quality between the two beam lines. Object 2 remained in its position of 5.5 cm from the scintillator in order to match the distance Object 2 had been in FP15R. While some differences do exist between the two beam lines (e.g., the energy spectrum, the camera location within the light-tight box, and the shielding configuration), this study will compare overall system performance.

Time gates and associated energies, as well as equipment settings, can be seen in Table 9.4. For each of the radiographs in this study, 50 frames were taken, the ADC gain was set to 50, and the intensifier gain was set to 80. Corresponding flatfield images were taken, also with the same settings in Table 9.4. Note that all settings



Figure 9.33: Photograph of Object 2 at a distance of 78.7 *cm* from the scintillator.



Figure 9.34: Photograph of Object 2 at a distance of 5.5 *cm* from the scintillator.

Table 9.4: Equipment settings for the four Object 2 radiographs taken to compare FP60R image quality to that of FP15R, including the particle type, particle energy, added signal delay, camera gate width, and the number of integrated pulses per frame.

Particle Type	Energy (MeV)	Delay (ns)	Gate Width (ns)	Pulses per Frame
Neutron	10.0 to ∼600	1019.67	398.91	3.00×10^5
	∼0.1 to 2.5	116.89	873.11	3.00×10^5
Photon	All	990.0	10.0	6.00×10^5
Both	All	0.0	1784.0	1.25×10^5

match those used in FP15R, except for the delays and the time gate widths which had to be altered to match energy bin endpoints.

9.4.4 Long Exposure Radiographs

This study was conducted to determine how image quality is affected by exposure time. Although longer exposures deliver higher doses to the radiography object, increasing the exposure time improves image statistics by allowing more frames to be combined, which in turn improves the signal-to-noise ratio for the final image. Therefore, the purpose of this study was to determine how much of an improvement can be seen by taking long exposure radiographs.

Object 2 was placed within the camera's field of view at a distance of 50 cm from the scintillator. Also stacked within the field of view were the two LLNL objects (refer to Figures 9.19 and 9.20 for object diagrams), with the penetrameter object placed on top of the crack test object. The three objects were placed upon the piece of thick foam and two sets of four aluminum plates that had been stacked on an optical table. Object 2 was raised slightly higher than the other two object by another two aluminum plates on top of the foam. A diagram of this set-up can be seen in Figure 9.35, with a photograph shown in Figure 9.36.

Nine-hour exposures (equal to 1800 frames), along with corresponding flatfield images, were taken for 8 to 12 MeV and 12 to 16 MeV. The time bins and associated delays are listed in Table 9.1. For both radiographs in this study, 1800 frames were taken, 6.00×10^5 pulses per frame were integrated, the ADC gain was set to 50, and the intensifier gain was set to 80.

9.4.5 Depleted Uranium Radiographs

The final study radiographed the crack test object through three 1 in thick depleted uranium plates. This study was conducted to determine how well the system can image through thick, high-Z material and whether higher neutron energies are

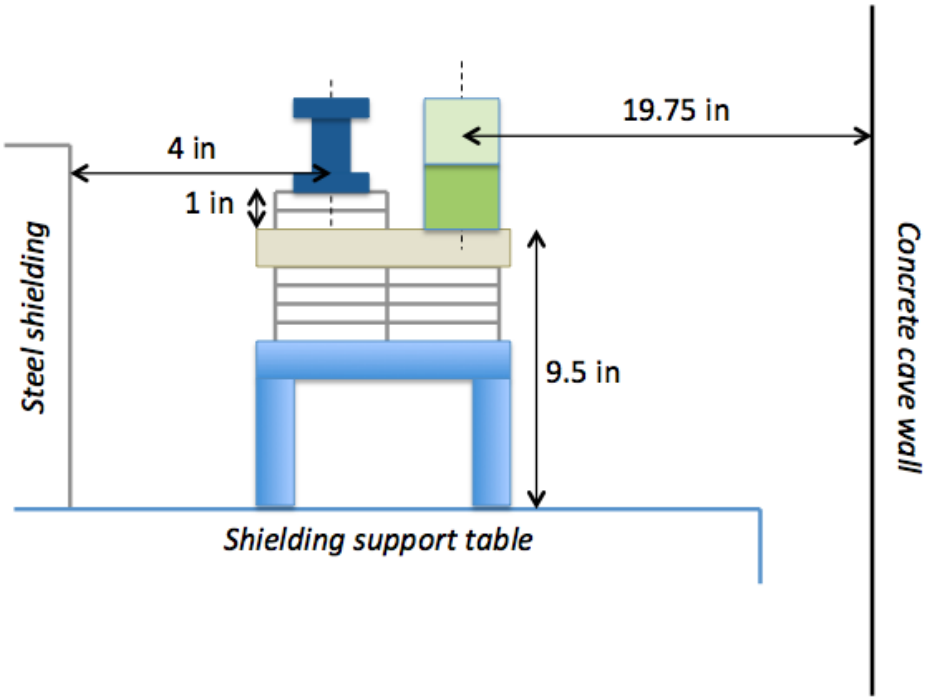


Figure 9.35: Not-to-scale diagram of the set-up for the long exposures of Object 2 (dark blue), the crack test object (dark green), and the penetrameter (green). The optical table (blue), aluminum plates (white with gray border), and the foam (beige) used to raise the height of the objects are also shown. The steel shielding, shielding support table, and concrete cave wall are shown for reference, and the point-of-view is from the beam looking toward the scintillator.

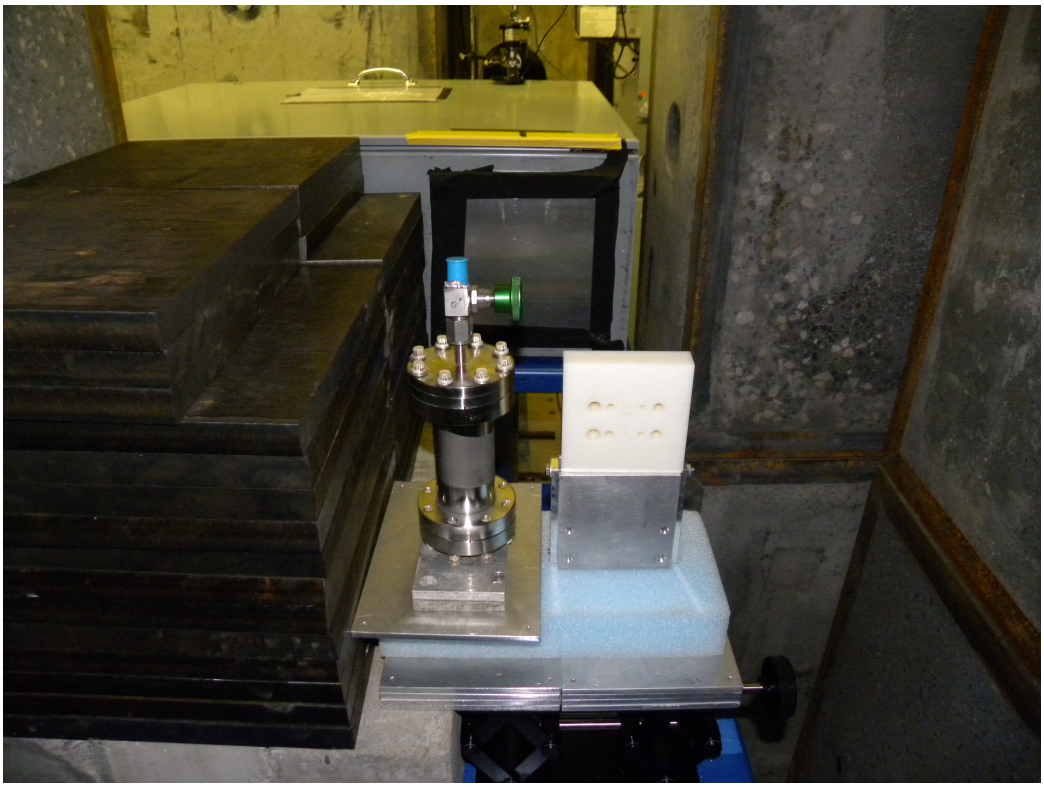


Figure 9.36: Photograph of the set-up for the long exposure radiographs. Object 2 is on the left, and the two LLNL objects are stacked on the right, with the penetrameter above and the crack test object below.

necessary when compared to Object 2. Other analysis was completed to determine the impact of having a long exposure flatfield image but a short exposure radiograph, which would reduce dose to the radiography object while possibly improving the signal-to-noise ratio.

For this study, the crack test object was placed behind the three DU plates so that, if the crack test object was visible through the DU, its image was generated from direct source neutrons and not from scatter off the DU plates. It is much harder to image with the DU between the scintillator and the object, and so this configuration was intentionally selected to be more challenging.

The center of the translation stage was moved to a distance of 83 cm from the scintillator. The three plates were set on top of a 4 in tall steel beam pipe collimator, with the rectangular DU plate sandwiched between the two semi-circular DU plates (Figure 9.37). The back of the DU plate farthest from the scintillator (from the viewpoint of the scintillator) was at a distance of 87.3 cm from the scintillator face. The crack test object was placed on the side of the semi-circular plate closest to the beam pipe, with a photograph of the crack test object from above shown in Figure 9.38. All handling of the DU was done by LANSCE staff for safety reasons. Time gates and associated energies, as well as equipment settings, can be seen in Table 9.5. For each of the radiographs in this study, three sets of 200 frames were taken (yielding 600 total frames), the ADC gain was set to 50, and the intensifier gain was set to 80. Corresponding flatfield images were taken, also with the same settings in Table 9.5.

9.5 Results and Conclusions

The data from the various studies outlined in this chapter were post-processed using ImageJ and according to the process previously described in Section 5.2.6 to convert pixel values into σt. However, unlike results in Chapter 5 which combined frames by averaging them together, frames from FP60R experiments were combined using the

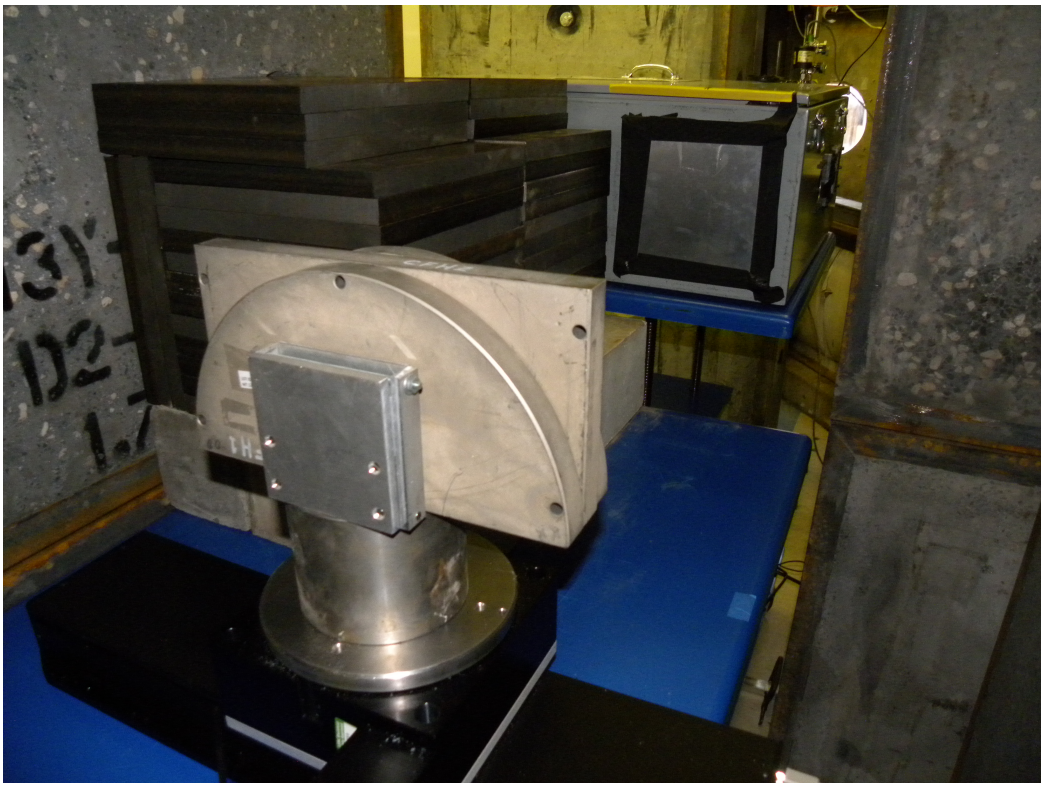


Figure 9.37: Photograph of the experimental set-up to radiograph the crack test object behind three DU plates.

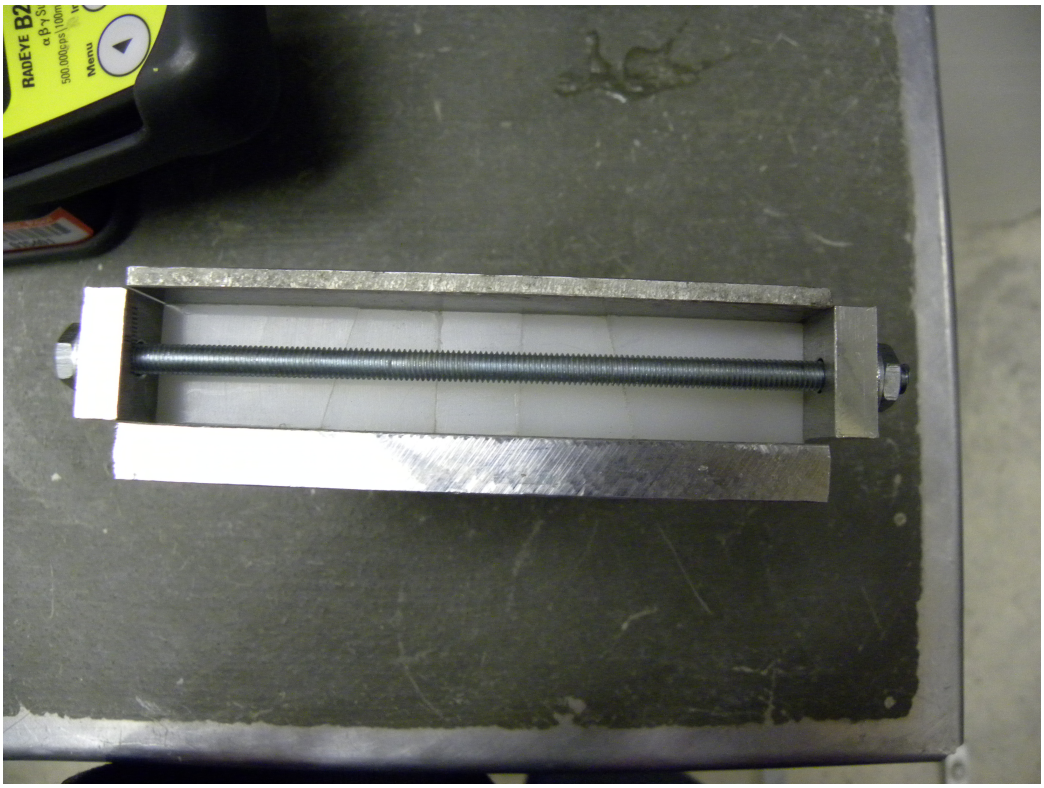


Figure 9.38: Photograph of the top of the crack test object.

Table 9.5: Equipment settings for the three radiographs of the crack test object, taken through 3 *in* of DU, including the particle type, particle energy, added signal delay, camera gate width, and the number of integrated pulses per frame.

Energy (MeV)	Delay (ns)	Gate Width (ns)	Pulses per Frame
8 to 12	1376.75	98.58	6.00×10^5
12 to 16	1396.23	48.35	6.00×10^5
50 to 70	1123.58	32.01	6.00×10^5

median pixel value. The final image thus used the median pixel value as calculated by ImageJ among all frames, which better eliminated stars in the final post-processed images. Once the frames were combined and the flatfield (also combined by this median process) was divided out, the typical process of applying a natural *log* filter and multiplying the result by -1 was conducted to convert pixel values to σt. A second median filter was then applied with a radius of 1 pixel in order to further smooth noise and remove stars.

The reader will notice the fission chamber appears in the radiographs included in this section. The fission chamber, round in shape and with periodic holes in its frame, could not be eliminated by dividing out the flatfield. This is most likely due to shifts in the beam spot during the LANSCE run cycle that cause flatfield features (e.g., the fission chamber) to not be in the same location as in the radiograph. The fission chamber is thus an artifact and not indicative of features within the object. It is possible that the fission chamber artifact may obscure features within the radiography object. Thus, future experiments will need to move the fission chamber out of the camera's field of view.

A final comment will be made on the effort in this chapter to eliminate the differences in flux levels between energy bins. Such a step was necessary to make fair comparisons between radiographs generated with different energy bins. This was accomplished by normalizing each radiograph to the lowest average flatfield intensity, which was determined from a ROI that consisted of the entire flatfield image. For example, if Flatfield A had an average intensity that was twice that of Flatfield B, Radiograph A would only use half of the frames that Radiograph B used. Similarly, Flatfield A would combine only half of the frames as Flatfield B. This normalization method took into account variations in flux level that result in changing the start time and width of the time gate. This effort improves upon data post-processing that is shown in Chapter 5.

As an example of the effect of flux normalization, a plot of normalized to unnormalized FP60R data was generated for a 10 to 600 MeV neutron radiograph of

Object 2 located at a distance of 5.5 cm from the scintillator (Figure 9.39). This plot shows that, as expected, the overall statistics decrease when frames are discarded, which causes the normalized line-out to appear less smooth. As an additional observation, normalization did not affect the contrast levels in the flatfield image. This is because neutrons in the selected energy bin (in this case, 10 to 600 MeV) have the same probability of interacting with the scintillator and the radiography object whether the data is normalized or not to the flux. Rather, normalization only affects the number of neutrons used to form an image so that flux differences between the various energy bins may be addressed on a statistical basis. This process should allow for fair comparison between energy bins that may contain different amounts of flux due to the polyenergetic nature of the LANSCE spectrum.

9.5.1 Optimal Source Energy

The first study, and possibly one of the most important of those discussed in this chapter, was conducted with the goal of finding the optimal neutron energy(ies) for use with TiGReSSE. Radiography data was normalized to the average flatfield intensity, with Table 9.6 listing the number of frames out of 100 that were used for the five energy bins studied. This number of frames was used for generating the radiography image, as well as the flatfield image, to account for differences in flux in the various energy bins.

The radiographs can be seen in Figures 9.40 through 9.44, after rotating them 1.5° counter-clockwise to straighten the object in the field of view. The radiographs were independently set to their optimal contrast range to best see internal features; thus, contrast ranges do not match between the five energy bins.

The features of interest within Object 2 are indicated in Figure 9.45. These features were captured by two ROIs, shown in Figure 9.46, so that averaged vertical line-outs could be generated to determine if, and how well, these features are seen in the various energy bins. The averaged vertical line-outs for this study can be seen

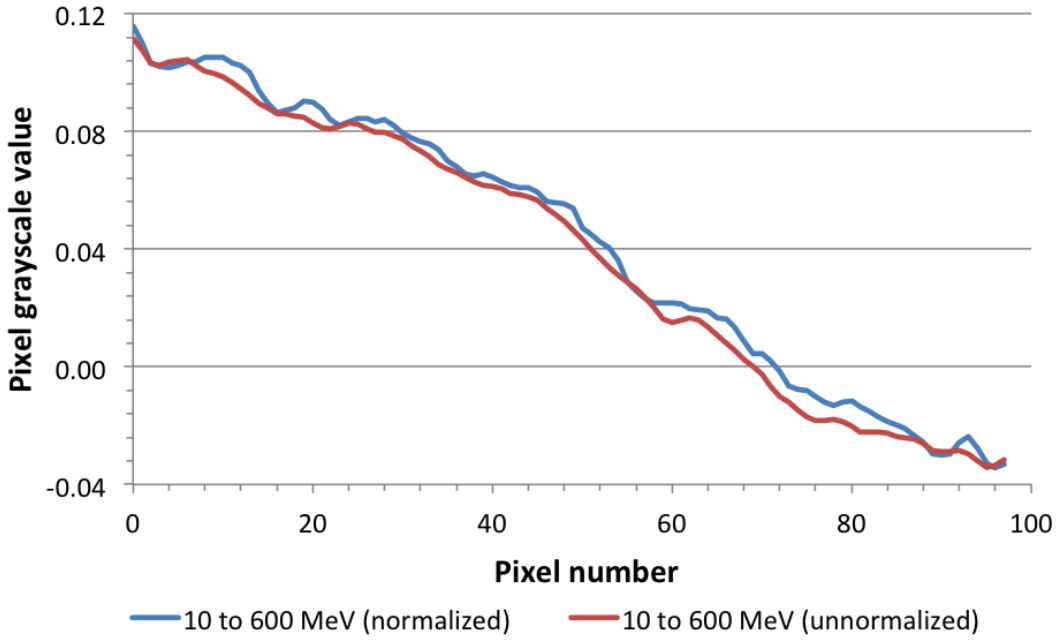


Figure 9.39: Averaged vertical line-outs for the normalized 10 to 600 MeV radiograph (27 frames) and the unnormalized 10 to 600 MeV radiograph (all 100 frames were used), both taken of Object 2 in FP60R. Note that while smoothness is affected by normalization, contrast is not.

Table 9.6: The number of frames, rounded up to the nearest whole number, used to generate the radiography and flatfield images for the optimal energy study. A varying number of frames was used in order to normalize the images to the average flatfield intensity.

Energy (MeV)	Number of Frames Used
2 to 3	84
8 to 12	64
9 to 11	100
12 to 16	92
50 to 70	79

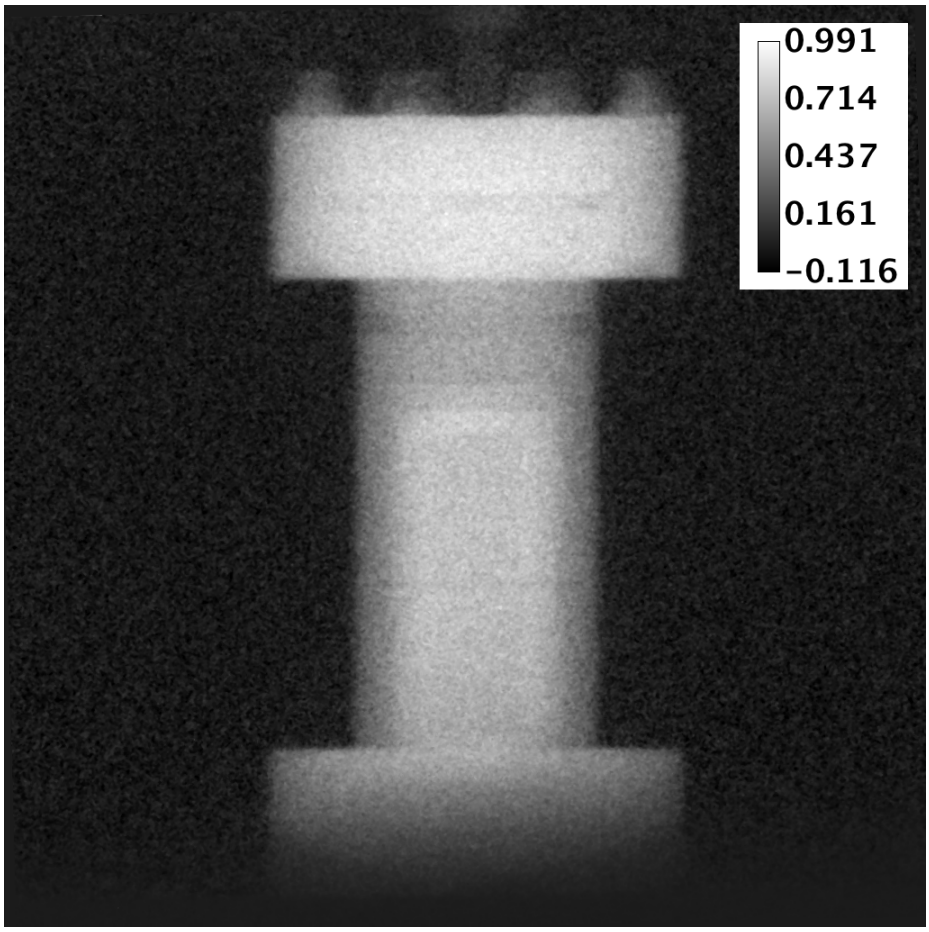


Figure 9.40: FP60R radiograph of Object 2 using 2 to 3 MeV neutrons and 84 frames. The image was rotated 1.5° counter-clockwise to straighten the object in the field of view.

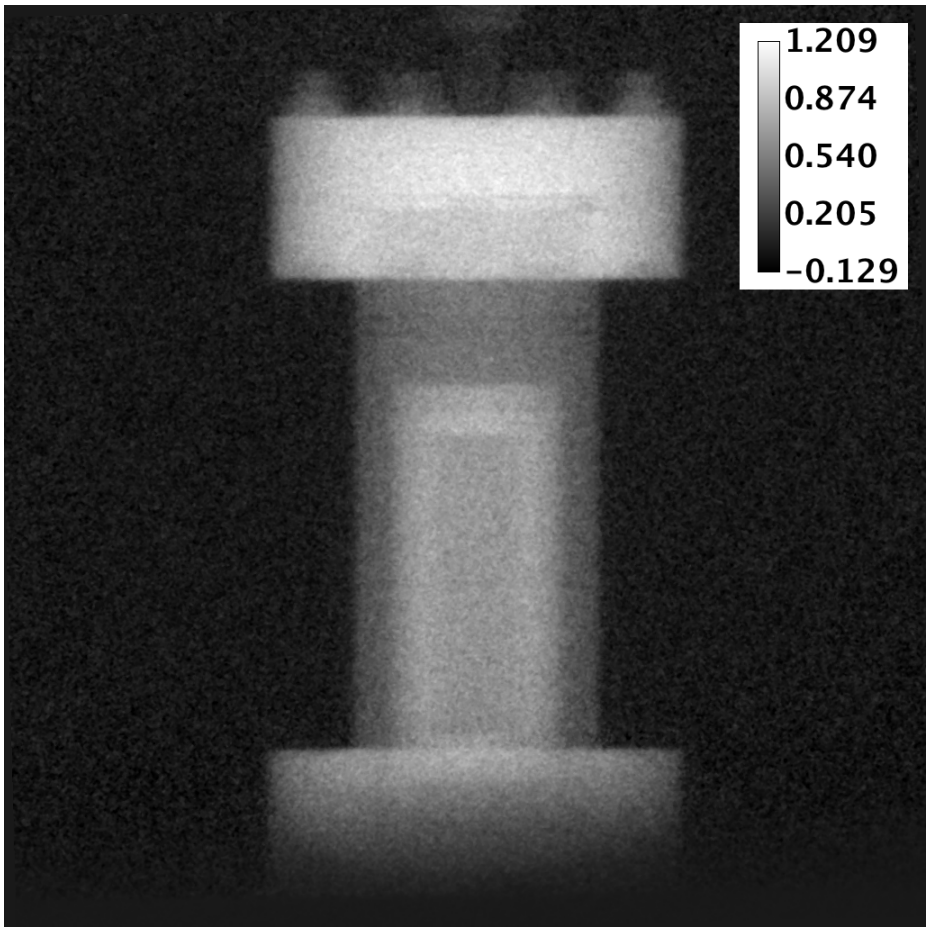


Figure 9.41: FP60R radiograph of Object 2 using 8 to 12 MeV neutrons and 64 frames. The image was rotated 1.5° counter-clockwise to straighten the object in the field of view.

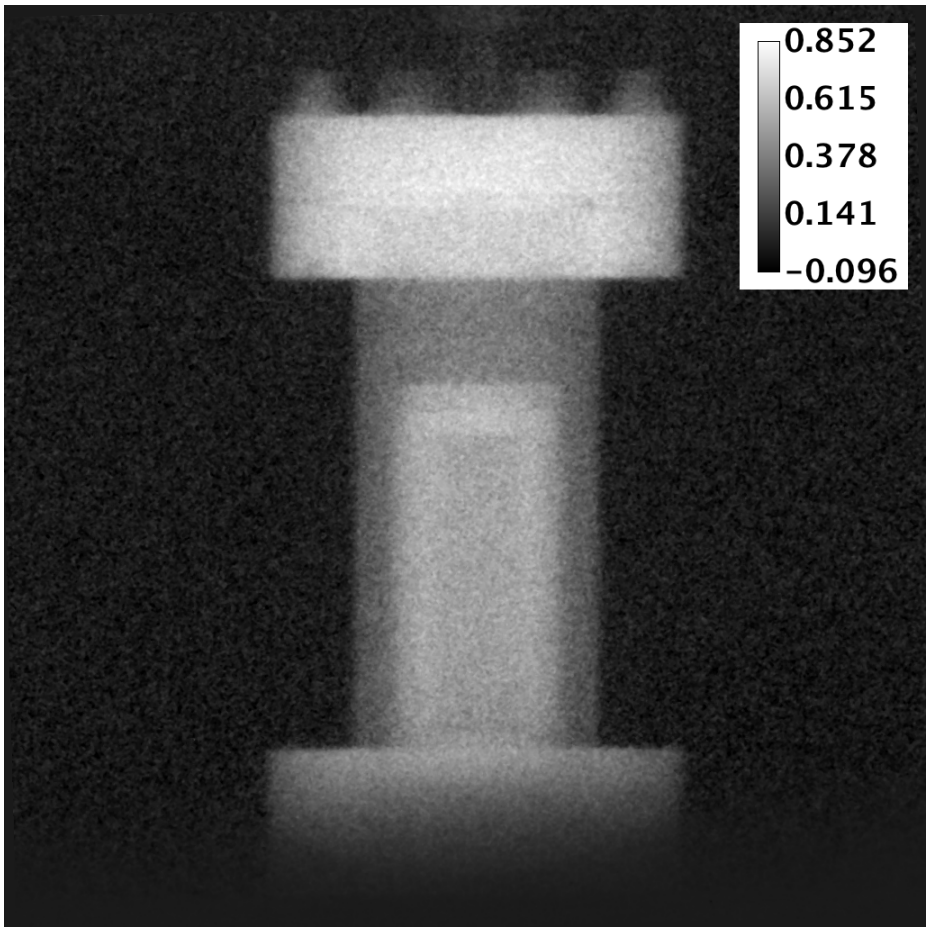


Figure 9.42: FP60R radiograph of Object 2 using 9 to 11 MeV neutrons and 100 frames. The image was rotated 1.5° counter-clockwise to straighten the object in the field of view.

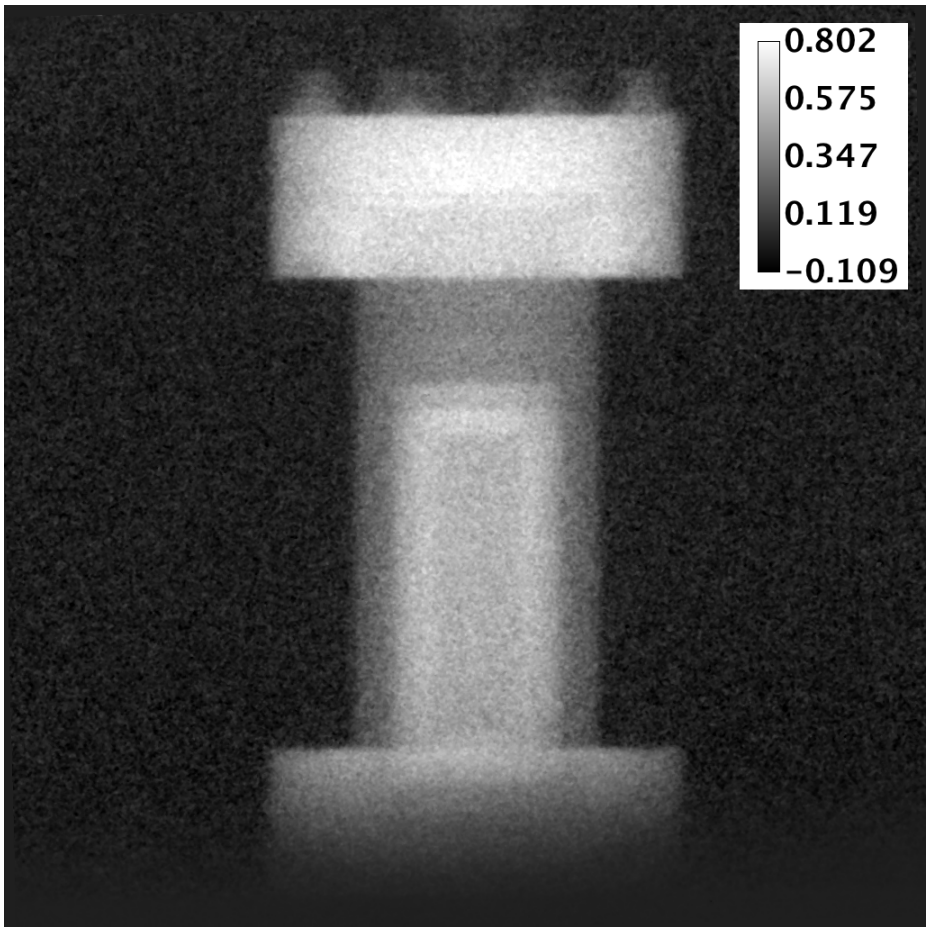


Figure 9.43: FP60R radiograph of Object 2 using 12 to 16 MeV neutrons and 92 frames. The image was rotated 1.5° counter-clockwise to straighten the object in the field of view.

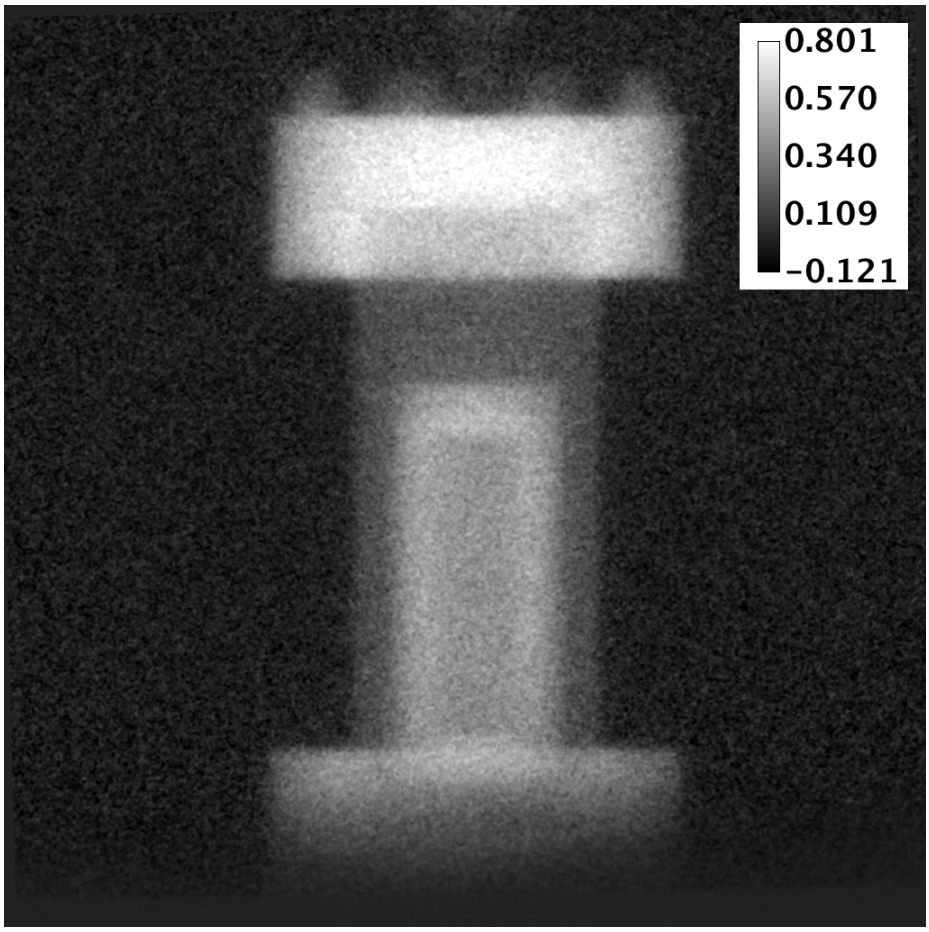


Figure 9.44: FP60R radiograph of Object 2 using 50 to 70 MeV neutrons and 79 frames. The image was rotated 1.5° counter-clockwise to straighten the object in the field of view.

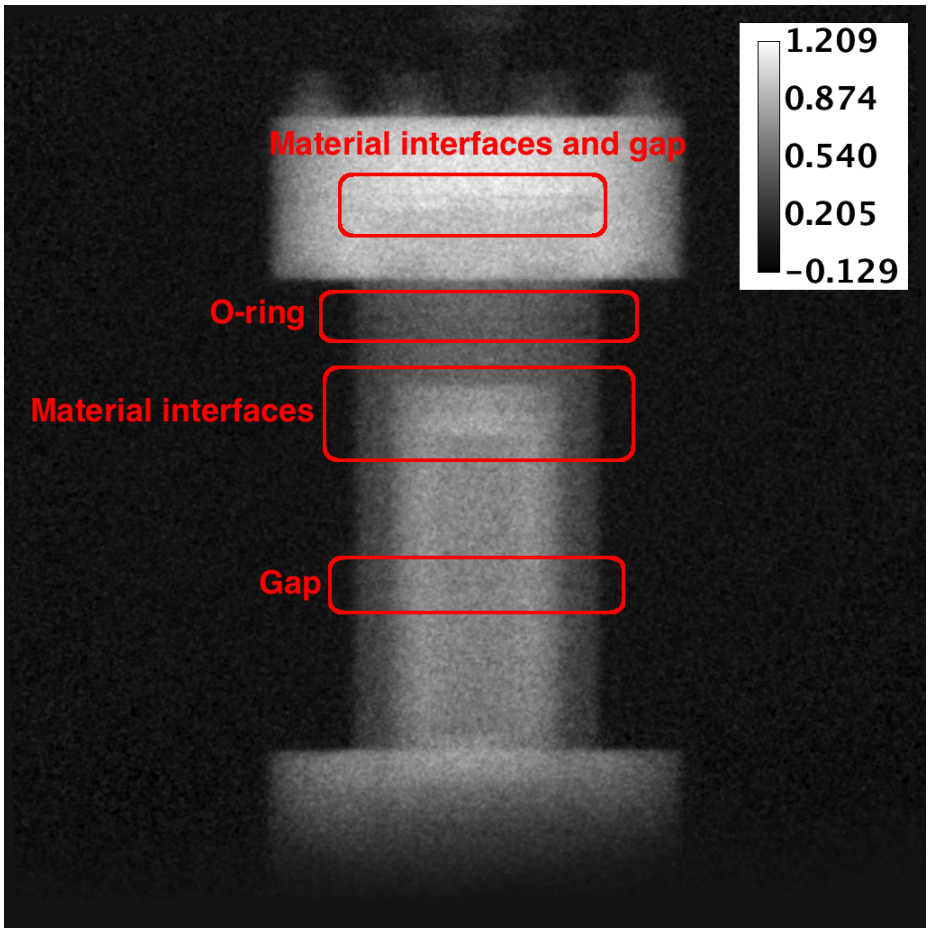


Figure 9.45: Features of interest indicated on the FP60R radiograph of Object 2 that was generated with 8 to 12 MeV neutrons.

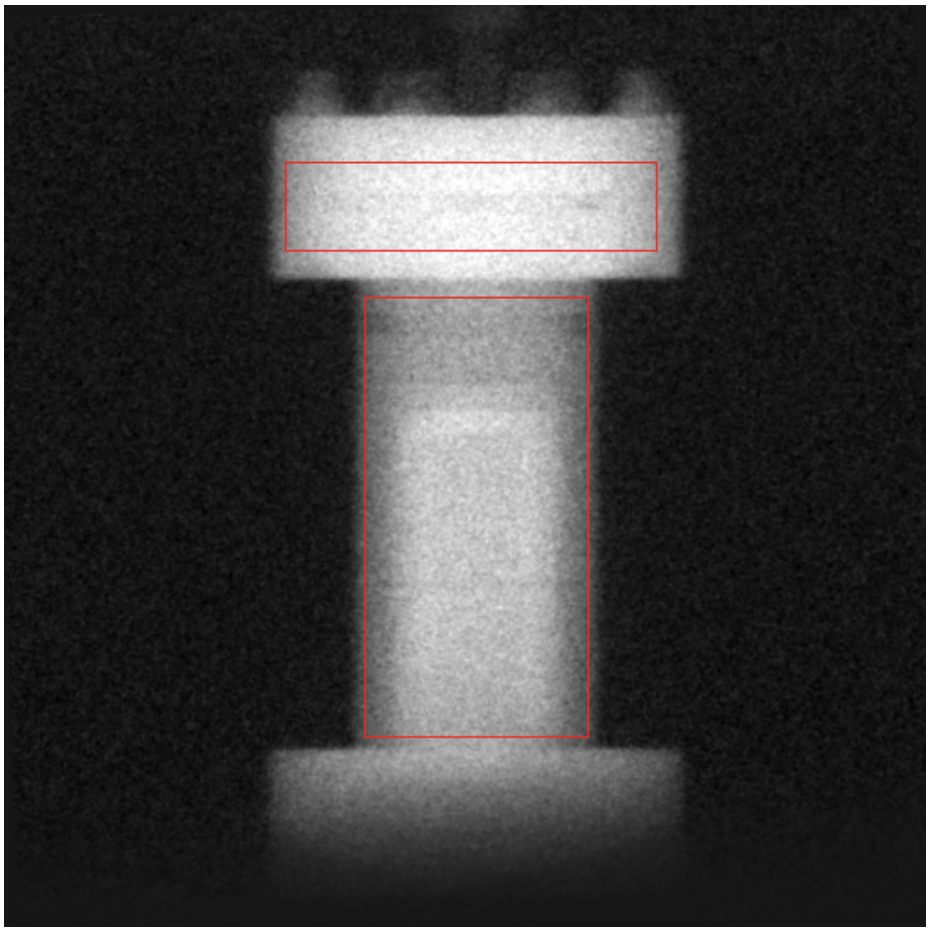


Figure 9.46: Two ROIs were selected on the radiographs of Object 2 to generate averaged line-outs and thus gauge the impact of neutron source energy on the ability to image internal features. ROIs are shown in red.

in Figure 9.47 and show that there are two gaps in each ROI, although these are not distinguishable by eye when inspecting the radiographs. The set of gaps in the middle ROI corresponds to the O-ring, while the set of gaps in the top ROI is a result of an angled gap between the two flange pieces (the two valleys) and the gold-coated stainless steel material region (the peak). These gaps are most apparent in the 2 to 3 MeV and 8 to 12 MeV line-outs, but are hard to distinguish from the noise for the other three energy bins. This is most likely a result of the energy-dependence of the gap materials and object geometry.

With respect to the pixel grayscale values, which have been manipulated to represent σt, the higher energy bins are seen to be less attenuated (i.e., having smaller pixel grayscale values) than the lower energy bins, which was to be expected according to the theory of neutron radiography as discussed in Chapter 1. An exception, however, is for 2 to 3 MeV and 8 to 12 MeV neutrons in the averaged vertical line-out of the top ROI, where the latter energy is more attenuated than the former. This is believed to be a result of the large amount of scatter in the 2 to 3 MeV energy range, which is a problem for the top ROI because this region is very thick when compared to the middle ROI. Increased scatter leads to increased fluence on the scintillator screen, which causes dark regions to appear artificially brighter and thus less attenuating than they otherwise would.

While the middle ROI correctly shows that 2 to 3 MeV neutrons are attenuated more than 8 to 12 MeV neutrons, the two line-outs are closer together in contrast value than one might expect. This perceived reduction in the attenuation of 2 to 3 MeV neutrons is also the result of scatter, but because this section of Object 2 is thinner, the scatter is not enough to increase the contrast above the 8 to 12 MeV contrast level like what was seen in the top ROI. It is thus expected that, if a uniform slab of a homogenous material were selected to radiograph in subsequent experiments, the scatter would be uniform and cause an artificial increase in transmission to be seen equally in two ROIs. Object 2, however, has an unequal scatter field which affects the line-outs of the two regions differently.

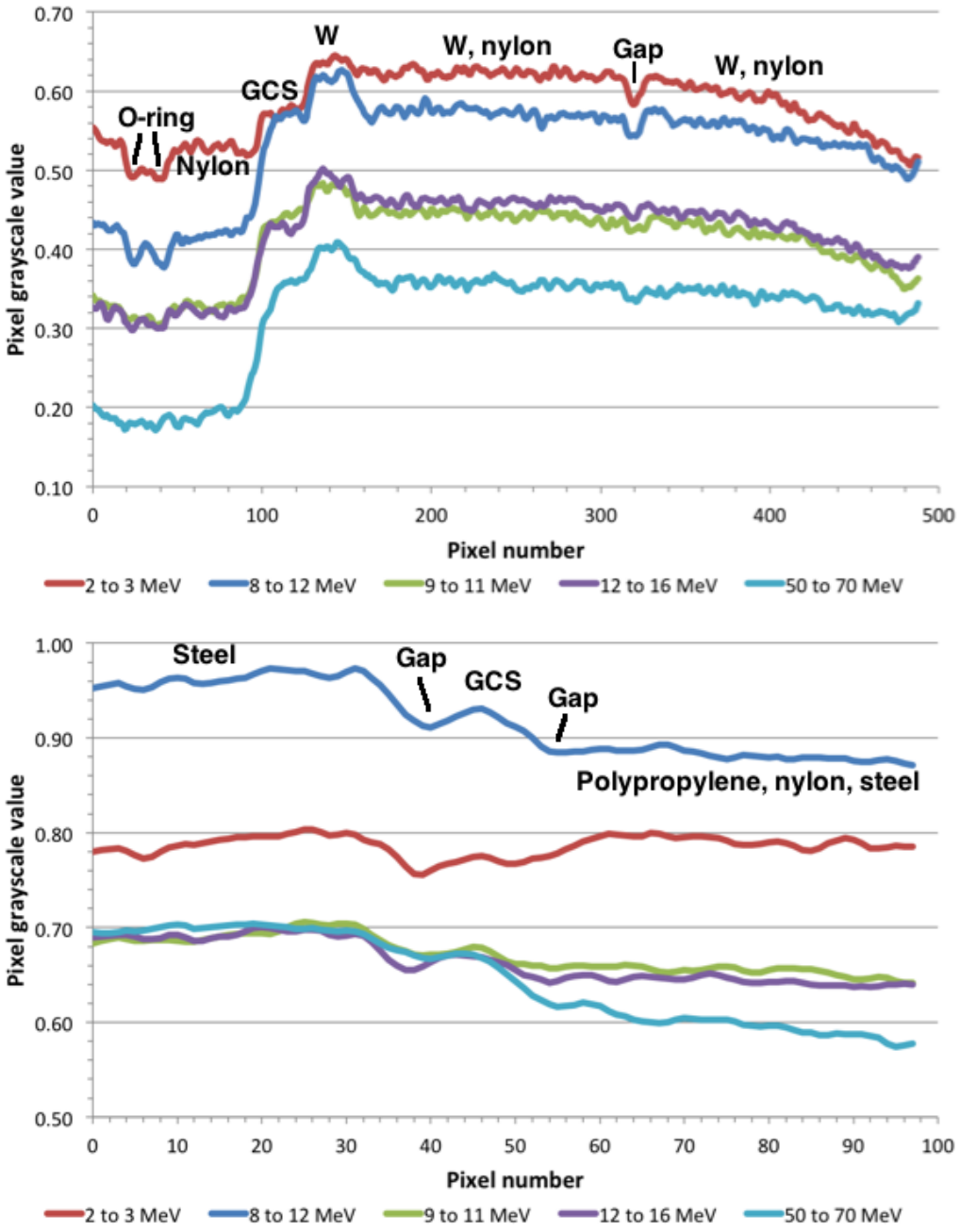


Figure 9.47: The line-outs associated with the optimal source energy study, which took radiographs of Object 2 with five different energy ranges. Regions and features are labelled, with "GCS" representing gold-coated steel. Only major materials were listed on the line-outs; for a full list, refer to the diagram of Object 2. Top: The averaged vertical line-out associated with the middle ROI. Bottom: The averaged vertical line-out associated with the top ROI.

Another interesting result was that the 9 to 11 MeV and 12 to 16 MeV line-outs have nearly the same contrast levels, even though their average energy is quite different (10 MeV versus 14 MeV). Additionally, the 12 to 16 MeV energy bin has better contrast resolution than the 9 to 11 MeV energy bin. This is believed to be a result of electronic noise, which forms a larger percentage of the data for shorter time gates than longer time gates and thus can artificially increase transmission. Noise results from data read-out, and if two radiographs have the same number of frames, they have the same amount of read-out noise. However, if there is less flux in a given energy bin because it is narrower in time or because the beam has less flux, then there is a larger percentage of the data that is attributable to noise. Future work should subtract background noise to address this problem.

As a final note, it appears both qualitatively and quantitatively that the 8 to 12 MeV energy bin is optimal for neutron radiography of Object 2 with TiGReSSE in FP60R. This may not, however, be the ideal energy range for all objects, which was shown to vary among objects in Chapter 5, or for all source or TiGReSSE configurations.

9.5.2 Optimal Location for Radiography Object

As described earlier in this chapter, this study examined the effect of object-to-scintillator distance on image quality. The centerline of Object 2 was placed either 5.5 cm or 78.7 cm from the scintillator, which will be referred to as "close" and "far", respectively. Radiographs were taken with neutrons 2.5 MeV and below in energy, since this energy bin is thought to have the most scatter and thus have a very obvious effect.The two radiographs had nearly the same average flatfield intensity, so all 100 frames were combined for both the image and the flatfield. Two different flatfield images were taken to account for the different support systems used at the two object locations; the structures would scatter differently and thus flatfields would not necessarily be the same.

The close and far radiographs are respectively shown at their optimal contrast levels in Figures 9.48 and 9.49. It can be seen in these two radiographs that the close radiograph was rotated 90° when it was relocated from its position at 78.7 *cm*, since the bolts at the top of the cylinder do not match in number between the two images. However, because the object is symmetrical along its centerline, this change should not noticeably impact the comparison.

During post-processing, the far radiograph was rotated 2.3° counter-clockwise, while the close radiograph was rotated 1.9° counter-clockwise. This was done to minimize blur in the line-outs that would result from a crooked image. The far radiograph was translated to approximate the location of Object 2 in the close radiograph so the ROIs would be in approximately the same location in the image. The two ROIs selected are shown in Figure 9.50.

Qualitatively, the close radiograph looks grainier and blurrier than the far radiograph. This observation was quantified by taking averaged vertical line-outs from the two ROIs (Figure 9.51). The line-outs show that the general contrast shape remains the same between the two object locations, but the 5.5 *cm* line-out is much noisier. The close line-out has lower contrast values because, even though the object materials and geometry remain the same, scatter is increased at 5.5 *cm* and the transmission is artificially increased. Additionally, the close line-out shows that the gold-coated steel region is not distinguishable from the nylon region like it is in the far line-out. It can thus be concluded from the line-outs that placing Object 2 farther from the scintillator improved image quality by reducing noise and increasing contrast resolution that enabled better detection of internal features.

In conclusion, the predictions made earlier in this chapter were seen to be valid: increasing the distance of the object from the scintillator reduces scatter into the scintillator and therefore improves contrast resolution. The close radiograph has smaller pixel grayscale values (which indicates increased transmission) when compared to the far radiograph because of the increased amount of scatter off the object into the scintillator; because both the close and far radiographs were generated

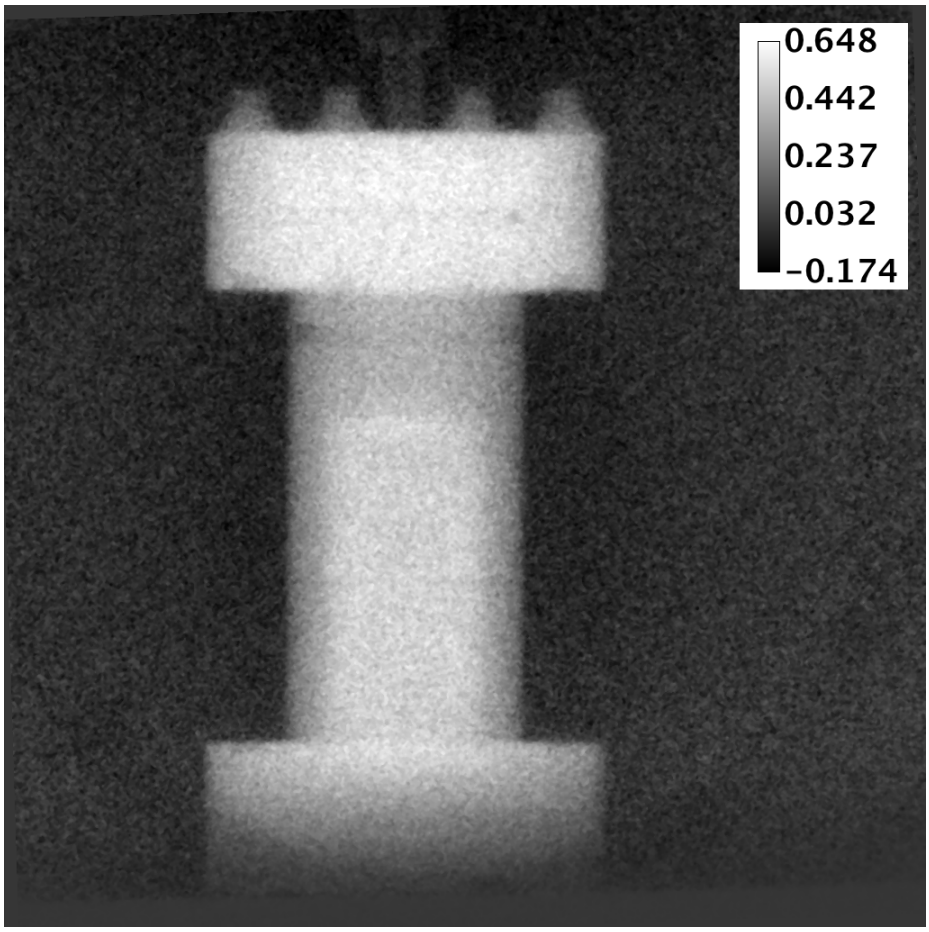


Figure 9.48: Close radiograph generated of Object 2 with neutrons of energy 2.5 MeV and below. The centerline of Object 2 is located 5.5 cm from the scintillator. The radiograph was rotated 1.9° counter-clockwise to straighten the object.

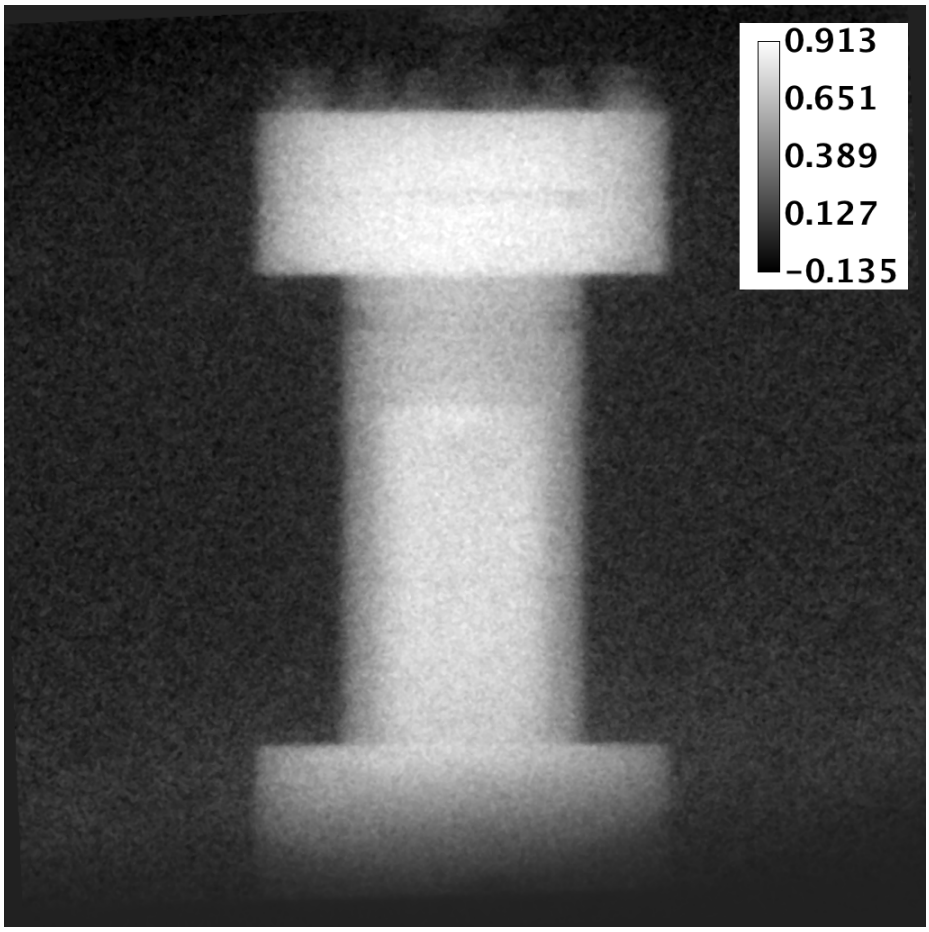


Figure 9.49: Far radiograph generated of Object 2 with neutrons of energy 2.5 MeV and below. The centerline of Object 2 is located 78.7 cm from the scintillator. The radiograph was rotated 2.3° counter-clockwise to straighten the object.

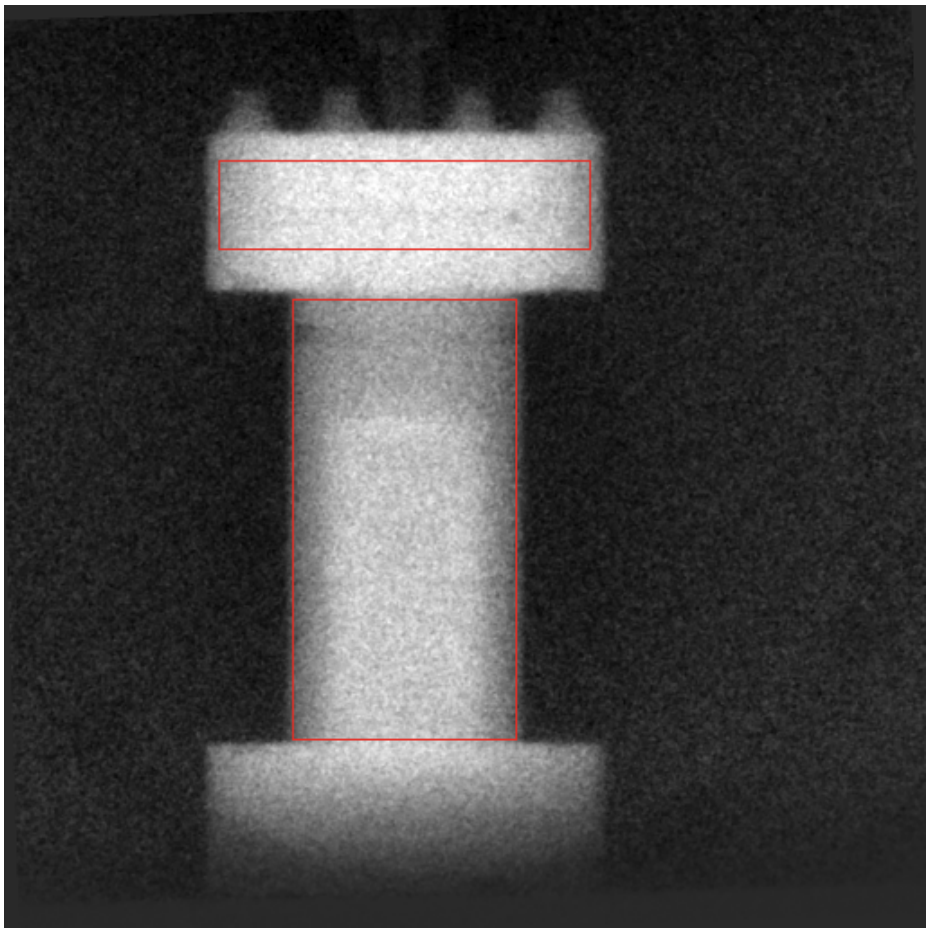


Figure 9.50: Regions of interest (red) on the close radiograph taken with 2.5 MeV and below neutrons in FP60R. These same ROIs were used on the far radiograph.

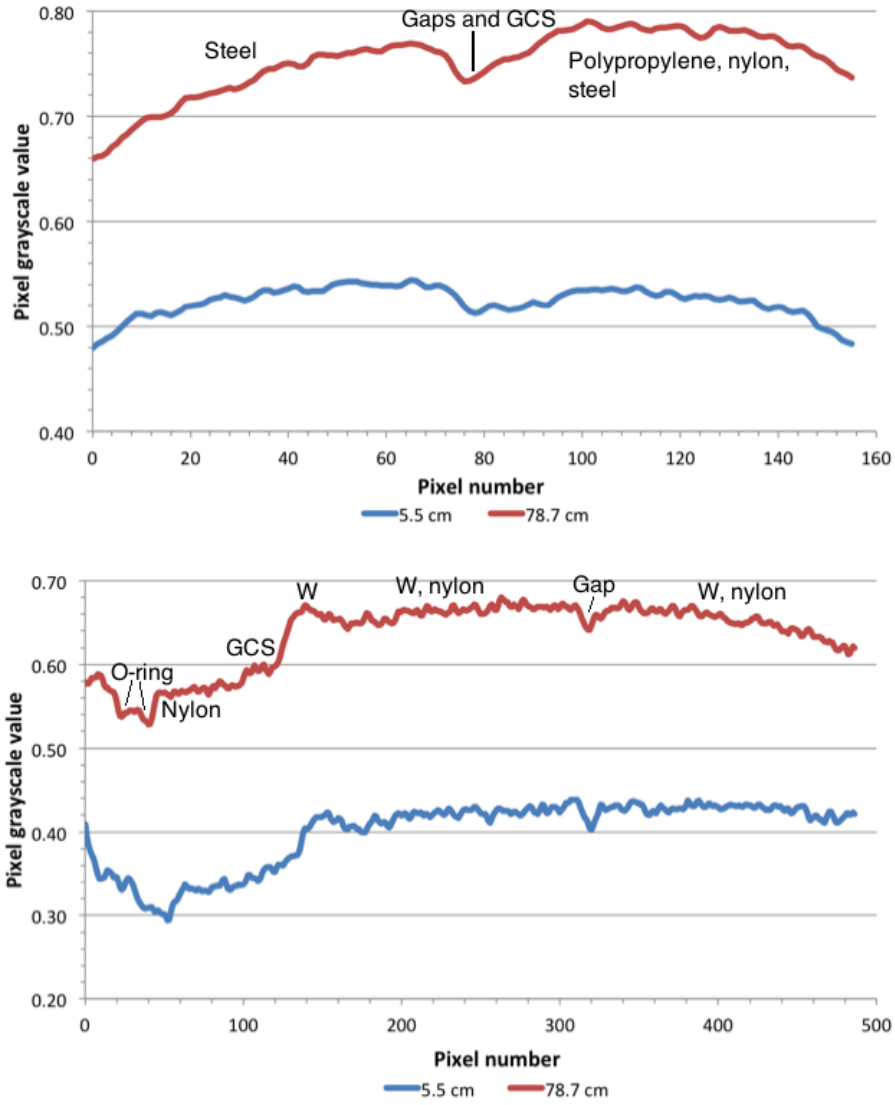


Figure 9.51: Averaged vertical line-outs taken to determine the impact of object location on image quality. Regions and features are labelled, with "GCS" representing gold-coated steel. Only major materials were listed on the line-outs; for a full list, refer to the diagram of Object 2. Top: Top ROI with the close radiograph shown in blue and the far radiograph shown in red. Bottom: Middle ROI with the close radiograph shown in blue and the far radiograph shown in red.

of the same object and with the same neutron source, the artificial increase in transmission can only be a result of scatter. Furthermore, the object distance for the far radiograph was between the calculated optimal object-to-detector distance that ranged from 75 *cm* and 100 *cm*, lending further support to these calculations. Thus, object location with respect to the scintillator does affect image quality, and further studies will need to be done to determine the optimal distance for each radiography object since the location is object- and source-dependent.

9.5.3 Comparison between FP60R and FP15R

Intentionally, this study did not normalize radiographs to the average flatfield intensity because the purpose of this study was to compare beam performance, and thus this variable could not be eliminated like it was in the other studies because source strength would obviously vary between the two beam lines. Figures 9.52 through 9.55 show the radiographs generated with the four time gates listed in Table 9.4. These figures compare FP60R and FP15R unnormalized radiographs at their optimal contrast ranges, and also include the FP15R radiograph at the same contrast range as the FP60R radiograph for additional comparison. These images are key to understanding beam behavior in the two flight paths.

Several conclusions can be drawn from visually comparing the four sets of radiographs. First, when FP60R and FP15R radiographs are set to equal contrast ranges, the FP60R radiographs are generally brighter than the FP15R radiographs and thus are more attenuated. This increased signal in FP15R is most likely a result of the scatter and activation products that were much worse in FP15R and that artificially increase transmission as seen in a radiograph. Another possible cause is that the FP15R radiographs were taken with the Generation I TiGReSSE design which placed the camera closer to the scintillator and therefore led to less geometric light loss within the system.

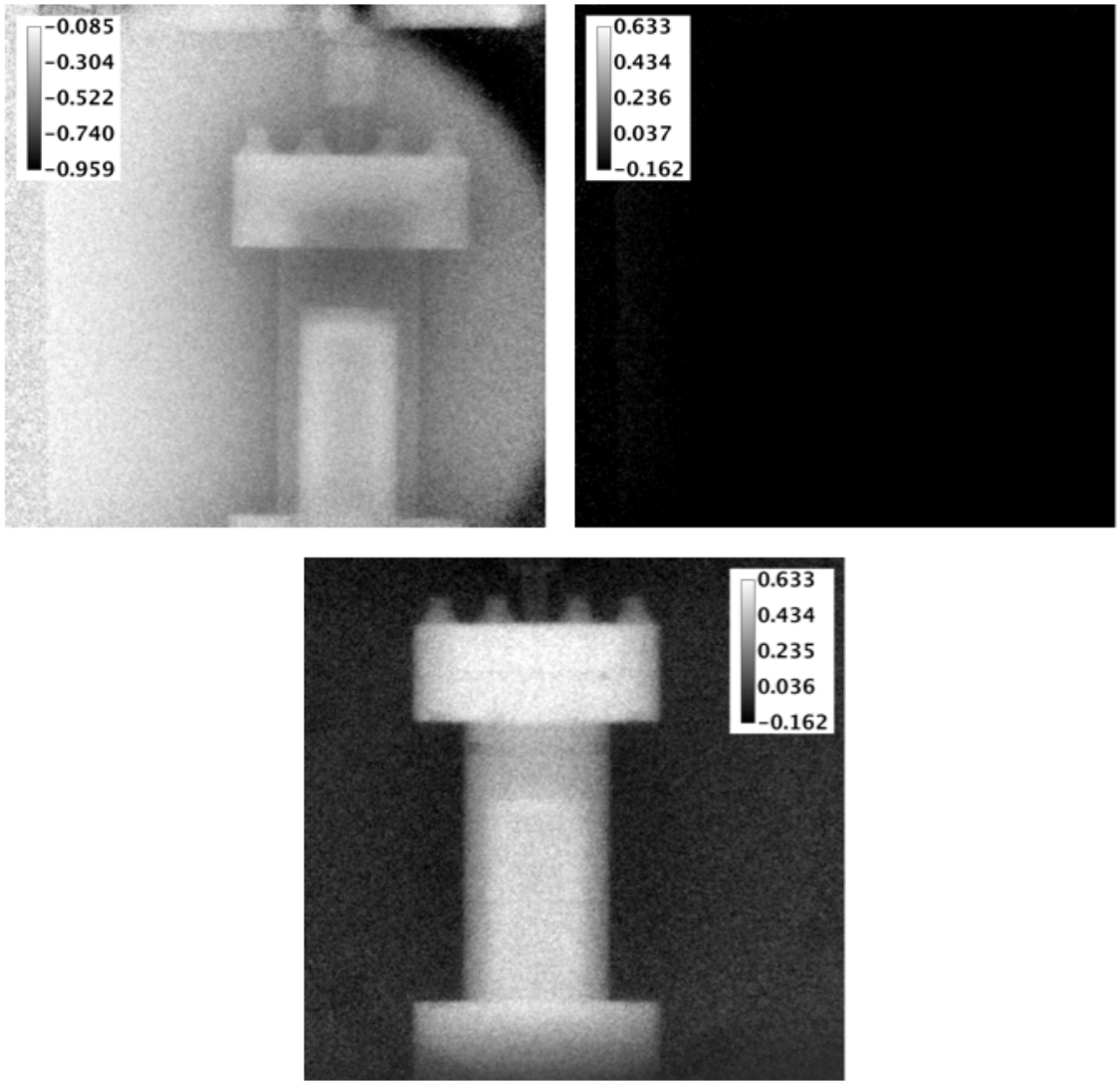


Figure 9.52: Radiographs from FP15R and FP60R, taken with 2.5 MeV neutrons and below. Top row: Radiographs from FP15R of Object 2, with the left radiograph at an optimal contrast range and the right radiograph at a contrast range matching that of the FP60R radiograph. Both radiographs were cropped. Note that the edge of the scintillator is visible because the mirror was misaligned. Bottom: Radiograph from FP60R of Object 2, set to an optimal contrast range, rotated, and cropped to the same size as the radiographs in the top row.

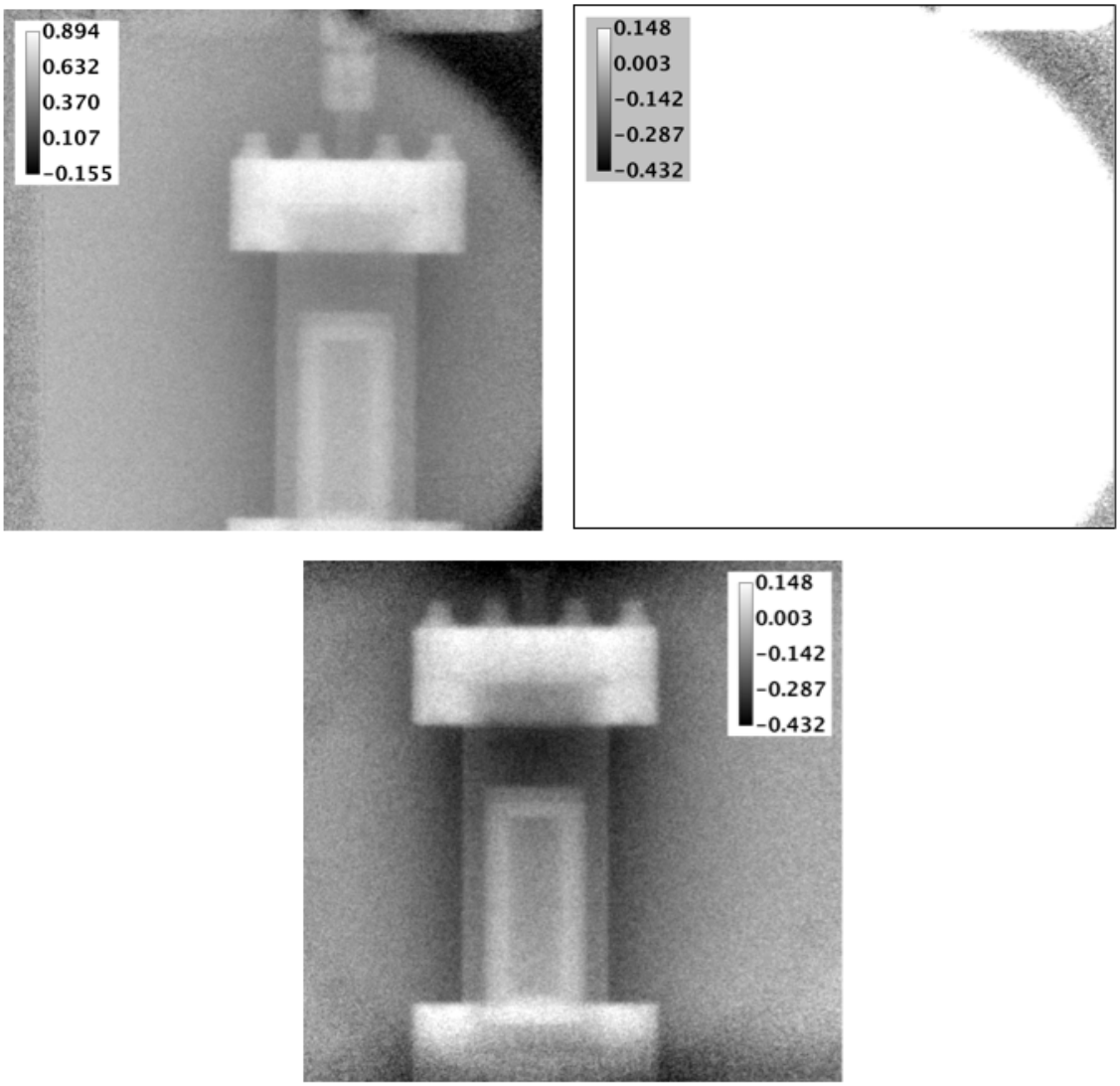


Figure 9.53: Radiographs from FP15R and FP60R, taken with 10 to 600 MeV neutrons and below. Top row: Radiographs from FP15R of Object 2, with the left radiograph at an optimal contrast range and the right radiograph at a contrast range matching that of the FP60R radiograph. Both radiographs were cropped. Note that the edge of the scintillator is visible because the mirror was misaligned. Bottom: Radiograph from FP60R of Object 2, set to an optimal contrast range, rotated, and cropped to the same size as the radiographs in the top row.

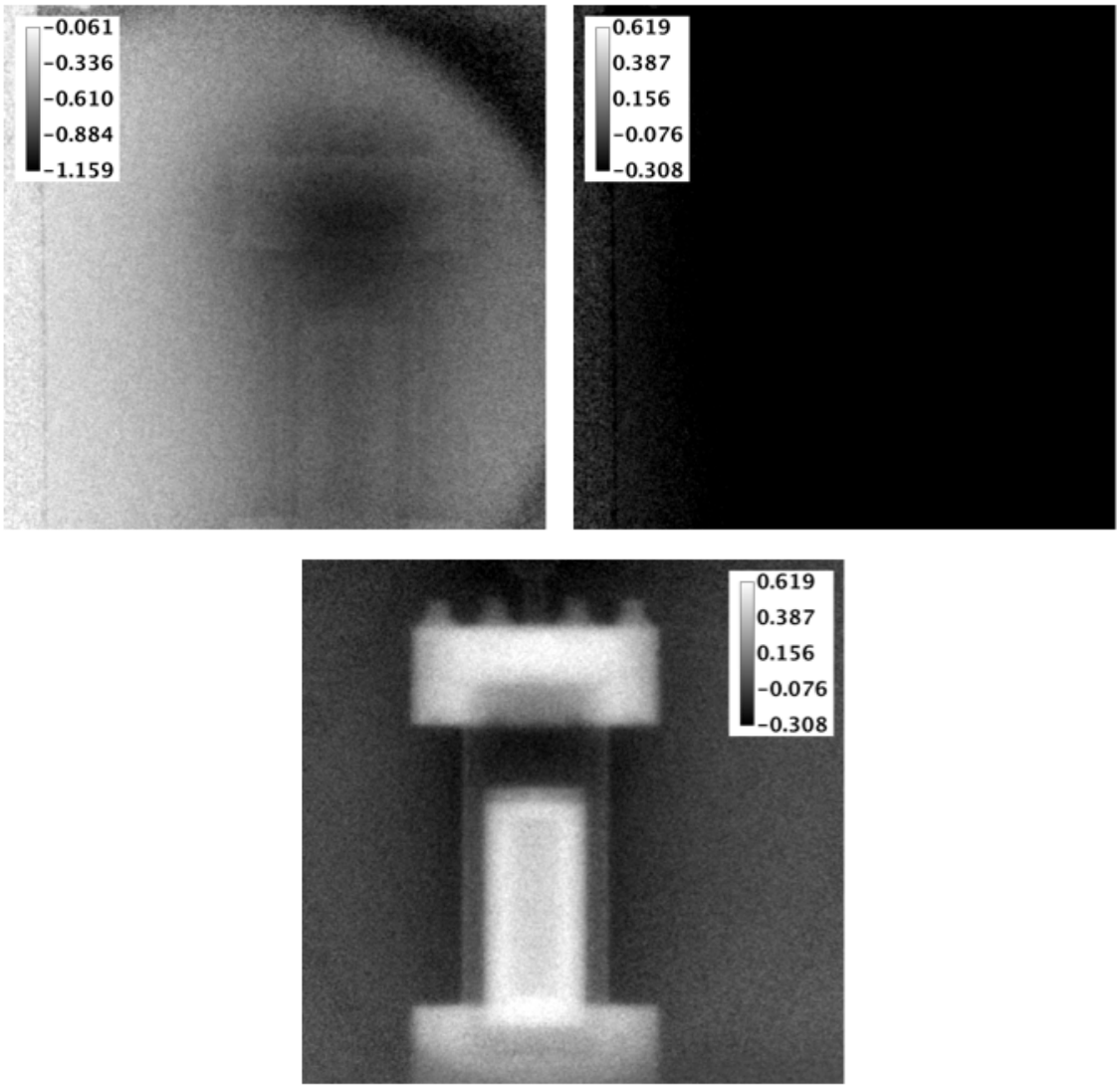


Figure 9.54: Radiographs from FP15R and FP60R, taken with spallation photons. Top row: Radiographs from FP15R of Object 2, with the left radiograph at an optimal contrast range and the right radiograph at a contrast range matching that of the FP60R radiograph. Both radiographs were cropped. Note that the edge of the scintillator is visible because the mirror was misaligned. Bottom: Radiograph from FP60R of Object 2, set to an optimal contrast range, rotated, and cropped to the same size as the radiographs in the top row.

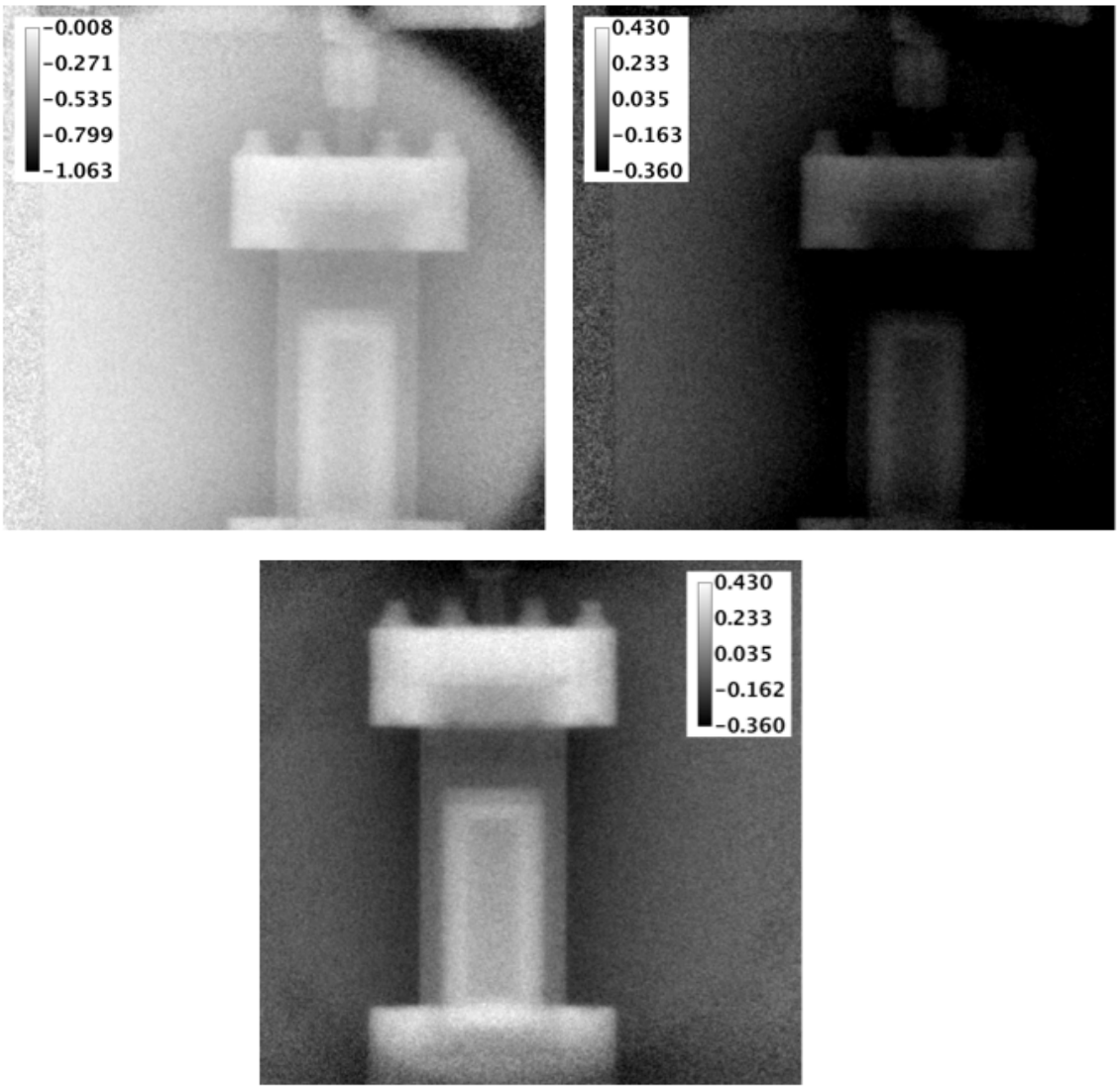


Figure 9.55: Radiographs from FP15R and FP60R, taken with the full LANSCE spectrum. Top row: Radiographs from FP15R of Object 2, with the left radiograph at an optimal contrast range and the right radiograph at a contrast range matching that of the FP60R radiograph. Both radiographs were cropped. Note that the edge of the scintillator is visible because the mirror was misaligned. Bottom: Radiograph from FP60R of Object 2, set to an optimal contrast range, rotated, and cropped to the same size as the radiographs in the top row.

One exception to this rule is the 10 to 600 MeV energy bin, where the FP15R radiograph is seen to be brighter than the FP60R radiograph when the contrasts are set to the same level. This means that, for this particular time bin, the FP60R signal is greater than that in FP15R. This is believed to be a result of the incorrectly-calculated time gate boundaries that caused the time gate in FP60R to actually bin 10 to 635 MeV neutrons. A wider bin has the potential to integrate a larger number of neutrons.

Other differences between FP60R and FP15R radiographs include a vertical shift in Object 2. In FP60R, Object 2 sits higher in the camera's field of view, which increases the amount of scatter into the scintillator and should reduce the quality of the FP60R radiographs. Thus, the results shown here are conservative in that FP60R radiographs would appear of better quality if Object 2 were lowered in the field of view.

Additionally, the FP60R radiographs were rotated 1.9° counter-clockwise to straighten them, and the FP15R radiographs were only rotated 0.3° counter-clockwise. It is thus possible that, if the mirrors were simply not aligned properly and Object 2 was indeed not placed so its base were parallel to the floor, there is more blur introduced in the FP60R radiographs than in the FP15R radiographs.

Finally, the surrounding environment was not the same between the two beam lines. FP15R had much more clutter in the beam line upstream from TiGReSSE. The concrete cave which was seen to be helpful in FP60R was actually a hindrance in FP15R and TiGReSSE had to be placed at a distance from it. The shielding configuration and the location of the camera within the light-tight box was also different between the two beam lines. Thus, results shown in this section also reflect the state of the beam line such as described here, as well as the properties of the beam itself.

With these caveats in mind, averaged vertical line-outs were taken for the two areas always chosen for Object 2: the joint in the top cap, and the central body of the object. The middle ROI for FP15R was not the same size as that for FPP60R

because of magnification differences, and, as a result, the two averaged line-outs did not line up along the x-axis. Thus, FP15R data for the middle ROI was translated to the right so that features line up in the plots. The ROIs, however, did match for the top of Object 2 but they were shifted vertically with respect to the other, since Object 2 was at a greater height above the floor in FP60R. The ROIs for the two sets of results are seen in Figure 9.56, and features of interest within those ROIs are shown in Figure 9.45.

A number of averaged vertical line-out plots were generated of the unnormalized data (Figures 9.57 and 9.58). These plots compare the four time gates used in both FP60R and FP15R, with one comparing line-outs for the top ROI and the other comparing line-outs for the middle ROI, respectively.

Comparing the FP60R line-outs to those for FP15R, the average grayscale pixel value is larger than that of FP15R for the 0.1 to 2.5 MeV, photon, and full spectrum radiographs. This indicates that, for these three time bins, the transmission is perceived as greater for FP15R. This is the result of activation products and scatter being present in FP15R due to poor beam collimation, which artificially increases scintillator brightness.

The exception to this generalization was seen to be the 10 to 600 MeV energy bin, which showed increased transmission for 10 to 600 MeV neutrons in FP60R. This may be accountable to the incorrect time gating that actually binned from 10 to 635 MeV, which would indeed be more transmissible, and thus the 10 to 600 MeV results are most likely unreliable. Overall, the FP15R line-outs have less-defined features than the FP60R line-outs, indicating that the signal-to-noise ratio is higher for FP60R. This is again due to the poor beam collimation, large amount of scatter, and high likelihood of activation products in FP15R that tend to blur features by reducing contrast.

Four plots were then generated, one for each energy bin, that held the energy bin constant to compare the two beam lines in one plot. Each plot shows averaged vertical line-outs for each beam line and for the two ROIs (Figures 9.59 and 9.60).

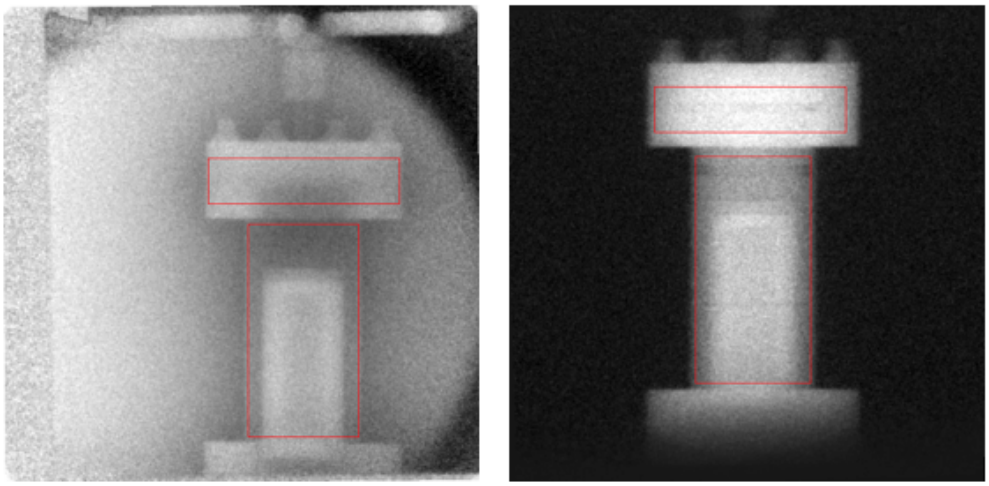


Figure 9.56: Regions of interest shown in red on 2.5 MeV and below neutron radiographs for FP15R (left) and FP60R (right).

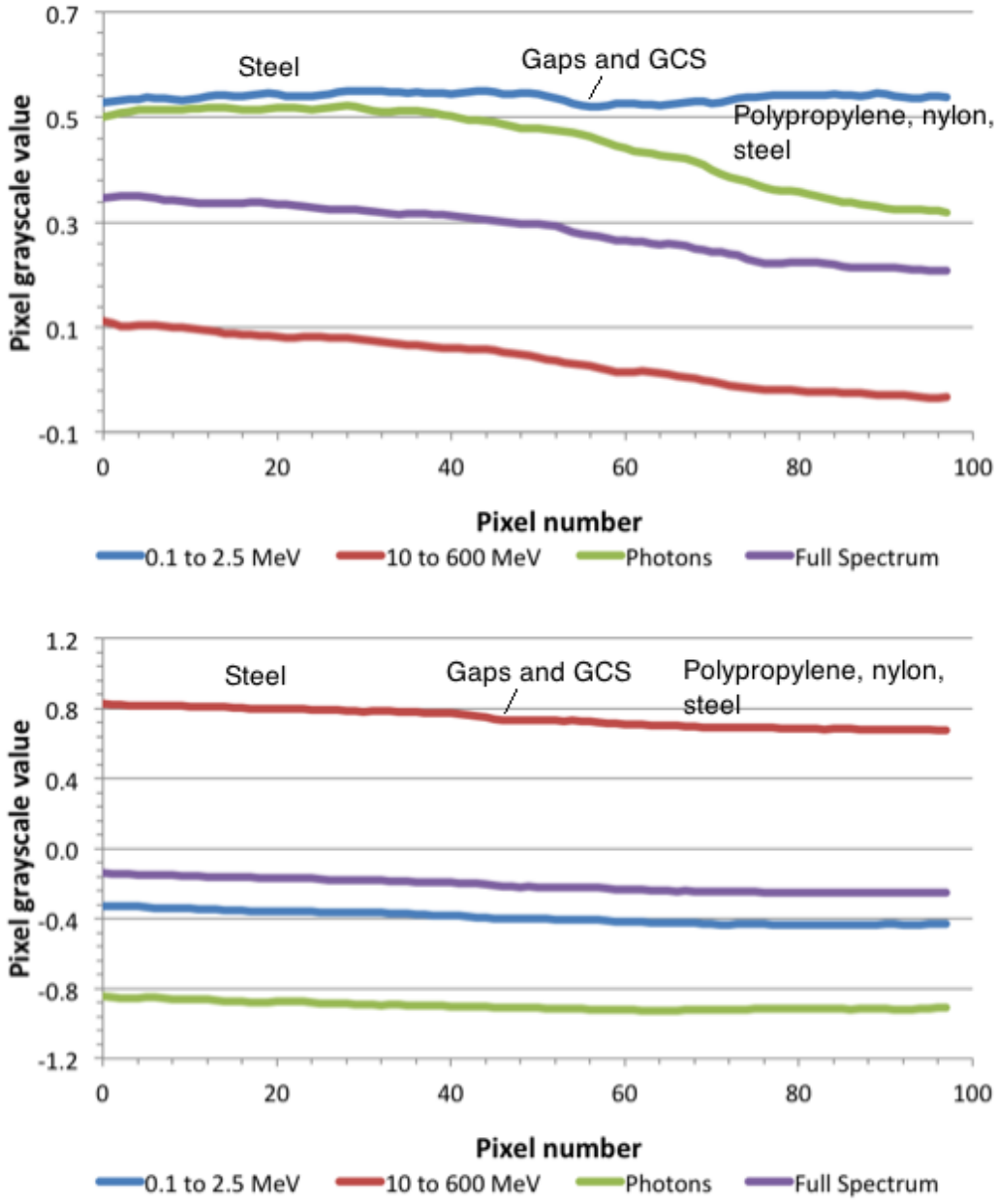


Figure 9.57: Averaged vertical line-outs taken for Object 2's top ROI in FP60R (top) and FP15R (bottom). Results plotted here have not been normalized to the average flatfield intensity. Regions and features are labelled. Only major materials were listed on the line-outs; for a full list, refer to the diagram of Object 2.

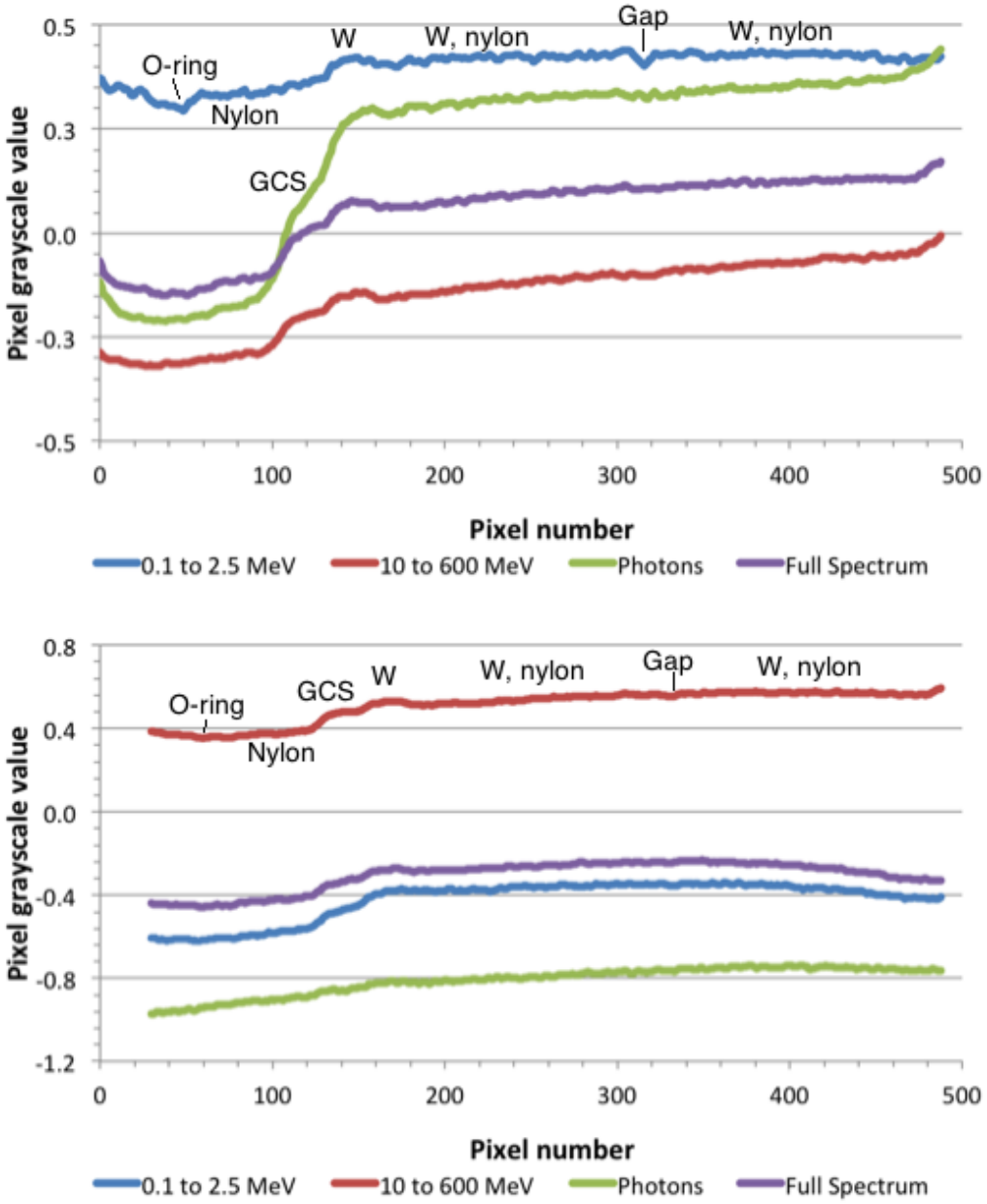


Figure 9.58: Averaged vertical line-outs taken for Object 2's middle ROI in FP60R (top) and FP15R (bottom). Results plotted here have not been normalized to the average flatfield intensity. Note that the FP15R data has been shifted to the right so features line up vertically. Regions and features are labelled, with "GCS" representing gold-coated steel. Only major materials were listed on the line-outs; for a full list, refer to the diagram of Object 2.

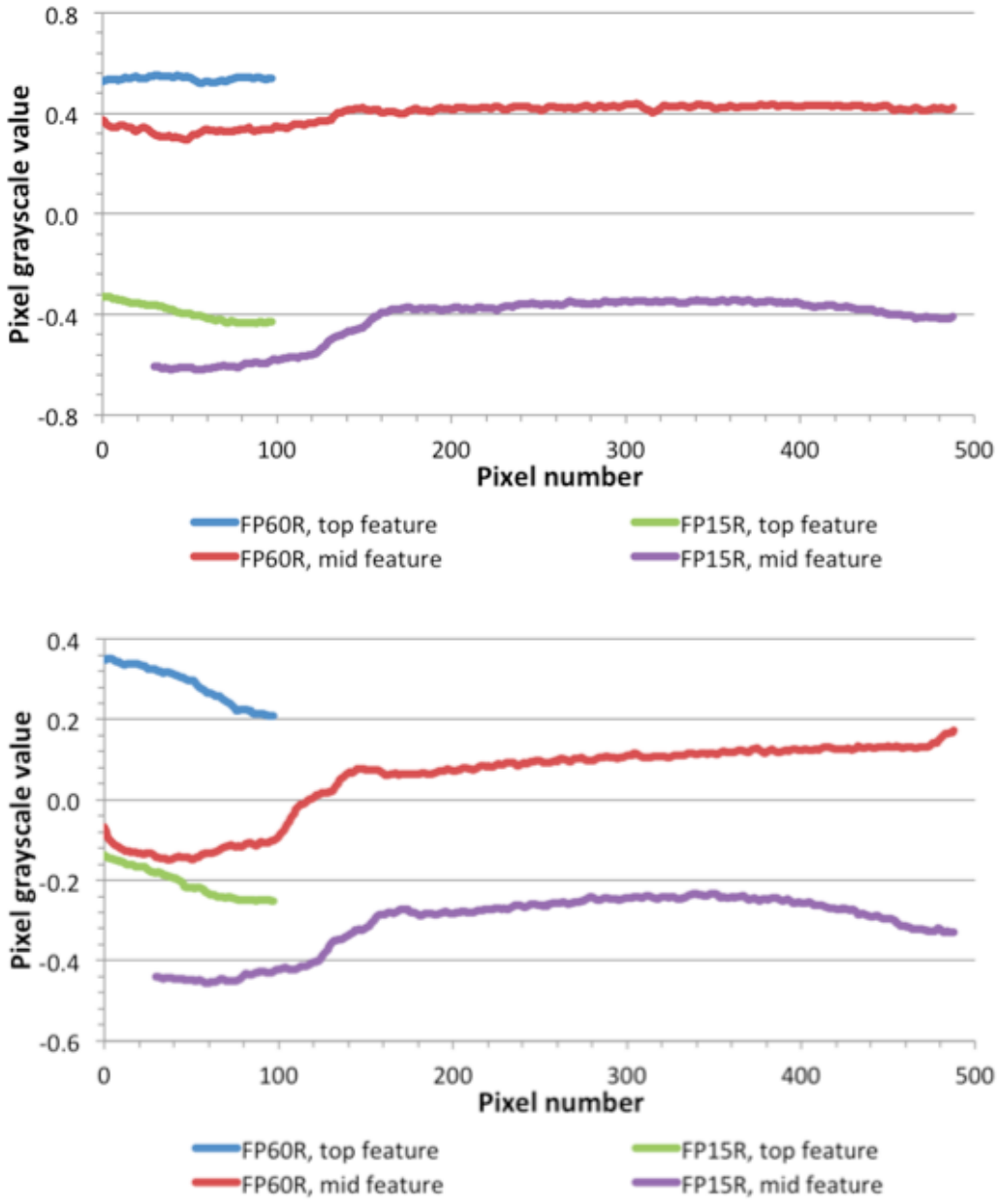


Figure 9.59: Averaged vertical line-outs taken for Object 2's top and middle ROIs for unnormalized radiographs generated in FP60R and FP15R. For FP60R, the top ROI is shown in blue and the middle ROI is shown in red. For FP15R, the top ROI is shown in green and the middle ROI is shown in purple. Top: Radiography data taken with neutrons of energy 2.5 MeV and below. Bottom: Radiography data taken with the full LANSCE spectrum.

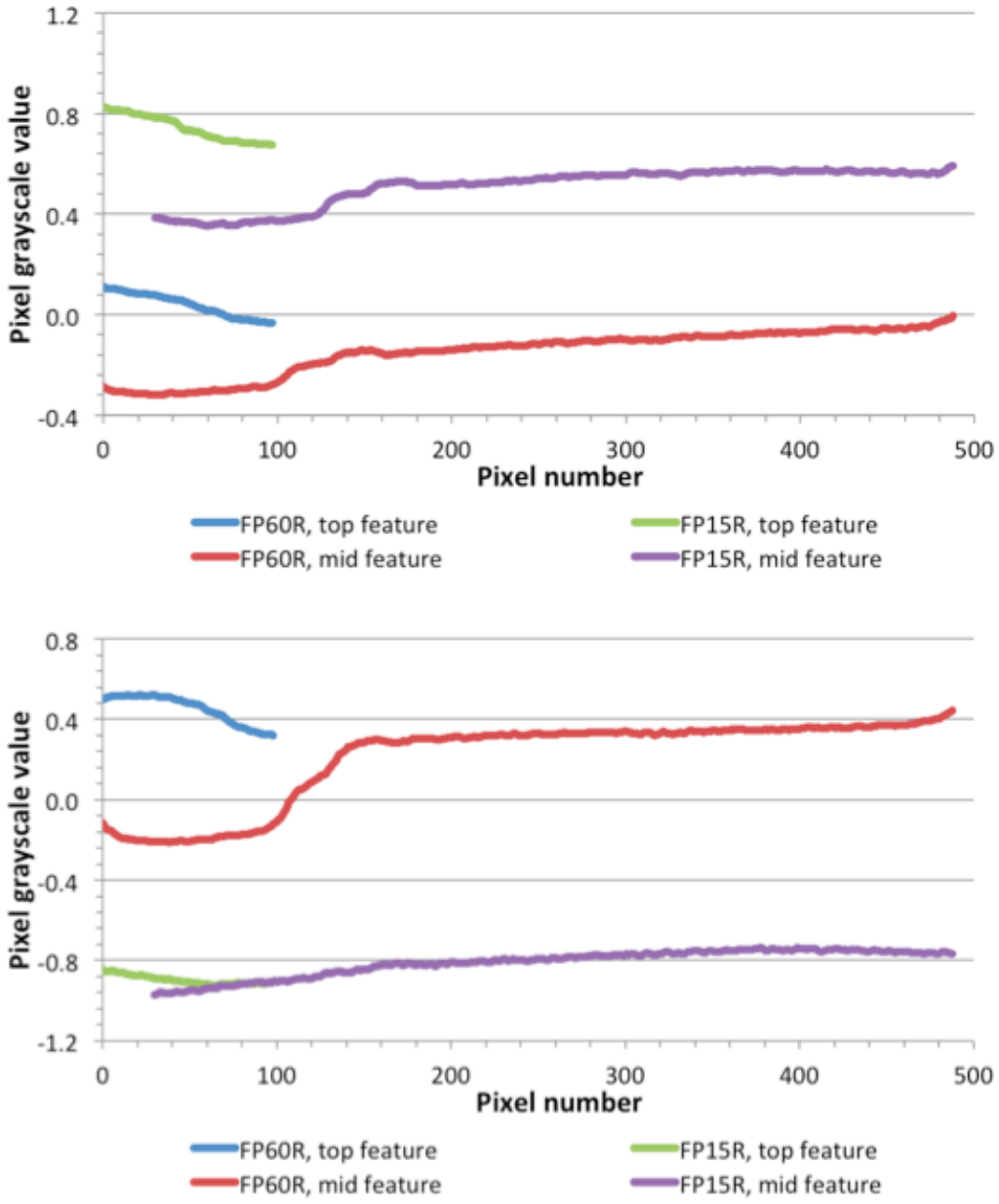


Figure 9.60: Averaged vertical line-outs taken for Object 2's top and middle ROIs for unnormalized radiographs generated in FP60R and FP15R. For FP60R, the top ROI is shown in blue and the middle ROI is shown in red. For FP15R, the top ROI is shown in green and the middle ROI is shown in purple. Top: Radiography data taken with neutrons of energy 10 to 600 MeV. Bottom: Radiography data taken with spallation photons.

The short line-out corresponds with the top ROI, while the long line-out corresponds with the middle ROI. These plots also yield the same conclusions as Figures 9.57 and 9.58: FP60R line-outs have grayscale values that are generally larger and have more defined line-out features than FP15R. Thus, FP60R is a better beam line for radiography because it has reduced scatter that artificially increases transmission while masking interior object features.

In summary of this study, FP15R generally had smaller σt values which indicates this beam line has a larger scatter source and more activation products. These results are not surprising, given the fact that TiGReSSE can resolve the photon and neutron peak in the FP60R time-of-flight scan but not in FP15R.

9.5.4 Long Exposure Radiographs

Radiographs generated with long exposure times were taken to study the improvement in image quality of increased exposure times (irrespective of dose deposited to the radiography object), as described in Section 9.4.4. The 8 to 12 MeV radiograph and its corresponding flatfield image were normalized to the 12 to 16 MeV flatbed $\bar{I}$ and thus only used 1268 frames, whereas the 12 to 16 MeV radiograph and its flatfield image used all 1800 frames (Figures 9.61 and 9.62, respectively). During post-processing, radiographs were rotated 1.2° counter-clockwise to straighten the objects and reduce blur in the line-outs.

Averaged line-outs were taken in ROIs within the three objects to evaluate whether TiGReSSE could detect their features. The five ROIs are shown in Figure 9.63, and the features of interest within these ROIs are labelled in Figure 9.64. The single ROI in the penetrameter object was read-out two different ways, which generated one averaged horizontal line-out (i.e., averaging columns of pixels) and one averaged vertical line-out (i.e., averaging rows of pixels) because features of interest exist in both directions. These two line-outs are shown in Figure 9.65.

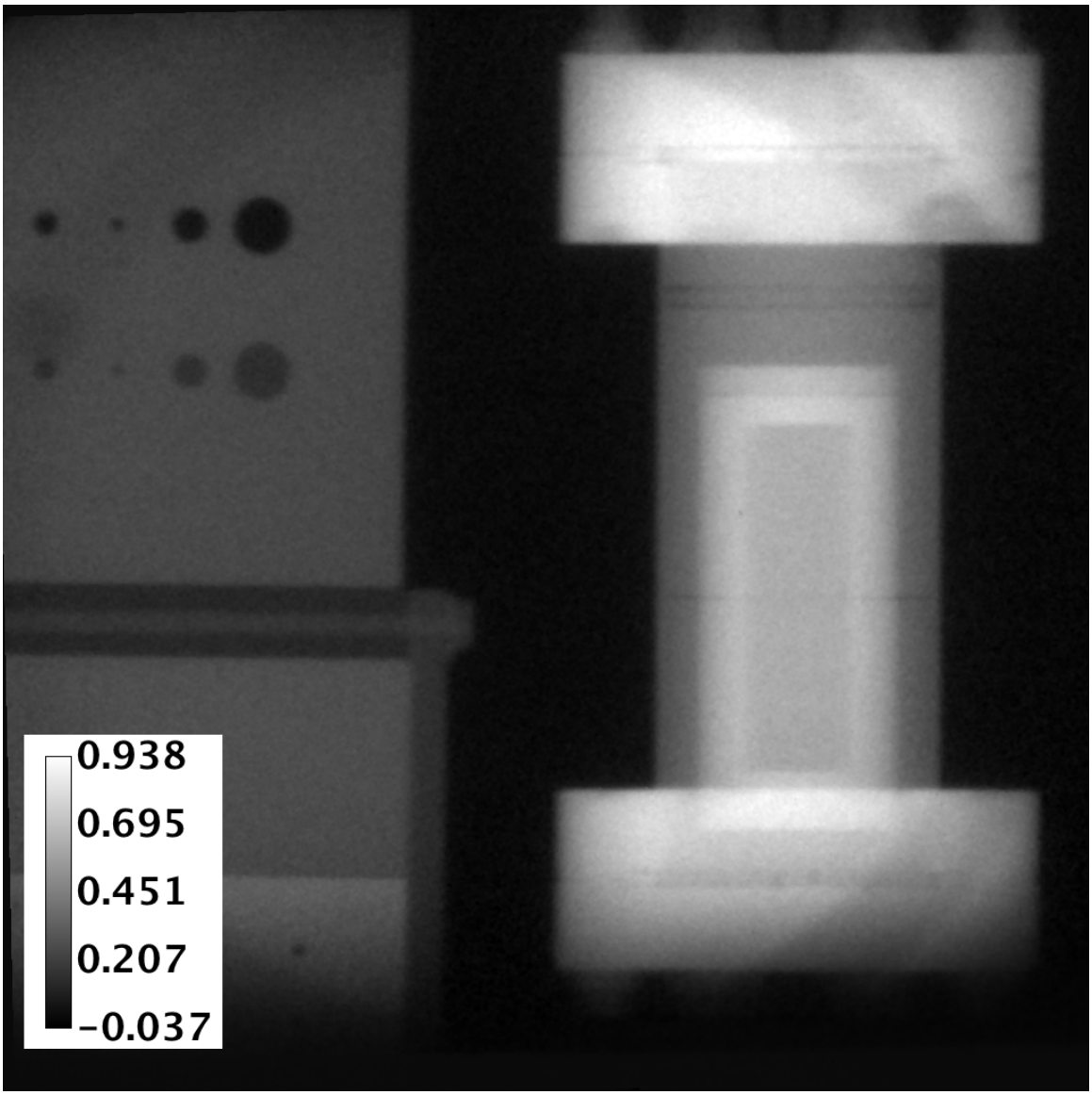


Figure 9.61: Long exposure radiograph of Object 2 (right), the penetrameter object (top left), and the crack test object (bottom left). This FP60R radiograph was generated with 8 to 12 MeV neutrons and with 1268 frames.

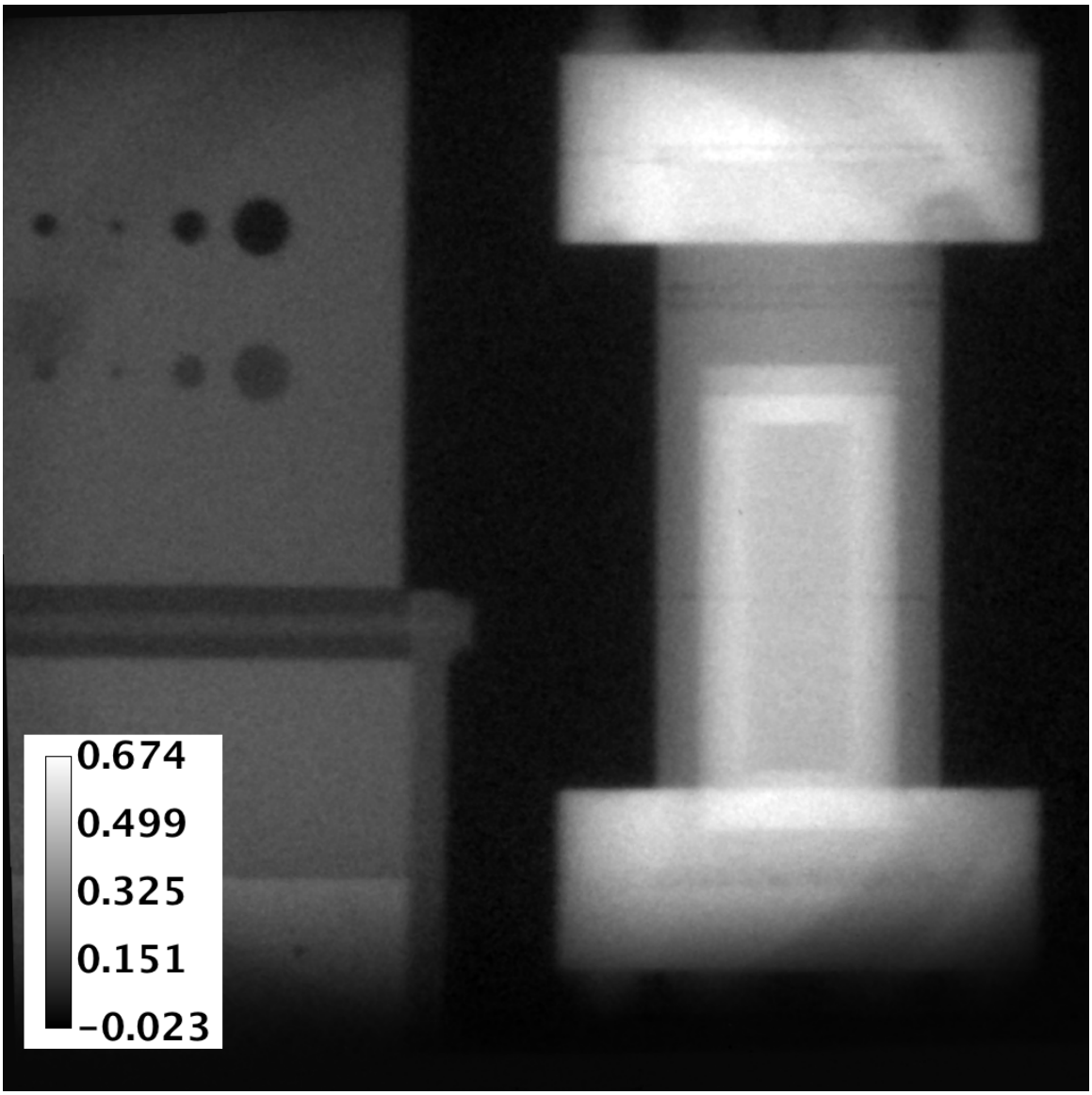


Figure 9.62: Long exposure radiograph of Object 2 (right), the penetrameter object (top left), and the crack test object (bottom left). This FP60R radiograph was generated with 12 to 16 MeV neutrons and with 1800 frames.

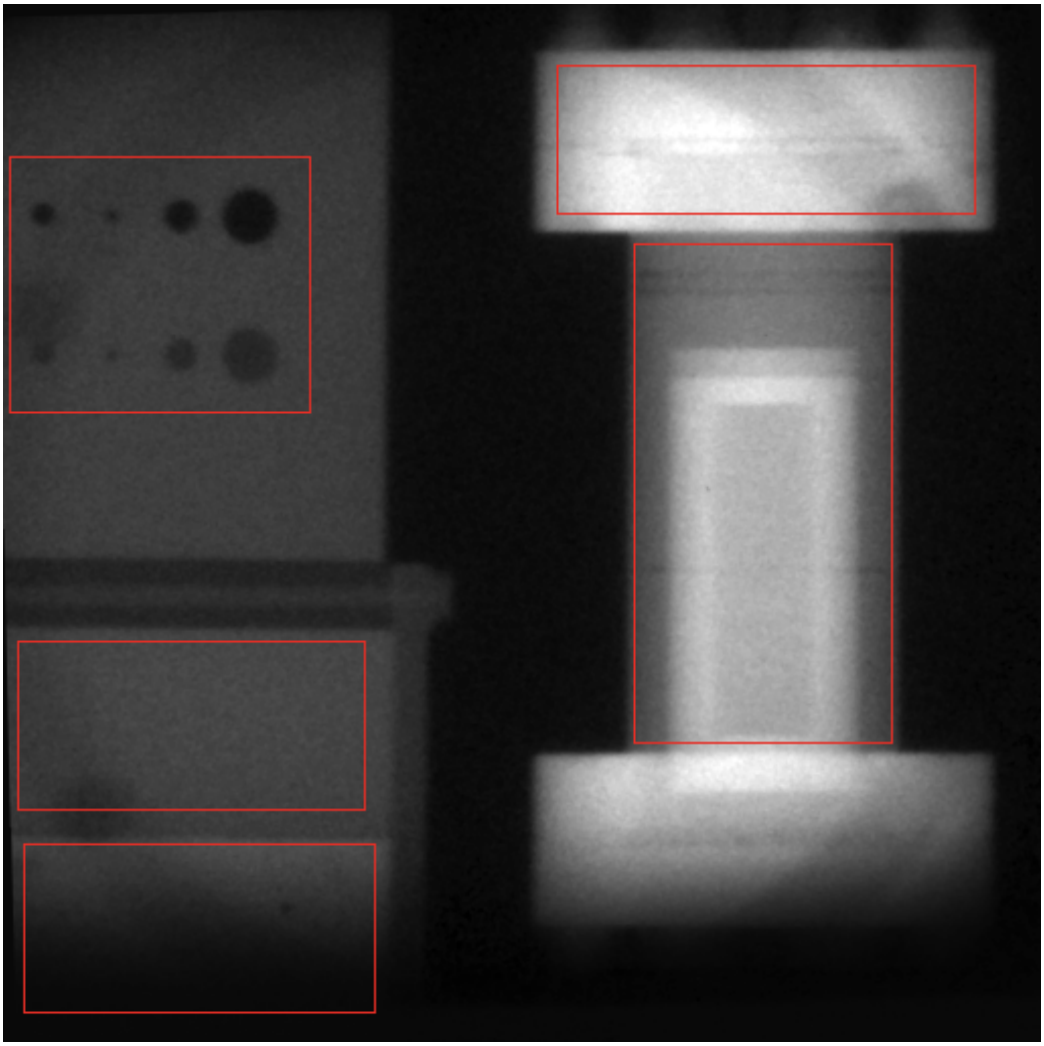


Figure 9.63: The five ROIs used to generate averaged line-outs of the 8 to 12 MeV and 12 to 16 MeV long exposure neutron radiographs of Object 2 (right), the penetrameter object (top left), and the crack test object (bottom left).

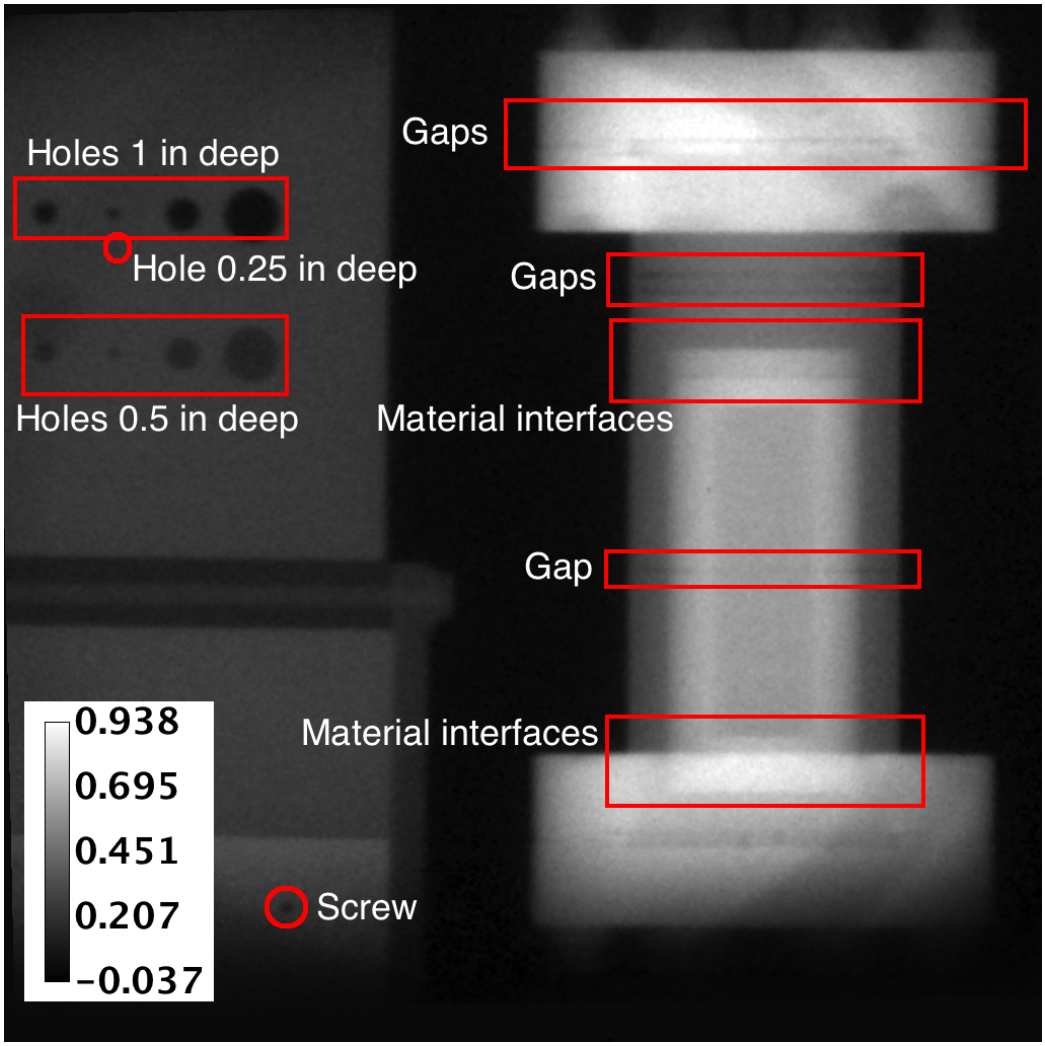


Figure 9.64: The features of interest in the long exposure radiographs, which are contained within the five selected ROIs, depicted on the 8 to 12 MeV normalized neutron radiograph.

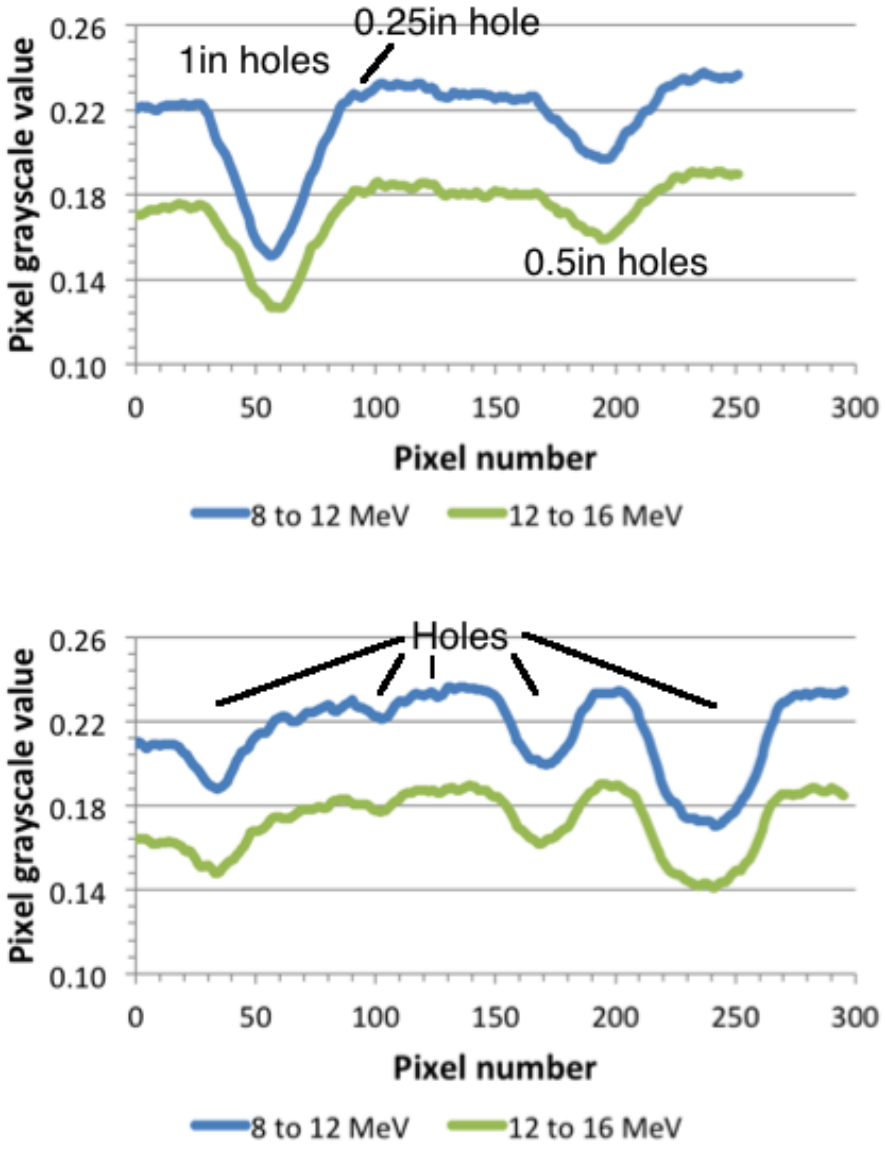


Figure 9.65: Averaged line-outs for the long exposure radiographs of the penetrameter object, with features of interest labelled with the hole depth indicated. Top: Averaged vertical line-out of the ROI in the penetrameter object for radiographs generated with 8 to 12 MeV and 12 to 16 MeV. Bottom: Averaged horizontal line-out of the ROI in the penetrameter object for radiographs generated with 8 to 12 MeV and 12 to 16 MeV.

These plots indicate that the contrast remains relatively constant whether the data averages row or column data. This is expected since line-outs are for the same material. A more interesting result is that the contrast of the hole features is dependent on the depth of the hole, as expected; the shallower holes have a shallower dip in the contrast level because they are more attenuating.

The smallest, shallowest hole that is discernible in the line-outs indicates the spatial and contrast resolution of the system. From the averaged vertical line-outs, the smallest visible hole has a 6 mm diameter and a depth of 0.25 in in a polyethylene block 1 in thick. This is thus the limiting contrast and spatial resolution at the object plane, which is a distance of 0.5 m from the scintillator. The 6 mm hole with a depth of 0.125 in is not resolvable in either the averaged vertical line-out or the radiograph.

The next object to be analyzed was the crack test object. Two ROIs were selected to take averaged line-outs, with one ROI in each of the two material regions of the object. Averaged vertical and horizontal line-outs were taken in the polyethylene and steel regions, respectively (Figure 9.66).

Drawing conclusions from these plots, it is evident that neither the cracks nor the holes are visible. This is because the penetrameter is 0.5 m away from the scintillator, and the blur is too great to see the cracks in the polyethylene. The penetrameter holes in the steel region (see Figure 9.20) are unfortunately out of the camera's field of view. Additionally, the one hole in the bottom right of the object (the result of a screw that holds the object together) is visible by eye, but not in the averaged horizontal line-out because its contrast value is reduced in the averaged line-out process. Thus, the crack test object would need to be radiographed much closer to the scintillator plane and in the center of the field of view to generate useful radiographs.

The final radiography object to analyze was Object 2. This object is especially interesting because it can be compared to previously-generated short exposures. The short exposures described in Section 9.5.1 were of Object 2 at a distance of 78.7 cm from the scintillator, whereas the long exposure radiographs were of Object 2 at an object-to-detector distance of 50 cm. Due to the differences in object placement, the

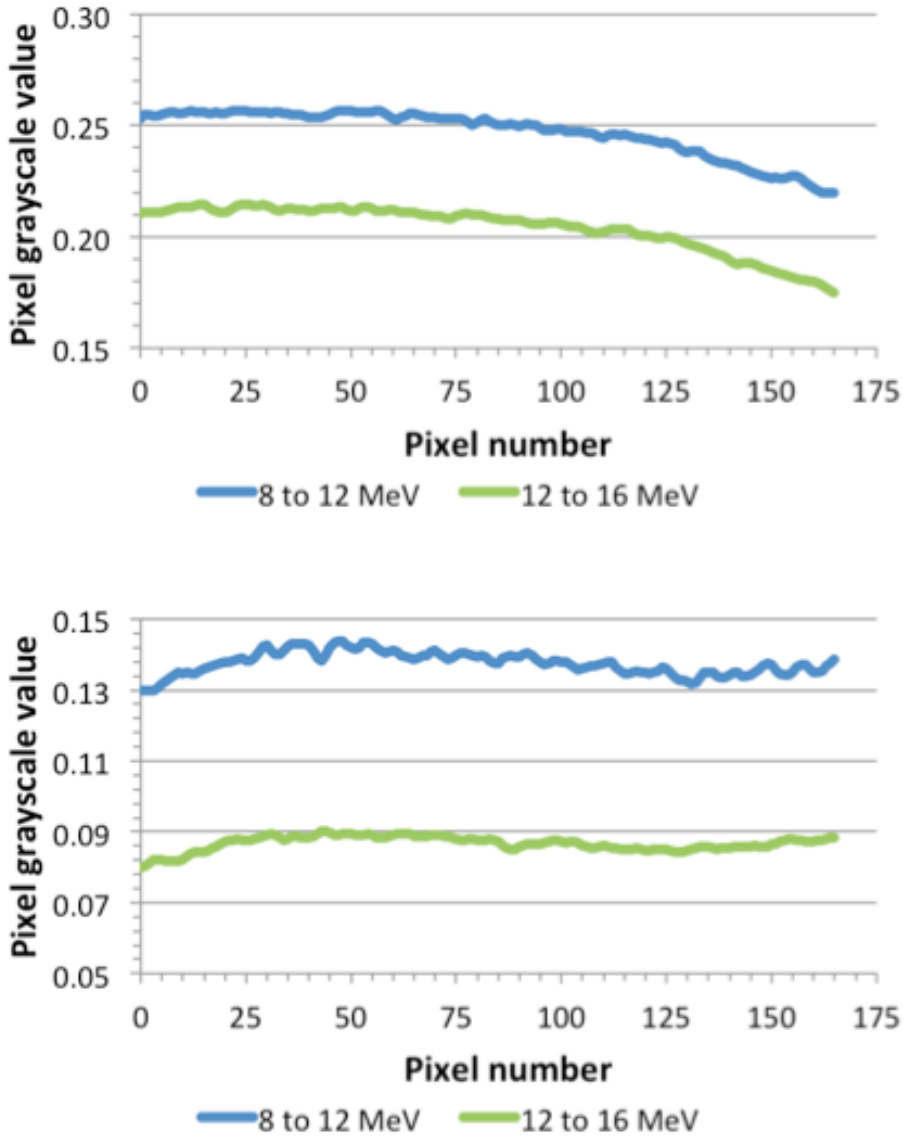


Figure 9.66: Averaged line-outs of the crack test object for the long exposure radiographs. No features of interest are seen in these line-outs. Top: Averaged vertical line-out of the ROI in the polyethylene region of the crack test object for radiographs generated with 8 to 12 MeV and 12 to 16 MeV neutrons. Bottom: Averaged horizontal line-out of the ROI in the steel region of the crack test object for radiographs generated with 8 to 12 MeV and 12 to 16 MeV neutrons.

optimal source radiographs cannot be used for an image quality comparison. However, a short exposure image can be generated from the long exposure image simply by combining fewer frames. It was assumed that 100 total frames were generated for a short exposure image, like was done in Section 9.5.1, and the radiograph and flatfield frames were normalized according to the flatfield brightness. Thus, out of the 1800 long exposure frames, the short exposure radiograph was generated with 70 frames for 8 to 12 MeV neutrons and 100 frames for 12 to 16 MeV neutrons. The short and long exposure radiographs are placed side-by-side in Figures 9.67 and 9.68.

Visually inspecting Figures 9.67 and 9.68 reveals that features are much clearer in Object 2 with the longer exposure radiograph and flatfield images. Material boundary changes are more readily identified because noise is greatly reduced. The differences between tungsten and nylon-filled hollow tungsten are also visible as different contrast levels in the long exposure radiograph. As expected, the section of the line-out is highest (most attenuating) where the largest amount of tungsten is found. Thus, differences in thickness for a given material are discernible with TiGReSSE, and future studies should determine what level of variation is detectable.

Two ROIs were selected in the top and middle sections of the object to remain consistent with other analyses within this chapter (Figure 9.63). Each ROI generated one averaged vertical line-out (Figure 9.69). Comparison of the line-out plots shows that the overall grayscale values are lower for the long exposure than the short exposure for 8 to 12 MeV neutrons. This is because lower grayscale values indicate a brighter image, which results from integrating more signal. As expected, the 12 to 16 MeV neutron radiograph line-outs are smaller in value than the 8 to 12 MeV neutron radiographs; this is due to increased transmission through Object 2 with increased source energy.

Interestingly, the exposure time did not affect the contrast level for the 12 to 16 MeV energy bin. Perhaps there is enough transmission in this energy bin that increasing exposure time and therefore increasing statistics does not have the same effect as in the lower 8 to 12 MeV energy bin. However, noise was still greatly

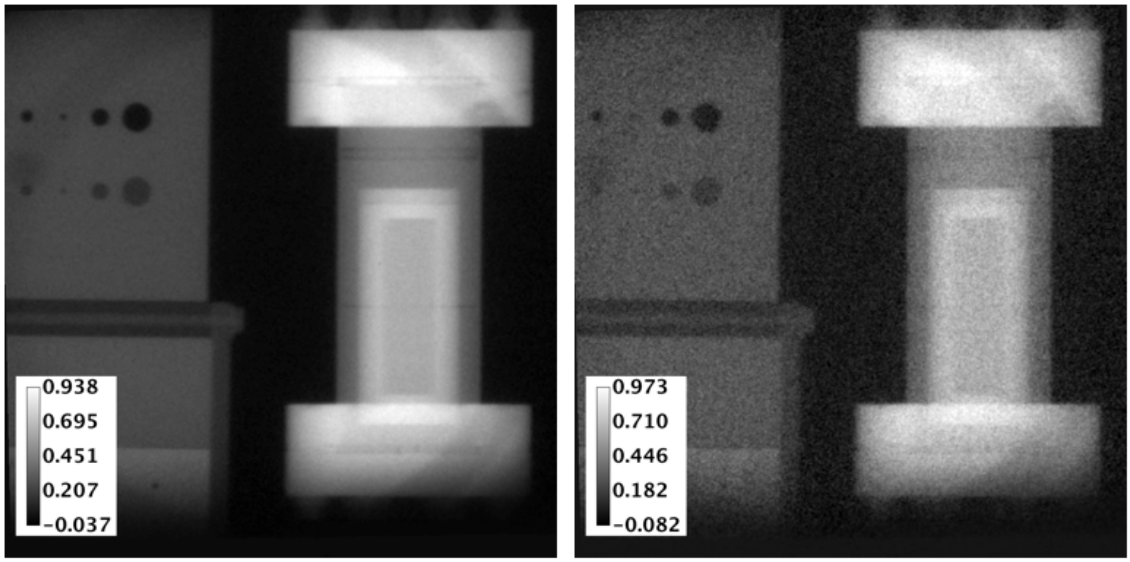


Figure 9.67: Long exposure (1268 frames) radiograph of Object 2 (left) compared to the short exposure (70 frames) radiograph (right). Both radiographs were taken in FP60R and used 8 to 12 MeV neutrons.

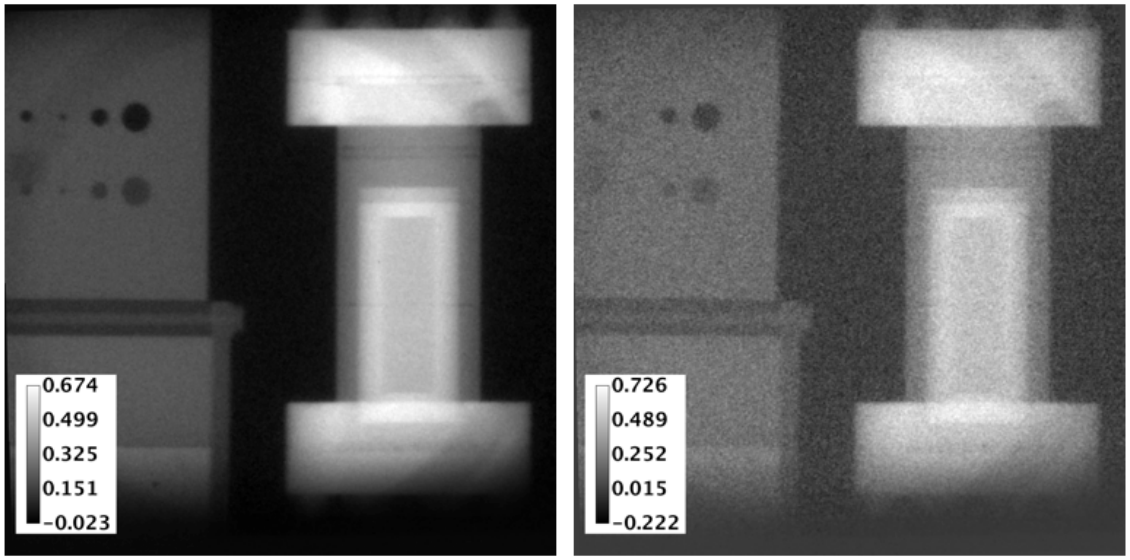


Figure 9.68: Long exposure (1800 frames) radiograph of Object 2 (left) compared to the short exposure (100 frames) radiograph (right). Both radiographs were taken in FP60R and used 12 to 16 MeV neutrons.

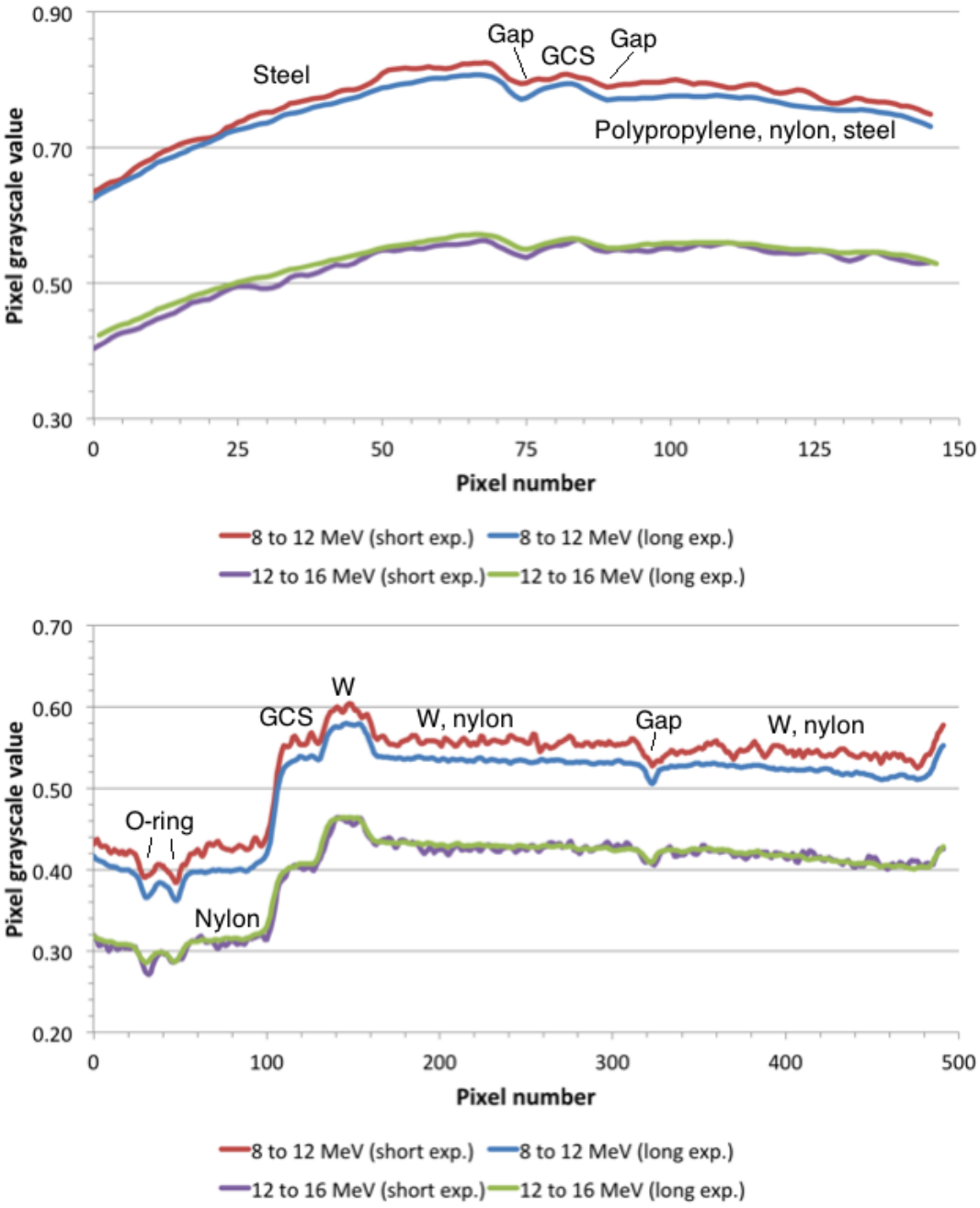


Figure 9.69: Averaged line-outs for the long exposure ("long exp.") and short exposure ("short exp.") radiographs of Object 2. Regions and features are labelled, with "GCS" representing gold-coated steel. Only major materials were listed on the line-outs; for a full list, refer to the diagram of Object 2. Top: Averaged vertical line-out of the ROI in the top of Object 2 for radiographs generated with 8 to 12 MeV and 12 to 16 MeV neutrons. Bottom: Averaged vertical line-out of the ROI in the middle of Object 2 for radiographs generated with 8 to 12 MeV and 12 to 16 MeV neutrons.

reduced with the long exposure. Therefore, increased exposure time does improve image quality. In the future, studies on dose need to be completed to determine the maximum exposure time that can be safely used while remaining below the dose-to-object safety threshold.

9.5.5 Depleted Uranium Radiographs

Effect of Increased Flatfield Exposure Times

The radiographs of the DU and crack test object were first analyzed as unnormalized images in order to study the effect of long versus short exposure flatfield images on image quality. It was thought that perhaps the flatfield image could be taken for a longer exposure time than the radiograph in order to improve image statistics while greatly reducing the dose to the radiography object. The flatfield image is taken of just the beam, and while dose would still be deposited on the TiGReSSE equipment, the dose to the object would be minimized. This would be particularly useful for dose-sensitive objects.

The data for this study was processed by combining each set of 200 frames using a median filter, and then summing the three sets together to yield a total of 600 frames. Results for this part of the study were not normalized to the flatfield average intensity. The number of flatfield frames were either from a long exposure (1800 frames) or a short exposure (100 frames, multiplied by six to approximately equal the scale of the 600 frame DU radiographs). In the case of the 50 to 70 MeV radiograph, there was no long exposure flatfield since they were only generated for the 8 to 12 and 12 to 16 MeV time gates. Thus, this comparison could only be conducted with two of the three energy bins used to image the DU plates and the crack test object.

Results, as expected, varied depending on the number of flatfield frames that were used in image post-processing. Qualitatively, the image quality improved if the final image was generated with a long exposure flatfield instead of a short exposure flatfield, even if the number of radiograph frames remained constant (i.e., 600 frames).

Figures 9.70 and 9.71 show the 8 to 12 MeV and 12 to 16 MeV radiographs, respectively, that were post-processed with either the long or short exposure flatfield images.

For ease of interpretation by the reader, Figure 9.72 labels features of interest on the 8 to 12 MeV radiograph processed with the long-exposure flatfield. It should be noted that there appears to be a crack in the upper-right section of the DU plates. Examining the flatfield radiograph, however, reveals that this crack is within the encasing of the fission chamber that is attached to the beam pipe. This feature is very obvious with 8 to 12 MeV and 12 to 16 MeV neutron radiographs. Overall, it is interesting that TiGReSSE was able to image a feature in the fission chamber from a great distance and from behind 3 in of DU.

The improvement in image quality was next quantitatively determined by taking averaged vertical and horizontal line-outs in the ROI indicated in Figure 9.73. The averaged line-outs were taken after rotating the radiographs 1.5° counter-clockwise. This region was selected to cover the hole in the three DU plates, seen at the top center of the radiographs, as well as the material boundaries within the crack test object and the steel-DU boundary at the bottom of the radiograph where the DU plates meet the support stand. The features from the fission chamber were ignored by the ROIs. The averaged vertical and horizontal line-outs for both short and long exposure flatfields can be seen in Figures 9.74 and 9.75, respectively.

The averaged vertical line-outs show that the crack test object's frame is visible, as is the crack test object's internal material regions. However, like in Section 9.5.4, its holes and cracks are not visible at this distance from the scintillator. Additionally, the DU attenuation is seen to increase as one moves from pixel 0 to ∼300 in the averaged vertical line-out. This is because, near the top of the radiograph, the DU is less thick on either side of the semi-circular DU plate (1 in versus 3 in) and these lower contrast values reduce the average line-out value. Thus, variations in thickness for a given material are again visible with TiGReSSE.

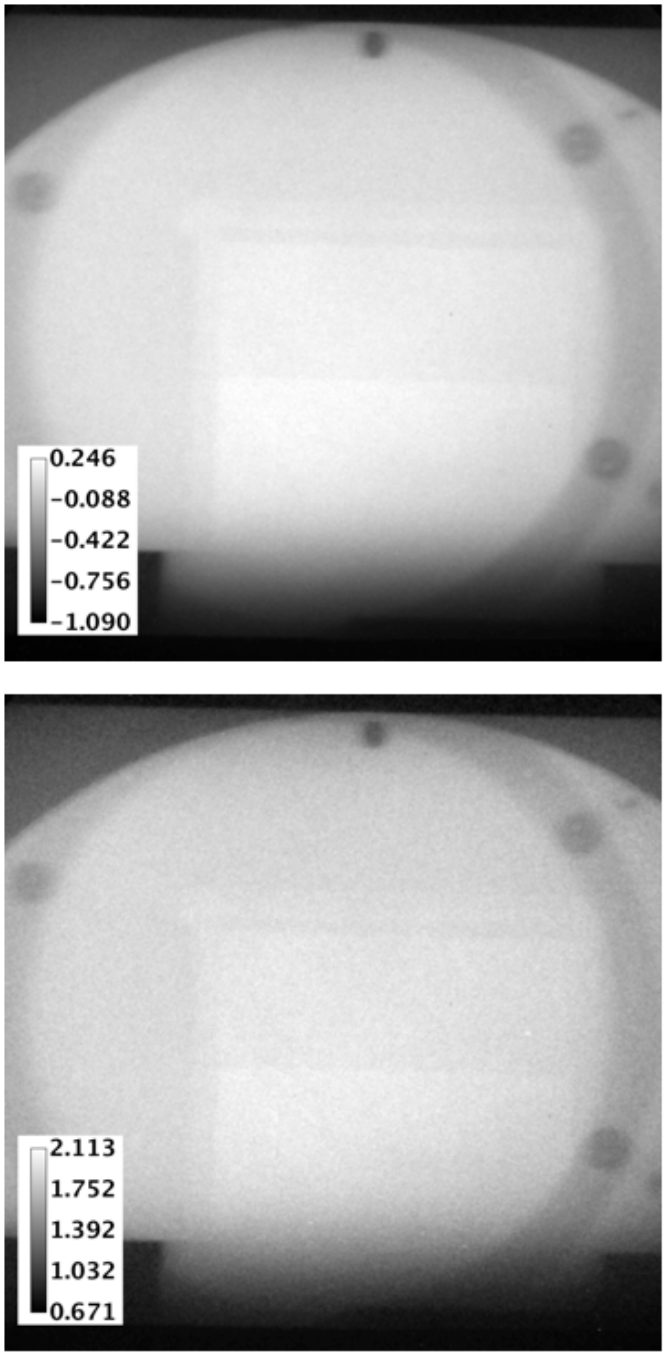


Figure 9.70: Radiographs of the crack test object through 3 *in* of DU and using the 8 to 12 MeV time gate. Top: Long-exposure flatfield used for normalization. Bottom: Short-exposure flatfield used for normalization. Note that the image quality is worse than the top radiograph.

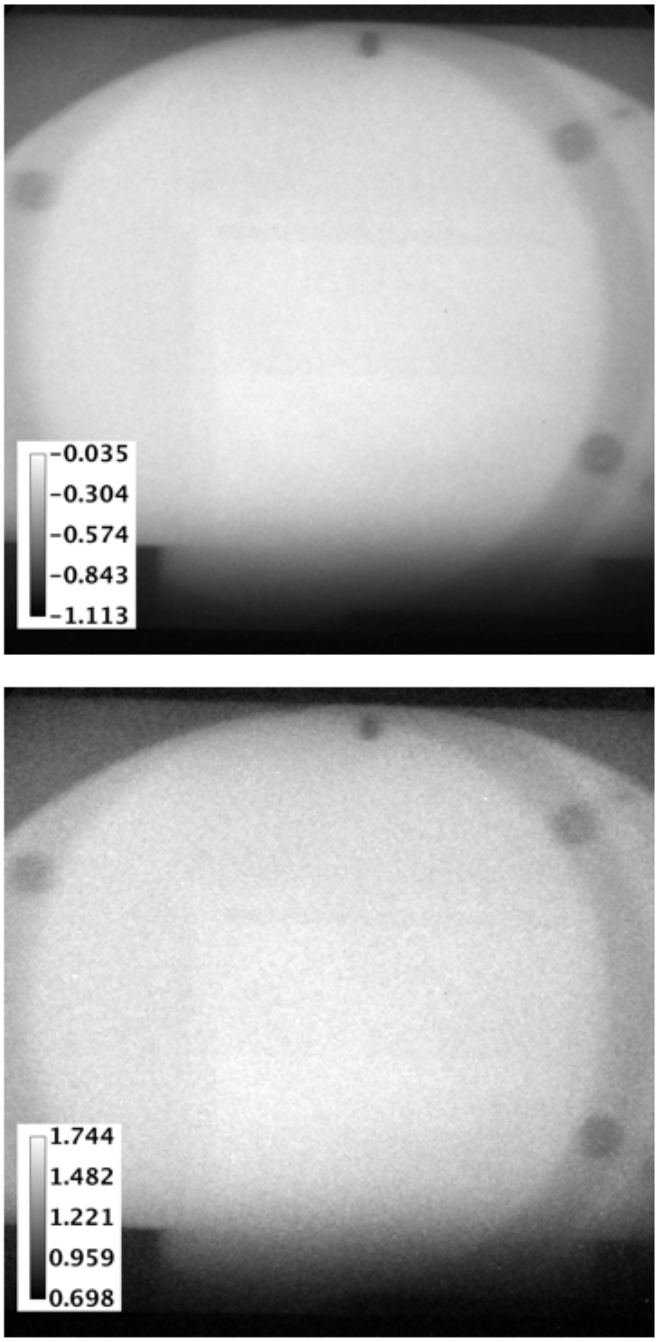


Figure 9.71: Radiographs of the crack test object through 3 *in* of DU and using the 12 to 16 MeV time gate. Top: Long-exposure flatfield used for normalization. Bottom: Short-exposure flatfield used for normalization. Note that the image quality is worse than the top radiograph.

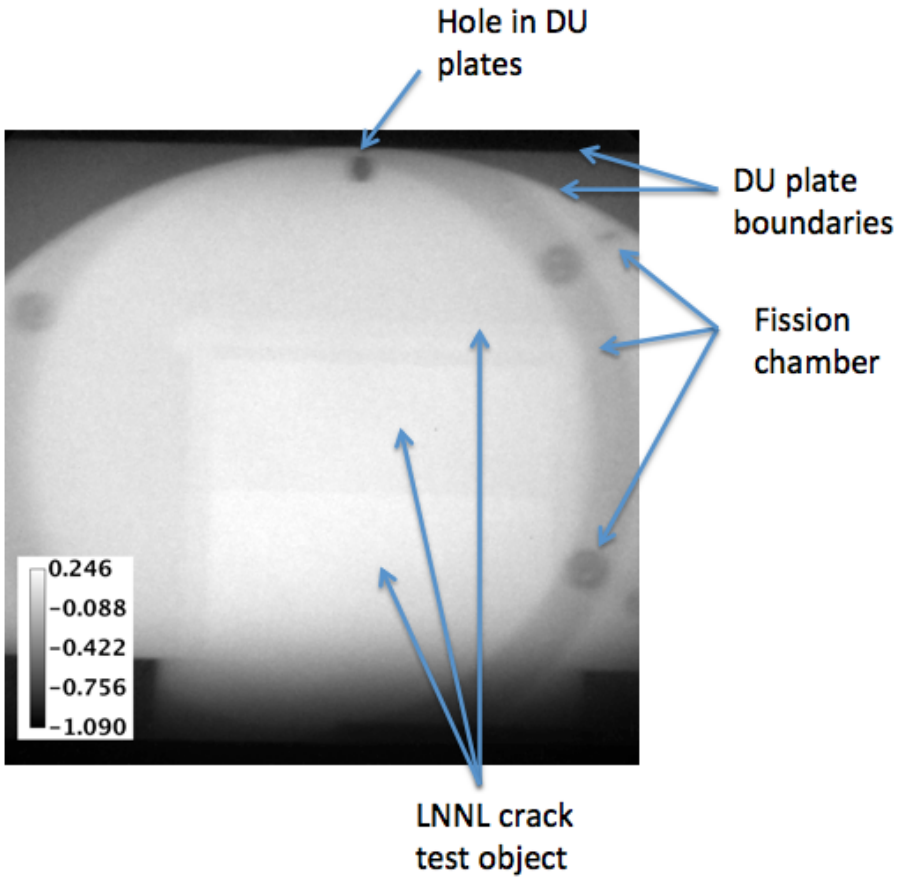


Figure 9.72: Features of interest in the 8 to 12 MeV radiograph processed with the long exposure flatfield. The fission chamber attached to the beam pipe can be seen as a circular object with three holes in it. The crack test object appears as three objects in this radiograph, and the boundaries of the DU plates are also visible.

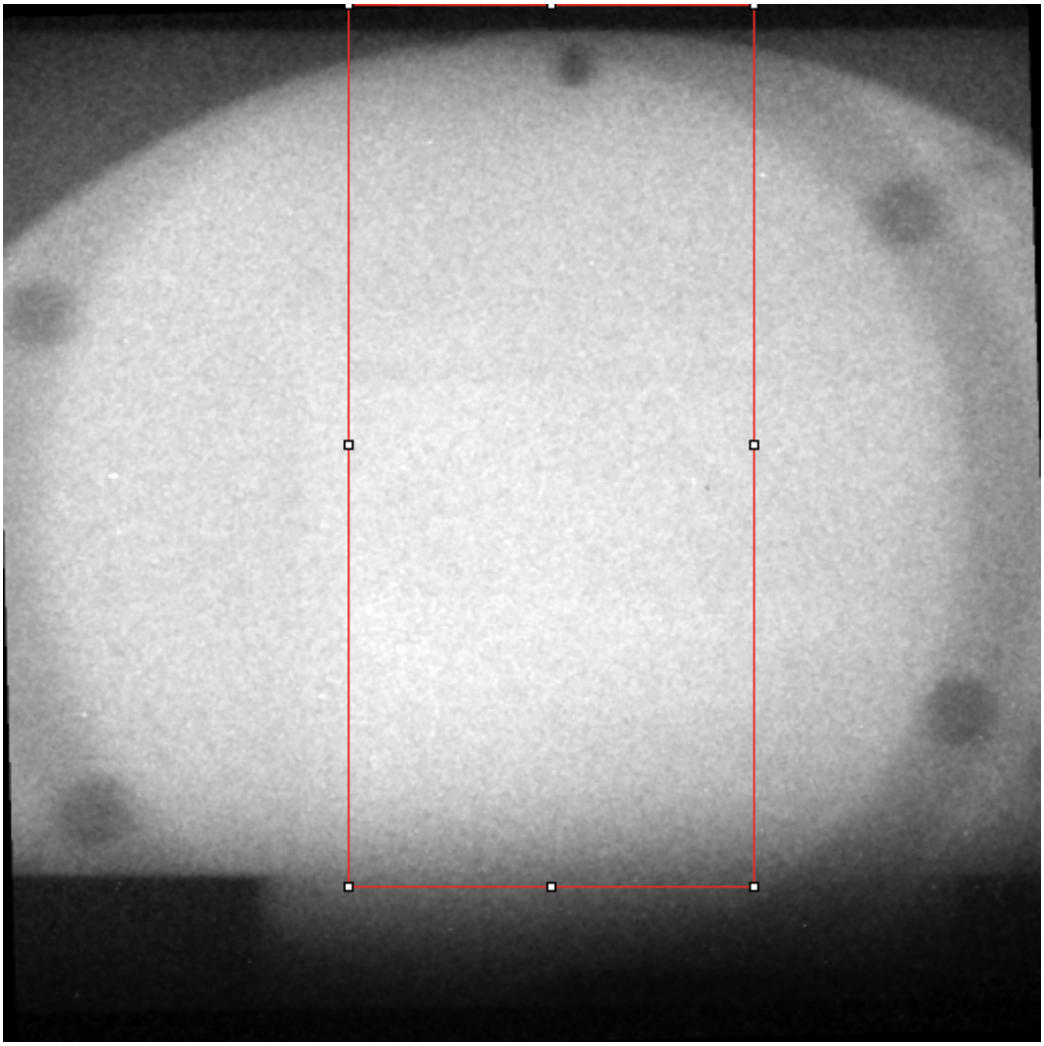


Figure 9.73: The ROI selected on the DU radiographs, after rotating the images 1.5° counter-clockwise, to generate averaged vertical and horizontal line-outs.

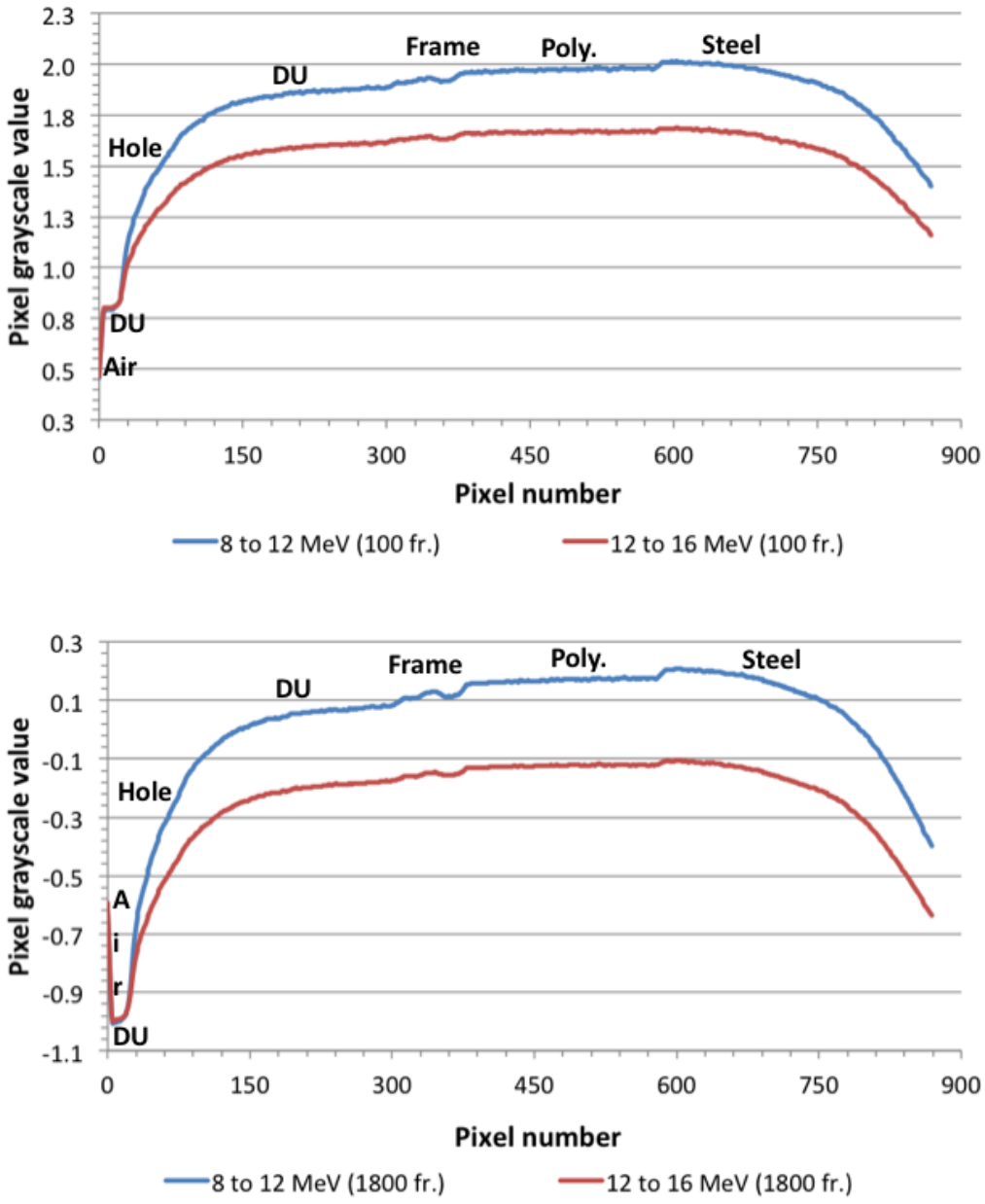


Figure 9.74: Unnormalized averaged vertical line-outs for the neutron radiographs of the DU plates and crack test object (labelled as "frame", "poly." (polyethylene), and "steel"). Features of interest in the radiograph are labelled on the plots. Top: Generated with the 600 frame ("fr.") flatfield image and 600 frame radiograph. Bottom: Generated with the 1800 frame flatfield and 600 frame radiograph.

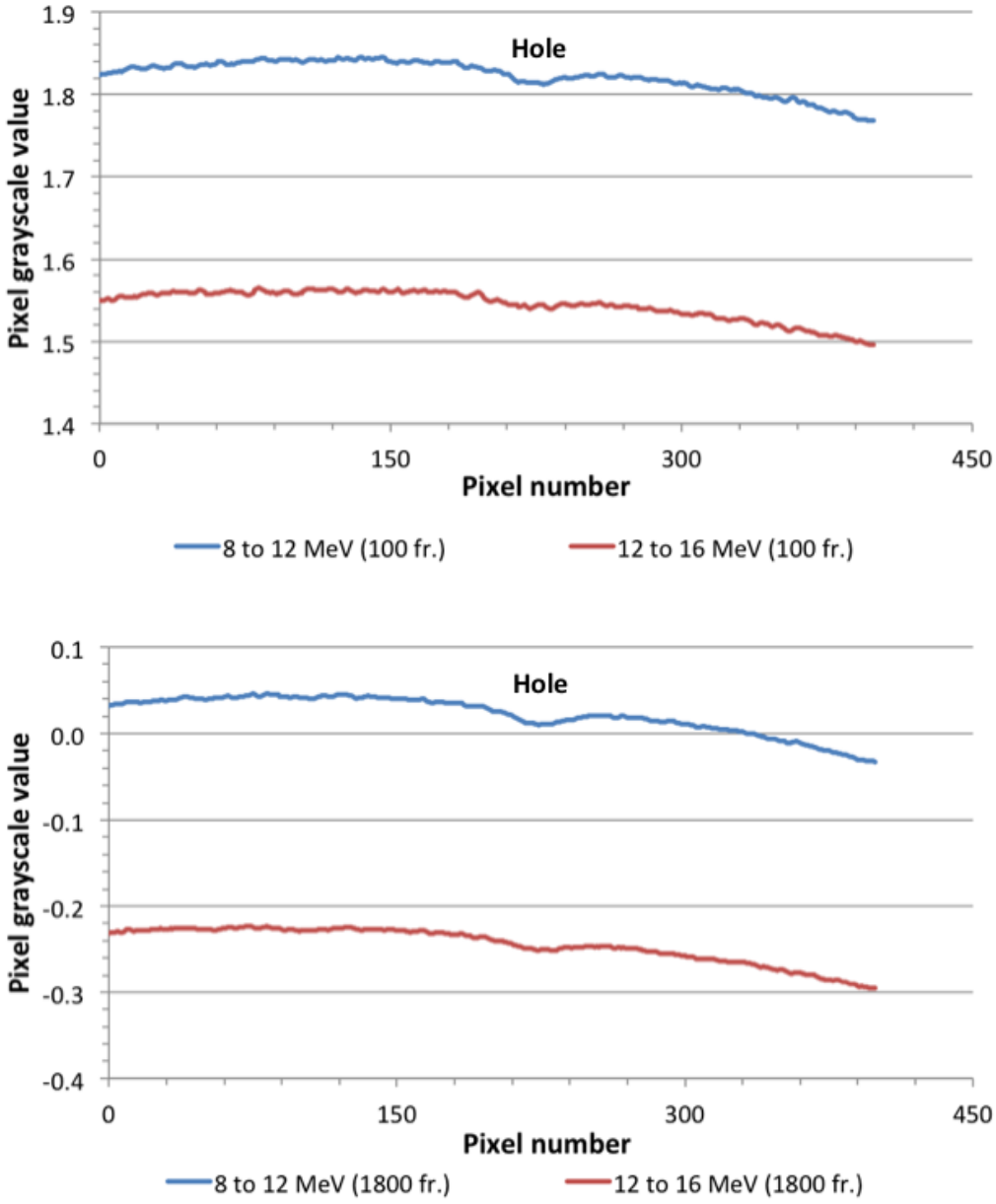


Figure 9.75: Unnormalized averaged horizontal line-outs for the neutron radiographs of the DU plates and crack test object (labelled as "frame", "poly." (polyethylene), and "steel"). Features of interest in the radiograph are labelled on the plots. Top: Generated with the 600 frame ("fr.") flatfield image and 600 frame radiograph. Bottom: Generated with the 1800 frame flatfield and 600 frame radiograph.

As for the averaged horizontal line-out, the three aligned holes in the DU plates are the only feature visible. It is much more obvious in this line-out than the averaged vertical line-out because the contrast of the hole gets averaged out in the vertical line-out due to the plate shapes and visible fission chamber.

As expected, the attenuation of the neutrons decreased as the incident neutron energy increased. The 8 to 12 MeV radiograph, with the largest, most positive pixel grayscale value, was the most attenuated, followed by the 12 to 16 MeV radiograph. However, even though increasing the energy increases transmission, the contrast range decreases with energy. This is seen in both the radiographs and line-outs, where features are less visible in the 12 to 16 MeV energy range even with the increased transmission.

Optimal Energy for High-Z DU

Having established that increasing the flatfield exposure time improves image quality, even if the number of radiograph frames remains constant, a second analysis of the DU radiographs was conducted to compare normalized data for all three energy bins: 8 to 12 MeV, 12 to 16 MeV, and 50 to 70 MeV neutrons. This second part of the study was conducted to determine the optimal energy for a thick, high-Z object and to see if it differed than the optimal energy for Object 2. Object 2 is less challenging to radiograph, and perhaps objects like the DU plates would benefit from higher neutron energies.

The images were normalized using the average flatfield intensity of the short exposure flatfield images (remember that no long exposure flatfield exists for the 50 to 70 MeV energy bin). Thus, respectively, the 8 to 12 MeV radiograph and flatfield used 415 and 69 frames; the 12 to 16 MeV radiograph and flatfield used 600 and 100 frames; and the 50 to 70 MeV radiograph and flatfield used 514 and 86 frames.

The normalized radiographs can be seen in Figure 9.76. It seems that the 8 to 12 MeV radiograph has the best contrast resolution, with contrast resolution

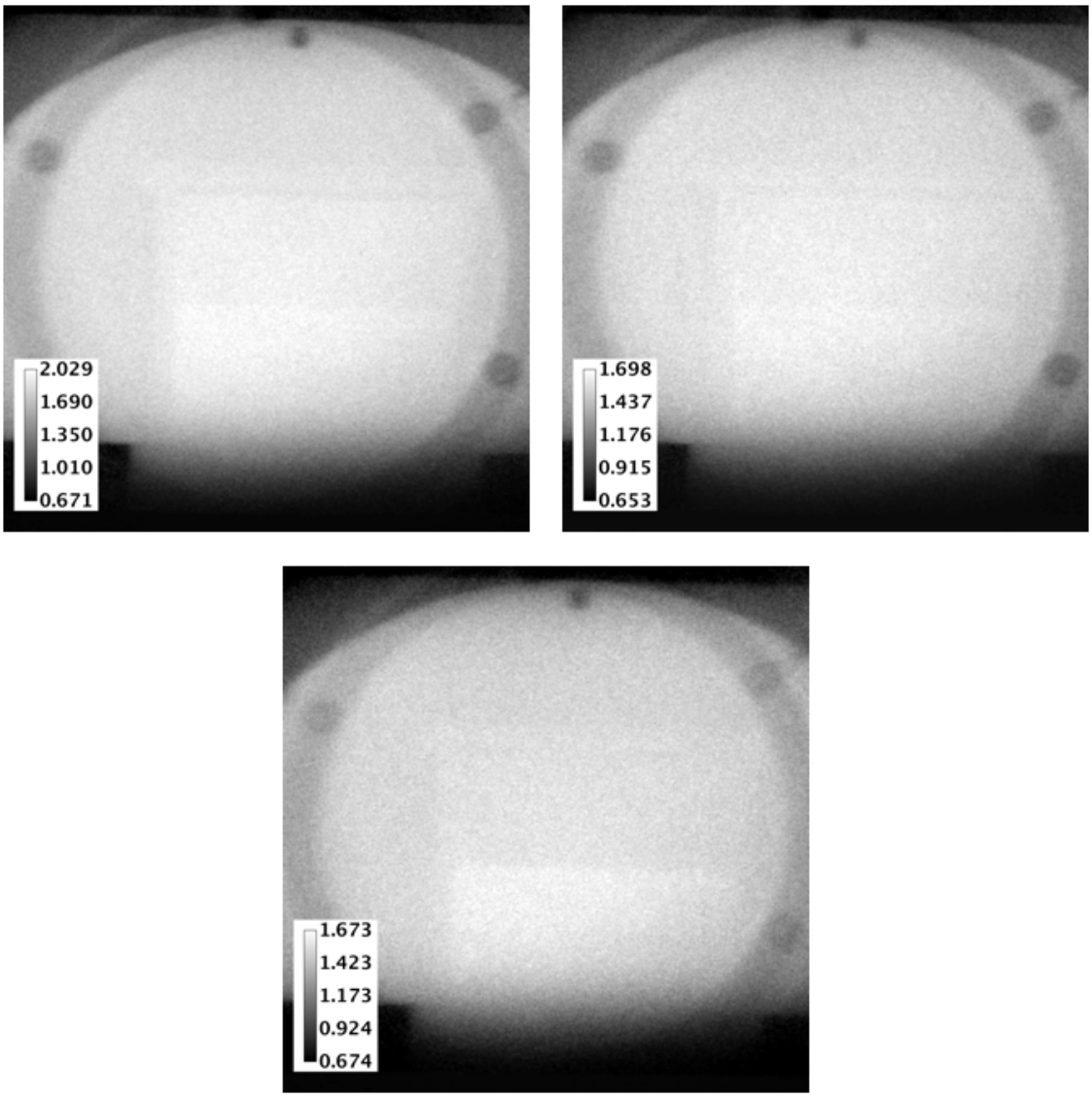


Figure 9.76: Radiographs of the crack test object through 3 *in* of DU at its thickest location. The average intensity of the short-exposure flatfield was used for normalization. The radiographs were formed with neutrons of 8 to 12 MeV (top left), 12 to 16 MeV (top right), and 50 to 70 MeV (bottom) in energy.

appearing to decrease with increasing neutron energy, although using a flatfield with more frames was shown to reduce this effect somewhat.

Averaged vertical and horizontal line-outs were taken in the same region of the normalized radiographs as that shown in Figure 9.73, again after rotating the radiographs 1.5° counter-clockwise. The line-outs can be seen in Figure 9.77. The conclusions stated earlier for the unnormalized data hold true for the normalized data: increasing neutron energy decreases attenuation but also decreases contrast resolution.

Additionally, contrast values are seen to increase as object thickness increases. While the DU thickness is 3 in for most of the configuration, the attenuation increases where the crack test object is located. Moreover, DU and steel is more attenuating than DU and polyethylene. All of these results are to be expected: adding more material causes transmission to decrease and scatter to increase.

Perhaps surprisingly, the 8 to 12 MeV energy bin once again appears to be the best interrogation energy. This is the same neutron energy that was found for Object 2 in Section 9.5.1, and the reasons for it being the optimal energy are also the same. Features are most easily visible in the radiographs and in the line-outs because the 8 to 12 MeV energy bin has the best contrast resolution for this particular object and experimental set-up.

However, using a long exposure flatfield image does improve the contrast resolution of 12 to 16 MeV neutron radiograph, so it is possible that a different technique is necessary with the higher energy neutrons to obtain the same contrast resolution as the lower energy neutrons. Moreover, a 14 MeV source is commercially available, whereas the proposed LLNL 10 MeV boosted D-D source is not, which also affects system design decisions. Future experiments should use a very difficult object (perhaps 10 in of DU, for example) to truly determine the optimal energy, and the cost of the source should obviously be taken into account for the final system design.

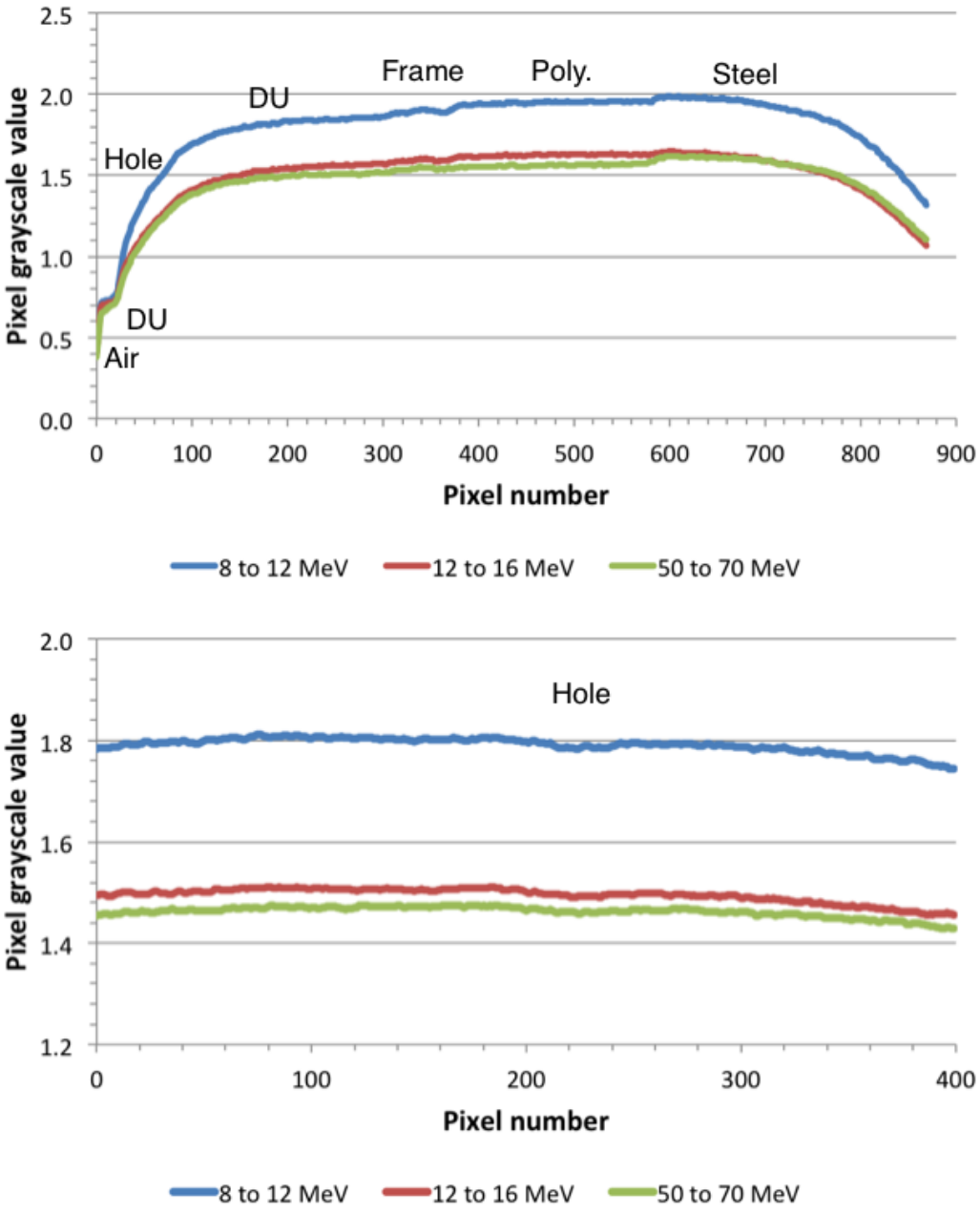


Figure 9.77: Normalized averaged line-outs for the neutron radiographs of the DU plates and crack test object (labelled as "frame", "poly." (polyethylene), and "steel"). Features of interest in the radiograph are labelled on the plots. Top: Averaged vertical line-out. Bottom: Averaged horizontal line-out.

9.5.6 Material Transmission Properties

Similar to the study outlined in Section 5.2.7, an analysis of the 8 to 12 MeV and 12 to 16 MeV DU radiography data was conducted to determine if pixel values represented σt. The methods remained the same, with the radiograph divided by the flatfield image to yield I/I_0 pixel values. Both the radiograph and the flatfield image were generated in post-processing by averaging 100 frames together, and a median filter with a radius of 1 pixel was applied at the very end to reduce noise (Figure 9.78). ROIs were selected in the 1 in and 3 in thick regions of the DU plates to find average I/I_0 values (Figure 9.79).

Experimental data was next compared to theoretical calculations. ENDF-B/VII.1 microscopic neutron total cross-section data for ^{238}U was used to approximate the isotopics of DU [52]. The microscopic cross-section data was found in 1 MeV increments for a neutron energy range of 8 to 16 MeV. The macroscopic total cross-section, Σ, was then generated for each increment according to Equation 5.10 with the assumption of $\rho = 18.95\ g/cm^3$. I/I_0 was then calculated for each increment according to Equation 5.8, and an average I/I_0 was then found for the 8 to 12 MeV and 12 to 16 MeV energy ranges and for the 1 and 3 in material thicknesses.

It was seen that calculated average I/I_0 values for the two DU thicknesses and the two radiograph energy bins did not match that of the experimental data (Table 9.7). This is because, as shown in Section 5.2.7, scatter and secondary particles are included in the experimental data but not the theoretical calculations. The results here, however, differ from those in Chapter 5 in that experimental transmission values were seen to correctly increase directly with energy. This is because scatter was reduced in FP60R when compared to FP15R, and the two energy ranges here contain less downscatter than those in FP15R (e.g., $\sim$0.1 to 10 MeV). Thus, experimental average I/I_0 data better matches theory.

MCNP6 simulations of the DU plates were then conducted to further evaluate radiography data. The three plates were modeled according to the diagram in

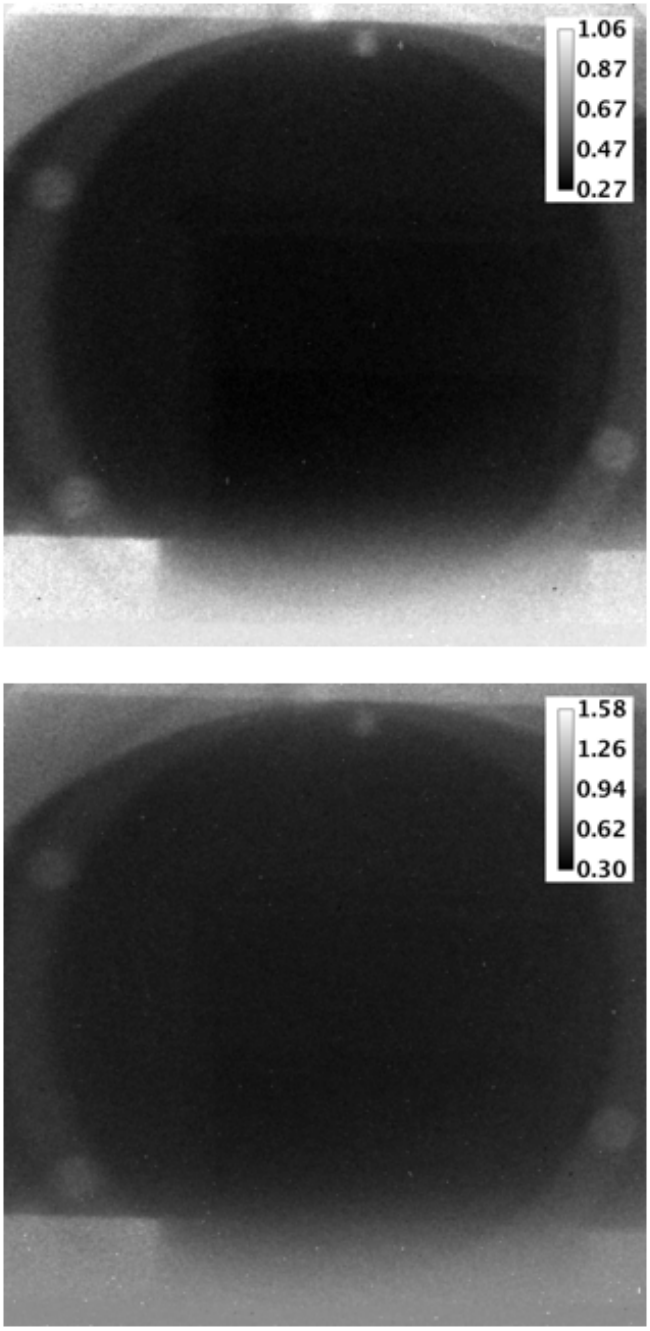


Figure 9.78: DU radiographs post-processed to represent I/I_0 values. Top: Radiograph generated with 8 to 12 MeV neutrons. Bottom: Radiograph generated with 12 to 16 MeV neutrons.

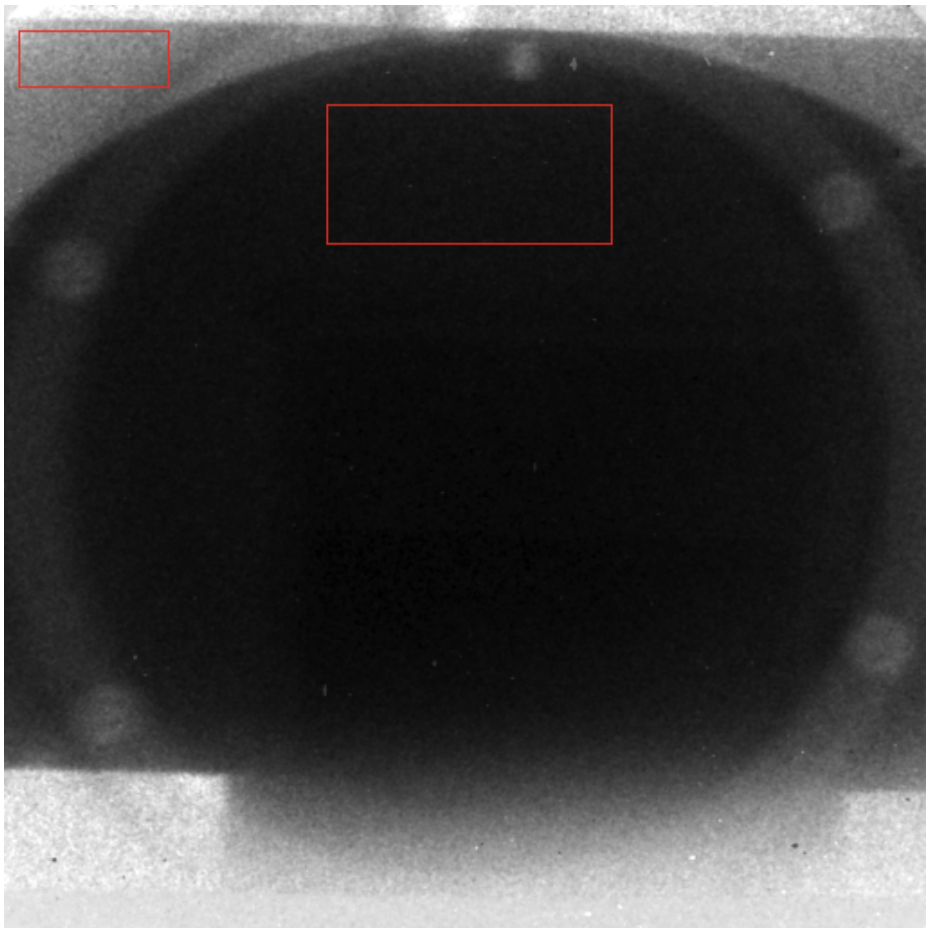


Figure 9.79: Two ROIs used to find the average I/I_0 value for 1 in and 3 in thicknesses of DU. The ROIs are shown in red on the 8 to 12 MeV neutron radiograph.

Table 9.7: Experimental and calculated transmission data for two thicknesses of DU: 1 *in* and 3 *in*.

DU Thickness	Data Source	8 to 12 MeV I/I_0	12 to 16 MeV I/I_0
1 *in*	Experimental	0.746	0.840
	Calculated	0.481	0.489
3 *in*	Experimental	0.346	0.460
	Calculated	0.112	0.117

Figure 9.22, with DU approximated as ^{238}U to match the theoretical calculations. No hole was simulated in the plates because its size was unknown. The three plates were placed on a steel collimator (4 *in* in height and diameter) like in the experiment, except the collimator was simulated as solid (the hole in the center of the collimator was not recorded during the experiments) and as pure iron, the main component of steel. The LLNL crack test object was not simulated, nor was the beam pipe or any other surrounding components that were present in the experiments.

The detector was modeled as EJ-212 and placed at a distance of 79.69 *cm* from the front of the DU plates as it had been in the experiments. The detector was shifted 6.01 *cm* lower than the DU plates in the Z direction to obtain a similar image to that in the experiment and was modeled to be 100% efficient.

An FMESH tally was placed over the detector with pixels 0.50×0.56 cm^2 in size. The tally formed direct and total (i.e., direct plus scatter) images for neutrons, as well as secondary photons. The source was simulated as a monodirectional disk source 15 *cm* in diameter and located at a distance of 100 *cm* from the front of the scintillator. The 8 to 12 MeV and 12 to 16 MeV source spectra were based upon the FP30L source definition provided by J. Hunter, with the probabilities of a given energy renormalized to generate a proper distribution. 5×10^7 neutrons were simulated.

Simulated total I/I_0 radiographs were first generated using post-processing to sum neutron and photon results together, and then divide the simulated total radiograph by the simulated total flatfield (Figure 9.80). Two ROIs were selected in similar locations to those in Figure 9.79 in order to find the average I/I_0 values for 1 *in* and 3 *in* thicknesses of DU (Figure 9.81).

Simulated total radiographs did not match experimental data, much like in Section 5.2.7, because downscatter was not accounted for in the source specification (Table 9.8). Additionally, other components in the flight path were not modeled, such as the crack test object, the concrete cave, the beam pipe, the light-tight box, and so on. Thus, the scatter field was not the same as in the experiment.

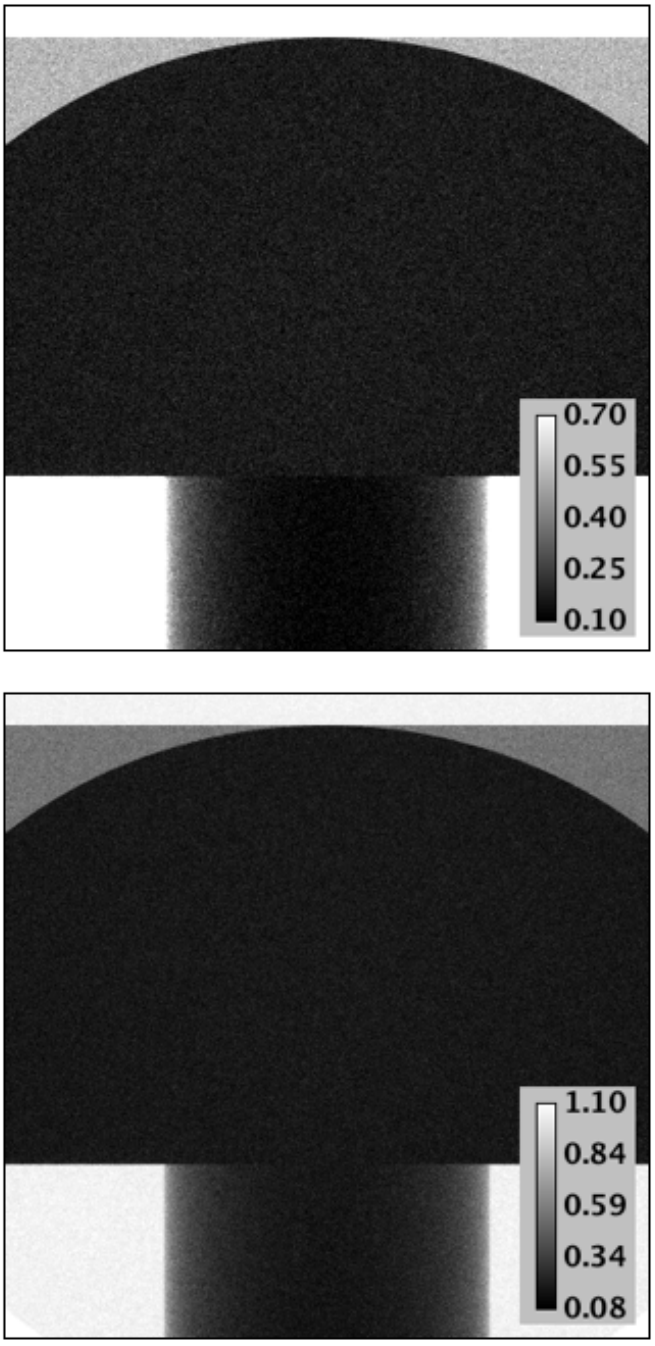


Figure 9.80: Simulated total (direct and scatter) neutron radiographs (including effects from secondary photons) for an 8 to 12 MeV neutron source (top) or a 12 to 16 MeV neutron source (bottom).

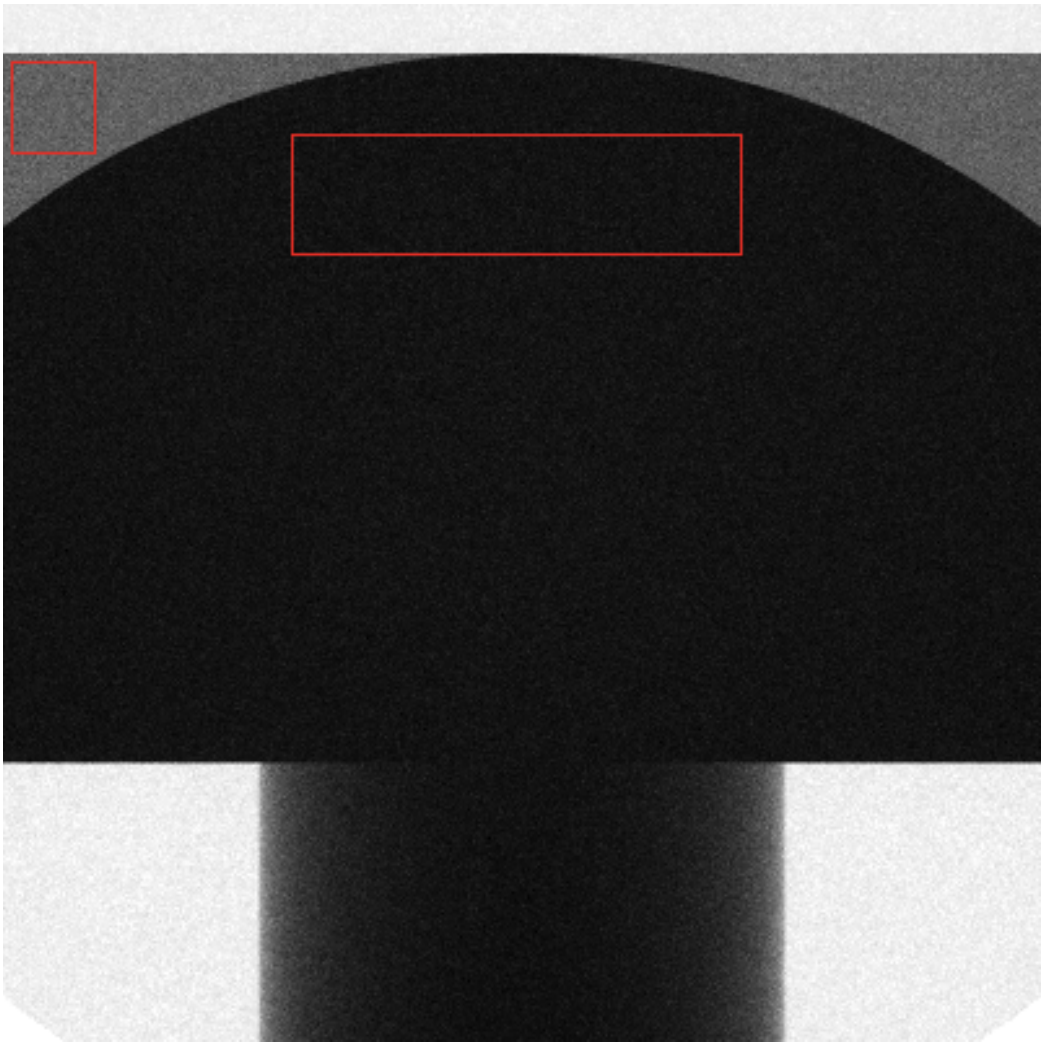


Figure 9.81: ROIs (red) used to find the average I/I_0 values for simulated radiographs of DU plates.

Table 9.8: Experimental and simulated total transmission data for two thicknesses of DU: 1 *in* and 3 *in*.

DU Thickness	Data Source	8 to 12 MeV I/I_0	12 to 16 MeV I/I_0
1 *in*	Experimental	0.746	0.840
	Simulated	0.530	0.544
3 *in*	Experimental	0.346	0.460
	Simulated	0.165	0.182

However, adding scatter like was done in the simulations did move average I/I_0 values toward the experimental I/I_0 values. This indicates that scatter artificially increases transmission.

Second, simulated direct radiographs were generated for comparison to theoretical calculations (Figure 9.82). Average I/I_0 values were found for the same ROIs shown in Figure 9.81 and were seen to match almost exactly with theory (Table 9.9). Any differences can be attributed to exact cross-section data being used by MCNP6, whereas calculations used average data. However, the two sets of data match almost exactly because scatter is not accounted for in either the direct simulations or the calculations. Thus, if scatter can be completely rejected, material identification becomes much easier because transmission values accurately represent σt.

Thus, as was shown in Section 5.2.7, the experimental transmission data does not match theory because of scatter effects. Incorporating scatter via simulated total radiographs caused transmission to artificially increase, whereas eliminating scatter via simulated direct radiographs caused average I/I_0 values to nearly match theory. Thus, scatter rejection is important not just for improving image quality but to also better identify materials within the radiograph. Finally, it was shown that FP60R data better mirrors theory than FP15R because scatter was reduced in the former. These results are expected to hold for other objects radiographed in FP60R.

9.5.7 Challenge Object

Some thought was given as to what would truly be a challenging material and/or object that could be built for TiGReSSE to radiograph in order to test the system limits. A challenging object was thought to be an empty SNF cask, and so simulated radiographs were generated and discussed in Chapter 8. However, SNF casks are difficult to come by and they could not be used to test TiGReSSE. Therefore, material transmission properties were investigated to determine potential components of a challenging radiography object.

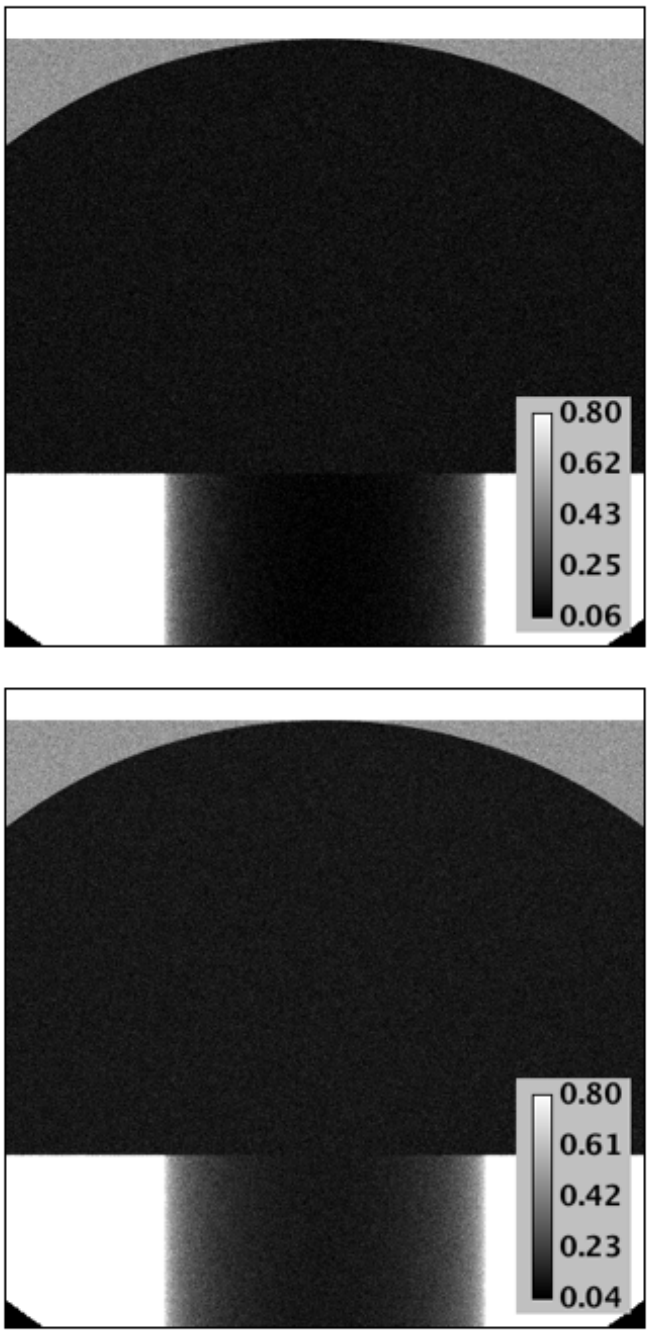


Figure 9.82: Simulated direct neutron radiographs generated with an 8 to 12 MeV neutron source (top) or a 12 to 16 MeV neutron source (bottom).

Table 9.9: Theoretical results and simulated direct transmission data for two thicknesses of DU: 1 *in* and 3 *in*.

DU Thickness	Data Source	8 to 12 MeV I/I_0	12 to 16 MeV I/I_0
1 *in*	Calculated	0.481	0.489
	Simulated	0.487	0.487
3 *in*	Calculated	0.112	0.117
	Simulated	0.116	0.116

The first step was to determine what percent of incident neutrons were transmitted through a material as a function of neutron energy. Materials studied were those used in FP15R and FP60R: borated polyethylene (Object 1), graphite (Object 1), lead (Object 1), uranium (DU object), and tungsten (Object 3). The microscopic total cross-section for borated polyethylene was calculated to match the properties of the borated polyethylene used during LANSCE experiments [70]. To calculate approximate transmission in the LANSCE flight paths, actual thicknesses of these materials were used. Relevant information is listed in Table 9.10. Energies studied covered most of the LANSCE spectrum: 1 MeV, 2.5 MeV, 5 MeV, 10 MeV, 20 MeV, 40 MeV, and 100 MeV. The upper limit was selected to be 100 MeV because above this point, cross-section data typically does not exist. In fact, the ^{238}U total cross-section data was only listed up to 30 MeV.

The transmission as a function of incident neutron energy, material type, and material thickness is shown in Table 9.11 and Figure 9.83. Of the objects radiographed at LANSCE, borated polyethylene was the most attenuating of 1 MeV neutrons as a result of its large ^{1}H content, and graphite was the least attenuating due to its cross-section. Tungsten was the second-most attenuating material for low-energy neutrons, which can be attributed to its large resonance region. At 100 MeV, neutrons were most attenuated by tungsten and least attenuated by borated polyethylene (potentially ^{238}U is a better attenuator than tungsten since its total cross-section was not listed for energies above 30 MeV, but this is not likely because its fission cross-section would improve transmission and it is less dense than tungsten).

Therefore, the most attenuating object radiographed in the FP15R and FP60R beam lines was the tungsten sphere, Object 3. This applied to all energies calculated, except 1 MeV neutrons, which were more attenuated by borated polyethylene due to the large hydrogen content. Additionally, borated polyethylene was more attenuating than the more dense graphite until 10 MeV, at which point it became less attenuating. It was seen, however, that, in general, the transmission decreased as material density increased.

Table 9.10: Materials and their thicknesses as used in FP15R and FP60R experiments. The thickness of tungsten is listed for the thickest part of the cylinder internal to Object 2. Isotopes used for ENDF/B-VII.1 total cross-sections are also listed [52].

Material	Thickness (cm)	Density (g/cc)	Isotopes
Borated polyethylene	9.75	0.95	^{1}H; ^{10}B; ^{12}C; ^{16}O
Graphite	7.98	1.70	^{12}C
Lead	10.20	11.35	^{207}Pb
Uranium	7.62	19.10	^{238}U
Tungsten	7.62	19.25	^{184}W

Table 9.11: Transmission through five materials radiographed in FP15R or FP60R: borated polyethylene ("b-poly."), graphite (^{12}C), lead (^{207}Pb), depleted uranium (^{238}U), and tungsten (^{184}W). Energies shown cover most of the LANSCE spectrum, and materials are listed in order of their increasing density. Transmission was calculated for experimental thicknesses of materials using ENDF/B-VII.1 total cross-section data (note: ^{238}U data only listed for energies up to 30 MeV.) [52].

	Transmission (%)				
Energy (MeV)	B-poly.	^{12}C	^{207}Pb	^{238}U	^{184}W
1	3.04	17.15	15.95	7.25	4.19
2.5	12.24	34.11	8.85	6.19	3.54
5	25.05	44.78	8.24	9.89	5.67
10	39.03	44.78	18.38	11.25	8.28
20	47.57	35.77	14.27	10.19	7.59
40	62.86	46.33	22.87	—	13.98
100	82.99	71.88	21.03	—	13.25

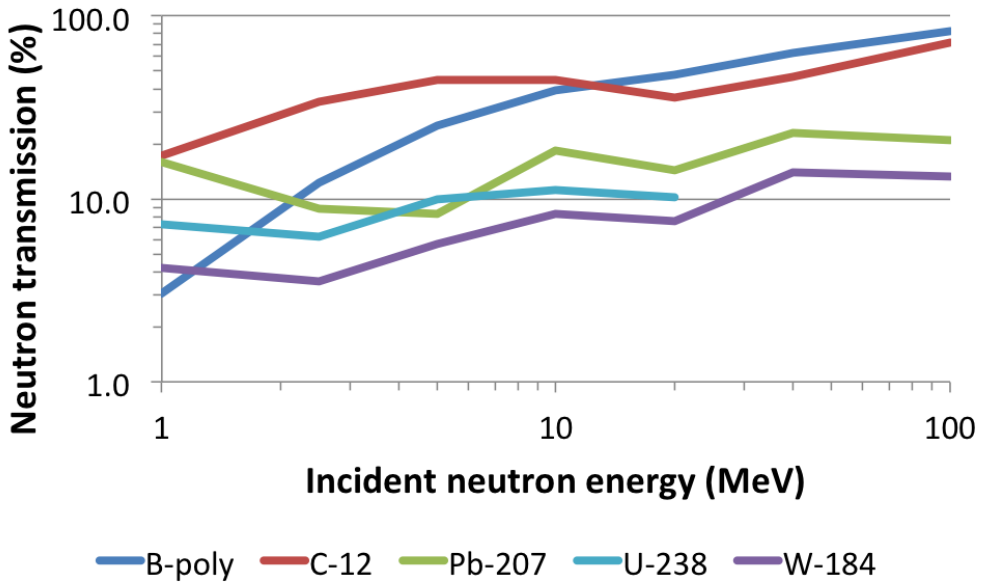


Figure 9.83: *Log* plot of transmission as a function of incident neutron energy for five materials radiographed in FP15R or FP60R: borated polyethylene ("b-poly."), graphite (^{12}C), lead (^{207}Pb), depleted uranium (^{238}U), and tungsten (^{184}W). Materials are listed in the legend according to increasing density, and calculations are based on ENDF/B-VII.1 total cross-section data (note: ^{238}U data only listed for energies up to 30 MeV) [52].

The most important conclusion, however, is that none of the objects radiographed in either FP15R or FP60R are particularly challenging to radiograph. The mean free path (MFP), or the average distance between collisions (typically listed in *cm*) for the five materials was calculated by taking the inverse of the macroscopic cross-section [52, 80]. It can be seen in Figure 9.84 that the borated polyethylene block and graphite cylinder have the largest MFPs, indicating that they are the easiest to penetrate with neutrons. High-Z materials like the depleted uranium plates and tungsten sphere, however, are not easy to penetrate and have much lower MFPs. The number of MFPs for the experimental thicknesses of these materials is shown in Figure 9.85, and it is seen that, particularly for high-energy neutrons, these objects were not of the necessary thickness to truly represent thick, dense objects.

The second step of the study was thus to describe a truly challenging object. Somewhat arbitrarily, it was decided that a thick, dense object would allow no more than 1% transmission of incident neutrons of a given energy, and thicknesses that would achieve such a loss in direct neutrons were calculated for the five materials radiographed at LANSCE [52]. A more challenging case of 0.1% transmission was also calculated for comparison, with both sets of results shown in Figure 9.86 [52]. These thicknesses were then compared to the actual material thicknesses radiographed at LANSCE, again indicating that more challenging objects will need to be purchased or designed to better test TiGReSSE capabilities (Figure 9.87). In most cases, the material thickness should be doubled in future tests.

For all energies, tungsten required the least amount of material to drop the incident flux to 1% or 0.1%. Although expensive, tungsten is thus the best material to challenge TiGReSSE if using the polyenergetic LANSCE beam. Although uranium is second in overall performance, it is difficult to store and handle and thus not recommended if tungsten is available. The plots also show that the thickness of borated polyethylene and graphite appears to grow exponentially as energy increases, whereas the heavy metals' increase in thickness appears to be more or less linear.

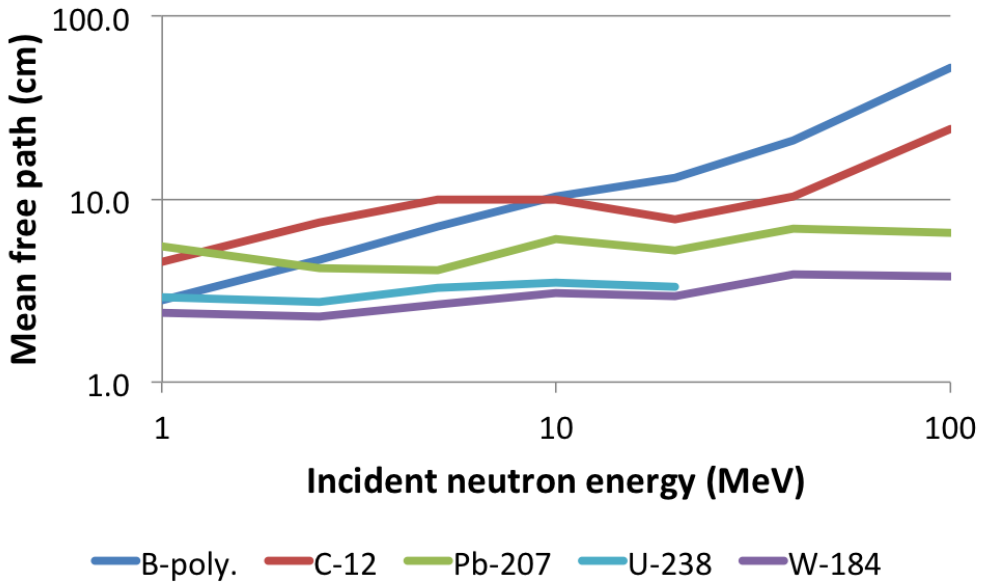


Figure 9.84: *Log* plot of mean free path as a function of incident neutron energy for five materials radiographed in FP15R or FP60R: borated polyethylene ("b-poly."), graphite (^{12}C), lead (^{207}Pb), depleted uranium (^{238}U), and tungsten (^{184}W). Materials are listed in the legend according to increasing density, and calculations are based on ENDF/B-VII.1 total cross-section data (note: ^{238}U data only listed for energies up to 30 MeV) [52].

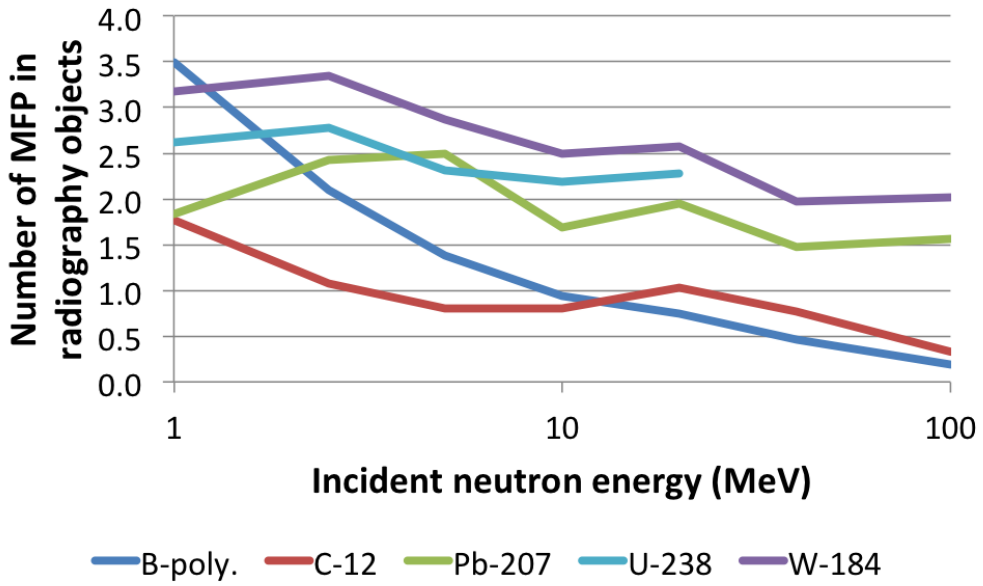


Figure 9.85: Semi-*log* plot of the number of mean free paths in each of the five materials radiographed in FP15R or FP60R: borated polyethylene ("b-poly."), graphite (^{12}C), lead (^{207}Pb), depleted uranium (^{238}U), and tungsten (^{184}W). Materials are listed in the legend according to increasing density, and calculations are based on ENDF/B-VII.1 total cross-section data (note: ^{238}U data only listed for energies up to 30 MeV) [52].

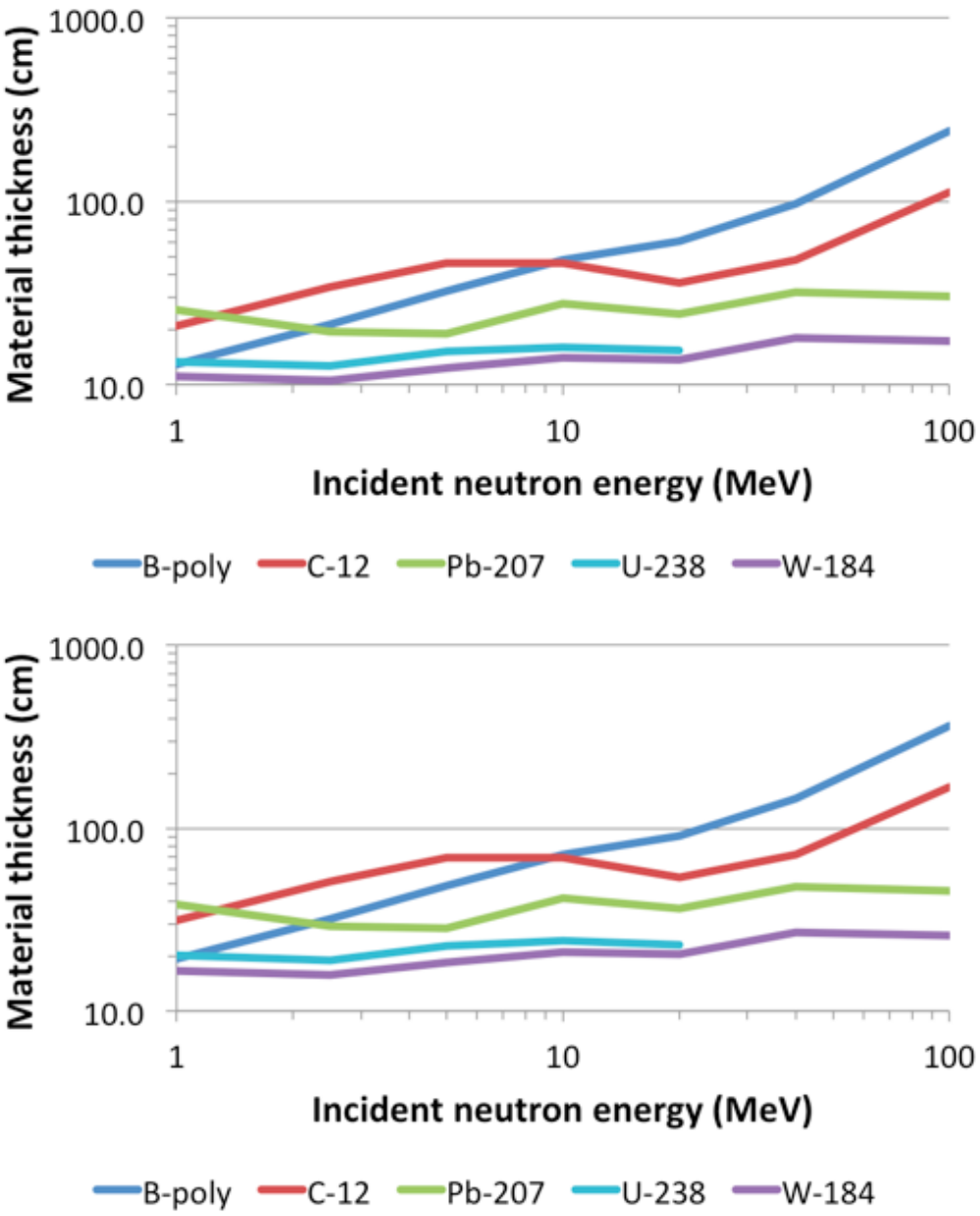


Figure 9.86: *Log* plot of the material thickness necessary, as a function of incident neutron energy, to reduce the incident neutron flux to 1% (top) or 0.1% (bottom) of its initial value. Materials are listed in the legend according to increasing density, and calculations are based on ENDF/B-VII.1 total cross-section data (note: ^{238}U data only listed for energies up to 30 MeV) [52].

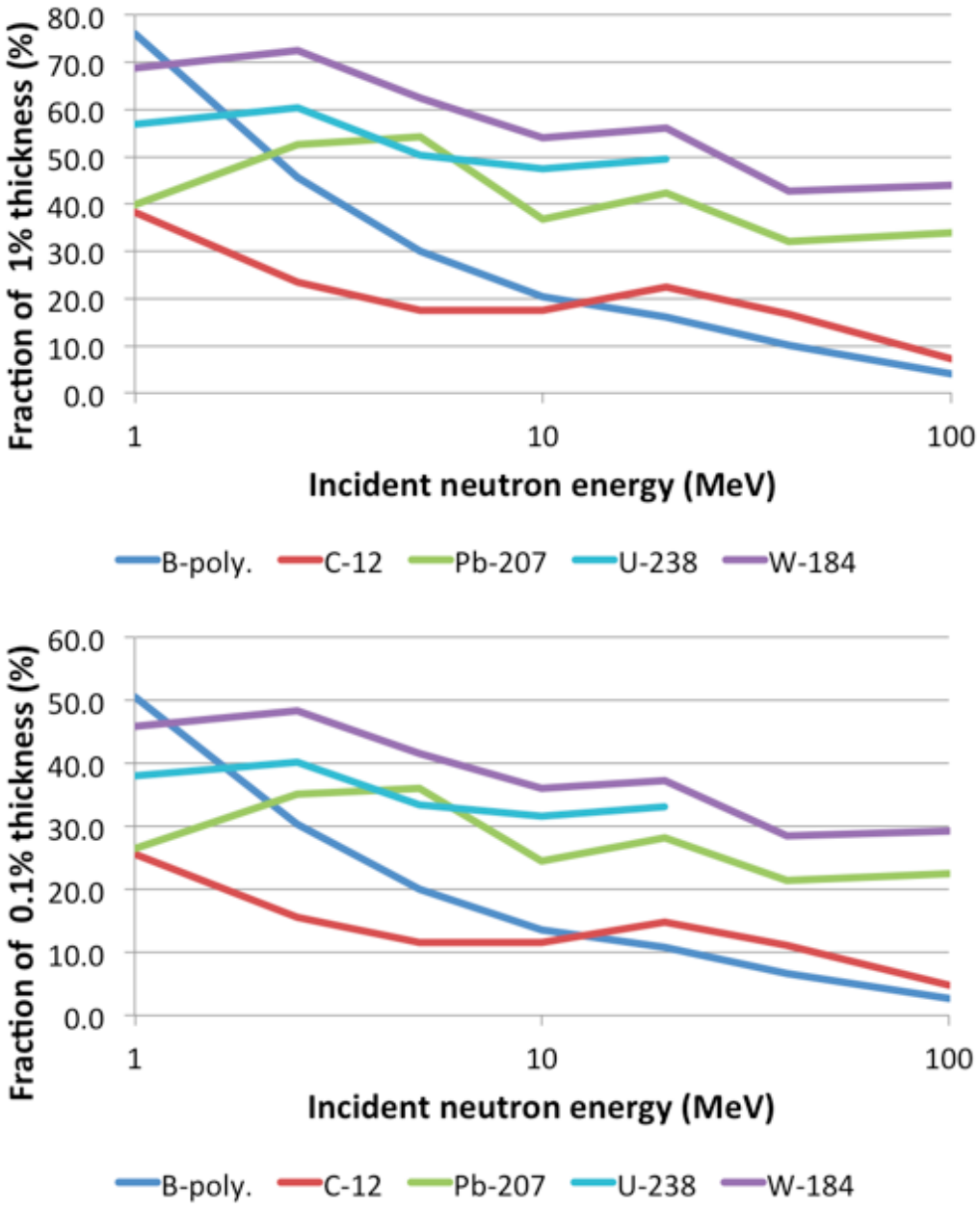


Figure 9.87: Semi-*log* plot of the fraction of the 1% (top) and 0.1% (bottom) thickness that was radiographed at LANSCE. Materials are listed in the legend according to increasing density, and calculations are based on ENDF/B-VII.1 total cross-section data (note: ^{238}U data only listed for energies up to 30 MeV) [52].

Therefore, the use of low-Z objects as challenge materials for high-energy neutrons is impractical and not recommended (e.g., 361.17 cm of borated polyethylene would be required to reduce the transmission of 100 MeV neutrons to 0.1% of the initial flux).

Finally, the transmission results were compared to what would be seen with 2.5 and 10 MeV monoenergetic x-ray sources. The graphite cylinder (part of Object 1) and the tungsten sphere (Object 3) were selected for this source particle comparison, with experimental thicknesses used to judge transmission. The NIST XCOM database of total attenuation coefficients (μ/ρ; units of cm^2/g) was used to determine x-ray transmission [81]. As can be seen in Figure 9.88, the graphite cylinder easily transmits both particle types, with neutrons slightly less transmissible due to increased scatter. The tungsten sphere, however, allows for only 0.21% transmission of 2.5 MeV x-rays and 0.09% of 10 MeV x-rays (note: the transmissibility of ^{184}W decreases from 2.5 to 10 MeV due to an increase in μ/ρ from an increased probability of pair production). Tungsten, however, allows 3.54% and 8.28% transmission of neutrons, respectively, which again highlights why TiGReSSE uses high-energy neutron sources for imaging thick, dense objects.

9.5.8 Comments on Line-out Noise

A large effort was made to address noise in radiographs so it would be minimized in line-outs. For both FP15R and FP60R, one method used for minimizing line-out noise was to take averaged line-outs for a region of interest, instead of using a single row or column of pixels which is much more vulnerable to noise. Additionally, the method for combining frames was switched from taking the average of the pixels (used to process FP15R data in Chapter 5) to taking the median of the pixels so that bright stars were discard instead of being averaged into the final pixel value.

Another method that was investigated for reducing noise in line-outs was using a histogram of the image to throw out pixel values that fell above a certain threshold (i.e., stars in the image). This method improved radiographs if used before combining

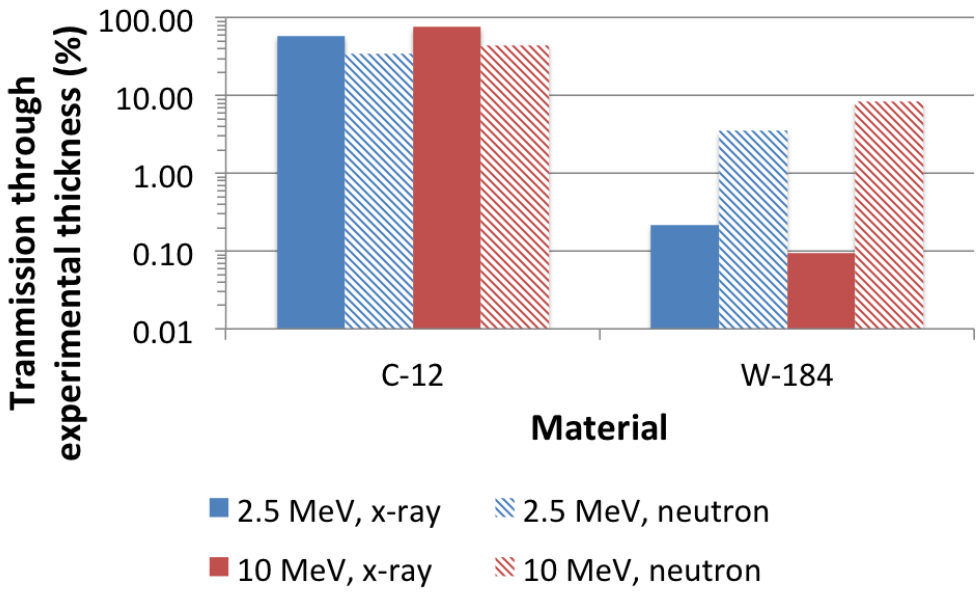


Figure 9.88: Semi-*log* plot of transmission through the experimental thicknesses of the graphite cylinder (^{12}C) and tungsten sphere (^{184}W) that were radiographed in FP15R. Monoenergetic neutrons of 2.5 and 10 MeV were compared to monoenergetic x-rays of the same energies. Neutron total microscopic cross-section data were taken from the ENDF/B-VII.1 library, while x-ray total attenuation coefficients were taken from the NIST XCOM database [52, 81].

frames with the median method and if no other post-processing was to be conducted on the radiograph. However, if this was done prior to combining frames with the median method (described at the beginning of this section and used to convert pixel values to σt), noise was actually increased in some cases and, in other cases, the noise simply moved to other parts of the line-out. Thus, the median method was seen to be the best overall post-processing method to reduce line-out noise.

9.5.9 Flatfield Images

An analysis was conducted of the FP60R flatfield images in a similar manner to that conducted in Section 5.2.8 except that the 100 flatfield frames were combined using the median pixel values (instead of the average pixel values). Line-out results were normalized to the number of pulse accumulations in each energy bin. The analysis was conducted first for the four energy bins selected to match FP15R and thus compare beam properties. The four energy bins covered the full spectrum, photons, and neutrons in energy from 10 to 600 MeV and from 2.5 MeV and below. The line used to calculate the line-out, as well as a plot of the line-outs, can be seen in Figure 9.89.

These results show that the four FP60R flatfield line-outs follow the same pattern in intensity levels as the corresponding four FP15R flatfield line-outs in Figure 5.58. The full spectrum has the largest intensity because it integrates the entire LANSCE pulse, whereas the other three energy bins only integrate part of the pulse. The 10 MeV and below flatfield is higher than 10 to 600 MeV because it contains more flux. The photon bin is still the bin with the lowest flux. Interestingly, the intensity of the flatfield images is much larger in FP15R than in FP60R. This indicates that there is more flux incident on the detector in FP15R than in FP60R, most likely because of the activation products and scatter that was so problematic in FP15R.

Next, the flatfield images for the remaining energy bins, which were used to determine the optimal source energy, were analyzed: 2 to 3 MeV, 8 to 12 MeV,

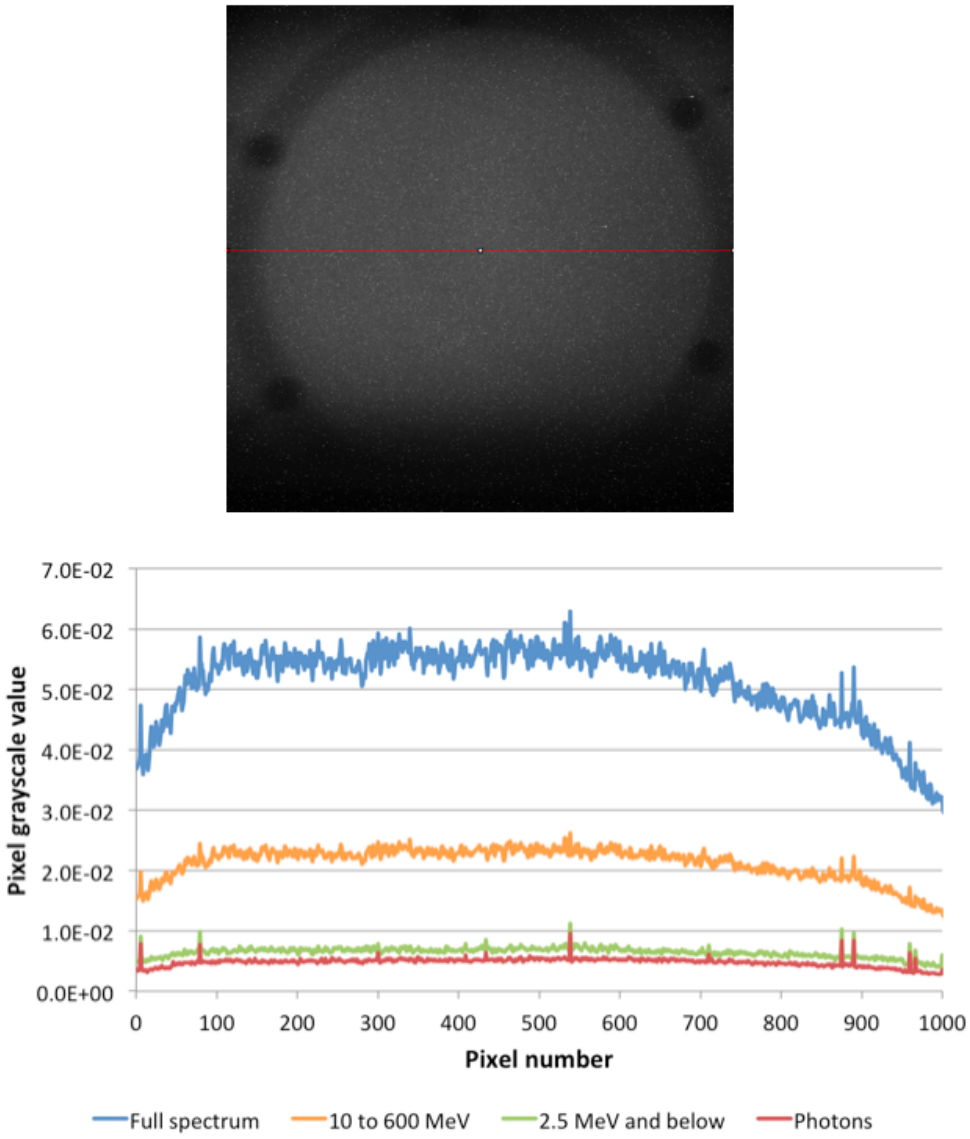


Figure 9.89: Top: Example of the line-out used to quantify FP60R beam non-uniformity. The line is demonstrated on the 2 to 3 MeV neutron flatfield. Bottom: Line-outs for the four flatfield images taken in FP60R that match some of the energy bins used in FP15R. Pixel grayscale values were normalized to the number of total pulse accumulations in each energy bin.

9 to 11 MeV, 12 to 16 MeV, and 50 to 70 MeV. The same line was used to generate the line-outs as that depicted in Figure 9.89, and all pixel values were normalized to the 6×10^5 pulse accumulations per frame. These flatfields also combined the 100 frames using the median pixel value. The plot of the five line-outs may be seen in Figure 9.90.

Not surprisingly, the plots mirror what was seen for the total average intensity in each flatfield image, which was used to normalize most of the radiographs in this chapter. It was thought that, because scintillator efficiency and FP60R flux decrease with increasing energy, the flatfield would be the largest for 2 to 3 MeV neutrons and smallest for 50 to 70 MeV neutrons. There are, however, variables of unknown quantity that are somehow affecting this prediction. For example, the additional flux from scatter and activation products is uncharacterized in this beam line, and it is possible that photon activation of the light-tight box and surrounding material from the previous pulse has not yet decayed by the time 50 to 70 MeV neutrons arrive at the scintillator.

Additionally, whereas the four energy bins shown in Figure 9.89 are relatively easy to compare to the flux profile in Figure 5.3—one bin contains everything below 10 MeV and another contains everything above 10 MeV—this is not the case for the five energy bins discussed here. Without the fission chamber data, which is unavailable because the detector was not functional for most of the experiment, it is impossible to see regional variations in the flux structure that may explain these anomalies. Thus, future experiments will need to be done in FP60R to explain the second set of results.

9.6 Summary

A number of studies were conducted in a different beam line at LANSCE, FP60R. It was found that FP60R produced better quality radiographs due to decreased noise from scatter and activation products, and the larger beam size allowed for more even

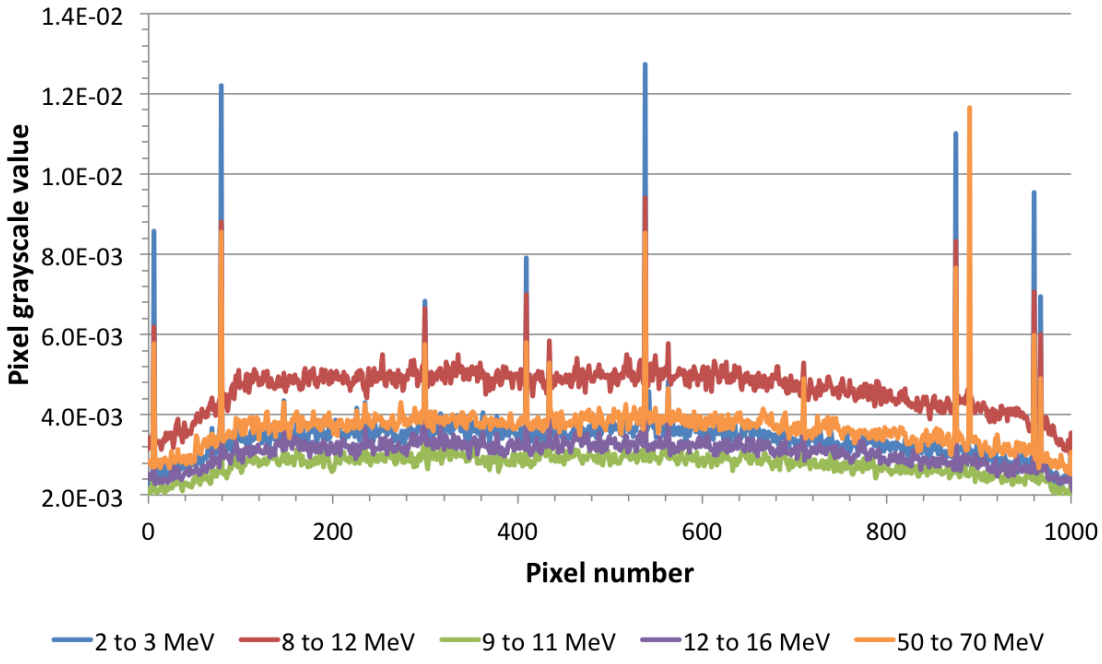


Figure 9.90: Line-outs for the five flatfield images taken in FP60R for several studies. Pixel grayscale values were normalized to the number of total pulse accumulations in each energy bin.

coverage of the scintillator. Additionally, the shielding set-up, whose design was outlined in Chapter 7, was shown to greatly reduce scatter into the camera volume. No doubt moving the camera within the light-tight box to make room for additional shielding also reduced scatter.

Other results showed that increasing the exposure time improves the signal-to-noise ratio in the radiographs, and that this benefit is seen even when just the flatfield exposure time is increased. Implementing this finding into future uses of TiGReSSE will limit dose to the radiography object while reducing noise in the radiograph. The long exposure radiographs also showed that, at an object-to-detector plane of 50 cm, the limiting object feature size is approximately a hole 6 mm in diameter and 0.25 in in depth located in 1 in of polyethylene. Future studies should be done to determine resolution in a range of materials and object geometries. No features were visible in the crack test object, most likely due to blur, and future experiments should place it closer to the scintillator in order to image its interior.

It was also found theoretically and experimentally that an optimal object-to-detector distance for the radiography object is between 75 and 100 cm. This places the object far enough away that most scatter misses the scintillator, but close enough to the scintillator to limit feature blur. Additional objects besides Object 2 should be used to further test this hypothesis because this distance is expected to be dependent on object features, materials, and measurement geometry.

Another interesting study imaged a polyethylene and steel object (the crack test object) through three DU plates with thickness ranging from 0 to 3 in along the stacked plates. While the crack test object features were not visible (e.g., cracks and holes), the material boundaries and the object's frame were visible. The hole in the three DU plates was also visible. While this experiment shows that TiGReSSE can image though high-Z material with relative ease, future experiments should attempt to image through even thicker pieces of DU to determine the system's optical thickness limit.

A final study was conducted to determine the optimal source energy for use with TiGReSSE. Initial results are mixed, showing that 8 to 12 MeV is better than 12 to 16 MeV, but 9 to 11 MeV is about the same or worse. It is difficult to say how much this is a result of the strange flatfield intensities shown in Figure 9.90. While it is true that radiographs and flatfields combined a number of frames that accounted for the variations in flatfield intensity, perhaps a better method exists or should be developed, in particular one that eliminates the energy-dependent variable of scintillator efficiency. Contrast resolution must also be taken into account, and has been shown to decrease as energy increases even though transmission increases. This result may not be object-dependent because the large, dense SNF cask in Chapter 8 also yielded this result. A final hesitation is the cost of the proposed 10 MeV source when compared to the cheaper 14 MeV source; it may be decided that the small added benefit shown here, if later proven to be correct, is not worth the large cost.

Taking all of these factors into account, it seems that for most objects the optimal source energy will be between 10 and 14 MeV. Contrast resolution was decreased substantially for 20 MeV neutron radiographs of the SNF cask, and experiments showed this result for the 50 to 70 MeV neutron radiographs, as well. More experiments, however, will need to be done to determine the flux spectrum in LANSCE and its impact on the results shown in this chapter, which will possibly lead to a new normalization method that will show more decisively what the optimal source energy is.

Overall, good progress was made with this series of experiments, and future work still remains to better quantify system resolution (e.g., taking knife-edge measurements and designing more representative penetrameters) and further narrow down the optimal source energy (e.g., designing a 14 MeV D-T source with the necessary timing and flux to allow for more accurate energy studies). Additional work remains to determine the optimal object-to-detector distance for each radiography object of interest within the 75 to 100 cm bounds.

Chapter 10

Conclusions and Future Work

This dissertation describes the work undertaken to develop a neutron radiography system, TiGReSSE ("Time Gating to Reject Scatter and Select Energy"), for NDA of thick, dense objects. This system was designed to be source-agnostic, such that it could be used with many pulsed high-energy neutron sources depending on the user's objectives. If used with a monoenergetic pulsed neutron source, TiGReSSE could reject scatter using TOF time gating, both from the surrounding environment and the object itself, and thus generate radiographs of thick, dense objects that currently incapable of being imaged with current system designs. If, however, TiGReSSE were to be used with a polyenergetic pulsed neutron source (or a monoenergetic pulsed source with a spallation target), downscatter and other sources of scatter could not be completely eliminated, but TOF time gating would allow for energy selection of the incident neutrons in order to vary contrast and preferentially see features of interest within the radiography object.

To design such a system, work was first conducted to approximate the time resolution that would be required to successfully reject scatter. A 10 MeV monoenergetic neutron source, modeled as a pencil beam in MCNP6, was incident on a graphite slab. It was found via calculations that scatter arrived only $\sim$1 to 3 ns after the direct signal. This led to the purchase of the Princeton Instruments PI-Max4

ICCD camera, which is capable of short, sub-ns time gates at high repetition rates (up to 1 MHz), as well as the Eljen EJ-212 fast plastic scintillator with decay times of only 2.4 ns. A very stable delay generator was also purchased to allow time-of-flight imaging to be conducted.

First system tests with a neutron source were conducted with a D-T generator and were very important in driving system design. It was found that TiGReSSE system geometry reduced the number of photons reaching the camera to values below the camera noise levels. The dark current was seen to increase as a function of temperature, and a liquid chiller was purchased to keep the camera cool and reduce electronic noise that could mask weaker sources. It was also found that a source strength of 1×10^6 neutrons per pulse was too weak for use with TiGReSSE if emitted into 4π, with only 2.01×10^4 of those neutrons reaching the scintillator.

A subsequent series of tests were conducted in FP15R at LANSCE. These tests showed the detrimental effect of scatter on radiograph quality and system electronics. In FP15R, scatter had many sources: downscatter from higher energies into lower energy time gates; activation products from a cluttered flight path; and the radiography object itself. Scatter was seen to be a larger problem at lower energies, due to the increased detector efficiency and increased downscatter. This scatter led to stars in images that skewed contrast adjustment of images, and also caused image grayscale values (after post-processing) to not match cross-section data. Partial scatter rejection was successfully demonstrated by eliminating scatter from the object at lower neutron energies. These tests, therefore, showed the importance of scatter rejection and the use of a pulsed monoenergetic source.

Results also showed that object features are visible at some neutron energies but not others, and that this optimal energy varies among radiography objects. Additionally, small features such as a sheet of paper between lead and borated polyethylene were visible, indicating that TiGReSSE has the potential to image small defects. These results show the importance of using a pulsed polyenergetic source for varying image contrast. Therefore, it is recommended that a monoenergetic pulsed

neutron source is used with a spallation target to allow for scatter rejection to improve image quality as well as to allow for energy selection to improve the likelihood of finding features that may not appear at the monoenergetic energy of choice.

Based on these initial tests, TiGReSSE was redesigned to reduce scatter. The ICCD camera was moved within the light-tight box so it was located farther from the direct beam. Additionally, the shielding design was updated to include lithiated polyethylene within the light-tight box and lead directly around the camera, while continuing to use 2 ft of steel outside the light-tight box. It was found that additional external shielding only increased scatter into the camera volume.

The redesigned Generation II TiGReSSE was shown to have reduced scatter into the camera in another LANSCE beam line: FP60R. These subsequent experiments built upon previous experiments by generating long exposure radiographs to better understand the impact of exposure time on radiograph quality, as well as demonstrating reduced scatter, from both the system redesign, as well as a flight path better designed for TOF radiography. Tests also showed that increasing source energy decreased contrast resolution, and that a hole with diameter of 6 mm and depth of 0.25 in in 1 in of polyethylene could be seen at a distance of 50 cm from the scintillator. A challenging configuration, 3 in of DU in front of the LLNL crack test object, was successfully imaged. It was also found that placing the radiography object at a distance of 50 to 75 cm from the scintillator reduced scatter from the object into the scintillator while maintaining spatial resolution.

To further characterize the system, the limiting spatial resolution was found to be 0.5 mm at the imaging plane. Above this line pair spacing, the contrast decreased too much to resolve features. Additionally, the scintillator efficiency was simulated with MCNP6 for neutron energies up to and including 20 MeV, and an average light yield was extrapolated for neutron energies up to 750 MeV. It was seen that the FP15R configuration was able to detect LANSCE neutrons of all energies, but that the FP60R configuration had a reduced ability because of increased geometric losses. Additionally, calculations showed that flux at the scintillator below $\sim 10^4$

is not detectable by TiGReSSE, which is corroborated by initial D-T experiments. Other MCNP6 simulations showed that the dose to the radiography object during NDA is reduced by decreasing the incident source energy, and that neutron dose is higher than x-ray dose; more x-rays are necessary to radiograph thick, dense objects, however, which most likely will cause total dose to be less with neutron radiography.

These results fall in line with FP60R experimental data and MCNP6 simulated radiographs of a spent nuclear fuel cask, both of which show that increasing the interrogation energy decreases contrast resolution. This is because of scatter and secondary particles, as well as an increase in mean free path that reduces detection efficiency and minimizes differences in material attenuation.

For all of these reasons, it is recommended that a neutron source energy be limited to 10 to 14 MeV. Such a source energy will increase contrast resolution and detector efficiency while reducing dose and maintaining the benefits of high-energy neutrons for radiographing thick, dense objects. This energy range is also large enough to allow a spallation target to be used to generate other energy neutrons for energy selection. Yet, if an object object is found that does require neutrons above 14 MeV in energy, TiGReSSE has been demonstrated to work with neutrons of energy up to 600 MeV and is thus more than capable of conducting NDA of such an object.

Future work still remains to further improve and characterize the system design. Work needs to be done to better understand the optimal neutron source energy, particularly by designing a very challenging radiography object that only allows 1% transmission of incident neutrons. Additionally, a monoenergetic source with pulse timing like that of LANSCE needs to be built to demonstrate total scatter rejection. Additionally, TiGReSSE can be improved by using fiberoptic coupling between the scintillator and the ICCD chip; such a redesign would limit light loss, improve detection efficiency, and improve the signal-to-noise ratio. Tests with a thinner scintillator should be conducted to determine whether the loss in detection efficiency is worth the increase in spatial resolution. The design of a better method for finding the start of the neutron pulse is also necessary, such as the use of a fast photon

detector serve as the true LANSCE trigger; such an improvement would increase time resolution of the system.

In summary, this project successfully developed two generations of TiGReSSE designs and demonstrated the benefits of both scatter rejection and energy selection at novel source energies. TiGReSSE is ready for further tests with even more challenging objects, and is well on its way to being deployable for radiographing thick, dense objects that cannot be imaged with existing x-ray or neutron radiography techniques.

Bibliography

[1] M. Willcox and G. Downes, "A review of common nondestructive tests," 2006. [Online]. Available: http://www.thefabricator.com/article/testingmeasuring/a-review-of-common-nondestructive-tests 1

[2] I. Anderson, R. McGreevy, and H. Bilheux, *Neutron Imaging and Applications: A Reference for the Imaging Community*, ser. Neutron Scattering Applications and Techniques. Springer Science+Business Media, 2009. xvii, 2, 4, 5, 6, 7, 8, 10, 12, 13, 14, 23, 29, 30, 33, 37, 41

[3] H. Barrett and W. Swindell, *Radiological Imaging: The Theory of Image Formation, Detection, and Processing*. Academic Press, 1981. 5, 29

[4] J. Bushberg, J. A. Seibert, E. Leidholdt, and J. Boone, *The Essential Physics of Medical Imaging*, 2nd ed. Lippincott Williams and Wilkins, 2002. 4

[5] R. Schirato, Personal communication, February 2015. 5, 23, 30, 32

[6] T. McDonald *et al.*, "Time-gated energy-selected cold neutron radiography," Los Alamos National Laboratory, Tech. Rep. LA-UR-98-833, 1998. 5, 41, 42

[7] Los Alamos Neutron Science Center, "Neutron and nuclear science (WNR) facility at LANSCE." [Online]. Available: http://wnr.lanl.gov/ 5

[8] F. Dietrich, J. Hall, and C. Logan, "Conceptual design for a neutron imaging system for thick target analysis operating in the 10-15 MeV energy range," *American Institute of Physics Conference Proceedings: Applications of Accelerators in Research and Industry*, vol. 392, pp. 837–840, 1997. 5, 50

[9] International Atomic Energy Agency, "Neutron generators for analytical purposes: IAEA radiation technology reports no. 1," 2012. [Online]. Available: http://www-pub.iaea.org/MTCD/Publications/PDF/P1535_web.pdf 5

[10] M. R. Hawkesworth and J. Walker, "Review: Radiography with neutrons," *Journal of Materials Science*, vol. 4, pp. 817–835, 1969. xvii, 7, 8, 9, 10, 14, 23, 47

[11] I. Mor *et al.*, "High spatial resolution fast-neutron imaging detectors for pulsed fast neutron transmission spectroscopy," *Journal of Instrumentation*, 2009. 7, 10, 37, 42

[12] D. Reilly, N. Ensslin, and H. Smith, *Passive Nondestructive Assay of Nuclear Materials*. Nuclear Regulatory Commission, 1991. 7, 55

[13] W. Hunger, R. Scherzer, and W. Enge, "Plastic detector technique in fast neutron radiography," *Nuclear Tracks*, vol. 3, pp. 53–68, 1979. 8, 41, 42

[14] E. Lehmann, P. Vontobel, G. Frei, and C. Bronnimann, "Neutron imaging – Detector options and practical results," *Nuclear Instruments and Methods in Physics Research A*, vol. 531, pp. 228–237, 2004. 8, 10, 37, 38, 42

[15] V. O. de Haan, T. H. J. J. van der Hagen, A. Federov, A. van Veen, and P. F. A. de Leege, "Conceptual design of a novel high-frame-rate fast-neutron radiography facility," *Nuclear Instruments and Methods in Physics Research A*, vol. 539, pp. 321–334, 2005. 12, 29, 30, 31, 33, 35, 36, 37

[16] G. Boreman, *Basic Electro-Optics for Electrical Engineers*, ser. Tutorial Texts in Optical Engineering. SPIE Optical Engineering Press, 1998, vol. TT31. xvii, xviii, 14, 17, 19, 20, 21, 22, 31, 32, 38, 204

[17] P. Vontobel, E. Lehmann, R. Hassanein, and G. Frei, "Neutron tomography: Method and applications," *Physica B*, vol. 385-386, pp. 475–480, 2006. xviii, 14, 15, 33, 34

[18] D. H. Kelly, "Spatial frequency, bandwidth, and resolution," *Applied Optics*, vol. 4, no. 4, pp. 435–437, 1965. xviii, 15, 24, 25, 27

[19] Wolfram Alpha, "Wolfram Alpha plotter widget," 2006. [Online]. Available: http://www.wolframalpha.com/widgets/view.jsp?id=feade1d2047977cd0cefdafc40175a99 xvii, 17, 18

[20] "University of Colorado-Boulder Physics 1010: The physics of everyday life," 2006. [Online]. Available: http://www.colorado.edu/physics/phys1010/phys1010_fa06/lectures/class13.pdf 17

[21] Edmund Optics, "Introduction to modulation transfer function." [Online]. Available: http://www.edmundoptics.com/technical-resources-center/optics/modulation-transfer-function 19

[22] B. Atkins, "Modulation transfer function – what is it and why does it matter?" [Online]. Available: http://photo.net/learn/optics/mtf/ xviii, 19, 24, 26

[23] Optikos Corporation, "How to measure MTF and other properties of lenses," 2008. [Online]. Available: http://www.optikos.com/wp-content/uploads/2013/11/How-to-Measure-MTF.pdf 23

[24] G. Boreman and S. Yang, "Modulation transfer function measurement using three- and four-bar targets," *Applied Optics*, vol. 34, no. 4, pp. 8050–8052, 1995. 24

[25] A. Theuwissen, "How to measure modulation transfer function (1)," 2014. [Online]. Available: http://harvestimaging.com/blog/?p=1294 xviii, 28

[26] Edmund Optics, "Imaging resource guide: Depth of field and depth of focus," 2014. [Online]. Available: http://www.edmundoptics.com/technical-resources-center/imaging/depth-of-field-and-depth-of-focus/ 31

[27] T. Gozani, "Understanding the physics limitations of PFNA – the nanosecond pulsed fast neutron analysis," *Nuclear Instruments and Methods in Physics Research B*, vol. 99, pp. 743–747, 1995. 33, 35, 43, 46

[28] D. Davis, "Kinetic energy at (very) high speeds," 2001. [Online]. Available: http://www.ux1.eiu.edu/~cfadd/1350/07WorkEnergy/RelKE.html 35

[29] J. Rynes *et al.*, "Gamma-ray and neutron radiography as part of a pulsed fast neutron analysis inspection system," *Nuclear Instruments and Methods in Physics Research A*, vol. 422, pp. 895–899, 1999. 36, 43, 46

[30] R. Loveman, J. Bendahan, T. Gozani, and J. Stevenson, "Time of flight fast neutron radiography," *Nuclear Instruments and Methods in Physics Research B*, vol. 99, pp. 765–768, 1995. 36, 43, 46

[31] T. Kamiyama and Y. Kiyanagi, "Time-of-flight neutron radiography with a blanking-type image intensifier," *Physics Procedia*, vol. 26, pp. 231–237, 2012. 36, 42

[32] Y. Kiyanagi, H. Sato, K. Iwase, and T. Kamiyama, "Recent progress of pulsed neutron imaging in Japan," *Physics Procedia*, vol. 26, pp. 219–222, 2012. 37

[33] N. Kardjilov *et al.*, "New trends in neutron imaging," *Nuclear Instruments and Methods in Physics Research A*, vol. 605, pp. 13–15, 2009. 37, 42

[34] G. Knoll, *Radiation Detection and Measurement*, 3rd ed. John Wiley and Sons, 2000. 39, 186, 187

[35] E. Bagge *et al.*, "Fast neutron radiography for extended objects by a plastic detector technique," *Nuclear Instruments and Methods: Section 8 (Applications in Dosimetry and Radiography)*, vol. 147, pp. 109–114, 1977. 41, 42

[36] E. H. Lehmann, G. Frei, G. Kuhne, and P. Boillat, "The micro-setup for neutron imaging: A major step forward to improve the spatial resolution," *Nuclear Instruments and Methods in Physics Research A*, vol. 576, pp. 389–396, 2007. 42

[37] T. Kai *et al.*, "First demonstration of neutron resonance absorption imaging using a high-speed video camera in J-PARC," *Nuclear Instruments and Methods in Physics Research A*, vol. 651, pp. 126–130, 2011.

[38] Y. Kiyanagi *et al.*, "Some experimental studies on time-of-flight radiography using a pulsed neutron source," *IEEE Transactions on Nuclear Science*, vol. 52, no. 1, pp. 371–374, 2005. 42

[39] D. Vartsky *et al.*, "Time-resolved fast neutron imaging: Simulation of detector performance," *Nuclear Instruments and Methods in Physics Research A*, vol. 542, pp. 206–212, 2005. 42

[40] K. Bergaoui *et al.*, "Design, testing and optimization of a neutron radiography system based on a deuterium-deuterium (D-D) neutron generator," *Journal of Radioanalytical and Nuclear Chemistry*, vol. 299, pp. 41–51, 2014. 43

[41] A. Swift, "Materials and configuration from NMIS type neutron imaging and gamma spectroscopy," Master's thesis, University of Tennessee-Knoxville, 2012. 43, 47

[42] M. Laubach, J. Hayward, X. Zhang, and J. Cates, "Timing and position response of a block detector for fast neutron time-of-flight imaging," *Nuclear Instruments and Methods in Physics Research A*, vol. 763, 2014. 43

[43] M. Wilke *et al.*, "The National Ignition Facility neutron imaging system," *Review of Scientific Instruments*, vol. 79, 2008. 44, 47

[44] C. Danly *et al.*, "Plastic fiber scintillator response to fast neutrons," *Review of Scientific Instruments*, vol. 85, 2014.

[45] F. Merrill *et al.*, "The neutron imaging diagnostic at NIF (invited)," *Review of Scientific Instruments*, vol. 83, 2012. 44, 47

[46] A. Tremsin *et al.*, "Scatter rejection in quantitative thermal and cold neutron imaging," *Nuclear Instruments and Methods in Physics Research A*, 2011. 47

[47] J. Goorley *et al.*, "MCNP6 user's manual," Los Alamos National Laboratory, Tech. Rep. LA-CP-13-00634, 2013. 49, 311

[48] B. Temple, "Differences between the TALLYX and FMESH cell tagging capabilities," Los Alamos National Laboratory, Tech. Rep. LA-UR-04-8244, 2004. 50

[49] J. Shultis and R. Faw, *An MCNP Primer*, Kansas State University, 2011. 50

[50] B. Rusnak, J. Hall, and S. Shen, "Rotating aperture deuterium gas cell development for high brightness neutron production," *Proceedings of 2005 Particle Accelerator Conference*, pp. 2074–2076, 2005. xix, 50, 52

[51] A. Swift, E. McKigney, R. Schirato, A. Robinson, and B. Temple, "A verification of MCNP6 FMESH tally capabilities," Los Alamos National Laboratory, Tech. Rep. LA-UR-14-24364, 2014. xix, 51, 54, 57, 59

[52] National Nuclear Data Center, "Evaluated Nuclear Data File (ENDF) Retrieval and Plotting," January 2016. [Online]. Available: http://www.nndc.bnl.gov/sigma/ xvi, xxvi, liii, liv, lv, 64, 154, 158, 159, 160, 465, 477, 478, 479, 480, 481, 482, 483, 484, 486

[53] Eljen Technologies, "EJ-212." [Online]. Available: http://www.eljentechnology.com/index.php/products/plastic-scintillators/64-ej-212 xiii, xx, 66, 67, 68, 86, 87, 88, 192

[54] "Polyvinyltoluene, mixed isomers." [Online]. Available: http://pubchem.ncbi.nlm.nih.gov/compound/16213094 xiii, 66, 86, 87

[55] Princeton Instruments, "PI-Max4: 1024 EMB." [Online]. Available: http://www.princetoninstruments.com/Uploads/Princeton/Documents/Datasheets/

PIMAX4/Princeton_Instruments_PI-MAX4_1024EMB_N1-6-9-14.pdf 68, 70, 89, 192, 195

[56] Princeton Instruments, *PI-Max4 System Manual*, 4th ed., September 2014. xx, 69, 70, 71

[57] First Surface Mirror LLC, "First Surface Mirror." [Online]. Available: http://www.firstsurfacemirror.com xx, 70, 72

[58] First Surface Mirror LLC, "Technical specifications." [Online]. Available: http://www.firstsurfacemirror.com/techspecs 70, 73

[59] Horiba Scientific, "Delta diode." [Online]. Available: http://www.horiba.com/scientific/products/fluorescence-spectroscopy/lifetime/tcspc-components/deltadiode/deltadiode-15899/ 73

[60] Horiba Scientific, "Horiba Scientific announces new Deltadiodes." [Online]. Available: http://www.horiba.com/us/en/scientific/news-events/latest-news/article/horiba-scientific-announces-new-deltadiodes-tm-18493/ xx, 73, 74

[61] Stanford Research Systems, "Digital delay generator: DG645– Ultra-low jitter delay generator." [Online]. Available: http://www.thinksrs.com/products/DG645.htm xx, 75, 76

[62] Thermo Scientific, *Instruction Manual: Pulsed Neutron Generator Model P 211*, A ed., July 2003. xxi, 84, 85

[63] J. Birks, *The Theory and Practice of Scintillation Counting*. Pergamon Press, 1964. xiii, 86, 87, 88

[64] National Nuclear Data Center, "ENDF data selection: H-1 (N,EL) H-1-L0, SIG." [Online]. Available: http://www.nndc.bnl.gov/exfor/servlet/E4sSearch2 xiii, 86, 87

[65] U. Bravar *et al.*, "FNIT: The fast neutron imaging telescope for SNM detection," *Non-Intrusive Inspection Technologies*, vol. 6213, 2006. 88, 90, 112

[66] Los Alamos Neutron Science Center, "About the neutron and nuclear science (WNR) facility." [Online]. Available: http://wnr.lanl.gov/_assets/about/about_wnr.php 91

[67] Los Alamos Neutron Science Center, "Neutron and nuclear science flight paths." [Online]. Available: http://wnr.lanl.gov/_assets/flight_paths/flight_paths.php xxi, xl, 91, 92, 93, 351

[68] Los Alamos Neutron Science Center, "Time structure of the LANSCE beam." [Online]. Available: http://wnr.lanl.gov/_assests/about/time_structure.php 91

[69] J. Shultis and R. Faw, *Radiation Shielding*. American Nuclear Society, 2000. 154, 182, 183, 221

[70] Shieldwerx, "Polyethylene-based shielding," 2015. [Online]. Available: http://www.shieldwerx.com/poly-based-shielding.html 154, 226, 476

[71] National Institute of Standards and Technology, "PSTAR: Stopping-power and range tables for protons." [Online]. Available: http://www.physics.nist.gov/PhysRefData/Star/Text/PSTAR.html xxviii, 183, 184

[72] National Institute of Standards and Technology, "ASTAR: Stopping-power and range tables for helium ions." [Online]. Available: http://www.physics.nist.gov/PhysRefData/Star/Text/ASTAR.hmtl xxviii, 183, 185

[73] T. Wilcox, "MCNP6 advanced tallies tutorial," Los Alamos National Laboratory, Tech. Rep. LA-UR-14-27128, 2014. 187

[74] Hamamatsu, "Image intensifiers," September 2009. [Online]. Available: https://www.hamamatsu.com/resources/pdf/etd/II_TII0004E.pdf 192

[75] Proxitronic, "Phosphor screens." [Online]. Available: http://www.finesensing.com/iiimaging/doc/PhosphorScreen.pdf 192

[76] Edmund Optics, "1-180, 101.6 x 101.6mm NBS 1963A positive target," 2016. [Online]. Available: http://www.edmundoptics.eu/test-targets/resolution-test-targets/nbs-1963a-resolution-target/85276/ xxix, 200

[77] Edmund Optics, "5.7" x 10" white, LED backlight," 2016. [Online]. Available: http://www.edmundoptics.com/illumination/led-illumination/led-backlights/metaphase-technologies-led-backlights/83874/ xxix, 201

[78] N. Koren, "Understanding image sharpness part 5: Lens testing," 2015. [Online]. Available: http://www.normankoren.com/Tutorials/ 204

[79] D. R. Leduc, "Dry storage of used fuel transition to transport: Fuel cycle research and development," Savannah River National Laboratory, Tech. Rep. FRCD-UFD-2012-000253, August 2012. 311

[80] J. Duderstadt and L. Hamilton, *Nuclear Reactor Analysis*. John Wiley and Sons, 1976. 480

[81] M. Berger *et al.*, "XCOM: Photon cross sections database," May 2015. [Online]. Available: http://www.nist.gov/pml/data/xcom/ lv, 485, 486

Vita

Alicia L. Swift is a nuclear engineering PhD student at the University of Tennessee (UT) and is conducting her dissertation research at Los Alamos National Laboratory on the topic of neutron radiography for non-destructive analysis. Previously, Alicia served as a Nonproliferation Graduate Fellow in the National Nuclear Security Administration's Office of Global Threat Reduction in Washington, D.C. from 2012 to 2013. Alicia also participated in the Center for Strategic and International Studies' Nuclear Scholars Initiative in 2013. Alicia obtained her MS in nuclear engineering and certificate in Nuclear Security Science and Analysis from UT in 2012, conducting her thesis research at Oak Ridge National Laboratory on treaty verification technology. Alicia received her BS with honors in nuclear engineering from the University of Florida in 2010. Alicia is highly involved with the American Nuclear Society, currently serving as Treasurer of the Nuclear Nonproliferation Policy Division and as an appointee to the Public Policy Committee.